Imperial College London

Doctoral Thesis

Imperial College London, Department of Aeronautics

Reduced-order particle-in-cell scheme for computationally efficient kinetic plasma modelling

Candidate:
Maryam Reza

Supervisor:
Dr. Aaron Knoll

Submitted in partial fulfilment of the requirements for Doctor of Philosophy (PhD) degree in Aeronautics at Imperial College London

September 2024

Statement of Originality

I, Maryam Reza, hereby declare that all the written materials and the illustrations presented in this doctoral thesis are my own work and have been derived from my research towards the PhD degree at Imperial College London.

Any materials, ideas or statements that is not my original work and/or not originated from my own PhD research is appropriately referenced.

I have already published the majority of the work reported in this thesis within Chapters 1 to 7 in different journal/conference articles. Any written and illustrated material adopted from these publications have been my original contributions to the papers.

The List of Publications (LoP) of this thesis reports all the articles and conference papers originated from this PhD research. The reused and/or adopted materials in Chapters 1 to 7 are from these publications.

The correspondence between the prior publications and the Chapters of this thesis are provided in the following. The hyperlink numbering used refers to that in the List of Publications.

Chapter 1: LoP journal articles no. 6, 7, and 12.

Chapter 2: LoP journal articles no. 2 and 11.

Chapter 3: LoP journal articles no. 1, 2, 10, and conference papers no. 1, 3, 4.

Chapter 4: LoP journal articles no. 3, 5, 6, 7, and conference papers no. 2 and 4.

Chapter 5: LoP journal articles no. 8 and 9.

Chapter 6: LoP journal article no. 4, and conference papers no. 4, 6, 7, and 8.

Chapter 7: LoP conference papers no. 4 and 5.

Copyright Declaration

The copyright of this thesis rests with the author. Unless otherwise indicated, its contents are licensed under a Creative Commons Attribution-Non Commercial 4.0 International Licence (CC BY-NC).

Under this licence, you may copy and redistribute the material in any medium or format. You may also create and distribute modified versions of the work. This is on the condition that: you credit the author and do not use it, or any derivative works, for a commercial purpose.

When reusing or sharing this work, ensure you make the licence terms clear to others by naming the licence and linking to the licence text. Where a work has been adapted, you should indicate that the work has been changed and describe those changes.

Please seek permission from the copyright holder for uses of this work that are not included in this licence or permitted under UK Copyright Law.

Abstract

Existing high-fidelity kinetic plasma simulations, such as particle-in-cell (PIC) method, can provide valuable insights into the physics of the $\mathrm{E} \times \mathrm{B}$ discharges unachievable with other numerical methods. However, their enormous computational cost does not allow for extensive parametric investigations and prohibits fully kinetic 3-dimensional simulations needed to properly study the multi-dimensional, multi-scale physics in real-size devices over real-world timescales.

The reduced-order PIC (RO-PIC) scheme, developed in this work and extensively verified in various $\mathrm{E} \times \mathrm{B}$ plasma configurations, serves as a promising computational tool, realizing self-consistent multi-dimensional kinetic modeling of plasma at a drastically reduced computational cost (up to several orders of magnitude) compared to the conventional PIC simulations.

The verified RO-PIC is used for extensive parametric investigations in 2D radial-azimuthal and axial-azimuthal Hall-thrusters-representative discharge settings. These studies demonstrated the RO-PIC's utility for investigating plasma phenomena across a broad parameter space of both fundamental and applied significance. Also, they have provided unique aggregated insights into the variations in the plasma instabilities, the electrons' cross-field transport, and the macroscopic plasma behavior with the changes in the system's operational and physical parameters.

In radial-azimuthal geometry, the studies reveal the dominance of various instabilities including Electron Cyclotron Instability (ECDI) and Modified Two Stream Instability (MTSI) with distinct consequences on plasma, under different electromagnetic field intensities and magnetic field curvatures. Along axial-azimuthal coordinates, the variation trends in plasma behavior and instabilities including Ion Acoustic Instability (IAI) and Transit Time Instability (ITTI) across diverse operating conditions are observed.

The application of RO-PIC as a predictive engineering tool is demonstrated through a first-of-its-kind attempt to self-consistently simulate an industrial 20-kW-class Hall thruster kinetically within practical timeframes, obtaining predictions of the experimental performance parameters with accuracies of $70 - 80\%$ across three simulated operating conditions.

Finally, future directions for further advancing the RO-PIC, including its extension to 3D, are outlined.

Acknowledgements

And here I am…writing these final words of my PhD thesis, concluding a fantastic and transformative educational and professional experience. I feel humbled and truly glad to be arriving at this point, content with all I have achieved through my research, and full of excitement and motivation for the future.

I would like to express my deepest gratitude to my PhD supervisor, Dr. Aaron Knoll. Your guidance has been invaluable as we navigated thrilling research frontiers. Your insightful perspectives and encouragement to think creatively have been truly inspiring. I am especially grateful for the trust you placed in me, allowing me the freedom to explore my own ideas, and for helping me realize my ambitions. Your genuine encouragement during challenging moments and your dedication to fostering an environment of growth and discovery have made the past three and a half years an amazing and unforgettable journey. Thank you, Professor, for being such an exceptional mentor.

I am profoundly thankful to my family for their unwavering support throughout this journey. Your love, patience, and understanding have been the foundation upon which I've built my achievements throughout my years of education. The countless sacrifices you made and the constant encouragement you provided have been a source of strength for me. I could not have reached this milestone without your belief in my abilities and your constant reassurance. Thank you for always being there for me and for giving me the confidence and inspiration to pursue my dreams.

To my husband, Farbod, who has been my rock, my partner, and my colleague for so many years now, words cannot fully express my gratitude. Your unending support, both personally and professionally, has been indispensable. Together, we have shared every high and low, celebrated every success, and faced every challenge with resilience and a strength that stems from our love. Our journey through this PhD has not only been a testament to our dedication to our professional dreams but also to our deep mutual respect, passion, and understanding. I am excited about the future we will build together, both in our personal lives and as collaborators in our professional endeavours. Farbod, thank you for being by my side every step of the way; I couldn't have done it without you.

And, just one last thing… who is to say that academic theses cannot have poems in them, at least "scientific" poems!? Let's set a precedent, shall we?

Chronicles of Reduced-order PIC

(A rhyming abstract, in collaboration with ChatGPT)

Plasmas pervade the cosmic stage,
In stars they burn, in space engage.
On Earth, in labs, its wonders we find,
Applications are diverse, for humankind.
In labs of science, minds aspire,
To tame this force, to reach higher.
Plasma's power, a cosmic art,
Propels us forward to above and beyond.
Plasma, a force that powers our quest,
Igniting the engines, we give it our best.
In labs, scientists work day and night,
To harness its power, to make things right.
Despite their presence vast and wide,
Their secrets still within them hide.
From space's thrust to fusion's dream,
A world of dynamics, complex, supreme.
Comprehensive insight, the keys we seek,
To predict and control, solutions unique.
Innovative pathways, technology's peak,
Fusion's promise, sustainable and sleek.
Fundamental questions yet to clear,
In plasma's dance, our grasp not near.
From stars to labs, a quest we face,
To predict and harness their fiery grace.
Prediction, control, the holy grail,
Technological leaps, we set to trail.
Yet hindered by models, fidelity high,
Computational bounds, stretch to the sky.

In plasma's realm, dimensions three,
A dance of scales, both vast and free.
Understanding sought, complex and steep,
In models' absence, our progress may sleep.
In pursuit of knowledge, we tirelessly strive,
To unlock the secrets, and keep innovation alive.
In plasma's realm, enigmatic and deep,
Kinetic simulations, their secrets to keep.
E×B discharges, mysteries unfold,
But computational costs, a barrier so bold.
In three dimensions, a vast expanse,
Yet limitations hinder our eager advance.
RO-PIC emerges, a beacon bright,
Efficient and agile, reducing the plight.
Parametric studies, once out of reach,
Now RO-PIC reigns, with lessons to teach.
RO-PIC, with efficiency's might,
Unlocks simulations, once out of sight
With unprecedented insights, it leads the way,
Predicting behaviors, in the plasma's sway.
So here we stand, on the brink of space,
With plasma's grace, we claim our place.
Plasma, the key, to our cosmic quest,
Guiding us onward, to places yet blessed.
Plasma thrusters whisper, gentle yet strong,
Pushing spacecraft where they belong.
With plasma thrusters, we reach afar,
To distant skies, past the nearest star.

In loving memory of my dear and greatly missed uncle, Navid, a kind, loving and curious soul whose passion for science and innovation always inspired me…

Contents

STATEMENT OF ORIGINALITY **2**

COPYRIGHT DECLARATION **3**

ABSTRACT **4**

ACKNOWLEDGEMENTS **5**

CONTENTS **8**

LIST OF FIGURES **10**

LIST OF TABLES **21**

LIST OF ACRONYMS **22**

LIST OF PUBLICATIONS **23**

CHAPTER 1 BACKGROUND AND PROBLEM STATEMENT **25**

1.1. OVERVIEW OF THE PHYSICS OF CROSS-FIELD PLASMA DISCHARGES 25

1.2. HALL THRUSTERS: PROVING GROUND FOR PLASMA PHYSICS STUDIES AND IMPORTANT TECHNOLOGY FOR SPACECRAFT PROPULSION 36

1.3. REVIEW OF THE AVAILABLE NUMERICAL APPROACHES TO STUDY PLASMAS 40

1.4. PARTICLE-IN-CELL SCHEME FOR KINETIC PLASMA MODELLING 41

1.5. PROBLEM STATEMENT: RESEARCH MOTIVATIONS AND OBJECTIVES 60

CHAPTER 2 REDUCED-ORDER PIC SCHEME: CONCEPT AND FORMULATION **62**

2.1. ORDER-REDUCTION IN THE CONTEXT OF PIC SIMULATIONS: RO-PIC CONCEPT 62

2.2. QUASI-MULTI-DIMENSIONAL PIC: THE DIMENSIONALITY-REDUCTION FORMULATION UNDERLYING RO-PIC ... 64

2.3. COMPUTATIONAL ADVANTAGE OF RO-PIC 77

2.4. STANDALONE VERIFICATIONS OF REDUCED-DIMENSION POISSON SOLVER (RDPS) 79

2.5. CONCLUSION 87

CHAPTER 3 VERIFICATIONS OF THE RO-PIC SCHEME AGAINST BENCHMARK PLASMA PROBLEMS **89**

3.1. AXIAL-AZIMUTHAL HALL-THRUSTER-REPRESENTATIVE BENCHMARK PROBLEM 90

3.2. RADIAL-AZIMUTHAL E×B DISCHARGE BENCHMARK PROBLEM 103

3.3. PENNING DISCHARGE BENCHMARK PROBLEM 110
3.4. NEUTRALS' PLUME EXPANSION (DSMC) TEST CASE 116
3.5. CONCLUSION 121
CHAPTER 4 INVESTIGATION OF THE PARAMETRIC VARIABILITY OF PLASMA INSTABILITIES AND TURBULENCE USING RO-PIC IN A RADIAL-AZIMUTHAL PLASMA CONFIGURATION 124
4.1. DESCRIPTION OF SETUP AND CONDITIONS 125
4.2. VARIATIONS WITH THE INTENSITY OF THE APPLIED FIELDS 127
4.3. INFLUENCE OF THE CURVATURE OF THE MAGNETIC FIELD 147
4.4. EFFECTS OF THE PRESENCE OF SECONDARY ELECTRON EMISSION 168
4.5. EFFECTS OF PLASMA NUMBER DENSITY 172
4.6. CONCLUSION 177
CHAPTER 5 INVESTIGATION OF THE PARAMETRIC VARIABILITY OF PLASMA INSTABILITIES AND TURBULENCE USING RO-PIC IN AN AXIAL-AZIMUTHAL PLASMA CONFIGURATION 181
5.1. DESCRIPTION OF SETUP AND CONDITIONS 181
5.2. VARIATIONS WITH OPERATING CONDITIONS: DISCHARGE VOLTAGE, ION CURRENT DENSITY AND MAGNETIC FIELD INTENSITY 184
5.3. INFLUENCE OF THE AXIAL PROFILE OF THE APPLIED MAGNETIC FIELD 208
5.4. CONCLUSION 212
CHAPTER 6 RO-PIC MODELLING OF A HIGH-POWER 20 KW-CLASS INDUSTRIAL HALL THRUSTER 216
6.1. RO-PIC AS A TOOL TO AID INDUSTRIAL DEVELOPMENT OF PLASMA TECHNOLOGIES 217
6.2. SIMULATIONS' SETUP AND CONDITIONS 218
6.3. RESULTS AND DISCUSSIONS 220
6.4. EFFECTS OF RADIAL DIMENSION 232
6.5. CONCLUSION 234
CHAPTER 7 CONCLUSIONS AND FUTURE WORK 235
7.1. SUMMARY AND CONCLUSIONS 235
7.2. FUTURE WORKS AND RESEARCH DIRECTIONS 236
BIBLIOGRAPHY 245
APPENDIX 255

List of Figures

FIG. 1.1: VARIOUS APPLICATIONS OF $\mathrm{E} \times \mathrm{B}$ PLASMAS: (A) A MAGNETRON [SOURCE], (B) A HALL THRUSTER [3], (C) A PENNING DISCHARGE [SOURCE] 26

FIG. 1.2: (A) STABLE (MAXWELLIAN) AND (B) UNSTABLE (NON-MAXWELLIAN) DISTRIBUTION FUNCTION 28

FIG. 1.3: SOLUTION OF THE ECDI'S 3D DISPERSION RELATION GIVEN BY EQ. 1.2; (A) FREQUENCY AND (B) GROWTH RATE VERSUS AZIMUTHAL WAVENUMBER (kz) FOR VARIOUS RADIAL WAVENUMBERS (ky). REPRODUCED FROM REF. [16] 30

FIG. 1.4: VARIATION OF IAI DISPERSION RELATION (EQ. 1.4) WITH (A) ELECTRON TEMPERATURE (Te) AT CONSTANT $ni = 1018\, m - 3$ AND (B) WITH ION NUMBER DENSITY (ni) AT CONSTANT $Te = 10\, eV$. 31

FIG. 1.5: NUMERICAL SOLUTION OF THE MTSI'S DISPERSION RELATION GIVEN BY EQ. 1.9 WITH THE PLASMA AND THE APPLIED FIELDS CONDITIONS CORRESPONDING TO A RADIAL-AZIMUTHAL BENCHMARK PROBLEM (SEE SECTION 3.2) 33

FIG. 1.6: SCHEMATIC OF HALL THRUSTER. ADAPTED VERSION OF THE ORIGINAL ARTWORK FROM REF. [51] 38

FIG. 1.7: SCHEMATIC OF THE MAGNETIC FIELD TOPOLOGY IN (A) MAGNETICALLY SHIELDED AND (B) CONVENTIONAL HALL THRUSTERS. 39

FIG. 1.8: ELECTROSTATIC PIC LOOP DIAGRAM INCLUDING THE MCC COLLISIONS AND THE NEUTRAL DYNAMICS MODULE. 48

FIG. 1.9: ILLUSTRATION OF INTERPOLATION COEFFICIENTS A IN 2D CELL. THE BLUE DOT REPRESENTS THE PARTICLE LOCATION, AND THE RED DOTS ARE THE PARTICLE'S SURROUNDING GRID NODES. 49

FIG. 1.10: ILLUSTRATION OF DIFFERENT CHARGED PARTICLES CURRENT CONTRIBUTIONS; (A) CATHODE PLANE BEING ON THE RIGHT BOUNDARY, (B) CATHODE PLANE BEING INSIDE THE DOMAIN IN THE CURRENT CONTINUITY SCHEME 51

FIG. 1.11: (A) SEE YIELD COEFFICIENT VERSUS INCIDENT ELECTRON ENERGY ACCORDING TO THE LINEAR MODEL. VAUGHAN MODEL ESTIMATION OF (B) TOTAL EMISSION COEFFICIENT (γV) FOR VARIOUS INCIDENT ANGLES AND (B) PARTIAL EMISSION COEFFICIENTS FOR NORMAL INCIDENT ANGLE VERSUS ELECTRON INCIDENT ENERGY. THE PLOTS ARE FOR BORON NITRIDE. 53

FIG. 1.12: INTERPOLATED FUNCTIONS OF (A) BIAGI 7.1 ELECTRON-NEUTRAL AND (B) PHELPS ION-NEUTRAL COLLISION CROSS SECTIONS FOR XENON TAKEN FROM LXCAT DATABASE [102]. 55

FIG. 1.13: FLOWCHART OF THE DSMC COLLISIONS ALGORITHM 60

FIG. 2.1: SCHEMATIC OF THE DOMAIN DECOMPOSITION CORRESPONDING TO THE REDUCED-ORDER GRID SYSTEM FOR RO-PIC SCHEME; (LEFT) DECOMPOSITION INTO MULTIPLE "REGIONS" USING A COARSE GRID, (RIGHT) THE 1D COMPUTATIONAL CELLS (FINE GRIDS) FOR DISCRETIZATION OF EACH REGION ALONG THE x AND y DIRECTIONS. 63

FIG. 2.2: SCHEMATIC ILLUSTRATING EXCHANGE OF DATA BETWEEN THE PARTICLES AND REDUCED-DIMENSION GRID IN RO-PIC. 65

FIG. 2.3: VISUALIZATION OF SAMPLING OF 2D PROFILES (RIGHTMOST COLUMN) ON THE REDUCED-DIMENSION x-GRID (TOP ROW) AND y-GRID (MIDDLE ROW) WITH VARIOUS NUMBERS OF REGIONS AS WELL AS THE RECONSTRUCTED PROFILES ON THE FULL-2D GRID (BOTTOM ROW) USING x- AND y-GRID VALUES PER EQ. 2.4.. 66

FIG. 2.4: SCHEMATIC OF THE COMPUTATIONAL GRID IN SINGLE-REGION DOMAIN DECOMPOSITION FOR REDUCED-DIMENSION POISSON'S EQUATION. 68

FIG. 2.5: SCHEMATIC OF THE MULTI-REGION DOMAIN DECOMPOSITION FOR THE REDUCED-DIMENSION POISSON'S EQUATION; (A) DEFINITION OF THE REGIONS, (B) COMPUTATION GRID ALONG x FOR SOLUTION OF ϕx, AND (C) COMPUTATION GRID ALONG y FOR SOLUTION OF ϕy..... 70

FIG. 2.6: SCHEMATIC OF (A) THE HORIZONTAL AND THE VERTICAL COMPUTATIONAL ELEMENTS ASSOCIATED WITH THE DIMENSIONALITY-REDUCTION APPROACH IN REGION $\Omega m, n$, (B) THE ELECTRIC FIELD COMPONENTS ACROSS THE SIDES OF THE VERTICAL ELEMENT FOR SOLVING POTENTIAL FUNCTION ALONG THE x-DIRECTION, (C) THE ELECTRIC FIELD COMPONENTS ACROSS THE SIDES OF THE HORIZONTAL ELEMENT FOR SOLVING POTENTIAL FUNCTION ALONG THE y-DIRECTION. 72

FIG. 2.7: SCHEMATIC ILLUSTRATING THAT AT THE LIMIT WHERE THE REGIONS ARE AS SMALL AS THE 2D CELLS, THE COMPUTATIONAL ELEMENTS ALONG x AND Y AXES COINCIDES THE CELLS OF A FULL-2D GRID, MAKING THE REDUCED-DIMENSION COMPUTATIONAL GRID EQUIVALENT TO THE FULL-2D GRID. 73

FIG. 2.8: SCHEMATIC ILLUSTRATING (A) THE REDUCED-DIMENSION COMPUTATIONAL GRID IN REGION $\Omega m, n$, (B) AND (C) STENCILS USED FOR THE DISCRETIZATION OF THE DERIVATIVES IN EQ. 2.28 AND EQ. 2.29, RESPECTIVELY. 75

FIG. 2.9: ILLUSTRATION OF THE STENCIL FOR THE CELLS REACHING THE REGION'S BOUNDARY ALONG THEIR LONG SIDES, USED FOR DISCRETIZATION OF THE LAST TWO TERMS ON THE RIGHT-HAND SIDE OF EQ. 2.28 AND EQ. 2.29. THESE TERMS REPRESENT THE INTEGRALS OF "CROSS-DERIVATIVES" WHICH ARE ONLY NON-ZERO ON THE SIDES OF THE CELLS WHICH ALIGN WITH THE REGION'S BOUNDARY.. 77

FIG. 2.10: VARIATION OF THE COMPUTATIONAL COST RATIO (VERSUS THE NUMBER OF REGIONS) IN QUASI-2D AND QUASI-3D SIMULATIONS COMPARED TO THE CORRESPONDING FULL-2D AND FULL-3D SIMULATIONS. THESE VALUES ARE CALCULATED ASSUMING 500 NUMBER OF CELLS ALONG EACH DIMENSION AND AN EQUAL NUMBER OF REGIONS ALONG ALL DIRECTIONS. NOTE THAT THE PLOT IS IN LOG-LOG SCALE. 79

FIG. 2.11: COMPARISON OF THE APPROXIMATE Q2D SOLUTIONS FROM THE REDUCED-DIMENSION POISSON SOLVER (RDPS) WITH VARIOUS NUMBER OF REGIONS AGAINST THE CORRESPONDING FULL-2D SOLUTION (BOTTOM ROW) FOR CASES 1-4 DEFINED IN **TABLE 2.1**. THE NUMBERS OF REGIONS ARE EQUAL ALONG BOTH DIMENSIONS ($M = N$), WHICH ARE DENOTED BY *NUMR*. .. 81

FIG. 2.12: COMPARISON OF THE APPROXIMATE Q2D SOLUTIONS FROM THE REDUCED-DIMENSION POISSON SOLVER (RDPS) WITH VARIOUS NUMBER OF REGIONS AGAINST THE CORRESPONDING FULL-2D SOLUTION (BOTTOM ROW) FOR CASES 5-8 DEFINED IN **TABLE 2.1**. THE NUMBERS OF REGIONS ARE EQUAL ALONG BOTH DIMENSIONS ($M = N$), WHICH ARE DENOTED BY *NUMR*. .. 82

FIG. 2.13: CONTOUR MAP REPRESENTATION OF PLOTS IN **FIG. 2.11**; COMPARISON OF THE RDPS' SOLUTIONS WITH VARIOUS NUMBER OF REGIONS AGAINST THE CORRESPONDING FULL-2D SOLUTION (BOTTOM ROW) FOR CASES 1-4 DEFINED IN **TABLE 2.1**. THE NUMBERS OF REGIONS ARE EQUAL ALONG BOTH DIMENSIONS ($M = N$), WHICH ARE DENOTED BY *NUMR*..... 83

FIG. 2.14: CONTOUR MAP REPRESENTATION OF PLOTS IN **FIG. 2.12**; COMPARISON OF THE RDPS' SOLUTIONS WITH VARIOUS NUMBER OF REGIONS AGAINST THE CORRESPONDING FULL-2D SOLUTION (BOTTOM ROW) FOR CASES 5-8 DEFINED IN **TABLE 2.1**. THE NUMBERS OF REGIONS ARE EQUAL ALONG BOTH DIMENSIONS ($M = N$), WHICH ARE DENOTED BY *NUMR*..... 84

FIG. 2.15: ERROR CONVERGENCE OF THE RDPS' SOLUTION; VARIATION OF THE NORMALIZED L2 ERROR (EQ. 2.40) BETWEEN THE FULL-2D SOLUTION AND THE APPROXIMATE Q2D SOLUTION FROM THE RDPS WHEN INCREASING NUMBER OF REGIONS FOR CASES 1-4 (LEFT), AND CASES 5-8 (RIGHT). THE y-AXIS IN BOTH PLOTS IS IN LOGARITHMIC SCALE..... 85

FIG. 2.16: COMPARISON OF THE RDPS' SOLUTION WITH VARIOUS NUMBER OF REGIONS AGAINST THE CORRESPONDING FULL-2D SOLUTION FOR CASE 9 (WITH PERIODIC BOUNDARY CONDITION ALONG THE y-AXIS) DEFINED IN **TABLE 2.1**. THE NUMBERS OF REGIONS ARE EQUAL ALONG BOTH DIMENSIONS ($M = N$), WHICH ARE DENOTED BY *NUMR*. 86

FIG. 2.17: CONTOUR MAP REPRESENTATION OF PLOTS IN **FIG. 2.16**; COMPARISON OF THE RDPS'S SOLUTIONS WITH VARIOUS NUMBER OF REGIONS AGAINST THE CORRESPONDING FULL-2D SOLUTION (RIGHTMOST COLUMN) FOR CASE 9 DEFINED IN **TABLE 2.1**. THE NUMBERS OF REGIONS ARE EQUAL ALONG BOTH DIMENSIONS ($M = N$) WHICH ARE DENOTED BY *NUMR*..... 87

FIG. 2.18: ERROR CONVERGENCE OF THE RDPS' SOLUTION FOR CASE 9; VARIATION OF THE NORMALIZED L2 ERROR (EQ. 2.40) BETWEEN THE FULL-2D SOLUTION AND THE APPROXIMATE SOLUTION FROM THE RDPS WHEN INCREASING NUMBER OF REGIONS. 87

FIG. 3.1: (A) SCHEMATIC OF THE COMPUTATIONAL DOMAIN AND SETUP, (B) AXIAL PROFILES OF THE IMPOSED MAGNETIC FIELD AND THE IONIZATION SOURCE IN THE AXIAL-AZIMUTHAL SIMULATIONS. 90

FIG. 3.2: TIME-AVERAGED (OVER $16 - 20\ \mu s$) AXIAL PROFILES OF PLASMA PROPERTIES FROM LOW-NUMBER-OF-REGION Q2D SIMULATIONS; (A) ION NUMBER DENSITY (ni), (B) AXIAL ELECTRIC FIELD (Ex), (C) ELECTRON TEMPERATURE (Te) AND (D) ELECTRIC POTENTIAL (ϕ). IN PLOT (D), THE DASHED CYAN CURVE REPRESENTS THE PLASMA POTENTIAL PROFILE FROM THE 1D AXIAL SIMULATION WITHOUT ANY AD-HOC ELECTRON TRANSPORT. 93

FIG. 3.3: NUMERICAL DISPERSION PLOTS OF AZIMUTHAL INSTABILITIES OBTAINED FROM 2D FFT OF THE SPATIOTEMPORAL SIGNAL OF THE AZIMUTHAL ELECTRIC FIELD FLUCTUATIONS (IN DIFFERENT REGIONS) FROM THE LOW-NUMBER-OF-REGION Q2D SIMULATIONS. 94

FIG. 3.4: AXIAL PROFILES OF THE TRANSPORT TERMS IN EQ. 1.20 FROM LOW-NUMBER-OF-REGION Q2D SIMULATIONS. THE FORCE TERMS ARE AVERAGED OVER $16 - 20\ \mu s$. 95

FIG. 3.5: COMPARISON BETWEEN THE AXIAL PROFILES OF THE TIME-AVERAGED (OVER $16 - 20\ \mu s$) PLASMA PROPERTIES FROM THE SINGLE-REGION Q2D SIMULATIONS WITH VARIOUS INITIAL NUMBER OF PARTICLES PER CELL ($Nppc$); (A) ION NUMBER DENSITY, (B) AXIAL ELECTRIC FIELD, AND (C) ELECTRON TEMPERATURE. 96

FIG. 3.6: TIME-AVERAGED (OVER $20 - 30\ \mu s$) AXIAL PROFILES OF PLASMA PROPERTIES FROM HIGH-NUMBER-OF-REGION Q2D SIMULATIONS; (A) ION NUMBER DENSITY, (B) AXIAL ELECTRIC FIELD, (C) & (D) AXIAL AND AZIMUTHAL ELECTRON TEMPERATURE, AND (E) & (F) AXIAL AND AZIMUTHAL ION TEMPERATURE..... 97

FIG. 3.7: VARIATION OF L2 ERROR IN THE PREDICTION OF PLASMA PROPERTIES FROM THE AXIAL-AZIMUTHAL Q2D SIMULATIONS COMPARED TO THE FULL-2D RESULTS IN REF. [69], ALONGSIDE THE COMPUTATIONAL TIME RATIO BETWEEN THE Q2D AND FULL-2D PIC SIMULATIONS PLOTTED AGAINST THE NUMBER OF REGIONS IN THE Q2D SIMULATIONS (M).. 98

FIG. 3.8: 2D MAPS OF THE ION NUMBER DENSITY (LEFT COLUMN), THE AZIMUTHAL ELECTRIC FIELD (MIDDLE COLUMN), AND THE ELECTRIC POTENTIAL (RIGHT COLUMN) FROM HIGH-NUMBER-OF-REGION Q2D SIMULATIONS AT THE TIME $t = 30\ \mu s$. THE DASHED LINES AND GREY PLANES SHOW THE LOCATION OF THE PEAK MAGNETIC FIELD INTENSITY. 99

FIG. 3.9: NUMERICAL DISPERSION PLOTS OF AZIMUTHAL INSTABILITIES OBTAINED FROM 2D FFT OF THE SPATIOTEMPORAL SIGNAL OF AZIMUTHAL ELECTRIC FIELD FLUCTUATIONS IN THREE AXIAL LOCATIONS FROM HIGH-NUMBER-OF-REGION Q2D SIMULATIONS. YELLOW CURVES ARE THE LOCAL DISPERSION RELATIONS (IN THE CORRESPONDING REGION), AND THE GREEN CURVES ARE THE UPSTREAM DISPERSION RELATION OF THE ION ACOUSTIC WAVES (AT $x = 0.4\ cm$) OBTAINED FROM EQ. 1.4. 100

FIG. 3.10: AXIAL PROFILES OF THE TRANSPORT TERMS IN EQ. 1.20 FROM HIGH-NUMBER-OF-REGION Q2D SIMULATIONS. THE FORCE TERMS ARE AVERAGED OVER $16 - 20\ \mu s$. 101

FIG. 3.11: COMPARISON BETWEEN THE TIME-AVERAGED AXIAL PROFILES OF PLASMA PROPERTIES FROM THE HIGH-NUMBER-OF-REGION Q2D SIMULATIONS WITH SINGLE ($N = 1$) AND MULTIPLE ($N = 10, 20$) HORIZONTAL REGIONS ALONG THE AZIMUTHAL COORDINATE..... 101

FIG. 3.12: COMPARISON OF THE 2D MAPS OF THE ION NUMBER DENSITY (LEFT COLUMN), THE AZIMUTHAL ELECTRIC FIELD (MIDDLE COLUMN), AND THE ELECTRIC POTENTIAL (RIGHT COLUMN) FROM THE HIGH-NUMBER-OF-REGION Q2D SIMULATIONS WITH SINGLE ($N = 1$) AND MULTIPLE ($N = 10, 20$) HORIZONTAL REGIONS ALONG THE AZIMUTHAL COORDINATE AT $t = 30\ \mu s$. THE DASHED LINES AND GREY PLANES SHOW THE LOCATION OF THE PEAK MAGNETIC FIELD INTENSITY. 102

FIG. 3.13: COMPARISON OF THE AXIAL PROFILES OF THE TIME-AVERAGED (OVER $20 - 30\ \mu s$) PLASMA PROPERTIES FROM THE Q2D SIMULATIONS (WITH $N = 20, M = 40$) WITH VARIOUS INITIAL NUMBER OF PARTICLES PER CELL ($Nppc$); (A) ION NUMBER DENSITY, (B) AXIAL ELECTRIC FIELD, AND (C) ELECTRON TEMPERATURE. 102

FIG. 3.14: SCHEMATIC OF THE COMPUTATIONAL DOMAIN AND SETUP OF THE RADIAL-AZIMUTHAL SIMULATIONS. 103

FIG. 3.15: TIME-AVERAGED (OVER $25 - 30\ \mu s$) RADIAL PROFILES OF THE ION NUMBER DENSITY (FIRST ROW) AND THE ELECTRON TEMPERATURE (SECOND ROW). PLOTS (A) AND (D) ARE FROM THE 1D RADIAL SIMULATION, (B) AND (E) FROM "LOW-ORDER" Q2D SIMULATIONS, AND (C) AND (F) FROM "HIGH-ORDER" Q2D SIMULATIONS.. 105

FIG. 3.16: VARIATION OF THE L2 ERROR IN THE PREDICTION OF ION NUMBER DENSITY AND ELECTRON TEMPERATURE FROM THE RADIAL-AZIMUTHAL Q2D SIMULATIONS COMPARED TO FULL-2D RESULTS FROM IPPL-2D CODE, ALONGSIDE THE COMPUTATIONAL TIME RATIO BETWEEN THE Q2D AND FULL-2D IPPL CODES PLOTTED AGAINST THE NUMBER OF REGIONS IN THE Q2D SIMULATIONS. 106

FIG. 3.17: AZIMUTHAL WAVENUMBER SPECTRUM OF INSTABILITIES OBTAINED FROM SPATIAL FFT OF THE AZIMUTHAL ELECTRIC FIELD SIGNAL AVERAGED OVER ALL RADIAL POSITIONS AND OVER THREE TIME INTERVALS; (A) & (D) $5 - 10\ \mu s$, (B) & (E) $15 - 20\ \mu s$, AND (C) & (F) $25 - 30\ \mu s$. 107

FIG. 3.18: FREQUENCY SPECTRUM OF INSTABILITIES OBTAINED FROM TEMPORAL FFT OF THE AZIMUTHAL ELECTRIC FIELD SIGNAL FROM "HIGH-ORDER" Q2D SIMULATIONS IN COMPARISON WITH THOSE FROM FULL-2D SIMULATION. THE FFTS ARE AVERAGED OVER ALL RADIAL AND AZIMUTHAL POSITIONS. 108

FIG. 3.19: 2D SNAPSHOTS OF THE PLASMA PROPERTIES FROM "HIGH-ORDER" Q2D SIMULATIONS AND THE 2D SIMULATION AT THE TIME OF LOCAL MAXIMUM (TOP PANEL) AND LOCAL MINIMUM (BOTTOM PANEL) OF THE SPATIALLY AVERAGED RADIAL ELECTRON TEMPERATURE 109

FIG. 3.20: COMPARISON OF TIME-AVERAGED RADIAL PROFILES OF (A) NORMALIZED ION NUMBER DENSITY, AND (B) NORMALIZED ELECTRON TEMPERATURE OBTAINED FROM THE 50-REGION Q2D SIMULATION WITH VARIOUS INITIAL NUMBER OF MACROPARTICLES PER CELL.. 110

FIG. 3.21: SCHEMATIC OF THE COMPUTATIONAL DOMAIN AND SETUP OF THE PENNING DISCHARGE SIMULATIONS. 111

FIG. 3.22: TIME-AVERAGED (OVER $200 - 500\ \mu s$) PROFILES OF PLASMA PROPERTIES AT THE MID-PLANE ($y = 0$) OF THE DOMAIN ALONG THE x-DIRECTION, FROM THE Q2D SIMULATIONS WITH VARIOUS NUMBER OF REGIONS, AND FROM THE FULL-2D IPPL PIC SIMULATION; (A) ION NUMBER DENSITY, (B) ELECTRON TEMPERATURE, AND (C) PLASMA POTENTIAL. 112

FIG. 3.23: TIME EVOLUTIONS OF THE LOCAL ION NUMBER DENSITY AT THE LOCATION OF THE VIRTUAL DENSITY PROBE (LEFT COLUMN) AND TEMPORAL FFT SPECTRA OF THE PROBE'S SIGNAL (COMPUTED OVER $50 - 500\ \mu s$ DURATION) FROM THE Q2D AND THE FULL-2D SIMULATIONS. THE HIGHEST PEAK IN THE FFTS CORRESPONDS TO THE SPOKE FREQUENCY. 113

FIG. 3.24: 2D SNAPSHOTS OF THE ION NUMBER DENSITY (TOP PANEL) AND x-COMPONENT OF THE ELECTRIC FIELD (BOTTOM PANEL) AT 5 DIFFERENT INSTANCES OVER ONE EVOLUTION CYCLE (WITH PERIOD T) OF THE SPOKE MODE FROM THE Q2D AND THE FULL-2D SIMULATIONS. 114

FIG. 3.25: VARIATION OF THE L2 ERROR IN PREDICTION OF PLASMA PROPERTIES FROM THE Q2D SIMULATIONS COMPARED TO FULL-2D RESULTS FROM IPPL-2D CODE IN THE PENNING DISCHARGE CASE, ALONGSIDE THE COMPUTATIONAL TIME RATIO BETWEEN THE Q2D AND FULL-2D IPPL CODES PLOTTED AGAINST THE NUMBER OF REGIONS IN THE Q2D SIMULATIONS.. 115

FIG. 3.26: FLOWCHART OF THE Q2D DSMC ALGORITHM. THE FINE GRIDS ALONG THE x AND y DIRECTIONS REFER TO THE Q2D GRIDS ILLUSTRATED IN **FIG. 2.1**.. 117

FIG. 3.27: SCHEMATIC OF THE COMPUTATIONAL DOMAIN AND SETUP OF THE NEUTRALS' PLUME EXPANSION TEST CASE. 118

FIG. 3.28: STEADY-STATE 2D DISTRIBUTION OF THE NEUTRALS' PROPERTIES FROM THE FULL-2D DSMC SIMULATION WITH COLLISIONLESS (TOP ROW), AND COLLISIONAL (BOTTOM ROW) NEUTRAL'S EXPANSION; THE PANELS FROM LEFT TO RIGHT REPRESENT THE NUMBER DENSITY, AXIAL DRIFT VELOCITY, RADIAL DRIFT VELOCITY, AND TEMPERATURE OF THE NEUTRALS. ... 118

FIG. 3.29: STEADY-STATE 2D DISTRIBUTION OF THE NEUTRALS' PROPERTIES FROM THE Q2D AND FULL-2D DSMC SIMULATIONS OF THE COLLISIONAL NEUTRALS PLUME EXPANSION TEST CASE; THE PANELS FROM LEFT TO RIGHT REPRESENT THE NUMBER DENSITY, AXIAL DRIFT VELOCITY, RADIAL DRIFT VELOCITY, AND TEMPERATURE OF THE NEUTRALS. 119

FIG. 3.30: STEADY-STATE AXIAL PROFILES OF THE NEUTRALS' PROPERTIES FROM THE Q2D DSMC SIMULATIONS WITH VARIOUS NUMBER OF REGIONS AND FROM THE FULL-2D DSMC SIMULATION OF THE COLLISIONAL NEUTRALS PLUME EXPANSION TEST CASE; (A) NEUTRAL NUMBER DENSITY, (B) NEUTRAL TEMPERATURE, (C) NEUTRALS' AXIAL DRIFT VELOCITY, AND (D) NEUTRALS' RADIAL DRIFT VELOCITY. 120

FIG. 3.31: VARIATION OF THE L2 ERROR IN THE PREDICTION OF NEUTRALS' PROPERTIES FROM THE AXIAL-RADIAL Q2D DSMC SIMULATIONS COMPARED TO FULL-2D DSMC RESULTS IN COLLISIONAL NEUTRALS' EXPANSION CASE, ALONGSIDE THE COMPUTATIONAL TIME RATIO BETWEEN THE Q2D AND FULL-2D DSMC SIMULATIONS PLOTTED AGAINST THE NUMBER OF REGIONS IN THE Q2D SIMULATIONS (M)..... 121

FIG. 4.1: VARIATION OF SPATIOTEMPORALLY AVERAGED (ACROSS ENTIRE DOMAIN AND OVER $20 - 30\ \mu s$) PLASMA PROPERTIES VS Ey (TOP ROW) AND VS Bx (BOTTOM ROW) FOR THE THREE PROPELLANTS; (A) ION NUMBER DENSITY, (B) & (C) RADIAL AND AZIMUTHAL ELECTRON TEMPERATURE, AND (D) TOTAL ELECTRON TEMPERATURE 129

FIG. 4.2: RADIAL PROFILES OF THE ION NUMBER DENSITY AVERAGED OVER ALL AZIMUTHAL LOCATIONS AND OVER THE TIME INTERVAL OF $20 - 30\ \mu s$ FOR THE THREE PROPELLANTS WITH VARIOUS Ey (TOP ROW) AND VARIOUS Bx (BOTTOM ROW). 129

FIG. 4.3: VARIATION OF SPATIOTEMPORALLY AVERAGED (ACROSS ENTIRE DOMAIN AND OVER $20 - 30\ \mu s$) RADIAL-TO-AZIMUTHAL ELECTRON TEMPERATURE RATIO VS Ey (LEFT) AND VS Bx (RIGHT) FOR THE THREE PROPELLANTS. 130

FIG. 4.4: RADIAL PROFILES OF THE RADIAL-TO-AZIMUTHAL ELECTRON TEMPERATURE RATIO AVERAGED OVER ALL AZIMUTHAL LOCATIONS AND OVER THE TIME INTERVAL OF $20 - 30\ \mu s$ FOR THE THREE PROPELLANTS WITH VARIOUS Ey (TOP ROW) AND VARIOUS Bx (BOTTOM ROW). 131

FIG. 4.5: RADIAL PROFILES OF THE NORMALIZED AXIAL ELECTRON CURRENT DENSITY AVERAGED OVER ALL AZIMUTHAL LOCATIONS AND OVER THE TIME INTERVAL OF $20 - 30\ \mu s$ FOR THE THREE PROPELLANTS WITH VARIOUS Ey (TOP ROW) AND VARIOUS Bx (BOTTOM ROW). 132

FIG. 4.6: 2D SNAPSHOTS OF THE NORMALIZED PLASMA PROPERTIES AT A TIME OF LOCAL MAXIMUM OF THE SPATIALLY AVERAGED Tex FOR XENON PROPELLANT WITH VARIOUS Ey (LEFT) AND VARIOUS Bx (RIGHT). 133

FIG. 4.7: AZIMUTHAL WAVENUMBER SPECTRA OF INSTABILITIES OBTAINED FROM AVERAGE SPATIAL FFTS (OVER ALL RADIAL POSITIONS AND OVER THE TIME INTERVAL OF $20 - 30\ \mu s$) OF THE AZIMUTHAL ELECTRIC FIELD SIGNAL FROM SIMULATIONS WITH VARIOUS Ey (TOP PANEL) AND VARIOUS Bx (BOTTOM PANEL) FOR THE THREE PROPELLANTS. 135

FIG. 4.8: FREQUENCY SPECTRA OF INSTABILITIES OBTAINED FROM AVERAGE TEMPORAL FFTS (OVER ALL RADIAL AND AZIMUTHAL POSITIONS) OF THE AZIMUTHAL ELECTRIC FIELD SIGNAL FROM SIMULATIONS WITH VARIOUS Ey (TOP ROW) AND VARIOUS Bx (BOTTOM ROW) FOR THE THREE PROPELLANTS. 136

FIG. 4.9: VARIATION OF THE NORMALIZED CHARACTERISTICS OF THE DOMINANT ECDI AND THE MTSI MODES VS Ey (TOP PANEL) AND VS Bx (BOTTOM PANEL) FOR THE THREE PROPELLANTS. 138

FIG. 4.10: VARIATION OF THE NORMALIZED MTSI'S GROWTH RATE VS THE NORMALIZED AZIMUTHAL WAVENUMBER AND THE Bx OBTAINED FROM THE SOLUTION OF THE MTSI'S DISPERSION RELATION IN EQ. 1.9 FOR THE XENON PROPELLANT. 140

FIG. 4.11: IONS' AZIMUTHAL PHASE-SPACE ($z - vz$) PLOTS FOR XENON WITH VARIOUS Ey (LEFT COLUMN) AND VARIOUS Bx (RIGHT COLUMN). 141

FIG. 4.12: RADIAL PROFILES OF THE TRANSPORT TERMS IN EQ. 4.1 FOR XENON PROPELLANT WITH VARIOUS Ey (TOP PANEL) AND VARIOUS Bx (BOTTOM PANEL). THE FORCE TERMS ARE AVERAGED OVER $20 - 30\ \mu s$. 143

FIG. 4.13: VARIATION OF SPATIOTEMPORALLY AVERAGED (ACROSS ENTIRE DOMAIN AND OVER $20 - 30\ \mu s$) FORCE TERMS IN THE ELECTRONS' AZIMUTHAL MOMENTUM EQUATION VS Ey (LEFT) AND VARIOUS Bx (RIGHT) FOR XENON PROPELLANT. 143

FIG. 4.14: SPATIALLY AVERAGED (OVER ENTIRE DOMAIN) DIVERGENCE-ANGLE DISTRIBUTION FUNCTIONS DUE TO THE RADIAL VELOCITY COMPONENT (Γx, TOP PANEL) AND DUE TO THE AZIMUTHAL VELOCITY COMPONENT OF THE IONS (Γz, BOTTOM PANEL) FOR THE THREE PROPELLANTS WITH VARIOUS Ey (TOP ROW IN EACH PANEL) AND VARIOUS Bx (BOTTOM ROW IN EACH PANEL). 145

FIG. 4.15: RADIAL DISTRIBUTION OF THE AZIMUTHALLY AVERAGED ION BEAM DIVERGENCE ANGLE DUE TO THE RADIAL AND AZIMUTHAL VELOCITY COMPONENTS OF THE IONS FOR THE THREE PROPELLANTS WITH VARIOUS Ey (TOP ROW IN EACH PANEL) AND VARIOUS Bx (BOTTOM ROW IN EACH PANEL). 146

FIG. 4.16: VARIATION OF SPATIOTEMPORALLY AVERAGED (ACROSS ENTIRE DOMAIN AND OVER $20 - 30\ \mu s$) DIVERGENCE ANGLE VS Ey (TOP ROW) AND Bx (BOTTOM ROW) FOR THE THREE PROPELLANTS. 147

FIG. 4.17: (A) SCHEMATIC OF THE MAGNETIC FIELD LINES, WITH THE LINES' INCIDENCE ANGLE AT THE INNER WALL ($\theta 1$) AND AT THE OUTER WALL ($\theta 2$) AS USED IN EQ. 4.5 ILLUSTRATED, (B) 2D SHAPE OF THE MAGNETIC FIELD LINES IN THE AXIAL-RADIAL ($y - x$) PLANE FOR VARIOUS θ, AND (C) RADIAL PROFILE OF THE AXIAL COMPONENT OF THE MAGNETIC FIELD (By) FOR VARIOUS θ.. 149

FIG. 4.18: VARIATION OF SPATIOTEMPORALLY AVERAGED (ACROSS ENTIRE DOMAIN AND OVER $20 - 30\ \mu s$) PLASMA PROPERTIES VS θ FOR THE THREE PROPELLANTS; (A) ION NUMBER DENSITY, (B) & (C) RADIAL AND AZIMUTHAL ELECTRON TEMPERATURE, AND TOTAL ELECTRON TEMPERATURE. 150

FIG. 4.19: RADIAL PROFILES OF THE ION NUMBER DENSITY AVERAGED OVER ALL AZIMUTHAL LOCATIONS AND OVER THE TIME INTERVAL OF $20 - 30\ \mu s$ FOR THE THREE PROPELLANTS WITH VARIOUS NEGATIVE (TOP ROW) AND POSITIVE (BOTTOM ROW) CURVATURES OF MAGNETIC FIELD. 150

FIG. 4.20: VARIATION OF SPATIOTEMPORALLY AVERAGED (ACROSS ENTIRE DOMAIN AND OVER $20 - 30\ \mu s$) RADIAL-TO-AZIMUTHAL ELECTRON TEMPERATURE RATIO VS θ FOR THE THREE PROPELLANTS. 151

FIG. 4.21: RADIAL PROFILES OF THE OF THE RADIAL-TO-AZIMUTHAL ELECTRON TEMPERATURE RATIO AVERAGED OVER ALL AZIMUTHAL LOCATIONS AND OVER THE TIME INTERVAL OF $20 - 30\ \mu s$ FOR THE THREE PROPELLANTS WITH VARIOUS MAGNETIC FIELD CURVATURES 152

FIG. 4.22: RADIAL PROFILES OF THE OF THE NORMALIZED AXIAL ELECTRON CURRENT DENSITY AVERAGED OVER ALL AZIMUTHAL LOCATIONS AND OVER THE TIME INTERVAL OF $20 - 30\ \mu s$ FOR THE THREE PROPELLANTS WITH VARIOUS NEGATIVE (TOP ROW) AND POSITIVE (BOTTOM ROW) CURVATURES OF MAGNETIC FIELD. 152

FIG. 4.23: 2D SNAPSHOTS OF THE NORMALIZED PLASMA PROPERTIES AT A TIME OF LOCAL MAXIMUM OF THE SPATIALLY AVERAGED Tex FOR XENON PROPELLANT WITH VARIOUS θ 153

FIG. 4.24: AZIMUTHAL WAVENUMBER SPECTRA OF INSTABILITIES OBTAINED FROM AVERAGE SPATIAL FFTS (OVER ALL RADIAL POSITIONS AND OVER THE TIME INTERVAL OF $20 - 30\ \mu s$) OF THE AZIMUTHAL ELECTRIC FIELD SIGNAL FROM SIMULATIONS WITH VARIOUS NEGATIVE (TOP PANEL) AND POSITIVE (BOTTOM PANEL) CURVATURES OF MAGNETIC FIELD FOR THE THREE PROPELLANTS. 155

FIG. 4.25: FREQUENCY SPECTRA OF INSTABILITIES OBTAINED FROM AVERAGE TEMPORAL FFTS (OVER ALL RADIAL AND AZIMUTHAL POSITIONS) OF THE AZIMUTHAL ELECTRIC FIELD SIGNAL WITH VARIOUS NEGATIVE (TOP PANEL) AND POSITIVE (BOTTOM PANEL) CURVATURES OF MAGNETIC FIELD FOR THE THREE PROPELLANTS. 156

FIG. 4.26: VARIATION OF THE NORMALIZED CHARACTERISTICS OF THE DOMINANT ECDI AND THE MTSI MODES VS θ FOR THE THREE PROPELLANTS. 157

FIG. 4.27: RADIAL PROFILES OF THE TRANSPORT TERMS IN EQ. 4.1 FOR XENON PROPELLANT WITH VARIOUS NEGATIVE (TOP ROW) AND POSITIVE (BOTTOM PANEL) CURVATURES OF MAGNETIC FIELD. THE FORCE TERMS ARE AVERAGED OVER $20 - 30\ \mu s$. 158

FIG. 4.28: VARIATION OF SPATIOTEMPORALLY AVERAGED (ACROSS ENTIRE DOMAIN AND OVER $20 - 30\ \mu s$) FORCE TERMS IN THE ELECTRONS' AZIMUTHAL MOMENTUM EQUATION (EQ. 4.1) VS θ FOR XENON PROPELLANT. 159

FIG. 4.29: SPATIALLY AVERAGED (OVER ENTIRE DOMAIN) DIVERGENCE-ANGLE DISTRIBUTION FUNCTIONS DUE TO THE RADIAL VELOCITY COMPONENT (Γx, TOP PANEL) AND DUE TO THE AZIMUTHAL VELOCITY COMPONENT OF THE IONS (Γz, BOTTOM PANEL) FOR THE THREE PROPELLANTS WITH VARIOUS NEGATIVE (TOP ROW IN EACH PANEL) AND POSITIVE (BOTTOM ROW IN EACH PANEL) CURVATURES OF MAGNETIC FIELD. 160

FIG. 4.30: RADIAL DISTRIBUTION OF THE AZIMUTHALLY AVERAGED ION BEAM DIVERGENCE ANGLE DUE TO THE RADIAL AND AZIMUTHAL VELOCITY COMPONENTS OF THE IONS FOR THE THREE PROPELLANTS WITH VARIOUS NEGATIVE (TOP ROW IN EACH PANEL) AND POSITIVE (BOTTOM ROW IN EACH PANEL) CURVATURES OF MAGNETIC FIELD. 161

FIG. 4.31: VARIATION OF SPATIOTEMPORALLY AVERAGED (ACROSS ENTIRE DOMAIN AND OVER $20 - 30\ \mu s$) DIVERGENCE ANGLE VS θ FOR THE THREE PROPELLANTS; (LEFT COLUMN) DIVERGENCE ANGLE DUE TO THE IONS' RADIAL VELOCITY COMPONENT, (RIGHT COLUMN) DIVERGENCE ANGLE DUE TO THE IONS' AZIMUTHAL VELOCITY COMPONENT. 162

FIG. 4.32: (A) A SCHEMATIC OF THE ADOPTED FIELD TOPOLOGY AND THE CROSS-SECTIONS CORRESPONDING TO CONFIGS. 1 & 2. (B) TO (E) RADIAL PROFILES OF THE STUDIED MAGNETIC FIELD CONFIGURATIONS. 163

FIG. 4.33: RADIAL PROFILES OF PLASMA PROPERTIES AVERAGED OVER ALL AZIMUTHAL LOCATIONS AND OVER THE TIME INTERVAL OF $20 - 30\ \mu s$ FOR XENON PROPELLANT WITH VARIOUS MAGNETIC FIELD CONFIGURATIONS; (A) ION NUMBER DENSITY, (B) ELECTRON TEMPERATURE, (C) RADIAL-TO-AZIMUTHAL ELECTRON TEMPERATURE RATIO, AND (D) NORMALIZED AXIAL ELECTRON CURRENT DENSITY. 164

FIG. 4.34: (LEFT PANEL) 2D SNAPSHOTS OF THE NORMALIZED AXIAL ELECTRON CURRENT DENSITY (Jey) AT FOUR DIFFERENT MOMENTS THROUGH THE DISCHARGE EVOLUTION CYCLE FOR DIFFERENT MAGNETIC FIELD CONFIGS. T REPRESENTS THE PERIOD OF THE CYCLE, WHICH IS DIFFERENT FOR EACH CONFIG. **(RIGHT PANEL)** 2D SNAPSHOTS OF THE NORMALIZED PLASMA PROPERTIES AT A TIME OF LOCAL MAXIMUM OF THE SPATIALLY AVERAGED Tex FOR XENON PROPELLANT WITH VARIOUS MAGNETIC FIELD CONFIGS. 164

FIG. 4.35: (A) AZIMUTHAL WAVENUMBER SPECTRA OF INSTABILITIES OBTAINED FROM AVERAGE SPATIAL FFTS, (B) FREQUENCY SPECTRA OF INSTABILITIES OBTAINED FROM AVERAGE TEMPORAL FFTS OF THE AZIMUTHAL ELECTRIC FIELD SIGNAL FROM SIMULATIONS WITH VARIOUS MAGNETIC FIELD CONFIGURATIONS FOR XENON PROPELLANTS. PLOT (C) DISPLAYS A ZOOM-IN VIEW OF PLOT (B) OVER $0 - 10MHz$ FREQUENCY RAGE. 165

FIG. 4.36: (A) SCHEMATIC ASSOCIATED WITH THE CALCULATION OF THE CROSS-FIELD VELOCITY, WHERE THE BLUE CURVE REPRESENTS THE MAGNETIC FIELD LINE. RADIAL PROFILES OF (B) AVERAGE ELECTRONS' AXIAL MOBILITY, AND (C) AVERAGE ELECTRONS' CROSS-FIELD MOBILITY OVER ALL AZIMUTHAL LOCATIONS AND OVER THE TIME INTERVAL OF $20 - 30\ \mu s$ FOR XENON PROPELLANT WITH VARIOUS MAGNETIC FIELD CONFIGURATIONS. 166

FIG. 4.37: NORMALIZED RADIAL AND AZIMUTHAL PARTICLES' VELOCITY DISTRIBUTION FUNCTIONS (VDF) FOR XENON PROPELLANT WITH VARIOUS MAGNETIC FIELD CONFIGURATIONS AT $t = 30\ \mu s$.. 167

FIG. 4.38: TOP ROW: SPATIALLY AVERAGED (OVER ENTIRE DOMAIN) DIVERGENCE-ANGLE DISTRIBUTION FUNCTIONS DUE TO (A) THE RADIAL AND (B) THE AZIMUTHAL VELOCITY COMPONENTS OF THE IONS; **BOTTOM ROW**: RADIAL DISTRIBUTION OF THE AZIMUTHALLY AVERAGED ION BEAM DIVERGENCE ANGLES DUE TO (A) THE RADIAL AND (B) THE AZIMUTHAL VELOCITY COMPONENTS OF THE IONS FOR XENON PROPELLANT WITH VARIOUS MAGNETIC FIELD CONFIGURATIONS. 168

FIG. 4.39: VARIATION OF THE SECONDARY ELECTRON EMISSION YIELD (γ) VS THE ELECTRON ENERGY (ϵ) FOR VARIOUS $\epsilon *$ VALUES ACCORDING TO THE LINEAR SEE MODEL (EQ. 4.10). 169

FIG. 4.40: RADIAL PROFILES OF PLASMA PROPERTIES AVERAGED OVER ALL AZIMUTHAL LOCATIONS AND OVER THE TIME INTERVAL OF $20 - 30\ \mu s$ FOR XENON PROPELLANT WITH VARIOUS SEE'S $\epsilon *$ VALUES. 170

FIG. 4.41: 2D SNAPSHOTS OF THE NORMALIZED PLASMA PROPERTIES AT A TIME OF LOCAL MAXIMUM OF THE SPATIALLY AVERAGED Tex FOR XENON PROPELLANT WITH VARIOUS SEE'S $\epsilon *$ VALUES..... 170

FIG. 4.42: (A) AZIMUTHAL WAVENUMBER SPECTRA OF INSTABILITIES OBTAINED FROM AVERAGE SPATIAL FFTS, AND (B) & (C) FREQUENCY SPECTRA OF INSTABILITIES OBTAINED FROM AVERAGE TEMPORAL FFTS OF THE AZIMUTHAL ELECTRIC FIELD SIGNAL FROM SIMULATIONS WITH VARIOUS SEE'S $\epsilon *$ VALUES FOR XENON PROPELLANTS..... 171

FIG. 4.43: VARIATION OF (A) SPATIOTEMPORALLY AVERAGED ELECTRONS' AXIAL MOBILITY (OVER $20 - 30\ \mu s$ AND OVER ENTIRE DOMAIN (μy) AND OVER THE CENTRAL PORTION OF THE DOMAIN WITH $xLx \in 0.2, 0.8\ (\mu y, center)$), AND (B) AVERAGE SEE YIELD γ (ACROSS ENTIRE EXTENTS OF BOTH INNER AND OUTER WALLS AND OVER $20 - 30\ \mu s$) VS SEE'S $\epsilon *$ VALUES. 172

FIG. 4.44: RADIAL PROFILES OF PLASMA PROPERTIES AVERAGED OVER ALL AZIMUTHAL LOCATIONS AND OVER THE TIME INTERVAL OF $20 - 30\ \mu s$ FOR XENON PROPELLANT WITH VARIOUS IONIZATION SOURCE PEAK INTENSITIES (S)..... 173

FIG. 4.45: 2D SNAPSHOTS OF THE NORMALIZED PLASMA PROPERTIES AT FOUR DIFFERENT MOMENTS THROUGH THE DISCHARGE EVOLUTION CYCLE FOR XENON PROPELLANT WITH FOUR DIFFERENT IONIZATION SOURCE PEAK INTENSITIES (S)..... 174

FIG. 4.46: (A) AZIMUTHAL WAVENUMBER SPECTRA OF INSTABILITIES OBTAINED FROM AVERAGE SPATIAL FFTS, (B) & (C) FREQUENCY SPECTRA OF INSTABILITIES OBTAINED FROM AVERAGE TEMPORAL FFTS OF THE AZIMUTHAL ELECTRIC FIELD SIGNAL FROM SIMULATIONS WITH VARIOUS IONIZATION SOURCE PEAK INTENSITIES (S) FOR XENON PROPELLANTS. 175

FIG. 4.47: VARIATION OF SPATIOTEMPORALLY AVERAGED (ACROSS ENTIRE DOMAIN AND OVER $20 - 30\ \mu s$) VALUES OF (A) RADIAL-TO-AZIMUTHAL ELECTRON TEMPERATURE RATIO, AND (B) ELECTRONS' AXIAL MOBILITY VS IONIZATION SOURCE PEAK INTENSITY (S). 176

FIG. 4.48: RADIAL PROFILES OF THE TRANSPORT TERMS IN EQ. 4.1 FOR XENON PROPELLANT WITH VARIOUS IONIZATION SOURCE PEAK INTENSITY (S). THE FORCE TERMS ARE AVERAGED OVER $20 - 30\ \mu s$. 176

FIG. 4.49: NORMALIZED RADIAL AND AZIMUTHAL PARTICLES' VELOCITY DISTRIBUTION FUNCTIONS (VDF) FOR XENON PROPELLANT WITH VARIOUS IONIZATION SOURCE PEAK INTENSITIES (S) AT $t = 30\ \mu s$.. 177

FIG. 5.1: AXIAL PROFILES OF (A) THE IMPOSED IONIZATION SOURCE FOR SIMULATIONS WITH VARIOUS ION CURRENT DENSITIES (J), (B) THE APPLIED RADIAL MAGNETIC FIELD FOR SIMULATIONS WITH VARIOUS MAGNETIC FIELD PEAK INTENSITIES (B). 184

FIG. 5.2: TIME-AVERAGED (OVER $20 - 30\ \mu s$) AXIAL PROFILES OF ION NUMBER DENSITY FOR THE THREE PROPELLANTS WITH VARIOUS V (TOP ROW), VARIOUS J (MIDDLE ROW), AND VARIOUS B (BOTTOM ROW).. 185

FIG. 5.3: TIME-AVERAGED (OVER $20 - 30\ \mu s$) AXIAL PROFILES OF ELECTRIC FIELD FOR THE THREE PROPELLANTS WITH VARIOUS V (TOP ROW), VARIOUS J (MIDDLE ROW), AND VARIOUS B (BOTTOM ROW).. 186

FIG. 5.4: TIME-AVERAGED (OVER $20 - 30\ \mu s$) AXIAL PROFILES OF ELECTRON TEMPERATURE FOR THE THREE PROPELLANTS WITH VARIOUS V (TOP ROW), VARIOUS J (MIDDLE ROW), AND VARIOUS B (BOTTOM ROW).. 186

FIG. 5.5: VARIATION OF THE PEAK VALUES OF THE AXIAL PROFILES OF ION NUMBER DENSITY, AXIAL ELECTRIC FIELD AND ELECTRON TEMPERATURE VS V (TOP ROW), VS J (MIDDLE ROW) AND VS B (BOTTOM ROW) FOR THE THREE PROPELLANTS. 190

FIG. 5.6: VARIATION OF SPATIOTEMPORALLY AVERAGED (ACROSS AXIAL EXTENT OF $1.5\ cm < x < 2.5\ cm$ AND OVER $20 - 30\ \mu s$) ION NUMBER DENSITY (ni) AND IONS' AXIAL DRIFT VELOCITY (Vix) IN THE PLUME VS V (TOP ROW), VS J (MIDDLE ROW), AND VS B (BOTTOM ROW) FOR THE THREE PROPELLANTS. 191

FIG. 5.7: VARIATION OF TEMPORALLY AVERAGED (OVER $20 - 30\ \mu s$) NORMALIZED ELECTRON CURRENT, NORMALIZED ION CURRENT AND ELECTRON-TO-ION CURRENT RATIO VS V (TOP ROW), VS J (MIDDLE ROW) AND VS B (BOTTOM ROW) FOR THE THREE PROPELLANTS. 193

FIG. 5.8: VARIATION OF THE AZIMUTHAL WAVENUMBER kz (LEFT PANEL) AND THE FREQUENCY ω (RIGHT PANEL) OF THE DOMINANT INSTABILITY MODE AT TWO AXIAL LOCATIONS (INSIDE THE CHANNEL AT $x = 0.375$ AND IN THE PLUME AT $1.625\ cm$) VS V (TOP ROW), VS J (MIDDLE ROW) AND VS B (BOTTOM ROW) FOR THE THREE PROPELLANTS. 195

FIG. 5.9: IONS' AZIMUTHAL PHASE-SPACE ($z - vz$) PLOTS IN THE PLUME ($1.25\ cm < x < 2.25\ cm$) FOR XENON WITH VARIOUS V (LEFT PANEL), VARIOUS J (MIDDLE PANEL), AND VARIOUS B (RIGHT PANEL). 197

FIG. 5.10: VARIATION OF THE RMS AMPLITUDE OF THE AZIMUTHAL ELECTRIC FIELD FLUCTUATIONS (LEFT COLUMN) AND ELECTRON NUMBER DENSITY (RIGHT COLUMN) FLUCTUATIONS IN THE PLUME VS V (TOP ROW), VS J (MIDDLE ROW) AND VS B (BOTTOM ROW) FOR THE THREE PROPELLANTS.. 198

FIG. 5.11: 2D SNAPSHOTS OF THE NORMALIZED ION NUMBER DENSITY (TOP PANEL) AND NORMALIZED AZIMUTHAL ELECTRIC FIELD (BOTTOM PANEL) AT $t = 30\mu s$ FOR XENON WITH VARIOUS V (LEFT COLUMN), VARIOUS J (MIDDLE COLUMN) AND VARIOUS B (RIGHT COLUMN).. 200

FIG. 5.12: 2D SNAPSHOTS OF THE NORMALIZED AZIMUTHAL ELECTRIC FIELD AT $t = 30\mu s$ FOR VARIOUS PROPELLANTS AT $B = 20$ AND $30\ mT$. DASHED BLACK LINES REPRESENT THE LOCATION OF THE CHANNEL EXIT PLANE 201

FIG. 5.13: AXIAL PROFILES OF THE TRANSPORT TERMS IN EQ. 1.20 FOR THE THREE PROPELLANTS WITH VARIOUS V (LEFT COLUMN), VARIOUS J (MIDDLE COLUMN) AND VARIOUS B (RIGHT COLUMN). THE FORCE TERMS ARE AVERAGED OVER $4\ \mu s$. 203

FIG. 5.14: VARIATION OF SPATIOTEMPORALLY AVERAGED (ACROSS ENTIRE DOMAIN AND OVER $4\ \mu s$) MAGNETIC FORCE TERM (LEFT COLUMN) AND ELECTRIC FORCE TERM (RIGHT COLUMN) IN EQ. 1.20 VS V (TOP ROW), VS J (MIDDLE ROW), AND VS B (BOTTOM ROW) FOR THE THREE PROPELLANTS. 204

FIG. 5.15: VARIATION IN THE AXIAL LOCATION OF THE PEAK VALUES OF DIFFERENT QUANTITIES VS V (TOP ROW), VS J (MIDDLE ROW), AND VS B (BOTTOM ROW) FOR THE THREE PROPELLANTS. 205

FIG. 5.16: NORMALIZED ION AXIAL VELOCITY DISTRIBUTION FUNCTION (IVDF) IN THE PLUME (OVER $1.5\ cm < x < 2.5\ cm$) AT $t = 30\ \mu s$ FOR THE THREE PROPELLANTS WITH VARIOUS V (TOP ROW), VARIOUS J (MIDDLE ROW), AND VARIOUS B (BOTTOM ROW). DOTTED LINES SHOW THE IONS' IDEAL EXHAUST VELOCITY GIVEN BY EQ. 5.1. 206

FIG. 5.17: NORMALIZED 1D1V IONS' DISTRIBUTION FUNCTIONS (AT $t = 30\ \mu s$) ALONG AXIAL DIRECTION AND AXIAL VELOCITY COMPONENT FOR THE THREE PROPELLANTS WITH VARIOUS J (TOP PANEL) AND VARIOUS B (BOTTOM PANEL). 207

FIG. 5.18: TIME-AVERAGED (OVER $20 - 30\ \mu s$) AXIAL PROFILES OF ION TEMPERATURE (Ti) FOR THE THREE PROPELLANTS WITH VARIOUS B. DASHED BLACK LINES REPRESENT THE LOCATION OF THE CHANNEL EXIT PLANE. 208

FIG. 5.19: AXIAL PROFILES OF THE APPLIED RADIAL MAGNETIC FIELD FOR SIMULATIONS WITH DIFFERENT B-FIELD DISTRIBUTION; (A) VARIOUS VALUES OF STANDARD DEVIATIONS (σ), AND (B) VARIOUS AXIAL LOCATIONS OF THE MAGNETIC FIELD PEAK (xp).... 208

FIG. 5.20: TIME-AVERAGED (OVER $20 - 30\ \mu s$) AXIAL PROFILES OF ION NUMBER DENSITY, AXIAL ELECTRIC FIELD, ELECTRON TEMPERATURE FOR XENON WITH VARIOUS VALUES OF STANDARD DEVIATION OF THE MAGNETIC FIELD PROFILE σ (TOP ROW), AND VARIOUS MAGNETIC FIELD'S PEAK LOCATIONS xp (BOTTOM ROW).. 209

FIG. 5.21: VARIATION OF SPATIOTEMPORALLY AVERAGED (ACROSS AXIAL EXTENT OF $1.5\ cm < x < 2.5\ cm$ AND OVER $20 - 30\ \mu s$) ION NUMBER DENSITY AND IONS' AXIAL DRIFT VELOCITY IN THE PLUME VS σ (TOP ROW) AND VS xp (BOTTOM ROW) FOR XENON..... 210

FIG. 5.22: VARIATION OF THE TEMPORALLY AVERAGED (OVER $20 - 30\ \mu s$) CURRENT TERMS VS σ (LEFT), AND VS xp (RIGHT) FOR XENON PROPELLANT. 211

FIG. 5.23: AXIAL PROFILES OF THE TRANSPORT TERMS IN EQ. 1.20 FOR XENON PROPELLANT WITH VARIOUS σ (LEFT COLUMN), AND VARIOUS xp (RIGHT COLUMN). THE FORCE TERMS ARE AVERAGED OVER $4\ \mu s$..... 212

FIG. 6.1: AXIAL PROFILES OF (A) THE NORMALIZED RADIAL MAGNETIC FIELD INTENSITY (B) INITIAL NEUTRAL DENSITY (LEFT AXIS) AND NEUTRALS' AXIAL VELOCITY (RIGHT AXIS) USED FOR THE THREE OPERATING CONDITIONS; CASE I, CASE II AND CASE III. 220

FIG. 6.2: COMPARISON OF THE NORMALIZED GLOBAL PERFORMANCE PARAMETERS FROM THE SIMULATIONS AGAINST EXPERIMENTAL VALUES FOR THE THREE OPERATING CONDITIONS [168]. 222

FIG. 6.3: TIME EVOLUTION OF THE DISCHARGE CURRENT FOR THE THREE SIMULATED OPERATING CONDITIONS. THE HIGHLIGHTED AREAS ISOLATE ONE CYCLE OF THE PERIODIC BEHAVIOR IN THE DISCHARGE AFTER REACHING THE QUASI-STEADY STATE. 224

FIG. 6.4: AVERAGE (OVER ALL AXIAL POSITIONS) TEMPORAL FFT PLOTS OF THE ION NUMBER DENSITY SIGNAL, FOR THE THREE SIMULATED CONDITIONS. 224

FIG. 6.5: SPATIOTEMPORAL MAPS OF (A) ION NUMBER DENSITY, (B) IONS' AXIAL DRIFT VELOCITY, (C) AXIAL ELECTRIC FIELD, (D) ELECTRON TEMPERATURE, (E) NEUTRAL NUMBER DENSITY AND (F) NEUTRALS' AXIAL DRIFT VELOCITY FOR THE THREE SIMULATED CONDITIONS. 226

FIG. 6.6: TIME-AVERAGED AXIAL PROFILES OF PLASMA PROPERTIES FOR THE THREE SIMULATED OPERATING CONDITION; (A) ION NUMBER DENSITY, (B) AXIAL ELECTRIC FIELD, (C) IONIZATION RATE, (D) PLASMA POTENTIAL, (E) NEUTRAL NUMBER DENSITY, (F) NEUTRALS' AXIAL VELOCITY, (G) ELECTRON TEMPERATURE, AND (H) ION MACH NUMBER. 228

FIG. 6.7: COMPARISON OF THE PREDICTED AXIAL DISTRIBUTION OF THE IONS' AXIAL DRIFT VELOCITY WITH THE LIF MEASUREMENTS FOR OPERATING CONDITION II. THE ERROR BARS ON THE TEST DATA REPRESENT ONE STANDARD DEVIATION OF THE MEASURED DISTRIBUTION. 229

FIG. 6.8: 1D1V VELOCITY DISTRIBUTION FUNCTIONS OF THE IONS ALONG THE AXIAL DIRECTION AND AXIAL VELOCITY COMPONENT FOR THE THREE SIMULATED OPERATING CONDITIONS DURING DIFFERENT MOMENTS OF THE DISCHARGE EVOLUTION CYCLE. 229

FIG. 6.9: NUMERICAL DISPERSION PLOTS OF AZIMUTHAL INSTABILITIES FOR THE THREE SIMULATED CONDITIONS, OBTAINED FROM 2D FFT OF THE SPATIOTEMPORAL SIGNAL OF AZIMUTHAL ELECTRIC FIELD FLUCTUATIONS OVER THE TIME WINDOW OF $400 - 600\ \mu s$..... 231

FIG. 6.10: AZIMUTHAL WAVENUMBER SPECTRA (TOP ROW) AND FREQUENCY SPECTRA (BOTTOM ROW) OF INSTABILITIES OBTAINED, RESPECTIVELY, FROM AVERAGE SPATIAL AND TEMPORAL FFT OF THE AZIMUTHAL ELECTRIC FIELD SIGNAL FROM THREE SIMULATIONS CASES. 231

FIG. 6.11: AZIMUTHAL VDF OF THE IONS RESIDING OVER THE ENTIRE AXIAL EXTENT OF THE DOMAIN, AVERAGED OVER $400 - 600\ \mu s$, FOR THE THREE SIMULATED CASES.. 232

FIG. 7.1: SCHEMATIC OF THE MAIN LOOP OF THE Q2D DL-PIC CODE. THE SAME IS VALID FOR A Q3D CASE. FIGURE ADOPTED FROM REF. [183]. 238

FIG. 7.2: SCHEMATIC OF THE MAGNETIC-FIELD-ALIGNED COARSE GRID UNDERLYING THE REDUCED-ORDER SCHEME FOR TWO DIFFERENT MAGNETIC FIELD TOPOLOGIES CORRESPONDING TO (A) CONVENTIONAL (UNSHIELDED) HALL THRUSTERS AND (B) MAGNETICALLY-SHIELDED HALL THRUSTERS. 240

FIG. 7.3: SCHEMATIC OF THE DOMAIN DECOMPOSITION CORRESPONDING TO THE REDUCED-DIMENSION GRID SYSTEM FOR FIRST-ORDER RO-PIC; (**LEFT**) DECOMPOSITION INTO MULTIPLE "REGIONS" USING A COARSE GRID, (**RIGHT**) THE 1D COMPUTATIONAL CELLS (FINE GRIDS) FOR THE DISCRETIZATION OF EACH REGION ALONG THE x AND y DIRECTIONS. THE RED LINES REPRESENT THE BOUNDARIES BETWEEN THE REGIONS WHICH COINCIDE WITH THE COMPUTATIONAL GRIDS. 242

List of Tables

TABLE 1.1: PARAMETERS IN VAUGHAN MODEL FOR PARTIAL COEFFICIENT YIELDS AND THEIR VALUES FOR BORON NITRIDE. 53

TABLE 2.1: DEFINITION OF THE 2D POISSON PROBLEMS FOR STANDALONE VERIFICATION OF THE REDUCED-DIMENSION POISSON'S SOLVER. 80

TABLE 3.1: SUMMARY OF THE MAIN COMPUTATIONAL AND PHYSICAL PARAMETERS USED FOR THE Q2D AXIAL-AZIMUTHAL SIMULATIONS. 92

TABLE 3.2: SUMMARY OF THE MAIN COMPUTATIONAL AND PHYSICAL PARAMETERS USED FOR THE Q2D AND THE FULL-2D RADIAL-AZIMUTHAL SIMULATIONS. 104

TABLE 4.1: LIST OF ALL THE SIMULATION CASES PERFORMED IN THE RADIAL-AZIMUTHAL COORDINATES 126

TABLE 5.1: LIST OF ALL THE SIMULATION CASES PERFORMED IN THE AXIAL-AZIMUTHAL COORDINATES 183

TABLE 6.1: SUMMARY OF THE MAIN PHYSICAL AND NUMERICAL AND PARAMETERS USED FOR THE Q2D AXIAL-AZIMUTHAL SIMULATIONS OF HT20K. 219

TABLE 6.2: HT20K OPERATING CONDITIONS USED FOR THE SIMULATIONS. 220

TABLE 6.3: PERFORMANCE PARAMETERS FROM THE Q2D SIMULATIONS OF THE HT20K IN THE THREE OPERATING CONDITIONS. .. 221

TABLE 6.4: COMPARISON OF THE PEAK FREQUENCIES OF THE DISCHARGE CURRENT SIGNAL FROM THE Q2D SIMULATIONS OF THE HT20K IN THE THREE OPERATING CONDITIONS WITH THE CORRESPONDING EXPERIMENTAL VALUES. 225

TABLE 6.5: COMPARISON OF SEVERAL PLASMA PARAMETERS IN IN AXIAL-AZIMUTHAL AND RADIAL AZIMUTHAL CONFIGURATIONS.. 233

List of Acronyms

CFL	Courant-Friedrichs-Lewy Criterion
CPU	Central Processing Unit
DL	Deep Learning
DMD	Dynamic Mode Decomposition
DNS	Reynolds-Averaged Navier-Stokes
DSMC	Direct Simulation Monte Carlo
ECDI	Electron Cyclotron Drift Instability
EVDF	Electron Velocity Distribution Function
FEM	Finite Element Method
FFT	Fast Fourier Transform
GPU	Graphics Processing Unit
IAI	Ion Acoustic Instability
ITTI	Ion Transit Time Instability
IVDF	Ion Velocity Distribution Function
LES	Large Eddy Simulation
MCC	Monte Carlo Collisions
MPI	Message Passing Interface
MTSI	Modified Two Stream Instability
ODE	Ordinary Differential Equation
PDE	Partial Differential Equation
PIC	Particle-In-Cell
Q2D	Quasi Two Dimensional
Q3D	Quasi Three Dimensional
RO-PIC	Reduced Order Particle-In-Cell
SCS	Space-Charge-Saturated
SEE	Secondary Electron Emission
VDF	Velocity Distribution Function

List of Publications

Select journal articles

1. **Reza M**, Faraji F, Knoll A, "Resolving multi-dimensional plasma phenomena in Hall thrusters using the reduced-order particle-in-cell scheme," *J Electr Propuls* **1**, 19 (2022) DOI: 10.1007/s44205-022-00019-6.
2. **Reza M**, Faraji F, Knoll A, "Concept of the generalized reduced-order particle-in-cell scheme and verification in an axial-azimuthal Hall thruster configuration," *J. Phys. D: Appl. Phys.* **56** 175201 (2023) DOI: 10.1088/1361-6463/acbb15.
3. **Reza M**, Faraji F, Knoll A, "Parametric investigation of azimuthal instabilities and electron transport in a radial-azimuthal E×B plasma configuration," *J. Appl. Phys.* **133**, 123301 (2023) DOI: 10.1063/5.0138223.
4. **Reza M**, Faraji F, Knoll A, Piragino A, Andreussi T, Misuri T, "Reduced-order particle-in-cell simulations of a high-power magnetically shielded Hall thruster," *Plasma Sources Sci. Technol.* **32**, 065016 (2023) DOI: 10.1088/1361-6595/acdea3.
5. **Reza M**, Faraji F, Knoll A, "Influence of the magnetic field curvature on the radial-azimuthal dynamics of a Hall thruster plasma discharge with different propellants," *J. Appl. Phys.* **134**, 233303 (2023) DOI: 10.1063/5.0176579.
6. **Reza M**, Faraji F, Knoll A, "Effects of the applied fields' strength on the plasma behavior and processes in E×B plasma discharges of various propellants: I. Electric field", *Phys. Plasmas.* **31**, 032120 (2024) DOI: 10.1063/5.0176581.
7. **Reza M**, Faraji F, Knoll A, "Effects of the applied fields' strength on the plasma behavior and processes in E×B plasma discharges of various propellants: II. Magnetic field", *Phys. Plasmas.* **31**, 032121 (2024) DOI: 10.1063/5.0176586.
8. **Reza M**, Faraji F, Knoll A, "Plasma dynamics and electron transport in a Hall-thruster-representative configuration with various propellants: I. Variations with discharge voltage and current density," *Plasma*, **7**(3), 651-679 (2024) DOI: 10.3390/plasma7030034.
9. **Reza M**, Faraji F, Knoll A, "Plasma dynamics and electron transport in a Hall-thruster-representative configuration with various propellants: II. Effects of the magnetic field topology," *Plasma*, **7**(3), 680-704 (2024) DOI: 10.3390/plasma7030035.
10. Faraji F, **Reza M**, Knoll A, "Enhancing one-dimensional particle-in-cell simulations to self-consistently resolve instability-induced electron transport in Hall thrusters," *J. Appl. Phys.* **131**, 193302 (2022) DOI: 10.1063/5.0090853.
11. Faraji F, **Reza M**, Knoll A, "Verification of the generalized reduced-order particle-in-cell scheme in a radial-azimuthal E×B plasma configuration," *AIP Advances* **13**, 025315 (2023) DOI: 10.1063/5.0136889.
12. Faraji F, **Reza M**, Knoll A, "Effects of the neutral dynamics model on the particle-in-cell simulations of a Hall thruster plasma discharge," *J. Appl. Phys.* **133**, 213301 (2023) DOI: 10.1063/5.0143292.

Select conference papers

1. **M. Reza**, Faraji F, Knoll A, "Reduced-order 'pseudo-2D' particle-in-cell scheme for the prediction of multi-dimensional phenomena in Hall thrusters," IEPC-2022-305, *In Procs. of 37th International Electric Propulsion Conference*, Boston, Cambridge, 19-23 June 2022.
2. **M. Reza**, Faraji F, Knoll A, "Reduced-order particle-in-cell scheme: Redefining kinetic modeling for electric plasma propulsion," AIAA 2024-2709, *In Procs. of 2024 SciTech Forum conference*, Orlando, Florida, 8-12 January 2024. DOI: 10.2514/6.2024-2709.
3. **M. Reza**, Faraji F, Knoll A, "Latest verifications of the reduced-order particle-in-cell scheme: Penning discharge and axial-radial Hall thruster case," AIAA 2024-2712, *In Procs. of 2024 SciTech Forum conference*, Orlando, Florida, 8-12 January 2024. DOI: 10.2514/6.2024-2712.
4. **Reza M**, Faraji F, Knoll A, "Technical Advancements at Imperial Plasma Propulsion Laboratory on the Building Blocks of Digital Twin Technology for Electric Propulsion," SP2024_061, *In Procs. of Space Propulsion Conference*, Glasgow, Scotland, 20-23 May 2024.
5. **Reza M**, Faraji F, Knoll A, Kutz JN, "Shallow Recurrent Decoder architecture with application to super-resolution enhancement of the reduced-order particle-in-cell scheme," IEPC-2024-503, *In Procs. of 38th International Electric Propulsion Conference,* Toulouse, France*,* 23-28 June 2024.
6. Faraji F, **M. Reza**, Knoll A, "Insights from reduced-order particle-in-cell simulations into the plasma behavior in a high-power magnetically shielded Hall thruster," IEPC-2022-306, *In Procs. of 37th International Electric Propulsion Conference*, Boston, Cambridge, 19-23 June 2022.
7. Faraji F, **Reza M**, Knoll A, "Digital Twins for a 21st-Century Transformation of the Electric Propulsion Sector: Vision 2030," SP2024_046, *In Procs. of Space Propulsion Conference 2024*, Glasgow, Scotland, 20-23 May 2024.
8. Faraji F, **Reza M**, Knoll A, "Digital twins for Electric Propulsion: concept, game- changing potentials, and building blocks", IEPC-2024-256, *In Procs. of 38th International Electric Propulsion Conference,* Toulouse, France*,* 23-28 June 2024.

Chapter 1 Background and problem statement

Plasmas are ubiquitous in the universe. From the intense nuclear fusion reactions powering stars to the vast expanses of interstellar space, plasma constitutes a significant portion of cosmic matter. Despite its prevalence, our understanding of plasma and its behavior has remained incomplete. The long-standing fundamental questions in plasma physics pose significant implications on our ability to predict and control plasmas for terrestrial applications.

In many plasma applications of industrial relevance, from magnetrons for material processing and Hall thruster for space propulsion to magnetic confinement devices for fusion, the intricate plasma dynamics is three dimensional in nature and covers a vast range of temporal and spatial scales. Obtaining a comprehensive understanding of the muti-dimensional picture of kinetic plasma processes enables the prediction and control of plasmas, paving the way for more efficient technological solutions, novel plasma applications and harnessing fusion energy as the sustainable energy source for the future. Nonetheless, our efforts toward acquiring an all-round knowledge of the 3D plasma phenomena are often impeded by the unavailability of a computationally viable self-consistent, high-fidelity model.

In this regard, development of a new modelling approach that can cut the computational burden of the traditional kinetic simulations while maintaining the fidelity in their prediction serves as making a leap towards unravelling questions in plasma physics that have remained unanswered for decades.

Throughout this work, we primarily focus on $E \times B$ plasma discharges and applications as proving ground for the methods developed within this research.

1.1. Overview of the physics of cross-field plasma discharges

Partially magnetized plasmas immersed in a perpendicular configuration of the electric and magnetic fields (which are referred to as $\mathrm{E} \times \mathrm{B}$ or cross-field configuration) found important applications across industries over the last decades. These applications range from magnetrons for plasma-assisted manufacturing to Hall thrusters for in-space plasma propulsion and plasma sources such as Penning discharge (**Fig. 1.1**). The operation of the $\mathrm{E} \times \mathrm{B}$ technologies mainly relies on effectively impeding the cross-magnetic-field electron current. $\mathrm{E} \times \mathrm{B}$ discharges are characterized by multi-dimensional

phenomena across a wide spectrum of spatiotemporal scales [1][2]. Moreover, their underlying plasma processes, such as instabilities and particles' transport, exhibit a multifaceted and highly coupled nature. The rich physics and abundance of complex plasma phenomena made $\mathrm{E} \times \mathrm{B}$ plasmas the subject of broad fundamental research on various aspects including plasma instabilities and their induced electrons' cross-field transport, as well as sheath physics and plasma-wall interactions.

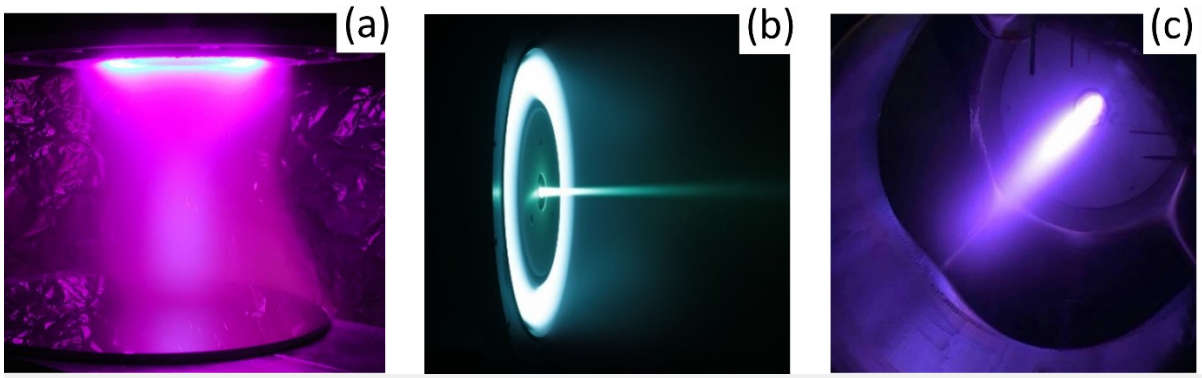


Fig. 1.1: Various applications of $\mathrm{E} \times \mathrm{B}$ plasmas: (a) A magnetron [Source], (b) A Hall thruster [3], (c) A Penning discharge [Source]

1.1.1. Plasma-wall interactions

At the interface of the plasma and a surface, electrons (due to their higher thermal mobility) tend to collide with the wall more frequently than ions. This results in a negative charge accumulation at the surface and establishment of an electric field directed towards the wall in its immediate vicinity. This electric field impedes the loss of more electrons to the wall while accelerating the ions so as to balance the flux of electrons towards the wall. At steady state, an equal flux of ions and electrons reaches the wall, hence, maintaining the surface potential at a constant value (sheath potential) relative to the plasma bulk's potential. In the vicinity of the wall's surface, a non-neutral layer called plasma sheath [4] forms, separating plasma bulk from the wall. The sheath region typically has a higher number density of ions than electrons, a necessary condition to "shield" the quasi-neutral bulk plasma from the negative wall potential. It is noteworthy that plasmas exhibit collective behavior that confines the Coulomb interactions between charged particles to within Debye sphere [4][5] (a sphere with radius of a Debye length). Accordingly, formation of a sheath is the response of the plasma to limit the influence of wall's negative potential to a distance in the order of a few Debye lengths (refer to Section 1.4.1). The sheath potential drop, i.e., the potential difference between the wall and bulk plasma, is a function of electron temperature.

1.1.2. Secondary Electron Emission (SEE), sputtering and erosion

Even though the sheath hinders most electrons from reaching the wall, those in the high-energy tail of the electrons' energy distribution function [6] will have high enough energy to overcome the sheath potential barrier and impact on the wall. When an electron hits the surface, depending on its pre-impact energy, multiple scenarios are possible: that "primary" electron can get elastically reflected, inelastically backscattered or, if the energy is above the so-called "emission threshold energy", it can cause a number of "secondary" electrons to be emitted out of the surface into the plasma. This last scenario is

referred to as Secondary Electron Emission (SEE). Since these emitted electrons are colder than the plasma primary electrons, the overall effect of SEE is to cool down the plasma by lowering the temperature of electron population.

The ratio between the flux of electrons from the wall entering the plasma and that of the primary impinging electrons is called total emission yield coefficient (γ). This coefficient depends on the primary electron energy and the angle of impact. The electron energy corresponding to $\gamma = 1$ is referred to as crossover energy (ϵ^*) which is a characteristic of the wall material.

As the primary electron energy approaches ϵ^*, γ increases due to a higher flux of electrons from the wall. Due to this increased flux, the potential profile in the immediate vicinity of the wall tends to flatten as a result of an accumulation of electrons, resulting eventually in a near-wall zero electric field. In this situation, the sheath is called to be in the Space-Charge Saturated (SCS) regime. The yield coefficient assumes a critical value (γ_{SCS}) which is proportional to the electron-ion mass ratio. It has been shown [7] that the SCS regime can be unstable, with certain instabilities developing so that the sheath returns to the unsaturated state.

While the sheath acts to repel the electrons away from the wall, as mentioned above, its potential drop accelerates ions towards the wall. Because ions gain energy in the sheath electric field, their impact on the wall can induce surface sputtering. Similar to SEE case, a sputtering yield coefficient (γ_s) can be defined as the average number of neutral particles ejected from the surface per incident ion. Sputtering yield is also a function of the impacting ion energy and angle of incident.

The surfaces in contact with plasma, e.g. the Hall thruster's channel walls, are constantly bombarded by ions which can cause sputtering of these surfaces. In the Hall thruster's acceleration region, high-energy ions accelerated by the strong electric field impact the ceramic channel, increasing sputtering rates near the exit plane and leading to gradual erosion of the channel material.

1.1.3. Plasma oscillations and instabilities

The plasma in $\mathrm{E} \times \mathrm{B}$ configuration is inherently non-quiescent, representing a variety of instabilities. This plasma is not in a thermodynamic equilibrium, and it tends to release its free energies through turbulence and radiation of electromagnetic waves to reach an equilibrium state. Instabilities in plasma can be caused by almost any kind of deviation from thermodynamic equilibrium which occurs in two general ways, based on which the instabilities can be divided into two main categories: macro-instabilities and micro-instabilities [8].

Macro-instabilities can occur due to any inhomogeneity in the thermodynamic quantities, such as pressure and temperature. As these instabilities depend on the configuration space [8] properties of the plasma, they can be adequately described by the fluid equations. Micro-instabilities, on the other hand, are kinetic in nature which arise due to deviation from Maxwellian distribution function [8]. Therefore, in most cases, they can only be appropriately treated using kinetic simulations (refer to Section 1.3). These instabilities are commonly excited under two conditions.

A) In the presence of two streams of particles in contact, or the existence of a current due to a relative drift between ions and electrons, the resulting particles' distribution functions have more than one peak (**Fig. 1.2** (b)). The existence of multiple extrema in the unperturbed velocity distribution function provides the possibility for the distribution function to have a gradient which satisfies the following relation at the velocities near the phase velocity of the wave (ω/k).

$$\frac{\omega}{k}\left.\frac{\partial f_0}{\partial v}\right|_{v=\frac{\omega}{k}} > 0 \qquad \text{Eq. 1.1}$$

In the above relation, f_0 is the unperturbed particles' distribution function, and ω and k are waves frequency and wavenumber, respectively. This is the necessary condition for appearance of instabilities as in such case, a net energy will transfer from particles to the wave during the wave-particles resonant interactions, which result in the growth of the waves. This process is opposite to the Landau damping [4][9], where the energy transfer occurs from wave to particles leading to damping of the waves. This condition (Eq. 1.1) is never met in a Maxwellian distribution function and, therefore, the waves propagating in a plasma with Maxwellian distributions are stabilized through Landau damping (**Fig. 1.2** (a)) [8].

As illustrated in **Fig. 1.2** (b), as a result of the resonant interactions with waves, the particles undergo heating and diffusion in the velocity space so as to eliminate the positive gradient and flattening the bump on the tail of the distribution function, and finally to bring the system back to a more stable state.

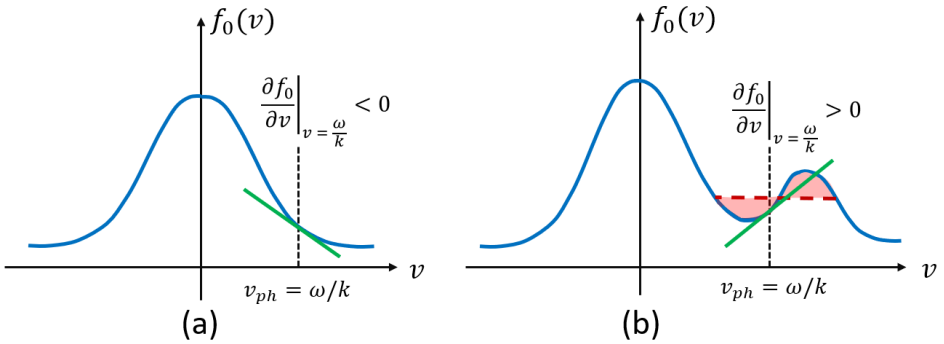


Fig. 1.2: (a) Stable (Maxwellian) and (b) unstable (non-Maxwellian) distribution function.

B) When plasma is subject to anisotropy. Anisotropies in the distribution function can appear, for example, in the presence of a magnetic field strong enough such that particles cyclotron frequency is larger than collision frequency. Otherwise, the collisions would smooth out the anisotropy.

In $\mathrm{E} \times \mathrm{B}$ discharges, both mentioned conditions exist which makes the plasma susceptible to a wide range of instabilities. In these configurations, the magnetic field is sufficient to create a substantial anisotropy in the electrons' distribution function. Besides, the $\mathrm{E} \times \mathrm{B}$ electrons motion resembles a large drift relative to the axially moving ions, providing the possibility to make the azimuthally propagating waves unstable.

In the following we provide a brief overview of the theoretical background of the important instabilities and oscillations in the cross-field plasma configuration. Regarding the notation of the coordinates' axes

used for the description of the instabilities, x represents the axial direction along the electric field (E), y denotes the radial direction parallel to the applied magnetic field (B), and z indicates the azimuthal coordinate along $\mathrm{E} \times \mathrm{B}$ direction.

1.1.3.1. Electron Cyclotron Drift Instability (ECDI)

One of the most influential azimuthal instabilities in $\mathrm{E} \times \mathrm{B}$ discharges is Electron Cyclotron Drift Instability (ECDI). It is a kinetic (microscopic) instability of high frequency ($1 - 10\ MHz$) and wavelengths on the order of electron Larmor radius which propagate in the azimuthal ($\mathrm{E} \times \mathrm{B}$) direction [2]. The waves' phase velocity is smaller than the electrons azimuthal drift, therefore the waves grow by taking energy from the drifting electrons. The ECDI excites as a result of a coupling between Doppler-shifted electrostatic Bernstein modes and the ion acoustic waves [10][11]. The ECDI has been studied extensively using theoretical, numerical, and experimental means over the past few decades [2][10][12][13].

The kinetic dispersion relation of the ECDI in the presence of stationary and uniform perpendicular electromagnetic fields can be obtained from a linearized perturbation of Vlasov's kinetic equation [4][6] for the electrons, fluid equations for the cold and unmagnetized ions, and Poisson's equation [14]-[16]. The resulting 3D dispersion relation is

$$1 + k^2\lambda_{De}^2 + g\left(\frac{\omega - k_z V_{de}}{\omega_{ce}}, \left(k_x^2 + k_y^2\right)\rho_e, k_y\rho_e\right) - \frac{k^2\lambda_D^2\omega_{pi}^2}{(\omega - k_x V_i)^2} = 0,$$

$$g(\Omega, X, Y) = \frac{\Omega}{2Y} e^{-X} \sum_{n=0}^{\infty} Z\left(\frac{\Omega - n}{\sqrt{2Y}}\right) I_n(X). \qquad \text{Eq. 1.2}$$

In the above equation, g is the Gordeev function, Z is the plasma dispersion function ($Z(\eta) = \frac{1}{\sqrt{\pi}}\int_{-\infty}^{+\infty} \frac{e^{-t^2}}{t-\eta} dt$), and I_n is the modified Bessel function of order *n*. k_x, k_y, and k_z are the axial, radial and azimuthal wavenumbers, respectively. ω is the frequency of the wave, $\omega_{pe} = \sqrt{\frac{n_e e^2}{m_e \epsilon_0}}$ is the electron plasma frequency, $\omega_{pi} = \sqrt{\frac{n_i e^2}{M_i \epsilon_0}}$ the ion plasma frequency, and $\omega_{ce} = \frac{eB}{m_e}$ is the electron cyclotron frequency. $\lambda_D = \sqrt{\frac{\epsilon_0 T_e}{e\, n_e}}$ is the Debye length, $V_{de} = \frac{E}{B}$ is the electrons' azimuthal $\mathrm{E} \times \mathrm{B}$ drift velocity, V_i is the ions' drift velocity, and $\rho_e = \frac{Ve_{th,\perp}}{\omega_{ce}}$ is the electron Larmor radius. In these relations, ϵ_0 is the permittivity of the free space, T_e is the electron temperature, $Ve_{th,\perp}$ is the electron thermal velocity in the plane perpendicular to the magnetic field, e is the unit charge, and n_e and n_i are the electron and ion number densities. Moreover, m_e and M_i denote the masses of the electron and ion particles, respectively.

Fig. 1.3 presents the solution of the ECDI's 3D dispersion relation for different values of k_y [16].

The 2D approximation of the dispersion relation perpendicular to the applied magnetic field (in the $x - z$ plane) shows that the unstable modes of the ECDI develop near a resonance condition given by Eq. 1.3 [14][17].

$$k_z = k_0 = N\frac{\omega_{ce}}{V_{de}} = N\frac{e}{m_e}\frac{B^2}{E} \;\; ; \;\; N = 1, 2, \ldots \qquad \text{Eq. 1.3}$$

The solution of the 3D dispersion relation [16] shows that, in the presence of a finite wavenumber along the magnetic field (i.e., $k_y \neq 0$), the sharp resonance-like behavior is smoothed out, and the dispersion relation given by Eq. 1.3 tends to an asymptotic curve representing the dispersion relation of the Ion Acoustic Instability (IAI) [18][19]. Furthermore, as demonstrated by Lampe et al. [20][21], the wave-particle interaction can result in resonance broadening, thereby smoothing out the cyclotron resonances. This will lead to transition to IAI, which occurs after a nonlinear growth stage when the ECDI's waves reach a sufficiently large amplitude.

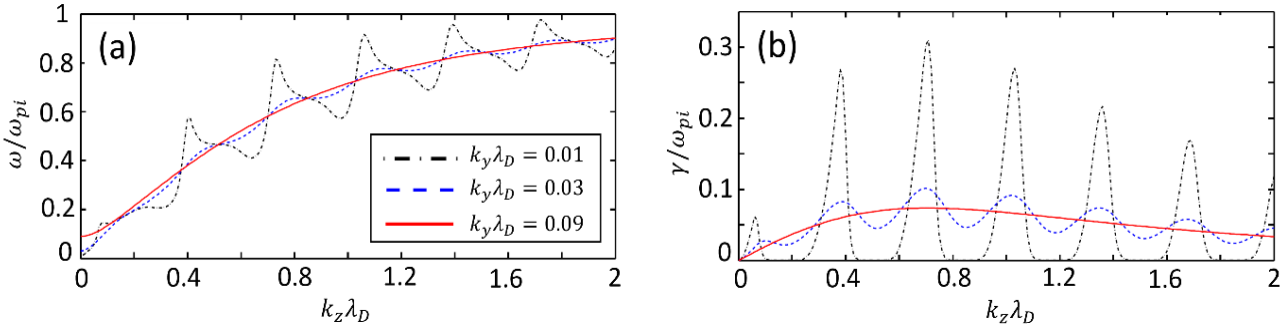


Fig. 1.3: Solution of the ECDI's 3D dispersion relation given by Eq. 1.2; (a) frequency and (b) growth rate versus azimuthal wavenumber (k_z) for various radial wavenumbers (k_y). Reproduced from Ref. [16], "Cavalier J et al, *Phys. Plasmas* **20**, 082107 (2013)," with the permission of AIP Publishing.

The significance of the ECDI roots in the multitude of consequences its presence has on the behavior of plasma. These include enhanced electron cross-field transport [22]-[25], considerable heating of the plasma [24][26], strong influence on and coupling to the SEE from the channel walls [7] in addition to an important role in exciting other plasma wave modes, specifically axial longitudinal ones [7]. In this regard, during the nonlinear growth of the instability, the wave-particle interactions result in heating of the bulk plasma. The increase in the electron temperature can modify the SEE regime that may lead to space-charge saturation of the near-wall sheath. It has been shown that the saturated sheath is unstable which causes the excitation of axially propagating electrostatic waves of high frequency [7].

1.1.3.2. Ion Acoustic Instability (IAI)

After a rapid non-linear growth phase, the ECDI reaches a pseudo-saturated state which marks its transition to Ion Acoustic Instability (IAI) with a linear growth rate. The frequency (ω) and the growth rate (γ) of the IAI are given by the following relations [2][17][18][20][21]

$$\omega \approx k_x V_{di} \pm \frac{k\lambda_D\omega_{pi}}{\sqrt{1 + k^2\lambda_{De}^2}}, \qquad \text{Eq. 1.4}$$

$$\gamma \approx \pm\sqrt{\frac{\pi m_e}{8m_i}}\frac{k_z V_{de}}{(1 + k^2\lambda_{De}^2)^{\frac{3}{2}}}, \qquad \text{Eq. 1.5}$$

Note that in the above equations $\lambda_D\omega_{pi} = c_s$, where c_s is sound speed. It is observed that the axial wavenumber of the instability is significantly smaller than the azimuthal wavenumber ($k_x \ll k_z$) [19][27][28], thus, in Eq. 1.4 and Eq. 1.5, we can assume $k \approx k_z$.

The variation in IAI dispersion ($\omega - k_z$) with electron temperature (T_e) and ion number density (n_i) is illustrated in **Fig. 1.4**. In the limit of the azimuthal wavelength being much larger than the Debye length, i.e., $k_z\lambda_D \ll 1$, Eq. 1.4 is simplified into the linear dispersion relation of the ion sound wave

$$\omega \approx k_z c_s \ . \qquad \text{Eq. 1.6}$$

The dominant mode of the IAI corresponding to the mode with the maximum growth rate satisfies $\frac{\partial \gamma}{\partial k_z} = 0$ condition. Accordingly, the characteristics of the instability's fastest growing mode, namely, the azimuthal wavenumber ($k_{z,max}$), the frequency (ω_{max}), and the phase velocity ($v_{ph,max}$) are obtained as

$$k_{z,max} \approx \frac{1}{\sqrt{2}\,\lambda_{De}} , \quad \omega_{max} \approx \frac{\omega_{pi}}{\sqrt{3}} , \quad v_{ph,max} \approx \sqrt{\frac{2}{3}} c_s , \qquad \text{Eq. 1.7}$$

where c_s is the ion sound speed. Ion-trapping is proposed as the saturation mechanism for the IAI [20][29]. The instability grows quasi-linearly until it reaches a sufficiently large amplitude that can trap significant population of the ions. At the saturation state, the approximate RMS amplitudes of the azimuthal electric field (δE_{RMS}) and electron number density ($\delta n_{e,\,RMS}$) fluctuations corresponding to the fastest growing mode of IAI are given by the expressions in Eq. 1.8 [18][30][31]

$$\delta E_{RMS} \approx \frac{T_e}{12\lambda_{De}} , \qquad \delta n_{e,\,RMS} \approx \frac{n_e}{6\sqrt{2}} , \qquad \text{Eq. 1.8}$$

where T_e and n_e represent the steady state electron temperature and number density, respectively.

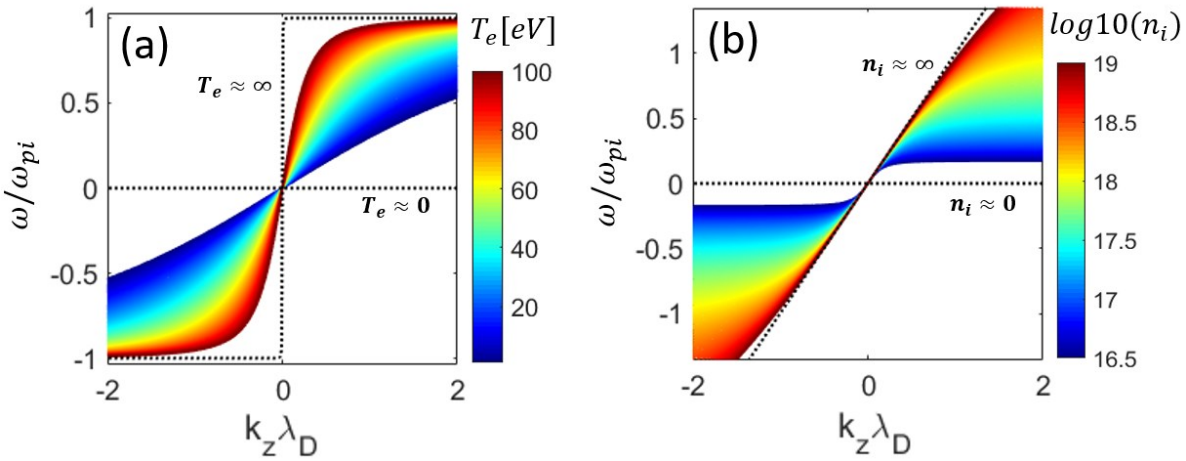


Fig. 1.4: Variation of IAI dispersion relation (Eq. 1.4) with (a) electron temperature (T_e) at constant $n_i = 10^{18}\ m^{-3}$ and (b) with ion number density (n_i) at constant $T_e = 10\ eV$. These plots are generated with the assumption of $k_x = 0$.

1.1.3.3. Modified Two Stream Instability (MTSI)

A theoretical investigation by McBride [32] showed that this mode is a fluid-like instability and is insensitive to the electron-to-ion temperature ratio (T_e/T_i). Janhunen et al. [12] and Taccogna et al. [28] numerically observed this instability as a relatively long-wavelength mode with a non-zero wavenumber along the radial directions ($k_y \neq 0$), the presence of which in the studied systems amplified the inverse energy cascade phenomenon.

In the simulations, the MTSI is observed to heat up electrons mainly in the direction parallel to the applied magnetic field [12][28][32]. Moreover, according to Ref. [32], the MTSI can heat up the ions perpendicular to the magnetic field almost to the same extent as it heats up the electrons parallel to field lines.

Boeuf and Smolyakov [2] derived the dispersion relation of the MTSI from the kinetic ECDI dispersion relation in the asymptotic case of cold electrons ($T_e \to 0$) and with a finite wavenumber component along the direction parallel to the magnetic field. Petronio et al. [33][34] derived a simplified 2D (in radial-azimuthal plane) fluid dispersion relation under the assumption of isothermal electrons with isotropic temperature and by treating ions to be cold and unmagnetized. The dispersion relation is obtained by linearizing a system of equations consisting of the continuity and momentum equations for both the electrons and the ions as well as Poisson's equations. The following dispersion relation was, hence, achieved

$$1-\left(\frac{\omega_{pi}}{\omega}\right)^2-\frac{m_i}{m_e}\frac{\omega_{pe}^2\,k_y^2}{\left(\omega-k_y\frac{E}{B}\right)^2k^2}-\frac{m_i}{m_e}\frac{\omega_{pe}^2\,k_z^2}{\left(\left(\omega-k_z\frac{E}{B}\right)^2-{\omega_{ce}}^2\right)k^2}=0. \qquad \text{Eq. 1.9}$$

Making certain simplifying assumptions, namely, $k_y \ll k_z$, $\omega \ll k_z V_{de}$, and $k_z V_{de} \ll \omega_{ce}/\omega_{pi}$, the MTSI's dispersion relation reduces to

$$\frac{\omega}{\omega_{pi}}=\left(1+\frac{m_i}{m_e}\frac{\omega_{pi}^2}{\omega_{ce}^2}-\frac{m_i}{m_e}\frac{k_y^2\omega_{pi}^2}{k_z^4V_{de}^2}\right)^{-1/2}. \qquad \text{Eq. 1.10}$$

The singularity of Eq. 1.10 characterizes the MTSI's fastest growing mode. Considering that $\frac{m_e}{m_i} \ll \frac{\omega_{pi}}{\omega_{ce}}$, the relationship between the radial and the azimuthal wavevector components of the MTSI's fastest growing mode is given by [34]

$$k_z=\sqrt{\frac{e}{m_e}\frac{B^2}{E}k_y}\,. \qquad \text{Eq. 1.11}$$

Despite the simplifications made to derive the analytical relation in Eq. 1.11, it well agrees in predicting the location of the fastest growing mode in the $k_y - k_z$ plane with that obtained from the kinetic dispersion relation as seen in **Fig. 1.5**. This figure illustrates the solution of the MTSI's dispersion relation (Eq. 1.9) for the plasma density and the field strength conditions of a radial-azimuthal community benchmark problem as an example [35]. Superimposed on these plots as dotted cyan curves are the loci of the (k_y, k_z) pairs that satisfy Eq. 1.11, hence, correspond to the MTSI's fastest growing mode.

From **Fig. 1.5** (b), it is noticed that the MTSI is unstable only when $k_z \leq \sqrt{\frac{e}{m_e}\frac{B^2}{E}k_y}$. Accordingly, in line with the findings of Ref. [34], the relationship given by Eq. 1.11 can properly define the boundary between the stable and unstable regimes of the MTSI.

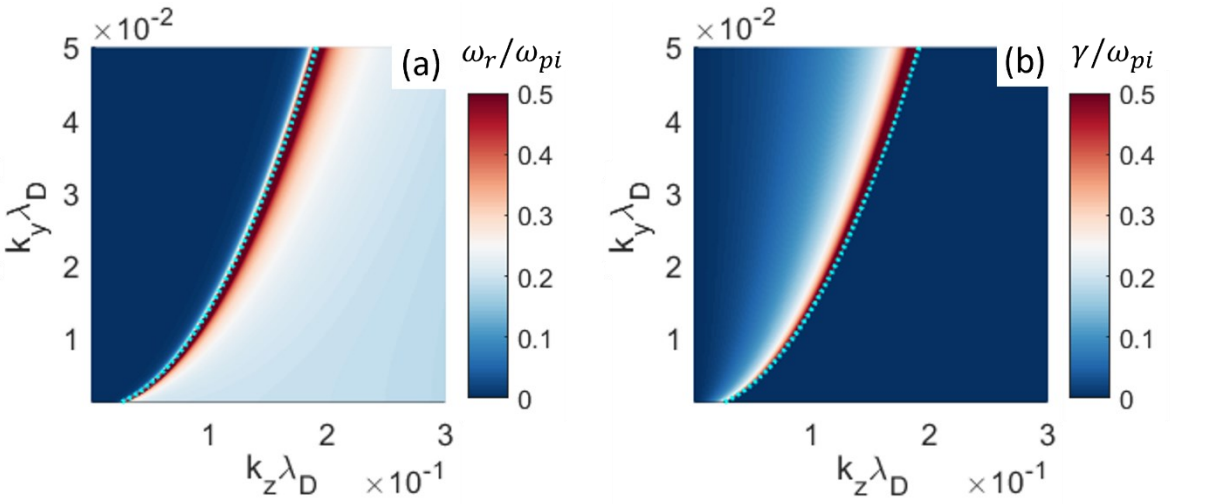


Fig. 1.5: Numerical solution of the MTSI's dispersion relation given by Eq. 1.9 with the plasma and the applied fields conditions corresponding to a radial-azimuthal benchmark problem (see Section 3.2), namely, xenon propellant, $n_i = 1.5 \times 10^{17}\ m^{-3}, E = 10\ kVm^{-1}$ and $B = 20\ mT$; (a) normalized real frequency (ω_r/ω_{pi}), and (b) normalized growth rate (γ/ω_{pi}) of the MTSI. The dotted cyan curves show the loci of the k_y and k_z pairs associated with the MTSI's fastest growing mode as determined by Eq. 1.11.

1.1.3.4. Ion Transit Time Instability

The Ion Transit Time Instability (ITTI) sometimes referred to as resistive instability in literature, is a predominantly axial mid-frequency oscillation in Hall thrusters. The frequency of these oscillations is in line with the inverse of the ions' transit time though the channel (0.1-1 MHz) and their phase velocity is close to the ion axial velocity [36]-[38].

Hagelaar [37] explained the dynamic of the transit-time oscillations. The acceleration region (defined by region of high electric field) oscillates towards the anode and away from it. When the acceleration zone moves towards the anode (upstream), ions in the process of acceleration do not experience the full accelerating voltage drop. Conversely, as the acceleration zone moves downstream, a phenomenon called "wave riding" causes the ions to undergo a larger voltage drop than that available for acceleration. Consequently, the resulting ion beam in the plume consists of two ion populations: (1) fast ions with energies exceeding the accelerating voltage, and (2) slow ions with lower energy than the voltage drop in the acceleration region. The flow of the low- and high-energy ion populations through the channel causes the ion current density profile to oscillate back and forth, which in turn translates into oscillations in the electric field profiles, and the cycle repeats.

Fernandez et al. [38] derived a 1D axial fluid dispersion relation of the instability from the linearized perturbed system of equations comprising continuity and momentum equations for electrons and ions, assuming quasi-neutral plasma, electrostatic fluctuations, and neglecting electron pressure [38]

$$\omega = k_x V_{i,x} - i\frac{\nu}{2} \pm \sqrt{-\left(\frac{\nu}{2}\right)^2 - i\nu k_x\left(V_{i,x} - V_{e,x}\right)}\,. \qquad \text{Eq. 1.12}$$

In the above relation, $\nu = e/m_i\mu_e$, where μ_e is the total axial electron mobility (representing all contributions to electrons' cross-field transport). In the limit of $k_x V_{i,x} \sim k_x V_{e,x} > \nu$ which is often the case in Hall thrusters, Eq. 1.12 leads to one stable and one unstable solution with the frequencies and growth rates given by Eq. 1.13 and Eq. 1.14, respectively

$$\omega \approx k_x V_{i,x} \mp \sqrt{\frac{(k_x V_{i,x} - k_x V_{e,x})\nu}{2}}, \quad \text{Eq. 1.13}$$

$$\gamma \approx \pm i \sqrt{\frac{(k_x V_{i,x} - k_x V_{e,x})\nu}{2}}. \quad \text{Eq. 1.14}$$

According to Eq. 1.14, the growth rate is proportional to $\sqrt{\nu}$, suggesting that the instability is particularly significant under conditions of low electron mobility.

Introducing electron pressure, the dispersion relation is modified to the following form

$$\omega = k_x V_{i,x} - i\frac{\nu}{2} \pm \sqrt{c_s^2 k_x^2 - \left(\frac{\nu}{2}\right)^2 - i\nu k_x (V_{i,x} - V_{e,x})}. \quad \text{Eq. 1.15}$$

In the limit of $k_x\, V_{i,x} \sim k_x\, V_{e,x} \sim k_x\, c_s > \nu$, the real frequency is approximated as

$$\omega \approx k_x (V_{i,x} \pm c_s)\,. \quad \text{Eq. 1.16}$$

Although the frequency and the growth rate are modified in the presence of electron pressure, the overall behavior of the instability remains unchanged including the scaling of the growth rate with the inverse of electron mobility [38].

The axial-azimuthal dispersion relation of the ITTI is derived by Petronio [33]. It was observed that while the non-zero azimuthal wavenumber (k_z) has a minor impact on the frequency of the instability, it can majorly affect the growth rate.

1.1.3.5. Breathing Mode Oscillations

In Hall thrusters, low-frequency (in the range of a few kHz) axial oscillations are known as breathing mode where the entire discharge oscillates in unison [39]-[42]. These oscillations are visible in the thruster's discharge current signal. Being an ongoing topic of research, there is still no consensus on the origin and the exact mechanism deriving the breathing mode instability. However, it is often associated with ionization processes and cyclic depletion and replenishment of neutrals through ionization and consequent cyclic variation in plasma density.

A simple 0D Predator-prey model is proposed by Fife et al. [43] explaining the breathing mode oscillation as a cyclic interaction between the electrons (predator) and neutrals (prey). The cycle begins with the electrons ionizing the neutrals, leading to increased plasma density, and reduction in neutral density. The rise in plasma density increases the ionization rate, which in turn depletes the neutrals. Consequently, with fewer neutral particles available, the ionization rate decreases, causing a decline in plasma density. As plasma density diminishes, so does the ionization rate, allowing neutral gas to accumulate, restarting the cycle. This simple model is described by the following equations

$$\frac{\partial n_i}{\partial t} + \frac{n_i V_{i,x}}{L_i} = \xi_i(T_e) n n_n \,, \qquad \text{Eq. 1.17}$$

$$\frac{\partial n_n}{\partial t} - \frac{n_n V_{n,x}}{L_i} = -\xi_i(T_e) n n_n \,, \qquad \text{Eq. 1.18}$$

where n_i and n_n are ion and neutral number densities, $V_{i,x}$ and $V_{n,x}$ are the axial velocity of the ions and the neutrals, respectively, L_i is the length of ionization region, and ξ_i is the ionization rate coefficient.

By applying a first-order linear perturbation analysis to Eq. 1.17 and Eq. 1.18, where the number densities are represented as $n_i = n_{i,0} + n_i' \exp(i\omega t)$ and $n_n = n_{n,0} + n_n' \exp(i\omega t)$, and considering the equilibrium which yields $n_{n,0}\xi_i = \frac{V_{i,x}}{L_i}$ and $n_{i,0}\xi_i = \frac{V_{n,x}}{L_i}$ and, a simple expression for breathing oscillations' frequency is obtained as

$$\omega = \frac{\sqrt{V_{i,x} V_{n,x}}}{L_i}. \qquad \text{Eq. 1.19}$$

It is noted that Eq. 1.19 provides an overly simplified representation of the breathing oscillations which fails to account for several important effects. As a result, more advanced 1D models are employed by different groups to describe the breathing mode mechanism and origin [42][44]-[47]. These studies showed that the role of the near-node region in the formation of this instability is important. In particular, Chapurin et al. [45] showed that the ion backflow towards the anode significantly impacts the breathing oscillations. Moreover, Lafleur et al. [47] observed that the breathing mode is linked to the time variation of the axial electric field and the nonlinearity in electron power absorption. Hara et al. [46] investigated the role of the perturbations in electron energy. They found that incorporating ion momentum and electron energy equations alongside ion and neutral continuity equations within a 0D model results in undamped ionization oscillations. Furthermore, a two-zone modified predator-prey model accounting for the coupling between the ionization instabilities in the near-anode and in the traditional ionization region is proposed by Dale et al. [48].

1.1.4. Electrons' cross-field transport

The efficient operation of $\mathrm{E} \times \mathrm{B}$ discharges, particularly Hall thrusters, typically relies on effective confinement of electrons' cross-field motion. Various contributions to electron cross-field transport can be identified by looking at the electron azimuthal momentum equation. This equation is derived by taking velocity (v_x) moment of the Boltzmann kinetic equation for electrons [6]. For simplicity, let us focus on a 2D axial-azimuthal ($x - z$) plane. Following the convention from Refs. [19][27][30], Eq. 1.20 represents the electrons' azimuthal momentum equation integrated over the azimuthal direction

$$-e n_e v_{e,x} B_y = \frac{\partial}{\partial t}\left(m_e n_e v_{e,z}\right) + \frac{\partial}{\partial x}\left(m_e n_e v_{e,x} v_{e,z}\right) + \frac{\partial}{\partial x}\left(\Pi_{e,xz}\right) - R_{en} - e n_e E_z \,. \qquad \text{Eq. 1.20}$$

In the above equation, the left-hand-side term is called the magnetic force (F_B). On the right-hand side (RHS), the first term is the temporal inertia (F_t), the second term is the convective inertia (F_I), the third term represents the viscos effects ($F_{\Pi_{xz}}$) corresponding to the off-diagonal component of the electron pressure tensor ($\Pi_{e,xz}$), and the fourth term represents the electron-neutral collision force. The

last term is the electric force term (F_E) comprising both the steady ($\bar{n}_e\bar{E}_z$) component, which is typically zero, and the fluctuating ($\tilde{n}_e\tilde{E}_z$) component.

Accordingly, the impact of the azimuthal instabilities on the electrons is due to the existence of a correlation between azimuthal oscillations in electron number density (n_e) and the azimuthal electric field (E_z) such that the spatiotemporal average of $\tilde{n}_e\tilde{E}_z$ term is non-zero. This term is interpreted as instability-enhanced "friction" force between electrons and ions [30] acting on the electrons in the opposite direction of their azimuthal drift, which then leads to an increased electron flux in the axial direction. Furthermore, based on the experimental observation and numerous numerical investigations, the current consensus is that azimuthal instabilities play a major role in the electron transport across the magnetic field [1][2].

1.2. Hall thrusters: proving ground for plasma physics studies and important technology for spacecraft propulsion

Hall thrusters are electrostatic plasma propulsion technology that have an extensive heritage of in-space application and are today prime candidates to access the next generation of near-Earth and interplanetary missions. Similar to other Electric Propulsion (EP) concepts, Hall thrusters provide specific impulse values of at least an order of magnitude higher than the chemical thrusters, thus offering huge propellant mass advantages at the satellite level. The great applied interest in the Hall thruster technology is mainly driven by the fact that, compared to other EP technologies on the market, Hall thrusters additionally feature a unique combination of high efficiency, high thrust-to-power ratio, ease of manufacturing and operational versatility. They are currently used for a variety of purposes such as attitude control, orbit maintenance and orbit raising. However, application of these devices and mission scenarios based on Hall propulsion systems are expanding. They are recently being considered for the emerging missions such as in-orbit servicing, transportation, and interplanetary exploration missions to farther destinations.

Hall Thrusters exist in a wide range of power levels from a few hundred Watts to tens of Kilowatts. Accordingly, the propulsive force (thrust) they generate ranges from a few mN to $1\ N$ depending on their operating power. Their specific impulse varies between 1000 to $3000s$.

Hall thrusters not only hold significant industrial relevance but also serve as proving ground to represent the complex physics in $\mathrm{E}\times\mathrm{B}$ plasmas, particularly instabilities and their interactions. This is because of several reasons: first, the plasma configuration in this device represents a perpendicular orientation of the applied electric (E) and magnetic (B) fields, featuring rich underlying physics owing to the presence of instabilities and turbulence that extend across a broad spectrum of spatial and temporal scales [1][2][10][39]. Second, the Hall thruster's $\mathrm{E}\times\mathrm{B}$ configuration closely matches many other industrially relevant low-temperature plasma sources. Third, Hall thrusters' setup presents a relative convenient accessibility and affordability for numerical and experimental physics studies, the insights from which can inform the research across the different plasma regimes and applications. All these factors make the industrially important, laboratory-scale Hall thruster plasma technology a suitable test

bed to investigate unknowns in fundamental plasma physics surrounding plasma instabilities' interactions with magnetic fields and their influence on charged particles' motion.

1.2.1. Overview of Hall thruster design concepts and operation principle

Hall thrusters are designed to ionize a neutral gas injected into their discharge channel, typically via DC electron bombardment, and to accelerate the resulting ions in order to generate thrust [49]. The geometry of a Hall thruster is such that the centerline of its discharge channel along the thruster's axis determines the axial coordinate. The wall-to-wall direction of the channel is the radial coordinate, and the direction along the channel circumference indicates the azimuthal coordinate, which completes a right-handed coordinate system. In an idealized case, the electric field is along the axial direction, whereas the magnetic field is radially oriented. The E-field is self-consistently generated and maintained, whereas the B-field is externally applied. The intensity of the B-field is such that the electrons are fully magnetized, but the ions are mostly non-magnetized and are accelerated under the influence of the electrostatic field. **Fig. 1.6** shows a schematic representation of Hall thrusters.

Typically, in Hall thrusters, the magnetic field features a strong gradient along the axial direction of the thruster's discharge channel, and a moderate gradient along the radial direction [49][50]. In conventional Hall thrusters, the field has a concave curvature in the axial-radial plane upstream of the axial location of the magnetic field peak intensity, which typically occurs near the exit plane of the channel. Downstream of the magnetic field peak, the field lines have a convex curvature. About the location of the B-field peak, the field lines are mostly radial with no notable curvature.

Hall thrusters typically have an annular axisymmetric channel made of dielectric materials like Alumina or Boron nitride. The channel is surrounded by a magnetic circuit consisting of a set of electromagnets to generate the field and a ferromagnetic body which is designed to provide a mainly radial magnetic field near the exit of the channel. At the back end of the channel, there is an annular anode which also serves as a gas distributor through which the propellant is injected. The cathode is placed in front of the channel (externally mounted) or at the center of the thruster (centrally mounted) to neutralize the ion beam exiting the thruster. The cathode has an emitter which emits electrons through thermionic emission [49]. The energy to overcome the work function of emitter material is provided by a heater during ignition phase, and by the plasma heat deposited on the surface of the emitter during steady operation.

The propellant is injected into the channel from the anode side and a voltage is applied between the anode and the cathode. The electrons emitted from the cathode, on their way towards the anode, must pass though the radial magnetic field. The Lorentz force due to the radial magnetic field and axial electric field put electrons in an azimuthal $\mathrm{E} \times \mathrm{B}$ drift. The azimuthal drift of electrons serves two purposes. First, it hinders electrons from reaching quickly to the anode and hence increases the residence time of electrons inside the channel besides increasing the energy of the electrons. Thus, the drifting electrons have enough time and energy to collide with neutrals and ionize them. The newly born secondary electrons together with those primary ones form an ionization avalanche which sustains the discharge. Second, the barrier that the electrons feel against their axial movement due to the radial magnetic field

resembles a resistance enabling the establishment and sustainment of a strong electric field in the near channel exit region that would otherwise be short-circuited. Ions on the other hand, remain unmagnetized (as their Larmour radius is larger than channel dimensions) which are accelerated out axially in this axial electric field and create thrust.

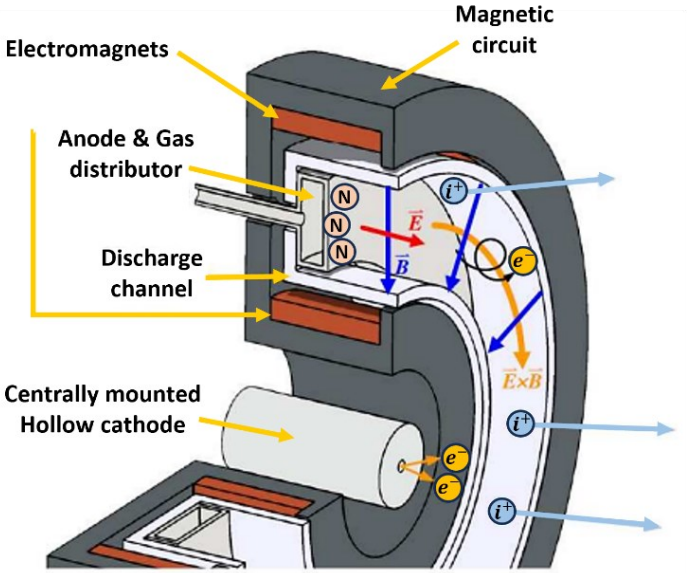


Fig. 1.6: Schematic of Hall thruster. Adapted version of the original artwork from Ref. [51], available in the public domain.

1.2.1.1. Magnetically shielded Hall thrusters

The erosion of thruster's ceramic channel, especially near the channel exit, is a major life-limiting factor for Hall thrusters. In recent years, there have been some attempts to mitigate the channel erosion and extend the operating life of these thrusters among which the technique of "magnetic shielding" has demonstrated great promise [52]-[55]. Magnetic shielding is achieved by designing the topology of magnetic field in a way to detach the plasma from the channel wall and minimize the plasma-wall interaction and, as a result, extend thruster's lifetime by at least one order of magnitude.

The idea of magnetic shielding is based on two principles: isothermality and equipotentiality of the magnetic field lines [52]. In partially magnetized plasmas, there is a significant disparity in electrons' mobility along and across the magnetic field directions. The substantial mobility of electrons along the magnetic field lines results in rapid achievement of their equilibrium along the field lines, thereby rendering them effectively isothermal in this direction ($\nabla_\mu T_e \approx 0$, where μ denotes the direction parallel to the local magnetic field's direction). Furthermore, the electrons' momentum equation along the magnetic field at equilibrium and in the absence of resistive forces is written as

$$\nabla_\mu P_e = \nabla_\mu (n_e K_b T_e) = e n_e \nabla_\mu \phi \qquad \text{Eq. 1.21}$$

Considering that $\nabla_\mu T_e \approx 0$, the above equation is simplified to

$$K_b T_e \nabla_\mu (n_e) = e n_e \nabla_\mu \phi \,. \qquad \text{Eq. 1.22}$$

Integrating Eq. 1.22 along the magnetic field line from $\mu = 0$ at which $n_e = n_{e,0}$ and $\phi = \phi_0$

$$\phi - \frac{K_b T_e}{e} \ln\left(\frac{n_e}{n_{e,0}}\right) = \phi_0 \,, \qquad \text{Eq. 1.23}$$

where ϕ_0 is referred to as the "thermalized potential" and was introduced by Morozov et al. [56] for the first time. Eq. 1.23 states that when the electron temperature and the variations in electron number density are sufficiently small, $\phi \approx \phi_0$. In other words, magnetic field lines tend to become equipotential, and the electric field establishes mostly in perpendicular direction to the magnetic field lines.

However, near the channel exit, plasma density, electron temperature and ion energy are high, resulting in maximum erosion in this region. Therefore, to be able to shield the channel walls especially near the channel exit, we need to manipulate the magnetic field topology to moderate the electron temperature in this region and, thereby allow the electric potential to be predominantly shaped by the magnetic field topology.

This is achieved through having a field line (called "grazing line") to be tangent to the channel chamfers at the exit region. The grazing line is required to penetrate deep into the channel and approach the anode surface where electron temperature is relatively low. As electrons freely move along the filed lines, the colder electrons in near anode region move along the grazing line towards the exit and moderate the electron temperature there. The lower electron temperature then provides the necessary condition for the equipotentiality along this line. Since the grazing line approaches the anode, the electric potential on this line is close to the anode potential, while the adjacent lines away from the wall are of lower potentials. This leads to the establishment of an electric field perpendicular to the wall in the exit region, where the line is almost tangent to the wall. This normal electric field retards ions from reaching the wall. Also, lower electron temperatures and large electric potential (close to that of the anode) cause lower potential drops perpendicular to the wall due to formation of a weaker sheath, thus, further reducing the ion flux to the wall. Additionally, the large curvature of magnetic field lines in this configuration gives rise to magnetic mirror effect which in turn impedes electrons' movement towards the walls in the exit region. **Fig. 1.7** schematically illustrates the magnetic shielding and the conventional magnetic field topologies.

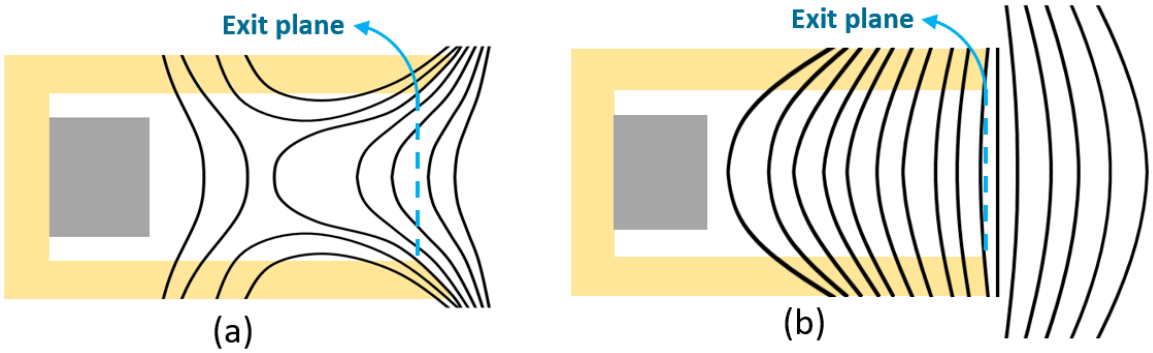


Fig. 1.7: Schematic of the magnetic field topology in (a) magnetically shielded and (b) conventional Hall thrusters.

1.2.1.2. The 3D nature of plasma interactions in Hall thrusters

Accurate prediction of plasma behavior in Hall thrusters requires a 3D kinetic model, as the underlying kinetic processes inherently involve all three dimensions. Regarding the significance of accounting for each dimension, firstly, the plasma properties have variation along the thruster's axis

which needs to be resolved. Furthermore, resolution in the axial direction captures the convection of the azimuthal instability into the near-plume region. Secondly, the wall losses can have a significant impact on thruster's performance and behavior which are captured in the radial direction. Besides, in magnetically shielded Hall thrusters due to the particular topology of the magnetic field, the radial gradients are significant which makes resolving this direction even more important than in conventional thrusters. Lastly, the resolution of azimuthal dimension in Hall thruster simulations is necessary in order to be able to self-consistently capture the azimuthal instabilities and their contribution to the electrons' axial transport.

In this regard, the ECDI, as one of the dominant role-players in the enhancement of the electrons' cross-field transport has a 3D nature. Moreover, this instability is among the most influential instabilities in Hall thruster as it can modify the plasma properties significantly by its resonant interactions with particles and heating. However, to capture accurately the characteristics of this instability and in turn its consequence on plasma, we need to resolve all the three spatial dimensions. Recent works have shown that ECDI is connected to the behavior of the plasma along the magnetic field (mostly radial) and in the direction of electric field (mostly axial). In fact, although this instability is mostly azimuthal, it has been discovered that its wavevector components along the magnetic field and the axial direction might be non-negligible [57][58]. As mentioned in Section 1.1.3.1, the finite wavenumber along the magnetic field can smooth out the resonant "comb-like" features in the instability's dispersion relation, facilitating its transition to the Ion Acoustic Instability [16][18]. Indeed, it has been recently discovered that, while the waves spectrum in 2D axial-azimuthal simulations exhibits discrete dominant modes (a possible artifact of not resolving the radial dimension), in reality, the instability's dispersion is more continuous over a wider range of wave modes [16][18].

Moreover, although it appears that Near-Wall Conductivity (NWC) phenomenon [59] plays a minor role in the electrons' transport (especially in magnetically shielded configurations), Secondary Electron Emission (SEE) may contribute to the saturation of the ECDI [7]. Therefore, the kinetic simulations of lower dimensionality (1D or 2D) have certain limitations and shortcomings. The 2D axial-azimuthal simulations predict stronger instabilities than 3D models and the experimental observations due to not accounting for the nonlinear coupling of the waves with secondary electrons emitted from the walls. This leads to a substantial overestimation of the waves' amplitude and electrons' transport [1].

Finally, another important instability, the MTSI, which has both azimuthal and radial wavevector components, cannot be captured in simulations that do not account for the radial dimension self-consistently. This instability is also observed to have a significant impact on the plasma, particularly in terms of heating and particles' transport [2][12][28], highlighting the importance of resolving it properly.

1.3. Review of the available numerical approaches to study plasmas

To predict plasma behavior and study the involved physical processes, there are different computational tools and numerical simulations which may vary significantly in terms of complexity, computational cost and fidelity. In general, the plasma modelling techniques can be divided into three main categories:

A) **Fully-fluid simulations**, which solve a system of conservation equations consisting of a hierarchy of velocity moments of Boltzmann's equation [60][61] for each species (electrons, ions and neutrals). The resulting system of equations is typically closed with the assumption of Maxwellian distribution functions for plasma species and neutrals. This assumption leads to simplifying approximations, such as assuming isotropic pressure and neglecting the off diagonal (viscus) terms in the pressure tensor in electron momentum equation. Sometimes the electron inertia terms are neglected as well, which reduces the equation to the "drift-diffusion" form [10]. The pressure term is normally ignored for ions as they are believed to remain cold throughout the thruster channel. This will then eliminate the need for solving the ion energy equation. For the case of assuming quasi-neutrality, the Poisson's equation is no longer needed as the electric field can be obtained from electron momentum equation (generalized Ohm's law [61]). Most of the available fluid models are 2D axisymmetric and used to simulate the distribution of plasma parameters in axial-radial dimensions.

B) **Kinetic simulations**, which are carried out either using Direct Kinetic (DK) [62] or particle-in-cell (PIC) approaches [63][64]. These models do not make any assumption on the particles' distribution functions. Direct Kinetic simulations are Eulerian approaches which resolve the evolution of distribution function by solving the Boltzmann's (or Vlasov's equation for a collisionless case) on a computational grid which includes velocity and configuration space (phase-space). DK simulations typically involve some approximations to overcome the computational expense associated with the additional dimensions introduced by the need for resolution of velocity space.

   The PIC simulations provide a Lagrangian alternative. In these models, the velocity distribution function is sampled, and each sample is represented by a macroparticle. The collection of the macroparticles then resembles a discretized version of the distribution function. The simulation integrates the equation of motion to advance the trajectory (velocity and position) of charged macroparticles under the influence of electromagnetic forces. Maxwell's equations are solved on a computational grid to compute the electromagnetic fields resulting from the motion and spatial distribution of the charged particles. The PIC models are usually combined with the Monte Carlo collision algorithm [65], leading to the PIC-MCC simulations that account for various types of elastic and inelastic collisions. A detailed description of PIC simulations is provided in Section 1.4.2.

C) **Hybrid fluid/PIC simulations**, in which ions are considered as particles and electrons are treated as fluid [61]. The fluid approximation of the electrons relies on their significantly shorter timescales compared to the timescale of the simulation. This prompts the assumption of the electrons' rapid thermalization and the achievement of an "equilibrium" state.

1.4. Particle-in-cell scheme for kinetic plasma modelling

The PIC simulations are suitable for the study of the kinetic behavior of complex plasmas such as those in Hall thrusters, due to their first principles treatment of the particle dynamics, and in turn high-fidelity and self-consistency of their prediction. The fluid and hybrid simulations, on the other hand,

involve approximations and assumptions, some of which are not appropriate to study dynamics of $\mathrm{E} \times \mathrm{B}$ plasmas and Hall thrusters. In particular, their underlying assumption of Maxwellian distribution function is not entirely valid for the plasma in Hall thrusters where the density and therefore interparticle collisions are not sufficient to "thermalize" the distribution function. Many phenomena in these devices are intrinsically due to deviations from Maxwellian distribution and kinetic interactions in velocity space such as micro-scale kinetic instabilities and their impact on plasma properties and electron transport.

One of the major limitations of fluid-based simulations is their inability to capture the instability-induced transport self-consistently. As a result, kinetic information that is not resolved with the fluid approximation needs to be incorporated in the simulation through ad-hoc empirical electrons' transport parameters and implementation of proper closure models. There have been some efforts to develop transport closure models for fluid-based simulations, most of which either rely at least partially on experimental data for reliable prediction [66] or are not generalizable to the various operation conditions [67].

Apart from the kinetic instabilities, there are other plasma processes for which fluid approximation is not suitable, such as plasma-wall interactions. The high energy tail of the particles' distribution function plays a significant role in the erosion of the confining walls of the device (ceramic channel in case of Hall thrusters) [68]. Therefore, to study the sheath dynamics and the erosion induced by the particle interactions with the walls, appropriate treatment of the electron distribution function and resolving the high-energy tail are necessary.

1.4.1. State-of-the-art and limitations of PIC modelling of technological plasmas

Although the traditional fully kinetic PIC codes are essential for prediction of the operation and performance of the Hall thrusters and similar plasma technologies, their remarkable computational and memory demands make them impractical for real-world applications. To provide a quantitative sense to this computational cost, according to Ref. [69], simulating $150\ \mu s$ of discharge evolution in a medium-power-class $5\ kW$ Hall thruster in the axial-azimuthal configuration would require more than a year on 1500 CPUs. Furthermore, recently a $10\ \mu s$-long 3D simulation is performed by Villafana et al. [70] to study high-frequency instabilities in a geometry representative of a medium-sized Hall thruster with a computational cost of 1.4×10^6 CPU hours. The enormous computational demand of such a short-duration 3D simulation evidences the unfeasibility of traditional PIC methods for practical purposes.

The computational cost associated with the PIC simulations stems from the following factors.

A) Strict requirements on the numerical parameters: These numerical parameters are computational grid's cell size (Δx), time step (Δt) and number of macro-particles per cell (N_{ppc}). The selection of the cell size and time step requires a knowledge of the involved spatial and temporal scales in plasma, namely the Debye length and the characteristic time corresponding to electrons oscillations [63][64]. Debye length is a typical distance over which charge perturbations can exist. In the face of an electric disturbance, plasma particles tend to collectively rearrange to mask the perturbations in a distance on the order of the Debye length [4]. This Debye shielding keeps the plasma quasi-neutral over length scales larger than the

Debye length. Therefore, in order to capture non-quasi-neutrality and the phenomena driven by it, the grid size needs to be less than the Debye length.

The plasma frequency is the frequency by which electrons oscillate in response to a charge disturbance to restore the charge neutrality [4]. The simulation time step must be smaller than the time scale of these oscillations. Another important time scale in the magnetized plasmas is related to the cyclotron motion of the electrons about magnetic field lines. However, as for typical plasma conditions in Hall thrusters and other low temperature $\mathrm{E} \times \mathrm{B}$ discharges, the cyclotron frequency is smaller than the plasma frequency, the time step is mainly restricted by plasma oscillations time scale. The Debye length (λ_D), plasma frequency (ω_{pe}) and cyclotron (ω_{ce}) frequency are defined as

$$\lambda_D = \sqrt{\frac{\epsilon_0 K_B T_e}{n_e e^2}}, \qquad \omega_{pe} = \sqrt{\frac{n_e e^2}{m_e \epsilon_0}}, \qquad \omega_{ce} = \frac{eB}{m_e}. \qquad \text{Eq. 1.24}$$

Accordingly, the stability of the PIC requires Δx and Δt to meet the following criteria [63][64]

$$\Delta x < \lambda_D\,, \qquad \Delta t < \frac{0.2}{\omega_{pe}}. \qquad \text{Eq. 1.25}$$

For the typical plasma conditions in Hall thrusters, the simulations require a cell size on the order of ten micrometers and a time step on the order of picoseconds.

B) Large disparity in the scales of the involved phenomena: The time scale of the phenomena taking place in Hall thrusters ranges from 10^{-12} to 10^{-3} seconds. The fastest processes are mainly driven by electron dynamics like plasma oscillations and micro-instabilities, and the slowest ones are regulated by heavy species (ions and neutrals) such as the breathing oscillations. This means that the time step must be very small to resolve the electron dynamics (which are discussed above), while the total simulated time needs to be long enough to capture at least a few cycles of breathing mode.

C) Numerical noise: Due to the discretized treatment of the particles' distribution functions, PIC simulations are subject to non-physical and spurious behaviors such as statistical noise, non-physical instabilities, non-conservations, and numerical heating. In general, the number of macroparticles per cell, which is a measure of the statistical quality of the sampled local distribution function in each computational cell, determines the noise level in PIC simulations.

The PIC algorithm is composed of Lagrangian particles and an Eulerian grid-based model for the electromagnetic fields. The underlying particle distributions are basically continuous in space which needs to get deposited onto the grid to represent the charge and current densities required for the solution of the electromagnetic fields. This corresponds to sampling a continuous variable with a sampling rate that is inversely correlated with the cell size, which in turn leads to aliasing effects. These aliasing effects are major sources of numerical instabilities in PIC simulations. In fact, the typical solvers used for solving the Maxwell's equations are most often stable per se, provided the CFL stability condition is respected. However, when coupled to a Lagrangian particle model, the solver becomes susceptible to numerical instabilities [71].

Furthermore, particles crossing the grid cells could cause high frequency noise which can be mitigated using higher order interpolation schemes for deposition of particles' charge on the grid, though at the expense of heavier computations. Although, in most cases the numerical noise itself is distinguishable from the physical modes (as the high frequency tail in the frequency spectrum), their consequence on the plasma (such as heating) is not.

Another main source of error in PIC simulations is numerical diffusion in velocity space and thermalization which distorts the particles' energy distribution function, which can occur due to finite number of macroparticles. This diffusion can be manifested as self-heating (i.e., an increase in the random kinetic energy of the particles) or thermalization which relaxes the particles' distribution functions towards a Maxwellian.

These numerical effects can be alleviated by reducing the cell size (which reduces aliasing effects) and increasing the number of macroparticle per cell to improve the statistics (which reduces the numerical diffusion and thermalization [72]), both ultimately translating into heavier computations.

1.4.1.1. Conventional speed-up techniques to tackle PIC's computational cost

There are some techniques commonly employed to tackle the enormous computational cost of the PIC simulations, the most popular of which are enumerated below.

A) **Scaling physical parameters:** These techniques are based on artificially scaling some physical parameters to either relax the numerical requirements (cell size and time step) or bridging the gap between the time scales related to the fast and slow species. In particular, increasing the free-space permittivity allows us to adopt larger cell sizes and time steps [73]. Also, scaling down the ion to electron mass ratio speeds up the ion dynamics which reduces the total time needed to be simulated [73]. Opposite to this is an approach called "speed-limited PIC", in which the electrons are slowed down, and their speed is restricted, allowing for larger time steps while maintaining the stability of the explicit PIC algorithm [74].

B) **Geometrical downsizing:** A smaller computational domain can be used as a representation of geometrically downscaled thruster. The downsizing is done according to the Hall thruster zeroth-order scaling laws [75] to maintain the relevant non-dimensional parameters constant. The relative self-similarity of the down-scaled and full-scale simulations is valid for limited scaling factors, as beyond some point the volume to surface ratio of plasma changes significantly. In such a case, due to being in close vicinity of the walls, the bulk plasma is non-neutral, and the physics is dominated by the sheath dynamics.

C) **Merging-splitting algorithm for macroparticles**: Usually, PIC simulations adopt a constant macroparticle weight for same species macroparticles. To ensure having enough number of macroparticles per cell throughout the domain, the macroparticles' weight must be determined based on the minimum number density in the system. Given the significant variation in number density along the thruster axis, most cells end up with more macroparticles than needed, resulting in an unnecessarily large total count of macroparticles. Assuming variable macroparticle weights can address this issue. They can then "merge" or "split" depending on

whether the number of macroparticles in a cell that they reside in is larger or smaller than required. The implementation of this algorithm, however, is complicated especially in terms of satisfaction of mass, momentum, and energy conservations [76].

D) Particles sub-cycling: Due to the difference in the velocity of various species and therefore their characteristics timescales, it is possible to use different time steps to update each species particles. This means that faster species get updated more frequently than the slower ones.

Application of some of these techniques, especially scaling of physical parameters and geometrical sizes, however, can alter physics quite substantially, and therefore needs a countermeasure to recover the true physics. The merging-splitting and particle sub-cycling are expected not to influence the results appreciably, but they do not offer remarkable computational advantage to make large scale simulations entirely affordable.

1.4.1.2. Recent techniques to alleviate PIC's numerical constraints

A) Energy Conserving (EC) and Direct implicit (DI) PIC methods: It was pointed out in Section 1.4.1 that the standard PIC algorithms, often referred to as "explicit momentum conserving (EM)", are limited by stringent numerical stability criteria particularly concerning the cell size and the timestep of the PIC simulations. In certain plasma physics problems, the phenomena of interest occur over length and timescales that are larger than the numerical constraints imposed by the EM PIC code. For these scenarios, methods that can enable circumventing the EM PIC constraints on the cell size and timestep are desirable.

The "explicit energy conserving (EC)" [77] and the "direct implicit (DI)" [78] PIC algorithms were proposed in the 1970s and 1980s as approaches to alleviate the strict cell size and timestep constraints of the EM PIC codes. Both methods involve rather straightforward implementations, although the DI PIC algorithm is relatively more complex than the EC PIC algorithm. A comprehensive explanation of these PIC methods along with their detailed assessment results for simulations of in a benchmark case can be found in Ref. [79].

As a brief overview, EC PIC [77] allows adopting cell sizes that are larger than the Debye length ($\Delta x \gg \lambda_D$). This PIC approach strictly conserves energy at the limit of $\Delta t \to 0$. At finite timesteps, the energy growth will still be diminishingly small as long as the plasma frequency is properly resolved, i.e., $\omega_{pe}\,\Delta t \leq 0.2$. The downsides of this approach are that by opting for energy conservation, the momentum of plasma is no longer conserved. Moreover, EC PIC is not suitable for modelling plasma problems involving accelerated beams of particles where the velocity of the beam is larger than the thermal velocity of the particles [80].

The DI PIC [78][81] modifies the standard PIC algorithm via a single linear correction [79] so as to allow for cell sizes larger the Debye length ($\Delta x \gg \lambda_D$) and also timesteps somewhat larger than the plasma oscillations' time scale ($\Delta t > 0.2\omega_{pe}^{-1}$). In practice, care must be taken when choosing the values of the cell size and the time step. In fact, the DI PIC approach is not necessarily energy conserving, but it is demonstrated in Ref. [79] to show good energy-conserving properties for the optimal cell-size-to-timestep ratio ($\Delta x/\Delta t$) of $0.1v_{th,e}$, with $v_{th,e}$ being the electrons' thermal velocity. The approach can break down if the simulations timestep

and cell size are simultaneously chosen to be much larger than the plasma frequency and the Debye length [79]. To address this problem, one can opt for fully implicit PIC simulations (see, e.g., Ref. [82]). Fully implicit PICs can provide exact charge and energy conservation with arbitrary cell size and time step selections. However, the fully implicit PIC is highly complicated to implement and, additionally, requires a fully nonlinear global solvers [82]. Hence, fully implicit PICs entail the highest computational cost compared to the EC PIC and DI PIC methods.

B) Sparse Grid (SG) method: The sparse grid (SG) method is a technique used in computational mathematics, particularly for addressing the computational burden of high-dimensional spaces. It aims to approximate functions or solve partial differential equations (PDEs) while keeping the involved computational costs to a minimum. The SG approach, which is based on a higher dimensional multiscale basis, was first introduced by Zenger in 1991 [83] and has since been extensively studied in the applied mathematics contexts [84]-[87].

The SG method involves constructing a sparse grid comprising a set of hierarchical sub-grids with different resolutions. Once the sparse grid is constructed, the solution to the problem is approximated by combining the solutions obtained from each sub-grid level, using a method known as the combination technique [84].

Resent works have implemented the SG method in electrostatic PIC simulations [88]-[91]. The SG discretization leads to a reduction in the number of grid cells from $O(N^d)$ of conventional approaches to $O(N.(logN)^{d-1})$, where d denotes the problem's dimension, and N is the number of cells along one dimension. The error of approximation can be reduced by using more sub-grids but at the cost of reducing the computational gain. According to Refs. [89][90], the speed-up factors achieved using SG PIC for a 2D problem ranges from $2-6.5$ depending on the accuracy of the approximate solution. The speed-up factors could reach up to about 70 times in 3D simulations.

1.4.2. Overview of conventional electrostatic PIC algorithm

As the applied magnetic field in Hall thrusters and similar $\mathrm{E}\times\mathrm{B}$ discharges is large compared to the current-induced field, the magnetostatic approximation is reasonably valid. Therefore, we focus on the electrostatic PIC simulation, where a temporally constant magnetic is externally imposed and only the electric field is allowed to vary as the simulation evolves.

This section provides an overview of the electrostatic PIC mathematical basis and numerical algorithm as well as introducing the conventional branches of the IPPL code, namely IPPL-1D and IPPL-2D, developed within this work. All branches of the IPPL code treat the velocity space along all the three velocity dimensions (3V).

1.4.2.1. Mathematical foundation of PIC

The electrostatic PIC algorithm is a statistical numerical modelling technique whose solution satisfies the Vlasov-Poisson's system of equations for plasma systems

$$\frac{\partial f_s(t,\boldsymbol{x},\boldsymbol{v})}{\partial t}+\boldsymbol{v}\cdot\nabla_x f_s(t,\boldsymbol{x},\boldsymbol{v})+\frac{q_s}{m_s}(\boldsymbol{E}+\boldsymbol{v}\times\boldsymbol{B})\cdot\nabla_v f_s(t,\boldsymbol{x},\boldsymbol{v})\ =0, \qquad \text{Eq. 1.26}$$

$$\boldsymbol{\nabla}^2\phi(t,\boldsymbol{x}) = -\frac{\rho(t,\boldsymbol{x})}{\epsilon_0} = -\frac{1}{\epsilon_0}\sum_{s=i,e} q_s\, n_s\,(t,\boldsymbol{x})\,, \qquad \text{Eq. 1.27}$$

where,

$$n_s(t,\boldsymbol{x}) = \int_{-\infty}^{+\infty} f_s(t,\boldsymbol{x},\boldsymbol{v})d^3\boldsymbol{v}\,, \qquad \text{Eq. 1.28}$$

and

$$\boldsymbol{E}(t,\boldsymbol{x}) = -\boldsymbol{\nabla}\phi(t,\boldsymbol{x})\,. \qquad \text{Eq. 1.29}$$

In the above equations, $f_s(t,\boldsymbol{x},\boldsymbol{v})$ is the distribution function of each plasma species (electrons or ions, $s \equiv e,i$), $\boldsymbol{v}$ is the velocity, q_s is the species' charge, m_s is the species' mass, $\boldsymbol{E}$ is the electric field, ϕ is the plasma electric potential, ρ is the charge density, and n_s is the species number density. $\boldsymbol{B}$ is the magnetic field, which is imposed and constant in electrostatic problems. The bold quantities are vectors. It is computationally impractical to integrate Eq. 1.26 to directly obtain the several dimensional distribution function of each plasma species. Accordingly, the so-called "PIC ansatz" is that the distribution function can be approximated by a collection of statistical samples of the distribution function of the following form, which are called "macroparticles" [92]

$$f_s(t,\boldsymbol{x},\boldsymbol{v}) = \sum_{p=1}^{N} \mathcal{W}_p\, S(\boldsymbol{x})\delta\left(\boldsymbol{v}-\boldsymbol{v}_p(t)\right). \qquad \text{Eq. 1.30}$$

In Eq. 1.30, $\mathcal{W}_p$ is the weight of each macroparticle (i.e., the number of real plasma particles it represents),$\boldsymbol{v}_p$ is the velocity of the macroparticle p, S is the shape factor in the physical 3-dimensional space (configuration space), and δ is the Dirac's delta function in the velocity space. For linear particle shapes, the shape factor in 1D, e.g., is $S_p(x) = S\left(\frac{x-x_p}{\Delta x}\right)$ with

$$S(x) = \begin{cases} 1-|x|, & |x| \le 1 \\ 0, & |x| > 1 \end{cases}, \qquad \text{Eq. 1.31}$$

and $\boldsymbol{x}_p$ being the position of the macroparticle p and Δx is the computational cell size.

Substituting Eq. 1.30 in Eq. 1.26, and taking first order moments in x and v, separately we retrieve the equations of motion (Eq. 1.32 and Eq. 1.33, respectively) for each macroparticle of species s [92]

$$\frac{d\boldsymbol{x}_p(t)}{dt} = \boldsymbol{v}_p(t), \qquad \text{Eq. 1.32}$$

$$m_p\frac{d\boldsymbol{v}_p(t)}{dt} = q_s\left(\boldsymbol{E}(t,\boldsymbol{x}_p) + \boldsymbol{v_p}(t)\times\boldsymbol{B}(t,\boldsymbol{x}_p)\right). \qquad \text{Eq. 1.33}$$

Thus, starting from an initial condition, by integrating the equation of motion (Eq. 1.32) for each macroparticle at every time step, the resulting distribution function (Eq. 1.30) will effectively satisfy the Vlasov equation (Eq. 1.26).

1.4.2.2. Numerical implementation of PIC

In the following, the details of the explicit electrostatic PIC algorithm as implemented in IPPL-1D and IPPL-2D codes together with a brief description of the main functions and modules are presented. The IPPL codes are written entirely in Julia language [93]. All branches of the IPPL code are parallelized on CPU using domain decomposition technique. The results of rigorous benchmarking of the individual

modules as well as the entire code in 1D and 2D standard benchmark cases are provided in Appendix A.1.

The PIC algorithm comprises a main loop which is executed at every time step (Δt) as illustrated in **Fig. 1.8**. The loop's core functions include particle pusher, electric field (Poisson) solver, scatter and gather functions, particles boundary conditions, particles sampling and injection, and diagnostics. The PIC algorithm will then couple with Monte Carlo Collision (MCC) function for electron-neutral and ion-neutral collisions, and neutral dynamics module based on either fluid Euler system of equations or Direct Simulation Monte Carlo Collision (DSMC) model.

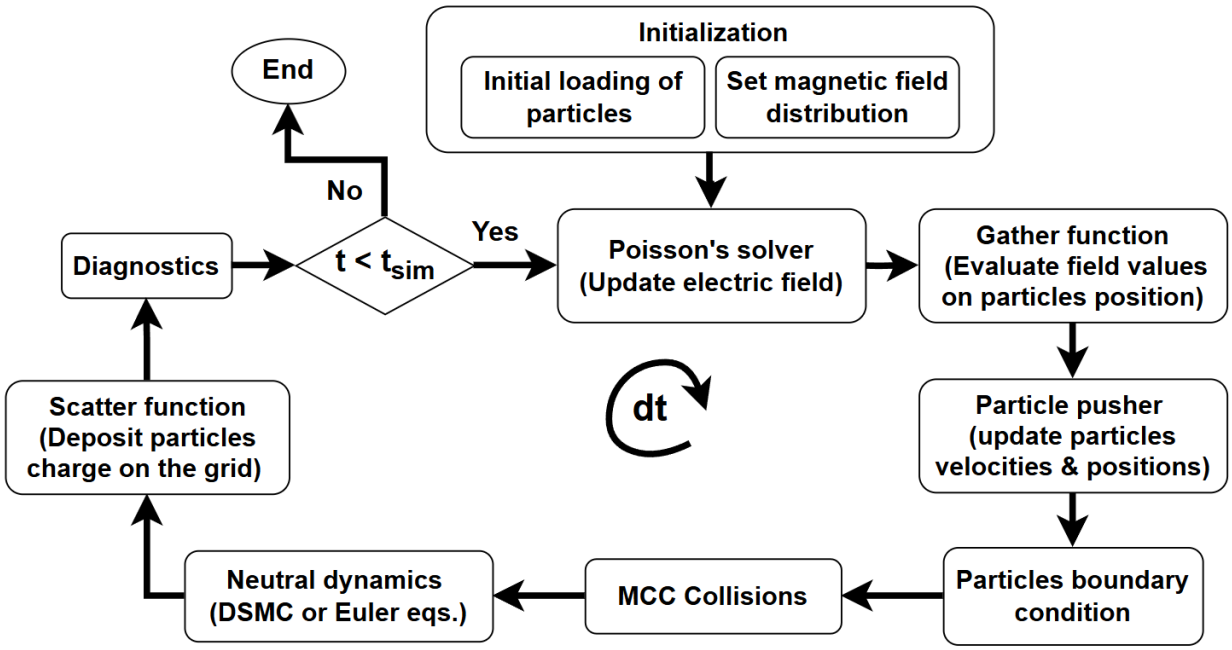


Fig. 1.8: Electrostatic PIC loop diagram including the MCC collisions and the neutral dynamics module.t_{sim} represents the total simulated time.

A) Particle pusher: The particles' position ($\boldsymbol{x}_p$) and velocity ($\boldsymbol{v}_p$) are updated by integrating the equation of motion under the influence of electromagnetic fields

$$m\frac{d\boldsymbol{v}_p}{dt} = e\left(\boldsymbol{E} + \boldsymbol{v}_p \times \boldsymbol{B}\right), \qquad \frac{d\boldsymbol{x}_p}{dt} = \boldsymbol{v}_p \qquad \text{Eq. 1.34}$$

The Boris method is applied for the integration of the velocity [94] of the electrons. According to the standard leapfrog method, the time grids for velocity and position are staggered by half a time step ($\Delta t/2$). This is achieved by rewinding all particles upon loading by $\Delta t/2$. In Hall thrusters, ions are often considered unmagnetized (due to their Larmor radius being larger than thruster's dimensions). As a result, ions are typically pushed electrostatically to save computations.

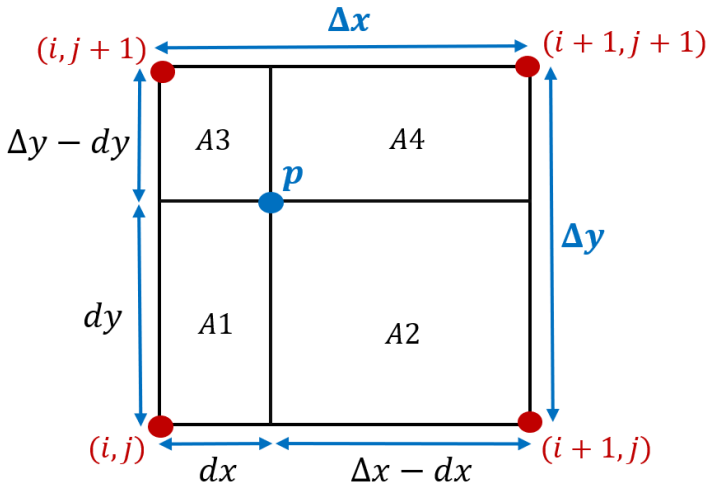
B) Field solver: The electric potential is obtained by solving Poisson's equation (Eq. 1.27) on the computational grid. The solver takes as input the charge density obtained by depositing the particles' charge on the grid. Representative boundary conditions for Hall thruster along different dimensions include: (I) along the axial direction, Dirichlet boundary conditions at both ends of the domain representing the anode and cathode potentials, (II) along the radial direction, either

Neumann condition to account for the dielectric ceramic walls or zero-Volt Dirichlet condition to represent grounded walls, and (III) along the azimuthal direction, a periodic boundary condition to mimic the periodicity. The electric field is then obtained per Eq. 1.29. IPPL code uses Julia's built-in direct matrix solver based on the LU decomposition method to solve Poisson's equation.

C) **Scatter and gather functions:** These functions are responsible for exchanging data between particles (which are continuous in space) and the grid (which is spatially discretized) through a first order (linear) interpolation. Scatter function linearly interpolates particles data on the grid for calculation of charge density (input to Poisson's equation) and calculation of macroscopic flow properties (diagnostics). The gather function evaluates the fields and other macroscopic properties on the particles positions by linearly interpolating the grid nodes' values surrounding the particle. The interpolation coefficients in 2D, e.g., are the partial areas given by $A1, A2, A3$ and $A4$, constructed by the particle location and the nodes of the cell in which the particle resides as illustrated in **Fig. 1.9**. Accordingly, particle's data β_p is scattered on the four surrounding nodes using Eq. 1.35, where $\Delta\beta$ represents the contribution of particle p to the value of β on the grid nodes. Moreover, Eq. 1.36 describes how the grid's data β is gathered at the particles' location based on its values on the neighboring nodes. In this relation, β_p is the collected data at the particle's position.

$$\Delta\beta(i,j) = A_4\beta_p, \quad \Delta\beta(i+1,j) = A_3\beta_p, \quad \Delta\beta(i,j+1) = A_2\beta_p, \quad \Delta\beta(i+1,j+1) = A_1\beta_p. \tag{Eq. 1.35}$$

$$\beta_p(x,y) = A_4\beta(i,j) + A_3\beta(i+1,j) + A_2\beta(i,j+1) + A_1\beta(i+1,j+1). \tag{Eq. 1.36}$$



$$A1 = \frac{dx\,dy}{\Delta x\,\Delta y}, \quad A2 = \frac{(\Delta x - dx)\,dy}{\Delta x\,\Delta y}, \quad A3 = \frac{dx\,(\Delta y - dy)}{\Delta x\,\Delta y}, \quad A4 = \frac{(\Delta x - dx)(\Delta y - dy)}{\Delta x\,\Delta y}.$$

Fig. 1.9: Illustration of interpolation coefficients a in 2D cell. The blue dot represents the particle location, and the red dots are the particle's surrounding grid nodes.

D) **Particle boundary conditions:** The representative boundary conditions on charged particles for Hall thrusters along different directions are as follows.

I) **Azimuthal direction**: Consistent with the periodic boundary condition applied on the electric potential along this direction, all particles reaching one azimuthal boundary will be reinjected into the domain from the opposite boundary while maintaining their velocities and positions along other dimensions.

II) **Axial direction**: On the anode side, electrons reaching the boundary are removed. Ions are recombined on the anode surface and will be reinjected into the domain as neutrals. Neutrals reaching the anode surface are specularly or diffusely reflected. Besides, at each time step, neutrals are injected from the anode surface with a constant rate corresponding to the thruster anode mass flow rate.

On the cathode side of the domain, ions and neutrals are removed. Also, electrons are constantly reinjected from the cathode plane to sustain the discharge. To calculate the rate of electron injection from the cathode, two different models are incorporated based on either of the following conditions.

II.I) Current continuity: In this model, we keep track of the number of electrons and ions reaching the anode or leaving the domain and inject electrons at a rate to satisfy the current continuity throughout the circuit. Different charged particle fluxes are illustrated in **Fig. 1.10**. In this figure, Γ_{ai} and Γ_{ae} are ion and electron fluxes to the anode, Γ_{oi} and Γ_{oe} are ion and electron fluxes leaving the domain from the right boundary. Also, Γ_{ce1} and Γ_{c2} are cathode electron current proportions, the first one enters the channel to sustain the discharge and the second neutralizes the ion beam in the plume. The discharge current is the total current reaching the anode which at steady state is equal to the cathode current

$$\Gamma_{ae} - \Gamma_{ai} = \Gamma_{ce1} + \Gamma_{ce2} \,. \qquad \text{Eq. 1.37}$$

Also, the current balance on the right boundary suggests

$$\Gamma_{oi} = \Gamma_{oe} + \Gamma_{ce2} \,. \qquad \text{Eq. 1.38}$$

Therefore, the flux of electrons to be injected from the cathode plane is obtained as

$$\Gamma_{ce1} = \Gamma_{ae} - \Gamma_{ai} - \Gamma_{oi} + \Gamma_{oe} \,. \qquad \text{Eq. 1.39}$$

Due to the electron removal at the right boundary, a large artificial sheath is formed near this boundary. A more appropriate treatment of cathode is proposed in Ref. [69] to avoid formation of the sheath. In this approach, instead of injecting cathode electrons exactly on the right boundary, the cathode emission plane is shifted slightly to the upstream (at a small distance about $1mm$ away from the right boundary). As now the cathode is placed inside the domain, the flux of injected electrons from cathode plane is

$$\Gamma_{ce} = \Gamma_{ce1} + \Gamma_{ce2} = \Gamma_{ae} - \Gamma_{ai} \qquad \text{Eq. 1.40}$$

In addition, to have the zero-potential condition on the cathode plane, a linear function is then subtracted from the solution of Poisson's equation ($\phi'(x)$) as below

$$\phi(x) = \phi'(x) - \frac{x}{x_c}\phi'(x_c) \,, \qquad \text{Eq. 1.41}$$

where x_c is the axial location of cathode injection plane. Notice that the new potential ($\phi(x)$) satisfies Poisson's equation as well.

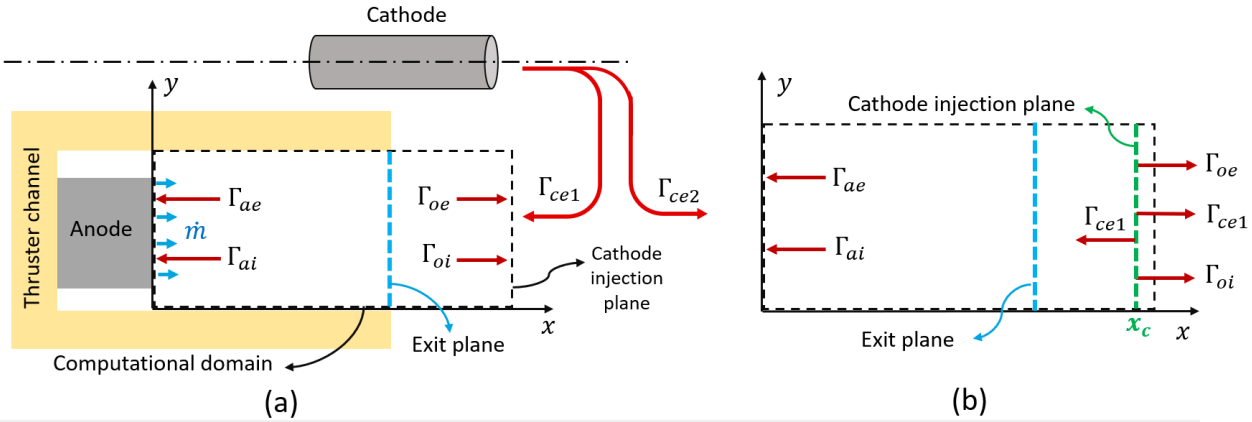


Fig. 1.10: Illustration of different charged particles current contributions; (a) cathode plane being on the right boundary, (b) cathode plane being inside the domain in the current continuity scheme.

II.II) Quasi-neutrality: Alternatively, we can inject from the cathode as many electrons as necessary to keep the cathode plane quasi-neutral. The number of electrons to be injected (N_e) corresponds to the difference between the ion and the electron number densities on the cathode plane which, in 2D, is obtained as

$$N_e = \sum_{j=1}^{N_j} \left(n_{i_j} - n_{e_j}\right)|_{x=x_c} \Delta V, \qquad \text{Eq. 1.42}$$

where n_i and n_e are ion and electron number densities, N_j is the number of cells across the cathode plane, ΔV is the cell volume, and x_c is the cathode axial location. According to this cathode boundary model, we only inject electrons if $N_e > 0$.This method is shown to be less sensitive to the injection temperature [69], which is unknown without modelling the cathode plasma itself and its coupling with thruster main plume. Besides, it is more suitable for the transient phase before reaching a quasi-steady state.

III) **Radial direction:** Ions impacting the radial walls are assumed to be recombined at the surface. Thus, the ions crossing the walls are removed, and neutral particles are introduced into the domain at the locations of the crossings. Neutrals are reflected at the walls' surfaces. Regarding the electrons, two different models are implemented to represent the SEE as the electrons colliding with the walls. These models determine the number of secondary electrons to be emitted based on their estimation of the secondary electron emission yield coefficient.

III.I) Linear model: The linear model assumes that the emission coefficient (γ) linearly increases with primary electron energy (ϵ) until reaching a maximum value (γ_{max}) beyond which γ remains constant and equal to γ_{max} regardless of the energy

$$\begin{cases} \gamma(\epsilon) = \gamma_0 + \dfrac{\epsilon}{\epsilon^*}(1-\gamma_0), & \epsilon < \epsilon_0, \\ \gamma(\epsilon) = \gamma_{max}, & \epsilon \geq \epsilon_0. \end{cases} \qquad \text{Eq. 1.43}$$

In the above equation, γ_0 is the probability of attachment, and ϵ^* is the crossover energy. For Boron Nitride (BN), which is the material typically used for Hall thruster's channel, $\gamma_0 \approx 0.578$, $\epsilon^* \approx 35.04\ eV$ and $\gamma_{max} \approx 2.9$. **Fig. 1.11** (a) plots the variation in γ versus

electron energy from the linear model. The linear model (Eq. 1.43) is obtained for each material by fitting a line to the experimentally measured total emission coefficient [95].

III.II) Monte Carlo-based model: In this model, depending on the energy and the impinging angle (θ) of primary electrons, they can either undergo elastic reflection, inelastic scattering or be absorbed and cause emission of a true secondary electron from the wall. The probabilities of the three mentioned events are determined by their respective partial yield coefficients. We adopted Vaughan fits to determine these coefficients [96]. Another possible model for the yield coefficients is Furman-Pivi model [97]. According to Vaughan model, the total emission coefficient (γ_V) is written as

$$\gamma_V(\epsilon,\theta) = \gamma_{max}(\theta)[\nu(\epsilon,\theta)\, exp(1-\nu(\epsilon,\theta))]^k, \quad \text{Eq. 1.44}$$

where,

$$\nu(\epsilon,\theta) = \frac{\epsilon-\epsilon_0}{\epsilon_{max}(\theta)-\epsilon_0}, \quad \text{Eq. 1.45}$$

$$\epsilon_{max}(\theta) = \epsilon_{max,0}\left(1+\frac{k_s}{\pi}\theta^2\right), \quad \text{Eq. 1.46}$$

$$\gamma_{max}(\theta) = \gamma_{max,0}\left(1+\frac{k_s}{2\pi}\theta^2\right). \quad \text{Eq. 1.47}$$

Following Vaughan approach, the coefficients for elastic reflection (γ_e), inelastic backscattering (γ_i), and the true SEE emission coefficient (γ_t) are then defined as

$$\gamma_e(\epsilon,\theta) = r_e\gamma_V(\epsilon,\theta) + \gamma_{e,max}\begin{cases}\nu_1(\epsilon)\exp\big(1-\nu_1(\epsilon)\big), & \epsilon_{e,0}<\epsilon<\epsilon_{e,max},\\ [1+\nu_2(\omega)]\exp\big(-\nu_2(\omega)\big), & \epsilon>\epsilon_{e,max},\end{cases} \quad \text{Eq. 1.48}$$

$$\gamma_i(\epsilon,\theta) = r_i\gamma_V(\epsilon,\theta), \quad \text{Eq. 1.49}$$

$$\gamma_t(\epsilon,\theta) = (1-r_e-r_i)\gamma_V(\epsilon,\theta), \quad \text{Eq. 1.50}$$

with

$$\nu_1(\epsilon) = \frac{\epsilon-\epsilon_{e,0}}{\epsilon_{e,max}-\epsilon_{e,0}}, \quad \text{and} \quad \nu_2(\epsilon) = \frac{\epsilon-\epsilon_{e,max}}{\Delta_e}. \quad \text{Eq. 1.51}$$

The definition of the parameters in the above equations together with their estimated values for Boron Nitride [95][98] are provided in **Table 1.1**. **Fig. 1.11** (b) and (c) present, respectively, the variation of the total emission coefficient with the incident energy and incident angle and the variation in the partial emission coefficients with the incident energy for the normal incident angle. Once these coefficients are determined, the occurrence of each of the three scenarios will be decided using a Monte Carlo approach according to Ref. [98].

Parameter	Definition	Value
ϵ_0	Emission threshold energy	13 $[eV]$
$\epsilon_{max,0}$	Primary electron energy at the maximum emission for normal incidence ($\theta = 0$)	500 $[eV]$
$\gamma_{max,\,0}$	Maximum electron emission coefficient for normal incidence ($\theta = 0$)	2.9
$\epsilon_{e,0}$	Threshold energy for the elastic reflection	2 $[eV]$
$\epsilon_{e,\,max}$	Primary electron energy at the maximum elastic reflection for normal incidence	10 $[eV]$
$\gamma_{e,max}$	Maximum elastic reflection for normal incidence	0.55
k_s	Surface smoothness factor (0: very rough, 2: polished)	1
r_e	Portion of the total emitted current consisting elastically reflected electrons	0.03
r_i	Portion of the total emitted current consisting of inelastically reflected electrons	0.07
Δe	Parameter controlling the decay of the "bumping" part of γ_e	12.0

Table 1.1: Parameters in Vaughan model for partial coefficient yields and their values for Boron Nitride [95][98].

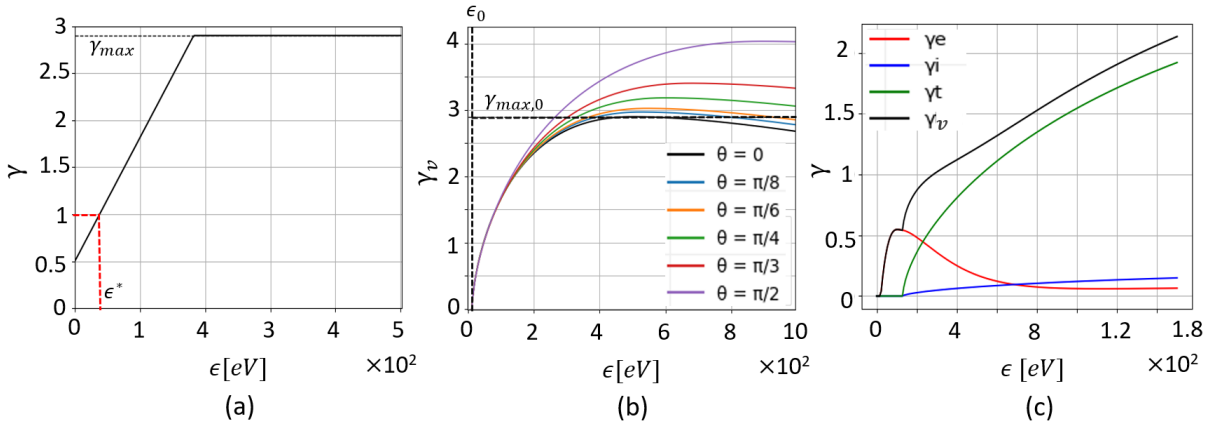


Fig. 1.11: (a) SEE yield coefficient versus incident electron energy according to the linear model. Vaughan model estimation of (b) total emission coefficient (γ_V) for various incident angles and (b) partial emission coefficients for normal incident angle versus electron incident energy. The plots are for Boron Nitride.

E) Particle sampling and injection: The simulation initialization typically involves loading particles for each species with their respective initial densities. Throughout the simulation, neutrals are injected from the anode surface at a constant rate corresponding to the thruster anode mass flow rate. Additionally, electrons are continuously reinjected from the cathode plane to sustain the discharge. Finally, electron-ion pairs resulting from ionization events from the electron-neutral Monte Carlo Collisions (refer to Section 1.4.2.3) are created and injected into the domain. For the initial loading of particles, we sample from a Maxwellian distribution function at a particular temperature using the Box-Muller sampling technique [99]. In cases of the anode and the cathode injections, the particles are sampled from drifting half-Maxwellian distribution functions. The random numbers for the sampling are generated using Julia's built-in Random Number Generator (RNG) function, which follows Xoshiro256++ algorithm [100].

F) Diagnostics: The output of the simulation is presented in terms of distributions of the macroscopic properties of the involved species including number density (n_s), drift velocity ($\boldsymbol{V}_s$), pressure tensor ($\pi_{ij,s}$) and temperature (T_s), where s denotes the species type which is either electrons, ions or neutrals. These properties are obtained by taking velocity moments (integrals)

of particles' distribution functions per Eq. 1.52 to Eq. 1.55. In PIC simulations, where particles serve as a discretized representation of the distribution function, the integration of the distribution function is equivalent to scattering the relevant particles data on the grid.

$$n_s = \int_{-\infty}^{\infty} f_s(\boldsymbol{v})\, d^3v\,, \qquad \text{Eq. 1.52}$$

$$\boldsymbol{V}_s = \frac{1}{n_s}\int_{-\infty}^{\infty} \boldsymbol{v}\, f_s(\boldsymbol{v})\, d^3v\,, \qquad \text{Eq. 1.53}$$

$$\pi_{ij,s} = m_s\left(\int_{-\infty}^{\infty} v_i\, v_j\; f_s(\boldsymbol{v}) d^3v - n_s \boldsymbol{V}_{s,i}\, \boldsymbol{V}_{s,j}\right), \qquad \text{Eq. 1.54}$$

$$T_s = \frac{m_s}{3K_B\, n_s}\left(\int_{-\infty}^{\infty} \boldsymbol{v}.\boldsymbol{v}\, f_s(\boldsymbol{v}) d^3v - n_s\, \boldsymbol{V}_s.\boldsymbol{V}_s\right), \qquad \text{Eq. 1.55}$$

1.4.2.3. Monte Carlo Collision module

Interparticle collisions need to be incorporated into simulations as another factor that influences the particles' movement in addition to the electromagnetic fields. The collisions can be modelled through probabilistic approaches following either Monte Carlo Collison (MCC) [65] or Direct Simulation Monte Carlo (DSMC, see Section 1.4.2.4) [101] schemes. In the MCC, collisions occur between source particles and a target "cloud" while the DSMC treats both source and target as particles. Therefore, MCC is much faster than DSMC, but it does not strictly conserve the momentum and energy of the system as the energy and momentum transfer to the target species is not accounted for. However, the MCC is a valid approximation when the density of the target species is much higher than that of the source. As the neutral density in Hall thruster is typically an order of magnitude larger than the plasma density, the MCC can represent with reasonable accuracy the collisions between the electrons/ions with the neutrals in Hall thruster.

The MCC is implemented for the electron-neutral and ion-neutral collisions. The electron-neutral collisions considered in this module are ionization, four levels of excitation and elastic momentum transfer scattering (doubly charged ionization is not taken into account)

- Isotropic elastic scattering: $e + Xe \rightarrow e + Xe$,
- Excitation: $e + Xe \rightarrow e + Xe^*$,
- Single ionization: $e + Xe \rightarrow 2e + Xe^+$.

The ion-neutral collisions include anisotropic scattering and charge exchange collision

- Isotropic elastic scattering/ backscattering: $Xe^+ + Xe \rightarrow Xe^+ + Xe$,
- Charge exchange collision: $Xe^+_{fast} + Xe_{slow} \rightarrow Xe^+_{slow} + Xe_{fast}$.

The energy threshold and collision cross sections as a function of the impact energy for xenon (**Fig. 1.12**) are derived from Biagi 7.1 and Phelps datasets from LXCat database [102].

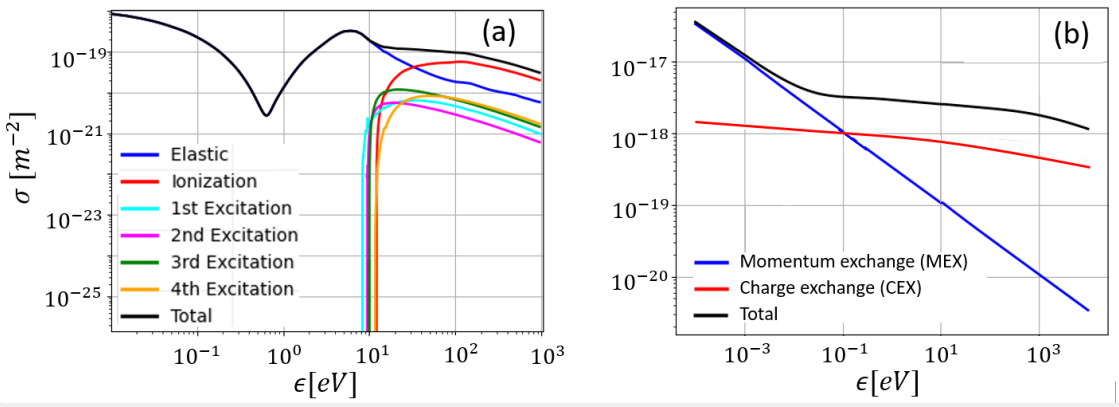


Fig. 1.12: Interpolated functions of (a) Biagi 7.1 electron-neutral and (b) Phelps ion-neutral collision cross sections for xenon taken from LXCat database [102].

The traditional implementation of MCC works by looping over all source particles where, for each particle, the collision probability is calculated based on the total collision cross section at the particle's energy

$$P_i = 1 - exp\left(-v_{r,i}\, n_t\, \sigma_{tot}(\epsilon_i)\, \Delta t\right) \quad \text{for} \quad 1 \le i \le N_p\,, \qquad \text{Eq. 1.56}$$

where N_p is the number of particles, n_t is the density of the target species at the location of the source particle, ϵ is the total kinetic energy of the particle, and σ_{tot} is the sum of all involved collision cross sections. Also, $v_{r,i}$ is the speed of the source particle relative to that of the target particle. The target velocity is randomly sampled from a drifting Maxwellian distribution with the target species' drift velocity and temperature at the location of the source particle.

Subsequently, this probability is compared against a uniformly distributed random number between 0 and 1 ($\mathcal{R}_1 \in U[0,1)$), and if the collision probability is greater than the random number, the collision takes place. To determine which type of collision gets executed, another random number ($\mathcal{R}_2 \in U[0,1)$) is compared with the individual collision frequencies (ν_j) normalized by the total collision frequency (ν_{tot}). The j^{th} type collision occurs, where $j \in [1, J]$ is the index of the collision type for which the following condition is met

$$\mathcal{R}_2 \le \frac{\nu_j}{\nu_{tot}} \qquad \text{for} \qquad j = 1\,,$$
$$\frac{\sum_1^{j-1} \nu_j}{\nu_{tot}} \le \mathcal{R}_2 \le \frac{\sum_1^{j} \nu_j}{\nu_{tot}} \qquad \text{for} \quad 2 \le j \le J\,. \qquad \text{Eq. 1.57}$$

The total collision frequency is obtained as

$$\nu_{tot} = v_{r,i}\, n_t\, \sigma_{tot}(\epsilon). \qquad \text{Eq. 1.58}$$

The standard implementation of MCC requires looping over all particles and computing the collision probability (P_i) for all of them that makes this approach computationally heavy. In this regard, Vahedi and Surendra [65] proposed an approach called "Null collision" method to execute the collision function only on a subset of particles. This method is based on the addition of a hypothetical collision type known as "null" collision with a collision frequency profile that, when added to the sum of the other collision frequencies (ν_{tot}), will bring the total collision frequency to a constant value over the entire range of energies, i.e., corresponding to the maximum of total collision frequency

$$\nu'_{tot} = \max_{x,\ \epsilon}(\nu_{tot}) = \max_{x}(n_t)\ \max_{\epsilon}(v_r\ \sigma_{tot}(\epsilon))\,, \quad \text{Eq. 1.59}$$

$$\nu_{null}(x,\epsilon) = \nu'_{tot} - \nu_{tot}(x,\epsilon). \quad \text{Eq. 1.60}$$

According to the new total collision frequency, the maximum fraction of particles that will undergo collision can be determined using

$$P_{null} = 1 - exp(-\nu'_{tot}\Delta t)\,. \quad \text{Eq. 1.61}$$

The check to determine the collision type is done as before (Eq. 1.57), except that here we have $J+1$ collision types, with the $(J+1)^{th}$ being the null collision for which no collision happens. The details of the execution of each collision can be found in Ref. [65].

1.4.2.4. Neutral dynamics

A rigorous treatment of the neutral flow involves kinetic DSMC model which takes into account the neutral-neutral and neutral-ion collisions. Nonetheless, because resolving the dynamics of neutrals over extended periods using the DSMC model is computationally intensive, a 1D fluid approximation can be alternatively used. In any case, considering the slower time scale of the neutrals, it is customary to update neutrals with a larger time step than electrons and ions to save computation. In the following the neutrals' fluid model based on 1D Euler system of equations and kinetic DSMC model are discussed.

A) Neutrals' fluid model using 1D Euler system of equations: Assuming neutrals in a Hall thruster as an adiabatic inviscid flow which vary mostly along the axial direction, their spatiotemporal evolution can be described through a 1D Euler system of equations

$$\frac{\partial \rho}{\partial t} + \frac{\partial(\rho u)}{\partial x} = S_1, \quad \text{Eq. 1.62}$$

$$\frac{\partial(\rho u)}{\partial t} + \frac{\partial(\rho u^2)}{\partial x} = -\frac{\partial P}{\partial x} + S_2, \quad \text{Eq. 1.63}$$

$$\frac{\partial \rho E}{\partial t} + \frac{\partial(\rho u E)}{\partial x} = -\frac{\partial P u}{\partial x} + S_3. \quad \text{Eq. 1.64}$$

In the above equations, ρ is the neutral density, u is the axial drift velocity, P is the pressure, and $E = e + \frac{1}{2}u^2$ is the specific total energy with e being the specific internal energy ($e = \frac{nk_BT}{\rho(\gamma-1)}$). In the relation for e, n is the number density, T is the neutral temperature, k_B is the Boltzmann constant, and γ is the heat capacity ratio. Using the ideal gas relation, $P = nk_BT$, the specific internal energy can be expressed as $e = \frac{P}{\rho(\gamma-1)}$. Moreover, in Eq. 1.62 to Eq. 1.64, S_1, S_2, and S_3 are the source terms for the continuity, momentum, and energy equations, respectively, which will be defined shortly. To numerically solve this system of equations, we write them in a general conservation form as

$$\frac{\partial U}{\partial t} + \frac{\partial \Gamma(U)}{\partial x} = S(U), \quad \text{Eq. 1.65}$$

which can be integrated using the first-order Euler scheme to march forward in time

$$U_i^{t+1} = U_i^t - \frac{\Delta t}{\Delta x}\left(\Gamma_{i+\frac{1}{2}} - \Gamma_{i-\frac{1}{2}}\right) + S\Delta t\,. \quad \text{Eq. 1.66}$$

In Eq. 1.66, U is the state vector of the conserved quantities, $\Gamma(U)$ is the vector of the corresponding fluxes, and $S(U)$ is the vector of the source terms. These vectors are defined as

$$U = \begin{pmatrix} \rho \\ \rho u \\ \rho E \end{pmatrix}, \quad \Gamma = \begin{pmatrix} \rho u \\ \rho u^2 + P \\ \rho u E + P u \end{pmatrix}, \quad S = \begin{pmatrix} -S_i \\ -u S_i \\ -u^2 S_i \end{pmatrix}. \qquad \text{Eq. 1.67}$$

Also, U_i^t is the state vector value at time t, $\Gamma_{i-\frac{1}{2}}$ and $\Gamma_{i+\frac{1}{2}}$ are the flux vectors at the left and right boundaries of the i-th cell, Δt is the timestep and Δx is the cell size. Moreover, S_i in Eq. 1.67 is the ionization source term defined as $\rho \nu_{ion}$, where ν_{ion} is the ionization frequency. It is noted that the energy change in the neutral flow due to ionization is typically neglected.

The described 1D Euler system of equations can be simplified by assuming the neutrals as an isothermal flow [61][69]. This assumption implies that the energy equation can be replaced with the equation of state, $P = \frac{\rho}{M} k_B T$, in which M is the atomic mass.

To solve the system spatially, we adopted the Weighted Essentially Non-Oscillatory scheme with 5 grid points (i.e., WENO-5). To calculate the inter-cell fluxes, we used the HLLC Riemann solver [103]. The algorithms used for these schemes are implemented as described in Ref. [104]. The neutrals' fluid model is also verified and benchmarked in Sod shock tube problem [105], and the results are provided in Appendix A.1.5.

Concerning the boundary conditions, at the cathode side of the domain, Neumann boundary condition is applied

$$\left.\frac{\partial U}{\partial x}\right|_{x=L_x} = \frac{U_{N_i} - U_{N_i-1}}{\Delta x} = 0 \Longrightarrow U_{N_i} = U_{N_i-1}. \qquad \text{Eq. 1.68}$$

At the anode boundary, a constant mass flow rate ($\dot{m}_a$) of neutrals is injected into the domain together with an additional variable mass flow rate ($\dot{m}_r$) that corresponds to the flux of ions recombined on the anode surface. Hence, following the approach suggested in Ref. [69], the flow properties at the anode boundary (i.e., the first computation cell) at the time $t+1$ can be written as

$$u_1^{t+1} = u_1^t + \Delta u\,, \qquad \text{Eq. 1.69}$$

$$\rho_1^{t+1} = \frac{\dot{m}_a + \dot{m}_a^t}{u_1^{t+1} A}, \qquad \text{Eq. 1.70}$$

$$P_1^{t+1} = \frac{\rho_1^{t+1}}{M} k_B T_{n0}\,. \qquad \text{Eq. 1.71}$$

In Eq. 1.69, Δu is defined as in Eq. 1.72 using the flow properties in the first (subscript 1) and the second (subscript 2) cells of the domain

$$\Delta u = \frac{u_1^2 (u_1 - C_{s1})[P_2 - P_1 - \rho_1 C_{s1}(u_2 - u_1)]}{\left(\frac{\dot{m}}{A} K_B N_A T_{n0} - \rho_1 C_{s1}\right)\left(\frac{\Delta x}{\Delta t} - (u_1 - C_{s1})\right)}. \qquad \text{Eq. 1.72}$$

In above relations, A is the cross-sectional area of the channel, N_A is the Avogadro's number, and C_{s1} is the sound speed in cell 1, defined as $\sqrt{\frac{\gamma P_1}{\rho_1}}$ with γ being the heat capacity ratio.

Different variants of the neutrals' fluid model described above with different levels of complexity are tested and compared in Ref. [106]. In the simplest case, assuming a temporally constant neutrals velocity profile, we only solve the continuity equation to obtain the temporal evolution of neutral density, considering their depletion due to ionization and replenishment from gas injection and ion recombination on the anode surface. This model is referred to as the "continuity only".

Increasing the complexity level by one step, the second neutrals' fluid model is the simplified version of the 1D Euler system, which accounts for the time variation of the density and velocity profiles of isothermal neutrals. This model is termed "1D Euler".

Finally, the most complex fluid description of the neutrals considered implemented in IPPL code solves the full 1D Euler system (Eq. 1.62 to Eq. 1.64), and additionally takes into account the axial momentum transferred from the ions to the neutrals through the ion-neutral collisions. This model is referred to as the "full 1D Euler + ion momentum transfer". The effect of the ion-neutral collisions on the momentum of the neutral atoms is introduced in the model as another source term (S_m) added to the right-hand side of Eq. 1.63. The energy transfer associated with ion-neutral collisions is also included as a source term in Eq. 1.64 in the form of uS_m.

The ion-neutral collisions, where considered, are simulated through the MCC method (Section 1.4.2.3).The momentum source term S_m can be either approximated as $-\rho_i(v_i - u)\nu_{in}$, where v_i is the ions' axial drift velocity and ν_{in} is the total ion-neutral collision frequency, or to be explicitly computed as the difference between the total axial momentum of the ions' population prior and after the collisions.

B) Neutrals' kinetic model with the DSMC collisions: DSMC module is implemented to simulate the collisions involving the heavy species particles including the elastic collisions between the neutrals (n-n) as well as the isotropic momentum exchange (MEX i-n) and the charge exchange (CEX i-n) collisions between the ion and neutral particles. The cross-section for the momentum exchange collisions between the neutrals is obtained according to Bird's Variable Hard Sphere (VHS) model [107]

$$\sigma = \pi \left(d_{ref} \left(\frac{v_{r,ref}}{v_r} \right)^a \right)^2 \qquad \text{Eq. 1.73}$$

in which $d_{ref} = 5.74 \times 10^{-10}\, m$, $v_{r,ref} = 209.8\, m/s$, and $a = -0.7$. In the above equation, v_r is the relative velocity between the colliding particle pair. The cross-sections for the MEX and CEX collisions are plotted in **Fig. 1.12** (b).

The DSMC algorithm starts with sorting the particles based on the cells in which they reside. In each cell, the maximum number of collision events (or collision pairs (n_p)) for each collision type is calculated as per the "no-time-counter" method (NTC) [63]

$$n_p = N_1 N_2\, W (v_r \sigma)_{max} \frac{\Delta t}{V_{cell}}. \qquad \text{Eq. 1.74}$$

In the above equation, N_1 and N_2 are the number of macroparticles of each species within the cell, V_{cell} is the cell volume, and W is the macroparticle weight (number of particles represented

by a macroparticle) of the species with the larger macroparticle weight, which typically corresponds to the neutrals' population. $(v_r\sigma)_{max}$ is initialized with an estimation and gets updated when a larger value than the initial estimation is encountered during the simulation. The number of collision pairs from Eq. 1.74 must be halved if the collision happens between two particles of the same species. Therefore, the total number of collision pairs in each cell is obtained as

$$n_p = \left(\frac{1}{2} N_n^2\, W_n (v_r\sigma)_{max,n} + N_n N_i\, W_n (v_r\sigma)_{max,MEX} + N_n N_i\, W_n (v_r\sigma)_{max,CEX}\right)\frac{\Delta t}{V_{cell}}, \qquad \text{Eq. 1.75}$$

where the indices "n" and "i" represent the neutrals and the ion species, respectively. To pick a collision pair in each cell, two random numbers $p_1 \in [1, N_n]$ and $p_2 \in [1, N_n + 2N_i]$ are selected, the type of collision for this pair is determined using a Monte Carlo method as illustrated in **Fig. 1.13**. The collision probability for each pair is defined as

$$P_i = \frac{v_r\sigma}{(v_r\sigma)_{max}}, \qquad \text{Eq. 1.76}$$

where σ is the cross-section of the selected collision type. To check for collision occurrence, the probability P_i from Eq. 1.76 is compared with a uniformly distributed random number. In case of the neutral-neutral or neutral-ion MEX collisions, the post-impact velocities of the involved particles are obtained based on the conservation of momentum and energy

$$\vec{v}'_{r1} = \frac{m_1\vec{v}_1 + m_2\vec{v}_2}{m_1 + m_2} + \frac{m_2}{m_1 + m_2}\, v_r\vec{R}, \qquad \text{Eq. 1.77}$$

$$\vec{v}'_{r2} = \frac{m_1\vec{v}_1 + m_2\vec{v}_2}{m_1 + m_2} - \frac{m_1}{m_1 + m_2}\, v_r\vec{R}, \qquad \text{Eq. 1.78}$$

where $\vec{R}$ is a unit vector of random direction. Assuming hard sphere interaction between the particles, the scattering will be isotropic. Thus, the scattering angles (ψ and ϕ) are defined as

$$\psi = \cos^{-1}(2\mathcal{R}_1 - 1), \quad \phi = 2\pi\mathcal{R}_2, \quad \text{where } \mathcal{R}_1 \text{ and } \mathcal{R}_2 \in [0,1). \qquad \text{Eq. 1.79}$$

In case of the neutral-ion CEX collision, the velocities of the two particles are simply swapped to update the colliding particles' velocity.

Eq. 1.77 and Eq. 1.78 are only true when the colliding particles are of equal macroparticle weights. However, to ensure the conservation of momentum and energy in case of unequal macroparticles weights over statistically large number of collision events, the velocity update is always performed for the particle with the smaller macroparticle weight (W_{p_2}), whereas the velocity of the particle with the larger macroparticle weight (W_{p_1}) is modified only if $\mathcal{R} > W_{p_2}/W_{p_1}$, where $\mathcal{R}$ is a uniformly distributed random number.

Regarding the typical boundary condition for Hall thruster simulations, neutrals that reach the anode surface or lateral walls are reflected, while those reaching the plume boundaries are removed. Also, ions impacting the anode surface and channel walls are assumed to recombine and are then reinjected into the domain as neutrals.

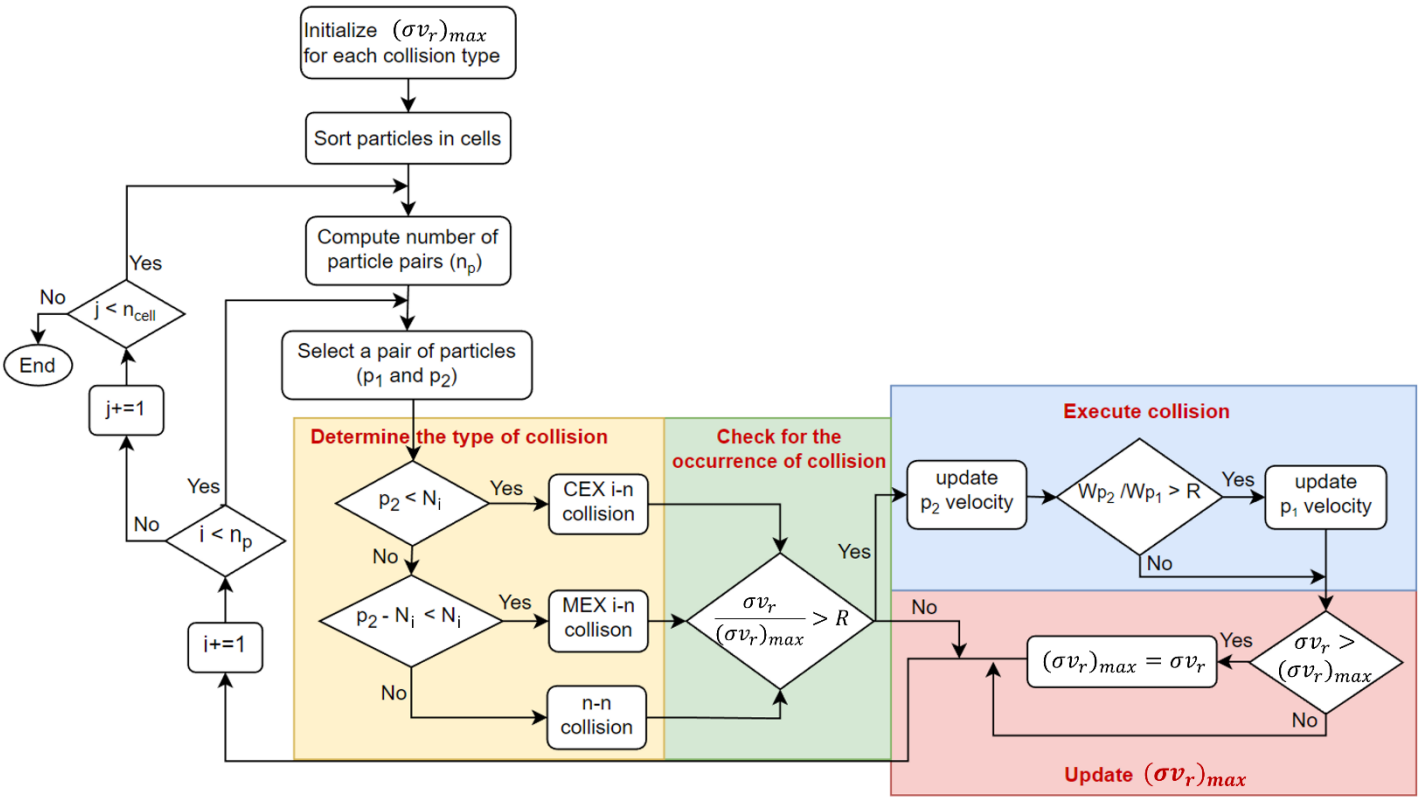


Fig. 1.13: Flowchart of the DSMC collisions algorithm.

1.5. Problem statement: research motivations and objectives

Motivation: Noting the predictive inadequacy and the lack of self-consistency of the less computationally demanding fluid-based plasma simulations on the one hand, and the kinetic nature of the of plasma processes in the $\mathrm{E} \times \mathrm{B}$ plasmas on the other, high-fidelity PIC simulations are the desired tools to study and predict the underlying plasma behavior. Nonetheless, the substantial computational cost of the traditional multi-dimensional PIC renders simulating real-size devices over timescales of real-world significance unfeasible without any physics-altering speed-up factors.

Furthermore, as evidenced from the large body of previous research in the literature [1][2][61][108][109], plasma processes in the $\mathrm{E} \times \mathrm{B}$ discharges such as instabilities and particles' transport exhibit a multifaceted and highly coupled nature. The characteristics of these phenomena and their impacts on the macroscopic plasma properties are remarkably dependent on the operating regime and the physical parameters of the plasma system. Despite the need for understanding these parametric variabilities, the conventional PIC codes cannot be effectively used for extensive parametric studies due to their remarkable computational resource demand.

Accordingly, from a scientific perspective, a computationally efficient high-fidelity model enables addressing long-standing questions in plasma physics and advances our understanding of the multi-dimensional plasma phenomena and their parametric dependencies. From an engineering viewpoint, such a predictive model facilitates the design and development of more efficient and reliable plasma technologies as well as unlocking new innovative technological solutions.

Objectives: In view of these needs and challenges, the present research is defined to primarily address the issue of enormous computational cost associated with kinetic electrostatic PIC simulations. Indeed, the stability criteria of the conventional PIC schemes require the use of very small grid sizes on the order of the Debye length ($O(10^{-6}\ m)$) as well as a statistically significant number of macroparticles ($O(10^{9}\ )$ in a full-2D PIC for a typical $E \times B$ device). The reduced-order PIC (RO-PIC) scheme aims to remarkably (by up to orders of magnitude) lower the computational cost of the PIC simulations by drastically reducing the total number of computational cells and, thus, the total number of macroparticles without affecting the stability of the PIC scheme. Achieving this objective is expected to pave the way toward the realization of computationally affordable high-fidelity 3D kinetic simulations of plasma devices. Accordingly, the objectives of this research are as follows:

Primary objective

- To devise a reduced-order kinetic-based approach (called reduced-order PIC scheme) capable of approximating the solution of the conventional multi-dimensional PIC simulations at a fraction of computational cost.

Secondary objectives

- Extensive verification of the scheme in well-established 2D benchmark cases across various E×B plasma configurations.
- Showcasing the capability of RO-PIC in enabling studies and simulations with scientific and applied significance that were previously impractical with conventional PIC codes.

Following the development of the RO-PIC PIC scheme, the achievement of secondary objectives entails a detailed characterization of the RO-PIC's prediction accuracy and computational advantage compared to the conventional full-2D PIC simulations. Furthermore, the demonstration of the RO-PIC capabilities is accomplished through (1) extensive high-fidelity parametric investigations of variations in plasma phenomena including instabilities and their impacts on global discharge characteristics across wide parameter spaces, and (2) self-consistent kinetic simulation of real-size Hall thrusters over sufficiently extended durations. Conducting the above studies with RO-PIC demonstrates its suitability for attaining a comprehensive understanding of plasma behavior as well as to its utility as a predictive tool.

Chapter 2 Reduced-Order PIC scheme: concept and formulation

The reduced-order PIC (RO-PIC) scheme developed within this research is an innovative approach that provides an approximation of the conventional PIC solution, resulting in a quasi-multi-dimensional representation of the problem at hand. The scheme relies on a novel dimensionality-reduction treatment that reduces the computational cost of conventional PIC simulations by up to 3 orders of magnitude depending on the desired order of approximation and the number of involved dimensions.

Broadly speaking, RO-PIC approximates a multi-dimensional problem by decomposing it into a number of coupled 1-dimensional problems along the involved simulation dimensions, which are much more computationally affordable. The number of these 1D problems determines the order of approximation of the RO-PIC. The formulation of the dimensionality-reduction technique offers a unique flexibility to have a trade-off between fidelity and computational gain of the simulation depending on its specific purpose and use case. This notion of "quasi-multidimensionality" is a unique feature of this approach that enables a continuous spectrum of choices for solution dimensionality anywhere in between a 1D and a full-2D/3D solution, all while ensuring the stability of the solution.

The proposed dimensionality reduction technique is a general concept enabling the reduced-order representation of the problem. In this work, we focus on the 2D electrostatic implementation of this scheme in PIC which leads to the development of quasi-2D electrostatic PIC plasma simulation. Nevertheless, the dimensionality reduction technique is believed that it is extendible to 3D and potentially to other numerical modelling techniques as well. The potential avenues and pathways for extension of the dimensionality-reduction formulation to a broader range of applications are enumerated in Section 7.2.5.

2.1. Order-reduction in the context of PIC simulations: RO-PIC concept

The traditional PIC simulations require the size of the computational grid cells to be smaller than the Debye length along the involved dimensions of the simulation. This is to capture non-quasi-neutralities that exist below the Debye scale as well as maintaining the stability of the simulation. The large number

of computational cells combined with the necessity of having a statistically large number of macroparticles per cell, makes the PIC simulations to be computationally expensive.

The order-reduction (dimensionality-reduction) underlying the reduced-order PIC is enabled through definition of a new computational grid system, the "reduced-order" grid. The adoption of this grid system in PIC allows increasing the cell size beyond the Debye scale along one or two simulation dimension(s) at a time (in 2D and 3D simulation, respectively) by an arbitrary amount, while keeping the cell size along the other dimension(s) compatible with ordinary PIC's requirements. Consequently, the number of computational cells and hence, the total number of macroparticles are reduced, resulting in reduced computations. The schematic of the reduced-order grid in 2D, also known as reduced-dimension or quasi-2D grid is illustrated in **Fig. 2.1**.

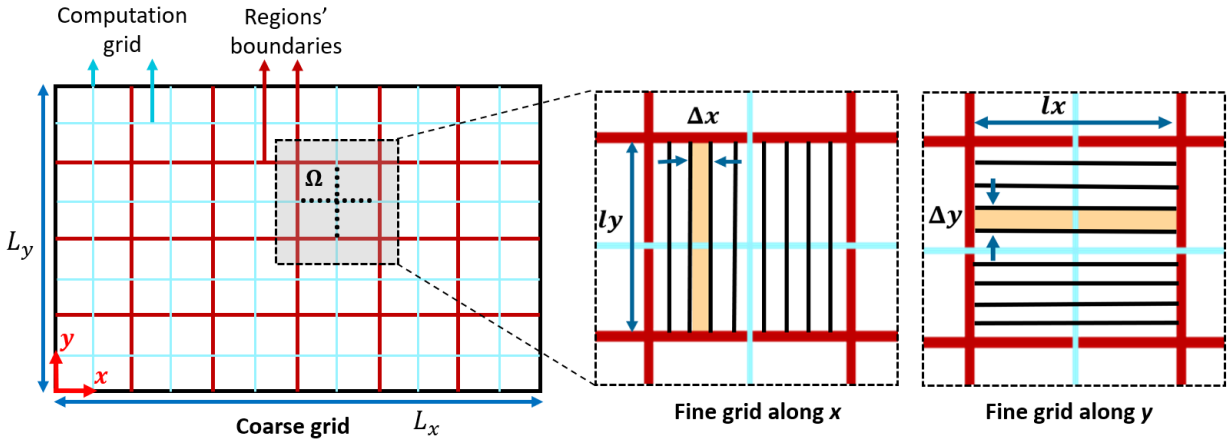


Fig. 2.1: Schematic of the domain decomposition corresponding to the reduced-order grid system for RO-PIC scheme; (left) decomposition into multiple "regions" using a coarse grid, (right) the 1D computational cells (fine grids) for discretization of each region along the x and y directions.

In the reduced-order grid system, the computational domain is decomposed into multiple rectangular (in 2D)/cubic (in 3D) subdomains or "regions", which can be thought of as the discretization of the domain using a "coarse" grid (**Fig. 2.1** (left)). Within any specific region, denoted as Ω on the left-hand side of **Fig. 2.1**, we discretize each simulation dimension separately using 1D "elongated" cells (orange-shaded elements in **Fig. 2.1** (right)). The criterion for the fine grids' cell sizes along the x and y directions, Δx and Δy, is the same as that in a conventional 1D PIC, i.e., smaller than the Debye length. This fine-discretization grids create a partial decoupling between the different coordinates within each region, resulting in remarkable reduction in the number of cells and, hence, the required total number of macroparticles. The vertical and horizontal fine grids in each region (**Fig. 2.1** (right)) capture separately the variations of the plasma properties along the x and y directions, respectively.

Such grid system establishes a new framework enabling quasi-multi-dimensional numerical simulations which provide an approximation of the full-multi-dimensional problem with arbitrary closeness to the corresponding full multi-dimensional solution. The order reduction technique, by construction, provides a flexibility for the user to determine the desired trade-off between level of predictions' accuracy and computational cost without affecting the stability of the solution. Indeed, the degree of "order reduction" (or approximation order) with respect to full 2D/3D and, consequently, the

computational cost of a reduced-order simulation depends on the fineness of the coarse grid, i.e., the number of regions. In other words, the aspect ratios of the horizontal and the vertical cells, $l_x/\Delta x$ and $l_y/\Delta y$ are directly proportional to the speedup factor achieved through this reduced-order scheme.

In this regard, at "low" approximation orders of a multi-dimensional problem (with few number of regions), RO-PIC captures an "average effect" of multi-dimensional phenomena and interactions that cannot be represented in a 1D setup, with the computational cost on apar with a 1D PIC simulation. At "high" approximation order limits, the scheme faithfully reproduces the results of traditional PICs while still featuring several factors of speedup. These will be demonstrated in detail, in the next chapter. Moreover, the underlying formulation of the reduced-order PIC scheme is mathematically proven to converge to 2D in the limit where the regions' extents are as small as the cell sizes in a 2D simulation ($lx = \Delta x\,, ly = \Delta y$). In this limit, the associated simulation cost is equivalent to a 2D simulation. However, in most cases, it is sufficient to choose the extents of the regions to be much larger than a 2D cell size.

The convergence behavior of the reduced-order simulation towards the outcome of a traditional PIC approach is case-dependent. This is because, the degree of coupling between different dimensions is heavily influenced by the underlying physical phenomena and the interactions involved within the system. For instance, in certain scenarios where the interdimensional interactions and couplings are relatively weak, the problem is effectively decomposable along the involved dimensions. In such a case, very few number of regions, or in the limiting case, treating the entire simulation domain as a single region, can produce a sufficiently accurate representation of the problem. In the presence of intrinsically multi-dimensional phenomena, the coupling between various dimension occurs over smaller scales, which require a more comprehensive treatment through the use of higher number of regions to capture the physics with a reasonable accuracy. In general, the selection of a proper number of regions is made in consideration with the underlying physics as well as the specific needs and purpose of the study.

2.2. Quasi-multi-dimensional PIC: the dimensionality-reduction formulation underlying RO-PIC

The incorporation of the reduced-order grid and the order-reduction formulation, which will be discussed shortly, into PIC leads to the development of reduced-order PIC (RO-PIC) scheme. The resulting PIC code based on RO-PIC scheme is a quasi-multi-dimensional PIC code which we referred to as quasi-2D (Q2D) when accounting for two dimensions and quasi-3D (Q3D) in the presence of three dimensions. The quasi-2D branch of IPPL code which is developed in this research is called IPPL-Q2D. Like IPPL-1D and IPPL-2D branches, IPPL-Q2D code is written entirely in Julia language [93]. Similar to the conventional branches of IPPL code, IPPL-Q2D is an electrostatic, explicit PIC simulation code which tracks all three components of the particles' velocity (3V in velocity space).

IPPL-Q2D, overall, follows the standard algorithm of the particle-in-cell method explained in detail in Section 1.4.2.2. The distinction between the reduced-order PIC code (IPPL-Q2D) and a conventional one (IPPL-2D) lies in the computational grid used for solving the electric potential and the electric field as well as for sampling the particle-based data (such as the electric charge) in space and gathering the

grid-based data (such as the electric field) from it onto the particles' position. Therefore, the formulation and implementation of the functions and modules that use or interact with the grid must be adjusted, namely the scatter and the gather functions as well as the Poisson solver.

2.2.1. Scatter and gather functions

The particles' information (e.g. charge density) in the reduced-order PIC is scattered onto the reduced-order computation grid (quasi-2D grid) corresponding to the dimensionality-reduction approach. Similarly, the field information used to update the particles' velocity and position are gathered from this computation grid. **Fig. 2.2** illustrates a schematic of the reduced-dimension grid and an arbitrary particle used to describe the scatter and gather formulations in the following.

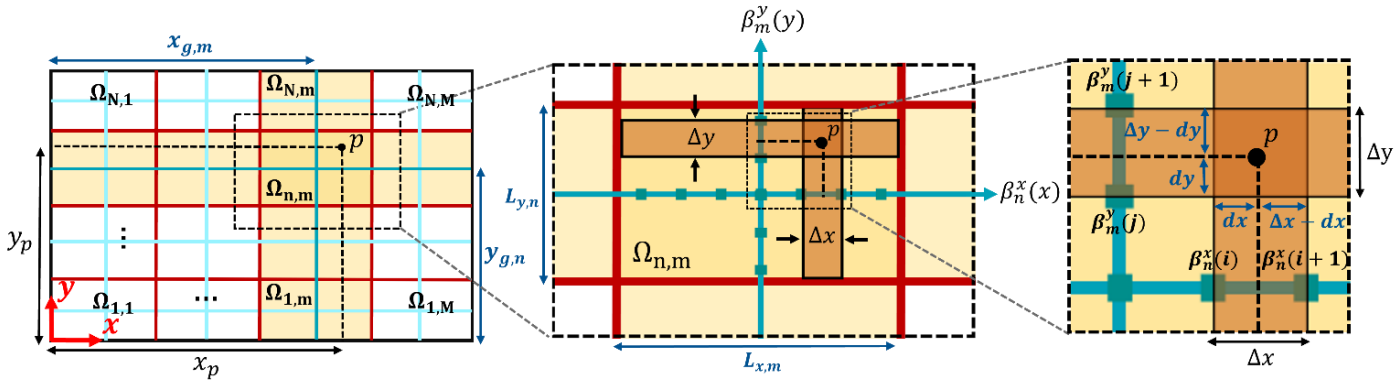


Fig. 2.2: Schematic illustrating exchange of data between the particles and reduced-dimension grid in RO-PIC.

The particles' data, denoted by β_p, is deposited once onto the refined grid along x (x-grid) according to Eq. 2.1 and once onto the grid along y (y-grid) direction given by Eq. 2.2. In these relations, $\Delta\beta_m^x$ and $\Delta\beta_n^y$ specifies the contribution of particle p to the value of β on the respective grids' nodes. The average of the two grid values will then reconstruct the distribution of the data on the full-2D grid using Eq. 2.3.

$$\Delta\beta_m^x(i) = \frac{\Delta x - dx}{\Delta x}\beta_p, \qquad \Delta\beta_m^x(i+1) = \frac{dx}{\Delta x}\beta_p\,, \qquad i \in \Omega_{n,m}, \qquad \text{Eq. 2.1}$$

$$\Delta\beta_n^y(j) = \frac{\Delta y - dy}{\Delta y}\beta_p, \qquad \Delta\beta_n^y(j+1) = \frac{dy}{\Delta y}\beta_p\,, \qquad j \in \Omega_{n,m}. \qquad \text{Eq. 2.2}$$

$$\Delta\beta(i,j) = \frac{1}{2}\left(\Delta\beta_m^x(i) + \Delta\beta_n^y(j)\right), \quad i,j \in \Omega_{n,m}\,. \qquad \text{Eq. 2.3}$$

Furthermore, we can gather the grid' data β^x and β^y at the particle's location using Eq. 2.4 in a similar manner, given by Eq. 1.36. In this relation, β_p is the gathered data at the particle's position

$$\beta_p(x,y) = \frac{1}{2}\left(\frac{\Delta x - dx}{\Delta x}\Delta\beta_m^x(i) + \frac{dx}{\Delta x}\Delta\beta_m^x(i+1) + \frac{\Delta y - dy}{\Delta y}\Delta\beta_n^y(j) + \frac{dy}{\Delta y}\Delta\beta_n^y(j+1)\right), \qquad x,y \in \Omega_{n,m}\,. \qquad \text{Eq. 2.4}$$

Notice that here, we employ 1D interpolation to exchange data independently between either of the grids (x-grid and y-grid) and the particles, in contrast to the full-2D method which uses 2D interpolation. This is in line with the principle behind the reduced-dimension grid, where each of the x- and y-grids captures the gradients along its respective direction and assumes the information to be uniform across their regions' extents (perpendicular to the corresponding grid direction).

Fig. 2.3 presents two examples illustrating the visualization of the projection of 2D profiles onto the x- and y-components (β^x and β^y) of the quasi-2D grid together with the reconstructed 2D profiles (β) from the x- and y-grid values according to Eq. 2.4.

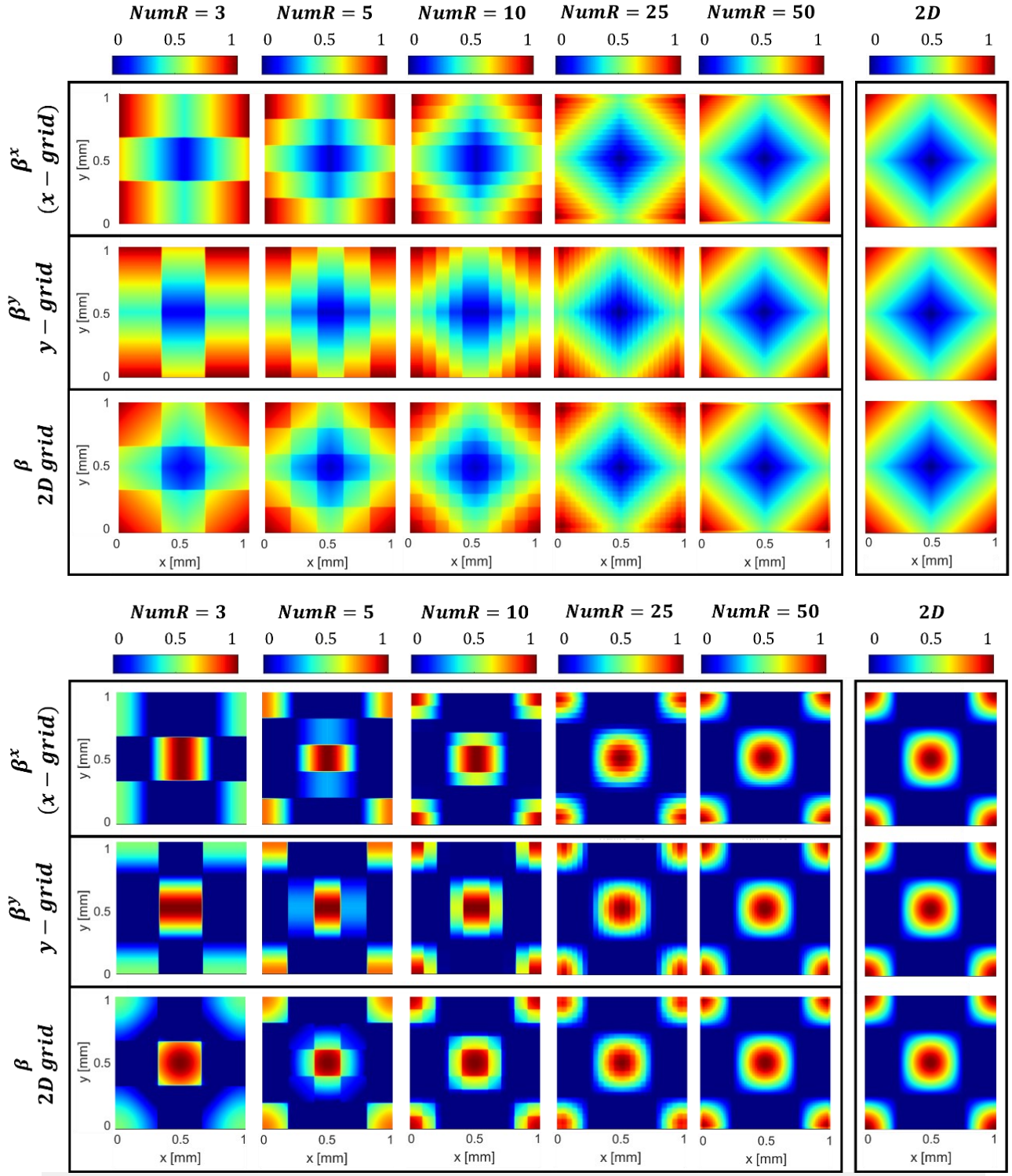


Fig. 2.3: Visualization of sampling of 2D profiles (rightmost column) on the reduced-dimension x-grid (top row) and y-grid (middle row) with various numbers of regions as well as the reconstructed profiles on the full-2D grid (bottom row) using x- and y-grid values per Eq. 2.4. The numbers of regions (denoted by *NumR)* are equal along both dimensions ($M = N$). The number of cells along either direction is 100. Top panel corresponds to the profile defined by Eq. 2.5 and bottom panel represent the distribution given by Eq. 2.6.

The 2D profiles in these examples are given by Eq. 2.5 and Eq. 2.6 (corresponding to top and bottom panels in **Fig. 2.5**, respectively)

$$\beta(x,y) = |x - 0.5| + |y - 0.5|, \qquad x,y \in [0,1] \qquad \text{Eq. 2.5}$$

$$\beta(x,y) = \cos(2\pi x)\cos(2\pi y), \qquad x,y \in [0,1] \qquad \text{Eq. 2.6}$$

These plots clearly demonstrate that the x-grid effectively captures the variation of β in a refined manner along the x-direction. Meanwhile, the value of β remains constant across the entire y-extents of the regions and varies abruptly from one region to another. Similarly, the y-grid represents the variations along the y-direction with no gradients across x-extents of the regions while accounting for variations along the x-direction coarsely with a resolution determined by the x-extents of the regions. In other words, the horizontal and vertical stripes decompose the domain into multiple 1D domains along the x- and y-coordinates, respectively, each spanning across the domain along one dimension and has a width equal to the extent of the regions.

As the number of regions increases, the resolution of the coarse grid improves, leading to a convergence of the distributions on the x- and y-grids towards each other. Ultimately, both distributions approach the full-2D distribution.

2.2.2. Reduced-dimension Poisson's equation

RO-PIC scheme uses the reduced-order grid system as its computational grid. As a result, the discretization of the differential equations used for solving the electromagnetic fields must be adjusted to become compatible with this new grid configuration. In this work we focus on electrostatic PIC which relies on Poisson's equation to obtain electric potential. Accordingly, in the following, we derive the formulation of the reduced-dimension Poisson's equation to be incorporated within electrostatic RO-PIC. Without losing generality, from this point forward, we present the methodology for a two-dimensional domain and, thus, the 2D Poisson's equation.

A) Single-region decomposition: To introduce the basic concepts behind the dimensionality-reduction approach, we start with presenting the formulation for the limiting case in which we use only one region covering the entire computational domain. In this case, as illustrated in **Fig. 2.4**, the 2D domain with the extents of L_x and L_y along the x and y directions, respectively, is represented by two perpendicular computation grids, one along x and one along y. The computational cells along x have the width Δx, and are extended over the entire L_y extent of the domain. Similarly, the computational cells along y have the width Δy and a length equal to L_x. It must be noted that Δx and Δy are determined according to the numerical requirement of the traditional PIC. We term this representation of the domain the "single-region" decomposition, since we have a single set of perpendicular grids representing the entire domain.

Note that the purpose of the reduced-order grid is to achieve a decoupling between the involved dimensions. In this regard, each grid, along x- or y- axis, captures the variation of the electric potential ($\phi(x,y)$) along its respective direction. Thus, we need to define two potential functions $\phi^x(x)$ and $\phi^y(y)$ representing the variables to be solved along their respective grids. We

emphasize that ϕ^x and ϕ^y are, by definition, only a function of the x- or y-coordinate, respectively, within this single region.

We then *approximate* the 2D potential function $\phi(x,y)$ as the superposition of these two potential functions, i.e.,

$$\phi(x,y) \approx \phi^x(x) + \phi^y(y). \qquad \text{Eq. 2.7}$$

Substituting Eq. 2.7 in the 2D Poisson's equation (Eq. 1.27)

$$\nabla^2\phi(x,y) = \frac{\partial^2\phi(x,y)}{\partial x^2} + \frac{\partial^2\phi(x,y)}{\partial y^2} = -\frac{\rho(x,y)}{\epsilon_0}, \qquad \text{Eq. 2.8}$$

and integrating once along the horizontal (x) and once along the vertical (y) extents of the computational cells yields a coupled system of 1D Ordinary Differential Equations (ODEs) for ϕ^x and ϕ^y, respectively, which is compatible with the definition of the reduced-order grid,

$$\frac{d^2\phi^x(x)}{dx^2}L_y + \frac{d\phi^y(y)}{dy}\Big|_{y_g+\frac{L_y}{2}} - \frac{d\phi^y(y)}{dy}\Big|_{y_g-\frac{L_y}{2}} = -\frac{1}{\epsilon_0}\int_{y_g-\frac{L_y}{2}}^{y_g+\frac{L_y}{2}} \rho(x,y)dy, \qquad \text{Eq. 2.9}$$

$$\frac{d^2\phi^y(y)}{dy^2}L_x + \frac{d\phi^x(x)}{dx}\Big|_{x_g+\frac{L_x}{2}} - \frac{d\phi^x(x)}{dx}\Big|_{x_g-\frac{L_x}{2}} = -\frac{1}{\epsilon_0}\int_{x_g-\frac{L_x}{2}}^{x_g+\frac{L_x}{2}} \rho(x,y)dx. \qquad \text{Eq. 2.10}$$

In the above equations, x_g and y_g are the y and x locations of the computation grid as shown in **Fig. 2.4** , respectively, with respect to the origin, and $\rho(x,y)$ is the 2D charge density distribution.

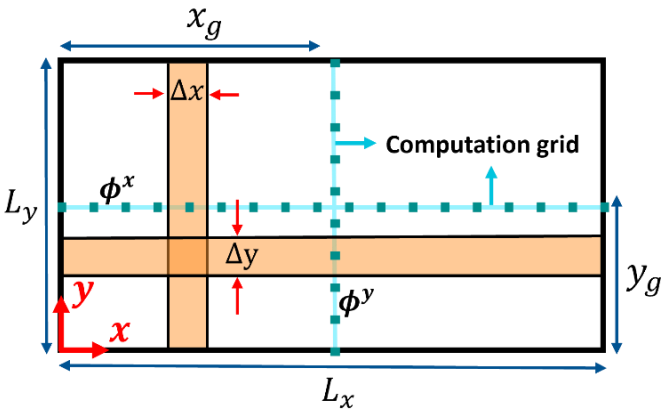


Fig. 2.4: Schematic of the computational grid in single-region domain decomposition for reduced-dimension Poisson's equation.

It is noted that, despite averaging out certain 2D variations in the potential profile with the single-region approximation, the Gauss's law (recovered by summing Eq. 2.9 and Eq. 2.10) is, on average, satisfied over the domain. This ensures the overall physical consistency of the solution.

B) Multi-region decomposition: We then extend the single-region decomposition formulation described above to the multi-region decomposition, where the 2D domain is now decomposed into a grid of $N \times M$ regions, denoted by $\Omega_{n,m}$ (**Fig. 2.5** (a)). The regions' boundary is defined such that it is equidistant from the two computational nodes adjacent to it. *Within each region*, there is a set of perpendicular grids along which the 1D potential functions ϕ_n^x and ϕ_m^y ($m \in [1,M]$ and $n \in [1,N]$), are resolved. ϕ_n^x is specific to the n-th horizontal stripe encompassing regions $\Omega_{n,j}$ where $j \in [1,M]$, and only varies along x and remain constant across the entire y-

extent of the regions $\Omega_{n,j}$ (**Fig. 2.5 (b)**). Similarly, ϕ_m^y pertains to the m-th vertical stripe which includes regions $\Omega_{i,m}$, $i \in [1, N]$, and only varies along y while remaining constant across the x-extent of the regions $\Omega_{i,m}$ (**Fig. 2.5 (b)**). Hence,

$$\phi_n^x = \phi_n^x(x)\,, \quad \forall x \in [0, L_x]\,, \quad y \in \left[y_{g,n} - \frac{L_{y,n}}{2}, y_{g,n} + \frac{L_{y,n}}{2}\right], \qquad \text{Eq. 2.11}$$

$$\phi_m^y = \phi_m^y(y)\,, \quad \forall x \in \left[x_{g,m} - \frac{L_{x,m}}{2}, x_{g,m} + \frac{L_{x,m}}{2}\right], \quad y \in [0, L_y], \qquad \text{Eq. 2.12}$$

where, $L_{x,m}$ and $L_{y,n}$ are the horizontal and vertical extents of the region $\Omega_{n,m}$. Also, $x_{g,m}$ and $y_{g,n}$ are the locations of the vertical and horizontal computation grids of the region $\Omega_{n,m}$, respectively, as depicted in **Fig. 2.5** (a).

Within the region $\Omega_{n,m}$, where $m = 1,2, \dots M$ and $n = 1,2, \dots, N$, the 2D potential function is then approximated as

$$\phi(x,y) \approx \phi_n^x(x) + \phi_m^y(y)\,, \qquad \forall x, y \in \Omega_{n,m}\,. \qquad \text{Eq. 2.13}$$

Similar to the approach followed for single-region decomposition, we substitute Eq. 2.13 in the 2D Poisson's equation and integrate separately along the x and y directions within each region. Note that here the integration is performed over the extent of the individual regions as opposed to the entire domain's length, as done in the single-region case. This leads to a general formulation for the reduced-dimension Poisson's system of equations in the form of a system of coupled of ODEs

$$\left(\frac{d^2\phi_n^x}{dx^2}\Big|_{x=x_i}\right)L_{y,n} + \left(\int_{y_{g,n}-\frac{L_{y,n}}{2}}^{y_{g,n}+\frac{L_{y,n}}{2}} \left(\frac{\partial \phi_m^y}{\partial x}\Big|_{x=x_i+\frac{\Delta x}{2}}\right) dy - \int_{y_{g,n}-\frac{L_{y,n}}{2}}^{y_{g,n}+\frac{L_{y,n}}{2}} \left(\frac{\partial \phi_m^y}{\partial x}\Big|_{x=x_i-\frac{\Delta x}{2}}\right) dy\right)\frac{1}{\Delta x}$$
$$+ \left(\frac{\partial \phi_m^y}{\partial y}\Big|_{y=y_{g,n}+\frac{L_{y,n}}{2}} + \frac{\partial \phi_n^x}{\partial y}\Big|_{y=y_{g,n}+\frac{L_{y,n}}{2}}\right) - \left(\frac{\partial \phi_m^y}{\partial y}\Big|_{y=y_{g,n}-\frac{L_{y,n}}{2}} + \frac{\partial \phi_n^x}{\partial y}\Big|_{y=y_{g,n}-\frac{L_{y,n}}{2}}\right) \qquad \text{Eq. 2.14}$$
$$= -\frac{1}{\epsilon_0}\int_{y_{g,n}-\frac{L_{y,n}}{2}}^{y_{g,n}+\frac{L_{y,n}}{2}} \rho(x,y)dy,$$

$$\left(\frac{d^2\phi_m^y}{dy^2}\Big|_{y=y_j}\right)L_{x,m} + \left(\int_{x_{g,m}-\frac{L_{x,m}}{2}}^{x_{g,m}+\frac{L_{x,m}}{2}} \left(\frac{\partial \phi_n^x}{\partial y}\Big|_{y=y_j+\frac{\Delta y}{2}}\right) dx - \int_{x_{g,m}-\frac{L_{x,m}}{2}}^{x_{g,m}+\frac{L_{x,m}}{2}} \left(\frac{\partial \phi_n^x}{\partial y}\Big|_{y=y_j-\frac{\Delta y}{2}}\right) dx\right)\frac{1}{\Delta y} \qquad \text{Eq. 2.15}$$
$$+ \left(\frac{\partial \phi_n^x}{\partial x}\Big|_{x=x_{g,m}+\frac{L_{x,m}}{2}} + \frac{\partial \phi_m^y}{\partial x}\Big|_{x=x_{g,m}+\frac{L_{x,m}}{2}}\right) - \left(\frac{\partial \phi_n^x}{\partial x}\Big|_{x=x_{g,m}-\frac{L_{x,m}}{2}} + \frac{\partial \phi_m^y}{\partial x}\Big|_{x=x_{g,m}-\frac{L_{x,m}}{2}}\right)$$
$$= -\frac{1}{\epsilon_0}\int_{x_{g,m}-\frac{L_{x,m}}{2}}^{x_{g,m}+\frac{L_{x,m}}{2}} \rho(x,y)dx.$$

In Eq. 2.14 and Eq. 2.15, x_i is the x-coordinate of computational node i along a horizontal grid and y_j is similarly the y-coordinate of node j along a vertical grid.

In Eq. 2.14 and Eq. 2.15, we note the appearance of the so-called "cross-derivative" terms, $\partial\phi_n^x/\partial y$ and $\partial\phi_m^y/\partial x$, that take into account the variations in ϕ_n^x and ϕ_m^y when transiting from one region to another along the y and x directions, respectively.

Moreover, recalling that, inside each region $\Omega_{n,m}$, ϕ_n^x is, by definition, constant along y, and ϕ_m^y is likewise constant along x, the integral terms within the second parentheses on the left-hand side of Eq. 2.14 and Eq. 2.15 are zero for the computational cells that reside entirely inside each region. In other words, the integrand terms $\frac{\partial \phi_m^y}{\partial x}|_{x=x_i+\frac{\Delta x}{2}}$ and $\frac{\partial \phi_m^y}{\partial x}|_{x=x_i-\frac{\Delta x}{2}}$ in Eq. 2.14 and, similarly, $\frac{\partial \phi_n^x}{\partial y}|_{y=y_j+\frac{\Delta y}{2}}$ and $\frac{\partial \phi_n^x}{\partial y}|_{y=y_j-\frac{\Delta y}{2}}$ in Eq. 2.15 are non-zero only when one side of a computational cell lies on a region's boundary.

The extension of multi-region decomposition of Poisson's equation to 3D is provided in Appendix A.2.

Having solved the coupled system of equations given by Eq. 2.14 and Eq. 2.15 for ϕ_n^x and ϕ_m^y with the appropriate boundary conditions, which are described in the next section, the electric field is determined within each region using $\vec{E} = -\vec{\nabla}\phi(x,y) = -\vec{\nabla}(\phi_n^x(x) + \phi_m^y(y))$.

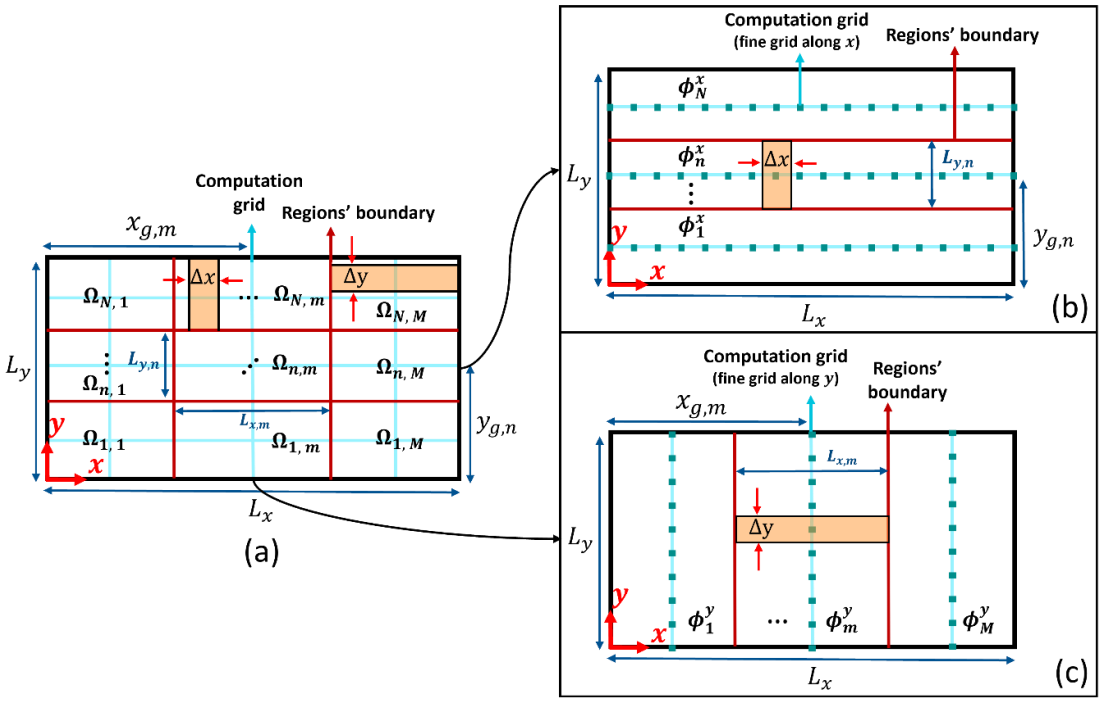


Fig. 2.5: Schematic of the multi-region domain decomposition for the reduced-dimension Poisson's equation; (a) definition of the regions, (b) computation grid along x for solution of ϕ^x, and (c) computation grid along y for solution of ϕ^y.

2.2.2.1. Boundary conditions of reduced-dimension Poisson's equation

The boundary conditions must also be adapted to be compatible with the reduced-dimension formulation, to solve the system of equations given by either Eq. 2.14 and Eq. 2.15 for a general multi-region decomposition or by Eq. 2.9 and Eq. 2.10 for special case of single-region application. In the following, we discuss the adaptation of three relevant boundary conditions, namely Dirichlet, periodic and Neumann boundary conditions consistent with the generalized multi-region equations.

A) Dirichlet boundary condition: Assume fixed potential Dirichlet boundary conditions at $x = x_b$ and $y = y_b$ boundaries such that

$$\begin{cases} \phi(x_b, y) = \xi_b(y), & y \in [0, L_y], \\ \phi(x, y_b) = \eta_b(x), & x \in [0, L_x]. \end{cases} \quad \text{Eq. 2.16}$$

Substituting Eq. 2.16 in Eq. 2.13 and integrating over the extents of the regions along x and y separately, yields the boundary conditions on ϕ_n^x and ϕ_m^y

$$\begin{cases} \phi_n^x(x_b) + \phi_m^{y0} = \dfrac{1}{L_{y,n}} \displaystyle\int_{y_{g,n}-\frac{L_{y,n}}{2}}^{y_{g,n}+\frac{L_{y,n}}{2}} \xi_b(y)\ dy, \quad n \in [1, N], \quad m = 1, x_b = 0 \text{ or } m = M, x_b = L_x \\ \phi_m^y(y_b) + \phi_n^{x0} = \dfrac{1}{L_{x,m}} \displaystyle\int_{x_{g,m}-\frac{L_{x,m}}{2}}^{x_{g,m}+\frac{L_{x,m}}{2}} \eta_b(x)\ dx, \quad m \in [1, M], \quad n = 1, y_b = 0 \text{ or } n = N, y_b = L_y \end{cases} \quad \text{Eq. 2.17}$$

where,

$$\begin{cases} \phi_m^{y0} = \dfrac{1}{L_{y,n}} \displaystyle\int_{y_{g,n}-\frac{L_{y,n}}{2}}^{y_{g,n}+\frac{L_{y,n}}{2}} \phi_m^y(y) dy, \\ \phi_m^{y0} = \dfrac{1}{L_{y,n}} \displaystyle\int_{y_{g,n}-\frac{L_{y,n}}{2}}^{y_{g,n}+\frac{L_{y,n}}{2}} \phi_m^y(y) dy. \end{cases} \quad \text{Eq. 2.18}$$

B) Periodic boundary condition: The periodic boundary condition along the x-axis, can be represented by as a zero-volt reference potential applied to ϕ_n^x at the domain boundaries in this direction ($x = x_b$), while leaving ϕ_m^y free. This approach of implementing periodicity follows the standard method employed in 1D simulations. Similarly, periodicity along the y-direction is achieved by imposing a zero-voltage reference potential on ϕ_m^y at the horizontal boundaries of the domain ($y = y_b$) and allowing ϕ_n^x to remain unconstrained.

$$\begin{cases} \phi_n^x(x_b) = 0, & n \in [1, N], \quad x_b = 0, L_x, \\ \phi_m^y(y_b) = 0, & m \in [1, M], \quad y_b = 0, L_y. \end{cases} \quad \text{Eq. 2.19}$$

C) Neumann boundary condition: Consider the following Neumann conditions at $x = x_b$ and $y = y_b$ boundaries

$$\begin{cases} \dfrac{\partial \phi(y)}{\partial x}|_{x=x_b} = \delta_b(y), & y \in [0, L_y], \\ \dfrac{\partial \phi(x)}{\partial y}|_{y=y_b} = \sigma_b(x), & x \in [0, L_x]. \end{cases} \quad \text{Eq. 2.20}$$

Similar to the approach followed for periodic boundary condition, the Neumann boundary condition is imposed on either ϕ_n^x or ϕ_m^y independently, which leads to

$$\begin{cases} \dfrac{\partial \phi_n^x(x)}{\partial x}|_{x=x_b} = \delta_b(y), & n \in [1, N], \quad x_b = 0, L_x, \\ \dfrac{\partial \phi_m^y(y)}{\partial y}|_{y=y_b} = \sigma_b(x), & m \in [1, M], \quad y_b = 0, L_y. \end{cases} \quad \text{Eq. 2.21}$$

2.2.2.2. Proof of convergence to full-2D Poisson's equation

The purpose of this mathematical proof is to demonstrate that the reduced-dimension Poisson's system of equations obtained from the application of the dimensionality-reduction technique converges to the 2D Poisson's equation *in the limit where the regions' extents approach the 2D cells' sizes*, i.e.

$$L_{x,m} = \Delta x, \quad \forall m \in [1, M] \quad \text{and} \quad L_{y,n} = \Delta y, \quad \forall n \in [1, N]\,. \qquad \text{Eq. 2.22}$$

Fig. 2.6, which depicts the schematic of the computational elements associated with dimensionality-reduction approach, along the x and y directions within region $\Omega_{m,n}$. In this figure, the terms E_N, E_S, E_E and E_W represent, respectively, the electric field components along the North, South, East, and West sides of a computational element. The electric field components, shown in **Fig. 2.6**, is consistent with the definition presented in Section 2.2.2, i.e., $\vec{E} = -\vec{\nabla}\left(\phi_n^x(x) + \phi_m^y(y)\right)$. The colored differential terms are the "cross-derivative" terms, with the blue ones being the terms that are always non-zero in Eq. 2.14 and Eq. 2.15, whereas the terms in red are only non-zero when one side of the computational element falls on a region's boundary.

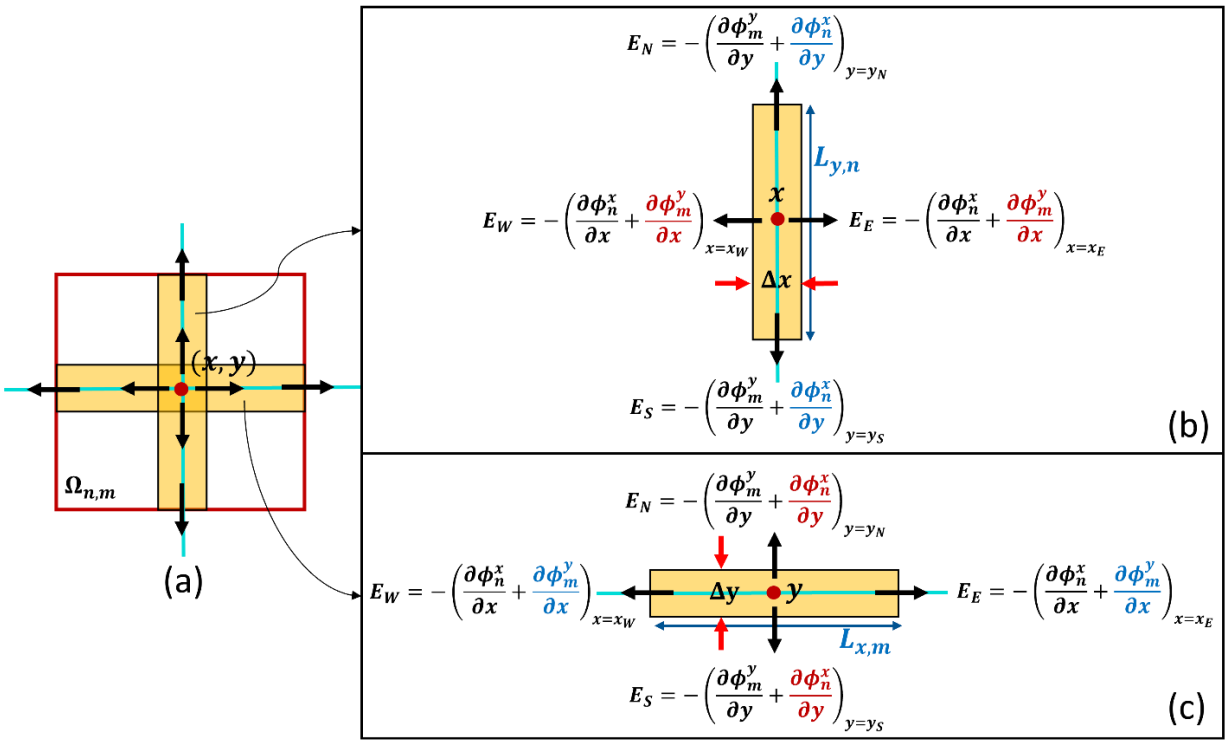


Fig. 2.6: Schematic of (a) the horizontal and the vertical computational elements associated with the dimensionality-reduction approach in region $\Omega_{m,n}$, (b) the electric field components across the sides of the vertical element for solving potential function ϕ_n^x along the x-direction, (c) the electric field components across the sides of the horizontal element for solving potential function ϕ_m^y along the y-direction.

At this point, we recall the integral form of Gauss' law, as given by

$$\int_{\delta S} \vec{E} \cdot d\vec{S} = \frac{Q}{\epsilon_0}, \qquad \text{Eq. 2.23}$$

in which $\vec{E}$ is the electric field vector, $\vec{S}$ is the vector representing the surface area of a computational element, and Q is the total charge enclosed within the computational volume. δS denotes the boundary of the computational cell.

Gauss's law can be written as in Eq. 2.24 and Eq. 2.25 for the vertical and the horizontal computational element in **Fig. 2.6**, respectively,

$$\int_{y_{g,n}-\frac{L_{y,n}}{2}}^{y_{g,n}+\frac{L_{y,n}}{2}} (E_E - E_W)dy + (E_N - E_S)\Delta x = \frac{\Delta x}{\epsilon_0}\int_{y_{g,n}-\frac{L_{y,n}}{2}}^{y_{g,n}+\frac{L_{y,n}}{2}} \rho dy, \qquad \text{Eq. 2.24}$$

$$(E_E - E_W)\Delta y + \int_{x_{g,m}-\frac{L_{x,m}}{2}}^{x_{g,m}+\frac{L_{x,m}}{2}} (E_N - E_S)dx = \frac{\Delta y}{\epsilon_0}\int_{x_{g,m}-\frac{L_{x,m}}{2}}^{x_{g,m}+\frac{L_{x,m}}{2}} \rho dx. \qquad \text{Eq. 2.25}$$

Replacing the definition of the electric field components into Eq. 2.24 and Eq. 2.25 and summing both equations yields

$$\begin{aligned}(L_y + \Delta y)\left(\frac{\partial \phi_n^x}{\partial x}|_{x_W} - \frac{\partial \phi_n^x}{\partial x}|_{x_E}\right) + (L_x + \Delta x)\left(\frac{\partial \phi_m^y}{\partial y}|_{y_S} - \frac{\partial \phi_m^y}{\partial y}|_{y_N}\right) + \Delta x\left(\frac{\partial \phi_n^x}{\partial y}|_{y_S} - \frac{\partial \phi_n^x}{\partial y}|_{y_N}\right) \\ + \Delta y\left(\frac{\partial \phi_m^y}{\partial x}|_{x_W} - \frac{\partial \phi_m^y}{\partial x}|_{x_E}\right) + \int_{x_{g,m}-\frac{L_{x,m}}{2}}^{x_{g,m}+\frac{L_{x,m}}{2}}\left(\frac{\partial \phi_n^x}{\partial y}|_{y_S} - \frac{\partial \phi_n^x}{\partial y}|_{y_N}\right)dx \\ + \int_{y_{g,n}-\frac{L_{y,n}}{2}}^{y_{g,n}+\frac{L_{y,n}}{2}}\left(\frac{\partial \phi_m^y}{\partial x}|_{x_W} - \frac{\partial \phi_m^y}{\partial x}|_{x_E}\right)dy = \frac{\Delta x}{\epsilon_0}\int_{y_{g,n}-\frac{L_{y,n}}{2}}^{y_{g,n}+\frac{L_{y,n}}{2}} \rho dy + \frac{\Delta y}{\epsilon_0}\int_{x_{g,m}-\frac{L_{x,m}}{2}}^{x_{g,m}+\frac{L_{x,m}}{2}}\end{aligned} \qquad \text{Eq. 2.26}$$

As we increase the number of regions, the lengths of the regions, $L_{y,n}$ and $L_{x,m}$ decrease. In the limit of having as many regions as there are computational cells ($M = N_i,\ N = N_j$, where N_i and N_j are the number of cells along x and y directions in 2D), the length $L_{y,n}$ approaches Δy and the length $L_{x,m}$ approaches Δx. In this situation, the computational elements along x and y directions effectively collapse on each other, and both coincide with the 2D computational cells as illustrated in **Fig. 2.7**. In other words, the reduced-dimension computational grid becomes equivalent to the full-2D grid.

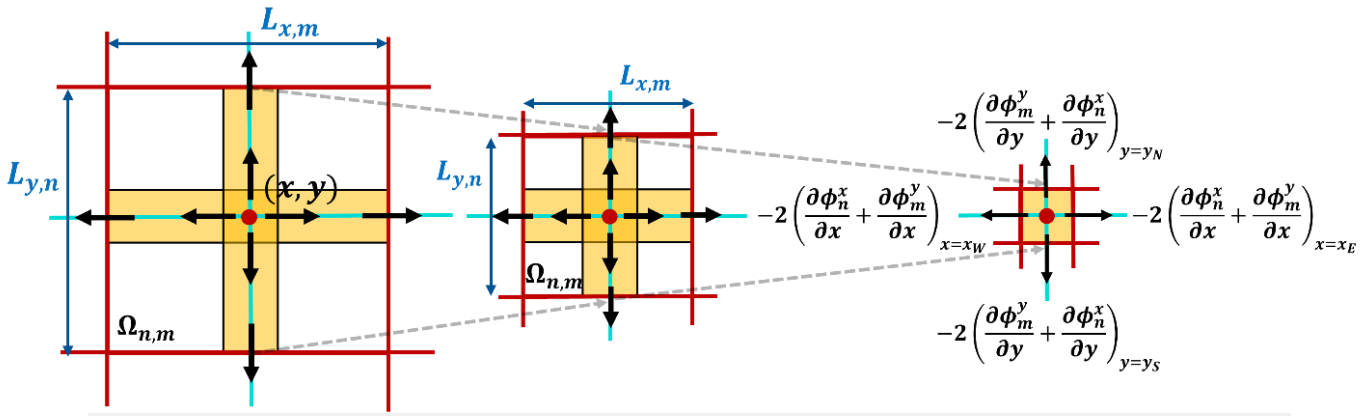


Fig. 2.7: Schematic illustrating that at the limit where the regions are as small as the 2D cells, the computational elements along x and y axes coincides the cells of a full-2D grid, making the reduced-dimension computational grid equivalent to the full-2D grid.

Consequently, in this limit we have $\phi_n^x(x) = \phi_m^y(y)$, since under this condition $x_g = x$ and $y_g = y$. Also, in this limit, Eq. 2.13 will no longer be an approximation and becomes exact. Given these, we find that $\phi_n^x(x) = \phi_m^y(y) = \frac{1}{2}\phi(x, y)$. Moreover, $L_{x,m} = \Delta x$ and $L_{y,n} = \Delta y$. Substituting these into Eq. 2.26 yields

$$2\Delta y\left(\left(\frac{\partial\phi(x,y)}{\partial x}\right)_{x=x_W}-\left(\frac{\partial\phi(x,y)}{\partial x}\right)_{x=x_E}\right)+2\Delta x\left(\left(\frac{\partial\phi(x,y)}{\partial y}\right)_{y=y_S}-\left(\frac{\partial\phi(x,y)}{\partial y}\right)_{y=y_N}\right)=\frac{2}{\epsilon_0}\rho(x,y)\Delta x\Delta y. \quad \text{Eq. 2.27}$$

Dividing both sides of Eq. 2.27 by 2 and by $\Delta x\Delta y$, the 2D Poisson's equation can be recovered. This proves the convergence of the dimensionality-reduction formulation towards the full-2D solution as $\frac{L_{x,m}}{\Delta x}$ and $\frac{L_{y,m}}{\Delta y}$ approaching unity and thereby verifying the mathematical consistency of the dimensionality-reduction formulation.

2.2.2.3. Numerical implementation of Reduced-dimension Poisson's equation in RO-PIC

The IPPL-Q2D code, which is based on the reduced-order PIC scheme, features an electric potential field solver, which we have termed "Reduced-Dimension" Poisson Solver, or RDPS. The RDPS numerically solves the system of coupled equations given by Eq. 2.14 and Eq. 2.15 using Julia's built-in direct matrix solve algorithm based on the LU decomposition method. However, for the solver's implementation in the PIC scheme, the terms corresponding to the gradients of the potential function ϕ_m^y in Eq. 2.14 and, similarly, the terms representing the gradients of ϕ_n^x in Eq. 2.15 are moved to the right-hand side and are, thus, calculated from the previous timestep of the simulation

$$\left(\frac{d^2\phi_n^x}{dx^2}|_{x=x_i}\right)L_{y,n}+\frac{\partial\phi_n^x}{\partial y}|_{y=y_{g,n}+\frac{L_{y,n}}{2}}-\frac{\partial\phi_n^x}{\partial y}|_{y=y_{g,n}-\frac{L_{y,n}}{2}}$$
$$=-\frac{1}{\epsilon_0}\int_{y_{g,n}-\frac{L_{y,n}}{2}}^{y_{g,n}+\frac{L_{y,n}}{2}}\rho(x,y)dy-\frac{\partial\phi_m^y}{\partial y}|_{y=y_{g,n}+\frac{L_{y,n}}{2}}+\frac{\partial\phi_m^y}{\partial y}|_{y=y_{g,n}-\frac{L_{y,n}}{2}} \quad \text{Eq. 2.28}$$
$$-\left(\int_{y_{g,n}-\frac{L_{y,n}}{2}}^{y_{g,n}+\frac{L_{y,n}}{2}}\left(\frac{\partial\phi_m^y}{\partial x}|_{x=x_i+\frac{\Delta x}{2}}\right)dy-\int_{y_{g,n}-\frac{L_{y,n}}{2}}^{y_{g,n}+\frac{L_{y,n}}{2}}\left(\frac{\partial\phi_m^y}{\partial x}|_{x=x_i-\frac{\Delta x}{2}}\right)dy\right)\frac{1}{\Delta x},$$

$$\left(\frac{d^2\phi_m^y}{dy^2}|_{y=y_j}\right)l_x+\frac{\partial\phi_m^y}{\partial x}|_{x=x_{g,m}+\frac{L_{x,m}}{2}}-\frac{\partial\phi_m^y}{\partial x}|_{x=x_{g,m}-\frac{L_{x,m}}{2}}$$
$$=-\frac{1}{\epsilon_0}\int_{x_{g,m}-\frac{L_{x,m}}{2}}^{x_{g,m}+\frac{L_{x,m}}{2}}\rho(x,y)dx-\frac{\partial\phi_n^x}{\partial x}|_{x=x_{g,m}+\frac{L_{x,m}}{2}}+\frac{\partial\phi_n^x}{\partial x}|_{x=x_{g,m}-\frac{L_{x,m}}{2}} \quad \text{Eq. 2.29}$$
$$-\left(\int_{x_{g,m}-\frac{L_{x,m}}{2}}^{x_{g,m}+\frac{L_{x,m}}{2}}\left(\frac{\partial\phi_n^x}{\partial y}|_{y=y_j+\frac{\Delta y}{2}}\right)dx-\int_{x_{g,m}-\frac{L_{x,m}}{2}}^{x_{g,m}+\frac{L_{x,m}}{2}}\left(\frac{\partial\phi_n^x}{\partial y}|_{y=y_j-\frac{\Delta y}{2}}\right)dx\right)\frac{1}{\Delta y}.$$

In this way, the system of equation is kind of decoupled, which is computationally beneficial as the size of the matrix to be solved can be reduced by half, by solving Eq. 2.28 and Eq. 2.29 separately. Moreover, we observed an increased robustness and stability of the solver when following this approach without any noticeable issues concerning the numerical artifacts and/or instabilities.

It is also important to mention that, before calculating the right-hand side derivative terms specified in the preceding paragraph and solely for the purpose of these calculations, a moving average filter with

a pre-fixed window size is applied to the solutions of the potential functions ϕ_n^x and ϕ_m^y . This is done to reduce the effect of noise in the calculation of these derivatives.

Eq. 2.28 and Eq. 2.29 are discretized on the reduced-dimension computational grid. In an arbitrary region $\Omega_{m,n}$ within a 2D domain, the reduced-dimension computational grid comprises two perpendicular 1D grids along x and y directions. These grids, depicted by the dark blue color in **Fig. 2.8** (a), intersect at the center of the region. According to the definition of the reduced-dimension grid, the node (i,j) on a 2D grid is reconstructed using independent contributions from the node i along x-grid (vertical cell in **Fig. 2.8** (a)) and the node j along y-grid (horizontal cell in **Fig. 2.8** (a)). Note that the values on x-grid are constant across the y-extent of the region and similarly, the values on y-grid are constant across the x-extent of the region. In other words, x and y components of the grid can be displaced perpendicular to their direction to anywhere within the region. Thus, a perpendicular grid passing through the node (i,j), shown in light blue in **Fig. 2.8** (a), is a replica of the computational grid with equivalent nodal values. We use this virtual grid just for illustrative purposes. The stencils used to discretize Eq. 2.28 and Eq. 2.29 are depicted in **Fig. 2.8** (b) and **Fig. 2.8** (c), respectively.

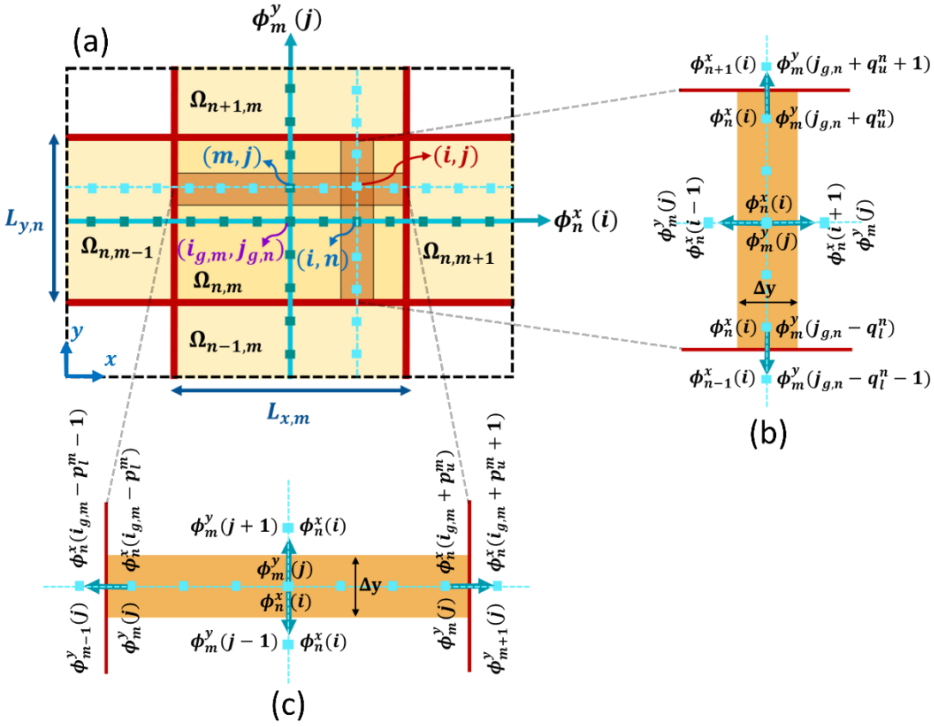


Fig. 2.8: Schematic illustrating (a) the reduced-dimension computational grid in region $\Omega_{m,n}$, (b) and (c) stencils used for the discretization of the derivatives in Eq. 2.28 and Eq. 2.29, respectively.

Accordingly, the discretization of the derivative terms in Eq. 2.28 and Eq. 2.29 are provided in the following. These include the second derivative in the first term in these equations which are discretized following the second-order accurate central finite difference scheme

$$\frac{d^2\phi_n^x}{dx^2}\Big|_{x=x_i} = \frac{\phi_n^x(i+1) - 2\phi_n^x(i) + \phi_n^x(i-1)}{\Delta x^2},$$

$$\frac{d^2\phi_m^y}{dy^2}\Big|_{y=y_j} = \frac{\phi_m^y(j+1) - 2\phi_m^y(j) + \phi_m^y(j-1)}{\Delta y^2}. \qquad \text{Eq. 2.30}$$

For the first derivatives, we use the first-order accurate forward difference. These include the derivatives in the second and the third terms in Eq. 2.28 and Eq. 2.29

$$\frac{\partial \phi_n^x}{\partial y}\Big|_{y=y_{g,n}+\frac{L_{y,n}}{2}} = \frac{\phi_{n+1}^x(i)-\phi_n^x(i)}{\Delta y}, \qquad \frac{\partial \phi_n^x}{\partial y}\Big|_{y=y_{g,n}-\frac{L_{y,n}}{2}} = \frac{\phi_n^x(i)-\phi_{n-1}^x(i)}{\Delta y}, \qquad \text{Eq. 2.31}$$

$$\frac{\partial \phi_m^y}{\partial x}\Big|_{x=x_{g,m}+\frac{L_{x,m}}{2}} = \frac{\phi_{m+1}^y(j)-\phi_m^y(j)}{\Delta x}, \qquad \frac{\partial \phi_m^y}{\partial x}\Big|_{x=x_{g,m}-\frac{L_{x,m}}{2}} = \frac{\phi_m^y(j)-\phi_{m-1}^y(j)}{\Delta x}, \qquad \text{Eq. 2.32}$$

as well as the derivatives in the second and the third terms in the right-hand side of these equations

$$\frac{\partial \phi_m^y}{\partial y}\Big|_{y=y_{g,n}+\frac{L_{y,n}}{2}} = \frac{\phi_m^y\left(j_{g,n}+q_u^n+1\right)-\phi_m^y\left(j_{g,n}+q_u^n\right)}{\Delta y}, \qquad \frac{\partial \phi_m^y}{\partial y}\Big|_{y=y_{g,n}-\frac{L_{y,n}}{2}} = \frac{\phi_m^y\left(j_{g,n}-q_l^n\right)-\phi_m^y\left(j_{g,n}-q_l^n-1\right)}{\Delta y}, \qquad \text{Eq. 2.33}$$

$$\frac{\partial \phi_n^x}{\partial x}\Big|_{x=x_{g,m}+\frac{L_{x,m}}{2}} = \frac{\phi_n^x\left(i_{g,m}+p_u^m+1\right)-\phi_n^x\left(i_{g,m}+p_u^m\right)}{\Delta x}, \qquad \frac{\partial \phi_n^x}{\partial x}\Big|_{x=x_{g,m}-\frac{L_{x,m}}{2}} = \frac{\phi_n^x\left(i_{g,m}-p_l^m\right)-\phi_n^x\left(i_{g,m}-p_l^m-1\right)}{\Delta x}. \qquad \text{Eq. 2.34}$$

In the above relations, $i_{g,m}$ and $j_{g,n}$ specify the index of the node at the center of the region $\Omega_{m,n}$ along the x-axis and the y-axis, respectively. Also, p_l^m and p_u^m represent the number of nodes, respectively, on the left side and on the right side of $i_{g,m}$ along the x-axis. Similarly, q_l^n and q_u^n denote the number of nodes on top and bottom of $j_{g,n}$ along the y-axis, respectively.

In the regions near the boundaries of the domain (where $m = 1, M$ or $n = 1, N$), these derivatives are computed as follows

$$\frac{\partial \phi_m^y}{\partial y}|_{y=0} = \frac{\phi_m^y(2)-\phi_m^y(1)}{\Delta y}; \quad n=1, \qquad \frac{\partial \phi_m^y}{\partial y}|_{y=L_y} = \frac{\phi_m^y(N_j)-\phi_m^y(N_j-1)}{\Delta y}; \quad n=N, \qquad \text{Eq. 2.35}$$

$$\frac{\partial \phi_n^x}{\partial x}|_{x=0} = \frac{\phi_n^x(2)-\phi_n^x(1)}{\Delta x}; \quad m=1, \qquad \frac{\partial \phi_n^x}{\partial x}|_{x=L_x} = \frac{\phi_n^x(N_i)-\phi_n^x(N_i-1)}{\Delta x}; \quad m=M. \qquad \text{Eq. 2.36}$$

Finally, Eq. 2.37 represents the discretized form of the last two integral terms on the right-hand side of Eq. 2.28. These terms are integrated over the long side (y-extent) of the vertical cells and involve first order "cross-derivatives" of potential function ($\frac{\partial \phi_m^y}{\partial x}$). It is important to note that, as depicted in **Fig. 2.9**, these terms are non-zero exclusively when either of the long vertical sides of the x-grid's cell coincides with the region's vertical boundary (when $i = i_{g,m}-p_l^m, i_{g,m}+p_u^m$). Additionally, within a given cell, only one of these two terms is non-zero — the one on the cell's boundary which is shared between the cell and the region.

$$\int_{y_{g,n}-\frac{L_{y,n}}{2}}^{y_{g,n}+\frac{L_{y,n}}{2}} \left(\frac{\partial \phi_m^y}{\partial x}\Big|_{x=x_i+\frac{\Delta x}{2}}\right) dy = \sum_{jj=j-q_l^n}^{j_{g,n}+q_u^n} \frac{\Delta y}{\Delta x}\left(\phi_{m+1}^y(jj)-\phi_m^y(jj)\right), \qquad i = i_{g,m}-p_l^m$$

$$\int_{y_{g,n}-\frac{L_{y,n}}{2}}^{y_{g,n}+\frac{L_{y,n}}{2}} \left(\frac{\partial \phi_m^y}{\partial x}\Big|_{x=x_i+\frac{\Delta x}{2}}\right) dy = \sum_{jj=j_{g,n}-q_l^n}^{j_{g,n}+q_u^n} \frac{\Delta y}{\Delta x}\left(\phi_{m+1}^y(jj)-\phi_m^y(jj)\right), \qquad i = i_{g,m}+p_u^m \qquad \text{Eq. 2.37}$$

Likewise, the discretization of the corresponding terms in Eq. 2.29, which represents the integrals of cross-derivatives ($\frac{\partial \phi_m^x}{\partial y}$) along the long side ($x$-extent) of the horizontal cells, is provided in Eq. 2.38. Similar to Eq. 2.37, these terms are only non-zero on either of the long horizontal sides of the y-grid's

cell when they align with the horizontal boundary of the region (when $j = j_{g,n} - q_l^n, j_{g,n} + q_u^n$) as shown in **Fig. 2.9**.

$$\int_{x_{g,m}-\frac{L_{x,m}}{2}}^{x_{g,m}+\frac{L_{x,m}}{2}} \left(\frac{\partial \phi_n^x}{\partial y}|_{y=y_j+\frac{\Delta y}{2}}\right) dx = \sum_{ii=i_{g,m}-p_l^m}^{i_{g,m}+p_u^m} \frac{\Delta x}{\Delta y}\left(\phi_{n+1}^x(ii) - \phi_n^x(ii)\right), \qquad j = j_{g,n} - q_l^n$$

$$\int_{x_{g,m}-\frac{L_{x,m}}{2}}^{x_{g,m}+\frac{L_{x,m}}{2}} \left(\frac{\partial \phi_n^x}{\partial y}|_{y=y_j-\frac{\Delta y}{2}}\right) dx = \sum_{ii=i_{g,m}-p_l^m}^{i_{g,m}+p_u^m} \frac{\Delta x}{\Delta y}\left(\phi_n^x(ii) - \phi_{n-1}^x(ii)\right), \qquad j = j_{g,n} + q_u^n \quad \text{Eq. 2.38}$$

It is worth highlighting that even though mathematically, the region sizes could be chosen as small as the individual cells, the numerical implemnetation requires the regions to include at least two nodes along each dimension. This requirement ensures numerical consistency in the computaion of the descretized derivative terms on the opossing sides of the cells. As a result, the largest numbers of regions that can be used in the quasi-2D simulations are $M = \frac{N_i}{2}$ and $N = \frac{N_j}{2}$.

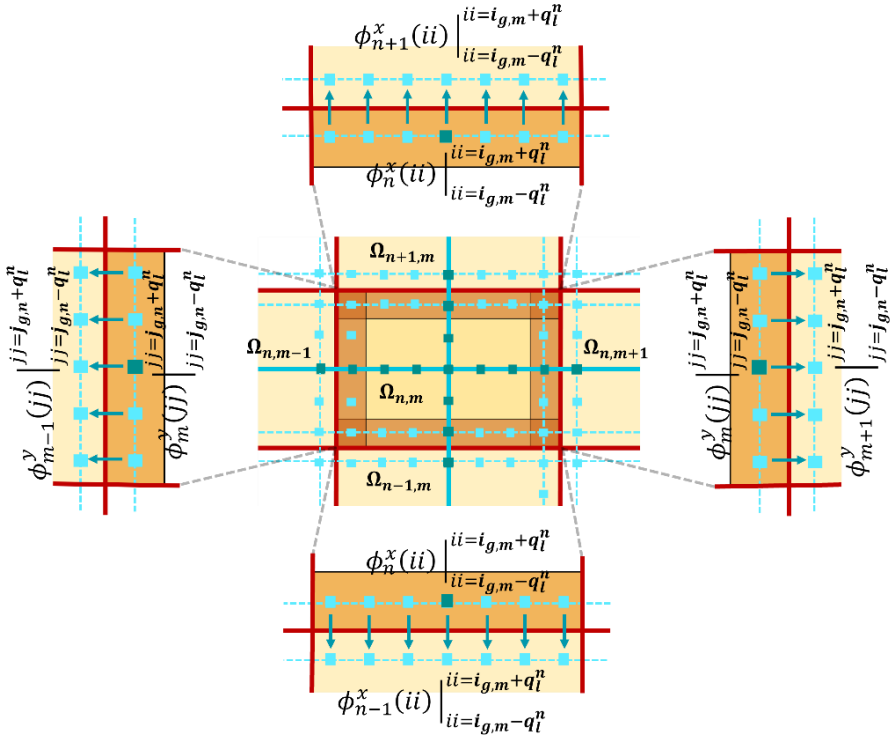


Fig. 2.9: Illustration of the stencil for the cells reaching the region's boundary along their long sides, used for discretization of the last two terms on the right-hand side of Eq. 2.28 and Eq. 2.29. These terms represent the integrals of "cross-derivatives" which are only non-zero on the sides of the cells which align with the region's boundary. (left) $i = i_{g,m} + p_u^m$, (right) $i = i_{g,m} - p_l^m$, (bottom), $j = j_{g,n} - q_l^n$, and (top) $j = j_{g,n} + q_u^n$.

2.3. Computational advantage of RO-PIC

The computational advantage of RO-PIC over the conventional PIC stems from the reduced total number of cells, thereby lower total number of macroparticles for the same number of macroparticles per cell. This reduction alleviates the computational and memory requirements of the PIC simulation. In addition to easing the computational burden on particle-based computations, the reduced number of

cells can also decrease the size of the matrix to be solved in the Poisson solver, which often represents a computational bottleneck in 3D problems.

Accordingly, the computational gain achieved with a quasi-2D simulation compared to a traditional PIC scales linearly with the ratio of the regions' extent to the cell size ($l_x/\Delta x$ or $l_y/\Delta y$, see **Fig. 2.1**). In fact, in a quasi-2D simulation, using M and N regions along the x and y directions with N_i and N_j numbers of cells along the x and y grids, respectively, we will have a set of two grids; the x-grid consists of $N_{cell,x} = N \times N_i$ total cells and the y-grid comprises $N_{cell,y} = M \times N_j$ cells. Therefore, the total number of unknowns in the reduced-dimension Poisson's equation to be solved is $N_\phi = N \times N_i + M \times N_j$ instead of $N_\phi = N_i \times N_j$ in the full-2D Poisson's equation. Moreover, considering that the particles are shared between the two grids, the total number of particles (N_p) in the simulation is determined by the larger number of cells between the two grids, i.e. $N_p = N_{ppc} \times max\big(N \times N_i, M \times N_j\big)$, where N_{ppc} is the number of microparticles per cell.

Extending the RO-PIC approach to 3D (refer to Appendix A.2) brings about even greater computational gain. Specifically, the speedup factor scales quadratically with the ratio of the regions' extents to the cell sizes ($l_x l_y/\Delta x \Delta y$ or $l_y l_z/\Delta y \Delta z$ or $l_x l_z/\Delta x \Delta z$). In this regard, in a quasi-3D simulation with M, N and P regions and N_i, N_j and N_k cells along each simulation dimension, the reduced-dimension computational grid consists of three fine grids; The x-grid is defined by $N_{cell,x} = N \times P \times N_i$ the y-grid by $N_{cell,y} = M \times P \times N_j$ and the z-grid by $N_{cell,y} = M \times N \times N_k$ number of cells. This leads to an unknown matrix with a size of $N_\phi = N \times P \times N_i + M \times N_j + M \times N \times N_k$ in the RDPS in contrast to $N_\phi = N_i N_j N_k$ in a full-3D Poisson solver. Also, the total number of macroparticles in the simulation is $N_p = N_{ppc} \times max\big(N \times P \times N_i, M \times P \times N_j, M \times N \times N_k\big)$.

The low-order approximations of the reduced-order scheme correspond to the limit where $\frac{l_x}{\Delta x} \gg 1$ and $\frac{l_y}{\Delta y} \gg 1$ (or equivalently, $M \ll N_i$ and $N \ll N_j$) in quasi-2D, and $\frac{l_x l_y}{\Delta x \Delta y} \gg 1$, $\frac{l_y l_z}{\Delta y \Delta z} \gg 1$ and $\frac{l_x l_z}{\Delta x \Delta z} \gg 1$ (or $M \ll N_i$, $N \ll N_j$ and $P \ll N_k$) in quasi-3D simulation. In this limit, the computational cost decreases from $O(n^2)$ for a full-2D simulation and $O(n^3)$ for a full-3D simulation to $O(n)$ for quasi-2D and quasi-3D simulations, where n represents the cell count along a single coordinate.

With higher approximation orders we still gain several factors of speedup. This is because sufficiently accurate predictions can be achieved with the regions' extents being several factors larger than the cell sizes, as will be demonstrated in the next section in standalone Poisson's problem and in the subsequent chapter for the plasma cases.

Fig. 2.10 shows the scaling of the computational cost in a quasi-2D and a quasi-3D simulation with various number of regions compared to the respective full-2D and full-3D PIC simulations. This example assumes a domain with 500 cells along each direction and equal number of regions along the involved dimensions.

It is worth noting that the same scaling is valid for the memory requirements of the RO-PIC relative to conventional PIC simulations.

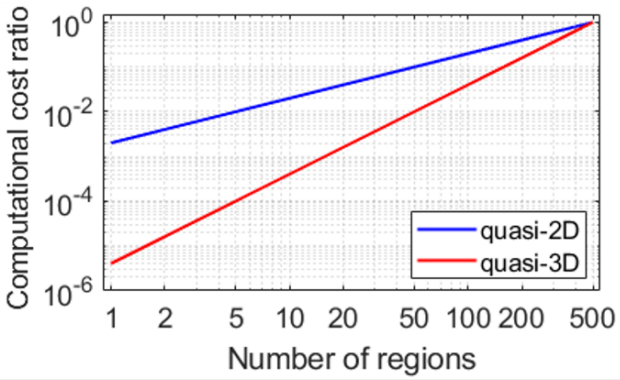


Fig. 2.10: Variation of the computational cost ratio (versus the number of regions) in quasi-2D and quasi-3D simulations compared to the corresponding full-2D and full-3D simulations. These values are calculated assuming 500 number of cells along each dimension and an equal number of regions along all directions. Note that the plot is in log-log scale.

2.4. Standalone verifications of Reduced-Dimension Poisson Solver (RDPS)

In this section we compare the qausi-2D approximations provided by RDPS (which numerically solves Eq. 2.14 and Eq. 2.15) across various numbers of regions with the corresponding full-2D solution. We conducted this comparison across several test cases featuring different source terms and boundary conditions to assess the convergence behavior of RDPS across a wide range of scenarios.

In Section 2.2.2.2 we mathematically proved that the formulation developed for the dimensionality reduction of Poisson's equation, converges to the 2D Poisson's equation in the limit where the number of regions is the same as the number of 2D computational cells, i.e., $N = N_j$ and $M = N_i$. Here, we intend to numerically demonstrate that by increasing the number of regions or, equivalently, the approximation order, the approximate solution from the RDPS converges to the full-2D solution. Furthermore, these examples show to what extent the low-number-of-region quasi-2D approximations of a 2D Poisson problem are representative of the full-2D solution.

To this end, nine different two-dimensional Poisson test cases are considered. The definition of these problems including their source terms ($S(x,y)$) and the boundary conditions are presented in **Table 2.1**. These definitions refer to the 2D Poisson's equation in the following form

$$\frac{\partial^2\phi(x,y)}{\partial x^2}+\frac{\partial^2\phi(x,y)}{\partial y^2}=S(x,y), \qquad x\in[0,L_x]\,, y\in[0,L_y]. \qquad \text{Eq. 2.39}$$

In all cases, the domain is a Cartesian $(x-y)$ plane of unit length (of arbitrary unit, e.g. millimeters) along the x and y directions. For simplicity, the permittivity of free space (ϵ_0) is assumed to be one for all problems. The number of computational cells in both x and y directions are $N_i = N_j = 100$ for all cases. Hence, according to discussion in Section 2.2.2.3 regarding the numerical implementation of RDPS, the maximum number of regions allowed along either direction is $N = M = 50$. The boundary conditions in the first eight cases (cases 1-8) are the Dirichlet condition along both x and y dimensions, whereas the last case (case 9) features the periodic boundary condition along x and the Dirichlet condition along y direction.

Case No.	Source terms ($S(x,y)$)	Boundary Conditions
1	$S = 0$	$\phi(0,y) = \frac{y}{1+y^2};\ \phi(L_x,y) = \frac{y}{4+y^2}$ $\phi(x,0) = 0;\ \phi(x,L_y) = \frac{1}{(1+x)^2+1}$
2	$S = x^2 + y^2$	$\phi(0,y) = \sin(\pi y)$ $\phi(L_x,y) = \exp(\pi L_x)\sin(\pi y) + 0.5y^2$ $\phi(x,0) = 0\ ;\ \phi(x,L_y) = 0.5x^2$
3	$S = \exp(xy)$	$\phi(0,y) = 5(y^2 - y);\ \phi(L_x,y) = -y(y-1)^4$ $\phi(x,0) = 0.5\sin(6\pi x)\ ;\ \phi(x,L_y) = \sin(2\pi x)$
4	$S = 100(x-0.5)^3$	$\phi(0,y) = 0;\ \phi(L_x,y) = 0$ $\phi(x,0) = -(0.5)^3;\ \phi(x,L_y) = (0.5)^3$
5	$S = 0$	$\phi(0,y) = 0;\ \phi(L_x,y) = 0$ $\phi(x,0) = 1;\ \phi(x,L_y) = 0$
6	$S = \frac{1}{\left((x-0.5)(y-0.5)\right)^2}$	$\phi(0,y) = 0;\ \phi(L_x,y) = 0$ $\phi(x,0) = 0;\ \phi(x,L_y) = 0$
7	$S = \begin{cases} -1 & \text{if } x = y = 0.4 \\ 1 & \text{if } x = y = 0.6 \\ 0 & \text{if otherwise} \end{cases}$	$\phi(0,y) = 0;\ \phi(L_x,y) = 0$ $\phi(x,0) = 0;\ \phi(x,L_y) = 0$
8	$S = 0$	$\phi(0,y) = \frac{1}{y-0.5};\ \phi(L_x,y) = \frac{1}{y-0.5}$ $\phi(x,0) = \frac{1}{x-0.5};\ \phi(x,L_y) = \frac{1}{x-0.5}$
9	$S = ysin(5\pi x) + exp(-50((x-0.5)^2 + (y-0.5)^2))$	$\phi(0,y) = 0;\ \phi(L_x,y) = 0$ $\phi(x,0), \phi(x,L_y)$: Periodic B.C.

Table 2.1: Definition of the 2D Poisson problems for standalone verification of the reduced-dimension Poisson's solver.

This selection of problems encompasses different levels of complexity regarding source terms and boundary conditions, leading to solutions with distinct characteristics. For instance, the potential distributions in cases 3-5 feature strong gradients. Case 6 and 7 are characterized by singularities in their charge distributions which are reflected in their resulting potential profiles. Also, case 8 represents discontinuous variation in the boundary conditions which creates abrupt jumps in the solution. The demonstration of the ability of the RDPS to provide representative approximations of the 2D solution in a diverse set of scenarios is necessary to establish the versatility of the approach.

Fig. 2.11 and **Fig. 2.12** show, respectively, the approximate solutions of the Poisson problems in cases 1-4 and cases 5-8 from the RDPS for various number of regions N and M. These plots correspond to the evolution of the RDPS approximate solution when N and M are increased simultaneously from 3 to 50 regions. The plots represent the reconstructed 2D potential distributions from the solutions of the potential functions ϕ_n^x and ϕ_m^y as per Eq. 2.13. Although, these 3D figures provide a good visual representation of the solution, for a closer comparison between various quasi-2D approximation orders and the full-2D solution, we can look at the corresponding contour plots in **Fig. 2.13** and **Fig. 2.14**.

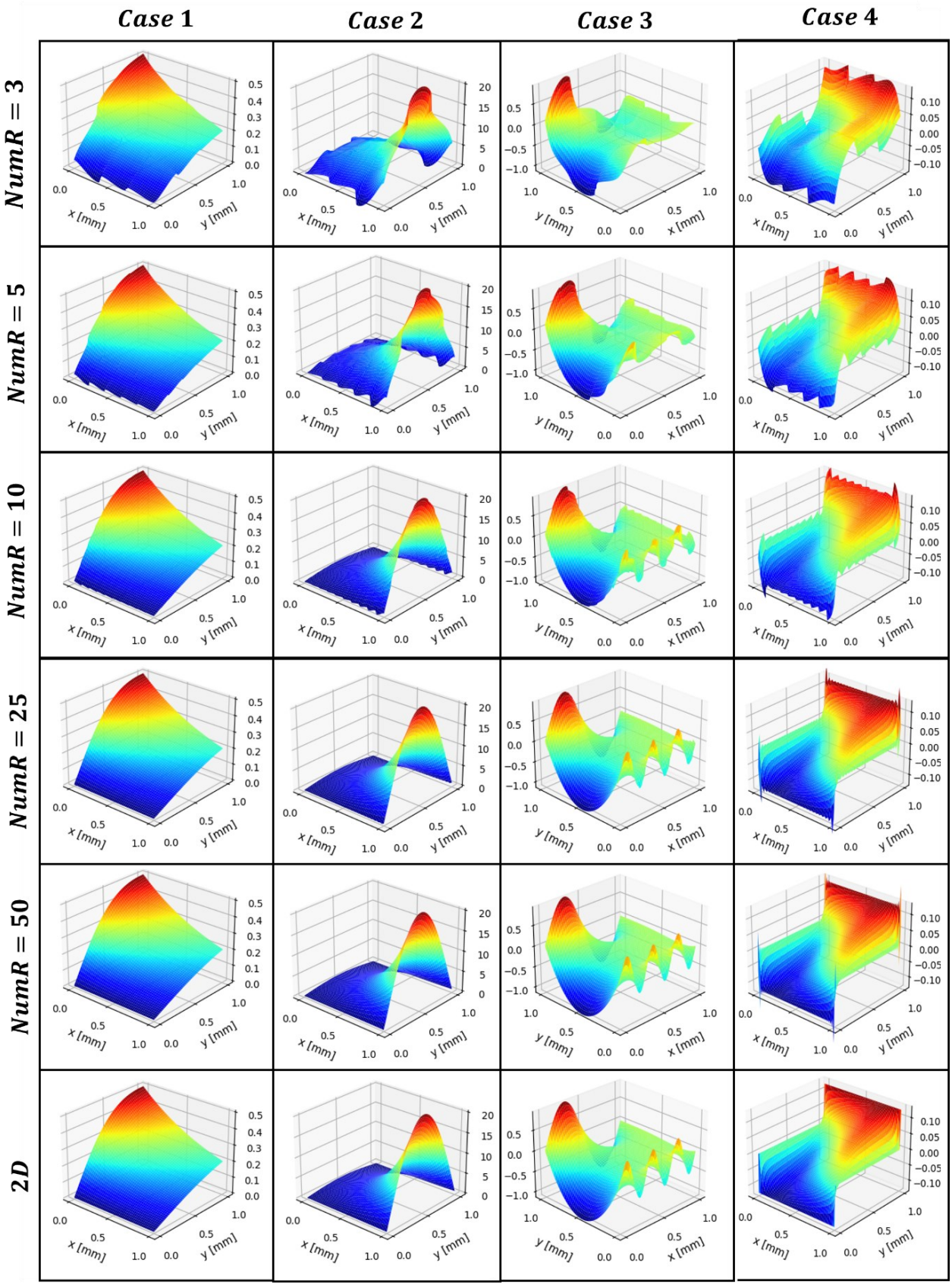


Fig. 2.11: Comparison of the approximate Q2D solutions from the Reduced-Dimension Poisson Solver (RDPS) with various number of regions against the corresponding full-2D solution (bottom row) for cases 1-4 defined in **Table 2.1**. The numbers of regions are equal along both dimensions ($M = N$), which are denoted by *NumR*.

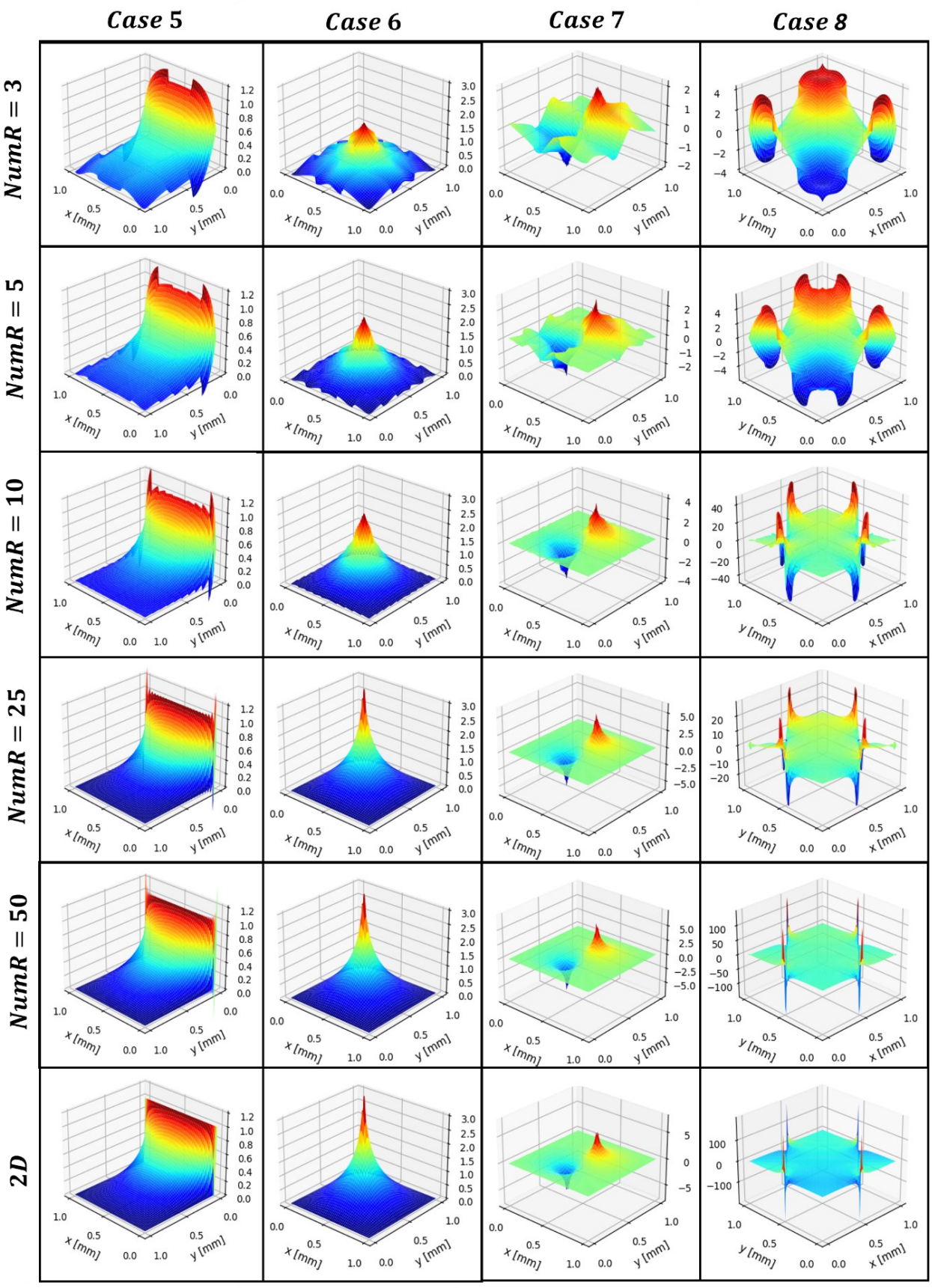


Fig. 2.12: Comparison of the approximate Q2D solutions from the Reduced-Dimension Poisson Solver (RDPS) with various number of regions against the corresponding full-2D solution (bottom row) for cases 5-8 defined in **Table 2.1**. The numbers of regions are equal along both dimensions ($M = N$), which are denoted by *NumR*.

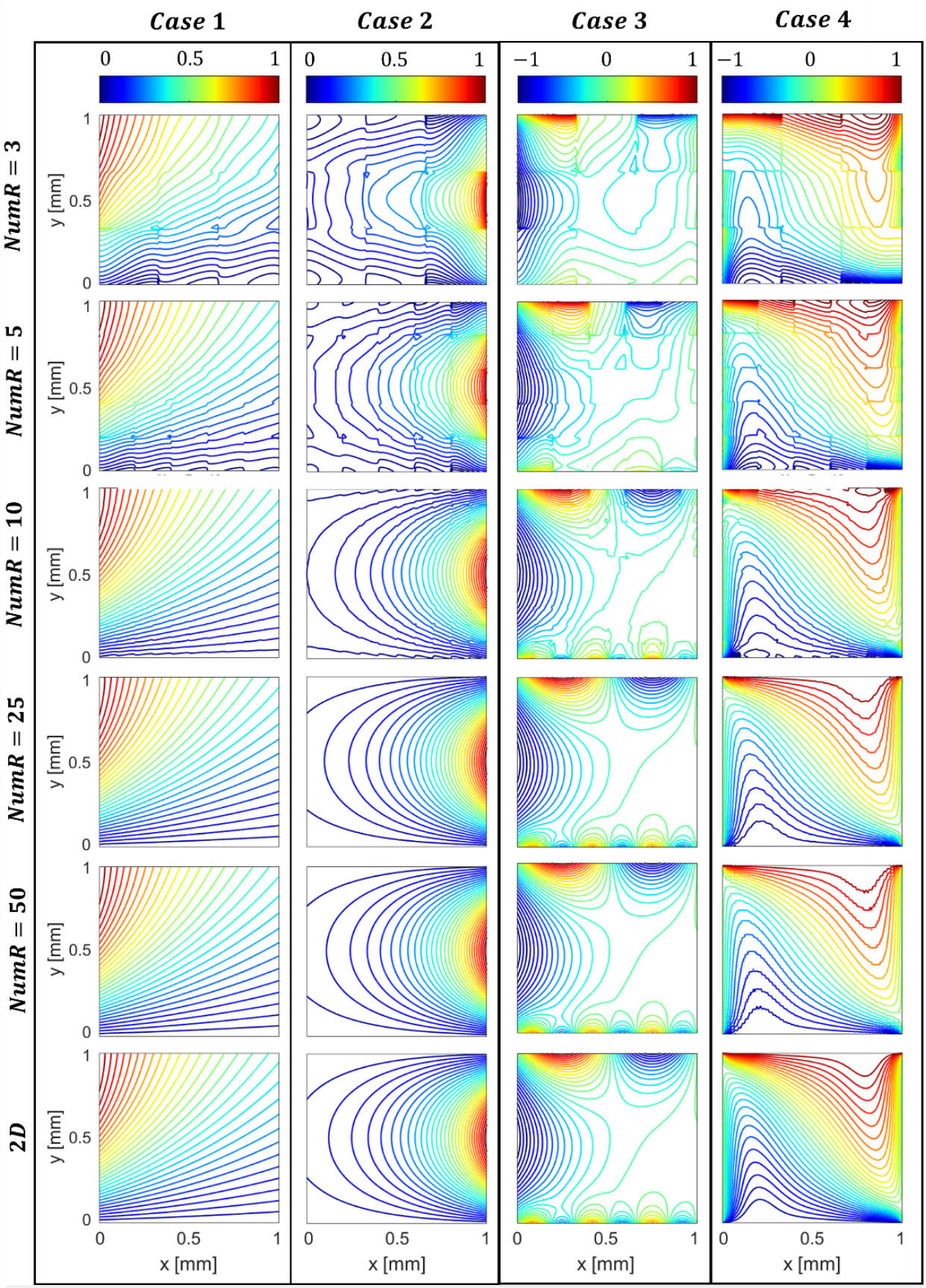


Fig. 2.13: Contour map representation of plots in **Fig. 2.11**; comparison of the RDPS' solutions with various number of regions against the corresponding full-2D solution (bottom row) for cases 1-4 defined in **Table 2.1**. The numbers of regions are equal along both dimensions ($M = N$), which are denoted by *NumR*.

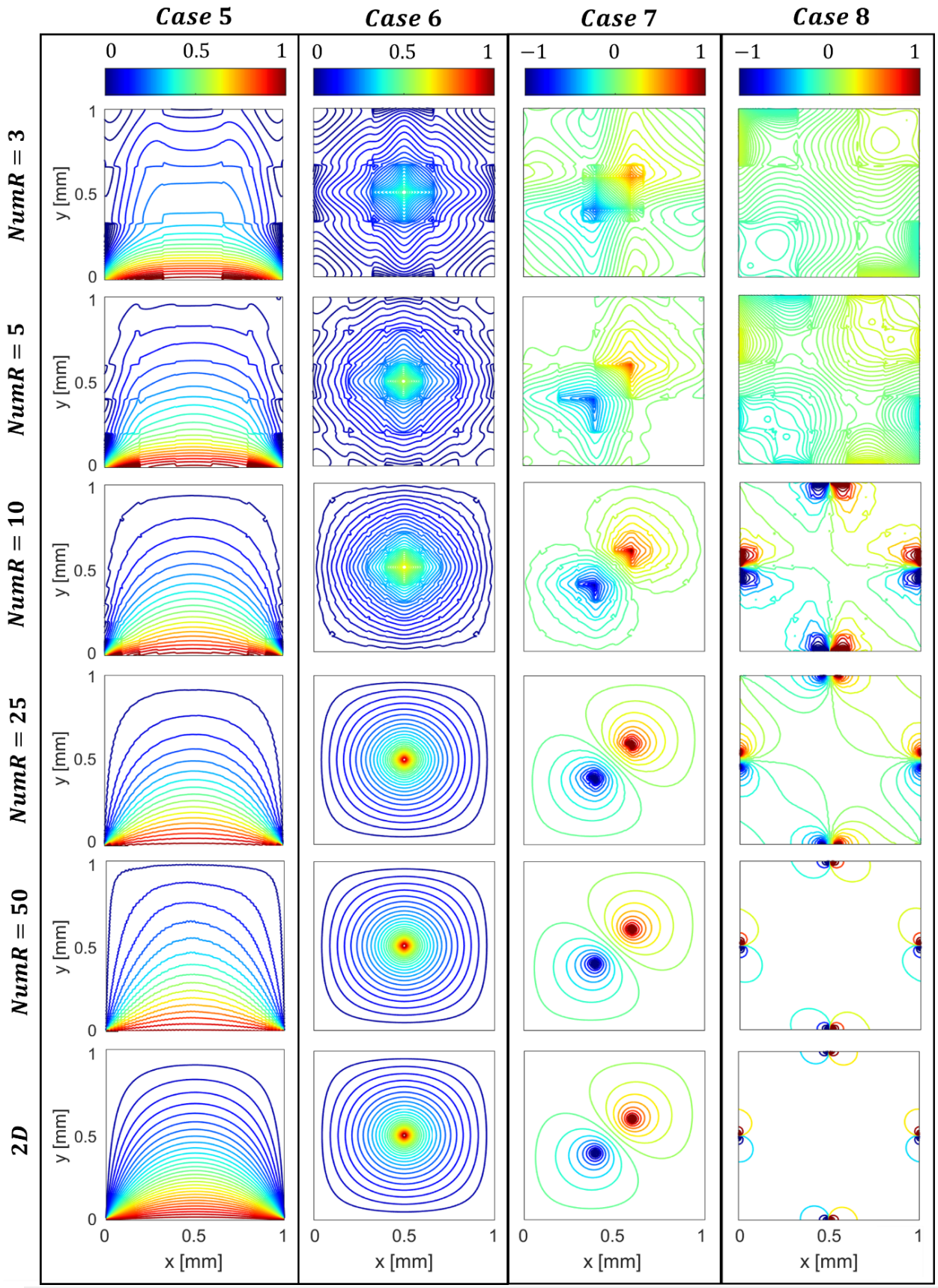


Fig. 2.14: Contour map representation of plots in **Fig. 2.12**; comparison of the RDPS' solutions with various number of regions against the corresponding full-2D solution (bottom row) for cases 5-8 defined in **Table 2.1**. The numbers of regions are equal along both dimensions ($M = N$), which are denoted by *NumR*.

It is noticed from these figures that first all, at low-number-of-region limit ($M, N \leq 10$), the quasi-2D successfully provides a coarse approximation to the full-2D solution. At this low-order approximation limit, the quality of the solution in terms of smoothness and in general, the degree of closeness to 2D solution is case-dependent. Second, with increasing number of regions, the quasi-2D solution becomes smoother, ultimately converging to the 2D solution with 50 regions. This converging behavior is observed in all test cases which verifies the broad applicability of the underlying formulation.

The error convergence characteristics of the RDPS solutions for the studied cases is provided in **Fig. 2.15**. The error is defined as the normalized L2 norm of the difference between the quasi-2D approximation (ϕ_{Q2D}) from RDPS with different number of regions and the full-2D solution (ϕ_{2D})

$$Error = \frac{\sqrt{\sum_{i=1}^{N_i}\sum_{j=1}^{N_j}\left(\phi_{2D}(i,j) - \phi_{Q2D}(i,j)\right)^2}}{\sqrt{\sum_{i=1}^{N_i}\sum_{j=1}^{N_j}(\phi_{2D}(i,j))^2}}. \qquad \text{Eq. 2.40}$$

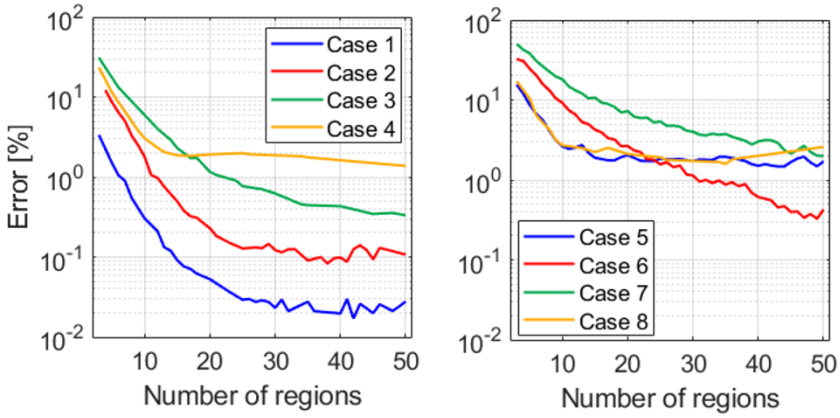


Fig. 2.15: Error convergence of the RDPS' solution; variation of the normalized L2 error (Eq. 2.40) between the full-2D solution and the approximate Q2D solution from the RDPS when increasing number of regions for cases 1-4 (left), and cases 5-8 (right). The y-axis in both plots is in logarithmic scale.

It is observed that the convergence behavior varies depending on the specific case. In case 1, which is characterized by smoothly varying solutions, the error remains consistently smaller compared to other cases across all approximation orders. For instance, with $N = M = 6$, the error is approximately $1\,\%$. Cases 4, 5 and 8 share similar convergence characteristics, with the error rapidly dropping. At the knee of their convergence curves ($N = M = 12$), the error drops below $2.5\,\%$ and remain relatively constant around the $1.5 - 2\,\%$ thereafter.

Case 2 and 3 exhibit a steady reduction in error with an increasing number of regions. Although, in case 3, the error is slightly larger than case 4 for $M, N < 17$, it continues to decrease below 0.5% at higher number of regions. This consistently decreasing trend is also observed in the convergence curves of cases 6 and 7, albeit with higher values of error. In case 6, for $M, N < 20$, the error surpasses other cases except for case 7. However, it decreases to $2.5\,\%$ for $M = N = 20$ and falls below 0.5% beyond 40 regions. Case 7 shows the largest error among all cases across the entire range of number-of-regions. At $M = N = 20$, the error is approximately $7\,\%$, reducing to $2.5\,\%$ at the highest approximation order.

It's worth noting that Case 6 and Case 7, which exhibit the largest errors at low-number-of-regions approximations, represent extreme scenarios. Case 6 involves a charge distribution with a singularity, while case 7 includes discontinuities created by point charges. These peculiar characteristics contribute to the challenges in accurately approximating the solutions, particularly at lower approximation orders. Additional test problems featuring oscillatory charge distribution or oscillatory boundary conditions with various wavelengths are provided in Appendix A.3, presenting the convergence behavior of RDPS in these examples.

Next, we present the quasi-2D approximate solution for case 9 with periodic boundary condition along the y-direction, which is a typical condition applied along the azimuth in Hall thruster simulations that involve this coordinate. As a result, it is necessary to verify the correctness of the implementation of the periodic boundary condition in the reduced-dimension solver.

Fig. 2.16 and **Fig. 2.17** illustrate, respectively, the 3D plots and contour maps demonstrating the various approximate solutions for this problem from RDPS corresponding to the same numbers of regions in previous cases. While the potential is computed over $\frac{y}{L_y} \in [0,1]$, in **Fig. 2.17**, the potential solution is duplicated along the y direction to visually inspect the fulfilment of periodic condition along this direction. Looking at these figures, the approximate solution obtained using only a few regions ($M, N = 3, 5$) is seen to qualitatively resemble the full-2D solution. Moreover, as evident in the contour plots, the solutions exhibit seamless periodicity along the y-axis.

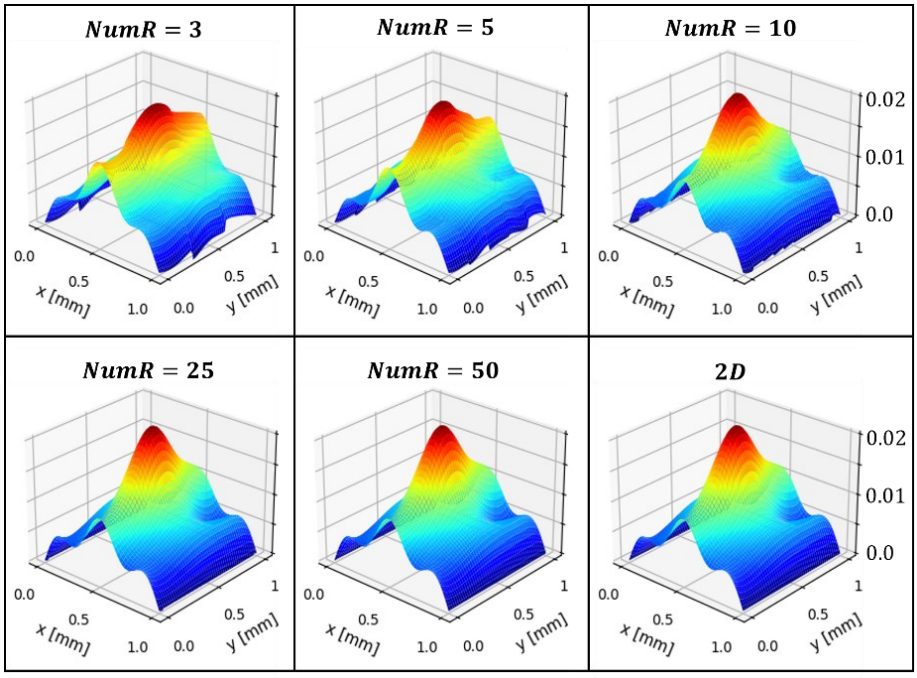


Fig. 2.16: Comparison of the RDPS' solution with various number of regions against the corresponding full-2D solution for case 9 (with periodic boundary condition along the y-axis) defined in **Table 2.1**. The numbers of regions are equal along both dimensions ($M = N$), which are denoted by *NumR*.

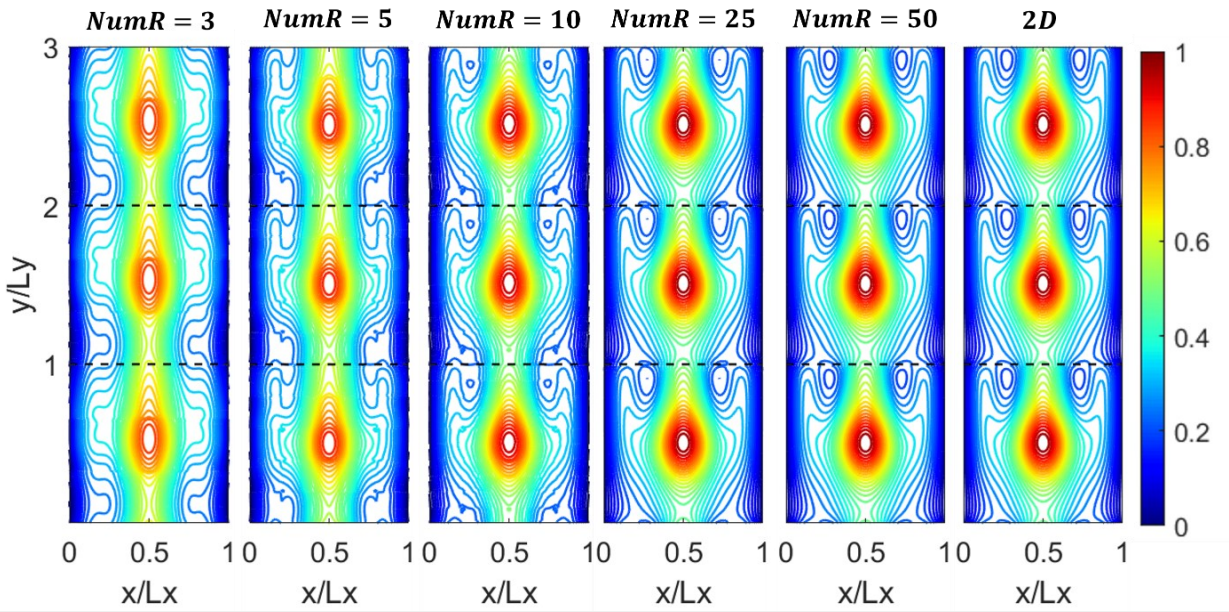


Fig. 2.17: Contour map representation of plots in **Fig. 2.16**; comparison of the RDPS's solutions with various number of regions against the corresponding full-2D solution (rightmost column) for case 9 defined in **Table 2.1**. The numbers of regions are equal along both dimensions ($M = N$) which are denoted by *NumR*. Potential is solved only for $\frac{y}{L_y} \in [0,1]$ and is duplicated twice along the y-direction to illustrate the satisfaction of periodicity condition.

Finally, the variation in error (calculated per Eq. 2.40), presented in **Fig. 2.18**, demonstrates a consistent decrease over the range of $M, N = 3 - 50$. In particular, the error measures about 4% at $M = N = 10$, drops below 1% when $M = N = 25$ and steadily decreases to less than 0.5% for $M, N > 30$.

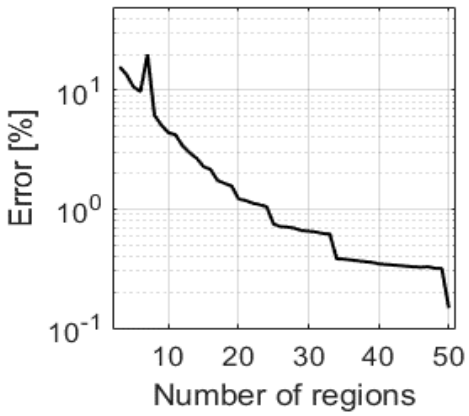


Fig. 2.18: Error convergence of the RDPS' solution for case 9; variation of the normalized L2 error (Eq. 2.40) between the full-2D solution and the approximate solution from the RDPS when increasing number of regions.

2.5. Conclusion

A novel dimensionality-reduction technique, based on a reduced-dimension computational grid, is introduced. This technique establishes a new framework for reduced-order modeling and development of quasi-multi-dimensional simulations with remarkably reduced computational cost. In particular, we developed an explicit electrostatic reduced-order PIC (RO-PIC) scheme by adopting the reduced-dimension grid and the adaptation of the grid-based functions. These include reformulation of the

Poisson's equation (and hence, development of the Reduced-Dimension Poisson Solver, RDPS) to be compatible with the reduced-dimension computational grid and adjustment of the scatter/gather functions to accommodate the new grid. The developed reduced-dimension Poisson's equation is presented for the limiting case of single-region as well as for a general multi-region domain decomposition. The degree of approximation achieved in the resulting quasi-2D/quasi-3D PIC will then be dependent on the number of regions used in the simulation.

In general, the approximate problem treatment at the "*low"* approximation order limit (low number of regions) implies that some accuracy is traded off for computational gain, which is inherent to any reduced-order model. We highlight that the approximation of the 2D potential function associated with the single-region domain decomposition has a limited applicability in terms of the solutions it can reproduce. However, the approximation given by Eq. 2.9 and Eq. 2.10 enables the lowest order quasi-multi-dimensional simulations (i.e., the single-region) that offer the maximum computational advantage over traditional PIC codes. Indeed, it's worth noting that at this approximate limit, the reduced-dimension Poisson's formulation comprises a system of equations integrated over the entire extents of the domain along each of the involved dimensions separately. Consequently, the interactions between the dimensions in single-region approximation are represented in an "average" sense. This approximation may be adequate for specific plasma configurations where there is a degree of decoupling between the physics along different dimensions, or when the detailed small-scale couplings are not critical for estimating the average effects of interest within the desired level of accuracy, depending on the specific objectives of the study.

On the other hand, a single-region simulation may not provide reasonable predictions for highly multi-dimensional geometries and/or plasma processes. Nonetheless, generalization of the single-region formulation to the "multi-region" domain decomposition provides the flexibility to choose an approximation order suitable for the physics of the problem and meets the required level of accuracy. In any case, it is important to recognize that a certain degree of approximation is inherent in any reduced-order representations.

We mathematically verified the convergence of the formulation of the reduced-dimension Poisson's equation to the full 2D Poisson's equation in the limit where the lengths of regions become as small as 2D cells' sizes. In addition, we numerically demonstrated in several standalone Poisson test cases, the consistency of the quasi-2D approximate solution corresponding to the reduced-dimension Poisson's equation and its convergence to full-2D solution as the number of regions increases. We observed different convergence behaviors in various cases, indicating the case-specificity of the required number of regions to achieve a certain accuracy.

In the next chapter, we will test the integration of the RDPS within PIC simulation and verify the entire RO-PIC (quasi-2D) code in various plasma configurations and characterize the convergence behavior of RO-PIC with number of regions across the studied plasma test cases. Additionally, we will present examples demonstrating instances where the single-region approximation yields remarkably accurate predictions, as well as cases where this approximation limit proves inadequate in representing the involved physical effects.

Chapter 3 Verifications of the RO-PIC scheme against benchmark plasma problems

Following the verification of the reduced-dimension Poisson's equation and the underpinning dimensionality-reduction approach in standalone Poisson test problems, the next step involves verifying the entire RO-PIC scheme.

Extensive verification of the IPPL-Q2D (quasi-2D) code, which is based on the RO-PIC scheme, is conducted across several well-established 2D plasma benchmark cases in different configurations. These include (a) axial-azimuthal Hall thruster-representative problem, (b) radial-azimuthal E×B discharge problem, and (c) Penning discharge case. Additionally, the dimensionality-reduction concept has been extended to the Direct Simulation Monte Carlo (DSMC) technique, resulting in a Q2D DSMC treatment of the neutrals' dynamics and collisional interactions, which is then integrated into the PIC loop leading to the Q2D PIC-DSMC code. The Q2D DSMC model is verified in a canonical problem of neutrals' plume expansion.

The IPPL-Q2D is tested extensively across various approximation orders including "low-order" and "high-order" approximations of the 2D problem achieved using different numbers of regions. To rigorously assess the prediction fidelity of the RO-PIC, comprehensive comparisons are conducted in terms of the plasma properties' profiles, the instabilities' spectra and their induced electrons' transport, where relevant.

In each case, the convergence of the Q2D predictions to the corresponding full-2D simulation results is verified. As pointed out for the standalone Poisson's problems, prediction accuracies and the convergence behavior are observed to be dependent on the specific case and the involved physics. In the axial-azimuthal coordinates, even a single-region decomposition can be sufficient to capture an average effect of the azimuthal instabilities on electrons' mobility, hence, self-consistently resolving the axial profiles of the plasma properties at computational costs equivalent to those of a 1D PIC problem. Whereas in Penning discharge problem, only "high-order" Q2D approximations can indistinguishably reproduce the full-2D results, in which case the Q2D simulations still provide several factors of speed-ups over full-2D.

These verifications demonstrate the versatility and generalizability of the RO-PIC and its enabling dimensionality-reduction technique.

3.1. Axial-azimuthal Hall-thruster-representative benchmark problem

As pointed out in Section 1.1.4, azimuthal instabilities are observed to have a significant role in enhancing the electrons' cross-field transport in Hall thrusters [10]. As a result, in a PIC simulation, achieving self-consistency with respect to the electron transport necessitates resolving the azimuthal coordinate. In this regard, demonstrating the capability of the RO-PIC scheme in reproducing the full-2D predictions in the axial-azimuthal coordinates is an important step toward achieving self-consistent predictions with a remarkable computational efficiency.

In this section, we present the results of verification of the quasi-2D (Q2D) simulations in the axial-azimuthal coordinates against the full-2D results for the benchmark problem in Ref. [58]. The verifications are performed using both "low-order" and "high-order" approximation limits of RO-PIC.

3.1.1. Setup and conditions of the problem

The simulations represent a 2D Cartesian plane of a Hall thruster along the axial-azimuthal coordinates with the setup adopted from the well-established benchmarking effort in Ref. [58]. The schematic representation of the simulation domain and the coordinate system is illustrated in **Fig. 3.1** (a), where x and z denote the axial and the azimuthal direction, respectively. The left boundary of the domain represents the anode, whereas the cathode boundary is located at the right-hand side of the domain. The domain's axial extent (L_x) is $2.5\ cm$, corresponding to $0.75\ cm$ of a Hall thruster's discharge channel and $1.75\ cm$ of the near-plume. The near-anode region is not included in these simulations. The azimuthal length of the domain (L_z) is $1.28\ cm$. Consistent with the benchmark settings in Ref. [58], the sizes of the computational cell along both axial and azimuthal directions are $\Delta x = \Delta z = 50\ \mu m$. This corresponds to the number of nodes of $N_i = 512$ along the x-axis and $N_k = 250$ cells along the z-axis. The timestep of the simulations is $\Delta t = 5 \times 10^{-12} s$.

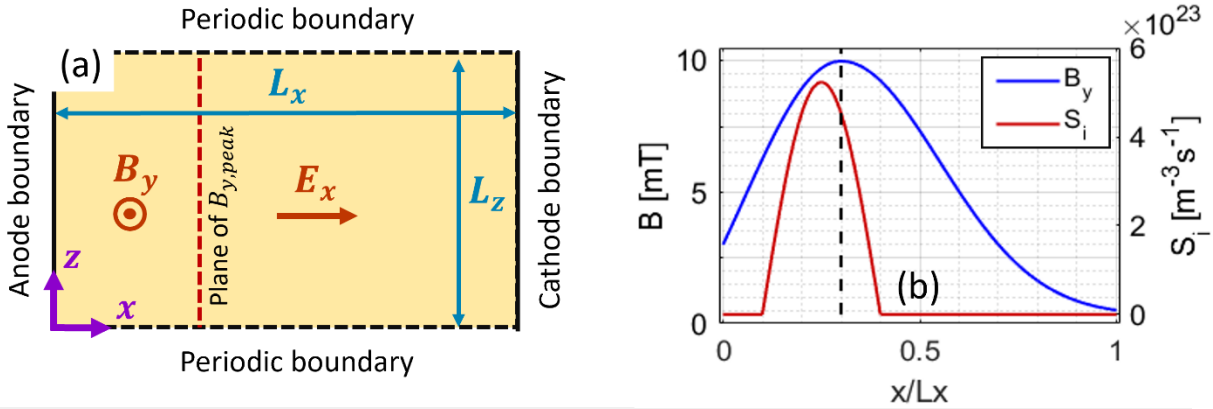


Fig. 3.1: (a) Schematic of the computational domain and setup, (b) axial profiles of the imposed magnetic field and the ionization source in the axial-azimuthal simulations.

The applied magnetic field (B) is purely radial and has a 1D Gaussian profile along the axial direction given by Eq. 3.1 [58], with its peak intensity of $10\ mT$ occurring at the channel exit plane (x_p = $0.75\ cm$). The magnetic field profile is plotted in **Fig. 3.1** (b).

$$B(x) = A_k \exp\left(-\frac{(x - x_p)^2}{2\sigma^2}\right) + C_k\ , \qquad k = 1{,}2 \qquad \text{Eq. 3.1}$$

In Eq. 3.1, $k = 1$ for $x \leq x_p$, $k = 2$ for $x > x_p$ and $\sigma = 0.625\ cm$. A_k and C_k are constant values which are obtained given $B(0) = 6\ mT$, $B(L_x) = 1\ mT$, $B(x_p) = 10mT$.

The collisional processes are neglected. To maintain a quasi-steady state in the system, a temporally invariant ionization source (S_i) is imposed according to the benchmark's definition in Ref. [58]. The axial distribution of the ionization source, presented in **Fig. 3.1** (b), is a cosine function spanning over $x = 0.25\ cm$ to $x = 1\ cm$ within the channel. In the nominal benchmark condition, the peak value of S_i is $5.23 \times 10^{23}\ m^{-3}s^{-1}$ which establishes an average ion current density of $J_M = 400\ Am^{-2}$. Moreover, under the benchmark operating conditions, the discharge voltage applied between the anode and the cathode is $200\ V$. Therefore, as the boundary condition of the potential solver (RDPS), a $200\ V$ and $0\ V$ Dirichlet conditions are applied at the anode and the cathode boundaries, respectively. A periodic boundary condition is imposed along the z-coordinate. The application of the potential boundary conditions follows the description provided in Section 2.2.2.1.

The simulation is initialized by loading electrons and the ions uniformly throughout the simulation domain as electron-ion pairs with the initial density of $n_0 = 5 \times 10^{16}\ m^{-3}$. The particles are randomly sampled from Maxwellian distribution functions at the temperatures of $10\ eV$ for the electrons and $0.5\ eV$ for the ions. The initial macroparticle per cell for each species is $N_{ppc} = 150$.

Regarding the particles' boundary conditions, both the ions and the electrons crossing either the anode or the cathode boundaries are removed from the simulation. To maintain the discharge, at each timestep electrons are injected into the domain from the cathode side. We used two different cathode boundary conditions as described in Section 1.4.2.2. Accordingly, the number of injected electrons obtained following either current continuity scheme (for the low-number-of-region simulations presented in Section 3.1.2) or quasi-neutrality condition (for the high-number-of-region simulations discussed Section 3.1.3) at the cathode plane. The re-injected electrons are sampled from a Maxwellian distribution at $10\ eV$. Moreover, along the azimuthal direction, the periodic boundary condition is implemented such that the particles leaving the domain at one end are injected back from the other end while maintaining their axial positions and their velocities.

The total simulated time for the simulations with low numbers of regions is $20\ \mu s$, and the results are averaged over the interval of $16 - 20\ \mu s$, which is in line with the benchmark's definition. However, for the simulations with high numbers of regions, the total simulated time is $30\ \mu s$, and the results are averaged over the interval of $20 - 30\ \mu s$ to be consistent with the results presented in Ref. [69], with which we have compared our simulation results. A summary of the simulation parameters and conditions is provided in **Table 3.1**.

Parameter	Value [unit]	
Physical Parameters		
Initial plasma density (n_0)	5×10^{16} [m^{-3}]	
Electron injection temperature ($T_{e,0}$)	10 [eV]	
Ion injection temperature ($T_i, 0$)	0.5 [eV]	
Discharge Voltage (V_d)	200 [V]	
Magnetic field's peak ($B_{y,peak}$)	10 [mT]	
Ionization source's peak ($S_{i,peak}$)	5.23×10^{23} m^{-3}s^{-1}	
Initial plasma density ($n_{p,init}$)	5×10^{16} [m^{-3}]	
Computational Parameters		
Time step (Δt)	5×10^{-12} [s]	
Axial domain length (L_x)	2.5 [cm]	
Azimuthal domain length (L_z)	1.28 [cm]	
Cell size ($\Delta x = \Delta z$)	50 [μm]	
Number of computational nodes along x (N_i)	512	
Number of computational nodes along z (N_k)	256	
	Low-number-of-region	High-number-of-region
Initial number of macroparticles per cells (N_{ppc})	300	100
Total simulation time (t_{sim})	20 [μs]	30 [μs]
Final averaging time window (t_{avg})	$16 - 20$ [μs]	$20 - 30$ [μs]
Number of regions along x (M)	1, 2, 3	10, 20, 40, 80
Number of regions along z (N)	1	5, 10, 20, 40
Cathode boundary condition (CBC)	Current continuity model	Quasi-neutrality model

Table 3.1: Summary of the main computational and physical parameters used for the Q2D axial-azimuthal simulations.

3.1.2. Verification results with low-number-of-region RO-PIC simulations

The results are provided for Q2D simulations with single, double, and triple regions along the axial coordinate ($M = 1, 2, 3$). In general, the boundary between regions and, hence, the relative extents of the regions in double- and triple-region simulations can be adjusted arbitrarily based on the axial variations in the azimuthal physics and the characteristics of the azimuthal instabilities. For instance, one regions' boundary can be set at the location of the maximum magnetic field intensity, which is shown in this setup to be coinciding with the axial location of the ion sonic point. This is because recent evidence [58][69] suggests that around the axial location of the ion sonic point, the characteristics of the azimuthal instabilities undergo a transition. The sensitivity of the results to the location of the boundary between the regions in the double-region Q2D simulation for this test case is investigated in Ref. [19]. Given the minimal sensitivity observed in this test case, we opted for equal extents among all regions for the present verification. Moreover, in these simulations, a single region is considered along the azimuthal direction ($N = 1$).

Fig. 3.2 presents the comparison between the time-averaged plasma properties from the Q2D simulations and the full-2D benchmark results reported in Ref. [58]. It is observed that all Q2D simulations provide a remarkably similar prediction of the time-averaged profiles across all plasma properties compared with the results of the full-2D reference simulation.

In **Fig. 3.2** (d), we have additionally shown the axial profile of the electric potential from a full-1D PIC simulation performed using IPPL-1D without any ad-hoc collisionality (the dashed cyan curve). This demonstrates that in the absence of the azimuthal instabilities, the axial electron transport in the simulation is insufficient, and the electric potential cannot be sustained at the expected level near the anode side of the domain. However, observing the plasma potential profiles from the Q2D simulations, it is clear that even "low-order" approximation limit of the RO-PIC scheme is able to self-consistently incorporate the necessary instability-induced electron transport for the sustainment of the plasma potential. Note that RO-PIC achieved this with the computational cost equivalent to a 1D PIC simulation.

The predictive capability of the low-number-of-region Q2D simulations are verified across a wide range of operating conditions in the axial-azimuthal coordinates. The results of these verifications are provided in Appendix A.4.1.

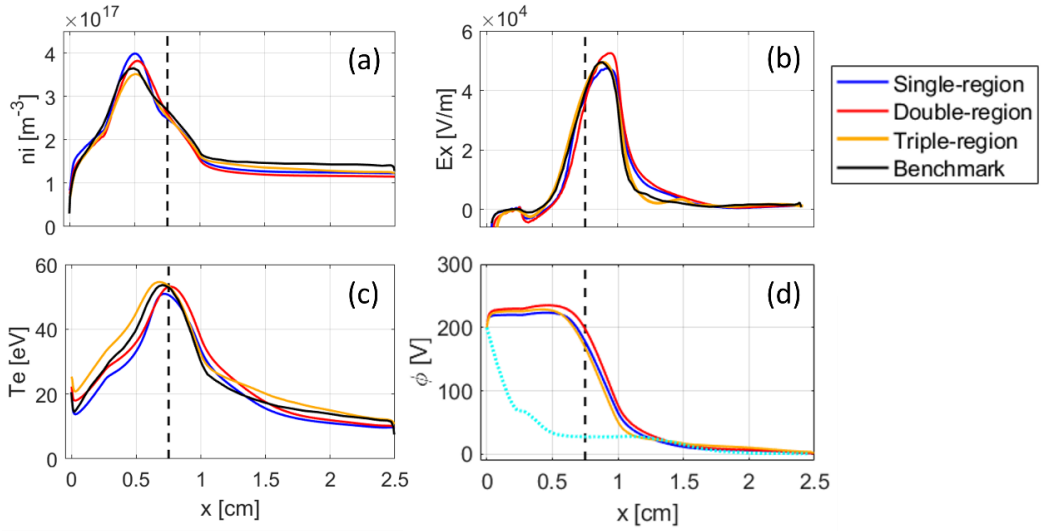


Fig. 3.2: Time-averaged (over $16 - 20\ \mu s$) axial profiles of plasma properties from low-number-of-region Q2D simulations; (a) ion number density (n_i), (b) axial electric field (E_x), (c) electron temperature (T_e) and (d) electric potential (ϕ). In plot (d), the dashed cyan curve represents the plasma potential profile from the 1D axial simulation without any ad-hoc electron transport. Dashed black lines show the location of magnetic field's peak. The benchmark results are from Ref. [58].

To assess the simulations predictions of the characteristics of the azimuthal instabilities we compared the numerical dispersion maps ($k_z - \omega$) of the azimuthal waves with the theoretical dispersion relation of the Ion Acoustic Instability (IAI) in **Fig. 3.3**. The comparison is made with the IAI dispersion relation since, it is shown in literature [10][18] that, at the quasi-steady state of the simulation, the excited waves are in the pseudo-saturated state, accompanied by a transition to the ion acoustic waves.

In each region, the numerical dispersion maps are obtained by applying 2D Fast Fourier Transform (FFT) to the spatiotemporal signal of the azimuthal electric field (E_z) on the azimuthal grid within the respective region. The theoretical dispersion relation of the ion acoustic instability is calculated using Eq. 1.4 in the ions' reference frame ($k_x V_{di} = 0$). In the plots of **Fig. 3.3**, the yellow curves are the local dispersion relations, calculated using the averaged plasma properties in each region, whereas the green curves are the ion acoustic dispersion relation corresponding to the plasma properties in Region

I. In the dispersion plots, the frequencies and wavenumbers are normalized with respect to the ion plasma frequency (ω_{pi}) and the Debye length (λ_D), respectively.

In **Fig. 3.3**, it is evident that the predicted dispersion characteristics in Region I are in very close agreement with the theoretical dispersion relation of the ion acoustic waves. Furthermore, it is seen that, going from Region I to II (in double- and triple-region simulations) and from Region II to III (triple-region simulations), the waves' dispersion plots increasingly deviate from the local ion acoustic dispersion relation (yellow curves). However, they remain closely consistent with the ion acoustic dispersion relation of Region I (green curves). This demonstrates that RO-PIC captures the downstream convection by the ion beam of the waves excited in Region I, an important feature regarding the dynamics of the azimuthal instabilities that has been also reported in Refs. [68][69]. This difference between the upstream (yellow) and downstream (green) dispersion relations is related to the instabilities' convection with the ion flow represented by $k_x V_{di}$ term in Eq. 1.4.

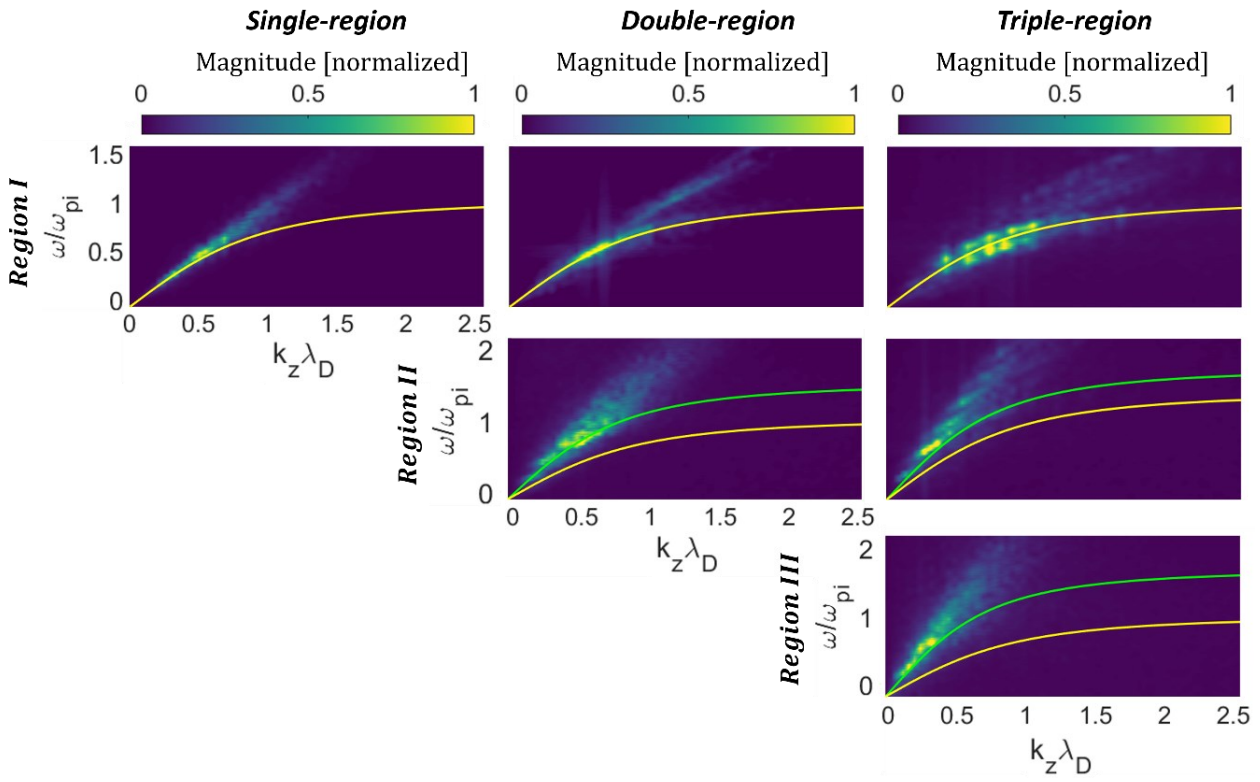


Fig. 3.3: Numerical dispersion plots of azimuthal instabilities obtained from 2D FFT of the spatiotemporal signal of the azimuthal electric field fluctuations (in different regions) from the low-number-of-region Q2D simulations. Yellow curves are the local dispersion relations (in the corresponding region), and the green curves are the dispersion relation of the ion acoustic waves in Region I obtained from Eq. 1.4.

The sensitivity of the results to the simulated azimuthal length is evaluated for the triple-region Q2D simulation as an example in Appendix A.4.1. This analysis verifies that, consistent with the minor sensitivity observed in the full-2D simulations reported in Ref. [69], the Q2D simulations exhibit a minimal sensitivity to the domain's azimuthal extent.

Finally, we examine various contributions to the electrons' axial transport in terms of the axial profiles of the momentum terms in the electron azimuthal momentum equation (averaged over the azimuthal

direction) given by Eq. 1.20. These include the magnetic force (F_B), on the left-hand side of Eq. 1.20, the viscous effects (F_Π), the convective inertia force (F_I), and the electric force term (F_E) representing the contribution of the azimuthal instabilities to cross-field transport. The RHS terms indicates the sum of all terms on the left-hand side of Eq. 1.20, i.e. $RHS = F_\Pi + F_I + F_E \approx F_B$.

Fig. 3.4 shows the axial distributions of the electron transport terms in the Q2D simulations. These profiles exhibit a high degree of similarity with the full-2D results reported in Ref. [69]. In this regard, the magnetic force term distribution and hence, the profile of the overall electron transport from the Q2D simulations, is found to be in line with the 2D profiles [58][69], with the results from the triple-region simulation demonstrating closest agreement. In addition, the dominant contribution of the electric force term (F_E), especially in the near-plume where the transport is primarily is driven by the instabilities [1][2], is captured in all three simulations.

Another important observation is that the RHS term perfectly matches the magnetic force term everywhere, evidencing the satisfaction of the momentum equation. This underlines the absence of any notable numerical effects that could have otherwise influenced the obtained results.

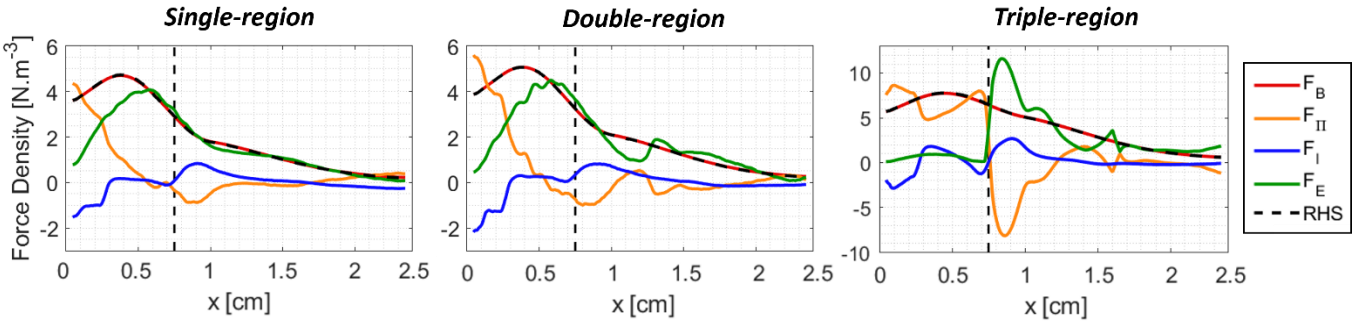


Fig. 3.4: Axial profiles of the transport terms in Eq. 1.20 from low-number-of-region Q2D simulations. The force terms are averaged over $16 - 20\ \mu s$. F_B is the magnetic force, F_Π is the viscous effects, F_I is the convective inertia force, F_E is the electric force term, and RHS represents the sum of F_Π, F_I and F_E . F_t (temporal inertia) contribution was almost zero, and it is thus not displayed. Dashed black lines show the location of magnetic field's peak.

3.1.2.1. Sensitivity to number of macroparticles per cell

To assess the impact of the initial number of macroparticles per cell (N_{ppc}) on the Q2D simulations in the low-number-of-region limit, the single-region simulation is performed with different N_{ppc} ranging from 75 to 2400. It is observed from the axial profiles of the time-averaged plasma properties in **Fig. 3.5**, that like the full-2D PIC simulations, the Q2D simulations are indeed sensitive to the value of N_{ppc}. However, from 300 to 2400 macroparticles per cell, the sensitivity is rather moderate. In addition, the simulations with 1200 and 2400 macroparticles per cell have almost identical predictions indicating a converging behavior with respect to N_{ppc}.

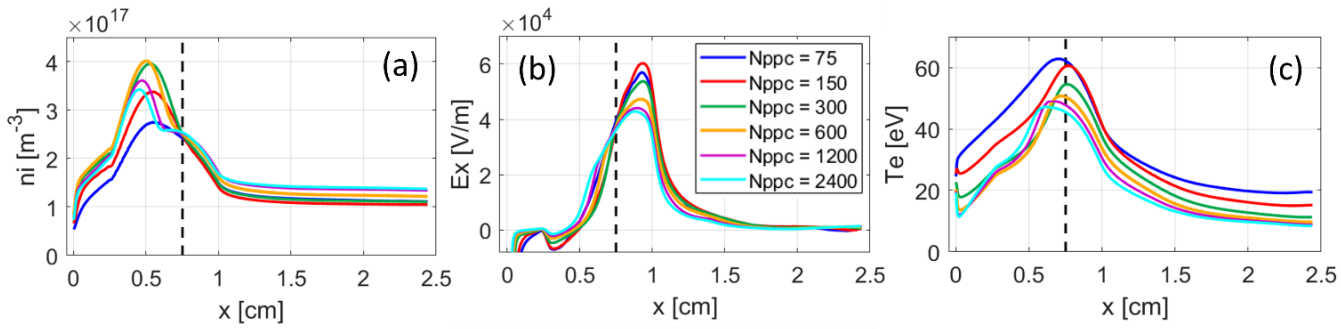


Fig. 3.5: Comparison between the axial profiles of the time-averaged (over $16 - 20\ \mu s$) plasma properties from the single-region Q2D simulations with various initial number of particles per cell ($Nppc$); (a) ion number density (n_i), (b) axial electric field (E_x), and (c) electron temperature (T_e).

3.1.3. Verification results with high-number-of-region RO-PIC simulations

In this section, we present the verification of the RO-PIC simulation using "high-order" approximations of the 2D problem. The verification involves Q2D simulations with relatively high numbers of regions including the following cases: case $\boldsymbol{i}$: $N = 5,\ M = 10$, case $\boldsymbol{ii}$: $N = 10,\ M = 20$, case $\boldsymbol{iii}$: $N = 20,\ M = 40$, and case $\boldsymbol{iv}$: $N = 40,\ M = 80$. Even though the number of regions along either direction can be chosen independently, we used twice as many regions along the x-coordinate compared to the z-coordinate ($M = 2N$), proportional to the domain's length along respective direction. In this way the regions' extents along both directions are almost equal ($L_{x,m} = L_{y,n}$). The regions' extents are also uniform across all regions in each direction ($L_{x,1} = L_{x,2} = \cdots = L_{x,M}\ ,\quad L_{y,1} = L_{y,2} = \cdots = L_{y,N}$).

Note that the cathode boundary condition in the 2D reference case adopted for the high-number-of-region simulations is different from the benchmark case used for the low-number-of-region simulations. Accordingly, the reference 2D results are slightly different than those in Section 3.1.2.

The comparison of the obtained time-averaged axial distributions of the plasma properties from these Q2D simulations against the reference results from the full-2D simulation in Ref. [69] is shown in **Fig. 3.6**. In these plots, the species' axial ($T_{s,x}$) and azimuthal ($T_{s,z}$) components of the temperature are defined as

$$T_{s,x} = \frac{m_s}{K_B\, n_s}\left(\int_{-\infty}^{\infty} v_x^2\, f_s(\boldsymbol{v}) d^3v - n_s\, \boldsymbol{V}_{s,x}^2\right), \qquad \text{Eq. 3.2}$$

$$T_{s,z} = \frac{m_s}{K_B\, n_s}\left(\int_{-\infty}^{\infty} v_z^2\, f_s(\boldsymbol{v}) d^3v - n_s\, \boldsymbol{V}_{s,z}^2\right), \qquad \text{Eq. 3.3}$$

where s represents either electrons or ions, v_x and v_z are the axial and azimuthal velocities, $\boldsymbol{V}_{s,x}$ and $\boldsymbol{V}_{s,z}$ are the axial and azimuthal drift velocities, $f_s(\boldsymbol{v})$ is the particles' distribution function, n_s is and m_s is the particle's mass.

The plots in **Fig. 3.6** clearly indicate that increasing the number of regions leads to the convergence of the plasma profiles to those from the 2D simulation. The predicted profiles in case ii ($N = 10,\ M = 20$) are very close to the profiles obtained from case iii ($N = 20,\ M = 40$) and case iv ($N = 40,\ M = 80$). Moreover, the axial profiles of case iv ($N = 40,\ M = 80$) are in perfect agreement with the 2D

results. These observations suggest that, in terms of the axial plasma distributions, increasing M and N beyond their values in case ii ($N = 10,\ M = 20$) does not majorly affect the accuracy of the Q2D simulation, since case ii has already replicated the full-2D results with sufficient fidelity.

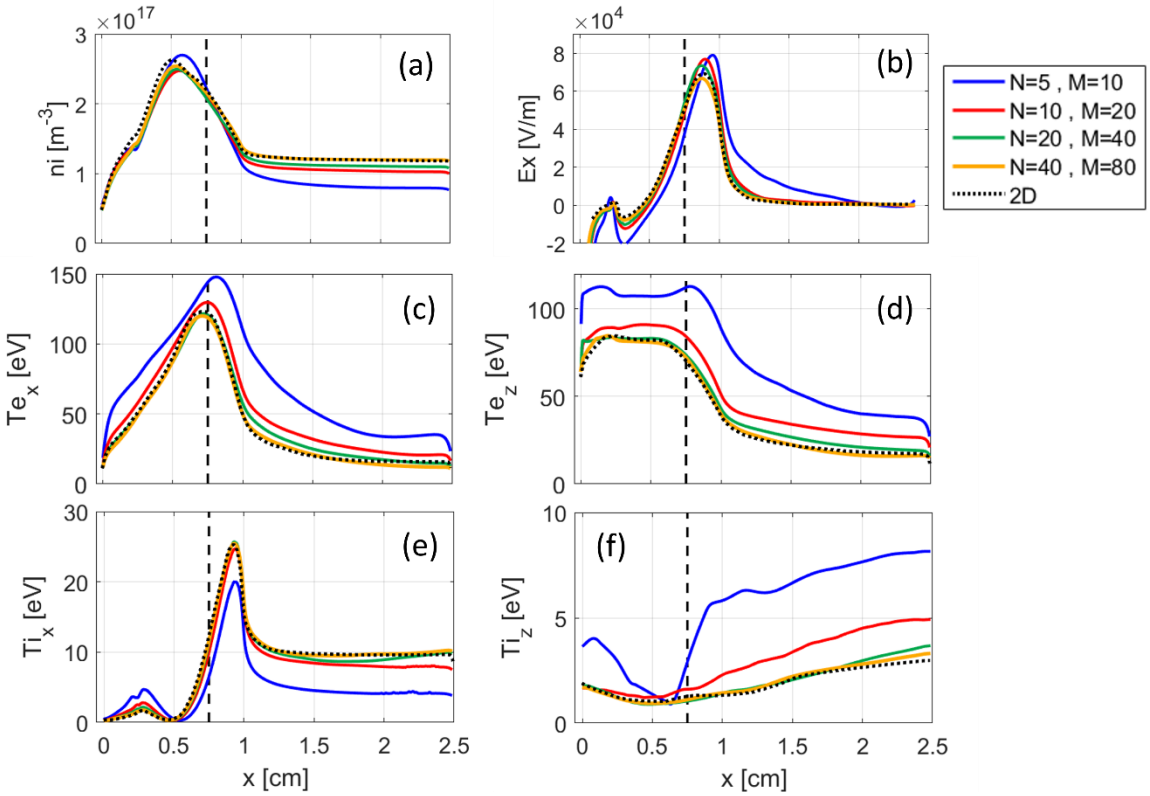


Fig. 3.6: Time-averaged (over $20 - 30\ \mu$s) axial profiles of plasma properties from high-number-of-region Q2D simulations; (a) ion number density (n_i), (b) axial electric field (E_x), (c) & (d) axial and azimuthal electron temperature ($T_{e,x}$ & $T_{e,z}$) , and (e) & (f) axial and azimuthal ion temperature ($T_{i,x}$ & $T_{i,z}$). Dashed black lines show the location of magnetic field's peak. The 2D reference results are from Ref. [69].

To provide quantitative accuracy metrics for the "high-order" Q2D simulations, we refer to **Fig. 3.7**, which shows the variation of the L2 errors in predictions of various plasma properties versus the number of regions used along the axial direction (M). The L2 error represents an average of the normalized node-by-node difference between the time-averaged axial profiles from the Q2D (P_{Q2D}) and the full-2D (P_{2D}) simulations given by

$$Error = \frac{\sqrt{\sum_{i=1}^{N_i}\left(P_{2D}(i) - P_{Q2D}(i)\right)^2}}{\sqrt{\sum_{i=1}^{N_i} P_{2D}(i,j)^2}} \qquad \text{Eq. 3.4}$$

Superimposed on the plot in **Fig. 3.7**, we plotted the computational time ratio between the Q2D and full-2D PIC simulations. Although, in general, this ratio represents the number of CPU-hours consumed by a Q2D simulation relative to a corresponding full-2D PIC simulation, with the assumption of an identical number of CPUs used for both the Q2D and the full-2D simulations, this ratio translates into the ratio between the time it takes for the respective simulations to complete. The ratio is calculated in accordance with the discussion in Section 2.3 regarding the computational benefit of the RO-PIC scheme.

We observe from **Fig. 3.7** that the error in the predictions of all plasma properties decreases from case i to case iv. The error values for case iv are almost within the margin of error ($5\ \%$) observed among various 2D codes participated in the Hall thruster axial-azimuthal benchmarking activity [58]. Meanwhile, the Q2D simulation of case iv takes only $15\ \%$ of the computational time required for a full-2D simulation. Furthermore, it is noteworthy that the Q2D simulation of case ii ($N = 10,\ M = 20$) only consumes $5\ \%$ of the 2D simulation's time to complete in spite of its fairly acceptable error figures, which are approximately $10 - 20\ \%$ across all properties.

To contextualize these speed-up and error figures in comparison with the previous accelerated PIC algorithms, it is noted that, according to Ref. [90], the predictions of Sparse Grid (SG) PIC (refer to Section 1.4.1.2) for the same problem involve 20 % error compared to the standard PIC method, while yielding only 3 times speed-up. The error is reduced to $7\ \%$ at the limit where the SG PIC provides no computational advantage over conventional PICs.

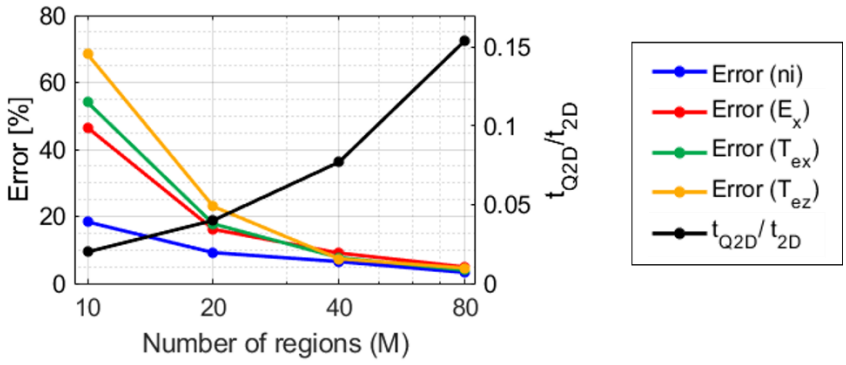


Fig. 3.7: Variation of L2 error in the prediction of plasma properties from the axial-azimuthal Q2D simulations compared to the full-2D results in Ref. [69], alongside the computational time ratio between the Q2D and full-2D PIC simulations plotted against the number of regions in the Q2D simulations (M). The L2 error is calculated using Eq. 3.4 for the time-averaged axial profiles. M denotes the number of regions along the axial direction which in these simulations are twice the number regions along the azimuthal direction (N).

We then look at the 2D maps of fluctuations as seen from the snapshots of the of plasma properties shown in **Fig. 3.8**. It is noticed that, in cases i ($N = 5,\ M = 10$) and ii ($N = 10,\ M = 20$), the fluctuations have primarily an azimuthal wavevector component upstream of the location of the magnetic field's peak. However, in cases iii and iv (i.e., $N = 20,\ M = 40$ and $N = 40,\ M = 80$, respectively), the n_i and E_z maps clearly exhibit inclined fluctuations near the anode. This serves as evidence that, in these cases, the RO-PIC is able to resolve the axial wavevector component (k_x) of the azimuthal instabilities.

In this regard, it is underlined that, should the regions' axial extent ($L_{x,m}$) be smaller than the waves' axial wavelength (λ_x), i.e., $L_{x,m} \ll \lambda_x$, the Q2D simulations are indeed expected to be able to capture the axial component of the wavevector. This criterion is met in both cases iii and iv. For instance, focusing on case iii, as it can be noticed from the $x - z$ map of the azimuthal electric field fluctuations in **Fig. 3.8**, the azimuthal wavelength (λ_z) of the waves is about $1\ mm$. Now, we recall that, typically, the instabilities' wavelength along the axial direction is much larger than that along the azimuthal direction ($\lambda_x \gg \lambda_z$) [27]. Therefore, noting that the axial length of the vertical regions in case iii is $L_{x,m} = 0.625\ mm$, we have $L_{x,m} < \lambda_z$ and $\lambda_z \ll \lambda_x$, thus, $L_{x,m} \ll \lambda_x$. This same analysis is valid for case iv,

where the length of the vertical regions is even smaller than that in case iii while the waves' azimuthal wavelength is almost the same.

Furthermore, the 2D fluctuation maps for cases iii and iv in **Fig. 3.9** are found to be in remarkable agreement with the similar maps from the 2D simulation in Ref. [69] in terms of the azimuthal wavelength and the tilt in the waves before the channel exit plane. Moreover, in the 2D simulation, the instabilities were observed to become almost purely azimuthal downstream of the channel exit plane, which is also seen in the fluctuation maps of cases iii and iv.

These observations, together with the remarkable accuracy in predicting the axial plasma profiles as well the computational cost figures presented in **Fig. 3.7**, points to the capability of the RO-PIC scheme in the "high-order" approximation limit in successfully capturing the underlying physics in the same manner as a full-2D simulation, albeit at a notably reduced computational cost.

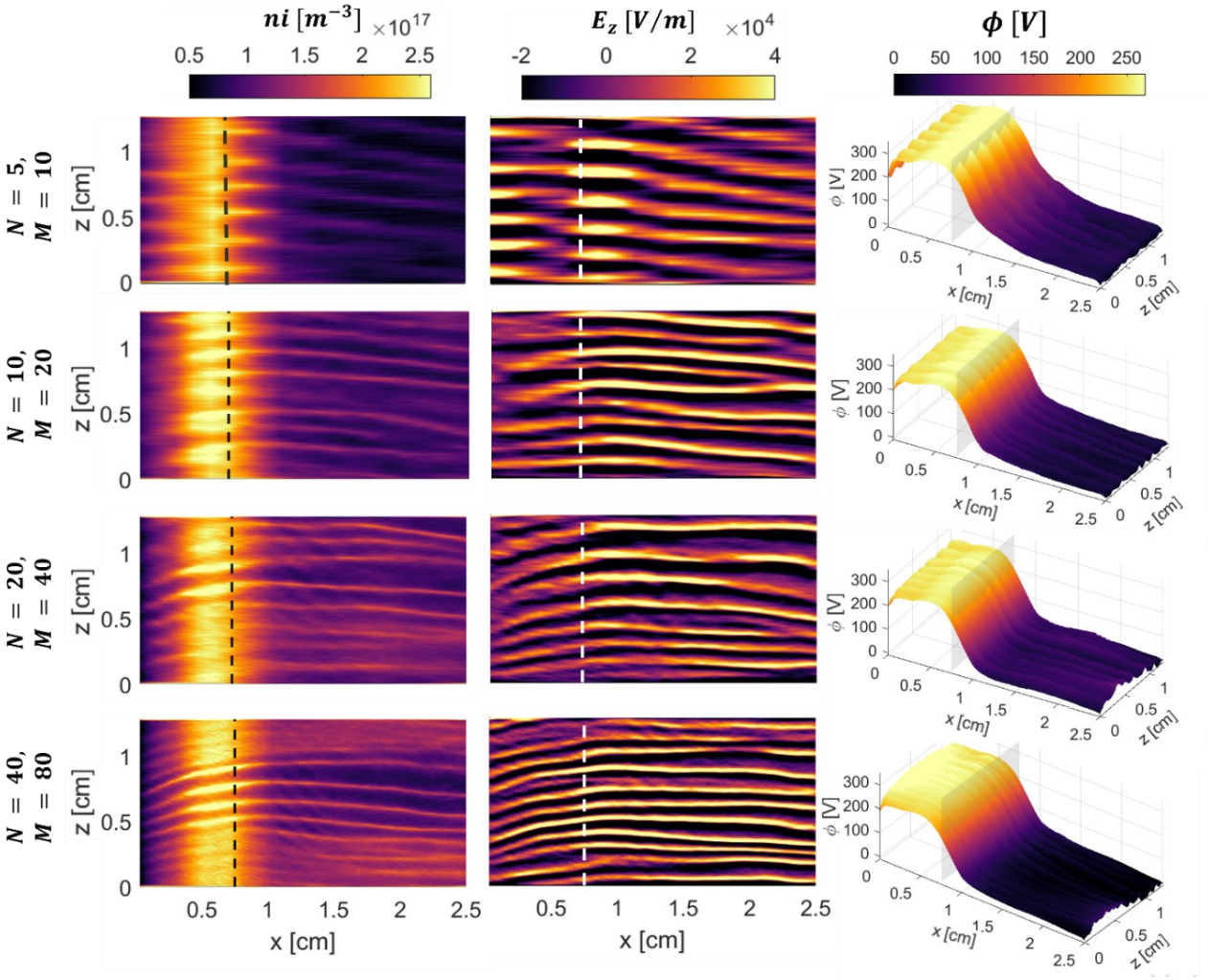


Fig. 3.8: 2D maps of the ion number density (left column), the azimuthal electric field (middle column), and the electric potential (right column) from high-number-of-region Q2D simulations at the time $t = 30\ \mu s$. The dashed lines and grey planes show the location of the peak magnetic field intensity.

Fig. 3.9 illustrates the numerical dispersion maps of the azimuthal electric field fluctuations at three axial locations from the "high-order" Q2D simulations in comparison with the theoretical IAI dispersion relation (Eq. 1.4). These are plotted in the same way as the plots in **Fig. 3.3**. Looking at the dispersion

plots, we notice that there is only a minor variation in the frequencies and wavenumbers of the dominant waves across different "high-order" simulation cases.

All cases show a change in the dominant wavenumbers from larger to smaller values when moving from inside the channel ($x = 0.4\ cm$) toward the near-plume ($x = 2\ cm$). In addition, the waves show a broader dispersion in the near-plume region. The predicted waves' characteristics agree with the theoretical IAI dispersion relation calculated for the upstream location corresponding to $x = 0.4\ cm$ (green curves in **Fig. 3.9**) across all cases and axial locations. Also, as pointed out in Section 3.1.2, from $x = 0.4\ cm$ to $x = 2\ cm$, the increasing deviation seen in the waves' local dispersion and the upstream IAI's dispersion relation is the evidence of the downstream convection of the azimuthal waves by the ion beam.

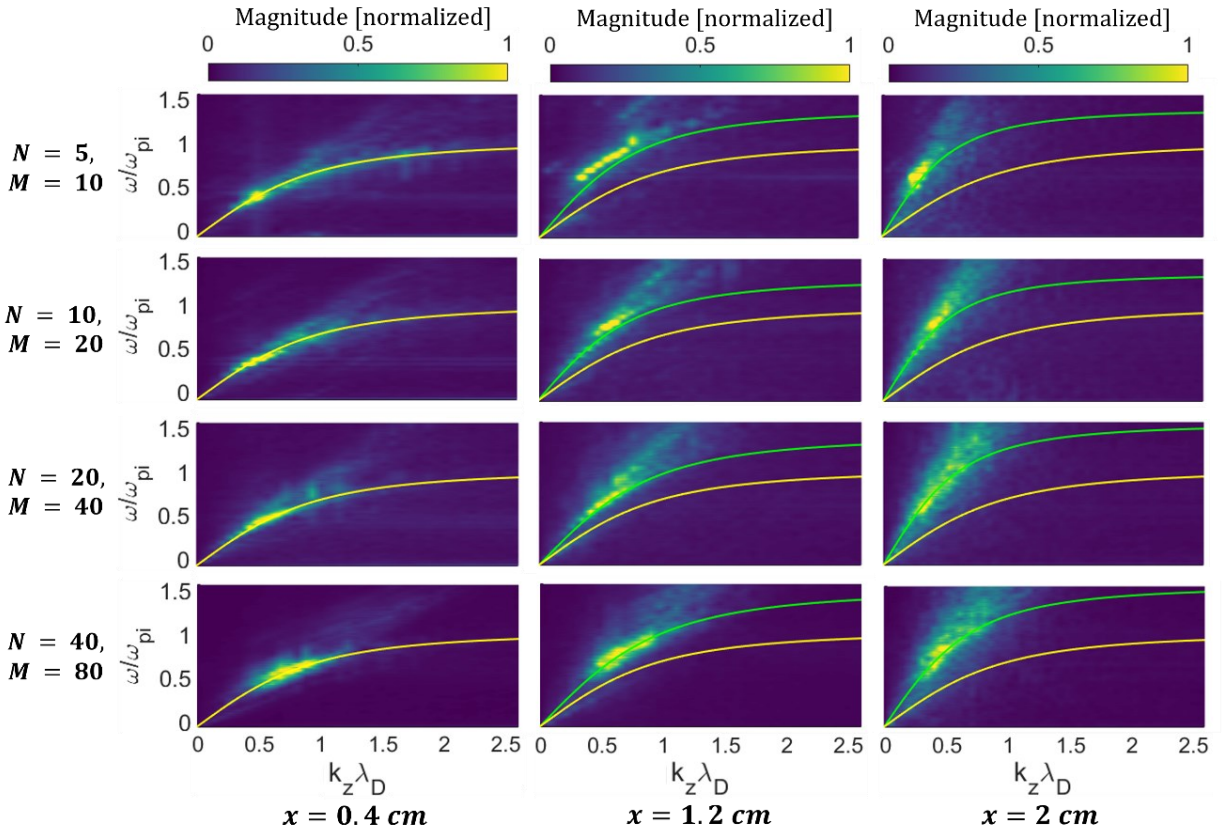


Fig. 3.9: Numerical dispersion plots of azimuthal instabilities obtained from 2D FFT of the spatiotemporal signal of azimuthal electric field fluctuations in three axial locations from high-number-of-region Q2D simulations. Yellow curves are the local dispersion relations (in the corresponding region), and the green curves are the upstream dispersion relation of the ion acoustic waves (at $x = 0.4\ cm$) obtained from Eq. 1.4.

Finally, **Fig. 3.10** provides the axial profiles of the force terms in the electrons' azimuthal momentum equation (Eq. 1.20) from the "high-order" Q2D simulations. Apart from case i ($N = 5,\ M = 10$), the profiles in the other cases exhibit a high degree of similarity among themselves, confirming convergence of the simulations beyond case ii ($N = 10,\ M = 20$) in terms of the predictions of the individual contributions to the electrons' axial transport as well.

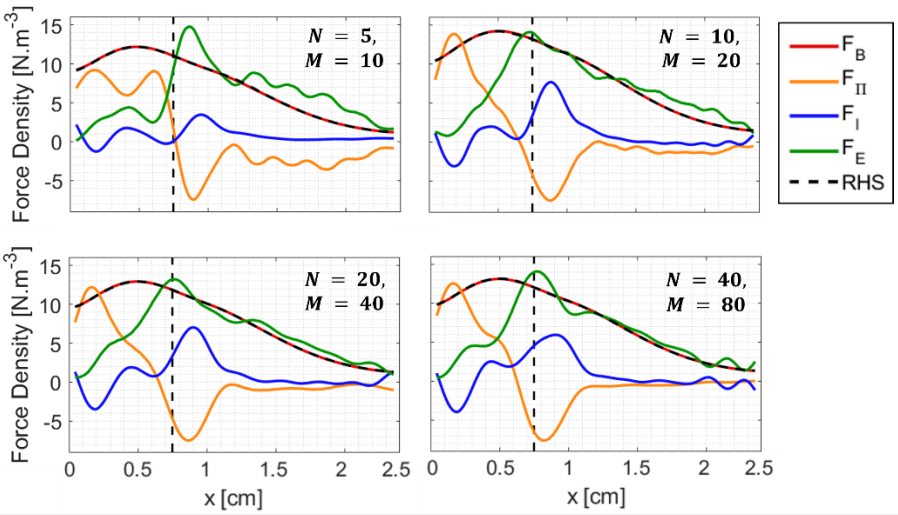


Fig. 3.10: Axial profiles of the transport terms in Eq. 1.20 from high-number-of-region Q2D simulations. The force terms are averaged over $16-20\ \mu s$. F_B is the magnetic force, F_Π is the viscous effects, F_I is the convective inertia force, F_E is the electric force term, and RHS represents the sum of F_Π, F_I and F_E . F_t (temporal inertia) contribution was almost zero, and it is thus not displayed. Dashed black lines show the location of magnetic field's peak

3.1.3.1. Sensitivity to the number of regions along the azimuthal direction

The current understanding of the plasma behavior in the axial-azimuthal coordinates of Hall thrusters indicates that the axial electric field does not have a notable gradient along the azimuthal direction. As a result, one may wonder if it might be actually necessary to divide the azimuthal coordinate into multiple regions in the Q2D axial-azimuthal simulations, since such a division would be essentially intended to resolve the azimuthal gradients of the axial electric field. The results and analysis here are aimed at answering this question. To this end, we have carried out "high-order" Q2D simulations with only a single horizontal region along the azimuth. These new simulation cases have domain decompositions with $N=1, M=20$ and $N=1, M=40$, and their results are compared against the corresponding simulations with $N=10,\ M=20$ and $N=20, M=40$.

It is noticed from **Fig. 3.11** that the time-averaged axial plasma profiles from the simulations with $N=1$ exhibit only minor deviations compared to the corresponding profiles from the simulations with multiple regions along the azimuthal coordinate.

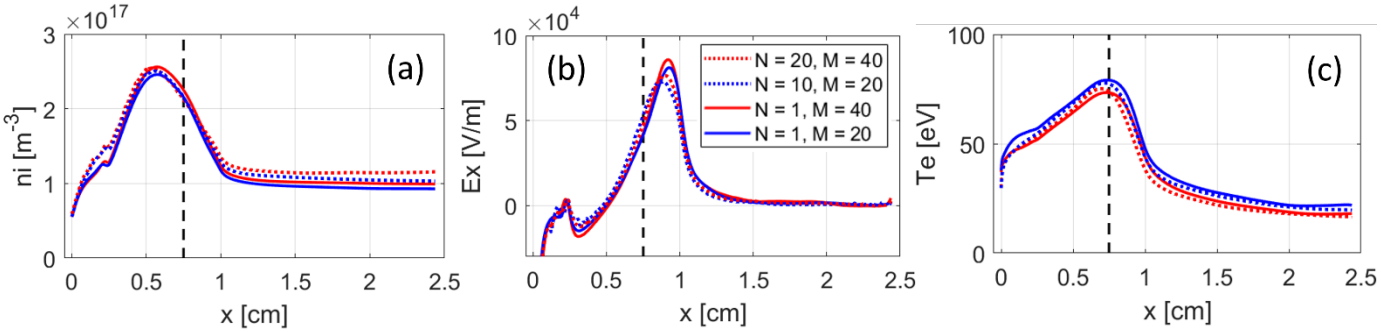


Fig. 3.11: Comparison between the time-averaged axial profiles of plasma properties from the high-number-of-region Q2D simulations with single ($N=1$) and multiple ($N=10, 20$) horizontal regions along the azimuthal coordinate.

In addition, in **Fig. 3.12**, we have compared the 2D maps of plasma fluctuations from the simulations with $N=1,\ M=40$ and $N=20,\ M=40$. We observe that also in terms of the overall characteristics

of the instabilities, the results from the two simulations do not show any significant difference. The simulation with $N = 1$ effectively captures all main features of the 2D plasma distributions captured in the simulation with $N = 20$.

These results show that, in general, having a priori understanding of the physics of a specific problem, can inform the decision regarding the optimum domain decomposition (i.e., the number of regions) such that the computational gain from the RO-PIC scheme could be maximized while maintaining the fidelity of the predications.

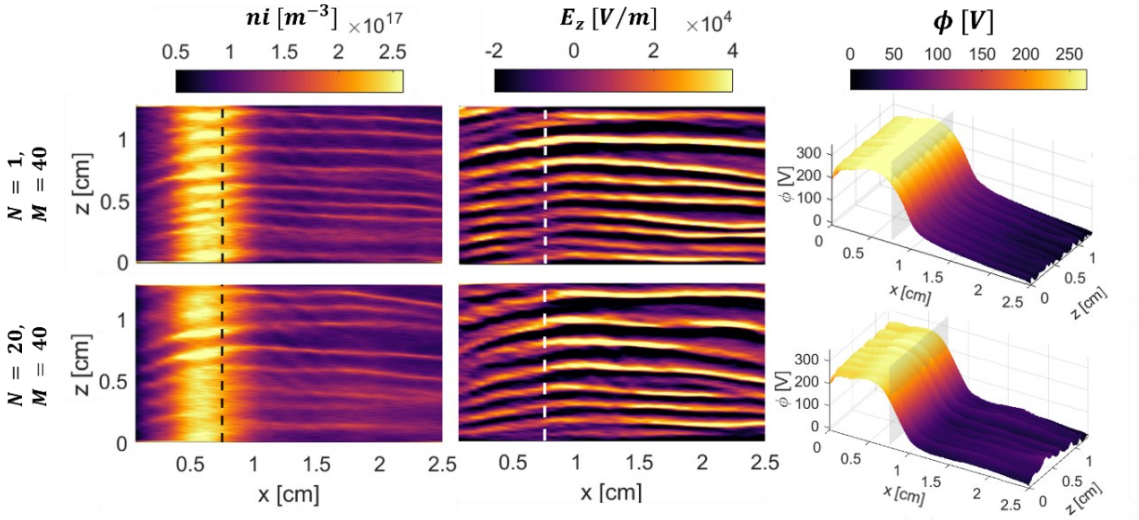


Fig. 3.12: Comparison of the 2D maps of the ion number density (left column), the azimuthal electric field (middle column), and the electric potential (right column) from the high-number-of-region Q2D simulations with single ($N = 1$) and multiple ($N = 10, 20$) horizontal regions along the azimuthal coordinate at $t = 30\ \mu s$. The dashed lines and grey planes show the location of the peak magnetic field intensity.

3.1.3.1. Sensitivity to number of macroparticles per cell

The sensitivity of the "high-order" Q2D simulations to the initial number of macroparticles per cell (N_{ppc}) is analyzed by comparing the results from case iii ($N = 20$ and $M = 40$) with various N_{ppc} including $50, 100, 200$ and 400. Looking at the resulting time-averaged axial plasma profiles in **Fig. 3.13**, it is noticed that the results are only marginally sensitive to the value of the N_{ppc}. The observed sensitivity of the Q2D simulations to N_{ppc} value is in the same level as the sensitivity noted in the 2D simulations [58][69].

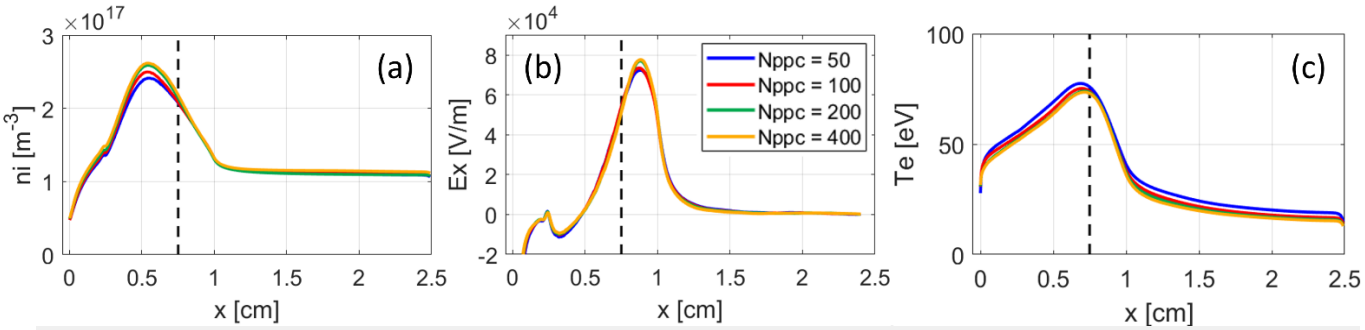


Fig. 3.13: Comparison of the axial profiles of the time-averaged (over $20 - 30\ \mu s$) plasma properties from the Q2D simulations (with $N = 20, M = 40$) with various initial number of particles per cell ($Nppc$); (a) ion number density (n_i), (b) axial electric field (E_x), and (c) electron temperature (T_e).

3.2. Radial-azimuthal E×B discharge benchmark problem

Prior research into the physics of plasma in a radial-azimuthal $\mathrm{E} \times \mathrm{B}$ configuration has revealed the development of important plasma instabilities [12][110] and intricate interactions between them, which can be affected by the inclusion of the physics along the radial dimension [7]. Thus, verifying the Q2D PIC in the radial-azimuthal configuration ascertains the ability of the RO-PIC scheme in resolving closely coupled, highly two-dimensional phenomena, hence, gaining additional confidence in the general applicability of the scheme.

In this section, the results of the verification of the Q2D simulations in the radial-azimuthal coordinates using the benchmark case in Ref. [35] are presented. The Q2D simulations are performed across a wide range of approximation orders from single-region to near full-2D limit of RO-PIC.

3.2.1. Setup and conditions of the problem

The simulation configuration resembles the radial-azimuthal cross-section of a Hall thruster with the setup and conditions exactly following that of the community-wide radial-azimuthal benchmark activity [35]. The computational domain represents a 2D Cartesian $(x - z)$ plane with equal lengths of $1.28\ cm$ along both simulation directions ($L_x = L_z = 1.28\ cm$). In terms of the axes notation, x, y, and z denote, respectively, the radial, axial, and azimuthal directions. A stationary axial electric field (E_y) of magnitude $10\ kVm^{-1}$ and an external radial magnetic field (B_x) of intensity is $20\ mT$ are applied. The schematic of the simulation domain and the directions of the imposed electric and magnetic fields relative to the coordinate system are illustrated in **Fig. 3.14**. The cell sizes are $\Delta x = \Delta z = 50\ \mu m$ which correspond to $N_i = N_k = 256$ cells along either dimension. The time step is $\Delta t = 1.5 \times 10^{-11}\ s$.

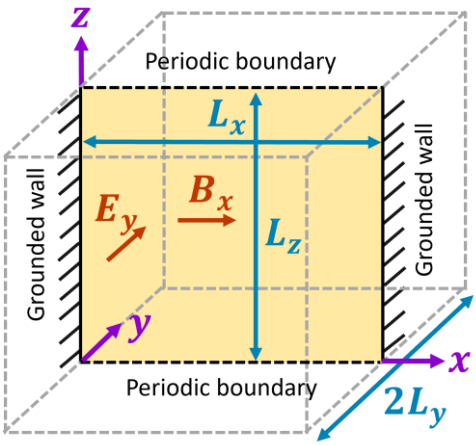


Fig. 3.14: Schematic of the computational domain and setup of the radial-azimuthal simulations.

Initially, electrons and ions are sampled from Maxwellian distribution functions at the temperatures of $10\ eV$ and $0.5\ eV$ for electrons and ions, respectively, and are loaded as electron-ion pairs over the $(x - z)$ simulation plane with a uniform density of $n_0 = 5 \times 10^{16}\ m^{-3}$. The initial number of macroparticles per cell is $n_{ppc} = 100$. The simulations are collisionless. To compensate for the fluxes of particles to the wall and establishment of a quasi-steady state density in the simulations, a temporally fixed particle injection source is imposed. The injection source is azimuthally uniform and follows a

cosine profile along the radial direction, spanning from $x = 0.09\ cm$ to $x = 1.19\ cm$ with the peak value of $8.9 \times 10^{22}\ m^{-3}s^{-1}$. This leads to establishment of an average ion axial current density of $100\ Am^{-2}$. At each time step, electron-ion pairs are injected according to the profile of the injection source with velocities sampled from Maxwellian distributions at the initial temperatures of the respective species.

As the simulations do not resolve the axial (y) direction, to represent the downstream convection of the azimuthal waves and to limit the growth of the particles' energy in the simulations [17], a finite virtual axial extent of $L_y = 1\ cm$ is considered for the domain. Along the axial direction, we do not solve the Poisson's equation. Rather, the particles crossing the domain's boundaries along the y-direction are resampled from a Maxwellian at their respective initial temperatures and reloaded onto the simulation plane at the same radial and azimuthal positions.

As for the boundary conditions for the electric potential, a zero-volt Dirichlet condition mimics the grounded walls along the radial direction. A periodic condition is applied along the azimuthal direction. All particles reaching the walls are removed with no secondary electron emission (SEE) considered. To reflect periodicity condition along the azimuthal coordinate, particles crossing the azimuthal boundaries are reinjected from the opposing boundary while retaining their velocities and radial positions.

The total simulation duration is $30\mu s$, with the averaging and data post-processing window spanning over $25 - 30\ \mu s$ which corresponds to when the simulation has reached a quasi-steady state. **Table 3.2** presents a summary of the numerical and physical parameters.

Parameter	Value [unit]
Physical Parameters	
Initial plasma density (n_0)	5×10^{16} [m^{-3}]
Electron injection temperature ($T_{e,0}$)	10 [eV]
Ion injection temperature ($T_i, 0$)	0.5 [eV]
Axial electric field (E_y)	10 [kVm^{-1}]
Radial magnetic field (B_x)	20 [mT]
Ionization source's peak ($S_{i,peak}$)	5.23×10^{23} m^{-3}s^{-1}
Initial plasma density ($n_{p,init}$)	5×10^{16} [m^{-3}]
Potential at walls (ϕ_w)	0 [V]
Computational Parameters	
Time step (Δt)	1.5×10^{-11} [s]
Total simulation time (t_{sim})	30 [μs]
Final averaging time window (t_{avg})	$25 - 30$ [μs]
Domain length ($L_x = L_z$)	1.28 [cm]
Virtual axial length (L_y)	1 [cm]
Cell size ($\Delta x = \Delta z$)	50 [μm]
Number of computational nodes along each direction ($N_i = N_k$)	256
Initial number of macroparticles per cells (N_{ppc})	100
Number of regions in Q2D simulations, NumR ($M = N$)	1, 3, 5, 10, 25, 50, 100

Table 3.2: Summary of the main computational and physical parameters used for the Q2D and the full-2D radial-azimuthal simulations.

3.2.2. Verification results

The Q2D simulations are performed using different number of regions (NumR) as listed in **Table 3.2**. In the Q2D simulations discussed in this section, an equal number of regions are used along the radial and the azimuthal directions with uniform extents. The reference full-2D results against which the outcomes of the Q2D simulations are compared are obtained from the IPPL-2D code. The results of the benchmarking of the IPPL-2D code are provided in Appendix A.1.7.

For reference, we also report the results from a 1D radial and a 1D azimuthal PIC simulations that we carried out using the same conditions and setup of the full-2D/Q2D simulations but adapted accordingly for the 1D simulations. In the 1D radial case, the same ionization source as that described in Section 3.2.1 is used. However, for the 1D azimuthal simulation, noting that the average plasma density remains constant throughout the simulation, the initial plasma density ($n_{i,0}$) is increased to $1 \times 10^{17}\ m^{-3}$, which corresponds to the average steady state density value in the 2D simulation.

Fig. 3.15 presents the time-averaged radial distributions of the ion number density (n_i) and the electron temperature (T_e) from the 1D radial simulation, from the Q2D simulations at "low" and "high" approximation orders, and from the full-2D simulation.

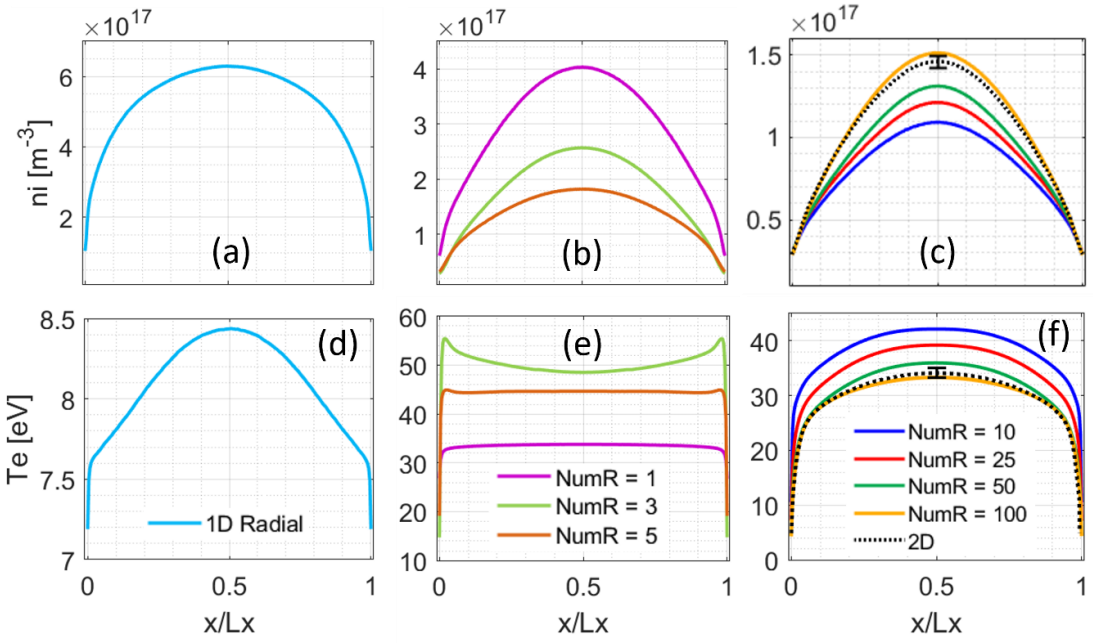


Fig. 3.15: Time-averaged (over $25 - 30\ \mu s$) radial profiles of the ion number density (first row) and the electron temperature (second row). Plots (a) and (d) are from the 1D radial simulation, (b) and (e) from "low-order" Q2D simulations, and (c) and (f) from "high-order" Q2D simulations. The reference 2D profiles are shown in plots (c) and (f) are from IPPL-2D. In plots (c) and (f), the $\pm$ 2.5 % error band superimposed at the peak values corresponds to the observed difference among the 2D codes participated in benchmark activity [35]). Note the difference in the y-axis scale among plots (a) to (c) and (d) to (f). $NumR$ denotes the number of regions used in Q2D simulations ($NumR = M = N$).

Looking at the radial profiles of the plasma properties from the "high-order" Q2D simulations (**Fig. 3.15**) (c) & (f)), it is evident that, by increasing the number of regions, the Q2D results converge to the full-2D ones at the 100 number-of-regions limit. The results from 100-region Q2D simulation indicate

an error of about 2.5% in the peak value of both the ion number density and the electron temperature compared to the 2D results. This is deemed a reasonably small error considering that it is consistent with the error observed among various 2D codes that participated in the radial-azimuthal benchmark activity [35].

Now, referring to the plot (b) in **Fig. 3.15**, it is observed that, by increasing the number of regions from 1 to 5, the ion number density profile consistently approaches the 2D one. Regarding the profiles of the electron temperature in the "low-order" simulations (plot (e) in **Fig. 3.15**), it is interesting to note that value of the electron temperature at the mid radial location (x/L_x = 0.5) predicted by "single-region" simulation is very close to the corresponding value from the 2D simulation.

Moreover, despite the discrepancy observed in the predicted ion density from the single-region simulation compared to that from the 2D simulation, upon comparing the single-region profiles against those from the 1D radial simulation (**Fig. 3.15** (a) and (d)), it is evident that the single-region simulation provides a substantial improvement over the 1D radial results. In particular, the average mutual effects of the physical mechanisms along the azimuthal and radial directions are captured by the single-region simulation. This is evident in the elevated electron temperature in the single-region simulation (relative to the 1D radial simulation) due to particles' heating by the azimuthal waves, and a corresponding decrease in the ion number density. Additionally, the shape of the ion number density profile from the single-region simulation closely resembles that from the 2D simulation as a result of capturing an average effect of the interactions between the radial and azimuthal processes.

Fig. 3.16 shows the convergence of the L2 error in the Q2D predictions with increasing number of regions together with the computational speedup achieved in each Q2D simulation compared to a full-2D PIC. The L2 error is computed based on the difference in the time-averaged radial profiles of n_i and T_e from the Q2D and full-2D simulations as per Eq. 3.4. It is noticed that in 10-region simulations the errors in both plasma properties are below $25\ \%$ with the computation time being only $4\ \%$ of that of the full-2D simulation. The 50-region Q2D simulation yields an L2 error of $12\ \%$ in n_i and $5\ \%$ in T_e while offering a 5-fold computational speedup compared to a full-2D simulation.

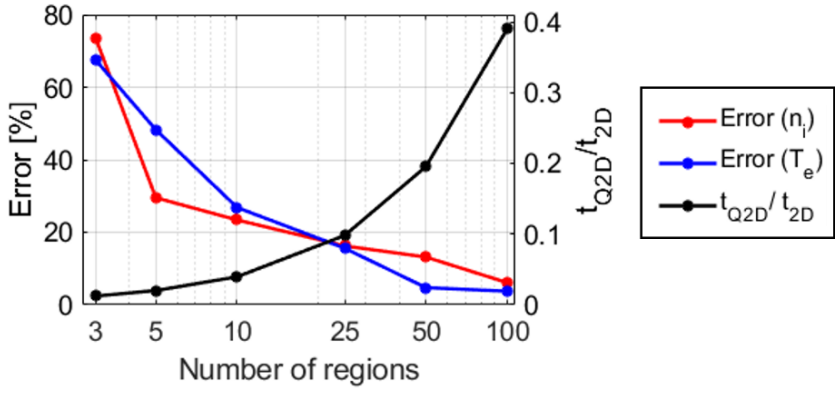


Fig. 3.16: Variation of the L2 error in the prediction of ion number density (n_i) and electron temperature (T_e) from the radial-azimuthal Q2D simulations compared to full-2D results from IPPL-2D code, alongside the computational time ratio between the Q2D and full-2D IPPL codes plotted against the number of regions in the Q2D simulations. The L2 error is calculated using Eq. 3.4 for the time-averaged radial profiles. Note that the x-axis is in logarithmic scale.

A prominent aspect of this $\mathrm{E} \times \mathrm{B}$ discharge test case is the development of two particular azimuthal instability modes, namely, the Electron Cyclotron Drift Instability (ECDI) and the Modified Two Stream Instability (MTSI), which were introduced in Sections 1.1.3.1 and 1.1.3.3. Thus, plasma discharge in this case is primarily characterized by the two instabilities and their interactions.

The predictions of the azimuthal wavenumber (k_z) spectrum of the instabilities are presented in **Fig. 3.18**. These spectra are derived using the time-averaged (over three different time intervals) Fast Fourier Transforms (FFT) of the azimuthal electric field signal from the 1D azimuthal simulation, the Q2D simulations in low- and high-order approximation limits, and from the 2D simulation. The x-axis in the plots of **Fig. 3.18** represents the normalized azimuthal wavenumber (k_z/k_0), with the normalization factor (k_0) being the fundamental resonance wavenumber of the ECDI defined as $k_0 = \frac{\omega_{ce}}{V_{de}}$, where ω_{ce} is the electron cyclotron frequency, and V_{de} is the electrons' $\mathrm{E} \times \mathrm{B}$ drift velocity (see Section 1.1.3.1).

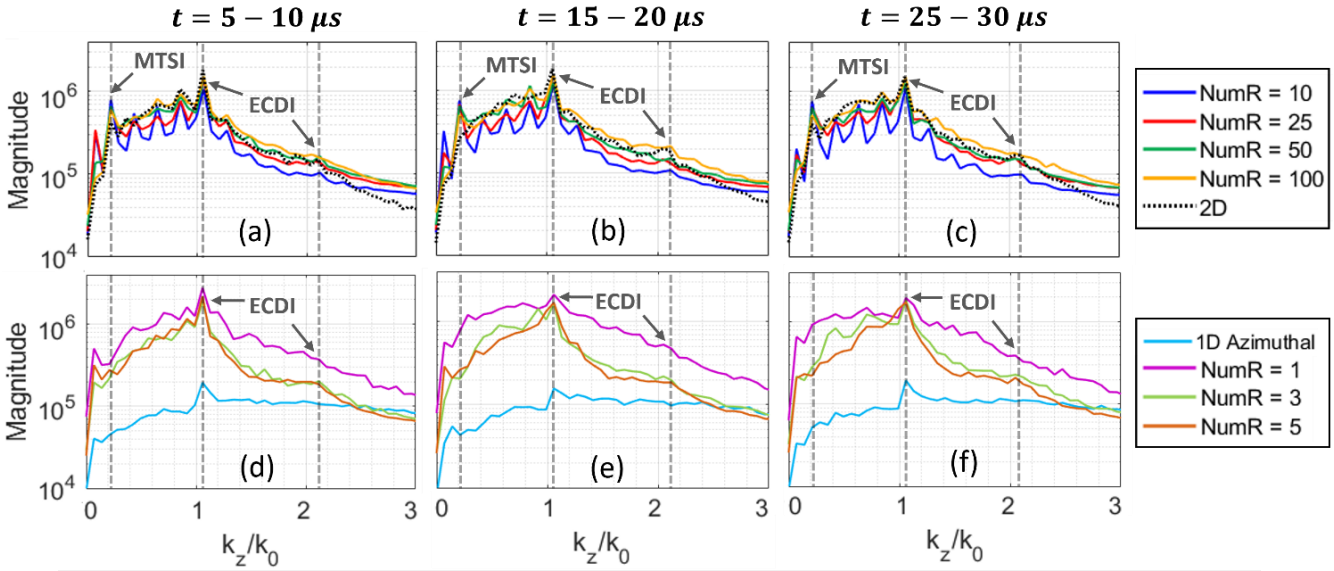


Fig. 3.17: Azimuthal wavenumber spectrum of instabilities obtained from spatial FFT of the azimuthal electric field signal averaged over all radial positions and over three time intervals; (a) & (d) $5-10\ \mu s$, (b) & (e) $15-20\ \mu s$, and (c) & (f) $25-30\ \mu s$. The top row is related to the "high-order" Q2D simulations and the full-2D simulation; the bottom row is related to the "low-order" Q2D simulations and the 1D azimuthal simulation.

Referring to the top-row plots in **Fig. 3.17**, we notice that the k_z spectrum captured by all "high-order" Q2D simulations are very similar to the that in full-2D. In particular, all "high-order" Q2D simulations perfectly agree with the 2D simulation regarding the prediction of the k_z values for the two dominant peaks in the instabilities' spectrum. The peak in the FFT plots at $\frac{k_z}{k_0} \approx 0.2$ is associated with the azimuthal component of the MTSI [35], whereas the peak at $\frac{k_z}{k_0} \approx 1$ corresponds to the first harmonic of the ECDI mode [35]. Also, a lower peak at $\frac{k_z}{k_0} \approx 2$, representing the second harmonic of the ECDI, is observed in the FFT plots of all "high-order" Q2D simulations, which is in line with the 2D simulation's FFT result.

In terms of the distribution of the absolute magnitudes of FFT spectrum across the azimuthal wavenumbers, the plots from the 50- and 100-region simulations are basically converged to the FFTs

from the 2D simulation within the three shown time intervals. The convergence of the Q2D results in these simulations is also evident from the frequency spectrum of the instabilities shown in **Fig. 3.18**.

Concerning the FFT plots from the "low-order" Q2D and the 1D azimuthal simulations (**Fig. 3.17**, bottom row), we see that the fundamental ECDI mode is present in all simulations. The 3-region and 5-region simulations also resolve the second harmonic of the ECDI. The MTSI is noticed to be absent in the "low-order" quasi-2D (and 1D azimuthal) simulations, most likely because, in these simulations, the radial wavenumber component of the MTSI is not properly captured so as to allow for the formation of the corresponding wave modes.

Comparing the FFT plot from the 1D azimuthal simulation with those from "low-order" Q2D simulations, we notice that accounting for the radial dimension even in the lowest approximation limit (single-region) substantially modifies the magnitude of the ECDI mode and the overall FFT spectrum towards the reference spectrum from the 2D simulation.

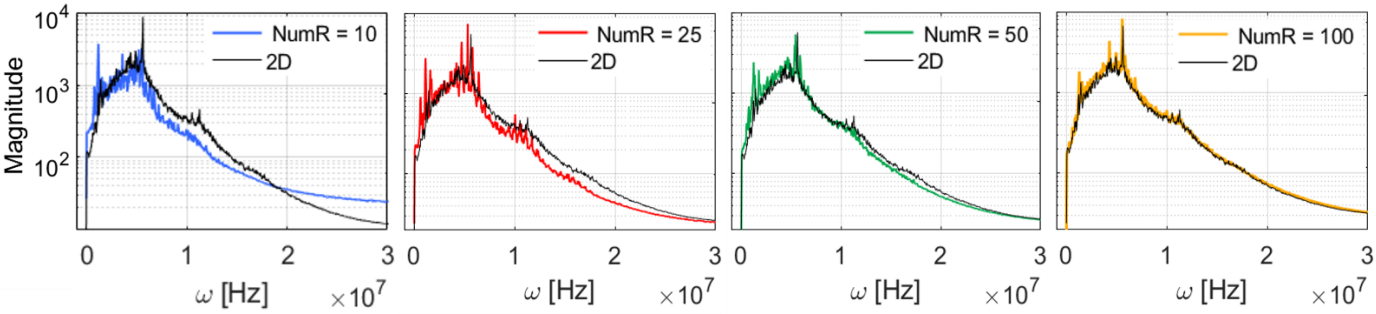


Fig. 3.18: Frequency spectrum of instabilities obtained from temporal FFT of the azimuthal electric field signal from "high-order" Q2D simulations in comparison with those from full-2D simulation. The FFTs are averaged over all radial and azimuthal positions.

The Q2D simulations, particularly with higher number of regions ($NumR \geq 10$) are also observed to properly capture the interactions between the dominant modes in the system. In fact, in this plasma configuration, the existing ECDI and MTSI modes exhibit a nonlinear coupling throughout the simulation, leading to a cyclic discharge behavior. Accordingly, the discharge oscillates between two distinct states corresponding to the local maxima and the local minima of the average radial electron temperature. When the radial electron temperature is at its local maximum, the MTSI is dominant, whereas the ECDI becomes more dominant when the radial electron temperature reaches a local minimum.

In this regard, **Fig. 3.19** illustrates the 2D snapshots of several plasma properties at a time instance corresponding to a local maximum (top panel), and a local minimum (bottom panel) of the spatially averaged radial electron temperature. It is evident from these plots that even with as few as 10 regions, the characteristic patterns of the fluctuations are faithfully represented. In particular, in all cases, both the azimuthal and radial wavenumber components of the MTSI are resolved, which is best visible from the 2D snapshots of the axial electron current density (J_{ey}) on the third row of top panel in **Fig. 3.19**. Moreover, the 50- and 100-region simulations provide predictions of the 2D distributions of the plasma properties which are almost indistinguishable from the full-2D results.

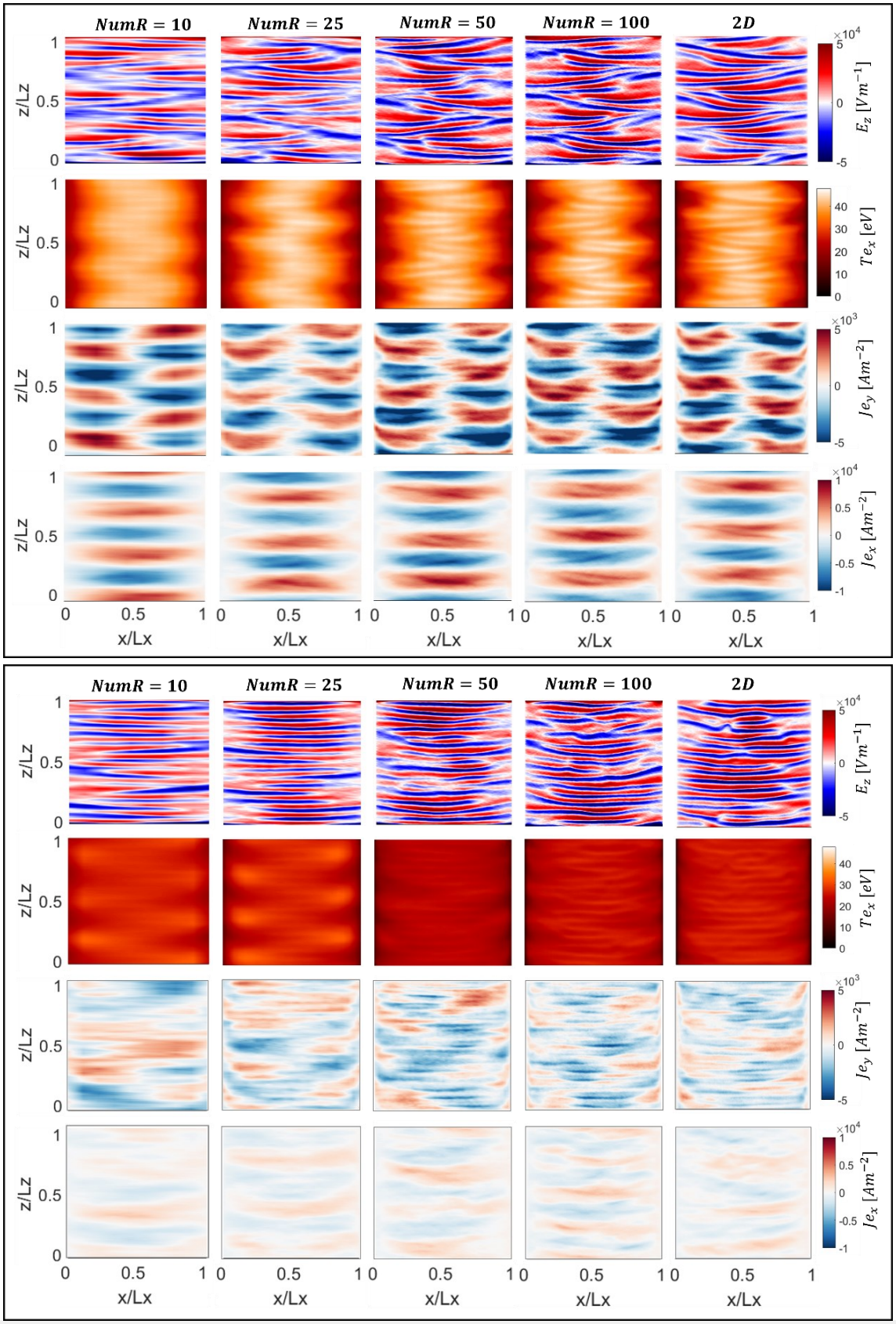


Fig. 3.19: 2D snapshots of the plasma properties from "high-order" Q2D simulations and the 2D simulation at the time of local maximum (top panel) and local minimum (bottom panel) of the spatially averaged radial electron temperature (Te_x). In each panel, the rows, from top to bottom, represent the azimuthal electric field (E_z), the radial electron temperature (T_{ex}), and the axial and radial electron current densities (J_{ey} & J_{ex}).

3.2.2.1. Sensitivity to number of macroparticles per cell

To evaluate the influence of the initial number of macroparticles per cell (N_{ppc}) on the Q2D results, we used the 50-region Q2D simulation with the of initial N_{ppc} ranging from 10 to 1024. The results in terms of the normalized, time-averaged, radial distributions of the ion number density and total electron temperature are shown in **Fig. 3.20**. Referring to plot (a) in this figure, the ion number density profiles are seen to have converged at a peak density ratio of about 2.45 for $N_{ppc} \geq 100$. Looking at plot (b) of **Fig. 3.20**, even though the convergence trend is not monotonic, the temperature profiles does not show any noticeable variation beyond $N_{ppc} = 200$. The simulation case with $N_{ppc} = 100$ has a maximum discrepancy of less than 10 % in normalized T_e compared to the simulations with higher N_{PPC} counts.

As a result, the Q2D simulations show a clear statistical convergence behavior when increasing the initial N_{ppc}, and an initial macroparticle per cell in the range of 100 to 200 can be sufficient to ensure statistically converged results. This convergence behavior of the Q2D simulation is consistent with the convergence trend observed for full-2D PICs in Ref. [35].

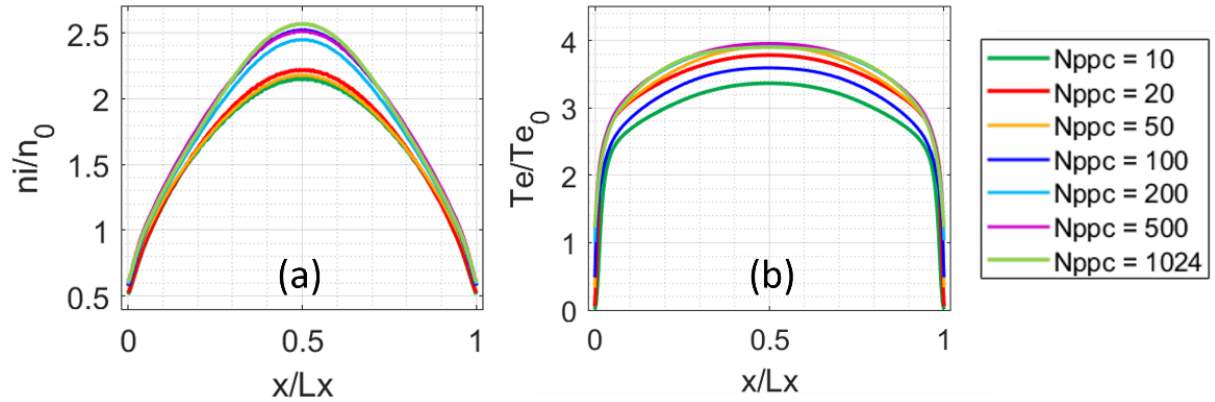


Fig. 3.20: Comparison of time-averaged radial profiles of (a) normalized ion number density, and (b) normalized electron temperature obtained from the 50-region Q2D simulation with various initial number of macroparticles per cell. $n_0 = 5 \times 10^{16}\ m^{-3}$ and $T_{e0} = 10\ eV$ denote the initial ion number density and electron temperature during initial particles' load.

3.3. Penning discharge benchmark problem

This test case intends to assess the ability of RO-PIC to resolve the underlying physics in a setup where the principal direction of the involved physical phenomena is constantly changing with respect to the coordinate system due to the formation of a large coherent structures called the spoke mode [111][112]. As described in Ref. [111], this problem is characterized by a "*vastly multi-scale physics*" and has a "*highly non-linear, turbulent, and global nature*". The occurrence of spoke leads to inefficiencies in an $\mathrm{E} \times \mathrm{B}$ device due to significant electron cross-field transport it induces [112][113].

In this verification case, we aim to assess the accuracy and the convergence characteristics of RO-PIC versus the degree of order-reduction (number of regions), and to further demonstrate the functionality and general applicability of RO-PIC for problems of complex physics.

3.3.1. Setup and conditions of the problem

The setup of the Penning discharge Q2D simulations is adopted from a newly defined benchmark problem within the $\mathrm{E} \times \mathrm{B}$ plasma community [114]. The benchmark problem is based on recent numerical research into the physics of the plasma within the Penning trap configuration, e.g., in Ref. [111], in order to investigate the formation and the characteristics of rotating spoke-like structures.

The simulation domain corresponds to a 2D Cartesian plane in the $x - y$ coordinates as depicted in **Fig. 3.21**. The length of the simulation domain is the same along the x and y directions and equal to $5\ cm$ ($L_x = L_y = 5\ cm$). The number of cells along either dimension is $N_i = N_j = 256$. The simulation time step is $\Delta t = 4 \times 10^{-11}\ s$ and the total simulation time is $500\ \mu s$. A uniform, constant magnetic field (B_z) is externally applied along the z-direction with an intensity of $10\ mT$. The ion species is Helium-4, and the ion particles are pushed electromagnetically using the Boris pusher [94] similar to the electrons.

All four boundaries of the domain are electrically grounded and perfectly absorbing. Thus, a zero-Volt Dirichlet potential boundary condition is applied to all sides of the domain. All particles crossing any of the four domain boundaries are removed from the simulation.

The simulation is collisionless. The domain is initially empty. A cylindrical particle injection source over a radius of $5\ mm$ is envisaged in the center of the domain [114]. This source injects the total number of macroparticles at each time step of $S_e = 49.932$ for electrons and $S_i = 19.973$ for ions. The injected electrons and ions are sampled from Maxwellian distribution functions at the temperature of $15\ eV$ and $0.025\ eV$, respectively. The macroparticle weight is $W_{mp} = 10^5$ for both electron and ion species. The time-averaging window for the plasma profiles is $200 - 500\ \mu s$.

A virtual ion density probe is placed within the simulation domain at the coordinates of $x = 1.25\ cm$ and $y = 0$, recording the local ion density throughout the simulation at this position.

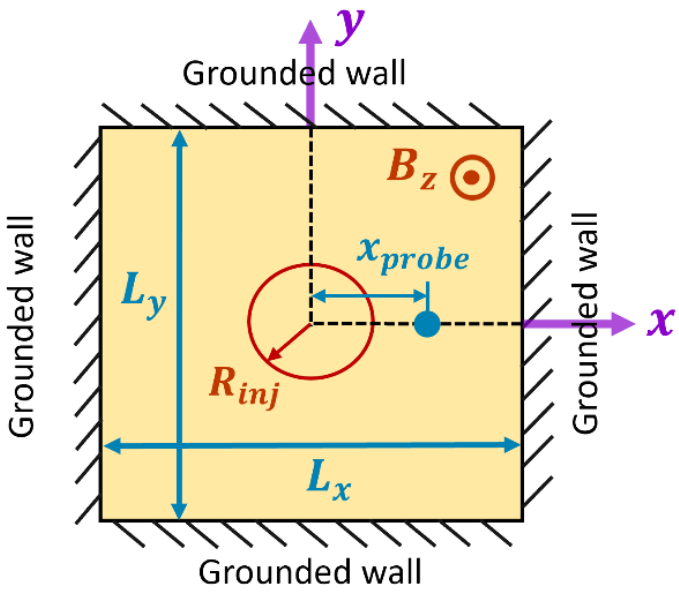


Fig. 3.21: Schematic of the computational domain and setup of the Penning discharge simulations.

3.3.2. Verification results

The Q2D simulations are performed with $15, 45$ and 100 regions along both dimensions of the domain. The extents of the regions are equal.

Fig. 3.22 shows the time-averaged profiles of the main output plasma properties along the x-direction. We have compared the obtained profiles from the Q2D simulations with various number-of-region domain decompositions against the full-2D results from IPPL-2D.

Looking at the three plots in **Fig. 3.22**, the convergence of the predicted profiles from the Q2D simulation to those of the full-2D is evident as the number-of-region increases from 15 to 100. The 100-region simulation is almost perfectly reproducing the 2D profiles, whereas the 45-region Q2D simulation provides a great approximation of the n_i and the ϕ properties, in particular. The profiles from the 15-region Q2D simulation show a higher level of discrepancy with respect to the 2D results, compared to the 45- and 100-region simulations.

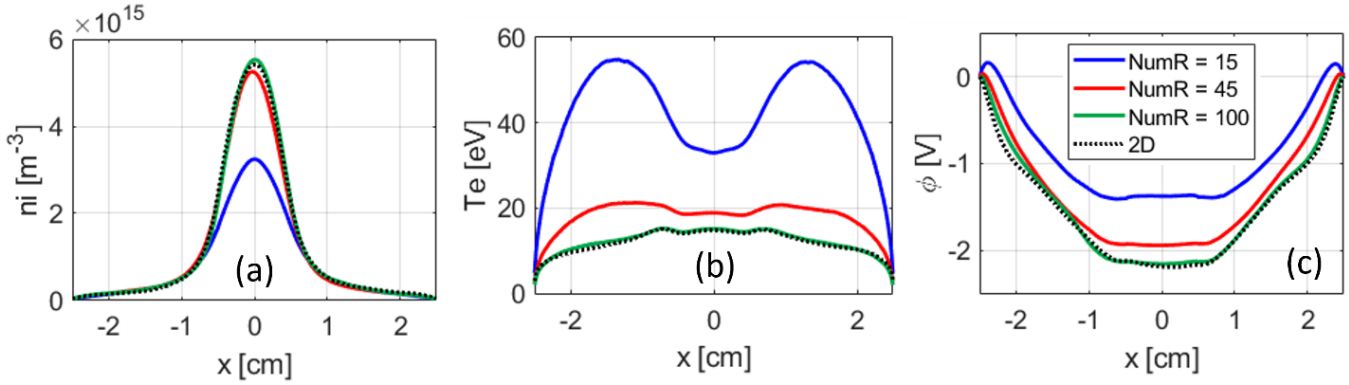


Fig. 3.22: Time-averaged (over $200 - 500\ \mu s$) profiles of plasma properties at the mid-plane ($y = 0$) of the domain along the x-direction, from the Q2D simulations with various number of regions, and from the full-2D IPPL PIC simulation; (a) ion number density (n_i), (b) electron temperature (T_e), and (c) plasma potential (ϕ).

We have also provided in **Fig. 3.23**, the time evolution of the local ion number density as measured by the virtual density probe as well as the temporal FFT of the corresponding density probe's signal from the Q2D and full-2D simulations.

We notice that the FFTs from all simulations feature three dominant peaks, with the highest peak representing the frequency of the rotating spoke. Interestingly, the spoke frequency from all the Q2D simulations is observed to be quite close to the full-2D's prediction. The highest discrepancy in the predicted frequency is about 20% for the 15-region simulation. The 100-region simulation shows a difference of only about 1.5 % in the predicted spoke frequency with respect to the full-2D simulation. The frequencies of the second and the third dominant peaks in the FFT spectrum of 100-region Q2D simulation also closely match those in the full-2D's spectrum. These frequencies from the 45-region simulation are in reasonably good agreement with the corresponding frequencies from the full-2D simulation.

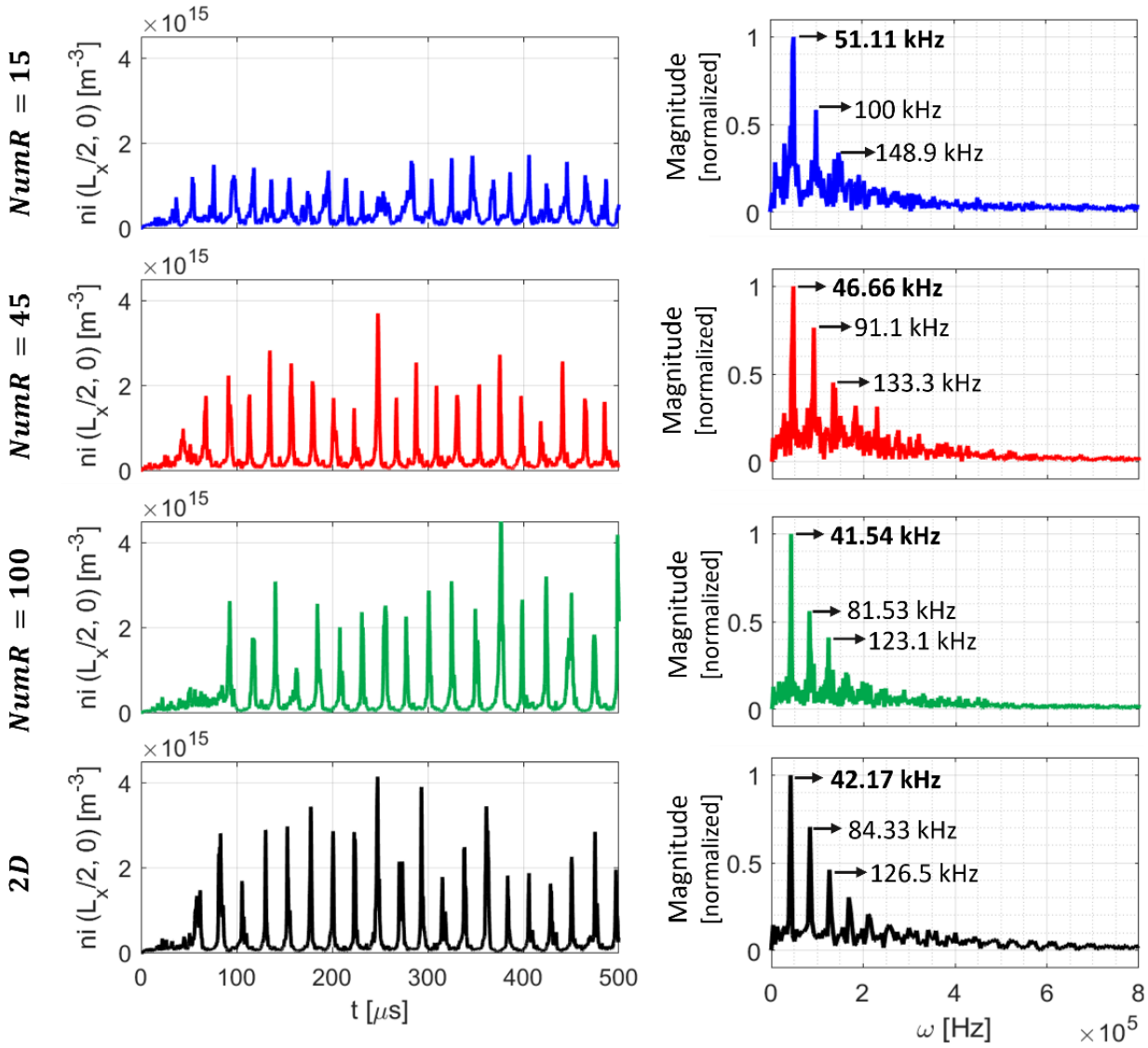


Fig. 3.23: Time evolutions of the local ion number density at the location of the virtual density probe (left column) and temporal FFT spectra of the probe's signal (computed over $50 - 500\ \mu s$ duration) from the Q2D and the full-2D simulations. The highest peak in the FFTs corresponds to the spoke frequency.

The spoke structure forms within the simulation, following the initial transient, that exhibits a counterclockwise rotation, leading to a quasi-periodic behavior of the discharge during the system's quasi-steady state. All Q2D simulations capture the formation of spoke and its counterclockwise rotation as seen in the 2D snapshots of the ion number density in the top panel of **Fig. 3.24**. This particularly demonstrates that all Q2D simulations have successfully resolved the essential underlying physics of the problem. Increasing the approximation order from 15 to 100 regions, the spatial details of snapshots from the Q2D simulations become increasingly more similar to the full-2D results. At the 100-region approximation limit, the spatial resolution of the Q2D PIC is indistinguishably close to that of the full-2D.

The 100-region simulation is used to simulate the discharge over an extended timeframe, up to $1200\ \mu s$, in order to assess possible variability of the discharge over the long terms. This study demonstrated that the discharge exhibits a minimal variation throughout the entire simulated time period (refer to Appendix A.4.3).

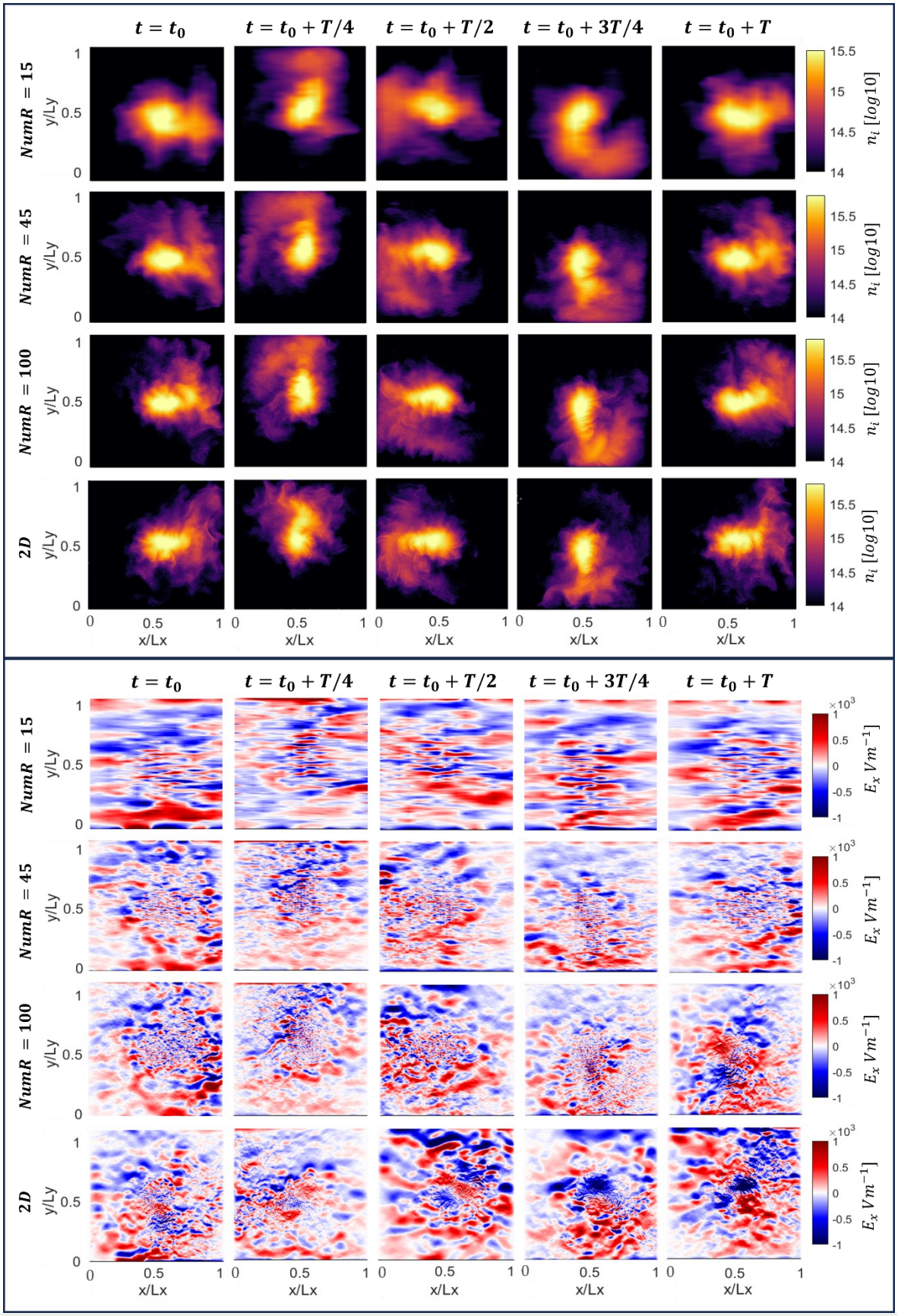


Fig. 3.24: 2D snapshots of the ion number density (top panel) and x-component of the electric field (bottom panel) at 5 different instances over one evolution cycle (with period T) of the spoke mode from the Q2D and the full-2D simulations.

Finally, the L2 error in the time-averaged plasma profiles, and the computational time ratio between the Q2D and the 2D simulation are presented in **Fig. 3.25**. In the lowest number-of-region simulation (15-region), the error in the predicted electron temperature is notably high, whereas the errors in the predictions of the ion number density and electric potential, which are about $20-30\%$, are deemed reasonable. This is achieved with a simulation that has less than 5 % of the computational time of a full-2D simulation. This indicates that this approximation order is less suited for the Penning discharge case if the aim would be to recover the 2D profiles with high accuracy. However, as seen earlier, even at this "low-order" approximation limit, the main behavior of the discharge and the characteristics of the spoke are adequately captured.

Moving to the "high-order" end of the problem approximation, the 100-region simulation is observed from **Fig. 3.25** to have an error of less than $3-4\%$ across all the relevant plasma properties while featuring a computational cost of about 40 % of the full-2D simulation.

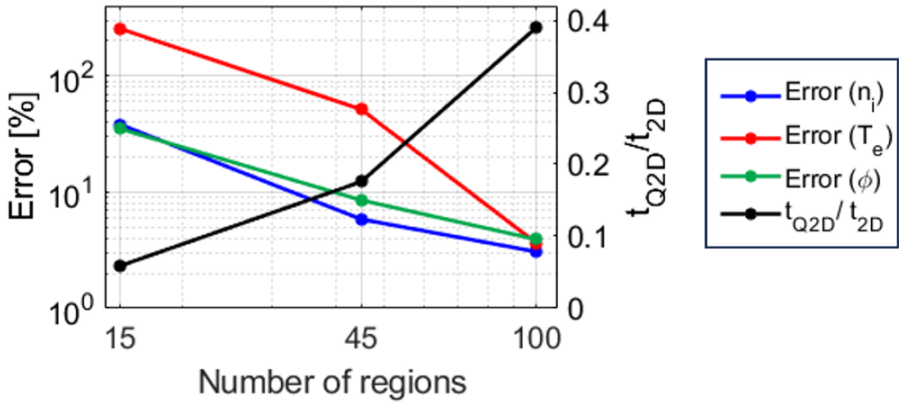


Fig. 3.25: Variation of the L2 error in prediction of plasma properties from the Q2D simulations compared to full-2D results from IPPL-2D code in the Penning discharge case, alongside the computational time ratio between the Q2D and full-2D IPPL codes plotted against the number of regions in the Q2D simulations. The L2 error is calculated using Eq. 3.4 for the time-averaged radial profiles. Note that the x-axis is in logarithmic scale.

The verification results presented so far were for the domain decompositions featuring uniform extents across all regions along a given dimension of the simulation domain. However, RO-PIC does *not* impose any restriction on choosing an arbitrarily non-uniform distribution of the regions' extents. A non-uniform domain decomposition can be informed by a very rough knowledge of the behavior of the macroscopic gradients in the system, particularly the gradients in the electric field. Accordingly, the extents of the regions can be locally refined to be compatible with the rapid local gradients or to meet a particular requirement on the solution's resolution in particular areas of the simulation domain. The adoption of non-uniform regions' extents is assessed in Appendix A.4.4 in both the radial-azimuthal $\mathrm{E}\times\mathrm{B}$ discharge benchmark problem and the Penning discharge benchmark case. The results presented in Appendix A.4.4 demonstrate the flexibility of the RO-PIC scheme to accommodate non-uniform regions' extent. They additionally show that an informed selection of the regions' extent based on the physics of the problem can lead to higher accuracy in the predictions with fewer regions. In other words, with a non-uniform distribution of the regions, it is possible to reduce the number of regions more readily without notably impacting the fidelity of the results, or to improve the accuracy of the results while maintaining the overall number of regions used in the simulation.

3.4. Neutrals' plume expansion (DSMC) test case

This test case serves as an example to demonstrate the generalizability of the dimensionality-reduction technique beyond the PIC simulation by applying the order-reduction technique to the DSMC method [101]. Moreover, in multi-dimensional partially ionized plasmas, the kinetic DSMC method is the de-facto approach to model the dynamics of the neutrals and to account for their collisional interactions. For instance, for Hall thruster simulations particularly in the axial-radial coordinates, which resolve the radial expansion of the neutrals, DSMC treatment of the neutrals is essential. However, like the conventional PIC simulation, the DSMC approach is computationally expensive. Moreover, if the DSMC module is to be used within the Q2D PIC simulation, the DSMC algorithm shall be adjusted to be compatible with the reduced-dimension grid and the overall Q2D description of the problem.

Accordingly, the purpose of this test case is to verify the Q2D adaptation of the DSMC method in a standalone manner before its integration as a Q2D neutral dynamics module into the IPPL-Q2D. The standalone verification of the Q2D DSMC is a precursor to the testing of the IPPL-Q2D in the axial-radial Hall thruster configuration whose results are presented in Appendix A.4.2.

3.4.1. Reduced-order adaptation of the DSMC (RO-DSMC)

As described in detail in Section 1.4.2.4, in a conventional DSMC algorithm, at each time step, particles are sorted based on the cells in which they reside. The maximum number of collision events (or collision pairs, n_g) in each cell is calculated according to the "no-time-counter" (NTC) method. Therefore, in each cell, n_g pairs of neutral particles are randomly selected, and if the collision occurs (based on the probability of collision between the selected pair), their velocities are updated following the conservation of momentum and energy before and after collision.

Here, the focus is on the Q2D adaptation of the DSMC algorithm to make it compatible with the Q2D computational grid associated with the RO-PIC scheme. This is achieved through modifying the conventional 2D DSMC method according to the algorithm illustrated in **Fig. 3.26**. The algorithm starts by initializing $(\sigma v_r)_{max}$ with an estimated value. We recall that, as illustrated in **Fig. 2.1**, the Q2D computational grid comprises two separate fine grids along the generic x and y directions of a 2D simulation domain. Accordingly, the Q2D modification of the DSMC method involves executing the main loop of the DSMC on both fine grids, separately. The DSMC's main loop on either grid is similar to the conventional DSMC's loop. It involves particle sorting within the corresponding cells of each x- and y-aligned grid, the calculation of the maximum number of collision events ($n_{g,x}$ within vertical cells of the x-grid, and $n_{g,y}$ within horizontal cells of the y-grid), the random selection of collision partners, checking for the collision occurrence, and the execution of the collision in case the collision happens. Hence, the only difference is that, in the Q2D DSMC scheme, the maximum number of collision events calculated for either x- or y-grid ($n_{g,x}$ and $n_{g,y}$, respectively) is halved. This is because the particles are shared between the two grids while the DSMC is being performed twice on the particles (once on each grid). As a result, halving the obtained $n_{g,x}$ and $n_{g,y}$ ensures the statistical consistency of the total collision events occurring in the DMSC-Q2D scheme with those in a corresponding full-2D DSMC.

Finally, in case of encountering a value for $(\sigma v_r)_{max}$ larger than the initial estimate during the collisions in either loop, the value of the parameter is updated accordingly.

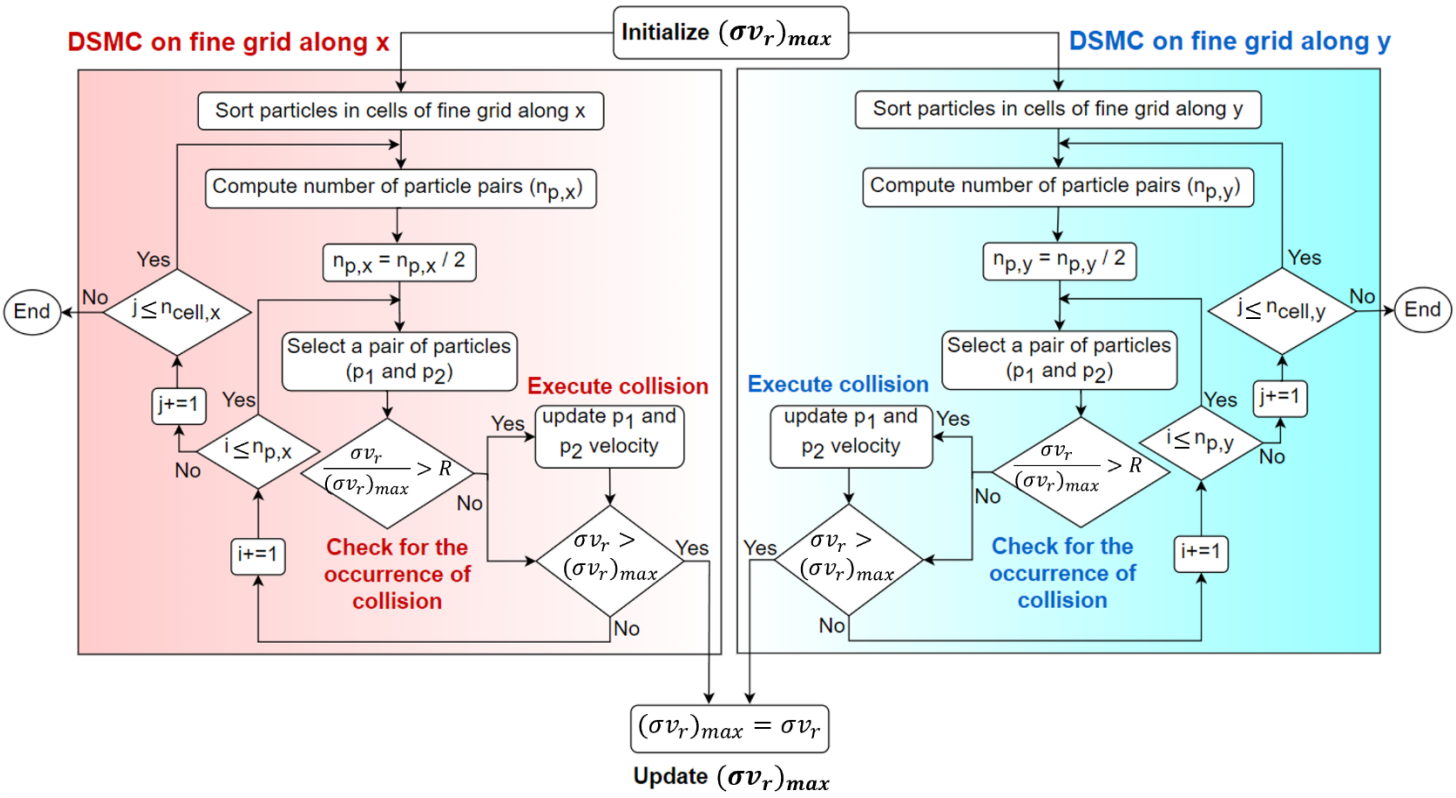


Fig. 3.26: Flowchart of the Q2D DSMC algorithm. The fine grids along the x and y directions refer to the Q2D grids illustrated in **Fig. 2.1**. $n_{cell,x}$ and $n_{cell,y}$ are the number of cells corresponding to the x-grid and the y-grid, respectively, σ is the collision cross section, v_r is the relative velocity of the colliding particles, and R is a random number selected from a uniform distribution between 0 and 1.

3.4.2. Setup and conditions of the problem

The test case resembles a miniaturized version of the expansion of a neutral flow in the plume of a Hall thruster. The computational domain is a Cartesian plane in $x - y$ coordinates with the dimensions $L_x = 13\ mm$ and $L_y = 8\ mm$ as depicted in **Fig. 3.27**. The neutrals are oxygen molecules and are injected at each time step with a constant mass flow rate that corresponds to the $n_{n,inj} = 5 \times 10^{24}\ m^{-3}$ and with the axial drift velocity of $V_{dn,inj} = 100 \frac{m}{s}$. The injection takes place on an injection plane that spans from $y_{inj,1} = 2\ mm$ to $y_{inj,2} = 4\ mm$. The neutrals are randomly sampled from a drifted half-Maxwellian distribution function with the temperature of $T_{n,inj} = 300\ K$. The number of computational cells along the axial (x) and the radial (y) directions are $N_i = 500$ and $N_j = 300$, respectively, to maintain the cell size below the minimum mean free path in the system. Also, the time step of $8 \times 10^{-8} s$ is adopted in accordance with the CFL (Courant-Friedrich-Lewy) criterion.

The neutral-neutral collisions are modeled through the Q2D DSMC algorithm. Regarding the boundary conditions on the neutral particles, we note that the bottom boundary of the domain corresponds to the axis of symmetry of a Hall thruster with an annular channel. Therefore, the particles

crossing the bottom boundary are specularly reflected to mimic the axisymmetric condition in an otherwise axisymmetric coordinate system. Neutrals reaching the rest of the boundaries of the domain are removed from the simulation.

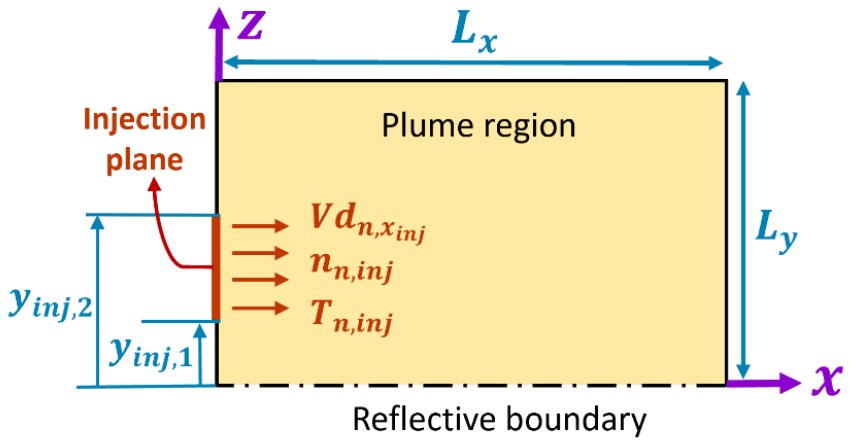


Fig. 3.27: Schematic of the computational domain and setup of the neutrals' plume expansion test case.

3.4.3. Verification results

Before assessing the Q2D DSMC scheme in the test case introduced above, we verify that the collisions in the defined case have indeed a significant impact on the neutrals' expansion profile so that the case can be considered as "collisional". This in turn ensures the suitability of the adopted case for our verification purposes. To this end, **Fig. 3.28** presents a comparison between the steady state distributions of the neutrals' properties from a collisionless and a collisional full-2D DSMC simulation. We highlight that the conditions in both simulations are kept exactly the same, except that, in the collisionless simulation, the DSMC collision function is inactivated, and the particles move along their trajectories with their initial load velocities.

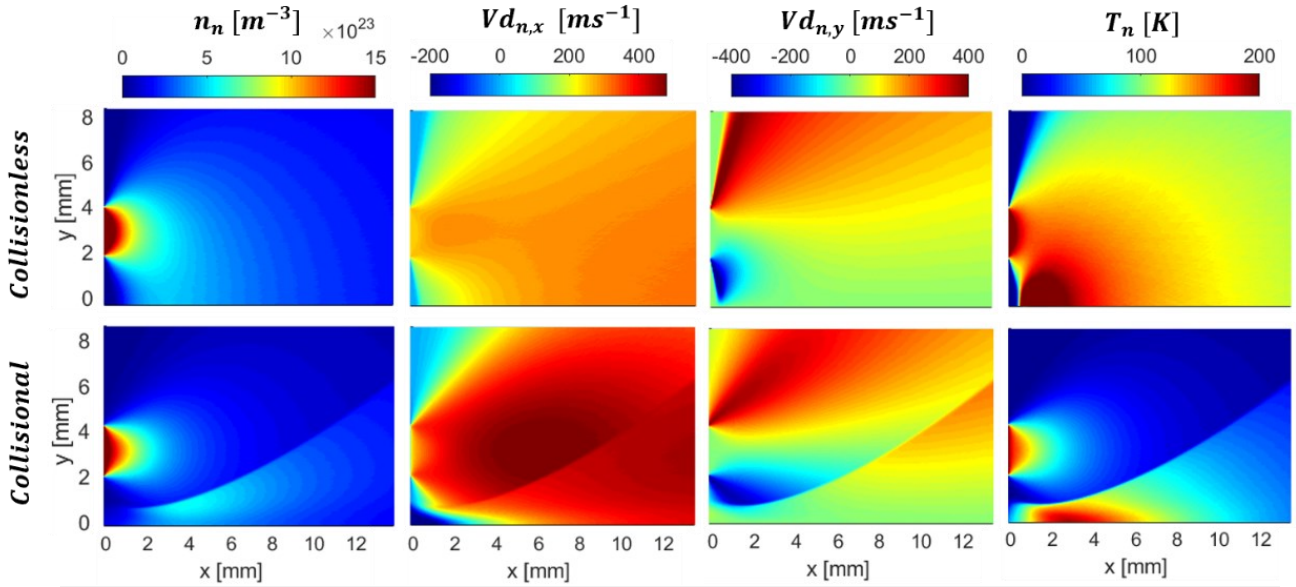


Fig. 3.28: Steady-state 2D distribution of the neutrals' properties from the full-2D DSMC simulation with collisionless (top row), and collisional (bottom row) neutral's expansion; the panels from left to right represent the number density (n_n), axial drift velocity ($V_{dn,x}$), radial drift velocity ($V_{dn,y}$), and temperature (T_n) of the neutrals.

It is evident from **Fig. 3.28** that the collisions remarkably changed the neutrals' profiles. In particular, in the presence of collisions, the axial drift velocity of the neutrals in the core region of the plume has increased significantly, while the neutral's temperature drops almost everywhere. This change in neutrals' profiles under collisional conditions is speculated to result from scattering and displacement of neutrals from the plume's central region caused by collisions. As the density decreases, the particles experience an increase in axial drift velocity, while their temperature decreases to conserve total energy of the neutral flow. Additionally, the formation of a diverging flow in front of the main plume is observed in the collisional case. This is because the collisions increase the neutrals' flux reaching the bottom boundary of the domain from where the particles are reflected towards the domain's center.

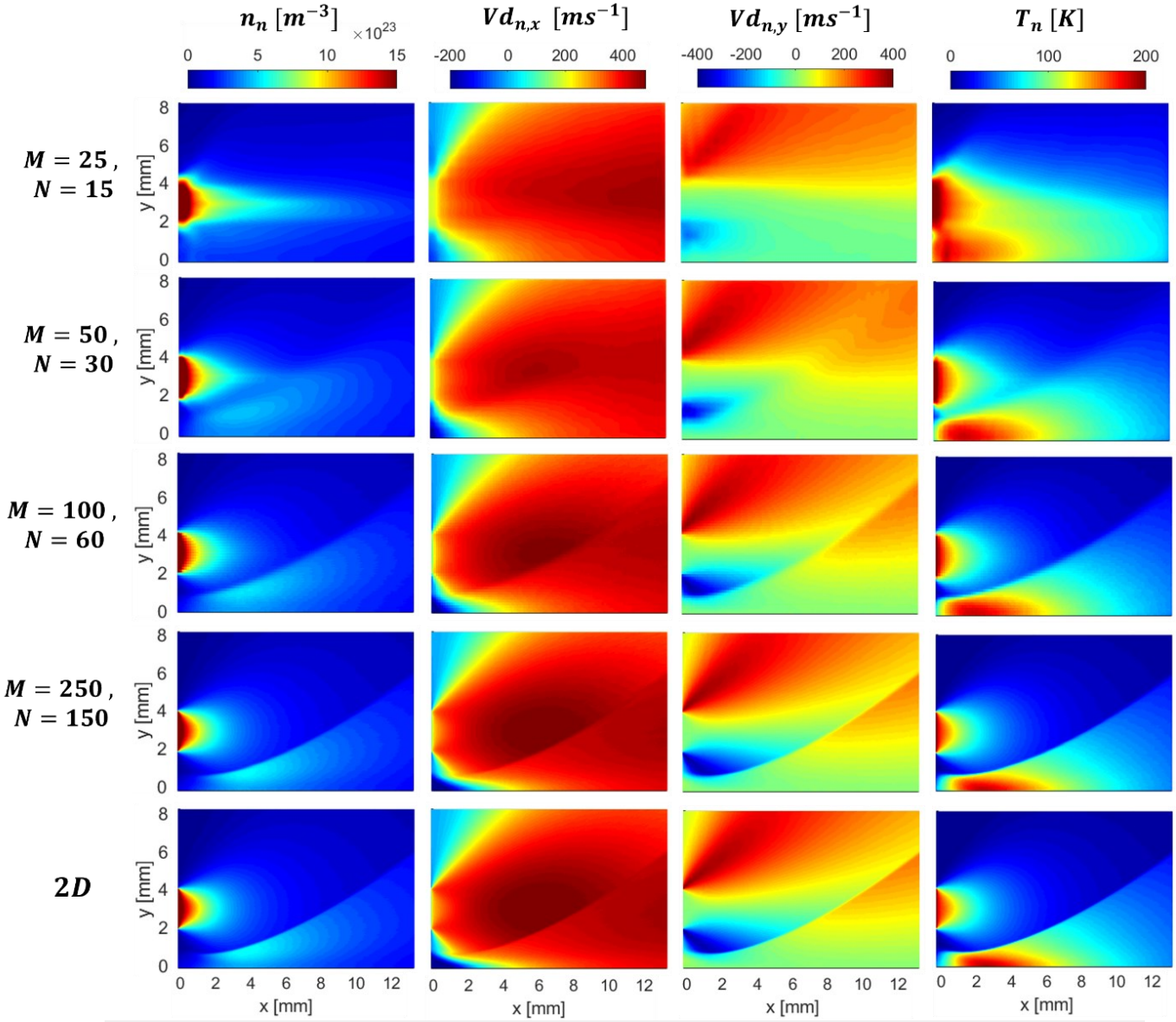


Fig. 3.29: Steady-state 2D distribution of the neutrals' properties from the Q2D and full-2D DSMC simulations of the collisional neutrals plume expansion test case; The panels from left to right represent the number density (n_n), axial drift velocity ($V_{dn,x}$), radial drift velocity ($V_{dn,y}$), and temperature (T_n) of the neutrals. M and N are the number of regions along the axial and the radial directions, respectively.

Following the above check, we proceed with the verification of the Q2D DSMC in the collisional neutrals' plume expansion test case. We performed the simulations using various number of regions including, case $\boldsymbol{i}$: $N = 15,\ M = 25$, case $\boldsymbol{ii}$: $N = 30,\ M = 50$, case $\boldsymbol{iii}$: $N = 60,\ M = 100$, and case $\boldsymbol{iv}$: $N = 150,\ M = 250$, where M and N represent the numbers of regions along x and y directions, respectively. The results are then compared against full-2D DSMC simulation.

Fig. 3.29 shows the resulting steady state 2D distributions of various neutrals' properties from these simulations. The plots in this figure visually illustrate the convergence of the Q2D DSMC solution to the full-2D profiles as the number of regions increases. In particular, at the low number of regions (case $\boldsymbol{i}$ and case $\boldsymbol{ii}$), the essential expansion behavior of the neutral flow is captured. At higher number of regions (case $\boldsymbol{iii}$ and $\boldsymbol{iv}$) the neutrals' distributions closely resemble the full-2D results.

For a quantitative comparison, the axial profiles of the neutrals' properties along the plume centerline ($y = 3\,mm$) from the Q2D simulations are plotted against the corresponding profiles from the full-2D simulation in **Fig. 3.30**. According to these plots, it is evident that the Q2D simulation corresponding to case $\boldsymbol{iii}$ ($M = 100, N = 60$) provides a reasonably well approximation of the full-2D profiles. Also, the axial profiles from case $\boldsymbol{iv}$ ($N = 150,\ M = 250$) perfectly coincide with those from the full-2D simulation.

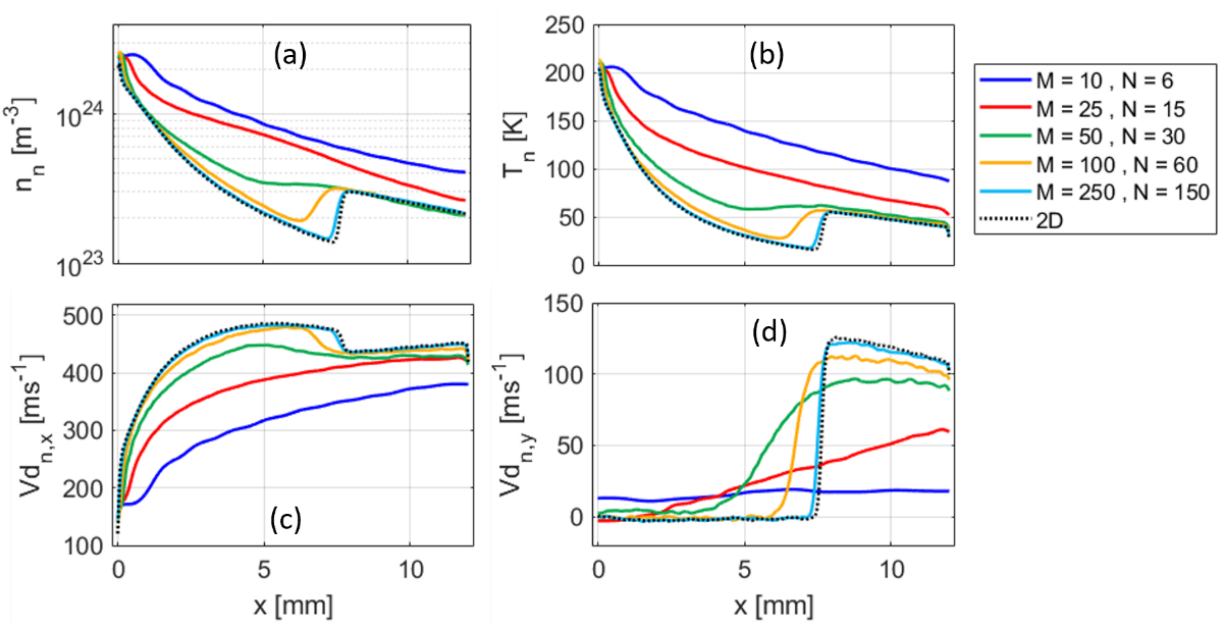


Fig. 3.30: Steady-state axial profiles of the neutrals' properties from the Q2D DSMC simulations with various number of regions and from the full-2D DSMC simulation of the collisional neutrals plume expansion test case; (a) neutral number density (n_n), (b) neutral temperature (T_n), (c) neutrals' axial drift velocity ($V_{dn,x}$), and (d) neutrals' radial drift velocity ($V_{dn,x}$).

Finally, to conclude the Q2D DSMC verification results, **Fig. 3.31** presents the variation of the error in the Q2D predictions of various neutrals' properties distributions with respect to the full-2D results, as well as the ratio of the computational time of the Q2D simulations to that of the full-2D, plotted against the number of regions (M). The error is calculated based on the L2 norm across the entire 2D distributions at steady state.

This convergence plot in **Fig. 3.31** exhibits a monotonic decrease in the Q2D simulations' error across various properties as the number of regions is increased. In particular, these results show that

a Q2D simulation with low number of regions ($M = 25, N = 15$, e.g.) can be well suited for parametric studies and order-of-magnitude approximations. Furthermore, a higher-order approximation of the problem with $M = 100, N = 60$ results in the reduction of the errors to below 50% in all predicted properties while yielding a five-fold speedup compared to a full-2D DSMC simulation.

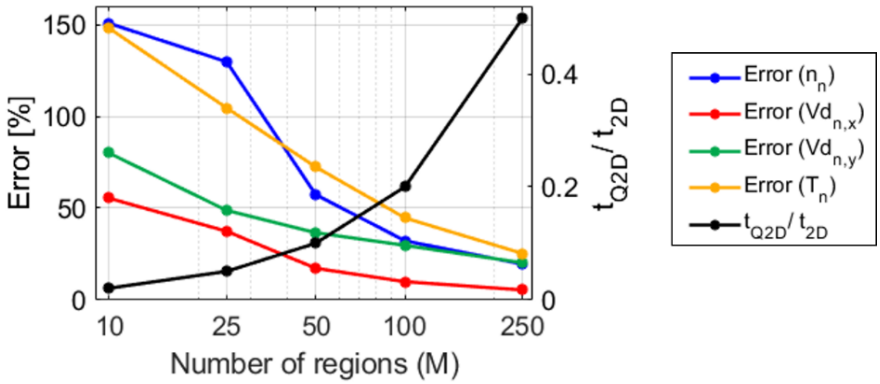


Fig. 3.31: Variation of the L2 error in the prediction of neutrals' properties from the axial-radial Q2D DSMC simulations compared to full-2D DSMC results in collisional neutrals' expansion case, alongside the computational time ratio between the Q2D and full-2D DSMC simulations plotted against the number of regions in the Q2D simulations (M). The L2 error is calculated using Eq. 3.4 over the entire 2D distributions at steady state. M denotes the number of regions along the axial direction which in these simulations are $5/3$ times the number regions along the axial direction (N). Note that the x-axis is in logarithmic scale.

3.5. Conclusion

The RO-PIC scheme (and the resulting Q2D PIC simulation) is tested and verified extensively against the full-2D results from conventional PIC in various plasma configurations and across wide range of approximation orders, which is determined by the number of regions used in the simulation. Rigorous assessment of the prediction fidelity of RO-PIC is conducted through comprehensive comparisons of the simulation results including the distribution of macroscopic plasma properties, instabilities' spectra and their induced electrons' transport, where relevant.

In a well-established 2D axial-azimuthal benchmark problem, we demonstrated that the "low-order" Q2D simulations, which offer about two orders of magnitude reduction in the computational cost compared to full-2D simulation counterpart, can self-consistently resolve the instability-induced electrons' cross-field transport in Hall thrusters. In particular, we showed that the single-region simulation provides a reasonably accurate, average representation of the azimuthal instabilities, and captures their overall effect on electron transport in a manner similar to 2D simulations. Also, "low-order" multi-region (double- and triple-region) simulations resolve several additional waves-related phenomena, the capture of which was previously believed achievable only through full-2D PIC simulations. These include the transition in waves' properties around the ion sonic point [58][115] and downstream convection of the waves excited upstream of the domain's exit plane by the accelerating ion beam [115]. We additionally demonstrated that, by increasing the number of regions, the predictions of "high-order" Q2D simulations converge to those from the 2D reference simulation. At an approximation limit that still offers about a factor of 6.5 reduction in computational cost, the Q2D

simulations are shown to reproduce the time-averaged plasma properties with less than 2% error, and accurately recover the features and characteristics of the azimuthal waves and their 2D distribution.

In a radial-azimuthal benchmark configuration, we verified that the Q2D simulation properly captures the involved intricate coupling and interactions between phenomena along the two dimensions. At the lowest-order end of the approximations, the single-region simulation, with the computational cost equivalent to that of a 1D PIC simulation, was shown to provide results that are notably improved with respect to the corresponding 1D radial and 1D azimuthal simulations. This improvement in the predictions was underlined to be due to the average mutual effects of the radial and azimuthal physical processes that are resolved by the single-region simulation. In addition, other low-order approximations, such as the 3- and 5-region simulations, lead to further improvement in the predictions particularly in terms of the instabilities' spectra. At the high-order end of the approximations, the simulations with 10 to 100 regions that yield about $25-2.5$ times speed-up compared to the full-2D simulation provide results that compare reasonably well with the full-2D ones. In all these cases, the characteristics of the instabilities are accurately captured. The predicted time-averaged plasma profiles involve less than 25% error in 25-region simulation and consistently convergence to full-2D toward 100-region simulation.

Recalling the principal idea behind the order-reduction of PIC simulations, it involves enabling approximation of a multi-dimensional problem with an arbitrary resolution. For many purposes where a very accurate prediction is not necessary, a simplified representation of the problem would be sufficient. The conventional approach is to simply reduce the problem to a lower dimension by neglecting the variation along one/two dimensions altogether, thereby reducing computational costs. Accordingly, a 3D or 2D problem will be treated as a 2D or 1D problem. However, it is important to recognize that most problems cannot be captured at all in lower dimensions, regardless of the extent of sacrifice we are willing to make regarding the accuracy of the predictions.

The Penning discharge test case is an example of such a scenario due to the 2D rotating nature of the spoke. Indeed, we observed that a "low-order" 15-region simulation captures a physics that a 1D simulation cannot resolve. Moreover, it provides an overall qualitative understanding of the behaviors and the processes to be expected, in particular a rather accurate estimation of the spoke's characteristics with only 5% error compared to the prediction of the full-2D simulation. Furthermore, the verification in the 2D Penning discharge problem demonstrates that the RO-PIC can successfully capture multi-dimensional phenomena, even when the principal direction of the system is variable.

We also extended the dimensionality reduction idea behind RO-PIC to the DSMC method. The resulting Q2D DSMC is tested in a problem of neutrals' plume expansion. This case is another example where the involved physics cannot be reduced to a 1D problem, regardless of the extents of the simplifications we make to the analysis of the problem. Nevertheless, the "low-order" approximation of Q2D DSMC is able to capture the overall behavior of the flow and provide reasonable estimates of the variations in the neutrals' properties. We verified that by increasing the number of regions, the Q2D DSMC solution converges to the full-2D DSMC solution. The verified Q2D DSMC then integrated within Q2D PIC simulations to develop Q2D PIC-DSMC model.

The verification results presented in this chapter verify the RO-PIC scheme as a viable, low-computational-cost alternative to the conventional multi-dimensional PIC simulations. Additionally, the Q2D DSMC model serves as an example demonstrating the applicability of the underlying dimensionality reduction approach to numerical models beyond PIC and indicating the promise of this approach to stand as a novel computational framework for reduced order approximation of any system of differential equations.

Chapter 4 Investigation of the parametric variability of plasma instabilities and turbulence using RO-PIC in a radial-azimuthal plasma configuration

RO-PIC, the cost-efficiency and accuracy of which have been verified in previous chapter, can change the current notion regarding the applicability and the utility of a PIC code toward extensive parametric investigations of plasma discharges. Throughout this chapter, we demonstrate the capability of the RO-PIC to enable exploring variation of the underlying plasma phenomena across a broad parameters space that is of significance from both fundamental and applied perspectives.

As demonstrated in Chapter 3, simulations with 50 regions achieve an optimal balance between accuracy and computational gain in the radial-azimuthal plasma configuration. At this level of approximation, the Q2D code offers a 5-fold speedup compared to a full 2D simulation, while faithfully reproducing the full-2D results, particularly, in terms of resolving the instabilities' characteristics. As a result, 50-region Q2D simulations are appropriate for the parametric studies presented in this chapter.

The parametric simulations in this chapter assess the influence of the intensity of the applied electromagnetic fields and the curvature of the magnetic field on the collisionless $E \times B$ plasma discharges in a radial-azimuthal configuration representative of a Hall thruster. Our investigations additionally look into how these variations are affected by the ion mass corresponding to different propellants, namely, xenon, krypton, and argon. The analyses are complemented by additional studies on the impact of the SEE and plasma number density.

It is underlined that the axial electric field intensity can be thought of as an operational parameter of a Hall thruster. However, in a given operating condition, the strength of the axial electric field also changes spatially along the thruster's axis [10][49][116], as well as dynamically in time within the thruster's breathing cycles [10][115][116]. Furthermore, in the context of $E \times B$ plasma technologies, the magnetic field intensity represents a design parameter. Particularly in the case of Hall thrusters, the topology of the applied magnetic field and its magnitude within the domain remains invariant over time. Despite this temporal constancy, the magnetic field typically features notable spatial variations by design.

Additionally, in modern Hall thrusters, the magnetic field topology most often features curved lines with a concave (negative) curvature upstream of the field's peak and a convex (positive) curvature downstream. Additionally, the advent of the magnetic shielding technique has led to Hall thruster designs with non-conventional field topologies that exhibit high degrees of concavity upstream of the field's peak.

Thus, the results of these parametric studies can represent the variation of the underlying phenomena in various cross sections of the Hall thruster's channel and at various instances throughout the discharges' breathing cycle.

*The derived aggregate insights from **70 high-fidelity Q2D PIC simulations,** discussed in this chapter, majorly advance our understanding of the parametric dependency of the physics of Hall-thruster-like cross-field plasma discharges. The results show that the factors studied induce notable variations in the spectra of the azimuthal instabilities. These variations consequently affect the macroscopic distribution of the plasma properties, the electrons' mobility, particles' distribution function and the divergence of the ion beam.*

4.1. Description of setup and conditions

The setup of the 2D radial-azimuthal $\mathrm{E} \times \mathrm{B}$ benchmark problem (described in Section 3.1.1) is adopted as a proving ground to demonstrate the RO-PIC utility for extensive parametric investigation and to provide an unprecedented collective insight regarding the parametric variability of the $\mathrm{E} \times \mathrm{B}$ across a wide parameter space.

The RO-PIC simulations are carried out using the IPPL-Q2D code, which is extensively verified in Chapter 3, employing the "high-order" approximation of the 2D problem corresponding to the domain decomposition of 50 regions along the radial and the azimuthal directions. As demonstrated in Section 3.2.2, Q2D simulations with 50 number-of-regions can reproduce the 2D results with sufficient accuracy, while offering a significant computational speedup (5 times) over the conventional 2D simulations. With 50 regions, the Q2D approximation involves an error of about $5 - 10\ \%$ in the plasma profiles, with the characteristics of the resolved instabilities being almost identical to those captured by the full-2D simulation. Accordingly, 50 number-of-regions represents an appropriate choice for parametric analyses and the study of physics in the present effort.

The parameters varied across simulations include magnitude of the imposed axial electric field (E_y), intensity of the applied radial magnetic field (B_y), and the curvature degree of the magnetic field topology, represented by incident angle of the magnetic field liens with the radial direction (θ). The values of the studied parameters are listed in **Table 4.1**.

Case No.	$E_y\ [kVm^{-1}]$	$E_y/E_{y,0}$	$B_x\ [mT]$	$B_x/B_{x,0}$	θ [°]	$S/S_0[m^{-3}]$	SEE/ $\epsilon^*\ [eV]$	Propellant
1	5	0.5	20	1	0	1	No	Xe, Kr
2	20	2	20	1	0	1	No	Xe, Kr, Ar
3	30	3	20	1	0	1	No	Xe, Kr, Ar
4	40	4	20	1	0	1	No	Xe, Kr, Ar
5	50	5	20	1	0	1	No	Xe, Kr, Ar
6	10	1	5	0.25	0	1	No	Xe, Kr, Ar
7	10	1	10	0.5	0	1	No	Xe, Kr, Ar
8	10	1	15	0.75	0	1	No	Xe, Kr, Ar
9	10	1	25	1.25	0	1	No	Xe, Kr, Ar
10	10	1	30	1.5	0	1	No	Xe, Kr
11	10	1	20	1	-60	1	No	Xe, Kr, Ar
12	10	1	20	1	-45	1	No	Xe, Kr, Ar
13	10	1	20	1	-30	1	No	Xe, Kr, Ar
14	10	1	20	1	-15	1	No	Xe, Kr, Ar
15	10	1	20	1	+15	1	No	Xe, Kr, Ar
16	10	1	20	1	+30	1	No	Xe, Kr, Ar
17	10	1	20	1	+45	1	No	Xe, Kr, Ar
18	10	1	20	1	+60	1	No	Xe, Kr, Ar
19	10	1	Config 1 (Fig. 4.32)			1	No	Xe
20	10	1	Config 2 (Fig. 4.32)			1	No	Xe
21	10	1	20	1	10	1	35	Xe
22	10	1	20	1	10	1	30	Xe
23	10	1	20	1	10	1	25	Xe
24	10	1	20	1	10	1	20	Xe
25	10	1	20	1	10	1	15	Xe
26	10	1	20	1	10	1	5	Xe
27	10	1	20	1	10	1/32	No	Xe
28	10	1	20	1	10	1/16	No	Xe
29	10	1	20	1	10	1/8	No	Xe
30	10	1	20	1	10	1/4	No	Xe
31	10	1	20	1	10	1/2	No	Xe
32	10	1	20	1	10	3	No	Xe
34	10	1	20	1	10	6	No	Xe

Table 4.1: List of all the simulation cases performed in the radial-azimuthal coordinates; E_y, B_x and S are the applied axial electric field, radial magnetic field and the ionization source's peak. $E_{y,0} = 10\ kVm^{-1}$, $B_{x,0} = 20\ mT$ and $S_0 = 5.23 \times 10^{23}\ \mathrm{m^{-3}s^{-1}}$ corresponding to the baseline conditions. θ is the incident angle of the magnetic field lines at the walls (refer to **Fig. 4.17** and Eq. 4.5) and ϵ^* is the crossover energy in the linear SEE model (refer to Eq. 1.43).

The results are presented for three industrially relevant propellants for $\mathrm{E} \times \mathrm{B}$ plasma technologies, namely, xenon, krypton, and argon. It is important to highlight that, as the simulations are collisionless, any observed variations among the propellants are solely attributed to the difference in the ions' mass. This enables us to isolate the effect of ion mass and to understand the extent to which the ion mass can change the variations in plasma behavior in response to the varying electric and magnetic fields.

Additionally, the impact of the (radial) gradient of the radial magnetic field (B_x) are assessed in curved magnetic field topologies, representative of magnetic shielding configuration in Hall thrusters (Config 1 and Config 2 in **Table 4.1**). We also, assessed the influence of various SEE rates (in separate set of simulations), determined by the value of crossover energy (ϵ^*), indicated in **Table 4.1.** In these simulations, the electrons' radial boundary condition is modified with respect to the baseline setup to account for the secondary electrons emitted from the walls.

Finally, since varying any of the above parameters alters the density that is established within the system, it is important to isolate the effect of plasma number density. Therefore, we studied the effect of density by varying the peak of the ionization source (S) which determines the steady-state plasma density. For these simulations, the cells' size (Δx and Δz) and the timestep (Δt) are adjusted accordingly to meet the numerical requirement of the simulation.

The variations in the plasma behavior are analyzed from several aspects, namely, the distribution of time-averaged plasma properties, dominant azimuthal instabilities and their characteristics, the electrons' cross-field transport, the particles' distribution functions and the divergence (expansion) of the ion beam.

Prior to analyzing the results, we made sure that all simulations had reached a quasi-steady state before the time window ($20 - 30\ \mu s$) used for the analyses.

4.2. Variations with the intensity of the applied fields

The results presented in this section build up on the work reported in Ref. [34], where the author carried out limited parametric studies on the MTSI and the ECDI in a radial-azimuthal setup that did not resolve the plasma sheath. In Ref. [34], the instabilities' characteristics for two values of the axial electric field were studied for the xenon propellant. Another recent research was carried out by Croes et al. [119]. In that work, for a single value pair of electric and magnetic field intensities, the authors assessed the characteristics of the ECDI and the electron transport due to this instability. Croes et al. adopted a collisional radial-azimuthal simulation setup that featured secondary electron emission [119]. They performed their studies using xenon, krypton, argon, and helium gases [119]. Most notably, the authors observed that, in line with the existing theories [14][16], the frequency of the ECDI depends on the ion mass [120]. However, they did not notice a notable variation in the electron transport with the choice of the gas type [119], an observation in line with the findings of Ref. [17].

The simulations in this section encompass a range of intensities for the applied axial electric field (E_x) from 5 to 50 kVm^{-1}, and various magnitudes for the applied radial magnetic field (B_x) ranging from of 5 to 30 mT.

4.2.1. Variations in the distribution of the plasma properties

We start by presenting the variation in the spatiotemporal average properties, specifically the ion number density and electron temperatures (**Fig. 4.1**). Additionally, **Fig. 4.2** provides the radial profile of the ion number densities. Several noteworthy trend can be observed from the plots in **Fig. 4.1**: first, from plot (a) and **Fig. 4.2**, the ion density (n_i) is the lowest for argon and the highest for xenon across various E_y and B_x values. However, n_i follows a similar general trend for the three propellants. In fact, n_i decreases as E_y increases from $5 - 20\ kVm^{-1}$, then, after experiencing a jump in values between $20 - 30\ kVm^{-1}$, it continues its decreasing trend beyond $E_y = 30\ kVm^{-1}$. Moreover, n_i exhibits a consistent trend of decrease with B_x. Beyond $B_x = 15\ mT$, the variation in the density becomes minimal, indicating an asymptotic trend.

Second, the general behavior observed in n_i, i.e. the non-monotonic behavior with E_y as well as the asymptotic trend with B_x, is also reflected in the variations of the radial electron temperature (T_{ex}) in plot (b). In this regard, T_{ex} is seen to be plateaued for E_y values within the range of $20 - 30\ kVm^{-1}$. It also increases with B_x up to $15\ mT$ after which it remains nearly constant. The inverse correlation that exists between T_{ex} and n_i is, in part, due to the temporal constancy of the imposed particle injection source in the simulations. It is noted that prescribing a fixed injection source creates a coupling between T_{ex} and n_i within the simulation [35]. If T_{ex} increases, the flux of particles to the wall increases and, since the rate of particles' injection is not dependent on the electron temperature (as opposed to a self-consistent ionization case, for example), the source cannot fully compensate for the particle losses to the wall. This leads to a reduction in the number density. Similarly, in case T_{ex} drops, the source overcompensates the particles loss to the wall and, hence, the density increases. Nevertheless, it is emphasized that the extent to which the observed correlation may hold in more realistic scenarios needs to be investigated in a setup with self-consistently resolved ionization process as well as the axial fluxes of the particles (hence, a 3D PIC simulation).

Third, from plot (c), the azimuthal electron temperature (T_{ez}) is observed to monotonically increases with E_y for all the propellants. Also, T_{ez} exhibits a slight increase with B_x up to $15\ mT$ for xenon and krypton, while it remains almost constant for argon. It then notably drops beyond $B_x = 15 - 20\ mT$.

Finally, the combined trends of T_{ex} and T_{ez} are aggregated in the total electron temperature (T_e) in plots (d), where it demonstrates a monotonic increase with E_y. Whereas with B_x, it initially increases and then drops with the peak values occurring for B_x in the range of $15 - 20\ mT$.

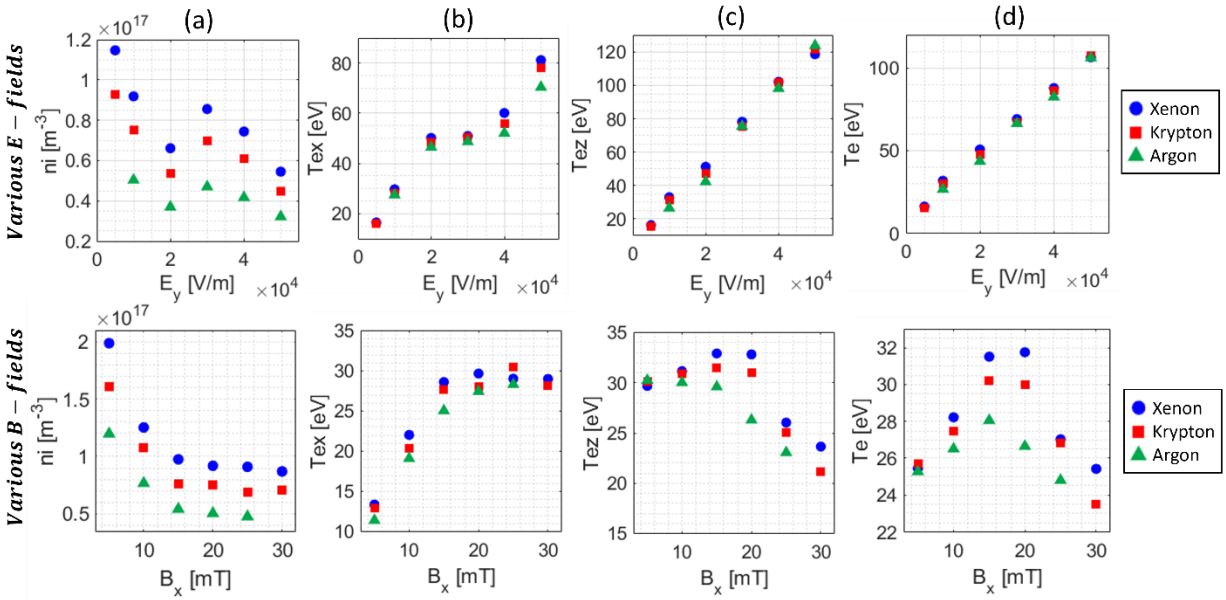


Fig. 4.1: Variation of spatiotemporally averaged (across entire domain and over $20-30\ \mu s$) plasma properties vs E_y (top row) and vs B_x (bottom row) for the three propellants; (a) ion number density (n_i), (b) & (c) radial and azimuthal electron temperature (T_{ex} & T_{ez}), and (d) total electron temperature (T_e).

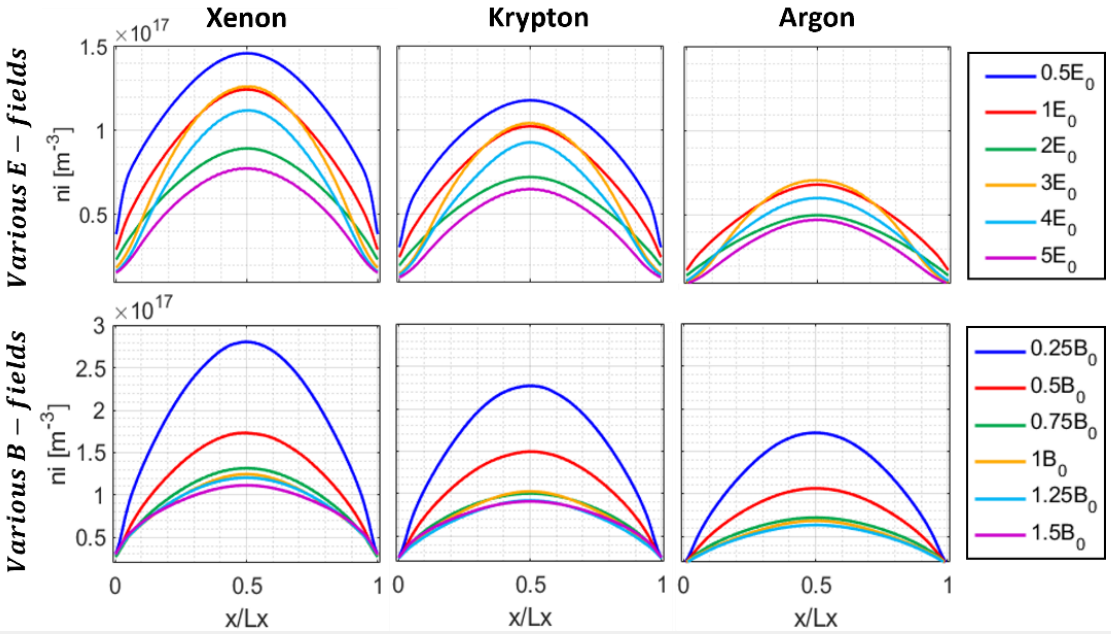


Fig. 4.2: Radial profiles of the ion number density (n_i) averaged over all azimuthal locations and over the time interval of $20-30\ \mu s$ for the three propellants with various E_y (top row) and various B_x (bottom row).

The observed trends in the electrons' temperatures (and hence the variation in the ion number density), are explained by the dominance of different underlying instability modes and variation of their amplitudes with the applied electromagnetic fields' intensity. As observed in the baseline simulation (with $E_y = 10\ kVm^{-1}$ and $B_x = 20\ mT$), the two dominant instabilities in this plasma configuration are the ECDI and the MTSI. Therefore, we can exploit our understanding of the different impacts that the MTSI and the ECDI modes have on plasma, particularly on the electrons' heating and the electrons' cross-field transport, to distinguish the relative dominance between the ECDI and the MTSI across various simulation cases prior to analyzing the FFT spectra of the plasma fluctuations.

Regarding the electron heating effects of the instabilities, it has been demonstrated that the ECDI has a significant role in the azimuthal heating of the electrons through particle-wave interactions along the azimuthal direction [24][26], whereas the MTSI is observed to heat up the electrons mainly in the radial direction parallel to magnetic field [12][28][32]. As a result, the ratio of the radial-to-azimuthal electron temperature (T_{ex}/T_{ez}), which is a measure of anisotropy, can be the first indirect indicator of the relative significance of these two instability modes. The radial profiles of the electron temperature ratio together with variation of its mean value throughout the domain vs E_y and B_x are presented in **Fig. 4.3** and **Fig. 4.4** for the three simulated propellants.

The T_{ex}/T_{ez} data points vs E_y in **Fig. 4.3** (left) are separated into two distinct clusters, which distinguishes two different "operating regimes": regime I, where $T_{ex}/T_{ez} \approx 1$ for E_y between $5-20\ kVm^{-1}$, and, regime II, where $T_{ex}/T_{ez} < 1$ for E_y between $30-50\ Vm^{-1}$. As the T_{ex}/T_{ez} ratio can serve as a measure of the relative strength of the MTSI and the ECDI, regime I should, hence, be characterized by the presence of strong MTSI modes with a radial heating that is almost comparable with or larger than the azimuthal heating caused by the ECDI. Whereas, in regime II, the MTSI should be mitigated leaving the ECDI as the dominant instability mode, thus, leading to a larger T_{ez} than T_{ex}. Furthermore, the temperature ratios are, overall, seen to be the highest for argon and the lowest for xenon in regime I, whereas the opposite is true in regime II. This means that argon exhibits a larger anisotropy in the electron temperature compared to the other two propellants.

Regarding the variation of the T_{ex}/T_{ez} ratio with B_x in **Fig. 4.3** (right), we see that, for the high values of B_x (25 and 30 mT), $T_{ex}/T_{ez} > 1$, suggesting that the MTSI shall be stronger than the ECDI (regime I). For low values of B_x (5 and 10 mT), $T_{ex}/T_{ez} < 1$, which indicates that the ECDI must be the dominant mode under these magnetic field conditions (regime II). At the intermediate magnetic field values (15 and 20 mT), particularly for xenon and krypton, $T_{ex}/T_{ez} \approx 1$. This implies that both the MTSI and the ECDI develop with comparable intensities in these cases. Nevertheless, for the argon simulation case with $B_x = 20\ mT$, the MTSI seems to be slightly stronger than the ECDI as the T_{ex}/T_{ez} ratio is moderately above unity.

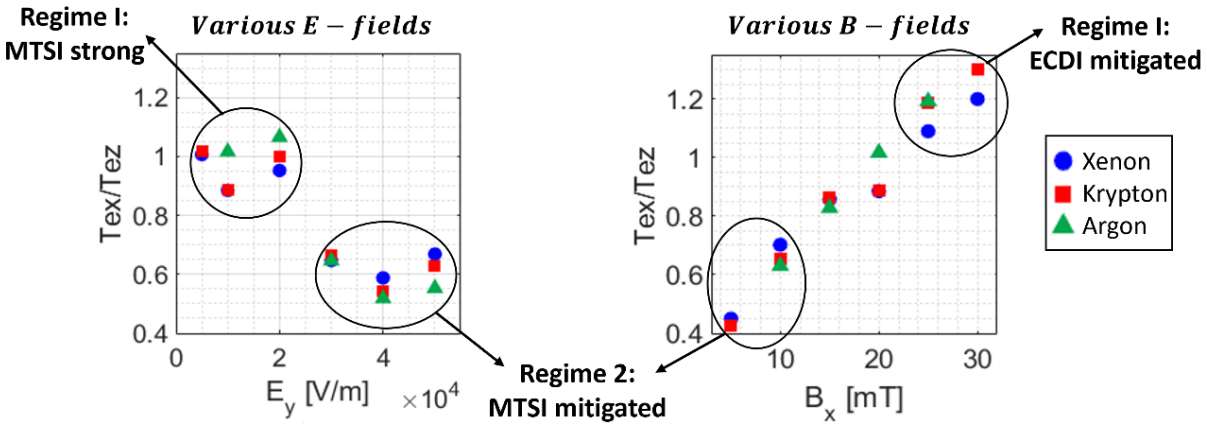


Fig. 4.3: Variation of spatiotemporally averaged (across entire domain and over $20-30\ \mu s$) radial-to-azimuthal electron temperature ratio (T_{ex}/T_{ez}) vs E_y (left) and vs B_x (right) for the three propellants.

As for the radial distribution of T_{ex}/T_{ez} (**Fig. 4.4**), various cases exhibit different profiles. For low values of E_y ($E_y = 0.5E_0, 1E_0$ and $2E_0$) as well as high values of B_x ($B_x = 1.25B_0$ and $1.5B_0$), T_{ex}/T_{ez} is large in the center of the domain and becomes smaller away from the centerline. On the other hand, cases with high E_y values ($E_y = 4E_0$ and $5E_0$), along with those with low B_x intensities ($B_x = 0.25B_0$ and $0.5B_0$) display a more uniform distribution of T_{ex}/T_{ez} across the radial extent of the domain. At $E_y = 3E_0$, T_{ex}/T_{ez} demonstrates greater values near the boundary compared to the central region.

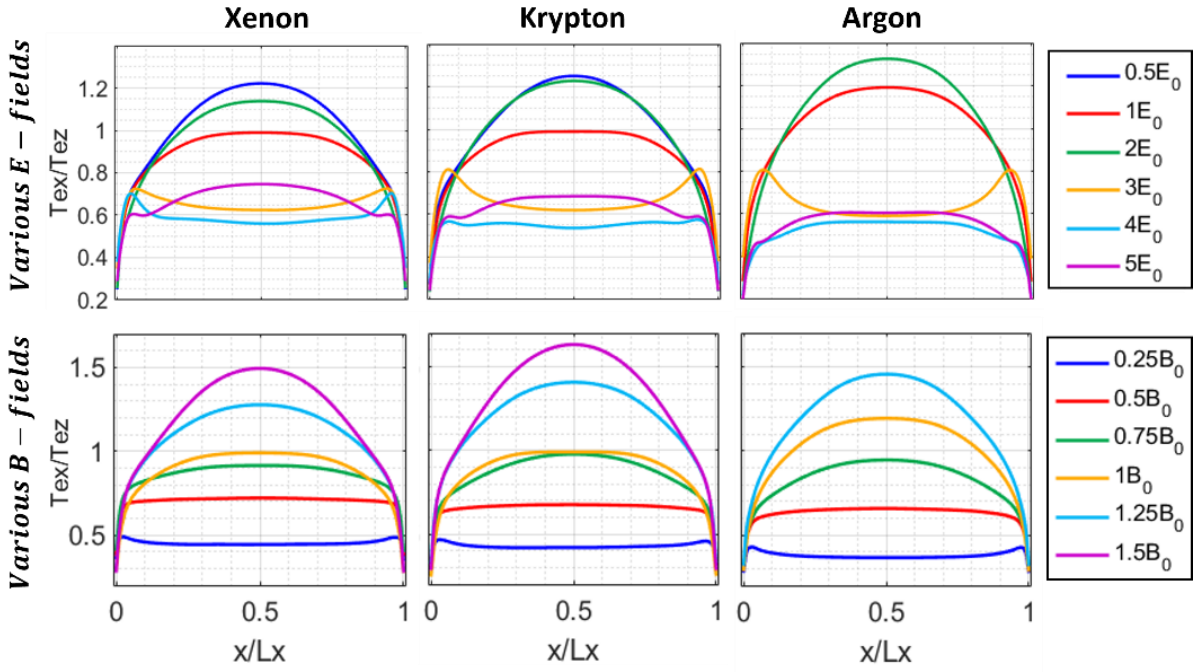


Fig. 4.4: Radial profiles of the radial-to-azimuthal electron temperature ratio (T_{ex}/T_{ez}) averaged over all azimuthal locations and over the time interval of $20 - 30\ \mu s$ for the three propellants with various E_y (top row) and various B_x (bottom row).

Looking at the plots in **Fig. 4.5**, which compares the radial distribution of the normalized axial electron current density ($J_{ey}/J_{ey,mean}$) for different simulation cases, we notice the correlation between the ECDI and the MTSI instabilities and the characteristic shape of the $J_{ey}/J_{ey,mean}$ profile. In fact, the dominance of either of the two instabilities is reflected in the radial distribution of $J_{ey}/J_{ey,mean}$.

In this regard, we observe in **Fig. 4.5** that, for the cases where the MTSI is the dominant mode, including cases with $E_y = 0.5E_0$, $2E_0$ and $B_x = 1.25B_0$, $1.5B_0$, J_{ey} exhibits peaks away from the center. In fact, the existence of two peaks on both sides of the centerline defines the characteristic profile of the electron transport induced by the MTSI. However, it is highlighted that a slightly different shape observed in the high-B_x simulations is attributed to the contribution of the viscosity (F_Π) to the transport, rather than the instabilities themselves. Indeed, as will be shown in Section 4.2.3 (**Fig. 4.12**), the isolated contributions of the instabilities exhibit the same characteristic shape of the MTSI-induced transport at high-B_x cases, while the additional set of peaks adjacent to the walls arise from the viscosity-induced transport.

In contrast, for the cases with larger axial electric field, $E_y = 3E_0, 4E_0, 5E_0$ and $B_x = 0.25B_0$, $0.5B_0$, in which the ECDI is dominant, J_{ey} is mostly concentrated toward the center with a peak occurring at

the centerline. Such a profile characterizes the electron transport driven by the ECDI. It is also noticed that in the $E_y = 4E_0$ and $5E_0$ cases, J_{ey} reverses its direction close to the walls.

Near the baseline condition of $E_y = 1E_0$ ($B_x = 1B_0$) and $B_x = 0.75B_0$, for xenon and krypton, the ECDI and the MTSI are of comparable amplitudes and their combined contributions to the electron transport has led to a rather uniform distribution of J_{ey} across the domain's radial extent. The same conditions for argon, nonetheless, results in the MTSI to develop with a rather larger amplitude relative to the ECDI (see also **Fig. 4.3**). This causes J_{ey} to be less uniform, having peaks toward the walls.

As a result, the overall distribution of the electrons' axial current density (J_{ey}) is strongly influenced by the instabilities established within plasma, thereby serving as the second indicator of the relative dominance of the ECDI and the MTSI.

The observations made in this section regarding the presence of the ECDI and the MTSI and their relative strength in the presence of various applied electromagnetic fields will be verified in the next section through a detailed examination of the instabilities' spectra.

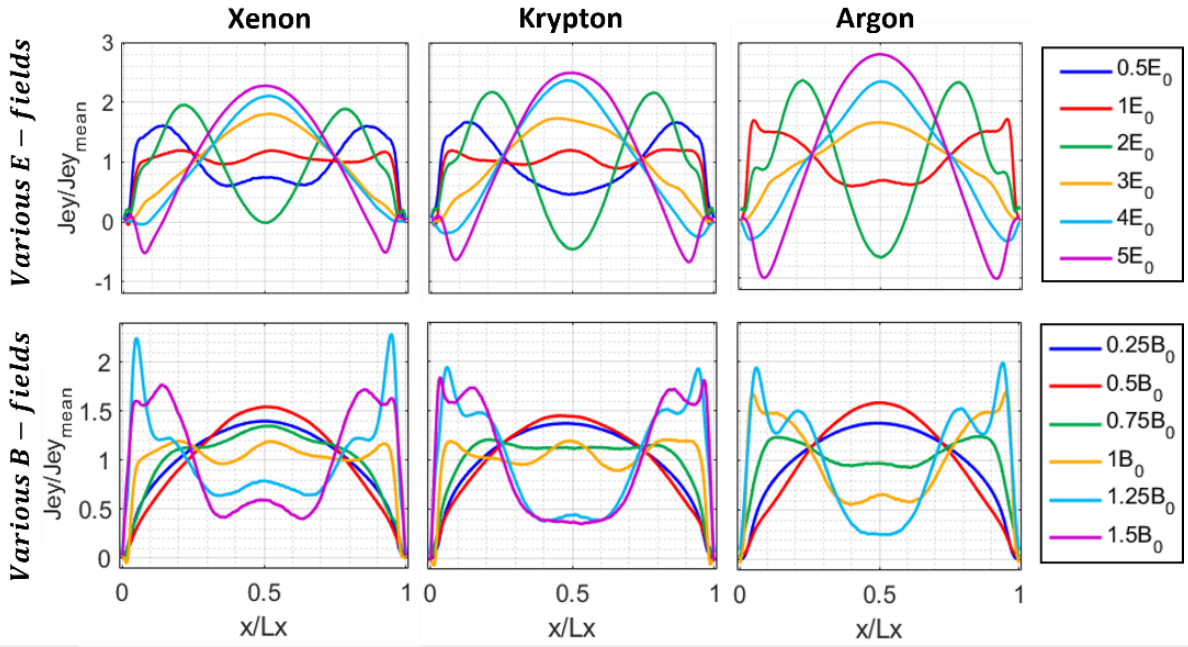


Fig. 4.5: Radial profiles of the normalized axial electron current density ($J_{ey}/J_{ey,mean}$) averaged over all azimuthal locations and over the time interval of $20 - 30\ \mu s$ for the three propellants with various E_y (top row) and various B_x (bottom row).

Before presenting a quantitative assessment of the resolved ECDI and MTSI modes, looking at the snapshots of the plasma properties provides a qualitative comparison of the dominant instabilities and the variations in their characteristics. In this regard, **Fig. 4.6** presents a sample of 2D snapshots of various plasma properties for xenon at an instant of time when the spatial averaged (over the entire domain) of T_{ex} is at its local maximum. This corresponds to the moments along the discharge evolution when the MTSI, if present in the simulation with a comparatively high amplitude, is fully developed.

On the left panel, the MTSI patterns (which are characterized by both azimuthal and radial wavevector components) are easily recognizable in the snapshots of the cases with $E_y = 0.5E_0, 1E_0,$

and $2E_0$. The $0.5E_0$ case also shows the formation of long wavelength azimuthal wave. In the remaining cases, the MTSI pattern gets distorted in the J_{ey} snapshots. However, the fluctuations still show a finite wavenumber in the radial direction except for the $5E_0$ case, in which the fluctuations become mostly azimuthal. The azimuthal wavelength of the waves becomes larger with increasing E_y, which we will demonstrate, later in this section, to be consistent with the relevant theory.

On the right panel, for the $0.5B_0$ case, MTSI-like patterns are not observed, and only azimuthal waves are visible. The simulation cases with $B_x = 0.75B_0$ and $1B_0$ feature both the ECDI-representative waves with short azimuthal wavelengths and the radial-azimuthal MTSI-like structures of longer azimuthal wavelengths. The ECDI waves become less distinct in the $1.25B_0$ case and are not observed in the $1.5B_0$ case. Furthermore, at the high magnetic field intensities ($1.25B_0$ and $1.5B_0$), a wave structure with a long azimuthal wavelength is developed as well.

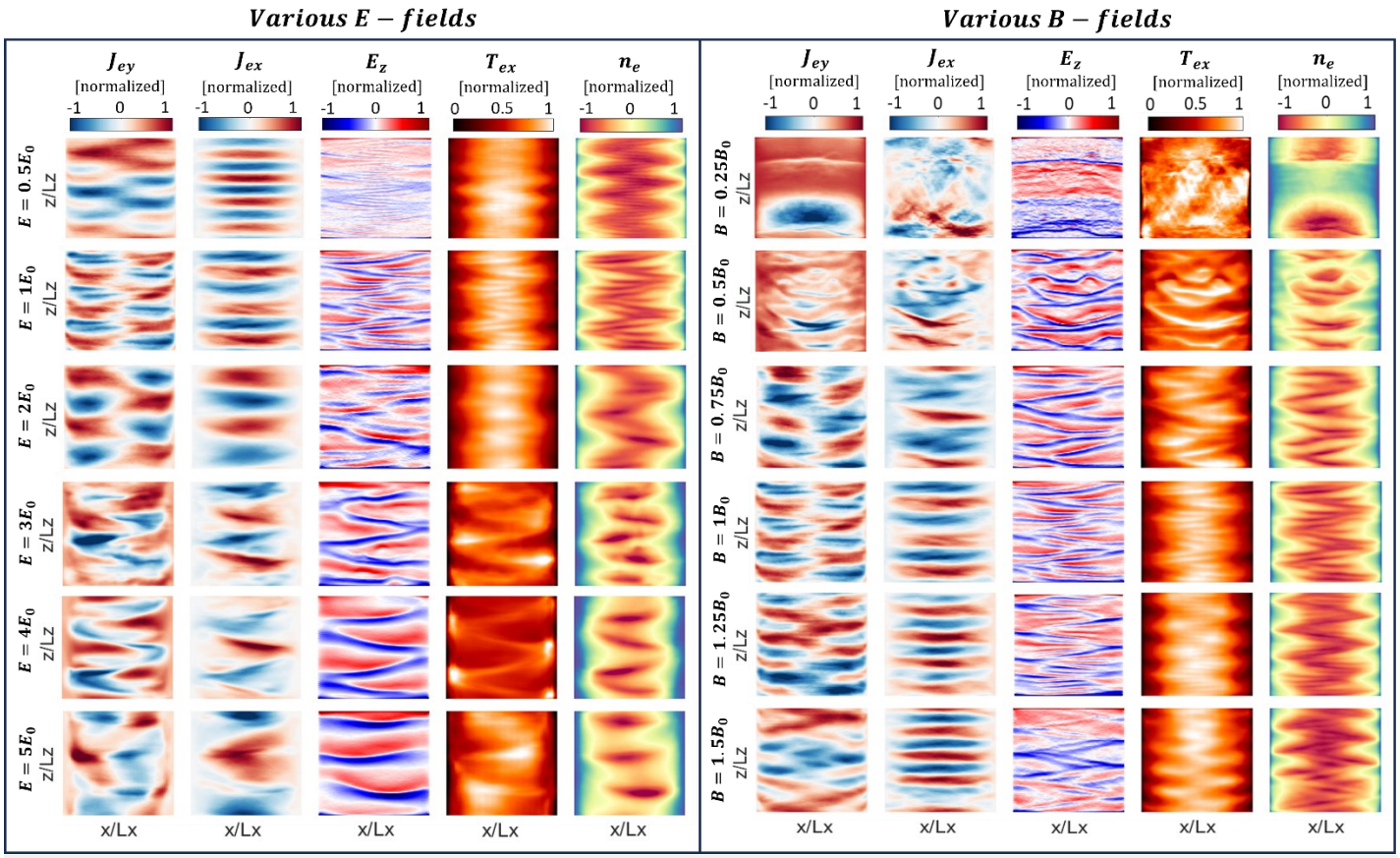


Fig. 4.6: 2D snapshots of the normalized plasma properties at a time of local maximum of the spatially averaged T_{ex} for xenon propellant with various E_y (left) and various B_x (right). The columns, from left to right, represent the axial and radial electron current densities (J_{ey} and J_{ex}), the azimuthal electric field (E_z), the radial electron temperature (T_{ex}), and electron number density (n_e).

4.2.2. Variations in the characteristics of the azimuthal instabilities

To assess the wavenumber and the frequency of the wave modes, we start by presenting the spatiotemporally averaged spatial FFTs of the azimuthal electric field (E_z) in **Fig. 4.7**. In these plots, the horizontal axis is normalized by the fundamental resonance wavenumber of the ECDI (given by Eq. 1.3) in each respective case.

We first focus on the variation of the k_z spectrum of the instabilities with E_y (top panel in **Fig. 4.7**). We observe that the cases with lower E-fields ($0.5E_0$, $1E_0$, and $2E_0$) contain distinct peaks at $k_z/k_0 \approx 0.1 - 0.3$ that coincide with the theoretical azimuthal wavenumber of the MTSI as estimated from Eq. 1.11. The MTSI's theoretical k_z is obtained by substituting the value of the radial wavenumber (k_x) of the MTSI mode in Eq. 1.11. The MTSI's k_x value from our simulations is about $245.5\ m^{-1}$, because the captured MTSI waves have a radial wavelength twice the radial size of the domain. The theoretical range of the MTSI's k_z is highlighted in the plots of **Fig. 4.7** by grey-shaded areas. In the $0.5E_0$ case, a long-wavelength mode has additionally appeared with a wavelength almost the same as the domain's azimuthal extent. We refer to this mode as the long-λ mode. The exact origin of this instability is not yet fully understood; however, it is conjectured to be the result of an inverse energy cascade of shorter wavelength instabilities, which happens in certain conditions. This can be observed from dispersion plots and the time evolutions of the k_z spectra of the instabilities which are provided in Appendix A.5.3 and Appendix A.5.4, respectively. In most cases where the long-λ instability appears, these plots exhibit a spectral cascade of energy from shorter wavelength instabilities (primarily the MTSI's harmonics) towards this long wavelength mode.

All FFT spectra additionally show the presence of the first harmonic of the ECDI ($k_z/k_0 \approx 1$) except for the $0.5E_0$ case with krypton. For the $0.5E_0$ case with krypton, the ECDI, even if might have been present in the simulations, has such a small amplitude that it is not evident in the average FFT plot. In most cases, the second harmonic of the ECDI ($k_z/k_0 \approx 2$) is also visible. The FFT spectrum of $5E_0$ case has a peak at the third ECDI harmonic as well for all the propellants (not specified in the figure).

Now, we look at the variation of the instabilities' k_z spectrum with B_x (bottom panel in **Fig. 4.7**). For the low B_x values ($0.25B_0$ and $0.5B_0$ cases) and for all the propellants, only the ECDI mode is dominantly visible at $k_z/k_0 \approx 1$. For the cases with the B-field intensity between $0.75B_0$ and $1B_0$, the theoretical estimation of the MTSI's azimuthal wavenumber is around $k_z/k_0 \approx 0.1 - 0.25$.

From $B_x = 0.75B_0$ case towards higher B-fields, the FFT spectra for all the propellants start to show peaks near the normalized theoretical azimuthal wavenumber of the MTSI at $k_z/k_0 \approx 0.25$. For the $0.75B_0$ case, the ECDI mode's magnitude is comparatively lower in krypton than in xenon, and it reaches its lowest value for argon. At $B_x = 1B_0$, the FFTs for all the propellants include both the ECDI and the MTSI peaks. For the case of argon, the intensity of the ECDI is nearly equal to that of the MTSI in contrast to the cases with xenon and krypton for which the ECDI is stronger than the MTSI.

In the high B-field range ($1.25B_0$ and $1.5B_0$), the MTSI is clearly present with high amplitude. The long-λ mode with a strength comparable to the MTSI's, is also visible in the spectra of these cases. At the highest B-field condition ($B_x = 1.5B_0$ for xenon and krypton, and $B_x = 1.25B_0$ for argon), the ECDI is not visible in the spatial FFT spectra.

The main observations from the instabilities' k_z spectra are summarized below:

- At low electric fields ($E \leq 2E_0$), both the MTSI and the ECDI exist at comparable amplitudes.
- At high electric fields ($E \geq 3E_0$), the MTSI is mitigated, and the ECDI dominates.
- At low magnetic fields ($B \leq 0.5B_0$), the MTSI is absent, and the ECDI is the dominant mode.

- At high magnetic fields ($B \geq 1.25B_0$), the MTSI and the long-λ mode are the dominant instabilities, and the ECDI is suppressed.
- At moderate magnetic fields ($0.75B_0 \leq B \leq 1B_0$), both ECDI and MTSI are present with comparable strengths.

These findings are consistent with the arguments made in Section 4.2.1 regarding the relative importance of the ECDI and the MTSI modes based on the temperature anisotropy (T_{ex}/T_{ez} ratio) in the system and the radial profile of the axial current density (J_{ey}).

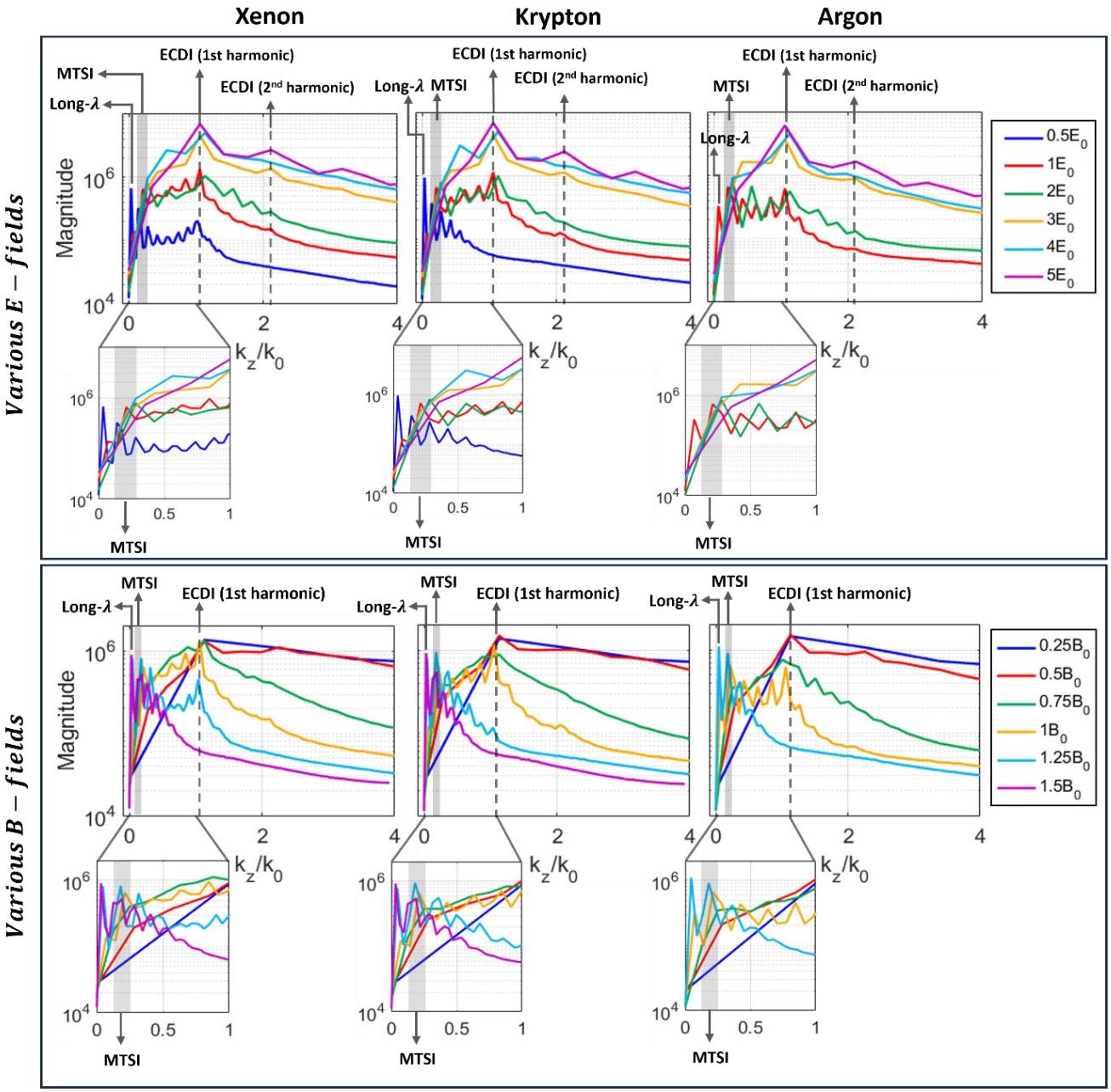


Fig. 4.7: Azimuthal wavenumber spectra of instabilities obtained from average spatial FFTs (over all radial positions and over the time interval of $20 - 30\ \mu s$) of the azimuthal electric field signal from simulations with various E_y (top panel) and various B_x (bottom panel) for the three propellants. k_0 represents the ECDI's fundamental wavenumber ($k_0 = \frac{\omega_{ce}}{V_{d_e}}$).

To determine the frequency spectra of the instabilities, we look at the spatially averaged temporal FFT plots of the E_z signal as is shown in **Fig. 4.8**. Complementary spectral analyses using the Dynamic Mode Decomposition (DMD) method [117][118][134] can assist with distinguishing the individual instability modes present in the system and to derive unambiguously their spatial structure together with their frequencies [135][136].

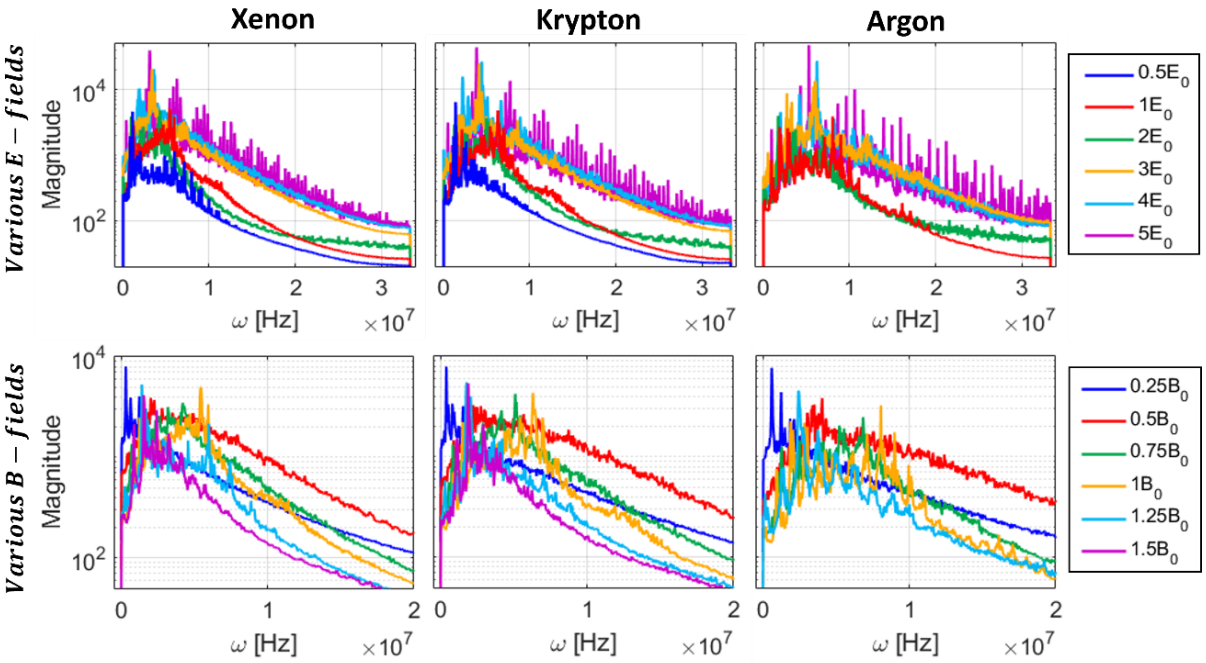


Fig. 4.8: Frequency spectra of instabilities obtained from average temporal FFTs (over all radial and azimuthal positions) of the azimuthal electric field signal from simulations with various E_y (top row) and various B_x (bottom row) for the three propellants.

The combined insights from the FFT spectral analysis are summarized in **Fig. 4.9**, where we plotted the numerically observed characteristics of the resolved ECDI and MTSI modes against the E_y and B_x values. Additionally, the theoretical estimations of the ECDI's and the MTSI's characteristics obtained from the corresponding theories (reviewed in Section 1.1.3.1 and 1.1.3.3, respectively) are superimposed on these plots. The characteristics of interest are the nondimensional azimuthal wavenumber ($\tilde{k}_z = k_z \lambda_D$), the nondimensional frequency ($\tilde{\omega} = \omega/\omega_{pi}$), and the nondimensional azimuthal phase velocity ($\tilde{V}_{ph} = V_{ph}/c_s$, where V_{ph} is the waves' phase velocity and c_s is the ion sound speed). It is also pointed out that, for the simulation cases in which the MTSI or the ECDI mode was not distinctly detected from the FFT analyses (the modes were strongly mitigated), the plots in **Fig. 4.9** only present the theoretical data points.

With regard to the theoretical comparisons, the $\tilde{k}_z$ values for the ECDI from the simulations are seen to be largely consistent with the theory across the simulated E_y and B_x ranges.

It is of interest to also investigate whether the ECDI modes share characteristics with the ion acoustic instability (IAI) modes, the transition to which are reported following the nonlinear growth and the pseudo-saturation of the instability [10][18]. In this regard, the characteristics of the fastest growing mode of the IAI from Eq. 1.7 are additionally superimposed on the ECDI's plot as horizontal black lines.

However, there is not sufficient agreement between the simulated characteristics of the ECDI and the theoretical characteristics of the IAI's fastest growing mode to provide evidence for the transition of the ECDI's waves to the IAI.

To evaluate this more closely, we have also provided in Appendix A.5.3, the comparison between the 2D dispersion maps of the azimuthal fluctuations with the IAI's theoretical dispersion relation (Eq. 1.4) for various E_y and B_x conditions with the xenon. Even though the dispersion map analyses are not entirely conclusive, some cases especially the baseline and those with $E_y = 30, 40\ km^{-1}$ and $B_x = 15\ mT$, exhibit a certain extent of resonance broadening around the dominant mode, which is a characteristic feature of the transition of the ECDI modes to the IAI [18].

Regarding the comparison of the MTSI's characteristics with theory, the theoretical and the simulated $\tilde{k}_z$ values show only minor discrepancies for the low E_y intensities where the MTSI appeared. For various B_x, the MTSI's simulated $\tilde{k}_z$ values show a good agreement with theory up to the $B_x = 15\ mT$. At the higher B_x values, the simulated wavenumbers show some deviation from the theory with a major discrepancy at $B_x = 30\ mT$.

Concerning the large discrepancy at $B_x = 30\ mT$, it is pointed out that we have taken the highest peak within the MTSI wavenumber range ($k_z/k_0 = 0.188$), as was highlighted in plots of the spatial FFT in **Fig. 4.7**, to represent the azimuthal wavenumber of the MTSI from the simulations. However, there also exists another nearby peak at $k_z/k_0 = 0.125$ with a slightly lower amplitude. This second, lower-amplitude peak coincides with the theoretical wavenumber of the MTSI from Eq. 1.11 for the $30\ mT$ case. Because it cannot be determined with full certainty which one of the two peaks corresponds to the MTSI in the simulation, we have added an error bar in the MTSI's $\tilde{k}_z$ plot (bottom panel in **Fig. 4.9**) for the $30\ mT$ case. The error bar covers the wavenumber interval between the two identified peaks.

To ensure that this special double-peak feature in the FFT spectrum is not due to the Q2D approximation, we verified the Q2D simulation of the $30\ mT$ case with the xenon propellant against a full-2D simulation of the same case in terms of the spatial and temporal FFT spectra of the instabilities. The results are provided in Appendix A.5.1. The 2D simulation also shows a broadening of the k_z/k_0 spectrum near the MTSI's azimuthal wavenumber (within $k_z/k_0 = 0.125 - 0.188$).

The theoretical MTSI's frequencies are obtained by solving the dispersion relation given by Eq. 1.9. To solve this equation, we substituted once the theoretical k_z from Eq. 1.11 and once the k_z as obtained from our simulations (in the E_y range where MTSI modes were observed in the spatial FFTs). The two resulting sets of theoretical frequencies are compared against the simulated $\tilde{\omega}$ values in **Fig. 4.9**.

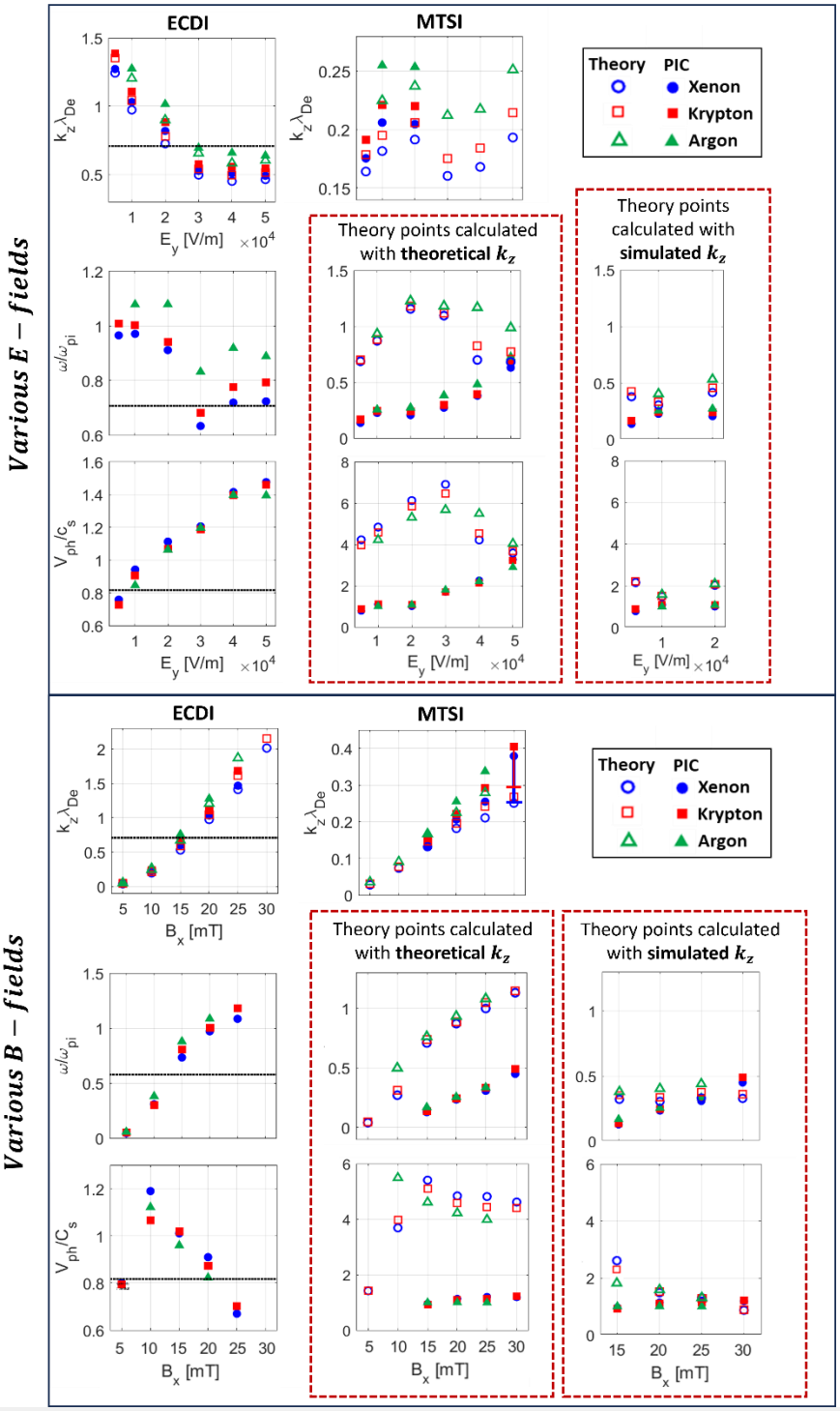


Fig. 4.9: Variation of the normalized characteristics of the dominant ECDI and the MTSI modes vs E_y (top panel) and vs B_x (bottom panel) for the three propellants. In each panel, (**top row**) normalized azimuthal wavenumber ($\tilde{k}_z = k_z\lambda_{De}$) compared against the theoretical wavenumber of the ECDI's first harmonic and the MTSI's fastest growing mode from Eq. 1.3 and Eq. 1.11, respectively; (**middle row**) normalized real frequency ($\tilde{\omega} = \omega/\omega_{pi}$); (**bottom row**) normalized azimuthal phase velocity ($\tilde{V}_{ph} = V_{ph}/c_s$). Superimposed on the ECDI plots, the horizontal black lines indicate the characteristics of the IAI's fastest growing mode of the from Eq. 1.7. The hollow markers on the MTSI frequency plot correspond to the solution to the instability's dispersion relation (Eq. 1.9); the theoretical data points on the middle-column frequency plot are from solving Eq. 1.9 with the k_z from Eq. 1.11, whereas the theoretical points on the right-column frequency plot are from solving Eq. 1.9 using the simulated k_z. The same is true for the phase velocity (bottom row, middle and right-most columns).

Focusing on the E_y range of $5-20\ kVm^{-1}$ and B_x range of $15-30\ mT$, for which both the simulated and the theoretical k_z values are available, we notice that the minor discrepancies observed between the normalized k_z values from the theory (Eq. 1.11) and the simulations in **Fig. 4.9** (top row in each panel, middle column) translate in a major variation in the theoretical values of the MTSI frequency from the dispersion relation in Eq. 1.9. This strong sensitivity of the frequency to the k_z value is expected, because Eq. 1.11 describes the wavenumber at the resonance condition for the MTSI where the $\omega - k_z$ dispersion relation has a very steep slope. Hence, a small variation in k_z can drastically change the theoretically predicted frequency and, in turn, the theoretical phase velocity. Accordingly, we observe that if we instead use the MTSI's simulated wavenumber to solve the dispersion relation in Eq. 1.9 to obtain the theoretical frequency and subsequently the theoretical phase velocity, the theoretical values become quite comparable with simulations' predictions of these two characteristics as seen in **Fig. 4.9** (second and third rows in each panel, right column).

Comparing the variation trends of the ECDI's and the MTSI's frequency with the E-field intensity from **Fig. 4.9**, it is seen that overall, the ECDI's frequency decreases with E_y whereas the MTSI exhibits the opposite trend. As a result, the frequencies of the ECDI and the MTSI are getting closer to each other as the electric field increases, which can facilitate the interactions of the two instabilities and the energy transfer between their associated waves. The enhanced interactions between the ECDI and the MTSI is a possible explanation for the mitigation of the MTSI under the elevated electric field conditions (i.e., for $E_y \geq 30\ kVm^{-1}$), and the growth of the ECDI as the single dominating mode at the high electric field values.

Furthermore, to explain why the MTSI is mitigated in the cases with low B-field intensities (i.e., for $B_x \leq 10\ mT$), we have plotted in **Fig. 4.10** the variation of the normalized MTSI's growth rate ($\tilde{\gamma} = \gamma/\omega_{pi}$) against the normalized azimuthal wavenumber ($\tilde{k}_z = k_z\lambda_D$) and B_x. The growth rate is obtained by solving the MTSI's dispersion relation (Eq. 1.9) at two fixed values of the normalized radial wavenumber ($\tilde{k}_x = k_x\lambda_D$) of 0.02 and 0.035. These specific $\tilde{k}_x$ values are selected because they indicate the two bounds of $\tilde{k}_x$ for the MTSI modes that were developed in the simulations across the various magnetic field intensities. The MTSI's theoretical $\tilde{k}_z$ is varied from about 0.02 to 0.25 as the B_x increases from $5\ mT$ to $30\ mT$. From the plots in **Fig. 4.10**, we observe that in the low magnetic field range, the growth rate of the MTSI's fastest growing mode is small, but it increases significantly as the magnetic field becomes stronger. This is consistent with our numerical observations that stronger MTSI modes occur at higher magnetic field magnitudes.

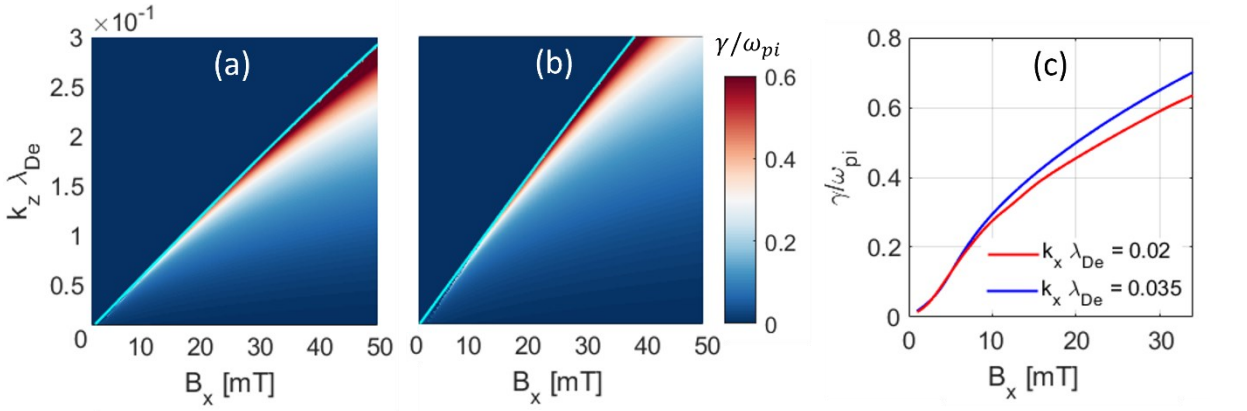


Fig. 4.10: Variation of the normalized MTSI's growth rate ($\tilde{\gamma} = \gamma/\omega_{pi}$) vs the normalized azimuthal wavenumber ($\tilde{k}_z = k_z\lambda_D$) and the B_x obtained from the solution of the MTSI's dispersion relation in Eq. 1.9 for the xenon propellant. To solve the dispersion relation, we have used $n_i = 1.5 \times 10^{17} m^{-3}$, $T_e = 30\ eV$, and $E_y = 10\ kVm^{-1}$. The dispersion relation is solved for two constant normalized radial wavenumber values ($\tilde{k}_x = k_x\lambda_D$) of (a) $\tilde{k}\_x = 0.02$, and (b) $\tilde{k}_x = 0.035$. The cyan curves in plots (a) and (b) indicate the azimuthal wavenumber of the MTSI's fastest growing mode as is determined from Eq. 1.11. Plot (c) shows the variation of $\tilde{\gamma}$ vs B_x for the MTSI's fastest growing mode with the two selected values of $\tilde{k}_x$.

Before proceeding with the rest of the discussion, we highlight that in order to gain confidence in the insights provided from these Q2D simulations, we verified the Q2D predictions of the instability's spectra for the cases with extreme fields, i.e., $E_y = 5E_0$ and $B_x = 1.5\ B_0$, with xenon propellant, against the full-2D simulations. The results of these verifications are presented in Appendix A.5.1.

In the Q2D simulation for $1.5\ B_0$ case we observed that the ECDI was absent in the k_z spectrum of the instabilities (**Fig. 4.7**). However, the k_z spectrum from the full-2D simulation exhibits a very small peak near the ECDI's first harmonic. Accordingly, we conclude that the ECDI is not entirely absent in the $1.5B_0$ condition. Rather, the ECDI mode is strongly suppressed to a very low amplitude. At such a low amplitude, the ECDI is likely falling close to the noise level of the Q2D simulations, which makes it undetectable from the spatial FFT of the Q2D results.

For the $E = 5E_0$ case, the full-2D and Q2D results are very similar. The full-2D results confirm that the occurrence of the multiple peaks in the temporal FFT (**Fig. 4.8**) in this case is not due to any numerical issues potentially caused by the Q2D simulation; rather, the multiple peaks are indeed present in the 2D simulation as well.

Furthermore, the outcomes of an analysis of the sensitivity of the instabilities' spectra to the radial and azimuthal lengths of the domain are presented in Appendix A.5.2 for the case of $E_y = 5E_0$ case. The results confirm that the mitigation of the MTSI in the high E-field cases, particularly at the extreme of E-field of $5E_0$, was not due to limited extent of the domain. This study additionally demonstrates that enlarging the domain size along the radial direction or along both the radial and azimuthal directions leads to the development of the long-λ wave mode.

As a concluding remark concerning the instabilities, we turn our attention to the saturation of the azimuthal instabilities. In this regard, the interaction of the ion particles with the azimuthal waves and

their tapping in the wave's potential wells – a phenomenon known as ion-wave trapping – is proposed as a saturation mechanism for the azimuthal instabilities including the ECDI [29]. This ion-wave trapping phenomenon is evident from the azimuthal ions' phase-space ($z - v_z$) plots, which are presented as a sample for xenon in **Fig. 4.11**. The characteristic "loops" in these plots indicate the ions being trapped in the waves' potential. The size of the loops along the azimuthal direction (z) is indicative of the wavelength of the azimuthal instabilities, and along the azimuthal velocity direction (v_z) is correlated with the combined effect of the amplitude and the phase velocity of the instability's waves.

The interactions of the ion particles with the azimuthal waves result in progressively increasing broadening of the ion velocity distribution functions (IVDF) in the azimuthal direction with increasing E-field. Moreover, the ions phase-space plot shows a turbulent distortion of ion flow in the phase-space for the $0.25B_0$ case. The significance of the ion-wave trapping diminishes with the increasing B_x values which result in the reduced azimuthal broadening of the IVDF at high B-fields intensities.

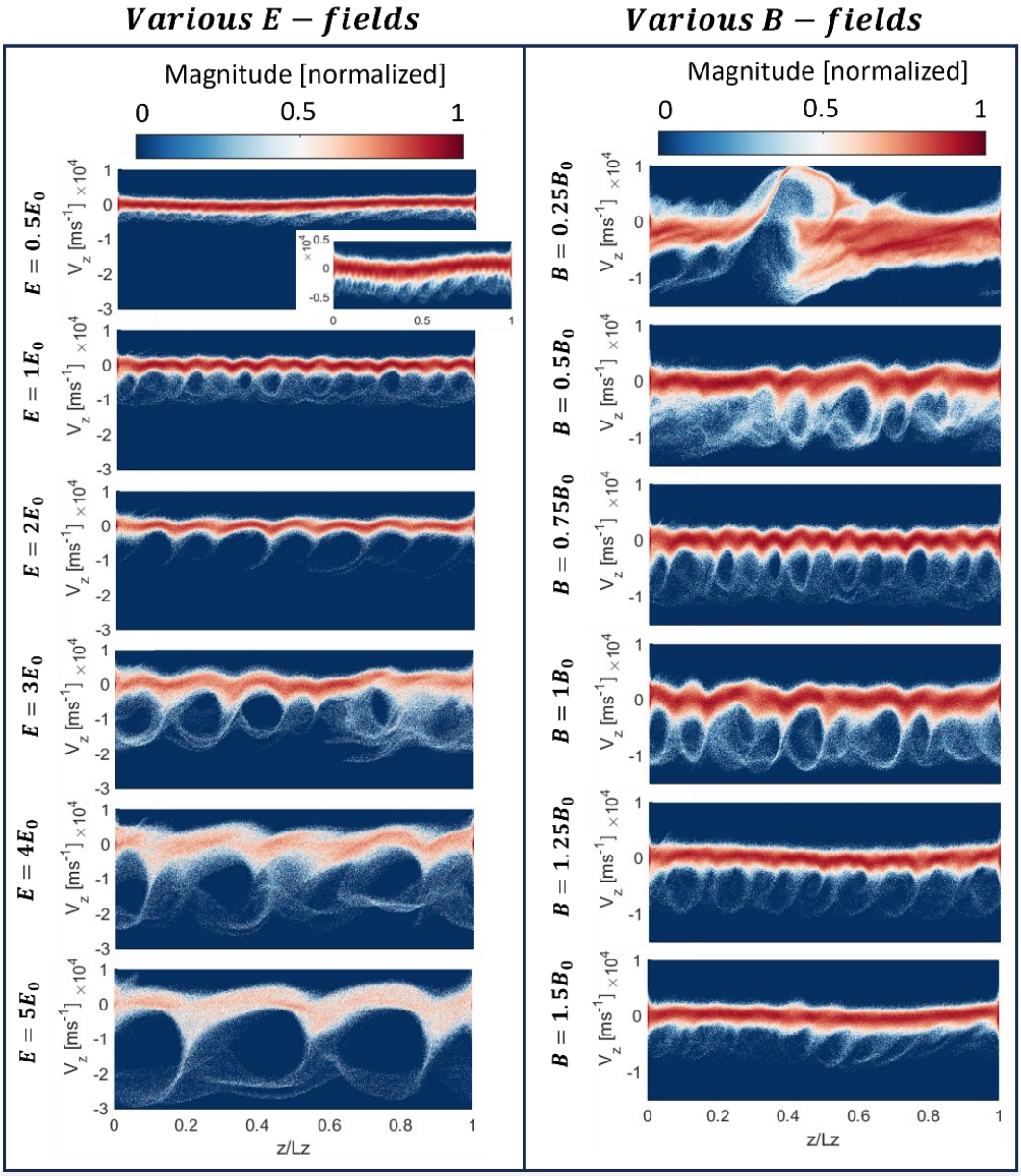


Fig. 4.11: Ions' azimuthal phase-space ($z - v_z$) plots for xenon with various E_y (left column) and various B_x (right column).

4.2.3. Variation in the electrons' cross-field transport

In this section, we examine the contribution of various terms in the electrons' azimuthal momentum equation (Eq. 1.20) to the electrons' cross-field transport in the presence of different E_y and B_x. Eq. 1.20 is rewritten below with the notations adapted according to the coordinate system convention in the radial-azimuthal case

$$-en_e v_{e,y} B_x = \frac{\partial}{\partial t}\left(m_e n_e v_{e,z}\right) + \frac{\partial}{\partial x}\left(m_e n_e v_{e,x} v_{e,z}\right) + \frac{\partial}{\partial x}\left(\Pi_{e,xz}\right) - en_e E_z \,. \qquad \text{Eq. 4.1}$$

This analysis is performed as an example for the xenon propellant. The resulting time-averaged radial profiles of different force terms in Eq. 4.1, along with their average values over the radial extent of the domain are shown, respectively, in **Fig. 4.12** and **Fig. 4.13**.

From these figures, it is evident that the F_E term, which represents the contribution of the azimuthal instabilities, distinctly plays the dominant role among other terms in all simulation cases. Therefore, the F_E profile determines the overall distribution of the cross-field transport across the domain indicated by the F_B term. The radial distribution of the F_E (and F_B) term in each case resembles the respective profile of the J_{ey} in **Fig. 4.5** for xenon. In fact, across all field intensities, the average value of the F_E term is $1-2$ orders of magnitude larger than the value of the second important term, i.e., F_Π which indicates the viscous effects (off-diagonal entry of the pressure tensor).

At lower E-field ($E_y \leq 2E_0$), the F_Π term exhibits an oscillatory profile around zero along radial direction, resulting in a mean value that is close to zero. At higher E-fields ($E_y \geq 3E_0$), the F_Π term remains positive over a more extended portion of the domain around the center and becomes negative near the walls, leading to larger mean values. Among various B_x cases, the relative role of F_Π is most significant at high B-field intensities ($B_x \geq 1.25B_0$). In this respect, although the mean value of the F_Π term is still small compared to the F_E (**Fig. 4.13**), the local value of this term near the walls has a noticeable effect on the total momentum distribution (F_B term) near the walls for $1.5B_0$ case, and across the domain for $1.25B_0$ condition. In addition, these results show that the convective inertia term (F_I) has a negligible role in cross-field transport across all E_y and B_x conditions.

As one last point concerning the plots in **Fig. 4.12** and **Fig. 4.13**, the discrepancy noticed between the left-hand side of Eq. 4.1 (F_B term) and the sum of the force terms on the right-hand side of this equation (RHS) is attributed to the momentum loss induced in the system by the application of the artificial boundary condition on the particles' motion along the axial direction. In this regard, as explained in Section 3.1.1, particles crossing the artificial boundaries of the domain along the axial direction are reloaded on the simulation plane with new velocities sampled from their initial distribution functions. This resampling of the particles amounts to a momentum loss (not accounted for in Eq. 4.1), which manifests as the discrepancy between the F_B and the RHS terms.

The imbalance between F_B and the RHS terms is particularly pronounced for the cases exhibiting relatively large axial electron fluxes, namely those with $E_y \geq 3E_0$ and $B_x < 1B_0$, due to the higher particle resampling rates in these cases.

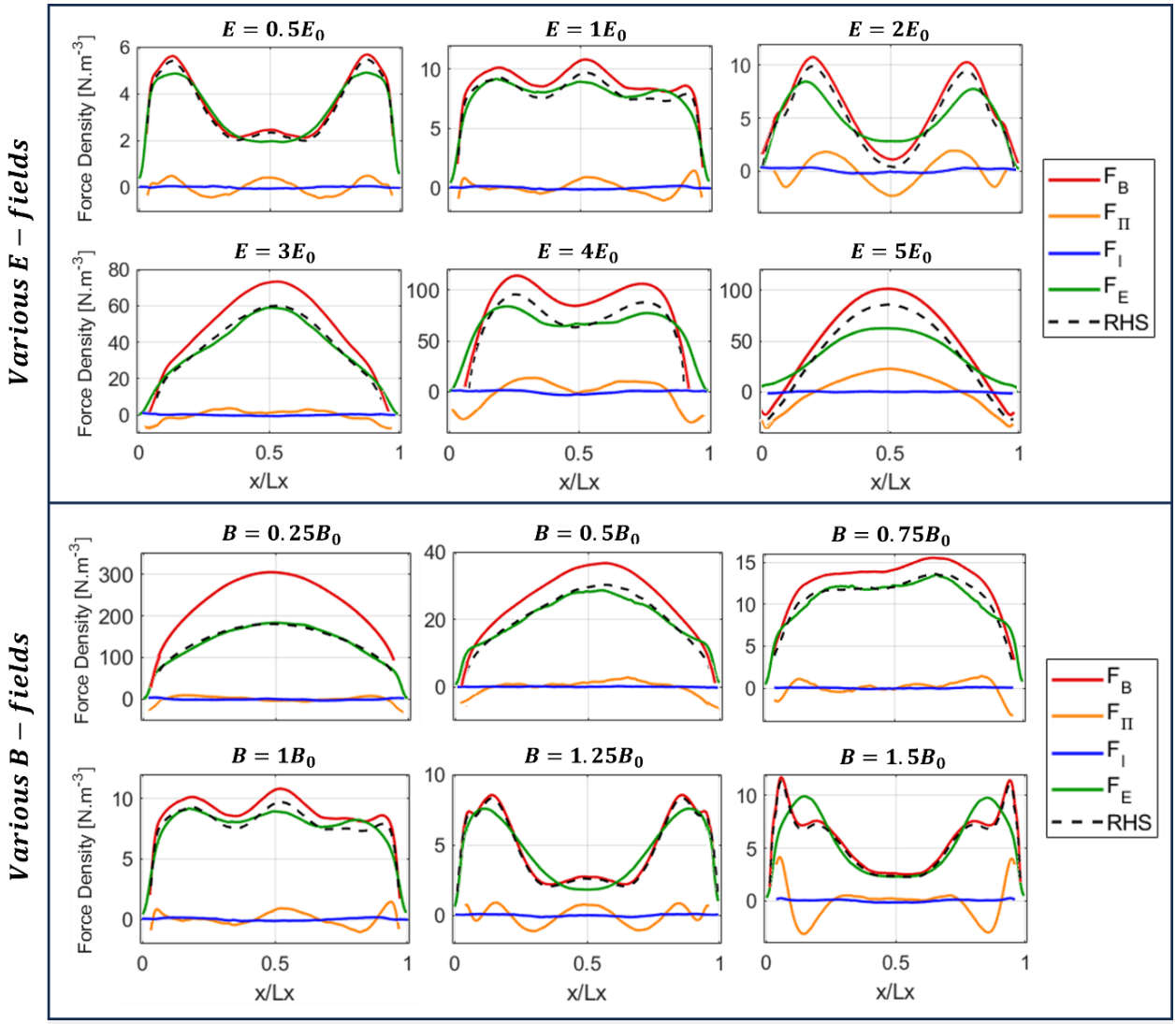


Fig. 4.12: Radial profiles of the transport terms in Eq. 4.1 for xenon propellant with various E_y (top panel) and various B_x (bottom panel). The force terms are averaged over $20-30\ \mu s$. F_B is the magnetic force, F_Π is the viscous effects, F_I is the convective inertia force, F_E is the electric force term, and RHS represents the sum of F_Π, F_I and F_E . F_t (temporal inertia) contribution was almost zero, and it is thus not displayed.

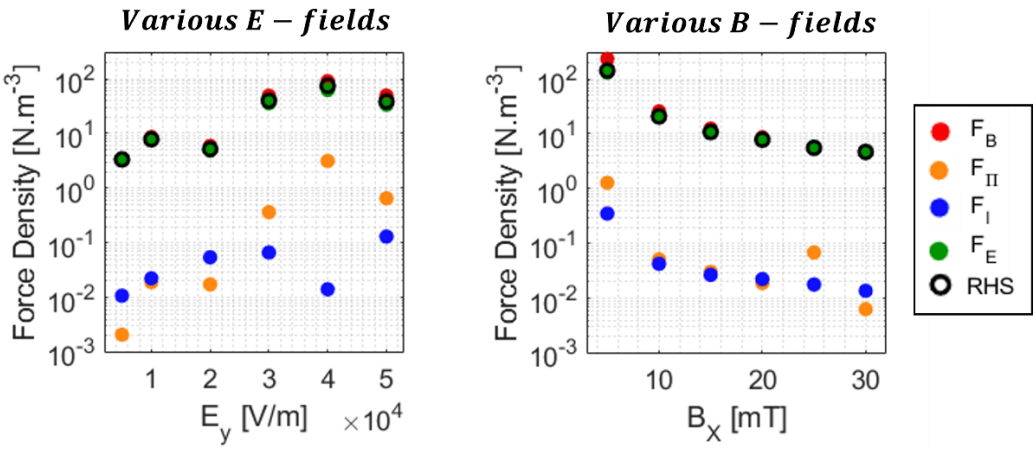


Fig. 4.13: Variation of spatiotemporally averaged (across entire domain and over $20-30\ \mu s$) force terms in the electrons' azimuthal momentum equation (Eq. 4.1) vs E_y (left) and various B_x (right) for xenon propellant.

4.2.4. Variations in the divergence of the ion beam

To quantify the level of beam divergence from the simulations, we defined an average divergence angle of the ion beam (α_{avg}) as

$$\alpha_{avg}(x) = \max\left(-\frac{\int_{-\frac{\pi}{2}}^{0} \alpha\, \gamma(\alpha, x) d\alpha}{\int_{-\frac{\pi}{2}}^{0} \gamma(\alpha, x) d\alpha},\ \frac{\int_{0}^{\frac{\pi}{2}} \alpha\, \gamma(\alpha, x) d\alpha}{\int_{0}^{\frac{\pi}{2}} \gamma(\alpha, x) d\alpha} \right). \quad \text{Eq. 4.2}$$

In the above equation, α represents the angle between the ion particles' trajectory and the axial (y) axis. Also, the function $\gamma(\alpha, x)$ introduces a novel concept that we term the "divergence-angle distribution function" or $I\alpha DF$ (in analogy with the $IVDF$ which denotes ion *velocity* distribution function).

We define α_x and α_z as the projections of α on the axial-radial and axial-azimuthal planes, respectively, i.e.,

$$\alpha_x = \tan^{-1}\left(\frac{v_{i,x}}{v_{i,y}}\right), \qquad \alpha_z = \tan^{-1}\left(\frac{v_{i,z}}{v_{i,y}}\right) \quad \text{Eq. 4.3}$$

where, $v_{i,x}$, $v_{i,y}$, and $v_{i,z}$ are, respectively, the ion particles' velocity along the radial, axial, and azimuthal directions. Accordingly, we can define ions' radial and azimuthal divergence-angle distribution function by $\gamma_x(\alpha_x, x)$ and $\gamma_z(\alpha_z, x)$, respectively. Substituting $\gamma_x(\alpha_x, x)$ and $\gamma_z(\alpha_z, x)$ in Eq. 4.2, we obtain the radial distribution of the average ion beam divergence due to the radial and the azimuthal ions' velocity components, $\alpha_{x,avg}(x)$ and $\alpha_{z,avg}(x)$. While $\alpha_{x,avg}$ characterizes the ions radial expansion and $\alpha_{z,avg}$ represents the ions azimuthal swirl, both angles measure the deviations of the ion flow from an axially directed beam.

Moreover, integrating these distribution functions along the domains' x-extent yields the integral distributions of ion particles over α_x and α_z, represented by Γ_x and Γ_z

$$\Gamma_x(\alpha_x) = \int_0^{L_x} \gamma_x(\alpha_x, x) dx, \qquad \Gamma_z(\alpha_z) = \int_0^{L_x} \gamma_z(\alpha_z, x) dx\,. \quad \text{Eq. 4.4}$$

The radial (Γ_x) and azimuthal (Γ_z) divergence-angle distribution functions of the ions, as per Eq. 4.4 are illustrated in **Fig. 4.14** for different E_y and B_x values. Regarding the variations of Γ_x with the field intensities, we notice that cases where the MTSI is strong, i.e., for $E_y \leq 1E_0$ and $B_x \geq 1B_0$, the ions are distributed over broader radial velocity angles, than in the cases where the ECDI is the dominant instabilities ($E_y \geq 2E_0$ and $B_x \leq 0.75B_0$). In fact, in these cases, Γ_x manifests two peaks at velocity angles $\alpha_x \approx \pm 45$ degrees, in contrast to the latter cases where the peak of Γ_x occurs at $\alpha_x = 0$.

Different behaviors are also observed for Γ_z distributions among these two sets of cases. In the cases where the ECDI is dominant ($E_y \geq 2E_0$ and $B_x \leq 0.75B_0$), Γ_z indicates an ion population with negative α_z angles, which represents the tapped ions drifting with the azimuthal phase velocity of the ECDI's azimuthal waves. Whereas in the presence of the MTSI, Γ_z exhibits a monotonic drop towards larger positive and negative α_z angles with a more symmetric distribution over negative and positive α_z angles.

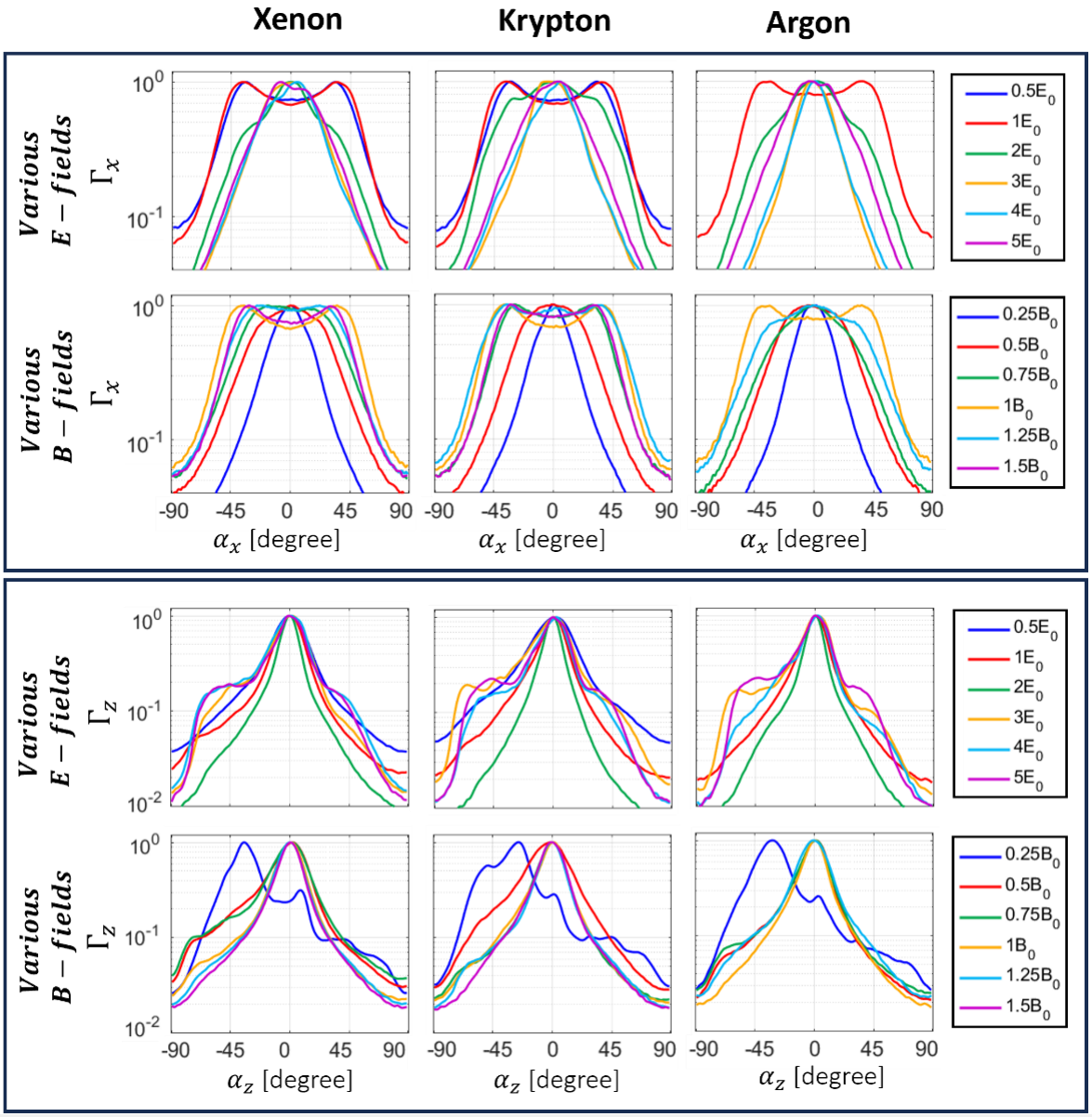


Fig. 4.14: Spatially averaged (over entire domain) divergence-angle distribution functions due to the radial velocity component (Γ_x, top panel) and due to the azimuthal velocity component of the ions (Γ_z, bottom panel) for the three propellants with various E_y (top row in each panel) and various B_x (bottom row in each panel).

The distribution of the average divergence angles due to the radial and azimuthal ion velocities, $\alpha_{x,avg}$ and $\alpha_{z,avg}$, are obtained using Eq. 4.2 and presented in **Fig. 3.15**. As expected from Γ_x distribution functions in **Fig. 4.14**, the cases with $E_y \leq 1E_0$ or $B_x \geq 1B_0$ (MTSI dominant) show significantly larger $\alpha_{x,avg}$ angles in the central region of domain compared to the cases with $E_y \geq 2E_0$ or $B_x \leq 0.75B_0$ (ECDI dominant). Contrarily, the conditions with the ECDI (or the long-λ mode in case of $E_y = 0.5E_0$) as the prevailing instability result in smaller $\alpha_{x,avg}$ angles.

These trends are summarized in **Fig. 4.16** in term of the mean values of $\alpha_{x,avg}$ and $\alpha_{z,avg}$ distributions across the radial extent of the domain, $\alpha_{x,mean}$ and $\alpha_{z,mean}$, as indicative quantities representing the overall ion beam divergence due to the radial and azimuthal velocity components of the ions, respectively.

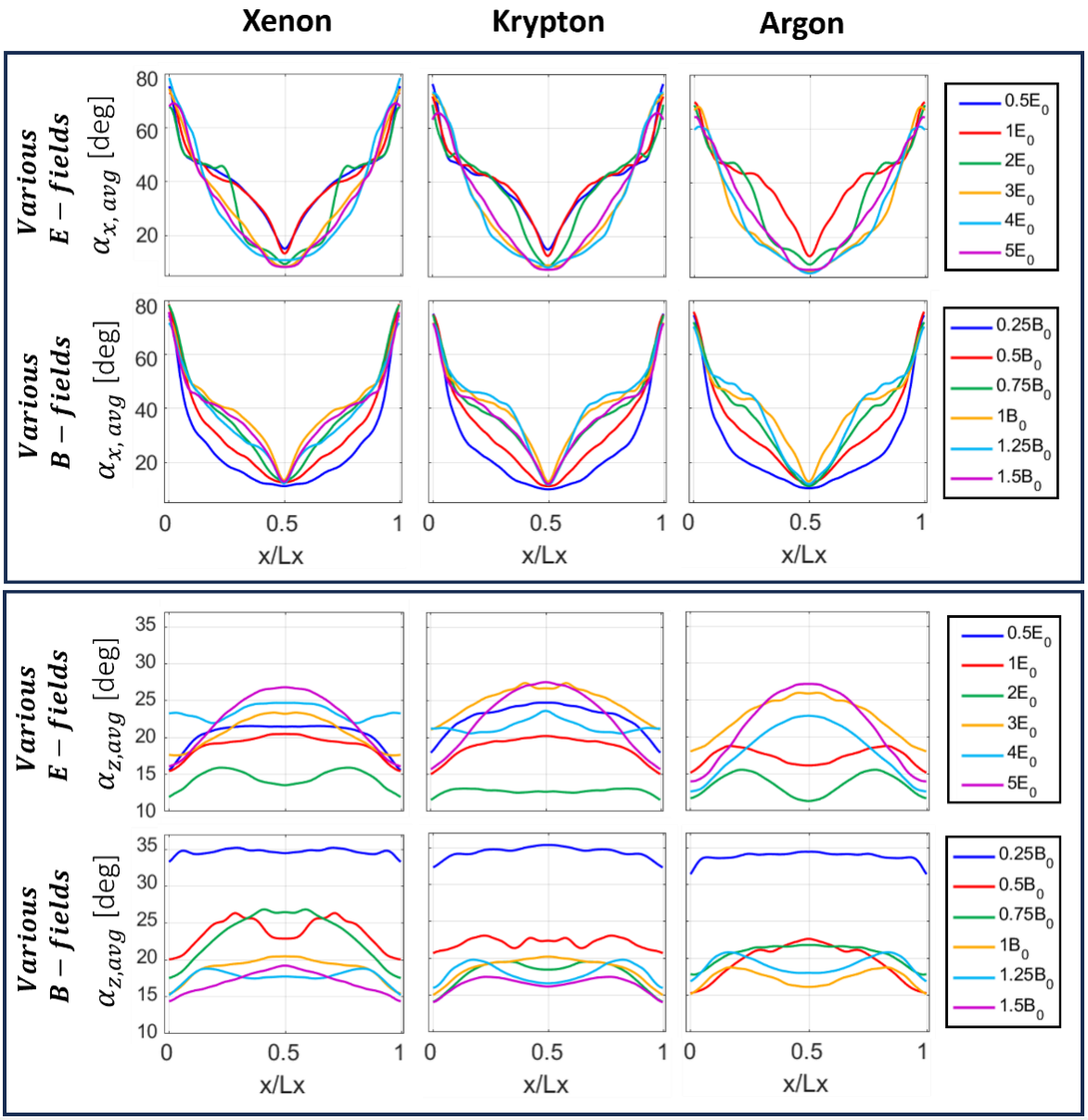


Fig. 4.15: Radial distribution of the azimuthally averaged ion beam divergence angle ($\alpha_{x,avg}$ & $\alpha_{z,avg}$, Eq. 4.2) due to the radial and azimuthal velocity components of the ions for the three propellants with various E_y (top row in each panel) and various B_x (bottom row in each panel).

These results reveal that the ion beam divergence caused by the MTSI (thus in conditions where the MTSI is strong), is mainly through affecting the radial component of the ion particles' velocities, and thus increasing α_x. This happens due to the radial wavenumber component of the MTSI's wave which scatters ions radially. On the other hand, the purely azimuthal ECDI's waves contribute to the divergence of the ion beam mainly by increasing the ions velocity component along the azimuthal direction, hence elevating α_z. Indeed, as seen in **Fig. 4.16**, in the low E-field and high B-field conditions, $\alpha_{x,mean} > \alpha_{z,mean}$, indicating that the ion beam divergence is dominated by the MTSI's contribution to $\alpha_{x,mean}$. Whereas in the high E-field and low B-field conditions, $\alpha_{x,mean}$ and $\alpha_{z,mean}$ are of comparable magnitudes, which means that the ECDI's contribution to $\alpha_{z,mean}$ is as large as the ions' radial expansion.

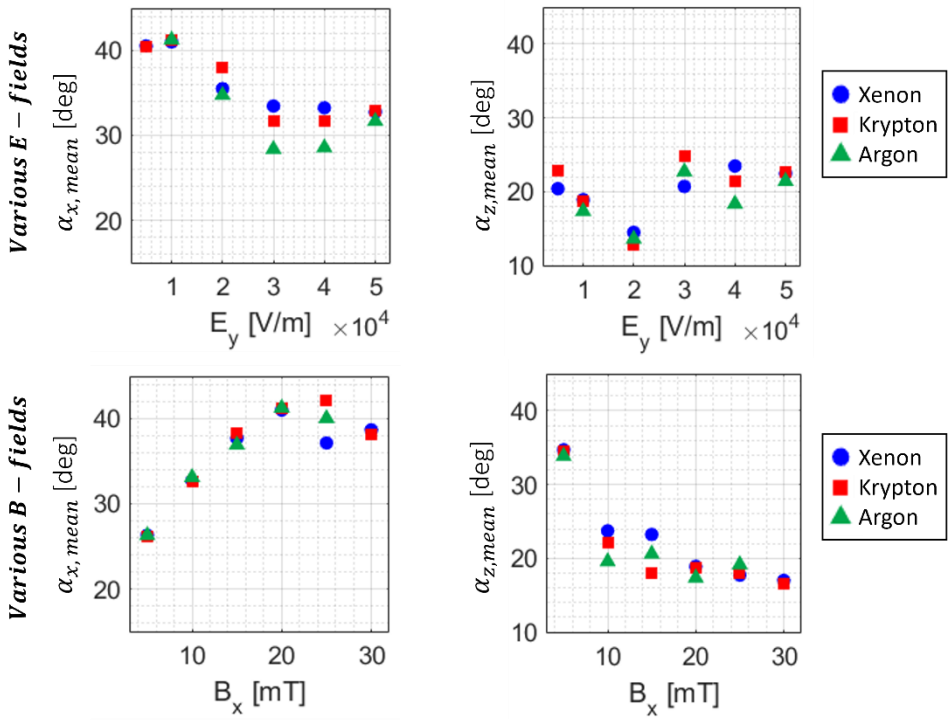


Fig. 4.16: Variation of spatiotemporally averaged (across entire domain and over $20-30\ \mu s$) divergence angle vs E_y (top row) and B_x (bottom row) for the three propellants; (left column) divergence angle due to the ions' radial velocity component, (right column) divergence angle due to the ions' azimuthal velocity component.

4.3. Influence of the curvature of the magnetic field

The effects of the axial gradients of the magnetic field on the plasma behavior in Hall thrusters have been the subject of several studies in the past years [121]-[125]. However, there has not been as much attention to the effects that the magnetic field curvature (radial gradients) has on the underlying plasma processes, particularly on the azimuthal instabilities and the resulting electron transport. Most high-fidelity studies of these two phenomena, which have been carried out in the setups resolving the radial coordinate, had assumed perfectly radial magnetic field lines [12][33][35].

Concerning the impacts of the B-field curvature on the plasma-wall interactions, there have been, nonetheless, a number of previous efforts. These activities were in part motivated by the emergence of the magnetically shielded Hall thrusters and their non-conventional magnetic field topologies. Refs. [52][126][127] carried out hybrid fluid-PIC simulations in the axial-radial coordinates to investigate the physics underlying the magnetic shielding concept as well as to analyze the variation in the distribution of the plasma properties, the sheath characteristics, and the plasma-wall interactions due to the consequent changes in the B-field topology. Authors in Refs. [128][129] also performed studies of similar scope on two specific industrial magnetically shielded Hall thrusters using axial-radial hybrid simulations. The focus of these works was on the 2D spatial distribution of the plasma properties, global power and current balances, and the interactions of the plasma with the radial walls [128][129].

The effects of the magnetic field curvature have also been assessed using fully kinetic PIC simulations. In this regard, Liu et al. [130] and Quan et al. [131] studied the influence of various degrees

of B-field's curvature on the plasma-wall interactions and the erosion phenomenon using 2D axial-radial and limited-domain radial-azimuthal simulations, respectively. They demonstrated that increasing the concavity of the field lines reduces the energy of the ions reaching the wall and, hence, lowers the erosion rate [131]. On the contrary, in the case of convex field lines, the erosion rate becomes highly significant at large degrees of positive curvature [131] . Marin-Cebrián et al. in Ref. [132] carried out 1D radial PIC simulations with various magnetic field curvatures and showed that, for negative curvatures, the electrons' distribution function becomes more isotropic, and the tail of the distribution function is greatly replenished. A concentrating effect in cases with concave field curvatures was observed, with the plasma density in the center of the domain becoming higher than the case with a constant radial magnetic field [132]. Taccogna et al. assessed, in a 1D radial setup, the effects of the magnetic field's inclination on the plasma sheath's characteristics in the presence of the secondary electron emission and with the plasma properties representative of different axial locations within the discharge channel of a Hall thruster [133].

To investigate the impact of the magnetic field's curvature on the dynamics of the plasma in the adopted simulation configuration, the applied magnetic field comprises a radially varying axial component (B_y) in addition to a uniform radial component ($B_x = 20\ mT$). We chose the same relation adopted in Ref. [132] to prescribe the variation of the B_y along the radial direction

$$B_y = B_x \tan\theta(r)\,; \qquad \tan\theta = \frac{L_x - x}{L_x}\tan\theta_1 + \frac{x}{L_x}\tan\theta_2 \qquad \text{Eq. 4.5}$$

where, θ_1 and θ_2 are, respectively, the incident angles of the magnetic field lines at the inner and the outer walls, as illustrated in **Fig. 4.17** (a). The magnetic field is assumed to be symmetric with respect to the channel centerline, hence, $\theta_1 = -\theta_2$. We highlight that, because simulations occur on a plane and do not resolve the variations along the axial dimension, the magnetic field does not have an axial gradient.

The Q2D simulations are performed with various degrees of magnetic field curvature, as parametrized by $\theta = \theta_1$. The field curvature parameter, θ, ranges from -60 to 60 degrees with a 15-degree increment. The case with $\theta = 0$ corresponds to the purely radial magnetic field topology of the baseline benchmark setup.

The concave field topology with negative curvature ($\theta < 0$) refers to the field lines curving toward the anode ($-y$ direction), which is representative of a typical magnetic field topology upstream of the axial location of the magnetic field peak ($x_{B,peak}$) within a Hall thruster's channel. Conversely, the convex field topology with positive curvature ($\theta > 0$) signifies the field lines curving toward the cathode ($+y$ direction), hence, resembling the conditions downstream of the $x_{B,peak}$ location. About the location of the B-field peak, which typically occurs near the channel's exit plane, the field lines are mostly radial with no notable curvature. Due to the general expected effect the curvature of the B-field has on the ion beam, the concaves (negative) curvature is often referred to as "ion focusing" in literature, while the field lines with convex (positive) curvatures are known as "ion diverging" or "ion expanding" [49].

The streamlines of the magnetic field and the radial variation of B_y in the simulated cases are illustrated, respectively, in **Fig. 4.17** (b) and (c).

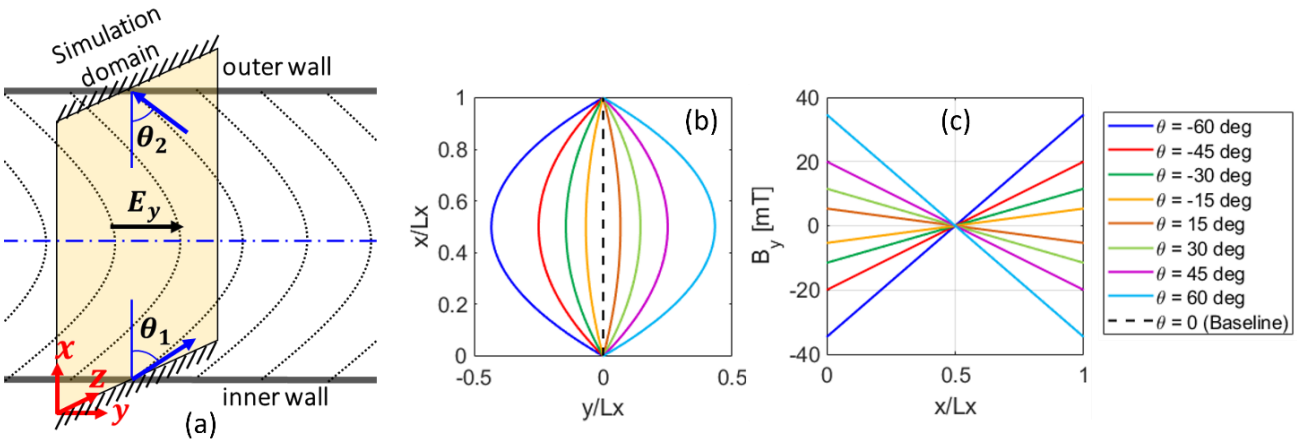


Fig. 4.17: (a) Schematic of the magnetic field lines, with the lines' incidence angle at the inner wall (θ_1) and at the outer wall (θ_2) as used in Eq. 4.5 illustrated, (b) 2D shape of the magnetic field lines in the axial-radial ($y-x$) plane for various θ, and (c) radial profile of the axial component of the magnetic field (B_y) for various θ.

Before discussing the results, it is noted that the same setup and conditions as those of Q2D simulations are simulated for xenon using the 1D radial PIC (IPPL-1D) in Appendix A.5.6, excluding the azimuthal direction and all the associated conditions. The comparison between the 1D results against the Q2D ones (provided in Appendix A.5.6) helps isolate and evaluate the contributions of *azimuthal* physics from the *radial* dynamics. These results highlight the significance of resolving azimuthal processes in such studies.

4.3.1. Variations in the distribution of the plasma properties

Fig. 4.18 presents the change in the spatiotemporal average of several plasma properties with respect to θ. Referring to **Fig. 4.18** (a), the number density (n_i) increases notably as θ approaches large negative values ($\theta = -60, -45$ degrees). However, it remains nearly identical for cases with $\theta = -30, -15$, and 0 degrees. In contrast, across the range of $\theta \geq -30$, n_i exhibits a more moderate variation. The time-averaged radial profiles of n_i are also shown in **Fig. 4.19**.

The general trend of n_i vs θ is consistent across all propellants, with xenon exhibiting the highest density, argon displaying the lowest, and krypton falling in between. However, there is an exception in the scenario with $\theta = -60$ degrees, where krypton demonstrates the highest density among the three propellants. We will see shortly that this exception is due to a slightly weaker MTSI mode for krypton at $\theta = -60$ degrees compared to the other two propellants. Apart from the direct effect of B-field curvature on the ion flux lost to the walls, the observed trends in n_i are in part the consequence of the variations in the radial electron temperature (T_{ex}). As discussed in Section 4.2.1, the setup of the problem creates a certain degree of coupling between n_i and T_{ex} due to imposing a temporally invariant ionization source and the absence of a self-consistent (T_e- dependent) ionization. Thus, the particle losses which are proportional to T_{ex} establish the observed inverse correlation between n_i and T_{ex}.

T_{ex} decreases almost monotonically from $\theta = -30$ to 45 degrees, and it increases slightly at $\theta = 60$ degrees. Across this range of B-field curvatures, argon consistently demonstrates the lowest T_{ex}, whereas xenon exhibits the highest values.

Looking at **Fig. 4.18** (c), T_{ez} has an overall increasing-decreasing trend with the magnetic field curvature, with the mean values of the azimuthal electron temperature being the highest at $\theta = 0$ for xenon and krypton and within the range of $\theta = 0$ to 30 degrees for argon. Finally, the combined behavior of T_{ex} and T_{ez} is represented by the total electron temperature (T_e) in **Fig. 4.18** (d).

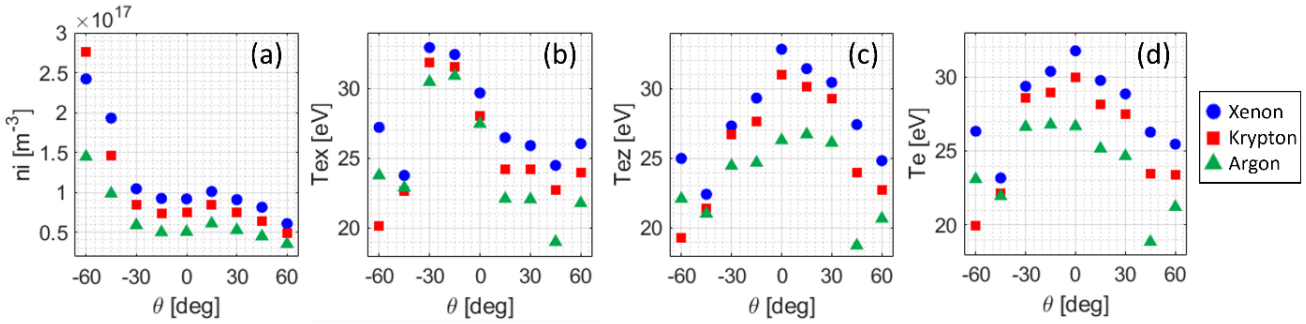


Fig. 4.18: Variation of spatiotemporally averaged (across entire domain and over $20 - 30\ \mu s$) plasma properties vs θ for the three propellants; (a) ion number density (n_i), (b) & (c) radial and azimuthal electron temperature (T_{ex} & T_{ez}), and total electron temperature (T_e).

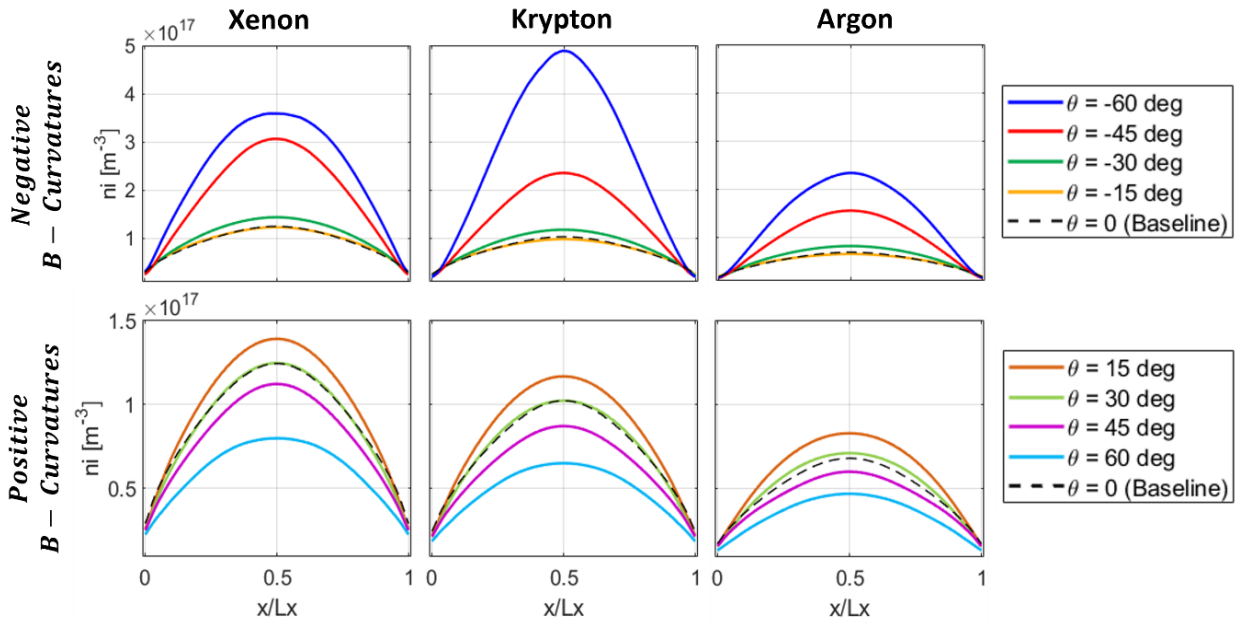


Fig. 4.19: Radial profiles of the ion number density (n_i) averaged over all azimuthal locations and over the time interval of $20 - 30\ \mu s$ for the three propellants with various negative (top row) and positive (bottom row) curvatures of magnetic field.

It is recalled from discussions in Section 4.2.1 that the established plasma profiles within the system, in particular, T_{ex} and T_{ez} and their comparative magnitudes are the outcome of the interplay between the instabilities and the relative strength of the developed modes. In this regard, based on the contributions of the ECDI and the MTSI to the electrons' heating along the azimuthal and the radial

directions, respectively, we identified the electron temperature anisotropy, represented by T_{ex}/T_{ez} ratio, as an indicative measure of the relative dominance of these two instability modes.

The variation in the spatiotemporally averaged T_{ex}/T_{ez} ratio across different curvature angles is plotted in **Fig. 4.20**. In this plot, we can distinctly identify the two regimes introduced in Section 4.2.1 (which were also observed among various field intensities in **Fig. 4.3**). Indeed, the presence of negative B-field curvatures results in $T_{ex}/T_{ez} > 1$, indicating the prevalence of the MTSI which is the characteristic of regime I. It is also noticed that for large negative curvatures, i.e., $\theta = -60$ and -45 degrees, the T_{ex}/T_{ez} is smaller compared to the lower negative curvatures ($\theta = -30$ and -15 degrees). We will show in Section 4.3.2 that, this is due to the appearance of the long-λ mode with a strong amplitude. This mode is seen in our simulations to heat up electrons mostly in the azimuthal direction.

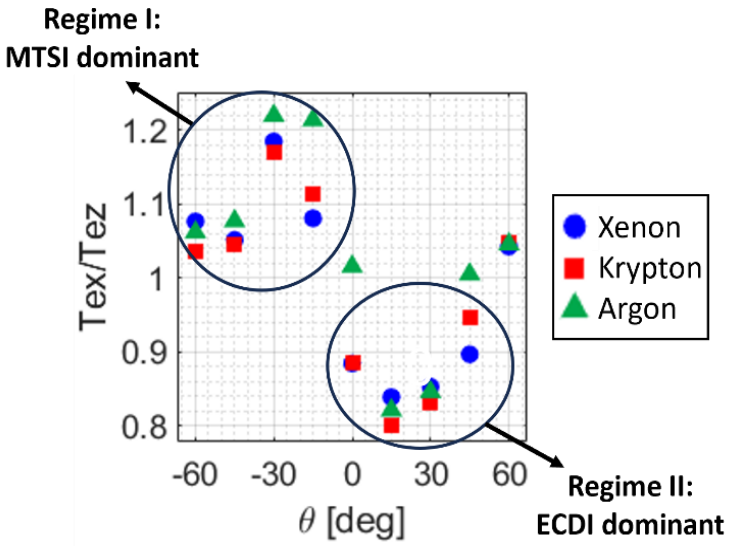


Fig. 4.20: Variation of spatiotemporally averaged (across entire domain and over $20 - 30\ \mu s$) radial-to-azimuthal electron temperature ratio (T_{ex}/T_{ez}) vs θ for the three propellants.

Contrarily, the positive curvatures lead, in general, to $T_{ex}/T_{ez} < 1$, which is attributed to the ECDI modes being the dominant instability, signifying regime II. A particular exception to this general observation is noticed for the case of $\theta = 60$ degrees, where the T_{ex}/T_{ez} ratio is slightly higher than 1 for all propellants. This implies that at $\theta = 60$ degrees, the MTSI mode must become relatively strong again. We will verify the variation of the dominant instability modes under various θ conditions in further detail in Section 4.3.2.

Additionally, the time-averaged radial profiles of the T_{ex}/T_{ez} ratio, provided in **Fig. 4.21**, demonstrate that, in general, the positive curvature of the B-field creates a more uniformly distributed temperature anisotropy across the domain compared to the B-fields with the negative or no curvatures.

Furthermore, it is demonstrated in Section 4.2.1 that the radial profile of the axial electron current density (J_{ey}) induced by different azimuthal instabilities exhibits distinct characteristics. We showed that, in the cases where the ECDI is the dominant instability, J_{ey} peaks at the centerline, whereas the MTSI's dominance leads to the concentration of J_{ey} away from the center and in some cases near the walls.

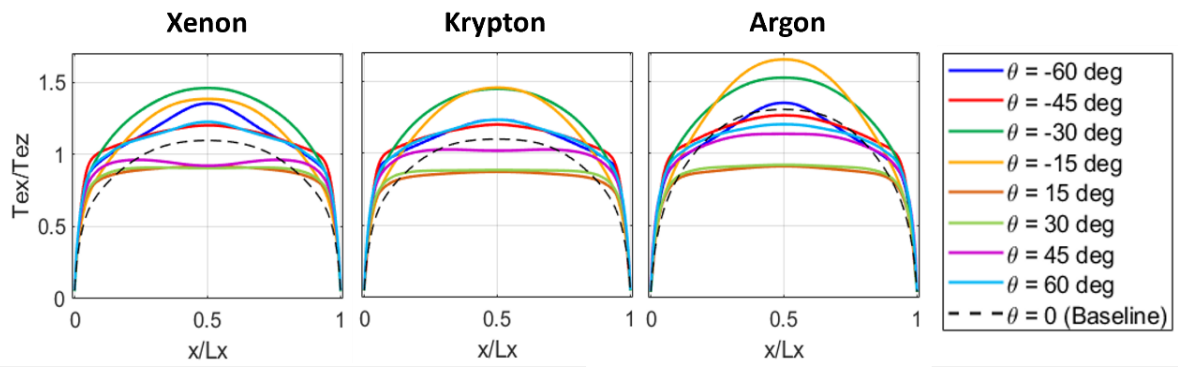


Fig. 4.21: Radial profiles of the of the radial-to-azimuthal electron temperature ratio (T_{ex}/T_{ez}) averaged over all azimuthal locations and over the time interval of $20-30\ \mu s$ for the three propellants with various magnetic field curvatures.

The radial distributions of the normalized axial electron current density ($J_{ey}/J_{ey,mean}$) are presented in **Fig. 4.22**. Consistent with the observations made in Section 4.2.1, we can see from **Fig. 4.22** that, for $\theta = -30$ and -15 degrees, where the MTSI is the dominant mode, J_{ey} is larger near the walls and reduces toward the center of the domain. Moreover, at $\theta = -60$ and -45 degrees, the J_{ey} profiles exhibit two peaks away from the centerline; however, the current density is primarily concentrated in the central portion of the domain rather than near the walls. This profile represents the combined electron current induced by both the MTSI and the long-λ mode. The presence of two peaks on both sides of the centerline is the characteristic shape of the MTSI-induced electron current, while the central concentration of the electron axial current density is due to the long-λ mode (the J_{ey} induced by long-λ mode has a centrally-concentrated characteristic shape similar to the ECDI).

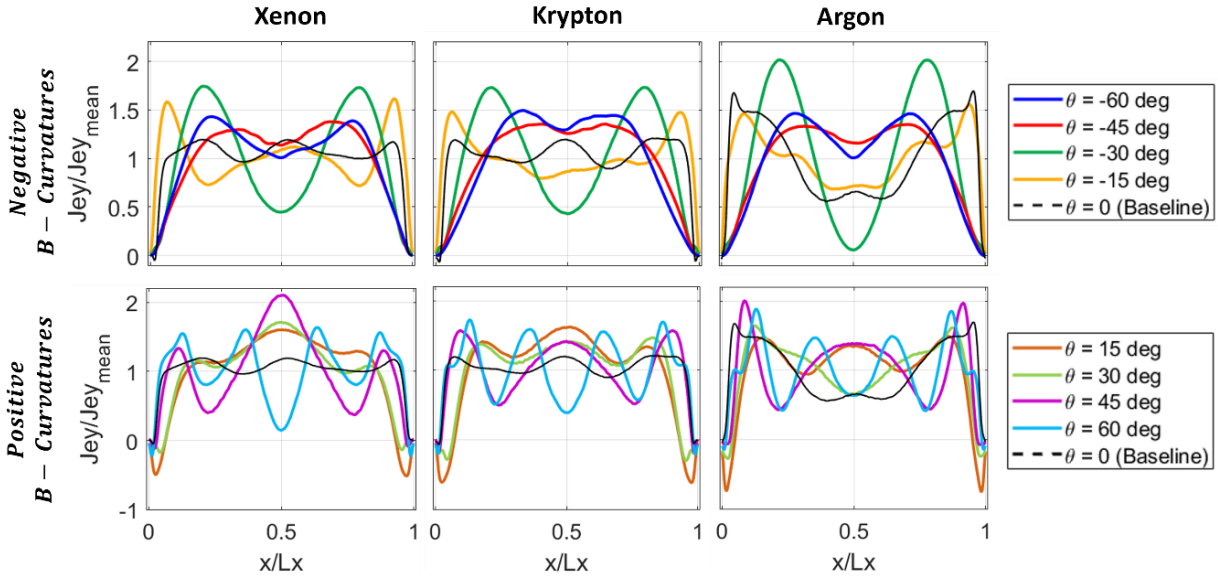


Fig. 4.22: Radial profiles of the of the normalized axial electron current density ($J_{ey}/J_{ey,mean}$) averaged over all azimuthal locations and over the time interval of $20-30\ \mu s$ for the three propellants with various negative (top row) and positive (bottom row) curvatures of magnetic field.

However, in cases with positive curvature, the contributions other than the azimuthal instabilities in particular the viscus effects are significant enough to substantially influence the J_{ey} profiles. Therefore, the discussion regarding the correlation between the observed characteristics of the electrons' axial

transport profile and the dominant instability in the system is deferred to Section 4.3.3, where we isolate the contribution of the instabilities from other factors.

Before moving on to the detailed evaluation of the instabilities' spectra, we refer to the 2D snapshots of the plasma properties in **Fig. 4.23**, which serve as a visual inspection of the dominant underlying instabilities across various θ values.

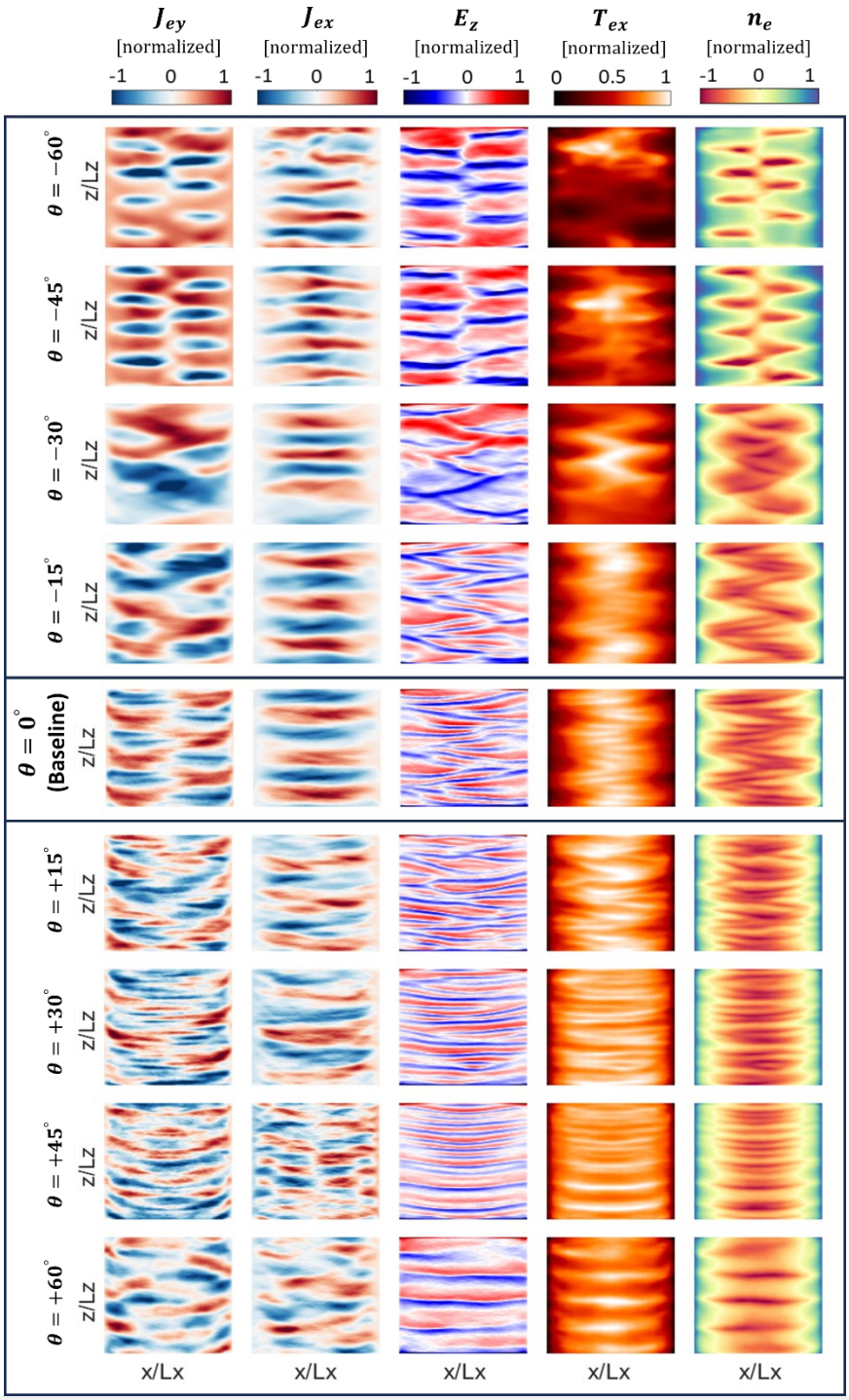


Fig. 4.23: 2D snapshots of the normalized plasma properties at a time of local maximum of the spatially averaged T_{ex} for xenon propellant with various θ. The columns, from left to right, represent the axial and radial electron current densities (J_{ey} and J_{ex}), the azimuthal electric field (E_z), the radial electron temperature (T_{ex}), and electron number density (n_e).

The snapshots are captured at a time instant corresponding to a local peak of the spatially averaged radial electron temperature (T_{ex}), during which the MTSI, if present, is strongest. It is evident from this figure that the negative- and the positive-curvature cases display distinctively different behaviors in terms of the spatial structures of the involved fluctuations.

In general, the negative curvature of the B-field tends to reinforce the development of the MTSI-representative patterns across the plasma properties, whereas the positive curvatures seem to suppress the MTSI, leaving the azimuthal waves of the ECDI as the primary instability modes in the system. The absence of the B-field curvature ($\theta = 0$) represents an intermediate scenario, where the snapshots exhibit patterns resembling both the ECDI and the MTSI. Moreover, traces of relatively long-wavelength structures associated with the long-λ mode is noticed in the negative curvature cases.

4.3.2. Variations in the characteristics of the azimuthal instabilities

The results of the FFT spectral analyses of the azimuthal fluctuations are used to investigate the variation in the instabilities' characteristics, including the wavenumber and the frequency across different θ values and various propellants. The average spatial and the temporal FFT spectra of the azimuthal electric field fluctuations are presented, respectively, in **Fig. 4.24** and **Fig. 4.25**.

Starting with the negative B-field curvature cases, we notice from the instabilities' k_z spectra in **Fig. 4.24**, that the ECDI (first harmonic) is developed only at $\theta = -15$ degrees. In this case, the ECDI's amplitude is lower for argon compared to xenon and krypton. Higher negative curvatures suppress the development of the ECDI. Accordingly, in the cases with $\theta \leq -30$ degrees, the ECDI is absent.

For, $\theta \leq -30$, the MTSI and the long-λ instability are the dominant instabilities, with the amplitudes that are nearly the same across all propellants. The long-λ instability also exits at $\theta = -15$ degrees, but with an intensity much lower than that of the MTSI. Furthermore, long-λ mode is significantly damped at $\theta = 0$ for xenon and krypton, whereas in the case of argon, its intensity is comparable with the mode's intensity at $\theta = -15$ degrees. Additionally, the temporal evolution of the instabilities' k_z spectrum for $\theta = -60$ and-45 degrees, provided in Appendix A.5.4, indicates an alternating energy transfer between the MTSI and the long-λ mode leading to a cyclic growth and damping of these modes throughout the discharge. For $\theta = -30$ degrees, however, the evolution plot of the k_z spectrum indicates the early establishment of the long-λ mode within the first few microseconds of the simulation through the energy cascade from shorter wavelength modes. In this case, the established long-λ mode persists throughout the simulation with relatively constant energy.

Looking at **Fig. 4.25**, a noteworthy observation is that, at $\theta = -30$ degrees, the frequency spectrum of the instabilities reveals the presence of instability modes with frequencies in the range of $20 - 25\,MHz$. The amplitudes of these modes decrease from xenon to krypton, and they are nearly suppressed in the case of argon. The DMD analyses in Ref. [137] enables discovering the spatial structure of these high-frequency modes. It is noticed that, at least for xenon, this mode with the

frequency of $\sim 20\ MHz$ shares the same wavelength and spatial structure as the MTSI mode with the frequency of about $1\ MHz$.

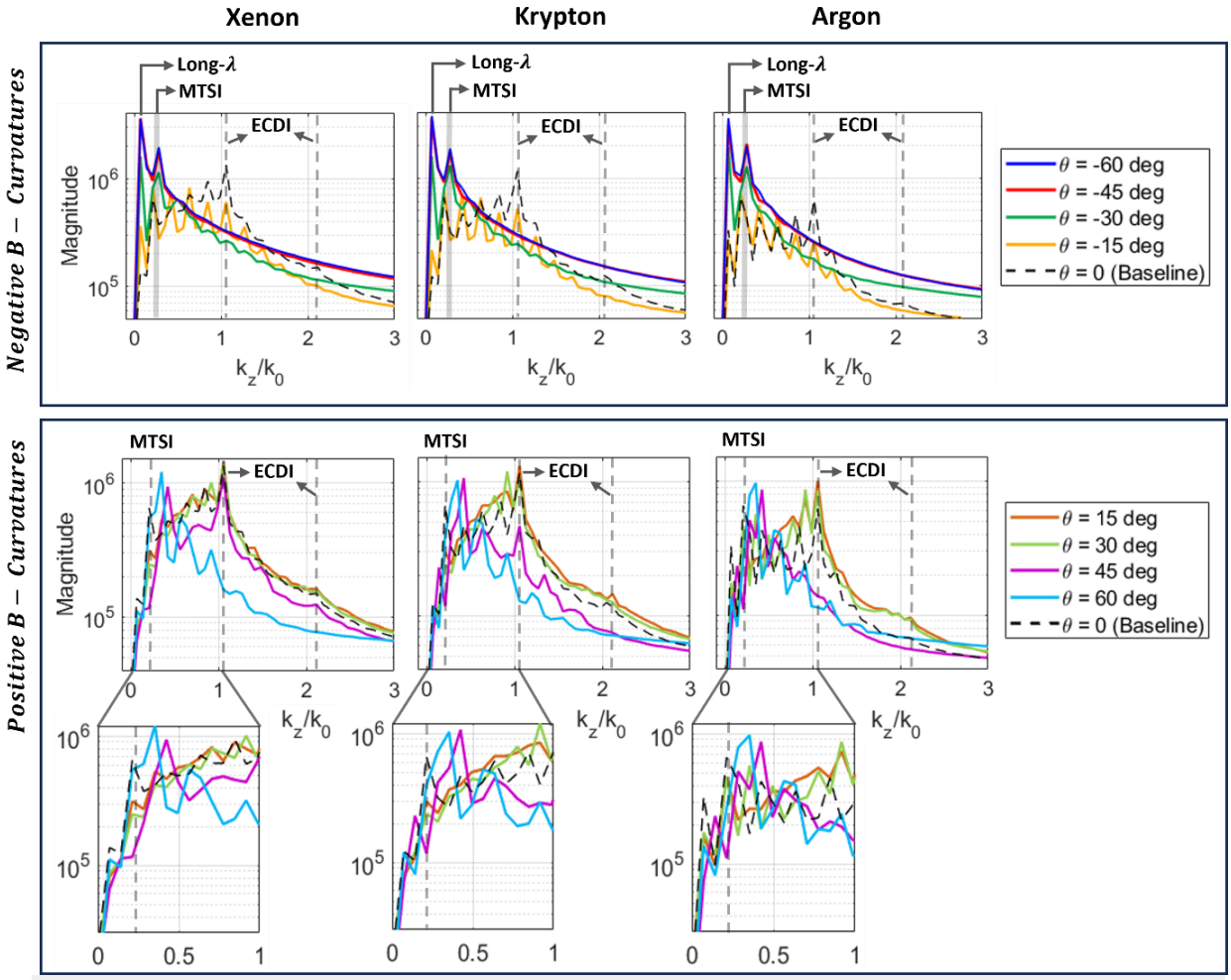


Fig. 4.24: Azimuthal wavenumber spectra of instabilities obtained from average spatial FFTs (over all radial positions and over the time interval of $20 - 30\ \mu s$) of the azimuthal electric field signal from simulations with various negative (top panel) and positive (bottom panel) curvatures of magnetic field for the three propellants. k_0 represents the ECDI's fundamental wavenumber ($k_0 = \frac{\omega_{ce}}{V_{de}}$).

Proceeding with the cases with positive B-field curvatures, it is evident from **Fig. 4.24**, that the positive curvatures in general contribute to the suppression of the MTSI, especially for xenon and krypton. In particular, the peaks associated with the MTSI in the k_z spectra of xenon and krypton at $\theta = 15$ and 30 degrees exhibit notably reduced amplitudes in comparison to the baseline case ($\theta = 0$). Whereas the MTSI's intensity for argon at these curvature values is comparable to the baseline simulation. The first harmonic of the ECDI is the dominant mode in the cases of $\theta = 15$ and 30 degrees. Additionally, the second harmonic of the ECDI is present in the cases of $\theta = 15$ and 30 degrees for all the propellants as well as for xenon in the case of $\theta = 45$ degrees.

The k_z spectra of the cases with $\theta = 45$ and 60 degrees for all propellants contain peaks at $k_z/k_0 \approx 0.42$ and $k_z/k_0 \approx 0.35$, respectively. However, it is not readily evident if these peaks could correspond to the MTSI since they represent larger azimuthal wavenumbers than those expected for the MTSI from

the baseline case (where $k_z/k_0 \approx 0.2$). In this respect, the DMD analysis results in Ref. [137] provided further insights into the nature of these modes by characterizing their spatial structures. We particularly understood that, at least for xenon at $\theta = 60$ degrees, the peak at $k_z/k_0 \approx 0.35$ is possibly linked to the MTSI as it presents a radial-azimuthal structure reminiscent of this instability.

Furthermore, the $\theta = 45$ degrees condition shows the largest discrepancy among different propellants in terms of the intensity of the ECDI. At this curvature level, the ECDI manifests its highest intensity for xenon, while it is mitigated for krypton and is absent for argon. In the case of $\theta = 60$ degrees, the nearest peak to the theoretical normalized wavenumber of ECDI's first harmonic ($k_z/k_0 = 1$) is shifted toward lower wavenumbers ($k_z/k_0 \approx 0.92$).

Referring to **Fig. 4.25**, it is noteworthy that, in the case of $\theta = 60$ degrees, the FFT spectrum exhibits numerous peaks across a wide range of frequencies. The DMD results [137] showed that these peaks with frequencies above $1.5\,MHz$ correspond to the modes with almost purely azimuthal spatial structures that resemble the ECDI.

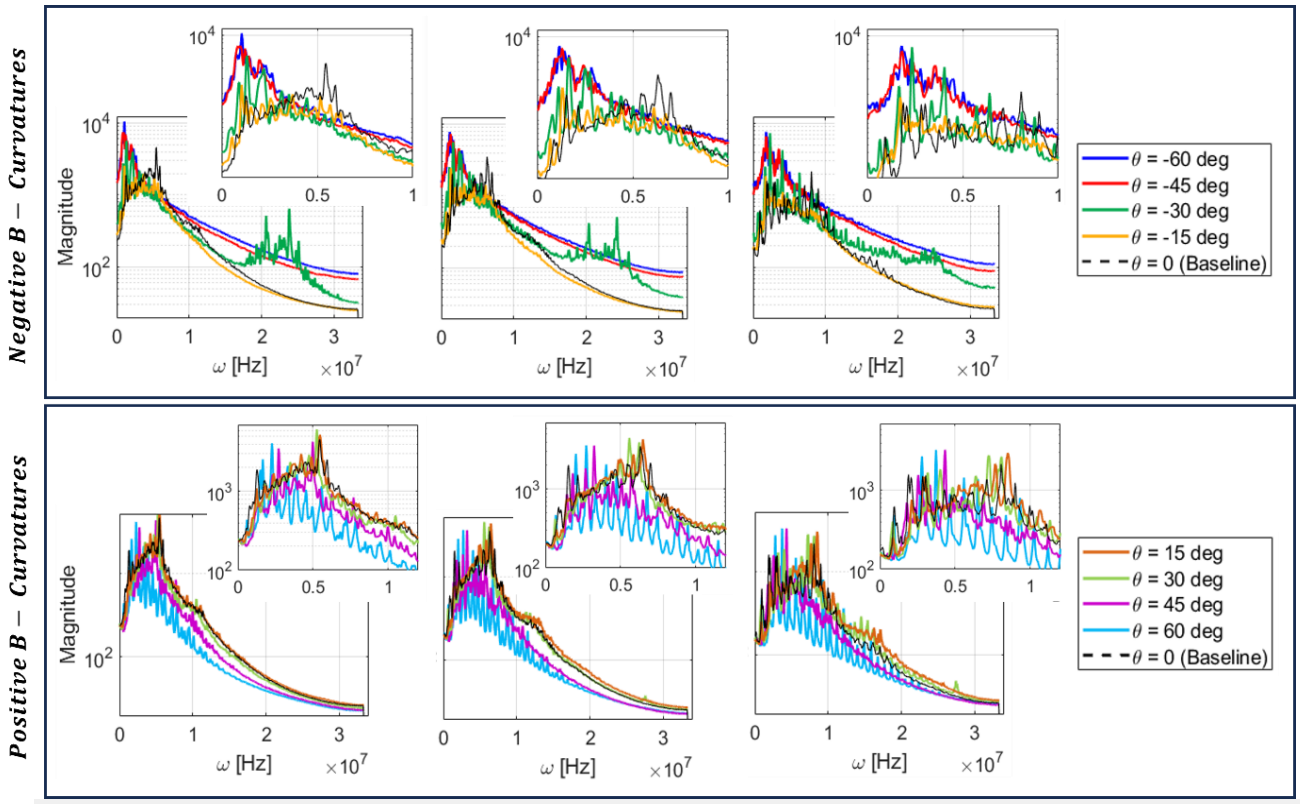


Fig. 4.25: Frequency spectra of instabilities obtained from average temporal FFTs (over all radial and azimuthal positions) of the azimuthal electric field signal with various negative (top panel) and positive (bottom panel) curvatures of magnetic field for the three propellants.

A summary of the salient findings observed from the spectra of the instabilities under various B-field curvatures is as follows:

- The negative curvature of the B-field ($\theta < 0$) tends to suppress the ECDI and the purely azimuthal instabilities (except for the azimuthal long-λ mode) while promoting the development of MTSI-like instabilities with both radial and azimuthal wavenumbers.

- The long-λ mode is progressively amplified with increasing negative curvature of the B-field.
- The positive curvature of the B-field ($\theta > 0$) hinders the formation of the MTSI and the instabilities with the radial-azimuthal structures in general.
- Under positive curvature conditions, the modes primarily consist of purely azimuthal instabilities, such as the ECDI across a range of frequencies and wavenumbers.

These findings indicate that under negative curvatures, the modes are dominated by radial-azimuthal MTSI-like patterns, and in the presence of the positive curvature, the modes almost entirely comprise purely azimuthal fluctuations.

Finally, **Fig. 4.26** provides a summary of the normalized characteristics of the ECDI and the MTSI modes (where present) across various θ for different propellants.

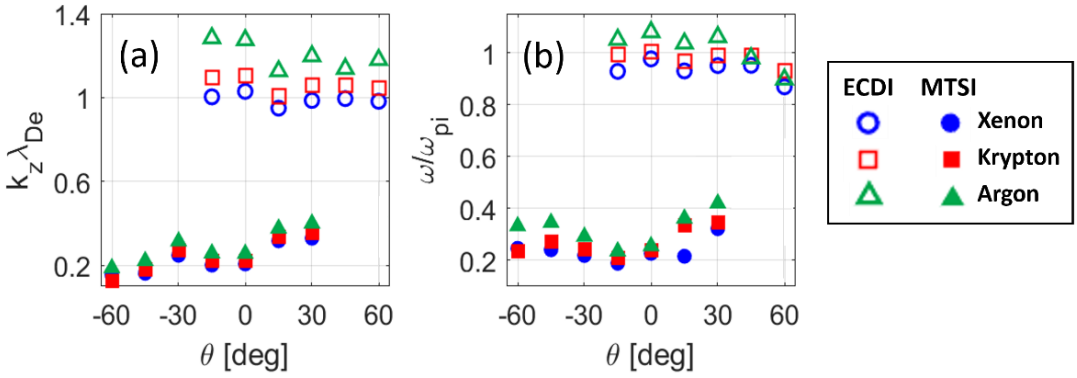


Fig. 4.26: Variation of the normalized characteristics of the dominant ECDI and the MTSI modes vs θ for the three propellants; (a) normalized azimuthal wavenumber ($\tilde{k}_z = k_z\lambda_{De}$), (b) normalized real frequency ($\tilde{\omega} = \omega/\omega_{pi}$), and (c) normalized azimuthal phase velocity ($\tilde{V}_{ph} = V_{ph}/C_s$).

Noting that, the negative curvatures typically occur upstream of the magnetic field peak (B_{peak}) along the centerline of the Hall thruster channel, while the positive curvature are present downstream of the axial location of B_{peak}, there is an inevitable correlation that between the direction of the axial gradient of magnetic field and concavity and convexity of magnetic field lines (i.e., $\theta < 0$ for $\frac{\partial B_x}{\partial y} > 0$ and $\theta > 0$ for $\frac{\partial B_x}{\partial y} < 0$). As a result, the distinct physical processes and behaviors observed for the cases with the negative and the positive curvatures, suggest, by the way of conjecture, that, besides the role of the axial gradients of the B-field, the field's curvature can be an additional significant factor contributing to the experimentally-observed differences in Hall thrusters' plasma dynamics before and after the B-field's peak. These differences include the experimental observations of the ECDI's waves in the near plume region [16][140][141] (after B-field's peak, where $\theta > 0$), while the ECDI is largely absent inside the channel (where $\theta < 0$). This is consistent with our simulation results which suggest ECDI is mostly present where the field's curvature is positive.

4.3.3. Variations in the electrons' cross-field transport

The time-averaged radial distributions of each of the force terms in Eq. 4.1 for various θ values with xenon propellant are compared in **Fig. 4.30**. In the presence of an axial component of the magnetic field, Eq. 4.1 includes an additional force term on the right-hand side, namely the axial magnetic field term given by $F_{B,y} = -qn_e v_{e,x} B_y$. In this case, the left-hand side term is the radial magnetic force term denoted by F_B. The variation of the spatiotemporal average of these terms with θ is plotted in **Fig. 4.28**.

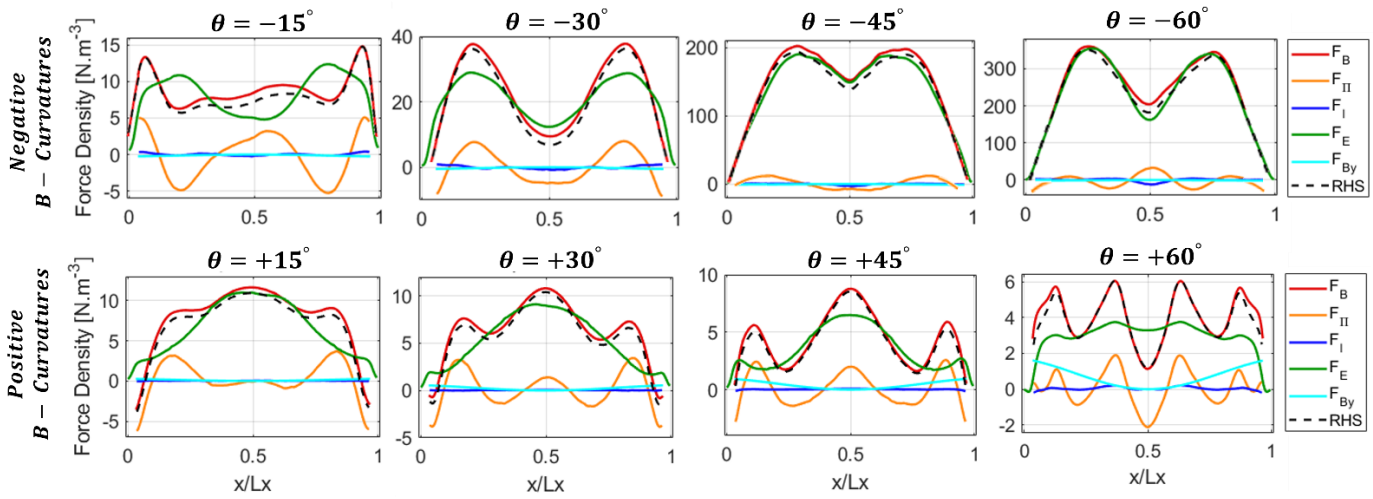


Fig. 4.27: Radial profiles of the transport terms in Eq. 4.1 for xenon propellant with various negative (top row) and positive (bottom panel) curvatures of magnetic field. The force terms are averaged over $20 - 30\ \mu s$. F_B is the radial magnetic force, F_Π is the viscous effects, F_I is the convective inertia force, F_E is the electric force, $F_{B,y}$ is the axial magnetic force term, and RHS represents the sum of F_Π, F_I and F_E . F_t (temporal inertia) contribution was almost zero, and it is thus not displayed.

It is observed in **Fig. 4.30**, that overall profiles of the electron transport (F_B or equivalently RHS) are primarily determined by the contributions of the azimuthal instabilities (F_E) and viscous pressure term (F_Π). Although as seen in **Fig. 4.28**, the average contribution of instabilities over entire domain is 1-2 orders of magnitude larger that of the average viscos effects (due to the oscillatory nature of F_Π around zero), the local values of F_Π term are large enough to significantly change the transports' profile.

In the cases with negative B-field curvatures, the F_E profile show the MTSI's transport profile, featuring two peaks on both sides of the centerline. Additionally, at $\theta = -45$ and -60 degrees, the significant increase in the F_E profiles with concentration toward the center is induced by the long-λ mode.

In the cases with positive θ values of 15 to 45 degrees, where the ECDI is the dominant instability the distribution of F_E is mostly concentrated in the center of the domain. However, in the case of $\theta = 60$ degrees as well as in the baseline case, the F_E distribution becomes more uniform in line with the coexistence of the ECDI and the MTSI.

The axial magnetic field force ($F_{B,y}$) is expected to become non-negligible toward the walls for large positive and negative curvatures, due to the notable the axial component of the magnetic in the regions adjacent to the walls at elevated θ values (refer to **Fig. 4.17**). Indeed, for $\theta = 60$ degrees, **Fig. 4.28**

shows that the radial average of the $F_{B,y}$ term is more significant than the pressure term (F_{Π}). Finally, the inertia force term (F_I) plays the least significant role in the axial electron transport in most cases.

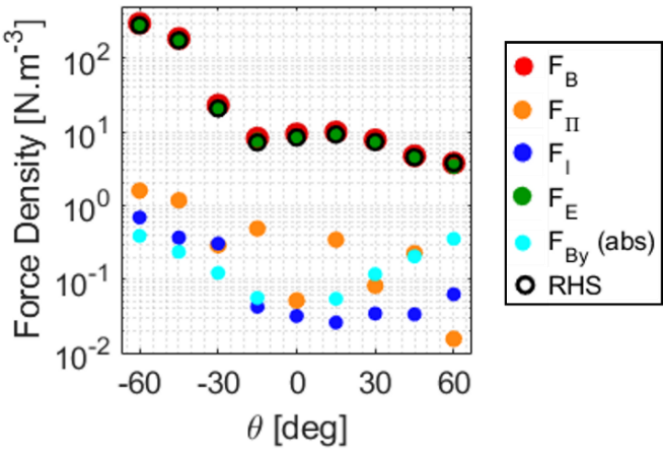


Fig. 4.28: Variation of spatiotemporally averaged (across entire domain and over $20-30\ \mu s$) force terms in the electrons' azimuthal momentum equation (Eq. 4.1) vs θ for xenon propellant.

4.3.4. Variations in the divergence of the ion beam

The ions' radial and azimuthal divergence-angle distribution functions, Γ_x and Γ_z, as defined in Section 4.2.4, under various B-field curvatures are presented in **Fig. 4.29**.

Regarding the variation in Γ_x (top panel in **Fig. 4.29**), for the negative-curvature cases, as θ varies from 0 to -60 degrees, the two peaks in the Γ_x around $\alpha_x = \pm(30-45)$ degrees merge and form one peak at $\alpha_x = 0$ degree, leading to significant reduction in the dispersion of Γ_x over the radial velocity angles. For the positive curvatures, as θ increases from 15 to 45 degrees, the flattened top of the Γ_x extends over a wider range of radial velocity angles. At $\theta = 60$ degrees, the Γ_x develops two peaks at about $\alpha_x = \pm 45$ degrees.

As for the trend of Γ_z (bottom panel in **Fig. 4.29**), the negative curvature of the field increases the population of the ions with non-zero azimuthal velocity angles. Specifically, at $\theta = -60$ and -45 degrees, where a strong long-λ mode had been observed, a notable ion population with the velocity angles of about $\alpha_z = -55$ to -70 degrees is noticed. In contrast, the impact of the positive curvature on Γ_z is minimal.

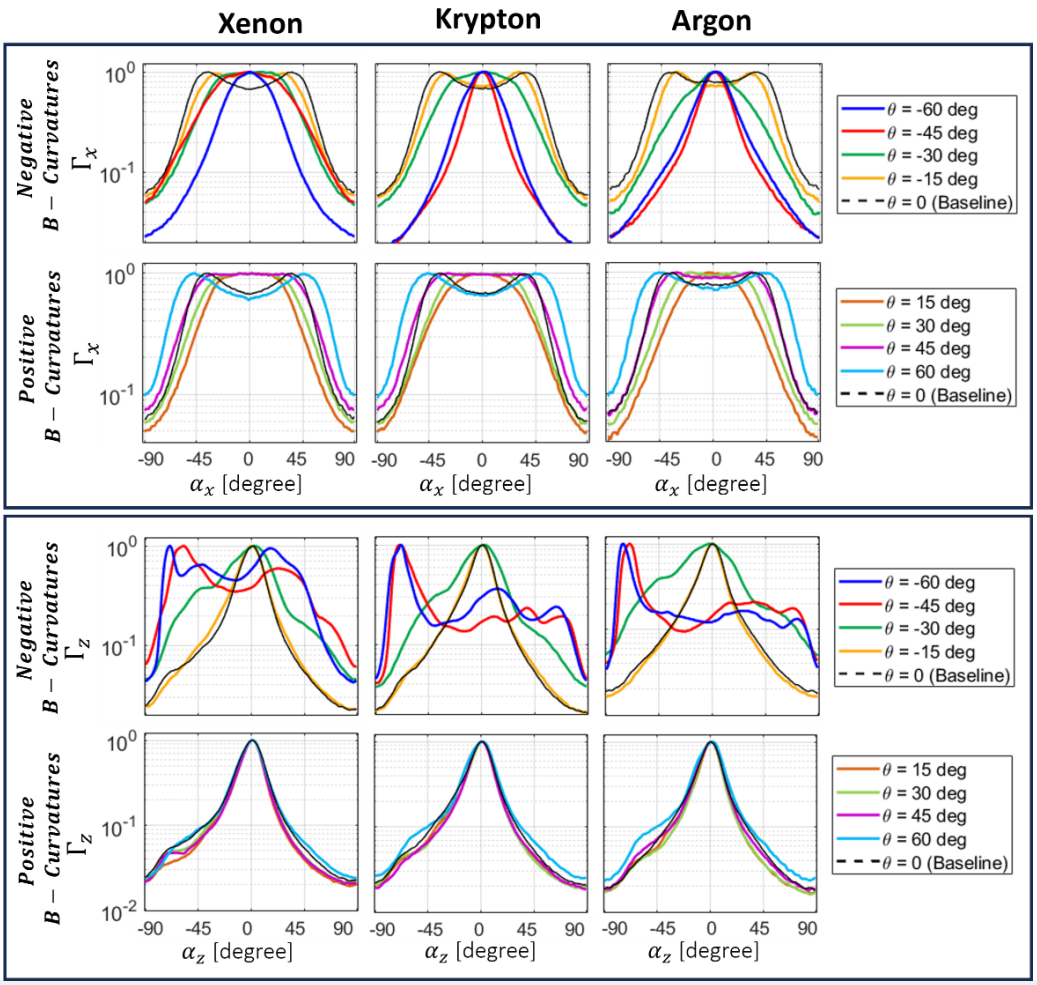


Fig. 4.29: Spatially averaged (over entire domain) divergence-angle distribution functions due to the radial velocity component (Γ_x, top panel) and due to the azimuthal velocity component of the ions (Γ_z, bottom panel) for the three propellants with various negative (top row in each panel) and positive (bottom row in each panel) curvatures of magnetic field.

Now, using our definition of the average divergence angles, $\alpha_{x,avg}$ and $\alpha_{z,avg}$, provided by Eq. 4.2, we obtain the radial profiles of the average ion beam divergence due to the radial and the azimuthal ions' velocity components. The resulting profiles are presented in **Fig. 4.30**.

Starting with the ion divergence angle ($\alpha_{x,avg}$) caused by their radial velocity (top panel in **Fig. 4.30**), the negative curvature of the magnetic field, in general, tends to reduce $\alpha_{x,avg}$ in the central part of the domain. This effect becomes consistently more significant toward higher negative curvatures. It is also observed that the case with $\theta = -45$ degrees displays a notable disparity in the $\alpha_{x,avg}$ profiles among the different propellants. Specifically, the central ion beam, characterized by the low radial divergence angles, extends over a substantially larger radial portion of the domain going from xenon to argon. On the other hand, the positive curvatures slightly enhance the ions' radial divergence angle.

Concerning the ion beam divergence ($\alpha_{z,avg}$) caused by the azimuthal component of the ions' velocity (bottom panel in **Fig. 4.30**), it is observed that, large negative curvatures ($\theta \leq -30$) substantially increase $\alpha_{z,avg}$. Furthermore, in the cases of $\theta = -60$ and -45 degrees, there is a consistent rise in

$\alpha_{z,avg}$ from xenon to argon. On the contrary, the positive curvature of the magnetic field moderately impacts the radial profile of $\alpha_{z,avg}$. In particular, the relationship between $\alpha_{z,avg}$ and the field's curvature displays a non-monotonic trend and exhibits distinct behaviors across various propellants.

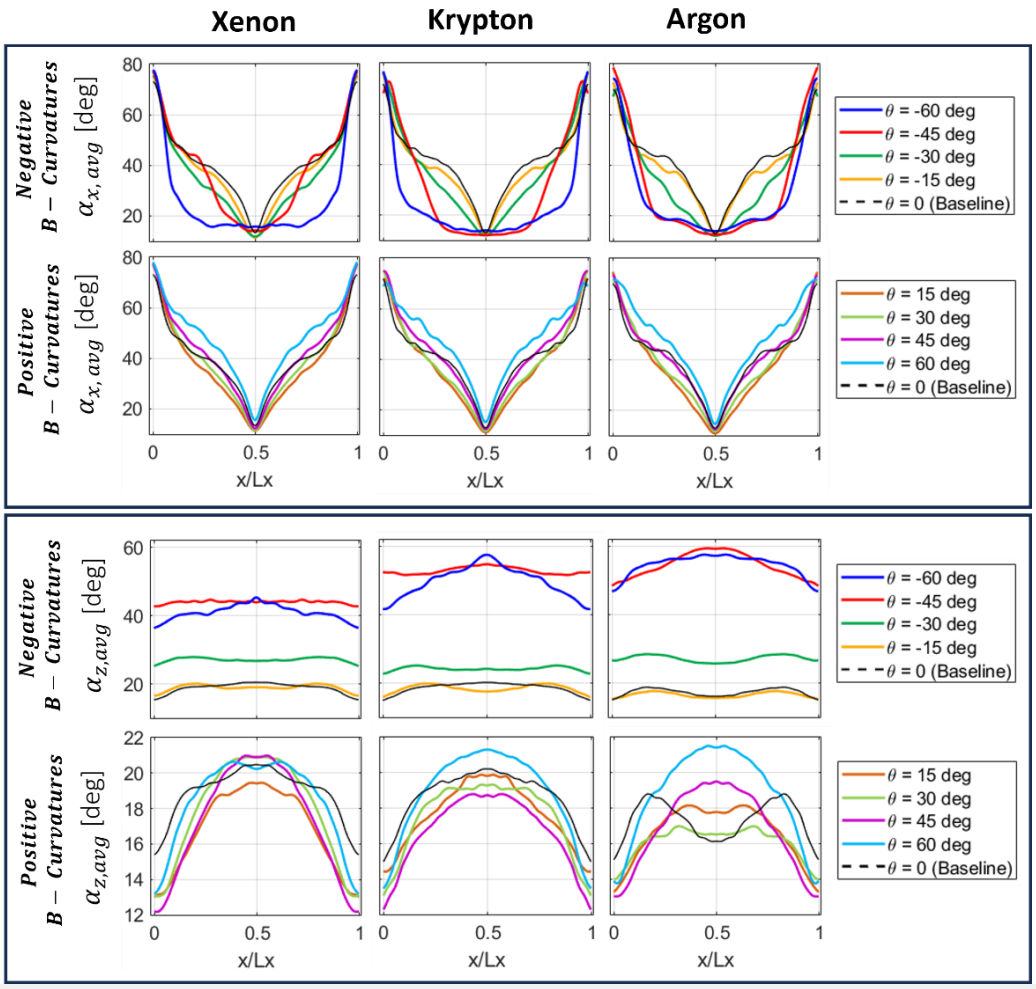


Fig. 4.30: Radial distribution of the azimuthally averaged ion beam divergence angle ($\alpha_{x,avg}$ & $\alpha_{z,avg}$, Eq. 4.2) due to the radial and azimuthal velocity components of the ions for the three propellants with various negative (top row in each panel) and positive (bottom row in each panel) curvatures of magnetic field.

To summarize the observed trends, we have plotted the variations of the mean (over the entire domain's extent) radial ($\alpha_{x,mean}$) and azimuthal ($\alpha_{z,mean}$) divergence angles against θ in **Fig. 4.31**. Similarly to Section 4.2.4, $\alpha_{x,mean}$ and $\alpha_{z,mean}$ serve as representative measures quantifying overall ion beam divergence.

In terms of the radial velocity angle ($\alpha_{x,mean}$), the negative curvature of the field has generally a confining effect, while the positive curvature tends to expand the ion beam. However, the main finding to emphasize is that, at high negative B-field's curvatures ($\theta \leq -45$ degrees), the beam divergence is primarily driven by the azimuthal ion velocity ($\alpha_{x,mean} < \alpha_{z,mean}$). This observation highlights another significance of resolving the azimuthal direction in the Hall thruster simulations, in addition to the well-known impact of the azimuthal instabilities on particles' transport. Specifically, in the absence of azimuthal physics, there is a risk of underestimating the ion beam divergence in the situations of a concave field topology with large degrees of curvature.

Nevertheless, across moderate negative curvatures as well as the entire positive curvature range ($\theta \geq -30$ degrees), the radial ion velocity is noticed to have the dominant influence on the ion beam divergence ($\alpha_{x,mean} > \alpha_{z,mean}$).

Finally, in terms of the correlation between our numerical results above and the experimental observations in the literature, we highlight that the observations of notably increased ion beam divergence for the magnetically shielded Hall thrusters [142][143], which feature rather large positive magnetic field curvatures in their near-plume region, are in line with our findings.

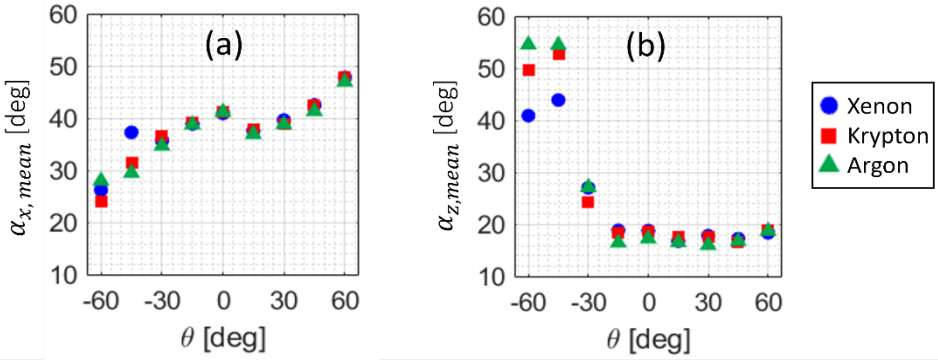


Fig. 4.31: Variation of spatiotemporally averaged (across entire domain and over $20 - 30\ \mu s$) divergence angle vs θ for the three propellants; (left column) divergence angle due to the ions' radial velocity component, (right column) divergence angle due to the ions' azimuthal velocity component.

4.3.5. Magnetic field curvatures representative of magnetically shielded Hall thruster configuration

So far, we have discussed the impact of the B-field curvature, considering an analytical form with a radially uniform radial component (B_x) and a linearly varying axial component (B_y) as given by Eq. 4.5. In this section, we focus on the curved magnetic field configurations representative of "magnetic-shielding" topology. **Fig. 4.32** (a) presents a 2D schematic of the adopted magnetic field topology and the channel cross-sections for which the simulations are performed. Plots (b) to (e) in **Fig. 4.32** show the radial profiles of the radial and axial components of the magnetic field, as well as the radial distributions of the magnetic field intensity (B) and the angle (θ) between the magnetic field lines and the radial coordinate (x) for the two studied magnetic field configurations. Note that in these configurations, the B_x component is not constat across the radial extent of the domain.

Config. 1 features a convex radial profile of B_x, with a magnitude increasing from $B_x = 0$ at the walls to the maximum value of $B_x = 20\ mT$ at the mid radial location. Config. 2 has instead has a concave B_x radial profile, with the maximum B_x occurring at walls and the minimum value of $B_x = 20\ mT$ being at the channel centerline. Config. 1 resembles the cross-sections of magnetically shielded Hall thrusters inside the discharge channel, whereas Config. 2 corresponds to the shielding topology slightly outside the channel and within the "magnetic lens" [50]. From plot (d) in **Fig. 4.32**, it is seen that the gradient in the magnetic field intensity is larger for Config. 2, which is expected to result in a more pronounced magnetic mirror effect due to a larger ∇B force, i.e., the force due to the gradient in the magnetic field pushing electrons away from the walls. In addition, plot (e) shows that, in Config. 1, the magnetic field

lines are parallel to the walls at the radial extremes of the domain, which is expected to result in a notably reduced flux of particles to the walls. Note that the magnetic field in both Config. 1 and Config. 2 has negative curvatures.

All other simulation conditions are kept identical to the baseline case described in Section 3.2.1. The simulations are performed only for xenon propellant as an example.

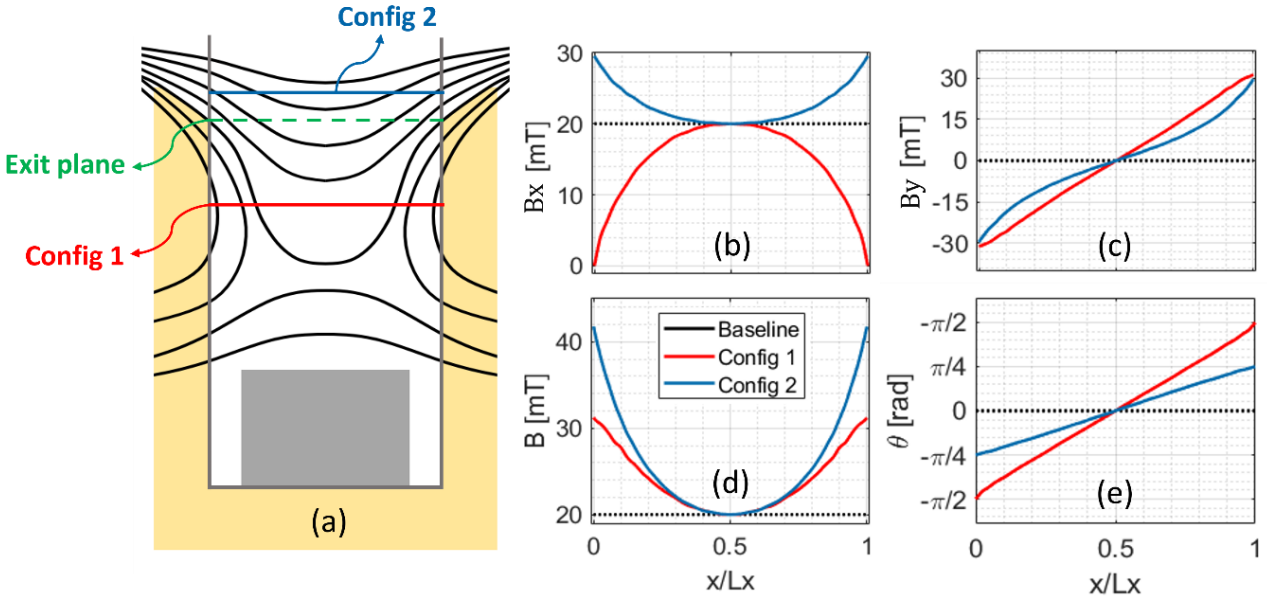


Fig. 4.32: (a) A schematic of the adopted field topology and the cross-sections corresponding to Configs. 1 & 2. (b) to (e) Radial profiles of the studied magnetic field configurations; (b) radial component (B_x), (c) axial component (B_y), (d) field intensity (B), and (e) angle between the tangent to the magnetic field lines and x-axis.

4.3.5.1. Variations in the distribution of the plasma properties

The time-averaged plasma profiles are presented in **Fig. 4.33**. Looking at plot (a) in this figure, it is observed that, for Configs. 1 and 2, n_i is much higher in the center of the domain compared to the baseline. This is expected outcome of the confining effect of the negative curvature of the B-field and is consistent with the trends observed in Section 4.3.1 (**Fig. 4.19**). The significant concentration of plasma density towards the center in Config. 2 is the result of effective confinement of the plasma due to the large ∇B force in this case.

Referring to plot (b), we notice that T_e in Config. 1 is relatively high similar to the baseline configuration, while in Config. 2, T_e is notably lower compared to the baseline. As will be shown later, the notably lower T_e for Config. 2 is due to the severe mitigation of the ECDI in this magnetic field configuration, which would have otherwise caused significant electron heating particularly in the azimuthal direction.

Moreover, from plots (d) and (e), it is evident that in Config. 1, $T_{ex}/T_{ez} > 1$ and J_{ey} displays the double-peak profile with the peaks occurring away from the centerline. These two characteristics suggest the dominance of the MTSI in this configuration. In Config. 2, however, $T_{ex}/T_{ez} \approx 1$ and the profile of J_{ey} is concentrated near the center, indicating that the MTSI is suppressed in this case. As the

ECDI is mitigated in Config. 2, the convex shape of the J_{ey} profile is due to the presence of the long-λ mode (refer to Section 4.3.5.2).

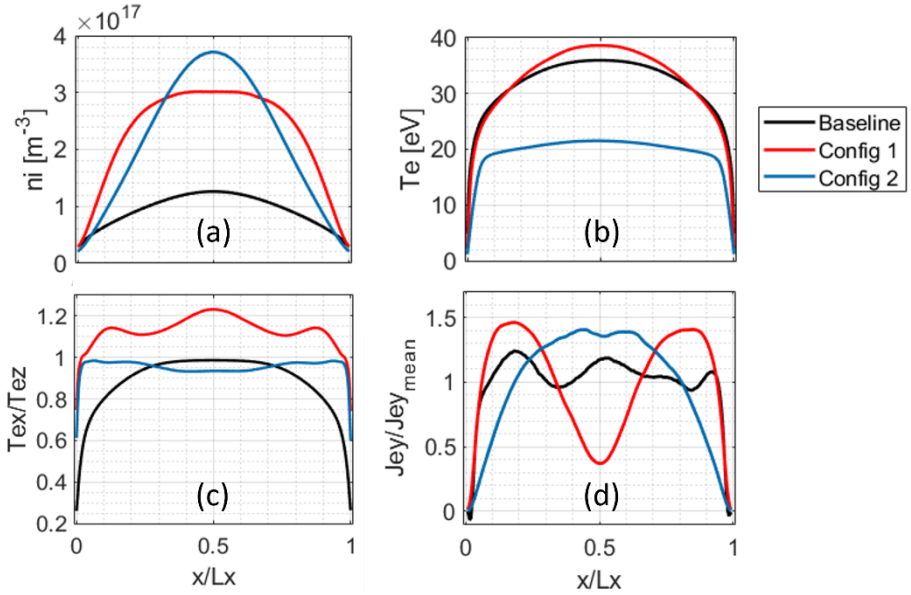


Fig. 4.33: Radial profiles of plasma properties averaged over all azimuthal locations and over the time interval of $20 - 30\ \mu s$ for xenon propellant with various magnetic field configurations; (a) ion number density (n_i), (b) electron temperature (T_e), (c) radial-to-azimuthal electron temperature ratio (T_{ex}/T_{ez}), and (d) normalized axial electron current density ($J_{ey}/J_{ey,mean}$).

Fig. 4.34 (left panel) illustrates the evolution of the 2D distribution of the electron axial current density (J_{ey}) at four different instants over one period of the discharge cycle (T).

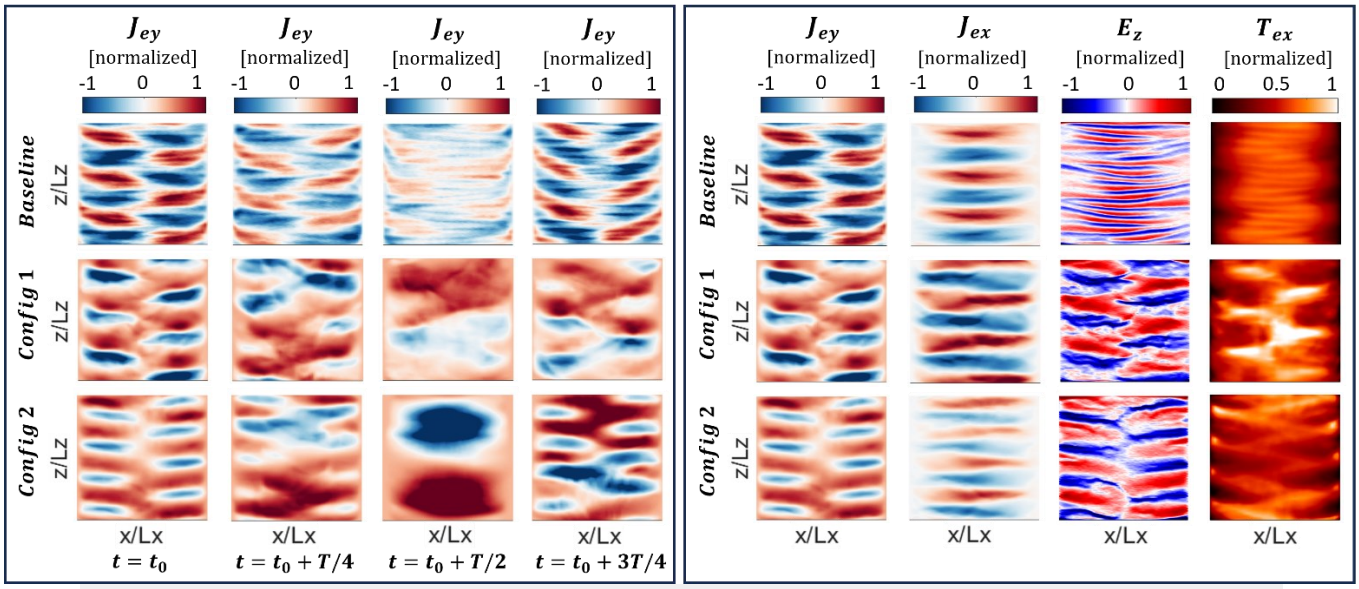


Fig. 4.34: (Left panel) 2D snapshots of the normalized axial electron current density (J_{ey}) at four different moments through the discharge evolution cycle for different magnetic field Configs. T represents the period of the cycle, which is different for each Config. **(Right panel)** 2D snapshots of the normalized plasma properties at a time of local maximum of the spatially averaged T_{ex} for xenon propellant with various magnetic field Configs. The columns, from left to right, represent the axial and radial electron current densities (J_{ey} and J_{ex}), the azimuthal electric field (E_z), the radial electron temperature (T_{ex}), and electron number density (n_e).

At $t = t_0$, the MTSI-like structures are dominant in all field configurations. This instability gradually mitigates at $t_0 + T/4$, until at $t_0 + T/2$, in Configs.1 and 2, the long-wavelength structure becomes eventually dominant, while in the baseline case, the ECDI takes over. Finally, the MTSI becomes fully formed and dominant again at $t = t_0 + T$, and the cycle repeats.

Moreover, **Fig. 4.34** (right panel) presents the 2D snapshots of various plasma properties at an instance of time when the MTSI-like structures are fully formed (corresponding to the local maximum of spatially averaged T_{ex}). The 2D snapshots for Configs. 1 and 2 show notably different structures with respect to each other and also compared to baseline configuration.

4.3.5.2. Variations in the characteristics of the azimuthal instabilities and the electrons' mobility

The azimuthal wavenumber (k_z) and the frequency spectra of the azimuthal instabilities are presented in **Fig. 4.35** for various B-Config simulations. Referring to this figure, we first notice that the ECDI mode is strongly suppressed in Configs. 1 and 2. For Config. 1, the first and second harmonics of the MTSI are observed, with the first harmonic occurring at the same k_z/k_0 and frequency as those for baseline case. For Config. 2, the first MTSI's harmonic is observed with a small amplitude, but it is slightly shifted to shorter wavelengths compared to the baseline and Config. 1. The frequency of the first MTSI's harmonic for Config. 2 is the same as that for the baseline and Config. 1, i.e., $1.2\ MHz$.

Additionally, in **Fig. 4.35** (a), we notice that for Config. 1 and 2, the long-λ mode at $k_z/k_0 \approx 0.07$ appears which constitutes the dominant mode in Config. 2. The long-λ mode is easily distinguished also in the frequency spectrum of Config. 2 in **Fig. 4.35** (c), at the frequency of $0.9\ MHz$. It is worth highlighting that the dominance of the MTSI and long-λ mode in Config. 1 and Config. 2 is in line with our observed trends in the instabilities' spectrum in the presence of large negative B-filed curvatures ($\theta \leq -45$ degrees) from **Fig. 4.24** and **Fig. 4.25**.

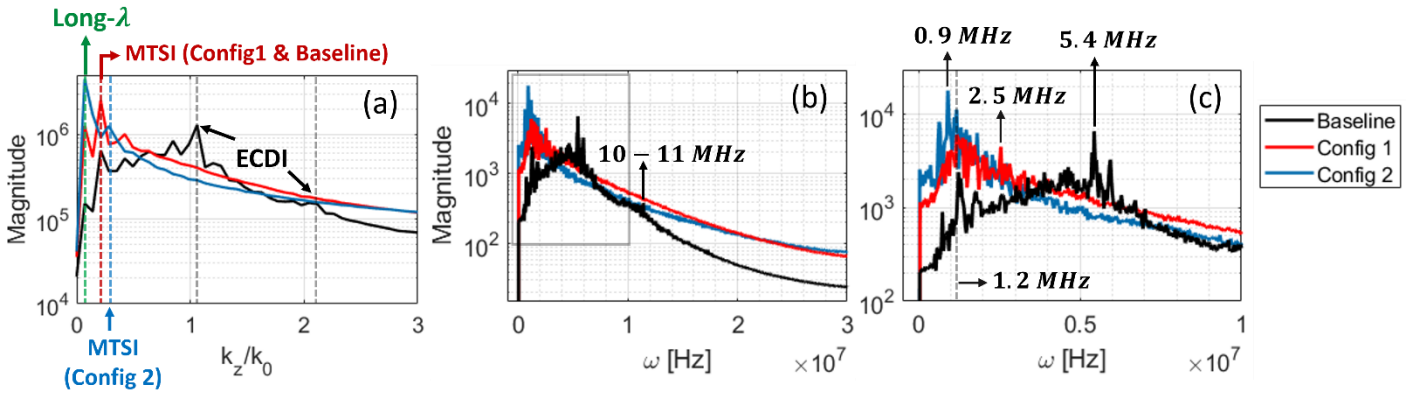


Fig. 4.35: (a) Azimuthal wavenumber spectra of instabilities obtained from average spatial FFTs, (b) frequency spectra of instabilities obtained from average temporal FFTs of the azimuthal electric field signal from simulations with various magnetic field configurations for xenon propellants. Plot (c) displays a zoom-in view of plot (b) over $0 - 10MHz$ frequency rage. In plot (a), k_0 represents the ECDI's fundamental wavenumber ($k_0 = \frac{\omega_{ce}}{V_{d_e}}$).

Moreover, as seen in the evolution plots in Appendix A.5.4, the MTSI and the long-λ mode in Config. 2 periodically exchange energy, which results in a cyclic and growth and damping of these two instabilities similar to what is observed for case with $\theta = -60$ degrees.

In Appendix A.5.3, the numerical $\omega - k_z$ dispersion maps of the azimuthal instabilities are provided. Although the $\omega - k_z$ spectrum in Config 2 is concentrated near the long-λ mode, the spectrum in Config. 1 is spread over wider ranges of ω and k_z.

We now assess the *axial* and *cross-field* mobility of the electrons. It should be noted that, in the baseline configuration, the magnetic field is purely radial and, thus, the axial and cross-field mobilities are equivalent. This is not the case in Configs. 1 and 2 due to the curvature of the field lines. The time-averaged electrons' *axial* mobility (μ_y), whose radial distribution for the three magnetic configurations is shown in **Fig. 4.36** (b), is obtained using the time-averaged axial electrons' velocity (v_{ey}) and the (constant) axial electric field (E_y) as given by Eq. 4.6. The time-averaged electrons' *cross-field* mobility ($\mu_\perp$), whose radial profile is seen in **Fig. 4.36** (c), is calculated using Eq. 4.7 to Eq. 4.9 and according to the schematic illustrated in **Fig. 4.36** (a).

$$\mu_y = \left|\frac{v_{ey}}{E_{ey}}\right|, \qquad \text{Eq. 4.6}$$

$$v_{e\perp} = \left|v_{ey}\cos\theta\right| + \left|v_{ex}\sin\theta\right|, \qquad \text{Eq. 4.7}$$

$$E_\perp = \left|E_y\cos\theta\right| + \left|E_x\sin\theta\right|, \qquad \text{Eq. 4.8}$$

$$\mu_\perp = \frac{v_{e\perp}}{E_{e\perp}}. \qquad \text{Eq. 4.9}$$

In the above equations, $v_{e\perp}$ is the electrons' cross-field velocity, v_{ex} is the electrons' radial velocity, $E_\perp$ is the magnitude of the electric field vector perpendicular to the magnetic field line at each radial location, E_x is the radial electric field component, and θ is the angle between the x-axis and the tangent to the magnetic field line.

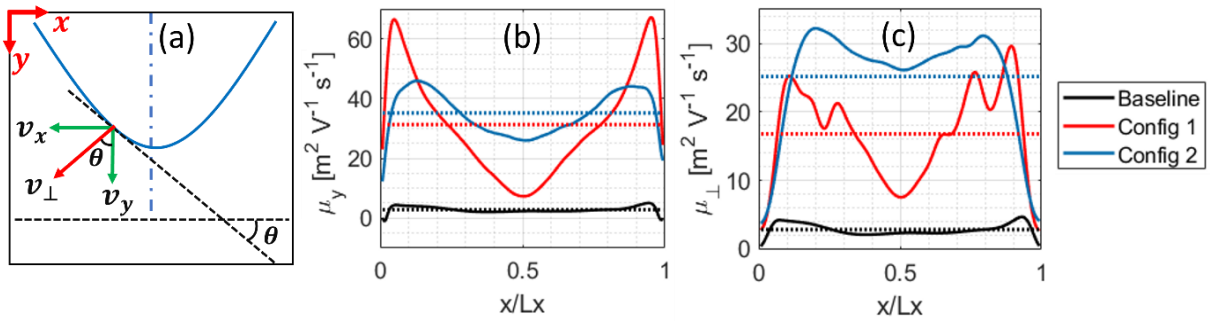


Fig. 4.36: (a) Schematic associated with the calculation of the cross-field velocity, where the blue curve represents the magnetic field line. Radial profiles of (b) average electrons' axial mobility, and (c) average electrons' cross-field mobility over all azimuthal locations and over the time interval of $20 - 30\ \mu s$ for xenon propellant with various magnetic field configurations. In plots (b) & (c), the dotted lines represent the radially averaged mobilities in the respective case.

It is observed in **Fig. 4.36** (b) that the radially averaged electrons' axial mobility is the highest for Config. 2, followed by that for Config. 1, which are both much higher than the that in the baseline case. The radial profile of μ_y for Config. 1 shows sharp increases toward the walls, which is due to the fact that the magnetic field lines in this configuration are parallel to axial direction near the walls (**Fig. 4.32** (e)). Hence, it is also of interest to look at the electrons' cross-field mobility ($\mu_\perp$) in **Fig. 4.36** (c). As it

was expected, the rise in the mobility profile near the walls for Config. 2 is now less significant, and the mean $\mu_\perp$ for Config. 2 is more distinctly higher than that for Config. 1.

4.3.5.3. Variations in particles' distribution functions and the ion beam divergence

To conclude the discussions in this section, we look at the normalized radial and azimuthal velocity distribution functions (VDFs) for the electrons and the ions shown in **Fig. 4.37**. It is observed from plot (a) that, unlike the baseline configuration, where the tail of the electrons' radial velocity distribution function is lost, the confinement of the plasma in Configs. 1 and 2 has led to the retainment of the tail of the EVDFs. Moreover, the EVDFs for Config. 1 span across broader ranges of velocities, which is consistent with the higher electron temperature observed for this configuration in **Fig. 4.33**.

Concerning the ions' velocity distribution functions, we notice, from the radial IVDF (plot (c)), that the distributions increasingly deviate from a Maxwellian from baseline to Config. 1 and Config. 2. Indeed, for Configs. 1 and 2, the IVDFs are depleted in the mid-velocity range, with the depletion being more significant for Config. 2. The azimuthal IVDFs for Configs. 1 and 2 (plot (d)) show a considerable broadening, which is again more pronounced for Config. 2. The broadening of the IVDFs, particularly for Config. 2, suggest a strong interaction between the ions and the long-λ waves, which seems to have caused a redistribution of the ions' energy from the radial direction to the azimuthal one.

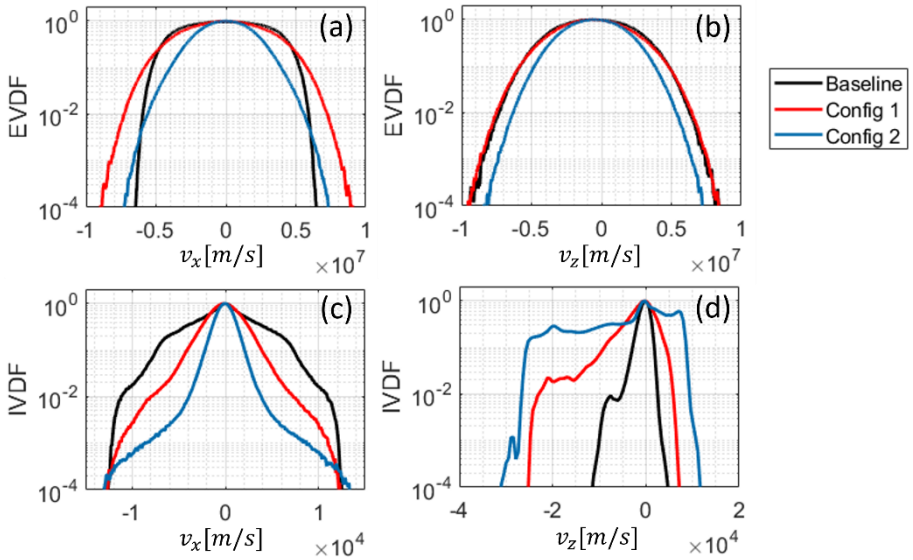


Fig. 4.37: Normalized radial and azimuthal particles' velocity distribution functions (VDF) for xenon propellant with various magnetic field configurations at $t = 30\ \mu s$. **Top row**: electrons' VDF along (a) the radial (x) and (b) the azimuthal (y) direction; **Bottom row**: ions' VDF function along (a) the radial and (b) the azimuthal direction.

Finally, the divergence-angle distribution functions, Γ_x and Γ_z, as well the radial distribution of the ion beam divergence angles, $\alpha_{x,avg}$ and $\alpha_{z,avg}$, are presented in **Fig. 4.38**. The negative curvatures of the B-field in Config 1 and 2 has significantly reduced the radial expansion of the ion beam (α_x), as seen in plots (a) and (c). This indicates the confining effect of these configurations on the ions. Nevertheless, plots (b) and (d) show that in Config 2, the presence of the long-λ mode remarkably increased ions' azimuthal swirling angle (α_z), thereby, leading to large divergence of the ion beam. Config 1, however,

does not exhibit significant change in α_z angle of the ions compared to the baseline configuration, thus yielding an overall reduction in the divergence of ion flow.

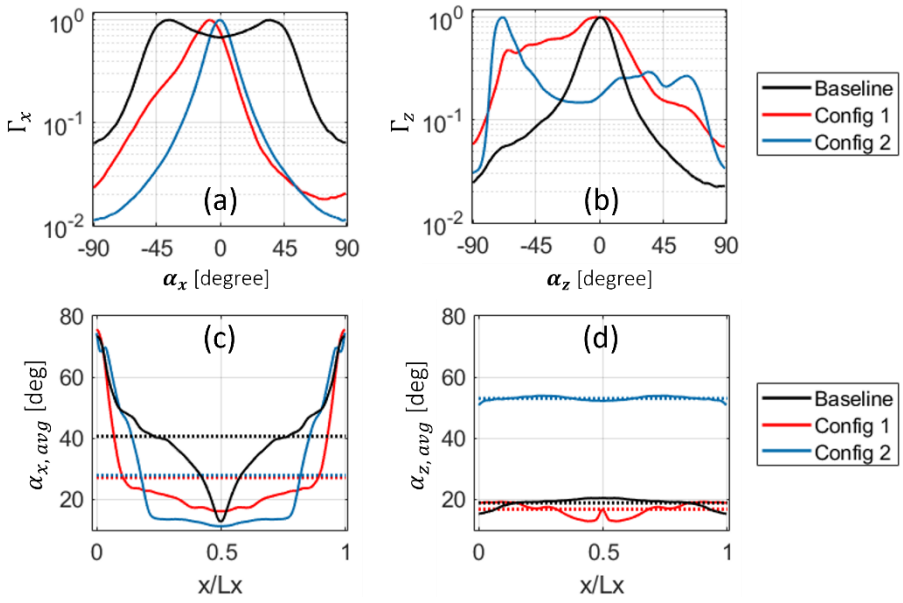


Fig. 4.38: Top row: spatially averaged (over entire domain) divergence-angle distribution functions due to (a) the radial and (b) the azimuthal velocity components of the ions; **Bottom row**: Radial distribution of the azimuthally averaged ion beam divergence angles due to (a) the radial and (b) the azimuthal velocity components of the ions for xenon propellant with various magnetic field configurations. The dotted lines in plots (b) & (c) represents the radially averaged values of divergence angles, $\alpha_{x,mean}$ & $\alpha_{z,mean}$.

4.4. Effects of the presence of secondary electron emission

The interactions between the ECDI and the secondary electrons emitted from the walls, together with their combined roles in "anomalous" cross-field transport of electrons, have been studied in Ref [7]. From their kinetic PIC simulations, the authors showed that, in the presence of high Secondary Electron Emission (SEE) rates, the "beam-plasma" instability is excited which induces very large axial electron currents. In Ref. [144], the effects of SEE on the sheath characteristics and the electrons' transport was investigated by performing a wide-range parametric study. The authors observed that increasing the SEE yield coefficient from 0 to 1 enhances the near-wall cross-field mobility of the electrons by a factor of 2 while decreasing the mobility in the bulk due to the cooling effect of secondary emitted electrons [144]. The results of Ref. [144] complemented prior investigations of the role of SEE in the electrons' dynamics and mobility in $\mathrm{E} \times \mathrm{B}$ configurations [145]-[148] by extending the analyses to a 2D radial-azimuthal configuration. In addition, in Ref. [149] the authors used a cylindrical 2D radial-azimuthal simulation and showed that an enhancement of the electron cross-field mobility can occur due the presence of a high-frequency sheath instability in the Space-Charge-Saturated (SCS) regime.

All the simulations results presented so far were with the assumption of neglecting the secondary electron emission (SEE) from the walls. In this section, we discuss the impact of the SEE on the main plasma properties and the instabilities in the radial-azimuthal simulations. Accordingly, for the simulations in this section, the electrons' radial boundary condition is different from the baseline setup.

Here the SEE from the walls is accounted for using a linear model described in Section 1.4.2.2. A linear SEE model provides a rather simple estimate of the SEE yield coefficient (γ) according to Eq. 1.43 which is rewritten below for convenience

$$\gamma(\epsilon) = \min\left(\gamma_{max}, \gamma_0 + \frac{\epsilon}{\epsilon^*}(1-\gamma_0)\right). \qquad \text{Eq. 4.10}$$

In the above equation, ϵ is the primary electron energy, γ_{max} is the maximum electron emission coefficient, γ_0 is the probability of attachment, and ϵ^* is the crossover energy, i.e., the energy at which the SEE yield coefficient is equal to 1. For these studies, we have kept the values of γ_{max} and γ_0 constant and equal to their corresponding values for Boron Nitride, which are $\gamma_{max} = 2.9$ and $\gamma_0 = 0.578$. However, the value of ϵ^* is varied over a broad range, from $5\,eV$ to $35\,eV$. Modifying the crossover energy values corresponds to changing the slope of the linear part of the $\gamma(\epsilon)$ as illustrated in **Fig. 4.39**.

The secondary emitted electrons are sampled from a Maxwellian at the assumed temperature of $2\,eV$. The simulations are conducted with xenon as propellant.

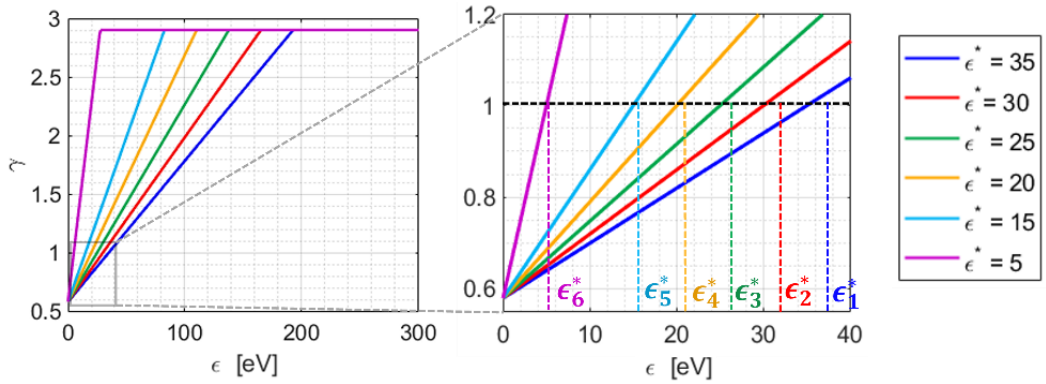


Fig. 4.39: Variation of the secondary electron emission yield (γ) vs the electron energy (ϵ) for various ϵ^* values according to the linear SEE model (Eq. 4.10).

4.4.1. Variations in the distribution of the plasma properties

From plots (a) and (b) in **Fig. 4.40**, it is noticed that decreasing the value of ϵ^* results in a consistent increase in the time-averaged ion number density and a decrease in the time-averaged electron temperature. In this regard, the higher emission rate of relatively cold secondary electrons reduces the T_e. This, in turn, reduces the radial flux of the particles lost to the wall, hence, increasing the ion number density in the bulk. Furthermore, plot (c) indicates that the presence of secondary electrons significantly increases the temperature anisotropy (relative to case with No SEE). Variation of the T_{ex}/T_{ez} ratio with ϵ^* is non-monotonic. The T_{ex}/T_{ez} ratio is higher in the presence of higher SEE rates ($\epsilon^* \leq 15\ eV$) compared to cases with lower SEE rates ($\epsilon^* \geq 20\ eV$).

The presence of SEE also substantially changes the profile of electrons' axial current density (plot (d)). In cases with low SEE rates ($\epsilon^* \geq 25\ eV$), J_{ey} is mainly concentrated near the center as opposed to the case with no SEE, where current density is spread across a more extended portion of the domain. Whereas the cases with high SEE rates ($\epsilon^* \leq 20\ eV$), the strong near-wall conductivity induces significant axial electron current, leading to the peaks in the J_{ey} profiles adjacent to the walls.

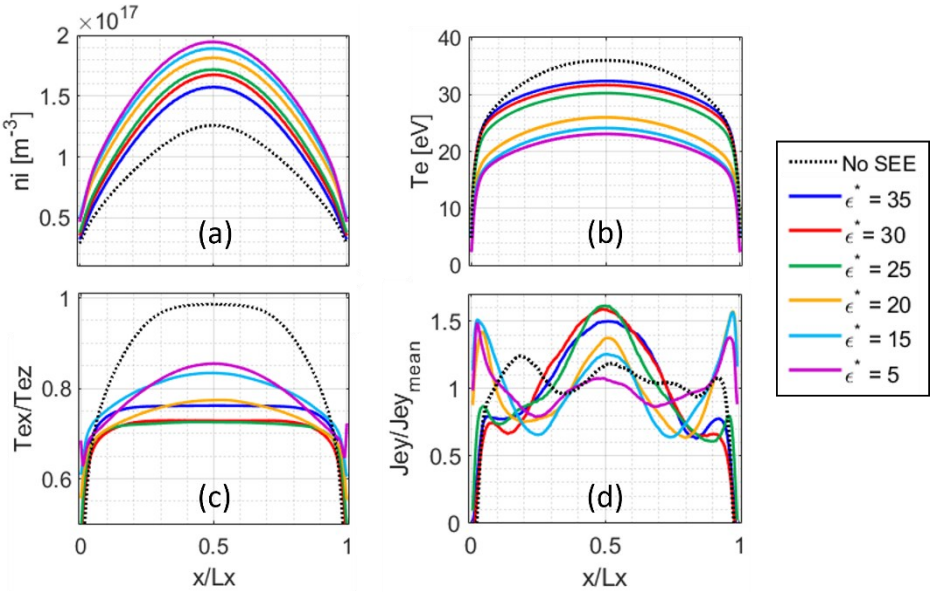


Fig. 4.40: Radial profiles of plasma properties averaged over all azimuthal locations and over the time interval of $20 - 30\ \mu s$ for xenon propellant with various SEE's ϵ^* values; (a) ion number density (n_i), (b) electron temperature (T_e), (c) radial-to-azimuthal electron temperature ratio (T_{ex}/T_{ez}), and (d) normalized axial electron current density ($J_{ey}/J_{ey,mean}$).

Fig. 4.41 presents the 2D snapshots of plasma properties for various ϵ^* values at a time of the local maximum of the spatially averaged T_{ex}, coinciding with the peak strength of the MTSI-like patterns.

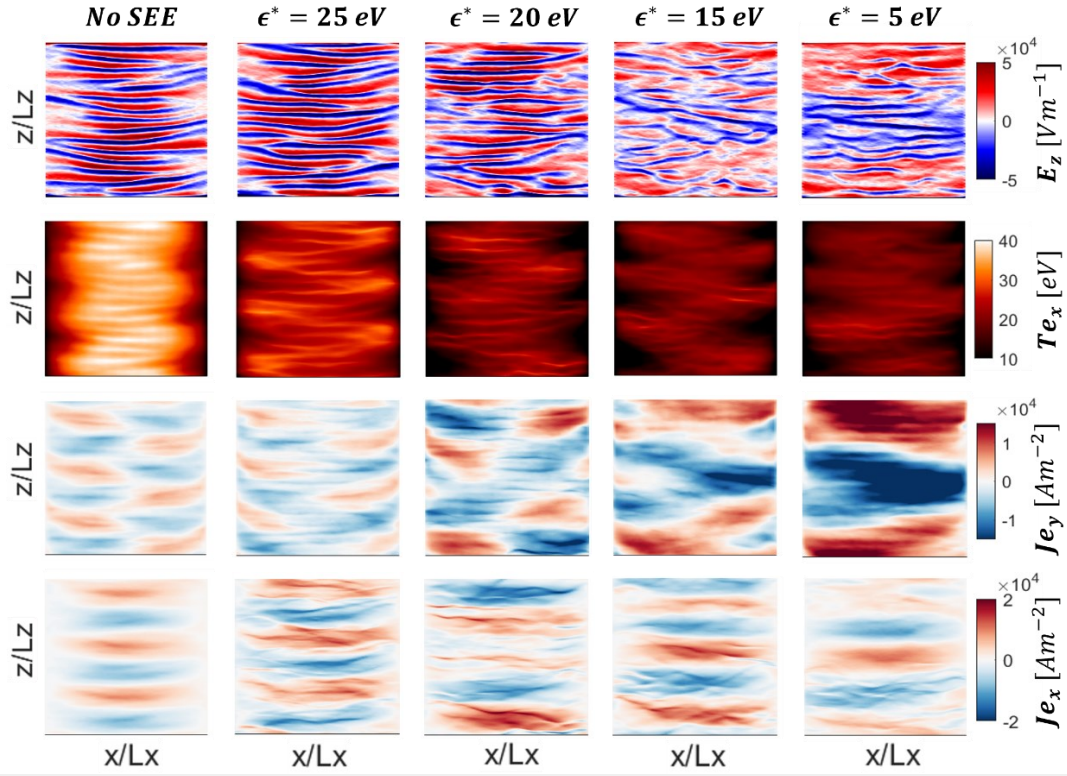


Fig. 4.41: 2D snapshots of the normalized plasma properties at a time of local maximum of the spatially averaged T_{ex} for xenon propellant with various SEE's ϵ^* values. The columns, from top to bottom, represent the azimuthal electric field (E_z), the radial electron temperature (T_{ex}) and the axial and radial electron current densities (J_{ey} and J_{ex}).

It is evident that when the SEE is taken into account and as the value of ϵ^* is reduced from $25\ eV$ to $5\ eV$, the 2D plasma distributions become increasingly different. In particular, an increasing cooling effect is clearly visible in the 2D snapshots of T_{ex} when the SEE rate becomes more and more significant. Furthermore, the long-wavelength instability mode is seen to become dominant for ϵ^* values of 5 and $15\ eV$. In this respect, we observe especially from the plots of E_z and J_{ey} in **Fig. 4.41** that, by decreasing ϵ^*, the 2D distributions change from those of the No-SEE case with dominant MTSI modes to those of the ϵ^* = 5 eV where the coherent structures corresponding to the long-λ mode appeared.

4.4.2. Variations in of the characteristics of the azimuthal instabilities and the electrons' mobility

To analyze more closely the characteristics of the observed wave modes in **Fig. 4.41**, we refer to **Fig. 4.42** which represent, the average spatial and temporal FFTs of the azimuthal electric field fluctuations. From these figures, it is evident that for ϵ^* values of 20 to $35\ eV$, the first harmonics of the ECDI and MTSI are clearly present with the ECDI being strongest. However, at $\epsilon^* = 15$ and $5\ eV$, the long-λ wave is the dominant mode with a frequency of about $1 - 1.3\ MHz$. This instability maintains an almost constant amplitude throughout the discharge as observed in the k_z evolution plots provided in Appendix A.5.4. In addition, in the case with $\epsilon^* = 5\ eV$, the MTSI is strongly damped, and the ECDI mode is not distinctly visible in the FFT spectra. In this case, the ECDI does not appear as a single dominant mode but seems to be present as a spectrum of modes around $k_z/k_0 \approx 1$ in plot (a) and $\omega \approx 5\ MHz$ in plot (c).

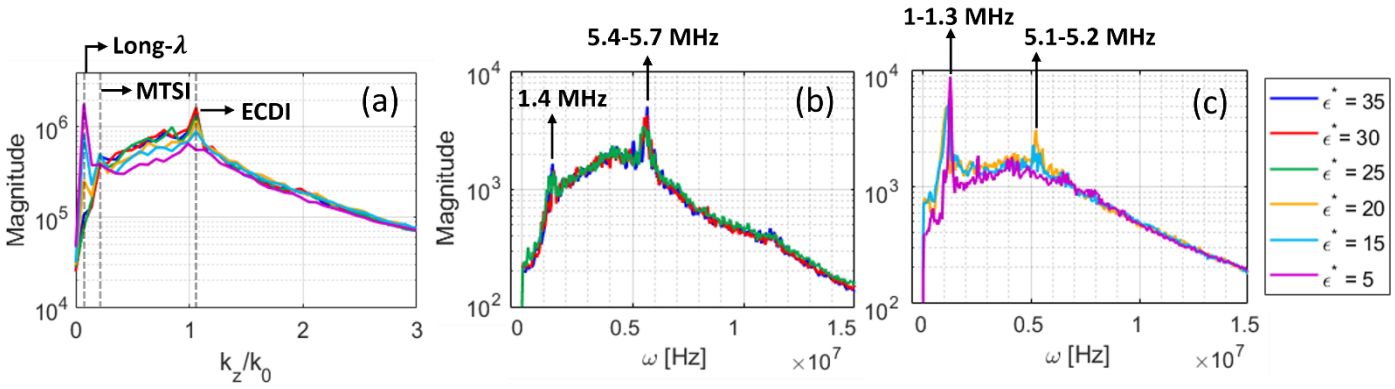


Fig. 4.42: (a) Azimuthal wavenumber spectra of instabilities obtained from average spatial FFTs, and (b) & (c) frequency spectra of instabilities obtained from average temporal FFTs of the azimuthal electric field signal from simulations with various SEE's ϵ^* values for xenon propellants. In plot (a), k_0 represents the ECDI's fundamental wavenumber ($k_0 = \frac{\omega_{ce}}{V_{d_e}}$).

The comparison between the $\omega - k_z$ dispersion plots of the azimuthal waves from various ϵ^* simulations and the theoretical dispersion relations of the Ion Acoustic Instability (IAI) in Appendix A.5.3 revealed that, for $\epsilon^* \geq 25$, the linear dispersion of the ion sound waves can be well fitted to the instability' dispersion maps. However, for $\epsilon^* \leq 20$, the numerical dispersions increasingly deviate from the IAI's dispersion relation. In particular, for the case of $\epsilon^* = 5\ eV$, the dispersion plot is characterized by a broadband spectrum around the frequency and wavenumber of the ECDI with a few distinct modes aligned at an angle with respect to the linear IAI's dispersion.

The spatiotemporal average values of the electrons' axial mobility over the entire domain (μ_y) and over the central portion of the domain away from the walls ($\mu_{y,center}$) for various ϵ^* cases are presented **Fig. 4.43** (a). The absence of the MTSI and the smeared ECDI modes at $\epsilon^* = 5\ eV$ are seen to have resulted in a reduction in the electrons' axial mobility, contrary to the overall trend of the μ with ϵ^* beyond this point. In fact, as ϵ^* is reduced, the total mobility and the mobility in the center of the domain increase. It is also noticed in **Fig. 4.43** (a) that as ϵ^* is reduced, the difference between μ_y and $\mu_{y,center}$ becomes larger, indicating the enhanced role of the near-wall conductivity due to the increasingly higher SEE rate, as presented in **Fig. 4.43** (b).

It is also interesting to note from **Fig. 4.43** (b) that, at $\epsilon^* = 5\ eV$, the time-averaged SEE rate (γ) is only slightly below 1, meaning that on average for every primary electron impacting the walls, one secondary electron is emitted. As the ϵ^* is increased to $15\ eV$, γ is stabilized at about the critical SEE yield value for xenon ($\gamma_{cr} = 0.985$), which corresponds to a space-charge saturated sheath (refer to Section 1.1.2). Increasing ϵ^* further leads to a monotonic decrease in γ.

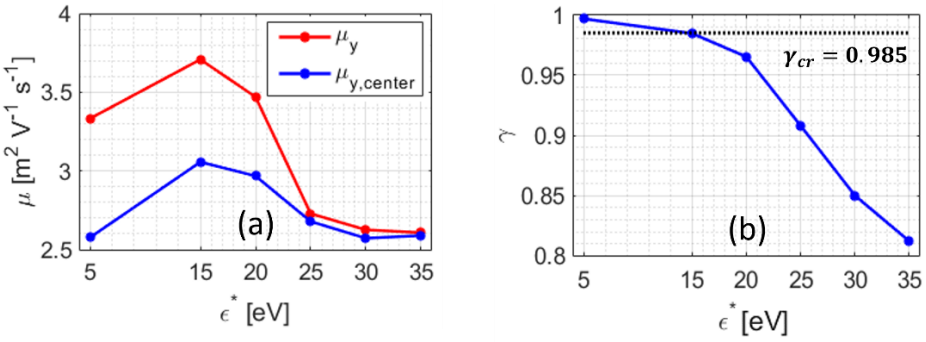


Fig. 4.43: Variation of (a) spatiotemporally averaged electrons' axial mobility (over $20 - 30\ \mu s$ and over entire domain (μ_y) and over the central portion of the domain with $\frac{x}{L_x} \in [0.2, 0.8]$ ($\mu_{y,center}$)), and (b) average SEE yield γ (across entire extents of both inner and outer walls and over $20 - 30\ \mu s$) vs SEE's ϵ^* values.

4.5. Effects of plasma number density

We have observed from the simulation results discussed so far that variation in virtually any discharge parameter will change the steady-state plasma density established within the system. Thus, it is of interest to isolate the impact of plasma number density (n_i), by varying n_i or, equivalently, the axial ion current density, as a separate parameter. Since the simulations feature a fixed imposed ionization source, as described in Section 3.2.1, the plasma density is controlled by the peak value (S) of this source profile. Accordingly, we performed several simulations for xenon propellant, varying the nominal peak of the ionization source, S_0, by a factor β ranging from $\frac{1}{32}$ to 6. In each simulation case, the initial plasma number density ($n_{i,0}$) is scaled by the respective factor β, while the computational cell sizes (Δx and Δz) and the timestep are adjusted by scaling them with a factor of $1/\sqrt{\beta}$.

4.5.1. Variations in the distribution of the plasma properties

The time-averaged radial distributions of the plasma properties are provided in **Fig. 4.44**. Plot (a) in this figure shows that, as the peak of the ionization source (S) is increased, the peak of n_i increases

from approximately 6×10^{15} to $8 \times 10^{17} m^{-3}$. The elevation of the ion (plasma) density results in development of higher intensity waves and consequently stronger wave-particle interactions. This will in turn cause more significant heating of the plasma by instability and, thus, increasingly higher electron temperatures. This trend is clearly observed in T_e profiles in plot (b).

The temperature ratio (T_{ex}/T_{ez}), shown in plot (c), demonstrates a non-monotonic behavior with S_0. T_{ex}/T_{ez} is highest in the cases with $S_0/32 < S \leq S_0/4$, while it is closer to unity for $S \geq S_0/2$ and $S = S_0/32$. Additionally, the J_{ey} profile exhibit notable concentration near the walls for $S < S_0$, whereas it is more uniformly distributed across the domain for $S \geq S_0$. In line with our previous observations, the trends in T_{ex}/T_{ez} and the J_{ey} profile are corelated with the dominant instability modes in each density condition, as will be discussed in Section 4.5.2 through the analysis of the instabilities' spectra.

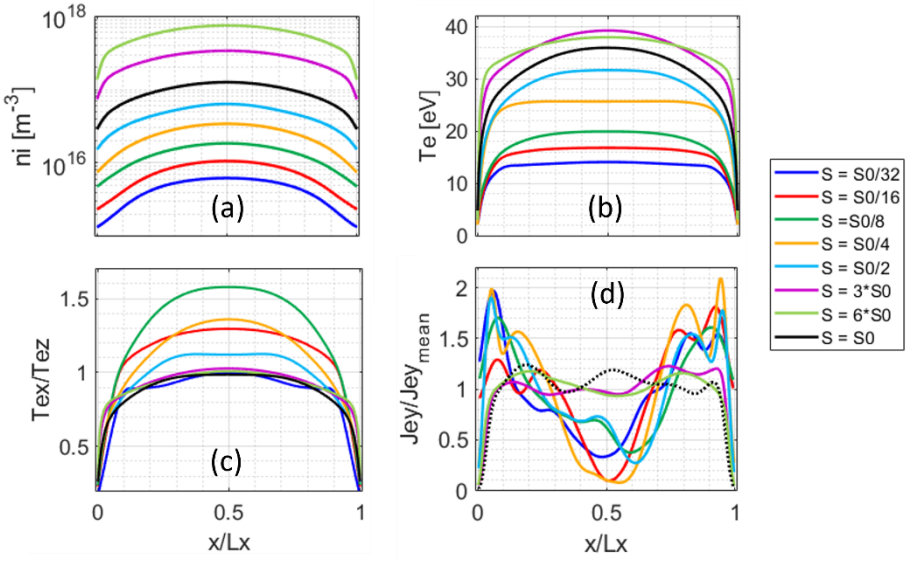


Fig. 4.44: Radial profiles of plasma properties averaged over all azimuthal locations and over the time interval of $20 - 30\ \mu s$ for xenon propellant with various ionization source peak intensities (S); (a) ion number density (n_i), (b) electron temperature (T_e), (c) radial-to-azimuthal electron temperature ratio (T_{ex}/T_{ez}), and (d) normalized axial electron current density ($J_{ey}/J_{ey,mean}$).

In **Fig. 4.45**, we have compared the 2D snapshots of various plasma properties through one evolution cycle of the discharge from the simulations corresponding to low and high plasma-number-density limits, namely, $S = S_0/16$ and $S = S_0/8$ vs $S = 3S_0$ and $S = 6S_0$. We notice that, in the low number density cases ($S = S_0/16$ & $S_0/8$), only MTSI-like structures are present. As the discharge evolves in one cycle, the first harmonic of the MTSI becomes dominant at $t = t_0 + T/4$, followed by the dominance of the second harmonic at $t = t_0 + T/2$.

In the high number density limit ($S = 3S_0$ & $6S_0$), the 2D plasma distributions are dominated by the long-wavelength mode superimposed on a spectrum of shorter wavelength ECDI and MTSI waves with lower amplitudes. The long-λ mode is seen to be always dominantly present, but its amplitude slightly varies over the discharge's evolution cycle.

The development of the long-λ mode at S = $3S_0$ case, where the plasma number density is in the same range of plasma density established in other simulation conditions featuring this instability (such

SEE level corresponding to $\epsilon^* = 5\ eV$ (Section 4.4), presence of high degree of B-field curvature with $\theta = -45$ and -60 degrees, and also at very low magnetic field intensity of $B_x = 5\ mT$), suggests that the formation of the long-λ mode mode is primarily driven by high plasma number density. Nevertheless, it is pointed out that the exact azimuthal wave content is case-dependent and varies depending on all plasma conditions.

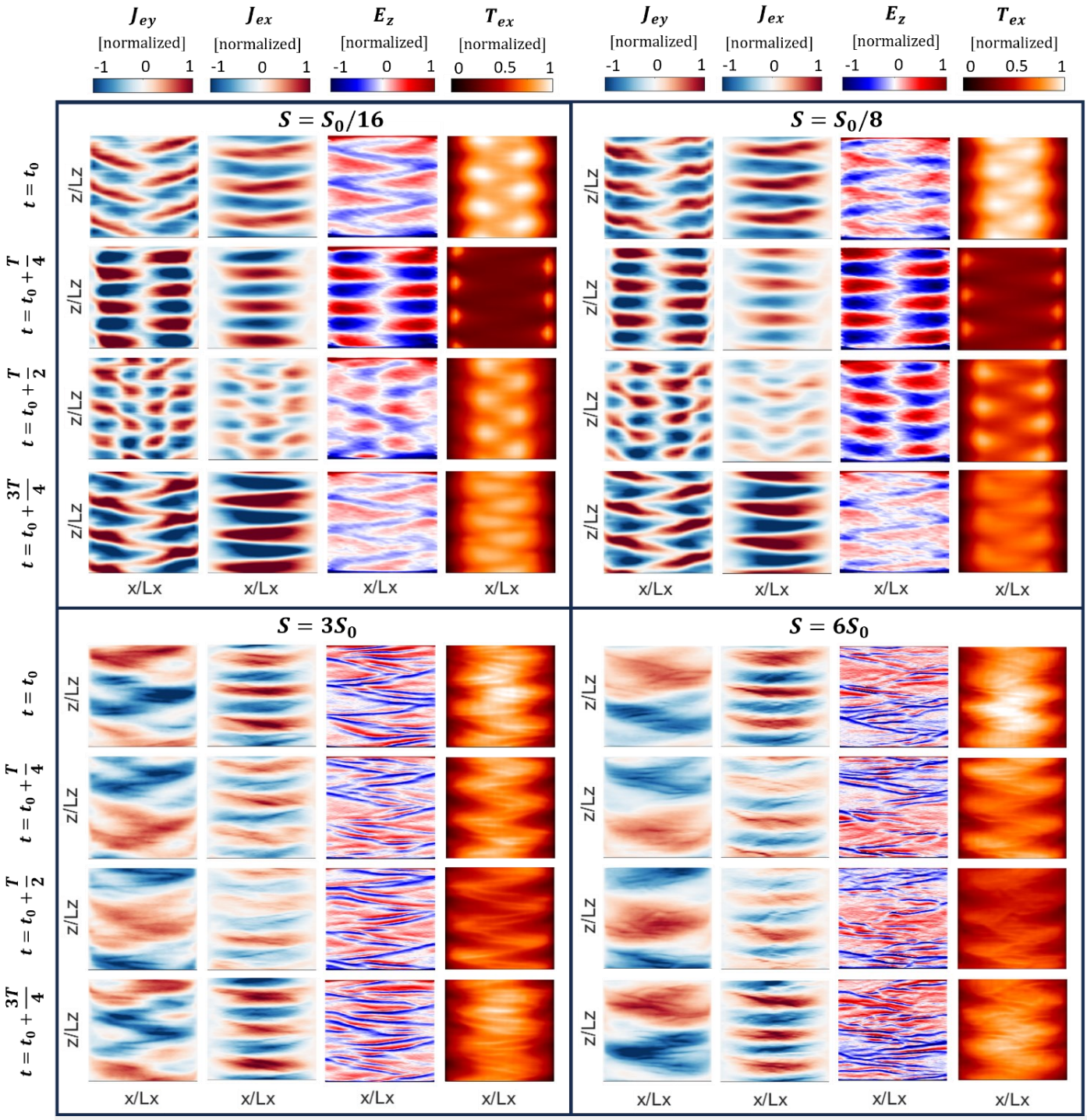


Fig. 4.45: 2D snapshots of the normalized plasma properties at four different moments through the discharge evolution cycle for xenon propellant with four different ionization source peak intensities (S). The columns, from left to right, represent the axial and radial electron current densities (J_{ey} and J_{ex}), the azimuthal electric field (E_z), the radial electron temperature (T_{ex}), and electron number density (n_e).

4.5.2. Variations in of the characteristics of the azimuthal instabilities and the electrons' cross field transport

The azimuthal wavenumber and the frequency spectra of the instabilities presented in **Fig. 4.46** clearly show that the azimuthal wave contents, and the overall magnitudes of the excited wave modes are remarkably affected by the plasma number density. From the instabilities' spectra, we can distinguish three distinct plasma regimes depending on the plasma number density, or the value of S.

In the first regime ($S_0/32 < S \leq S_0/4$), the ECDI is suppressed whereas the first and second harmonics of the MTSI establish as the dominant modes. At $S = S_0/4$, the ECDI exist but at much smaller amplitude compared to the MTSI.

In the second regime ($S_0/2 \leq S \leq S_0$), the MTSI's first harmonic along with the ECDI exist with comparable amplitudes. At $S = S_0/2$, the second harmonic of the MTSI is present with a notable intensity.

In the third regime ($S \geq 3S_0$), the ECDI mode is not observed as a single mode but rather as a continuous spectrum over a broad range of wavenumbers. Moreover, the long-λ mode and the first harmonic of the MTSI are distinctly visible with strong intensities.

Finally, at $S = S_0/32$, the long-λ mode together with the MTSI develop within the simulation with similar amplitude.

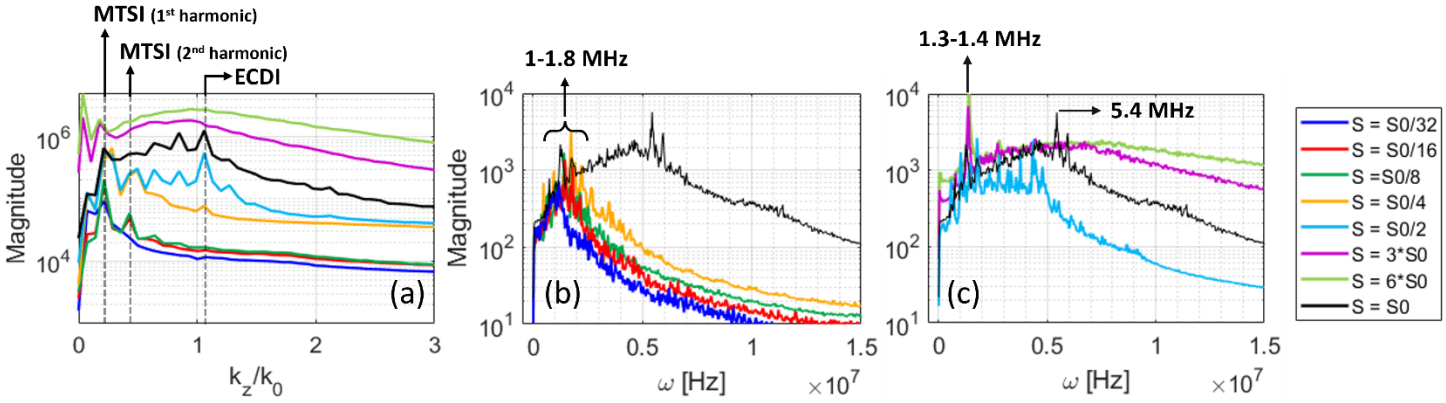


Fig. 4.46: (a) Azimuthal wavenumber spectra of instabilities obtained from average spatial FFTs, (b) & (c) frequency spectra of instabilities obtained from average temporal FFTs of the azimuthal electric field signal from simulations with various ionization source peak intensities (S) for xenon propellants. In plot (a), k_0 represents the ECDI's fundamental wavenumber ($k_0 = \frac{\omega_{ce}}{V_{d_e}}$).

These different regimes are also reflected in the relative values of the spatiotemporal average of the T_{ex}/T_{ez} ratio across simulated range of densities. Indeed, as depicted in **Fig. 4.47** (a), the temperature anisotropy ratios for different operating densities show a separation into three distinct clusters corresponding to the three mentioned regimes.

As a separate note regarding the instabilities' dispersion, it is highlighted that the plots provided in Appendix A.5.3 demonstrate that the numerical dispersion maps of the azimuthal waves for $S \geq S_0/4$ are somewhat in line with the linear projection of the IAI's dispersion relation.

Moving on to the effect of the plasma number density on the electrons' axial mobility, it is observed in **Fig. 4.47** (b), that the electrons' mobility rises monotonically with the plasma density. This is an expected behavior as the FFT plots in **Fig. 4.46** already indicated that the overall intensity of the excited wave modes increases with the plasma number density and so does their induced electron mobility.

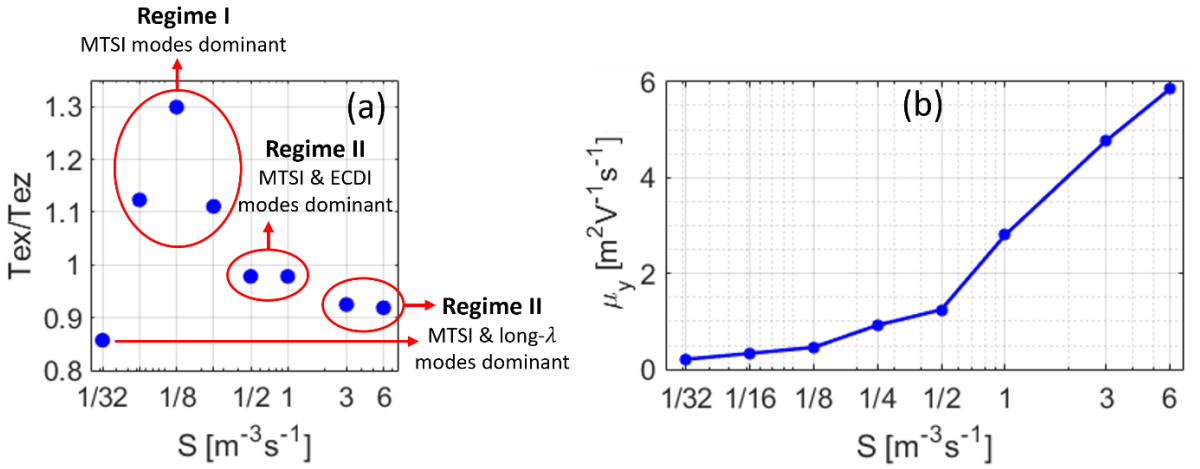


Fig. 4.47: Variation of spatiotemporally averaged (across entire domain and over $20 - 30\ \mu s$) values of (a) radial-to-azimuthal electron temperature ratio (T_{ex}/T_{ez}), and (b) electrons' axial mobility (μ_y) vs ionization source peak intensity (S).

Finally, to isolate the contribution of the instabilities to the electrons' axial transport, we plotted the radial distribution of the time-average force terms in the electrons' azimuthal momentum equation (Eq. 4.1) in **Fig. 4.48**. Consistent with our observation from the J_{ey} profiles in **Fig. 4.44** (d), the profile of the F_E term, representing the instabilities' transport contribution, exhibits peak values near the walls for $S \leq S_0/2$, indicative of the MTSI's transport pattern.

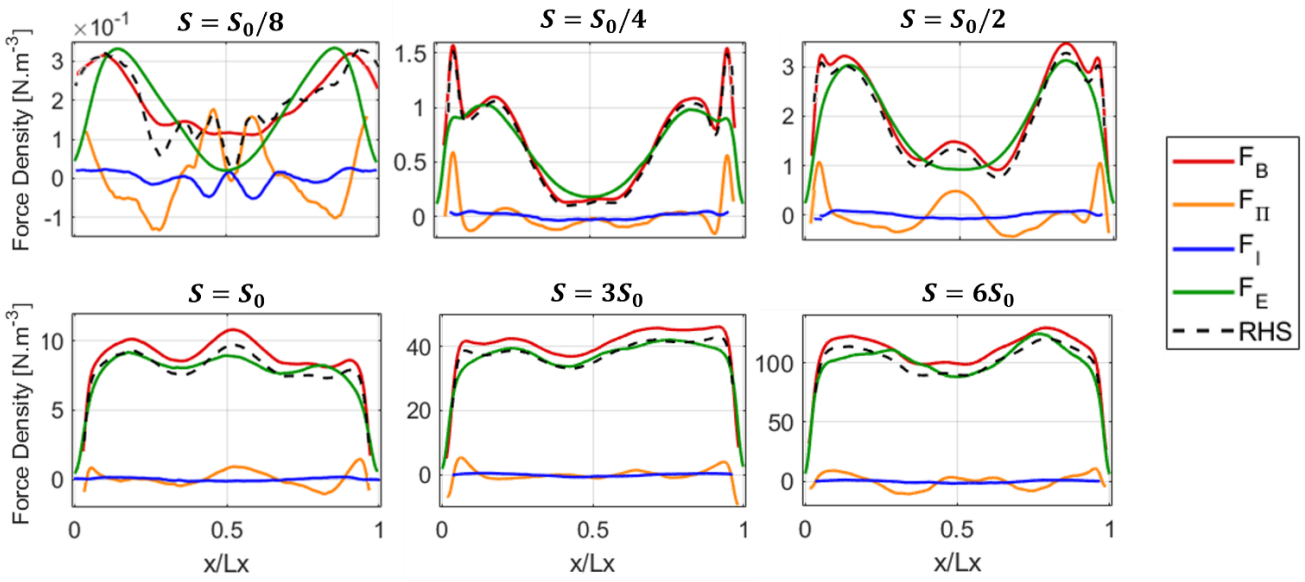


Fig. 4.48: Radial profiles of the transport terms in Eq. 4.1 for xenon propellant with various ionization source peak intensity (S). The force terms are averaged over $20 - 30\ \mu s$. F_B is the magnetic force, F_Π is the viscous effects, F_I is the convective inertia force, F_E is the electric force term, and RHS represents the sum F_Π, F_I and F_E . F_t (temporal inertia) contribution was almost zero, and it is thus not displayed.

Additionally, for $S > 1$, the more uniform F_E profile results from the combined effects of the MTSI and the long-λ mode as well as the broadband azimuthal waves. Indeed, the transport induced by the long-λ mode and the azimuthal waves is predominantly focused around the center. This, along with the high concentration of the MTSI's transport away from the center, leads to a more evenly distributed F_E profile.

Another interesting point to note is that, at low densities ($S \leq S_0/2$), the relative magnitudes of the viscus pressure term (F_Π) is large enough to tangibly influence the overall transport profile (F_B or RHS term). At higher densities, despite the larger absolute values of F_Π term, F_E term dominates the overall transport due to the presence of stronger waves.

4.5.3. Variations in particles' distribution functions

The normalized particles' velocity distribution functions along the radial and azimuthal directions are provided in **Fig. 4.49**. From the plot (a), we observe that, as the plasma density increases, the radial EVDF is increasingly broadened and progressively transitions toward a Maxwellian. The azimuthal EVDFs (plot (b)) show an increase in heating of the electrons along the azimuth for higher densities.

Furthermore, the broadening of the radial and azimuthal IVDFs, in plots (c) and (d), indicate the heating of the ion population along both directions. This heating is most significant along the azimuthal direction for the cases with $S = 3S_0$ and $6S_0$, where the long-λ mode develops and becomes dominant.

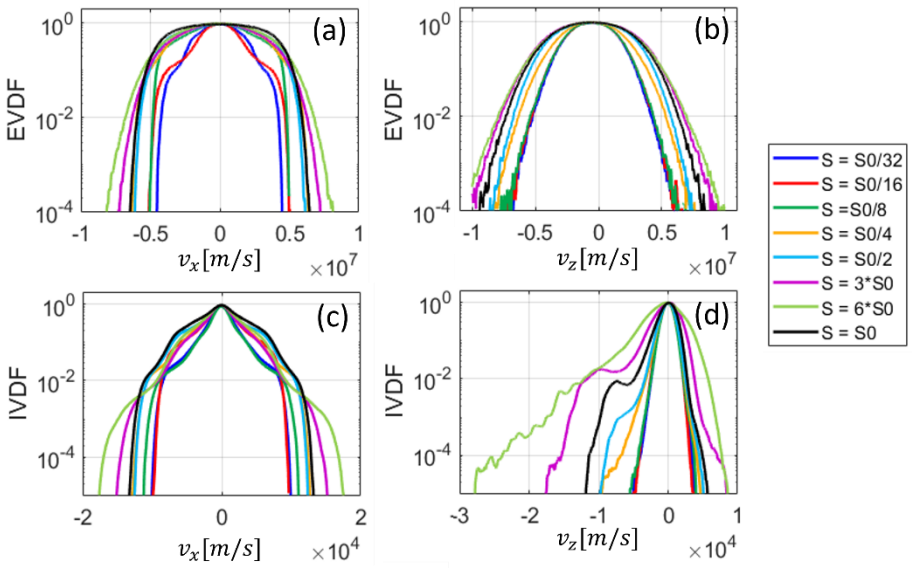


Fig. 4.49: Normalized radial and azimuthal particles' velocity distribution functions (VDF) for xenon propellant with various ionization source peak intensities (S) at $t = 30\ \mu s$. **Top row**: electrons' VDF along (a) the radial (x) and (b) the azimuthal (y) direction; **Bottom row**: ions' VDF along (a) the radial and (b) the azimuthal direction.

4.6. Conclusion

The global dynamics of plasma discharge and, hence, the performance of the $\mathrm{E} \times \mathrm{B}$ devices are driven by the intricate interactions among the underlying plasma phenomena including instabilities and turbulent mechanisms. Nonetheless, as evidenced throughout this chapter, the underlying plasma processes in the $\mathrm{E} \times \mathrm{B}$ discharges, including instabilities and their consequent impacts, exhibit a

multifaceted and highly coupled nature whose exact characteristics are very dependent on the operating condition and physical parameters of the system. Additionally, it is important to note that, in a Hall thruster, the magnetic field intensity varies along the axial direction. Moreover, during the thruster operation, the plasma discharge undergoes a back-and-forth motion over a beathing cycle, causing variation in the electric field at a given radial-azimuthal cross section of the channel [10][116]. The findings from this chapter indicate that these variations notably alter the underlying instability mechanisms at each axial location, influencing in turn the significance and/or the characteristics of the instability-induced heating and transport of the plasma species. Consequently, these changes can impact the device's performance, global stability, and operational lifespan.

Therefore, extensive parametric studies over a broad parameter space of plasma conditions are necessary to untangle the role of each individual physical factor and/or mechanism on path to gain a comprehensive understanding of the plasma phenomena, and thereby the global response of the plasma discharge. However, comprehensive characterization of these parametric dependencies, are, on one hand, hindered by the significant computational cost of conventional high-fidelity particle-in-cell (PIC) codes. On the other hand, experimental efforts have been limited by aspects such as probes' accessibility within often constrained geometries of $\mathrm{E} \times \mathrm{B}$ devices, the spatial and temporal resolution of the measurements as well as noise, the sensitivity of the sensors to plasma conditions and environmental interactions and potentially intrusive nature of the diagnostics, and often inability to independently control individual discharge parameters.

In this regard, we demonstrated in this chapter that the RO-PIC scheme, due to its computational efficiency and its ability of faithfully reproducing the results of conventional multi-dimensional PIC codes, serves as a viable tool enabling extended high-fidelity studies of plasma configurations over wide sets of plasma parameters. To this end we presented numerical insights from the total 70 parameter variations, including various applied electromagnetic field intensities, magnetic field curvatures, SEE rates and plasma densities. Through this parametric investigation we found out that the overall behavior of the discharge is determined by the dominant instabilities in the system.

The effects of each parameter studied in changing the dominant instabilities are summarized below:

A) **Effects of the axial electric field intensity ($\boldsymbol{E_y}$):** we observed that the intensity of E_y delimits two distinct regimes of the plasma behavior for the three studied propellants, characterized by the relative dominance of either the ECDI or the MTSI. In regime I which occurs for relatively low E-fields ($5 \leq E_y \leq 20\ kVm^{-1}$), the MTSI is the dominant instability mode. Regime II is associated with relatively high E-fields ($30 \leq E_y \leq 50\ kVm^{-1}$), where the MTSI becomes mitigated, giving room to the dominance of the ECDI. The intermediate E-fields ($20 < E_y < 30\ kVm^{-1}$) indicate the range of E_y values, at which the transition in the plasma regime occurs.

B) **Effects of the radial magnetic field intensity ($\boldsymbol{B_x}$):** we showed that the variation in the magnitude can also lead to establishment of the two observed regimes across all the studied propellants. In regime I which happens for relatively low B-fields ($5 \leq B_x \leq 10\ mT$), the MTSI mode is absent, and only the ECDI exists. For relatively high B-field values ($25 \leq B_x \leq 30\ mT$) corresponding to regime II, the ECDI was overall observed to be largely mitigated, with the

instabilities' spectra dominated by the MTSI and a long-wavelength wave mode. At moderate values of B-field ($15 \leq B_x \leq 20\ mT$), the MTSI and the ECDI coexist with comparable strengths.

C) **Effects of the magnetic field curvature (θ):** we demonstrated that curvature (concavity or convexity) of the B-field is another parameter that can separate plasma behavior into the two identified regimes. In general, concave field topologies (with negative curvatures, $\theta < 0$) are seen to suppress the ECDI and purely azimuthal instabilities, except for the azimuthal long-λ mode, while promoting the development of the MTSI-like instabilities as the dominant modes.
In contrast, the presence of convex fields (with positive curvatures, $\theta > 0$), generally, impedes the formation the radial-azimuthal instabilities like the MTSI, leaving primarily azimuthal instabilities such as the ECDI as the dominant instabilities. Therefore, concave field conditions correspond to regime I, whereas convex fields are associated with regime II.
Moreover, for a configuration representative of a cross-section of magnetically shielded Hall thrusters inside the discharge channel, we observed that the MTSI plays a dominant role. However, in a configuration indicative of the near-plume of the shielded thrusters, the long-λ mode is seen to grow as the strongest mode.

D) **Effect of the SEE rate (ϵ^*):** we showed that variation in the strength of the SEE phenomenon (determined by the value of crossover energy ϵ^*) changes the azimuthal wave content and the dominant instability modes. The ECDI is progressively suppressed with increasing SEE rate. For relatively low SEE rates ($\epsilon^* \geq 20\ eV$), the ECDI remains the dominant instability. However, in the presence of high SEE rates ($\epsilon^* \leq 15\ eV$), the ECDI is weakened and the long-λ mode becomes the dominant wave mode.

E) **Effect of plasma density (S):** changing the plasma number density (by adjusting the peak of ionization source S) was shown to modify the azimuthal wave content. At low plasma densities ($S_0/32 < S \leq S_0/4$), the ECDI is suppressed and the first and second harmonics of the MTSI were observed to be most prominent. At intermediate density range ($S_0/2 \leq S \leq S_0$), both the ECDI and the MTSI coexist with comparable amplitudes. At high plasma densities ($S \geq 3S_0$), the long-λ mode was noticed to coexist with a broadband spectrum of shorter-wavelength azimuthal wave modes. Additionally, elevated plasma density was seen to translate into stronger azimuthal waves overall, thereby causing more pronounced impacts on plasma including enhanced heating and electrons' cross-field transport.

We observed that each of these instabilities has distinct impacts on plasma, particularly on particles heating and the electrons' cross-field transport. In this regard, the ECDI contributes to the electrons' heating primarily along the azimuthal direction (which leads to $T_{ex} < T_{ez}$ in cases where the ECDI is dominant), whereas the MTSI heats up the electrons mostly in the radial direction (resulting in $T_{ex} > T_{ez}$ when the MTSI is dominant). In addition, the axial electron current induced by the ECDI is mostly focused around the central region of the domain as opposed to that carried by the MTSI, which is mainly concentrated near the walls. As such, we introduced two parameters, namely, the temperature anisotropy, which is defined as spatially average T_{ex}/T_{ez} ratio, and the radial profile of the normalized axial electron current density ($J_{ey}/J_{ey,mean}$), as two indicators for assessing the comparative strength of

the ECDI and the MTSI modes. We verified the consistency of the correlation between these two parameters with the dominance of the ECDI and the MTSI across the investigated parameter space.

Regarding the effect of these instabilities on the ions beam, it is noted that the MTSI primarily increases the ion beam divergence along the radial direction, while the ECDI enhances the spread of ions velocities mainly along the azimuthal direction. As a result, in conditions where the MTSI is strong, the ion beam divergence is attributed to the ions' radial velocity. Conversely, in the presence of the ECDI as the strongest mode, the ion beam divergence is dominated by the ions' azimuthal velocity. The distinct consequences of the MTSI and the ECDI are conjectured to be due to the fact that the MTSI has a radial wavenumber component while the ECDI is purely azimuthal.

The azimuthal long-λ wave mode characterized by an azimuthal wavelength in the range of the domains' azimuthal size and with the frequency of about 1 MHz develops due to an inverse energy cascade from the shorter wavelength instabilities in certain conditions. The long-λ instability found to have remarkable impacts on the plasma including notable electron's cross-field transport and strong interaction with the ions, leading to large ions' azimuthal drift and heating.

In studying the influence of ion mass under varying applied electric and magnetic field intensities and magnetic field curvatures, we found certain changes in the spectra of azimuthal instabilities. As most notable examples, simulation with krypton at $0.5E_0$, where the ECDI was weakened to the extent of being indistinguishable in time-averaged FFT plots. This was not the case for xenon in similar conditions. Also, at $\theta = -15$ degrees, the ECDI is significantly weakened in case of argon, and at $\theta = -15$ degrees, the amplitude of the ECDI gradually mitigates, changing to lighter propellants from xenon to argon. These variations in instabilities' spectra were reflected in the time-averaged plasma properties, such as electron temperature anisotropy and axial current density. The nondimensional characteristics ($\tilde{k}_z = k_z\lambda_{De}, \tilde{\omega} = \omega/\omega_{pi}$ and $\tilde{V}_{ph} = V_{ph}/C_s$) of the MTSI and ECDI showed only minor variations among propellants, since the variations due to the difference in ion mass are being captured within normalizing factors (λ_{De}, ω_{pi} and C_s).

Finally, it is essential to underscore the significance of experimental works in bolstering confidence in the insights provided. These experiments not only validate numerical observations but also offer additional insights derived from real-world devices and settings. However, recognizing the limitations of experiments, a synergistic approach integrating both numerical and experimental works is imperative to provide complementary insights.

Chapter 5 Investigation of the parametric variability of plasma instabilities and turbulence using RO-PIC in an axial-azimuthal plasma configuration

In $E \times B$ plasmas and, in particular, in electric plasma propulsion technologies like Hall thrusters, the global performance and stability of operation vary significantly across their operational envelope. The variability in operation of these devices stems from the inherent dependency of the underlying plasma phenomena and their interactions on the operating conditions. Establishing clear links between the involved plasma processes and the global operation of Hall thrusters requires a comprehensive characterization of these phenomena across the operating parameter space.

*The utility of RO-PIC in wide-ranging parametric investigations is further demonstrated in this chapter by providing insights from nearly **50 high-fidelity Q2D PIC simulations,** exploring the variation of an $E \times B$ plasma discharge in a Hall-thruster-representative axial-azimuthal configuration across various operating conditions. These include different voltages, current densities, magnetic field intensities and axial profiles, and propellant's ion masses.*

For these studies we used the Q2D simulation with an approximation order corresponding to 40 azimuthal regions and 20 axial regions ($N = 20,\ M = 40$), which we showed in Chapter 3 has a computational cost of only about 8 % of a full-2D simulation while capturing faithfully the underlying physics and providing an accurate prediction of plasma profiles.

Numerical parametric studies provide an effective pathway to isolate the effect of different operating parameters on plasma behavior in a more controlled environment of simulation. Additionally, comparison of the results of such parametric sweeps with the theoretical descriptions serve as a viable approach to stress-test the available theories and assess the extent of their validity under broad spectrum of $E \times B$ discharge conditions.

5.1. Description of setup and conditions

The simulations are performed in a setup that largely resembles that of the benchmarking effort in Ref. [58], which was described in detail in Section 3.1.1. The RO-PIC simulations with the domain decomposition corresponding to 40 azimuthal regions (M) and 20 axial regions (N) are used for these

simulations. As verified in Section 3.1.3, IPPL-Q2D code at this specific approximation level of the 2D axial-azimuthal problem, demonstrates a great agreement with the full-2D results (with only $5-10\,\%$ error in the prediction of the plasma profiles), while yielding about 13-fold speedup compared to the full-2D PIC simulation.

Regarding the setup of the problem, we emphasize that it represents a simplification to a real-world Hall thruster in several aspects. First, the ionization is imposed through a fixed injection source rather than being captured self-consistently. As a result, the low frequency discharge oscillations associated with breathing mode (see Section 1.1.3.5) are not represented nor are the focus of this study. Moreover, it is noted that in a real setting, the strength of the ionization and the relative positioning of the ionization zone with respect to the acceleration region changes over a breathing cycle. These variations influence the instantaneous plasma conditions and the high frequency instabilities. Although these effects are not captured within individual simulations, variations across simulations with different operating conditions can cast light on some of these effects. In other words, various conditions established within each simulation can represent the plasma state at different stages during the discharges' breathing cycle. Moreover, the quasi-static nature of the present setup enables effective isolation of various effects.

Second, the collisions are not accounted for; thus, the electrons' classic collisional scattering is absent in the simulations. Additionally, neglecting collisions means that any difference observed in the behavior of various propellants is due to the difference in the ion mass. This is in fact desired in this case since our intention has been to distinguish the direct potential effects of the ion mass from the effects of collision processes (due to the difference in the collision cross sections of different propellants).

Third, because of the absence of some energy loss mechanisms such as ionization and excitation as well as wall losses, the predicted temperatures are expected to be overestimated. Also, given that the simulations do not account for radial direction and wall interactions, the term "exit plane" which is referenced throughout the text and in the captions of the figures merely represents the location of the peak of the magnetic field profile and does not have any physical significance in terms of altering the boundary conditions. Subsequently, the terms inside the "channel" and in the "plume" refer to the axial locations before and after the B-field's peak, respectively. Finally, the near-anode region is not simulated, hence, the magnetic field values are relatively high near the left (anode-side) boundary of the domain.

Through this parametric study we assessed the variations in plasma behavior due to the changes in the operating conditions including the discharge voltage (V), the ion current density (J, which is indicative of mass flow rate), magnetic field intensity (B) with three different propellants namely xenon, krypton, and argon. The effect of axial profile of the magnetic field is additionally investigated. The studied operating parameters are listed in **Table 5.1**. The profiles of ionization sources used for various J simulations and the profiles of magnetic fields for various B intensity simulations are presented in **Fig. 5.1** (a) and (b), respectively.

Case No.	V $[V]$	V/V_0	J $[Am^{-2}]$	J/J_0	B $[mT]$	B/B_0	σ/σ_0	x_p $[cm]$	Propellant
1	100	0.5	400	1	10	1	1	0.75	Xe, Kr, Ar
2	300	1.5	400	1	10	1	1	0.75	Xe, Kr, Ar
3	400	2	400	1	10	1	1	0.75	Xe, Kr, Ar
4	600	3	400	1	10	1	1	0.75	Xe, Kr, Ar
5	200	1	50	0.125	10	1	1	0.75	Xe, Kr, Ar
6	200	1	100	0.25	10	1	1	0.75	Xe, Kr, Ar
7	200	1	200	0.5	10	1	1	0.75	Xe, Kr, Ar
8	200	1	800	2	10	1	1	0.75	Xe, Kr, Ar
9	200	1	400	1	5	0.5	1	0.75	Xe, Kr, Ar
10	200	1	400	1	15	1.5	1	0.75	Xe, Kr, Ar
11	200	1	400	1	20	2	1	0.75	Xe, Kr, Ar
12	200	1	400	1	30	3	1	0.75	Xe, Kr, Ar
13	200	1	400	1	10	1	0.25	0.75	Xe
14	200	1	400	1	10	1	0.5	0.75	Xe
15	200	1	400	1	10	1	2	0.75	Xe
16	200	1	400	1	10	1	Inf	0.75	Xe
17	200	1	400	1	10	1	1	0.5	Xe
18	200	1	400	1	10	1	1	1	Xe
19	200	1	400	1	10	1	1	1.25	Xe
20	200	1	400	1	10	1	1	1.5	Xe

Table 5.1: List of all the simulation cases performed in the axial-azimuthal coordinates; V, J and B are the applied voltage, total ion current density and the radial magnetic field's peak, respectively. Also, σ denotes the standard deviation of the magnetic field's Gaussian profile, and x_p represents the axial location of the magnetic field's peak. $V_0 = 200\ V,\ J_0 = 400\ Am^{-2}$, $B_0 = 10\ mT$, $\sigma_0 = 0.625 \times 10^{-2}$ and $x_{p,0} = 0.75\ cm$ corresponding to the baseline conditions.

The presented parametric studies are aimed to understand: (1) the variations in the macroscopic plasma properties, (2) the changes in the characteristics of the plasma fluctuations, particularly the ion acoustic and the ion transit time instabilities (where present), and the extent to which the available theories in the literature can describe the observed changes, (3) the variations in the electrons' cross-field transport and the significance of the contribution of various momentum terms to this phenomenon, and (4) the changes in the distribution function of the ion species. Even though a direct comparison between the simulations and the available experimental data in the literature is not possible due to the differences in the setup and the operating conditions, we compared instead the observed overall trends of the plasma profiles with the experimental results wherever possible.

All results discussed in the following sections correspond to the quasi-steady state of the system. The simulations reach a quasi-steady state (characterized by almost periodic oscillations) within less than $10\ \mu s$, and the time interval of $20 - 30\ \mu s$ is taken as the window for analysis of the data.

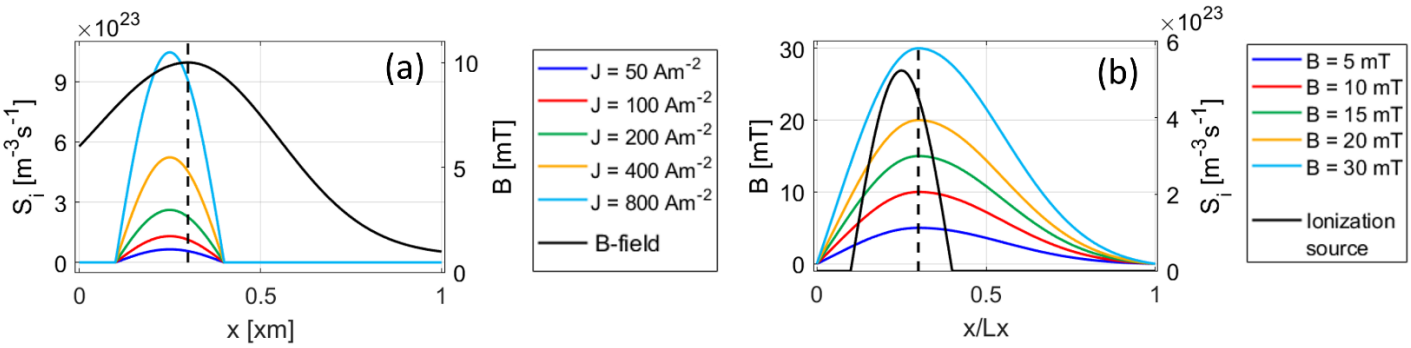


Fig. 5.1: Axial profiles of (a) the imposed ionization source for simulations with various ion current densities (J), (b) the applied radial magnetic field for simulations with various magnetic field peak intensities (B). The baseline magnetic field and ionization source profiles superimposed, respectively, on plots (a) and (b). Dashed black lines represent the location of the magnetic field peak that coincides with the channel exit plane.

5.2. Variations with operating conditions: discharge voltage, ion current density and magnetic field intensity

The studies in this chapter build upon and expand the insights provided by a number of prior works from literature. The physics of the instabilities and the instability-induced electrons' transport has been numerically investigated in 2D Hall-thruster-representative axial-azimuthal configuration in Refs. [18][24][27][28][30][34][58][69][150]- [152]. Among these works, Boeuf and Garrigues [18] and Charoy [27] studied the effects of the peak ion current density on the plasma discharge for xenon propellant in a similar simplified setup, in the presence of the imposed fixed ionization source. Boeuf and Garrigues [18] presented a detailed numerical-theoretical analysis of the Electron Cyclotron Drift Instability (ECDI) and its transition to the Ion Acoustic Instability (IAI). They also observed the development of the Ion Transit Time Instability (ITTI) at the low current densities and argued that this is correlated with the reduced electron transport at these conditions. Charoy [27] expanded the parametric investigation by exploring various magnetic field intensities in addition to different ion current densities in the same problem setup as Ref. [18]. The authors also analyzed the contribution of the force terms in the electrons' azimuthal momentum equation to the electrons' transport across the studied conditions and compared the contribution of the instabilities against the theoretical relation of the enhanced transport via electron-ion friction force proposed by Lafleur et al. in Ref. [120].

Building upon these prior efforts, we have expanded the parametric exploration to encompass a broader parameter space, which also includes variations in ion mass. We have additionally tested the relevant theories of plasma fluctuations, particularly related to IAI, with the numerical observations of the resolved instabilities across the studied parameter space. We highlight that compared to the works by Boeuf and Garrigues [18] and Charoy [27], which have used a cathode boundary condition based on the current-continuity approach, our parametric studies are carried out with a quasi-neutrality cathode condition [refer to Section 1.4.2.2]. This is an important distinction given the reported effects of cathode boundary conditions on axial-azimuthal PIC simulation results [27].

5.2.1. Variations in plasma profiles and currents

Fig. 5.2, **Fig. 5.3** and **Fig. 5.4** show the axial profiles of the time-averaged ion number density (n_i), axial electric field (E_x) and electron temperature (T_e), respectively. We observe that the typical features of an $\mathrm{E} \times \mathrm{B}$ discharge are represented across all operating conditions. These include the occurrence of the maximum number density around the center of the ionization zone (which is defined by the axial extent of the ionization source and highlighted by the grey area in the figures) upstream of the location of the magnetic field's peak (**Fig. 5.2**). **Fig. 5.3** demonstrates that in all operating conditions, the peak of the axial electric field occurs slightly downstream of the magnetic field's peak and the acceleration region (which corresponds to the region of high E_x values) and has an overlap with the ionization zone. A significant portion of the acceleration occurs after the B-field's peak (outside the channel). Additionally, it is noticed from **Fig. 5.4** that the peak of the electron temperature nearly aligns with the peak of the applied magnetic field in all cases.

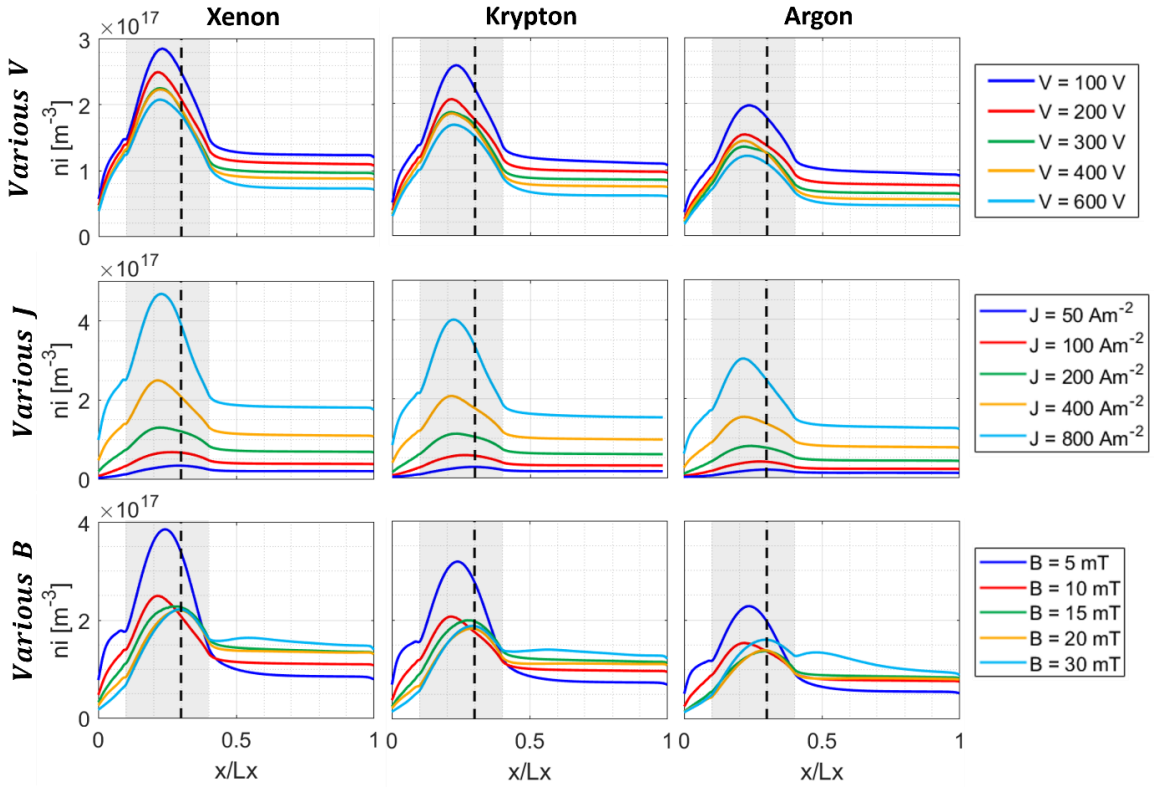


Fig. 5.2: Time-averaged (over $20 - 30\ \mu s$) axial profiles of ion number density (n_i) for the three propellants with various V (top row), various J (middle row), and various B (bottom row). Dashed black lines represent the location of the channel exit plane and grey boxes delimit the position of the ionization source.

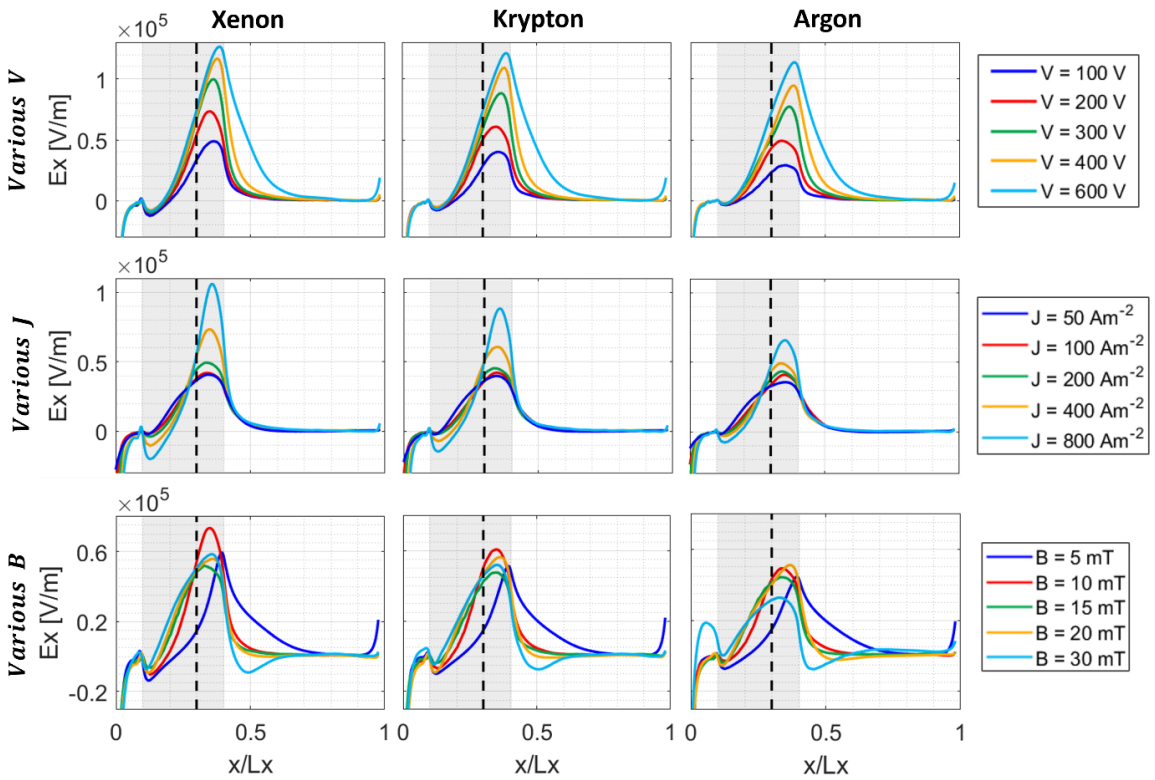


Fig. 5.3: Time-averaged (over $20 - 30\ \mu s$) axial profiles of electric field (E_x) for the three propellants with various V (top row), various J (middle row), and various B (bottom row). Dashed black lines represent the location of the channel exit plane and grey boxes delimit the position of the ionization source.

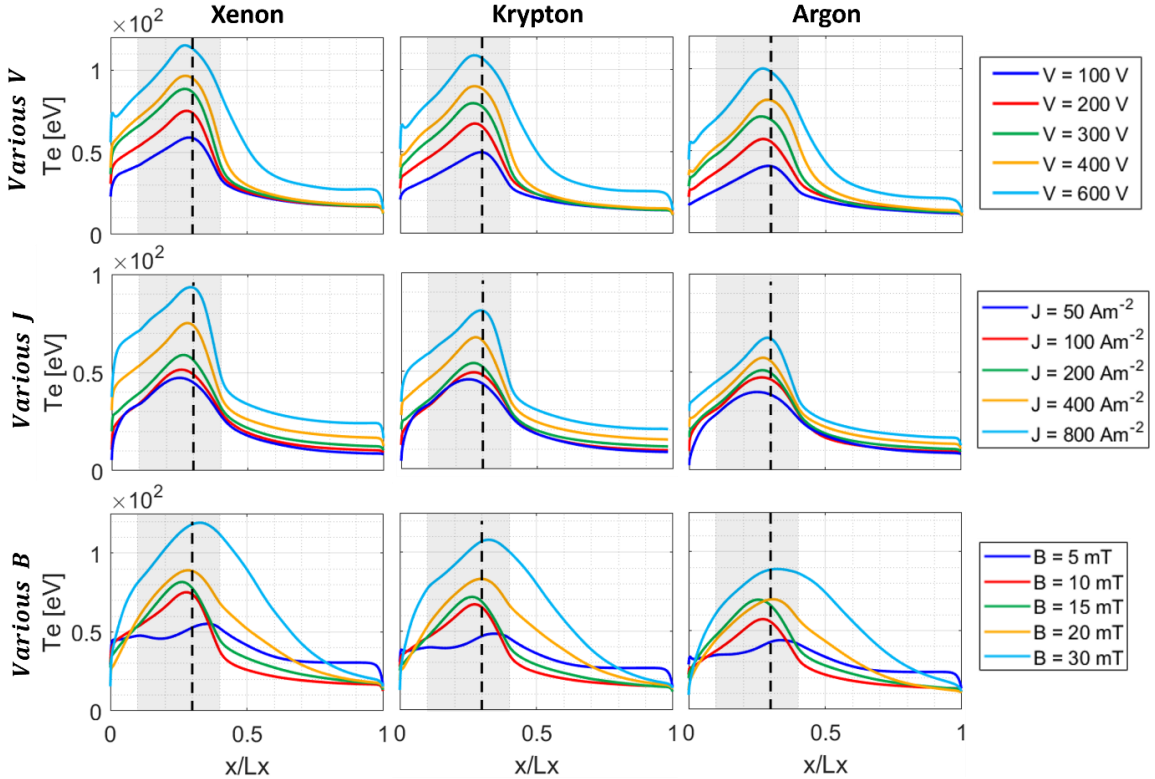


Fig. 5.4: Time-averaged (over $20 - 30\ \mu s$) axial profiles of electron temperature (T_e) for the three propellants with various V (top row), various J (middle row), and various B (bottom row). Dashed black lines represent the location of the channel exit plane and grey boxes delimit the position of the ionization source.

Starting with the variation of the plasma properties with the discharge voltage (V), increasing V from $100\,V$ to $600\,V$ expectedly leads to a consistent increase in the E_x profile, which accelerates ions to higher velocities, thereby causing a monotonic decrease in the overall n_i profile. The rate of the increase of the peak E_x with voltage seems to decrease at high voltages (from $V = 400$ to $600\,V$). This implies the reduced effectiveness of the magnetic barrier in confining the axial motion of the electrons, possibly due to higher electron temperatures (increased electron Larmor radius) at high voltages. In particular, at $V = 600\,V$, the reduced electron confinement is also evidenced by the sudden increase in the electron axial current reaching anode, as will be seen in **Fig. 5.7**. In practice, the magnetic field intensity is typically increased for operation at higher voltages to ensure effective electron confinement.

Moreover, as V increases, the width of acceleration zone (the region of high E_x magnitude) progressively expands and the location the peak of E_x profile shifts downstream. The elevated axial electric fields associated with higher voltages generate a more pronounced Joule heating [4][69], which leads to higher electron temperatures. These trends are similar among various propellants.

Experimental measurements have shown that increasing voltage leads to broadening and upstream shift of the acceleration zone [153]-[155]. Gawron et al. [156], on the other hand, observed that the spatial extent of the electric field decreases when V is increased. In Ref. [155] the authors emphasized that the obtained E_x profile from LIF measurement of ions' axial velocity is quite sensitive to the data postprocessing procedure. Additionally, Ref. [157] argued that the extent of acceleration layer is subject to misinterpretation as it depends on chosen definition of such extent, leading to previous data being erroneously interpreted as broadening of the acceleration region. Accordingly, they observed that in PPSX000 thruster, the width of the acceleration layer remains unchanged with increasing V, while in PPS100 thruster, the acceleration region narrows down when V increases. They, however, observed that the peak of the E_x profile shifts upstream toward the anode, consistent with other measurements [153]-[156]. It is speculated that the upstream movement of the acceleration layer is linked to the increased electron temperatures at higher voltages [157]. At higher temperatures, electrons have a larger Larmor radius, leading to less confinement by the magnetic field. As a result, they penetrate deeper into the magnetic barrier, causing the electric field to shift towards the anode. Ref. [153], on the other hand, hypothesized that the upstream shift of the acceleration zone is because of the narrowing down of the ionization zone due to higher electron temperature at higher voltages.

However, we observed in our simulations that, except for the voltage range between 100 to $200\,V$, the peak of the E_x profile shifts slightly downstream as voltage increases. The variation of the peak E_x with operating conditions can be seen from **Fig. 5.3**, which are also plotted in **Fig. 5.15** (note that here we consider the variation in the axial location of the peak E_x as a measure of upstream/downstream movement of the acceleration region). The opposite trend is most likely due to considering a fixed ionization source. Given that in these simulations the electrons' transport is self-consistently resolved, observing an opposite trend compared to the experiments undermines the less efficient electrons confinement as a plausible explanation for the upstream shift of the peak E_x. Instead, this upstream shift must be attributed to the ionization-related processes.

As for the variations with respect to the imposed ion current density (J), it is noticed that the profiles of n_i and T_e and the peak E_x rise monotonically with increasing J, although at much lower rates at low Js ($J = 50$ to $200\ Am^{-2}$). The increase in E_x peak is the consequence of Generalized Ohm's law [4][49], which suggests a direct relationship between current density and the established electric field. Later in this section, we will show that the axial electron current density consistently increases with J. As will be demonstrated in Sections 5.2.2 and 5.2.4, higher plasma density leads to the development of stronger azimuthal plasma fluctuations, thereby inducing larger axial electron transport. Although the enhanced axial electron mobility (equivalently, larger plasma conductivity and weaker electron confinement by the magnetic field) contributes to the reduction of the established electric field, this reduction does not compensate for the increase in the electrons axial current. Accordingly, the net result of these two opposing factors is the rise in E_x. Furthermore, it is noted that the acceleration region gets narrower as J increases, reducing the overlap between the acceleration and the ionization regions. The variation in the peak E_x across the simulated Js progressively decreases from heavier to lighter propellants (from xenon to argon). The elevated electron temperature at higher Js is attributed to the increased Joule heating as well as enhanced waves particle heating caused by stronger waves.

Most of these observations are consistent with the LIF measurements of Hall thruster plasma which showed that the intensity of E_x increases and the width of the high electric field region tends to become narrower when the anode mass flow rate increases [154][157]. However, Ref. [155] observed no modification of the shape of E_x with the mass flow rate. Regarding the location of the high E_x region, Hargus et al. and Mazouffre et al. [154][157] noticed an upstream movement, while in Ref. [155] a downstream shift of the E_x profile is observed with increasing mass flow rate. Such a non-unique trend might be due to differences in the tested operating conditions. In fact, our simulations show a non-monotonic behavior as well. At lower Js ($J = 50$ to $200\ Am^{-2}$), the peak E_x moves upstream, whereas at higher Js ($J = 200\ to\ 800\ Am^{-2}$), the peak E_x shifts downstream (**Fig. 5.15**, third column).

Across magnetic field peak intensities (B) in the range of 10 to $20\ mT$, the plasma profiles exhibit minor variations. However, the cases with the lowest and the highest magnetic field peak values show different behaviors. At $B = 5\ mT$, the density peak is much higher compared to the other cases. Also, the acceleration region is widened and shifted further downstream resulting in a lower overlap with the ionization region. This, in turn, causes the ions introduced into the domain in the ionization region to experience a larger portion of the potential drop, leading to their acceleration to higher velocities on average and consequently lower ion densities in the plume. The observed behavior in this case is most likely due to weaker azimuthal instabilities (hence, lower induced electrons' axial transport) upstream of the exit channel. The downstream shift of the acceleration region is also observed experimentally [153]-[155] at low magnetic field intensities. In Ref. [155], it is seen that at low B-field intensities, the high E_x region occurs entirely outside the channel, and it shifts upstream as B increases. Hargus et al. [154] also observed that most of the potential drop happens outside the channel. These experimental observations are in line with our numerical results.

At $B = 30\ mT$ (and to a lower extent at $B = 20\ mT$), the discharge becomes turbulent (as will be seen in Sections 5.2.2 and 5.2.4). In this condition, the magnetic field barrier is very strong and, thus,

severely limits the electrons' axial transport. As was also observed by Boeuf and Garrigues [18], the conditions where the electron conductivity is insufficient (such as at $J = 50\ Am^{-2}$), axial oscillations corresponding to the Ion Transit Time Instability (ITTI) are developed to balance the ion beam current. This is consistent with the theoretical dispersion relation of the ITTI presented in Section 1.1.3.4, which predicts an unstable mode when the electron conductivity is low. Moreover, Hagelaar et al. [37] noted that the intensity of the ITTI is strongest when I_i/I_0 ratio is closer to one. This is the case in our simulations for low current density and high B-field conditions.

In the $30\ mT$ case, the turbulent nature of the discharge affects the acceleration of the ions, which is reflected in the density profiles in the plume (**Fig. 5.2**). From the E_x and n_i profiles in **Fig. 5.3** and **Fig. 5.4**, it appears that these effects are stronger for argon than xenon and krypton. These effects significantly impacted the electric potential including appearance of a small bump in the potential profile downstream of the exit plane, which is observed as a dip in the E_x profiles (**Fig. 5.3**). The turbulence and a long-wavelength azimuthal instability (will be demonstrated in Section 5.2.2) seems to be causing substantial electron heating, leading to higher electron temperatures.

The peak E_x is generally lower at higher B-field intensities ($B \geq 15\ mT$) compared to that at $B = 10\ mT$ (except for argon at $B = 20\ mT$). Additionally, the width of the high E_x region increases from $B = 10\ mT$ to $B = 30\ mT$. These behaviors are consistent the experimental observations. In this regard, Hargus et al. [154] observed that the peak of the electric field is higher for the reduced B-field condition. Gawron et al. [156] noticed that the acceleration region expands with increasing B-field intensity. They explained that expansion of the acceleration region is due to the enlargement of the zone over which B-field is strong enough to effectively confine electrons [156]. However, in Section 5.3, we will show that increasing the extent of the magnetized region does not appreciably alter the width of the acceleration region.

As a summary of the observed trends, the variations of the peak values of the plasma profiles are presented in **Fig. 5.5** against the respective operating conditions.

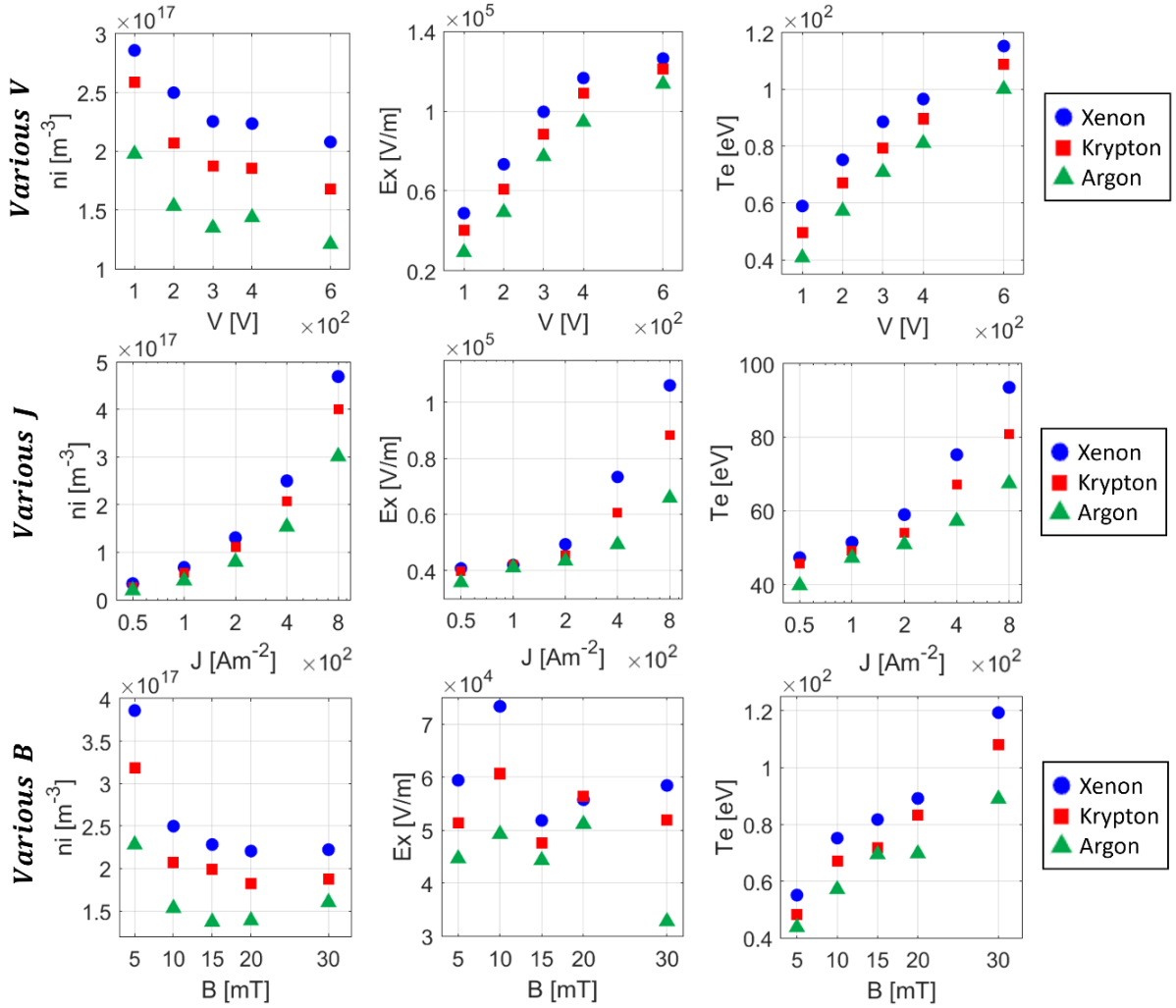


Fig. 5.5: Variation of the peak values of the axial profiles of ion number density (n_i), axial electric field (E_x) and electron temperature (T_e) vs V (top row), vs J (middle row) and vs B (bottom row) for the three propellants.

In addition, **Fig. 5.6** provides the variations of the spatiotemporal average of the ion number density and ions' axial drift velocity (V_{ix}) in the plume ($1.5\ cm < x < 2.5\ cm$), where ions are fully accelerated and their profiles are almost flat. The ideal exhaust velocity ($v_{exhaust}$) of ions calculated using Eq. 5.1, are superimposed on the V_{ix} plots

$$v_{exhaust} = \sqrt{\frac{2eV_d}{m_i}}. \qquad \text{Eq. 5.1}$$

As seen in the right column of **Fig. 5.6**, the V_{ix} values from simulation deviate from the ideal theoretical trends. This discrepancy is due to the fact that Eq. 5.1 does not account for energy losses. In reality, the voltage in Eq. 5.1 shall be the effective voltage available for the acceleration of ions (beam voltage, V_b), $V_b = \eta_e V_d$, with η_e being the energy efficiency [49]. The main energy loss mechanisms which can subtract from the beam voltage include ionization (and excitation), wall losses and voltage losses at the cathode (non-zero cathode coupling voltage). However, considering the absence of these loss mechanisms in this problem, the main source of acceleration inefficiency is due to the overlap between the acceleration and the ionization zones. This overlap causes the ions that are injected within the acceleration region to accelerate through only a partial potential drop, occurring downstream of their

injection location, which leads to velocities below their nominal velocity estimated by Eq. 5.1. However, there is a counter effect related to the sheath formed at the anode side of the domain which increases the bulk plasma potential and the potential drop through which ions are accelerated. This appears as a sharp decline near the left boundary in the E_x profiles in **Fig. 5.3**. The interplay of these two opposing factors explains the discrepancy between the ion axial velocities from the simulations and from Eq. 5.1.

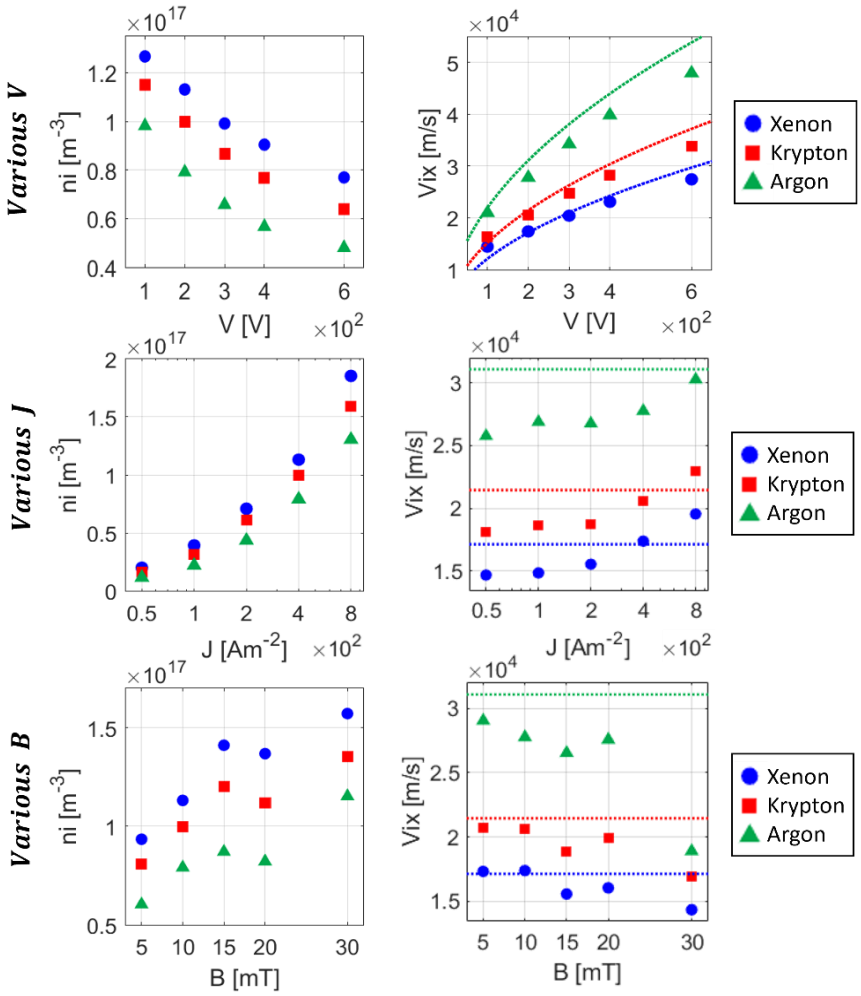


Fig. 5.6: Variation of spatiotemporally averaged (across axial extent of $1.5\ cm < x < 2.5\ cm$ and over $20 - 30\ \mu s$) ion number density (n_i) and ions' axial drift velocity (V_{ix}) in the plume vs V (top row), vs J (middle row), and vs B (bottom row) for the three propellants. The dashed lines in the right-hand side plots represent the ideal exhaust velocity for ions from Eq. 5.1.

In particular, the deviation of the ion velocities from the ideal values ($v_{exhaust}$) is consistently increased at higher discharge voltages. This is because at lower voltages the potential rise within the plasma bulk due to the anode sheath can almost compensate for (or exceed at $V = 100\ V$ with xenon) the acceleration inefficiency caused by the overlap of ionization and acceleration zones. However, as V increase, the effect of the anode sheath becomes less significant compared to the discharge potential drop, failing to balance the losses due to the acceleration inefficiencies. For the same reason, the deviation of the V_{ix} from $v_{exhaust}$ becomes more substantial from xenon to argon due to the consistent decrease in the sheath potential drop from xenon to argon, as seen in **Fig. 5.3**. Nevertheless, experimental measurements [154][157] indicated a constant voltage loss (about $60 - 75\ V$) across all

tested voltages, suggesting the independence of the voltage losses of the operating voltage. The discrepancy between our numerical results and experimental observations in the trend of voltage loss is most likely due to not accounting for all loss mechanisms in the simulation including ionization and wall losses as well as cathode coupling voltage.

Concerning the variations of V_{ix} with J, the discrepancy from ideal values diminishes from $J = 50\ Am^{-2}$ to $J = 400\ Am^{-2}$ because of the narrowing of the acceleration region, thereby a reduced overlap with the ionization zone, as well as increased anode sheath potential drop which compensates for increasingly larger portion of the acceleration non-idealities. Similar to the cases with various voltages, the discrepancy between the simulated and the ideal ion velocities becomes larger from xenon to argon which is attributed to the progressive decrease in the sheath potential from xenon to argon (**Fig. 5.3**). At $J = 800\ Am^{-2}$ with xenon and krypton, however, the anode sheath potential is large enough to overcompensate the acceleration inefficiencies, leading to ion velocities beyond the ideal values. In this condition with argon, the two effects are almost balanced and the V_{ix} is close to $v_{exhaust}$.

Regarding various B cases, we observe that, for xenon and krypton and for the B intensities of 5 and $10\ mT$, the simulated V_{ix} is quite consistent with the theoretical $v_{exhaust}$. At $5\ mT$, the shift in the peak of the E_x profile results in a reduced overlap between the acceleration and the ionization regions. At $10\ mT$, this overlap is still smaller compared to the cases with higher B intensities due to a narrower high-E_x zone in this condition. As B increases to 15 and $20\ mT$, the deviation between V_{ix} and $v_{exhaust}$ grows. A major discrepancy between V_{ix} and $v_{exhaust}$ occurs at $30\ mT$, with the deviation increasing substantially from xenon to argon. This disparity is believed to be due to the turbulent nature of the discharge under this extreme condition which has distorted the electric potential profile and led to an incomplete acceleration of ions. Nevertheless, in practice, operating at higher magnetic field intensities often corresponds to higher operating voltages. In any case, these results illustrate the consequences of not increasing the voltage when operating at higher magnetic fields.

In **Fig. 5.7**, we have illustrated the variation trends of several current ratios against the operating conditions, namely the normalized electron current (I_e/I_0), the normalized ion beam current (I_i/I_0), and the ratio of the electron current to the ion current (I_e/I_i). Note that the I_e/I_i ratio is a measure of inefficacy of the magnetic field barrier in confining electrons, which in turn impacts the total efficiency of the thruster.

The ion current is obtained from the simulation as the flux of ions crossing the cathode boundary of the domain (Γ_{ci}). The electron current is calculated by subtracting the ion current from the discharge current, I_d ($I_e = I_d - I_i$), where I_d is determined as the difference between the fluxes of electrons and ions reaching the anode boundary ($\Gamma_{ae} - \Gamma_{\mathrm{ai}}$).

The first row of **Fig. 5.7** shows that while I_e remains almost constant for xenon across voltages of 200 to $400\ V$, krypton and argon exhibit greater variability within this voltage range. From 400 to $600\ V$, I_e jumps by a factor of about 1.5 which, as mentioned before, is due to the weaker electron confinement by the fixed magnetic field. I_i appears to reach a plateau beyond $V = 300\ V$, indicating the maximum ion beam current that can be extracted with the imposed injection source intensity.

From the second row of **Fig. 5.7**, it is observed that as J increases, I_e/I_0 and I_e/I_i ratios become larger. This is mainly due to the enhanced electrons' axial transport induced by stronger azimuthal instabilities at higher J values. It is highlighted though that the unrealistically high electron currents at high J conditions are due to the fact that the baseline magnetic field of the setup does not necessarily correspond to an optimal Hall thruster condition. Note that the slopes of the I_e plots are different among various propellants. Another noteworthy observation is that at low J values of 50 and $100\ Am^{-2}$, the I_i/I_0 is near unity, meaning that most of the ions introduced into the domain by the injection source are accelerated downstream toward the cathode and are extracted at the cathode side. However, toward larger Js, the ratio of I_i/I_0 becomes increasingly less than 1 for all the studied propellants, implying that an increasing fraction of the ions drift toward the anode. A similar observation has also been reported in Ref. [18] from the xenon-propellant axial-azimuthal simulations.

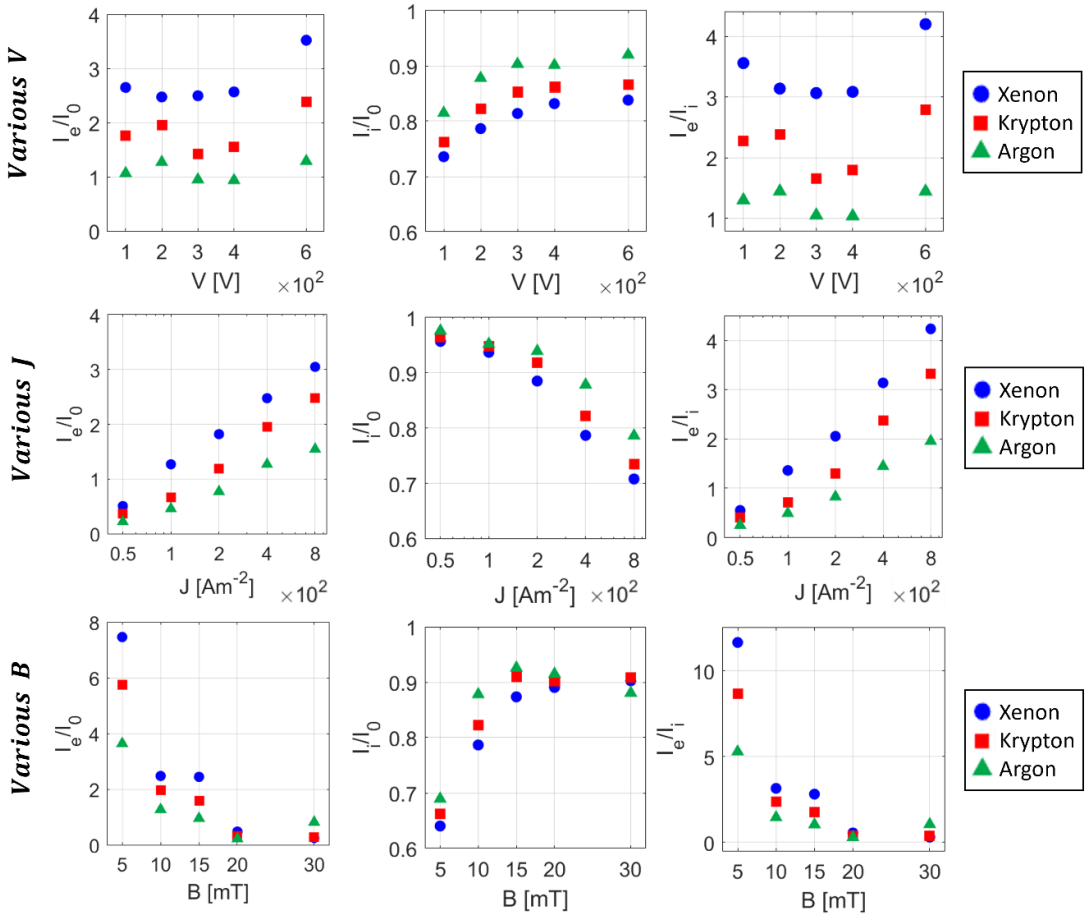


Fig. 5.7: Variation of temporally averaged (over $20-30\ \mu s$) normalized electron current (I_e/I_0), normalized ion current (I_i/I_0) and electron-to-ion current ratio (I_e/I_i) vs V (top row), vs J (middle row) and vs B (bottom row) for the three propellants. I_0 is the nominal total ion current imposed by the ionization source in each case.

With regard to the variation of currents with B in the third row of **Fig. 5.7**, we expectedly see that the electron current decreases with B for all the propellants due to stronger electron confinement. It is also noticed that, most notable changes in I_e occur between 5 and $10\ mT$, and between 15 and $20\ mT$. I_e seems to have reached an asymptotic value between 20 and $30\ mT$ for xenon and krypton. However, it shows a slight increase from 20 to $30\ mT$ in case of argon. The largest disparity in I_e among propellants occurs at $B = 5\ mT$. On the contrary, I_i has an increasing trend with the B intensity until it

almost reaches a plateau around $15\ mT$, indicating a threshold level for the fraction of ions that can be extracted at the cathode boundary.

5.2.2. Variations in the characteristics of the azimuthal instabilities

As was discussed in Section 1.1.3.1, one of the important instabilities developing along the azimuthal direction of a Hall thruster is known to be the ECDI. Previous studies in literature [19][27][58][158] have shown that in the adopted axial-azimuthal setup of the simulations in this work, the rapid non-linear growth of the ECDI cannot be captured. Instead, the simulations resolve the pseudo-saturated state of the ECDI, associated with a transition to relatively longer-wavelength Ion Acoustic Instability (IAI) modes of lower growth rates [20][21][23]. Hence, the dominant wave modes from our simulations are expected to represent ion-acoustic-like characteristics.

To assess the validity of this across various operating conditions, we have compared the numerical dispersion maps of the azimuthal instabilities (obtained from the simulations) with the theoretical linear and nonlinear dispersion relation of the IAI (given by Eq. 1.4 and Eq. 1.6). These comparisons are provided for xenon propellant as an example in Appendix A.6. In most cases, the numerical dispersion of the instabilities within the channel (at $x = 0.375\ cm$) aligns with the IAI's nonlinear dispersion relation. However, in the plume (at $x = 1.625\ cm$), the instabilities' dispersion matches the linear dispersion relation of ion sound waves, while exhibiting dispersion across a broader range of frequencies and azimuthal wavenumbers compared to inside the channel. Nonetheless, there are some exceptions to this behavior. In particular, at very low current density ($J = 50\ Am^{-2}$) as well as at high magnetic field intensities ($B = 20$ and $30\ mT$), the instabilities inside the channel display significant deviations from the IAI's dispersion relation. Moreover, at $B = 5\ mT$, the instabilities' dispersion in the plume is close to the nonlinear dispersion relation of the IAI.

Having observed an overall agreement between the instabilities' dispersion plots and the IAI's dispersion relation in most cases, we now aim to test the efficacy of the existing theories on the IAI (presented in Section 1.1.3.2) in estimating the characteristics of the numerically observed dominant wave modes across the studied operating conditions. To this end, we have compared the predicted characteristics of the azimuthal instabilities from simulations with their theoretical estimations at two axial locations: (1) at $x = 0.375\ cm$ which corresponds to the middle point of the discharge channel along the axis, and (2) at $x = 1.625\ cm$, situated midway within the plume region.

We first refer to **Fig. 5.8**, in which the azimuthal wavenumber (k_z) and the frequency (ω) of the dominant IAI wave mode from the simulations and the theory at the two axial locations are plotted. The numerical k_z and ω of the dominant mode are determined by identifying the highest peaks in the spatial and the temporal FFTs of the azimuthal electric field signal. These FFT plots are provided in Appendix A.6. Theoretical values, which are associated with the IAI's fastest-growing mode, are calculated from Eq. 1.7, with λ_{De} and the ω_{pi} being obtained using the time-averaged plasma properties at the respective axial locations from the simulations.

From **Fig. 5.8**, it is evident that, in general, the characteristics of instabilities vary from inside the channel toward the plume. A possible explanation for this variation is the downstream convection (with

the ion beam) of the waves excited in the near-anode region. Given the significant variation in plasma conditions from the anode to the plume region, the instabilities' dispersion relation changes as the waves are convected out with the ion beam [27][68][115] in accordance with the local plasma conditions.

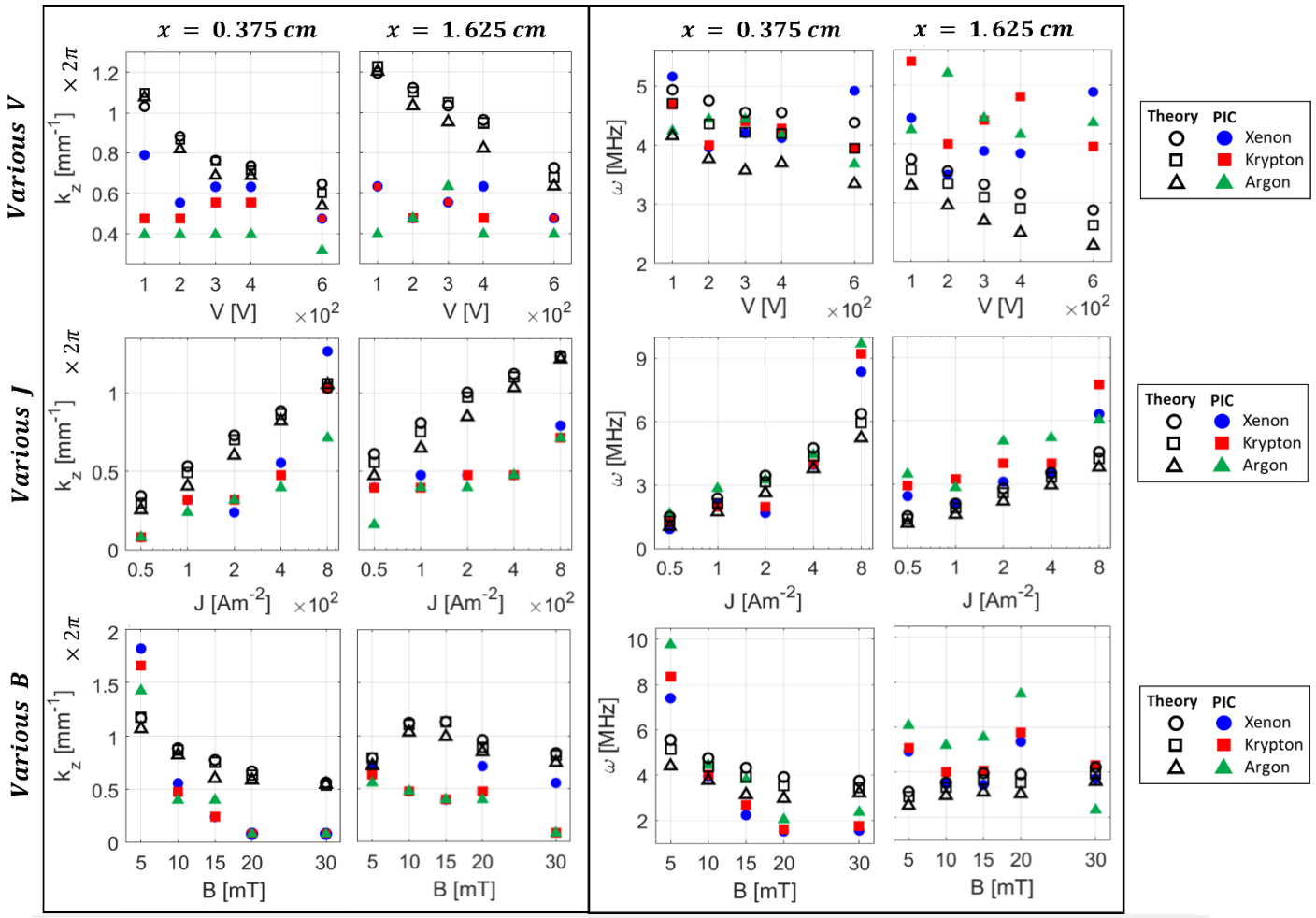


Fig. 5.8: Variation of the azimuthal wavenumber k_z (left panel) and the frequency ω (right panel) of the dominant instability mode at two axial locations (inside the channel at $x = 0.375$ and in the plume at $1.625\ cm$) vs V (top row), vs J (middle row) and vs B (bottom row) for the three propellants. The numerical predictions are compared against the corresponding theoretical values for the IAI's fastest-growing mode (Eq. 1.7). The dominant instability mode is identified as the mode with the largest amplitude in the spatial and temporal FFTs of the azimuthal electric field signal (presented in Appendix A.6).

Concerning the variations vs V, the theoretical relations predict a monotonic decrease in k_z and ω with V, which is a consequence of the trends of the time-averaged plasma properties versus V in **Fig. 5.2** and **Fig. 5.4**. However, it is noticed that the simulated wavenumber and frequency of the dominant wave mode do not exhibit a similar trend with V. At low voltages, the simulated k_z values are quite disparate with the theoretical ones both within the channel and in the near-plume. At higher voltages though, the agreement with the theory is seen to relatively improve. In the frequency plots, we notice that, within the channel, the agreement with the theory is rather acceptable. However, in the plume, the theoretically predicted frequency of the dominant IAI mode is consistently lower than the simulated value across the voltages and the propellants, except for the xenon at $200\ V$ (the baseline case), where the theory and the simulation are in close agreement.

The theory and the simulations agree on the overall increasing trend of k_z and ω with J both within the channel and in the plume, however, their values do not always exactly match. The most agreement is observed between the frequency values inside the channel up to $J = 400\ Am^{-2}$. Also, for xenon propellant in the plume, the theoretical frequencies are quite close to the simulated ones for $50\ Am^{-2} \leq J \leq 400\ Am^{-2}$.Interestingly, in the plume and within the ion current density range of $50 - 400\ Am^{-2}$, the wavenumber of the dominant mode for almost all three propellants is rather constant with J. Additionally, for $J \leq 400\ Am^{-2}$, k_z either increases or remains almost unchanged from channel to the plume. However, at $J = 800\ Am^{-2}$ for xenon and krypton, k_z is notably smaller in the plume compared to within the channel.

Regarding cases with various B, we primarily observe that inside the channel, k_z and ω of the dominant mode from the simulations show stronger variations with the B intensity than what is predicted by the theory. The closeness of the simulated characteristic of the instabilities to theory varies significantly across various magnetic field values and different propellants. Interestingly, at $B = 30\ mT$, the wavenumber of the instabilities increases significantly from within the channel to the plume for xenon, while, in cases of krypton and argon, the wavenumber remains relatively constant in this condition. It is also noted from the FFT plots in Appendix A.6 that for cases with $B = 20$ and $30\ mT$, the amplitude floors of the instability's frequency and wavenumber spectra inside the channel, are higher than in other cases for which the spectra are seen to rapidly fall off in magnitude toward high frequencies and wavenumbers. The elevated magnitudes of the tail of the spectra for the 20 and $30\ mT$ cases point to a turbulent state of the plasma.

Ion-wave trapping is proposed as a saturation mechanism for the azimuthal waves of the IAI. The saturated (RMS) amplitude of the IAI's fastest growing mode is given by Eq. 1.8. The ions whose azimuthal velocity (v_z) meets the following criterion [18][30][31] can be trapped within the waves' potential of amplitude $\delta\phi_{RMS}$ [30][120]

$$\left(v_z - \frac{\omega}{k_z}\right)^2 \leq 4\frac{q\delta\phi_{RMS}}{m_i} \qquad \text{Eq. 5.2}$$

Trapping of significant population of ions leads to the saturation of the waves. This occurs when $\frac{\omega}{k_z} \approx 4\frac{q\delta\phi_{RMS}}{m_i}$ [30]. For the fastest growing mode of IAI (substituting $k_{z,max}$ and ω_{max} from Eq. 1.7), the saturated amplitude of potential fluctuation is obtained as $\delta\phi_{RMS} = T_e/6\sqrt{2}$. This can be related to the amplitude of the electric field fluctuations through $\delta E_{RMS} = k_{max}\delta\phi_{RMS}$ relation, leading to Eq. 1.8.

To verify that the trapping of ions in the waves' potential have occurred in our simulations, we look at the ions' azimuthal phase-space shown in **Fig. 5.13**. We observe that except for the conditions of low current density ($J \leq 100\ Am^2$) and high B intensity ($B = 30\ mT$), the ions distribution is strongly affected by the azimuthal waves, featuring the characteristic loops in $z - v_z$ phase-space indicative of the ion-wave trapping. At $J = 50, 100\ Am^{-2}$ and $B = 30\ mT$, the amplitude of the waves (**Fig. 5.10**) is not strong enough to substantially impact the ions' azimuthal velocity distributions.

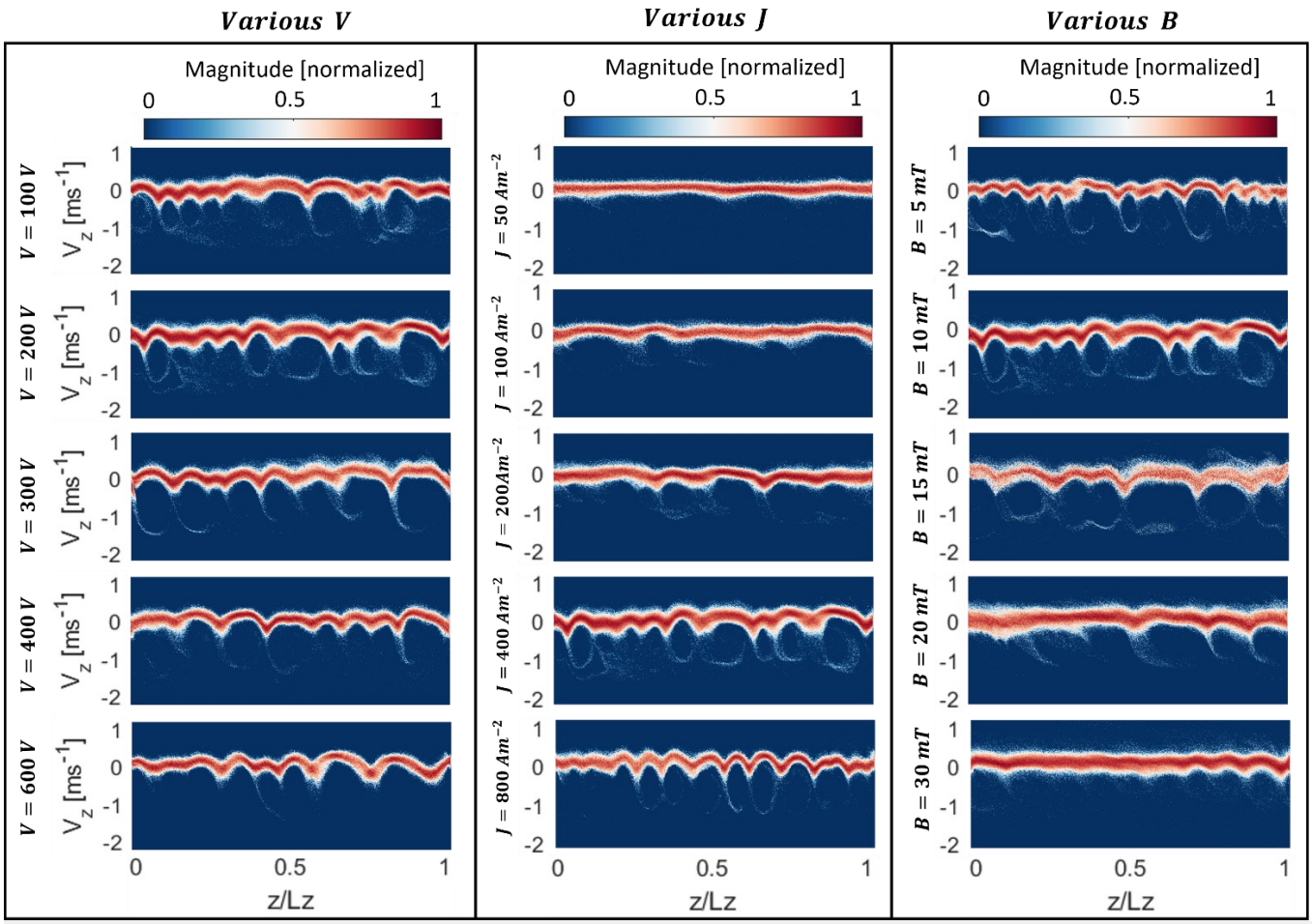


Fig. 5.9: Ions' azimuthal phase-space ($z - v_z$) plots in the plume ($1.25\ cm < x < 2.25\ cm$) for xenon with various V (left panel), various J (middle panel), and various B (right panel).

Fig. 5.10 compares the RMS amplitudes of the azimuthal electric field (δE_{RMS}) and the electron number density ($\delta n_{e,RMS}$) fluctuations in the plume (spatiotemporally averaged across $x = 1.25$ to $2.25\ cm$ and over $20 - 30\ \mu s$) from the simulations against the theoretical predictions. This comparison casts light on how closely the rather simple theoretical relation based on the ion-wave trapping saturation mechanism can explain the numerical observations concerning the waves' intensities across a broad range of operating conditions.

The simulated RMS amplitude (δE_{RMS}) is calculated according to the following definition

$$\delta E_{RMS} = \frac{1}{(t_2 - t_1)} \frac{1}{(x_2 - x_1)} \frac{1}{L_z} \int_{t_1}^{t_2} \int_{x_1}^{x_2} \sqrt{\int_0^{L_z} E^2(x,z,t)dz - \left(\int_0^{L_z} E(x,z,t)dz\right)^2}\, dx\,. \qquad \text{Eq. 5.3}$$

In the above relations, $E(x,z,t)$ is the spatiotemporal signal of the azimuthal electric field, x_1 and x_2 represent the spatial averaging window, and t_1 and t_2 denote the time averaging interval. Similarly, $\delta n_{e,RMS}$ is obtained using the spatiotemporal signal of electron number density ($n_e(x,z,t)$).

Looking at **Fig. 5.10**, the theory predicts a constant value for the normalized amplitudes of the number density fluctuations, which overall falls within the mid-range of the values observed in simulations across various operating conditions. Furthermore, the amplitudes of electric field fluctuations show substantial discrepancy from the theoretical predictions in some conditions. It is

recalled that the theoretical relation assumes the theoretical characteristics of the IAI's fastest growing mode. Therefore, the observed discrepancy between the simulated and theoretical saturation amplitudes can be in part attributed to the differences in the characteristics of modes between simulation and theory (as seen in **Fig. 5.8**). In general, the plots in **Fig. 5.10** shows that, at high voltages ($V \geq 400$), high current density ($J = 800\ Am^{-2}$), and low magnetic field ($B = 5\ mT$), the waves' amplitude grows beyond the theoretical ion-wave saturation value.

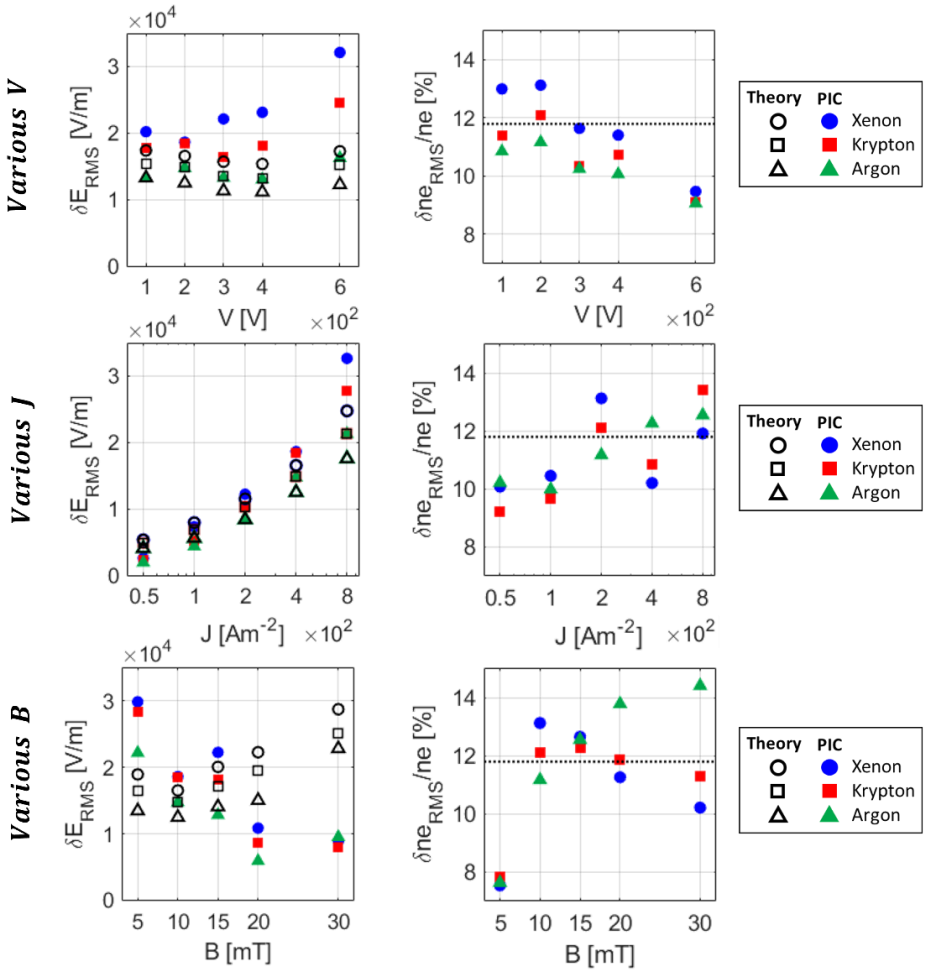


Fig. 5.10: Variation of the RMS amplitude of the azimuthal electric field fluctuations δE_{RMS} (left column) and electron number density δne_{RMS} (right column) fluctuations in the plume vs V (top row), vs J (middle row) and vs B (bottom row) for the three propellants. The RMS amplitudes represent the average across axial extent of $1.25\ cm < x < 2.25\ cm$ and over $20 - 30\ \mu s$. δne_{RMS} values are normalized by the respective average steady state electron number density in the plume (n_e). The numerical predictions are compared against the corresponding theoretical values for the fastest-growing ion acoustic mode (Eq. 1.8). Dashed black lines in the right column plots represent the theoretical values ($\frac{\delta ne_{RMS}}{n_e} = 1/6\sqrt{2}$).

The simulated δE_{RMS} values progressively deviate from the theoretical predictions towards higher voltages. In particular at $V = 600\ V$, there is a substantial difference between the δE_{RMS} from the simulations and the theory, with the deviation being more pronounced for xenon and krypton. Nevertheless, across different values of J, there is generally a good agreement between the numerical and theoretical values of δE_{RMS}. Contrarily, the theoretical and the simulated δE_{RMS} values (for all propellants) exhibit different trends with B. While the theoretical values for each propellant show a slight

decrease from 5 to $10\ mT$, and then an increasing trend for the higher B intensities, the simulated δE_{RMS} values, exhibit an overall decreasing behavior with B. At high B intensities ($B = 20\ ,30\ mT$) in particular, the substantial disparity could partly be due to the presence of a long wavelength instability, specially upstream the channel exit plane and the impacts of this instability on the downstream waves, which are more pronounced in cases of krypton and argon (will be seen in **Fig. 5.12**).

To visualize the observed behavior in the characteristics of the instabilities, the 2D snapshots of the fluctuations in ion number density and the azimuthal electric field (at $t = 30\ \mu s$) for xenon are presented in **Fig. 5.11**. The variation of the instabilities' wavelength with voltage is minor. However, the consistent decrease in the wavelengths (throughout the domain) with J is evidently visible. Additionally, we can see the substantial increase of the instabilities' wavelength with B intensity inside the channel.

The appearance of the instabilities of long wavelength (almost equal to the domains' azimuthal size) is also observed in the snapshots of cases with $B = 20$ and $30\ mT$ upstream of the domain. The snapshots of the E_z fluctuations for various propellants illustrated in **Fig. 5.12** show that the long-wavelength instability is extended further downstream in cases of krypton and argon.

DMD analysis [138][139] can help isolating the spatiotemporal structures of the dominant instability modes, reveal a non-zero axial component for this instability, in addition to the azimuthal wavenumber visible in these plots. The DMD results provided in Refs. [138][139] and FFT analyses show that the frequency of this mode is about $1 - 1.5\ MHz$. Same long wavelength instability with both axial and azimuthal wavenumbers is also detected for the low current density limit, i.e., $J = 50$ and $100\ Am^{-2}$ cases with the frequencies of about $1\ MHz$ and $0.6\ MHz$, respectively. The spatial structure and the frequency of this instability resembles that of the Ion Transit Time Instability (ITTI). This observation is consistent with the findings in Ref. [18] where the authors had also noted the presence of the ITTI at $J = 50\ Am^{-2}$ with a frequency on the order of $1MHz$. We will see in Section 5.2.4 that the ITTI has indeed influenced the ions' distribution function in these conditions.

Another noteworthy observation is that the instabilities involve non-zero axial wavenumbers inside the channel, whereas in the plume, the instabilities primarily constitute purely azimuthal oscillations. Also, as noticed in **Fig. 5.8**, the azimuthal wavenumber of the fluctuations undergoes a change from upstream to downstream of the exit plane in line with the variation in the local dispersion relation of the instabilities (determined by the local plasma properties). Eq. 1.7 suggests that the azimuthal wavenumber of the IAI's fastest growing mode is proportionally correlated with n_e/T_e ratio. Accordingly, the most remarkable change in k_z is observed at $B = 5\ mT$, which involves the largest variation in n_e/T_e ratio between the channel and the plume regions. This is in line with the observation in Ref. [69].

Finally, in cases with $B = 5\ mT$ and $V = 600\ V$ (and to some extent $400\ V$ case), the amplitude of oscillations is noticeably weaker inside the channel and stronger in the plume. For other operating conditions, the DMD analysis outcomes presented in Refs. [138][139] reveal that while a few instabilities modes display similar nonuniform amplitudes, the majority of the modes have a relatively uniform amplitude distribution across the domain in those conditions.

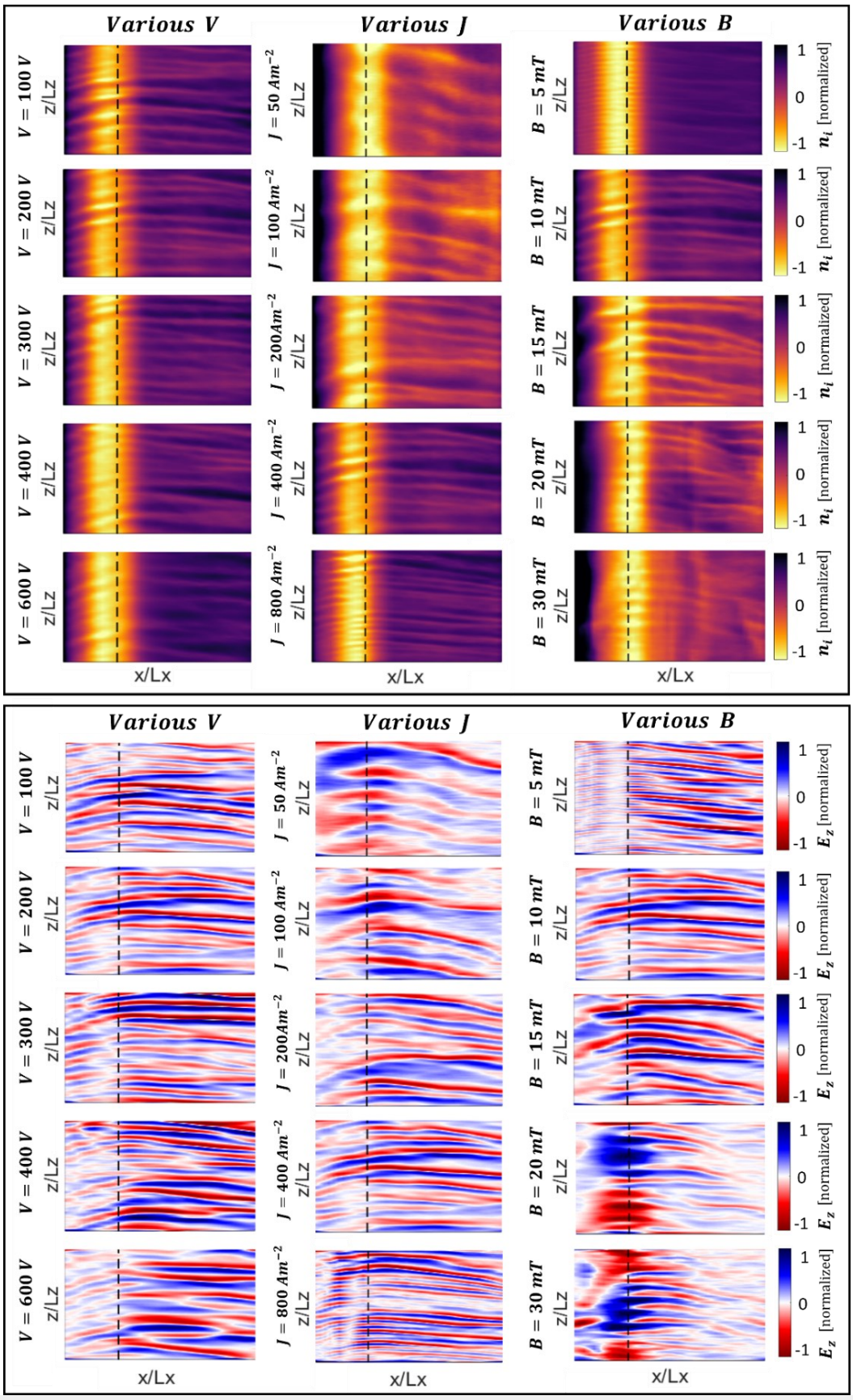


Fig. 5.11: 2D snapshots of the normalized ion number density n_i (top panel) and normalized azimuthal electric field E_z (bottom panel) at $t = 30\mu s$ for xenon with various V (left column), various J (middle column) and various B (right column). Dashed black lines represent the location of the channel exit plane.

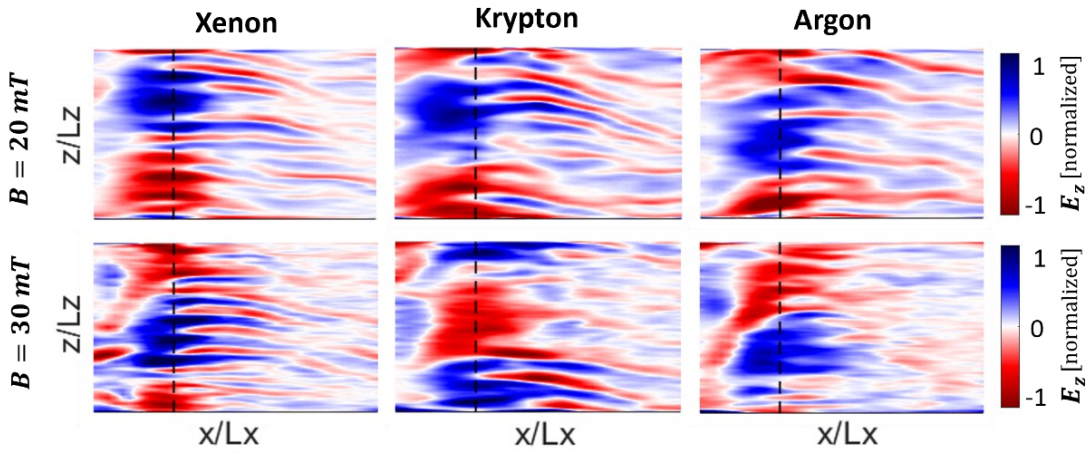


Fig. 5.12: 2D snapshots of the normalized azimuthal electric field E_z at $t = 30\mu s$ for various propellants at $B = 20$ and $30\ mT$. Dashed black lines represent the location of the channel exit plane.

5.2.3. Variation in the electrons' cross-field transport

The time-averaged axial profiles of the different mechanisms contributing to the electrons' cross-field transport across various operating conditions are compared in **Fig. 5.13**. These mechanisms are the force terms in the azimuthal momentum equation of the electrons (Eq. 1.20) which are reiterated here for convenience: $F_t = \partial_t(mn_e v_{e,z})$ is the temporal inertia, $F_I = \partial_x(mn_e v_{e,x} v_{e,z})$ is the convective (spatial) inertia, $F_\Pi = \partial_x(\Pi_{e,xz})$ is the viscous force term, and $F_E = e\tilde{n}_e \tilde{E}_z$ is the electric force term due to azimuthal fluctuations. The aggregate effects of these mechanisms on the electrons' azimuthal momentum are represented by the magnetic force term, $F_B = -en_e v_{e,x} B$ on the left-hand side of the Eq. 1.20. The F_t term is vanishingly small everywhere; therefore, it is discussed here.

Referring to the plots in **Fig. 5.13**, a number of common behaviors can be noticed across most simulation cases:

i) The F_Π term (orange curve) becomes a dominant contributor to the electron transport near the anode side of the domain, whereas, near the location of the magnetic field peak almost immediately after the exit plane, the F_Π values become negative.
ii) The F_I term exhibits almost symmetrical behavior with respect to the axial distribution of the F_Π term. The F_I profile peaks near the exit plane and becomes negative toward the anode side. Away from the near anode region, F_I values are nearly the negative counterparts of F_Π values, such that they almost cancel each other out.
iii) Apart from the near-anode region, in most cases, the F_E term has the dominant contribution to the electron transport, especially from near the magnetic field peak region into the plume.

Regarding the variations across operating conditions, the average of F_B and F_E terms (over the entire domain) are plotted against the operating conditions in **Fig. 5.14**. Another noteworthy aspect is the variation in the axial locations of the peak values of F_B and F_E terms ($x_{F_{B,max}}$ and $x_{F_{E,max}}$, respectively) which are presented in **Fig. 5.14**. As reference, the axial locations of the peak of the axial electric field ($x_{E_{x,max}}$) and electron temperature ($x_{T_{e,max}}$) are also provided in this figure.

The main observations from **Fig. 5.13**, **Fig. 5.14** and **Fig. 5.15** in terms of trends of variations of the force terms are summarized below.

Across various voltages (V): the values of the F_B term remain almost constant in the V range of 100 to $400\,V$. However, for krypton, some variability in the peak of F_B is noticed. At $V = 600\,V$, the F_B values notably increase for all the propellants. The profile of the F_Π term develops an additional peak near the exit plane with increasing V which increases the extent over which the F_Π is dominant. Furthermore, as V increases, the contributions of F_Π and F_I terms become increasingly comparable with that of F_E term. This observation can be traced to the generally larger electron drift and thermal velocities at higher voltages. Nevertheless, due to the symmetric behavior of F_Π and F_I terms, their contributions almost cancel out downstream the channel exit plane, leaving F_E as a primary determining factor in electrons' transport. In any case, looking at **Fig. 5.14** (top row) the proportion of F_E's role to the overall transport (represented by F_B) decreases with increasing V.

While $x_{F_{B,max}}$ remains relatively unchanged across various voltages, $x_{F_{E,max}}$ consistently shifts toward downstream as V increases for all propellants.

Across various total ion current densities (J): the behaviors of the different force terms are overall similar across Js, and increasing J mostly results in the magnitude of the terms to become almost proportionally larger. Moreover, the relative contribution of each term to the overall electrons' transport at each axial location remains almost the same across various Js. Both $x_{F_{B,max}}$ and $x_{F_{E,max}}$ exhibit consistent downstream shifts with increasing J.

Across various field intensities (B): the profiles of the force terms show a large degree of variability across B and do not follow a distinct trend. In particular, the cases with $B = 5\,mT$ and $B = 20 - 30\,mT$ represent two extremes in terms of the characteristics of the momentum force terms. At $5\,mT$, all force terms - F_I, F_Π, and F_E - have comparable magnitudes. The F_Π term is dominant near the exit plane exhibiting a large peak, while the peak of F_E occurs further downstream in the plume. The profiles of force terms in this case are nearly similar to those at $V = 600\,V$. This similarity is also reflected in the established E_x profiles in the $5\,mT$ and $600\,V$ cases as seen in **Fig. 5.3**. The $B = 30\,mT$ condition exhibits the largest disparity in force terms among different propellants. In case of argon, the F_E term has disproportionately large values. The F_Π term is less significant in this case at high B-fields ($B = 20 - 30\,mT$).

As the B increases, the $x_{F_{B,max}}$ and $x_{F_{E,max}}$ gradually shift upstream for xenon, getting further away from the channel exit plane. For krypton and argon, the movement of $x_{F_{E,max}}$ reverses towards downstream after $B = 15\,mT$.

In addition to the above observations, a "wavy" axial distribution is noted for the F_E and the F_I profiles in the plume at $V = 100\,V$ and $J = 800\,Am^{-2}$ for the xenon propellant, the exact root cause of which is not yet known.

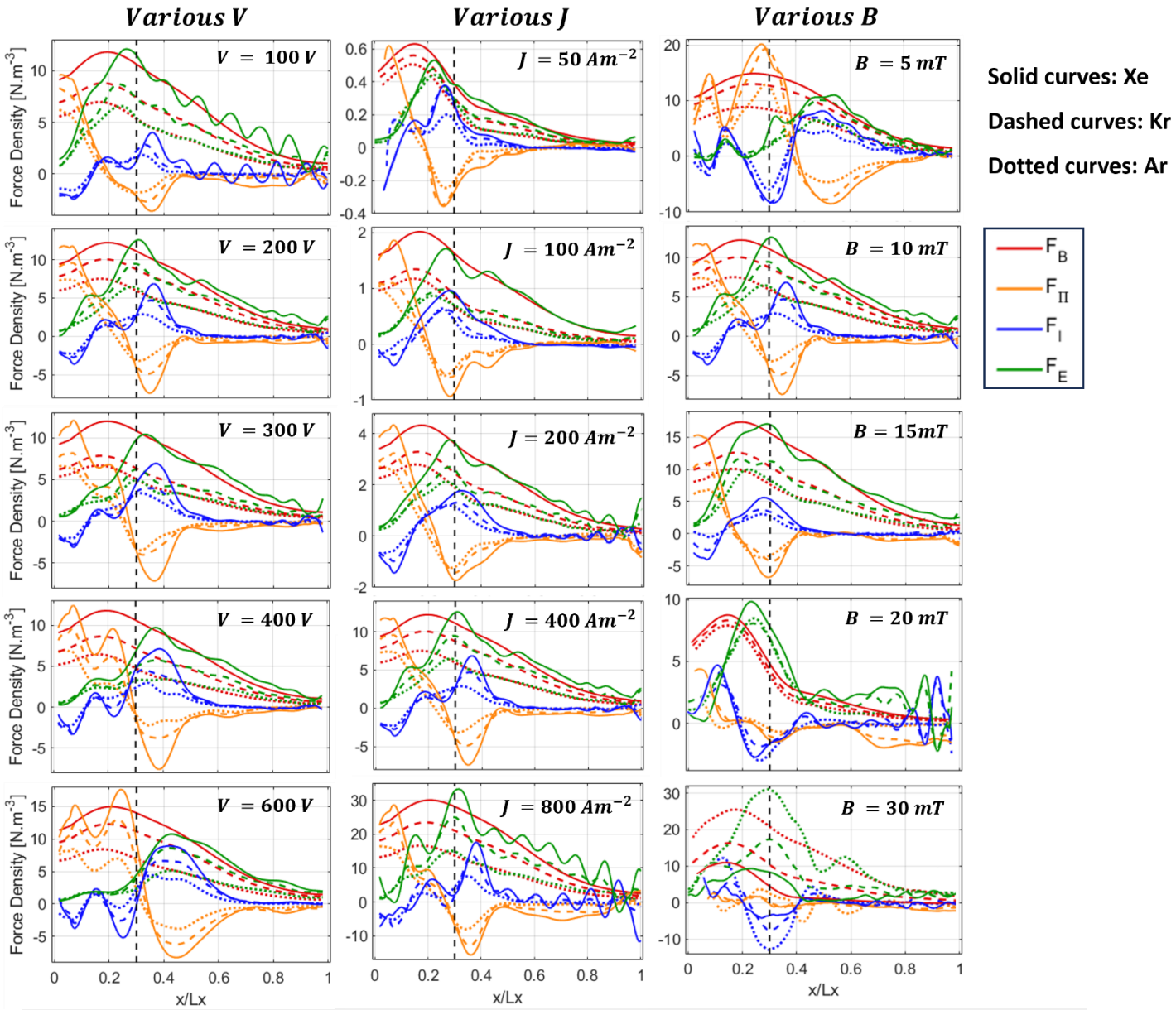


Fig. 5.13: Axial profiles of the transport terms in Eq. 1.20 for the three propellants with various V (left column), various J (middle column) and various B (right column). The force terms are averaged over 4 μs. F_B is the magnetic force, F_Π is the viscous effects, F_I is the convective inertia force, and F_E is the electric force term. F_t (temporal inertia) contribution was almost zero, and it is thus not displayed. Dashed black lines represent the location of the channel exit plane.

As a final remark, the relative "symmetry" between the viscous term ($F_{\Pi,}$) and the convective inertia (F_I) is an interesting observation that merits further investigation. This can be important for fluid simulations because if only one of the effects (and not both) is considered within the simulation, its contribution to electrons' transport may remain unbalanced, potentially leading to inaccuracies in the results. However, it is important to highlight that the assumption of a prescribed ionization source may alter the physics of the problem, and consequently, affect the transport terms. Hence, a deeper assessment needs to be performed in the presence of self-consistent ionization and collisional processes.

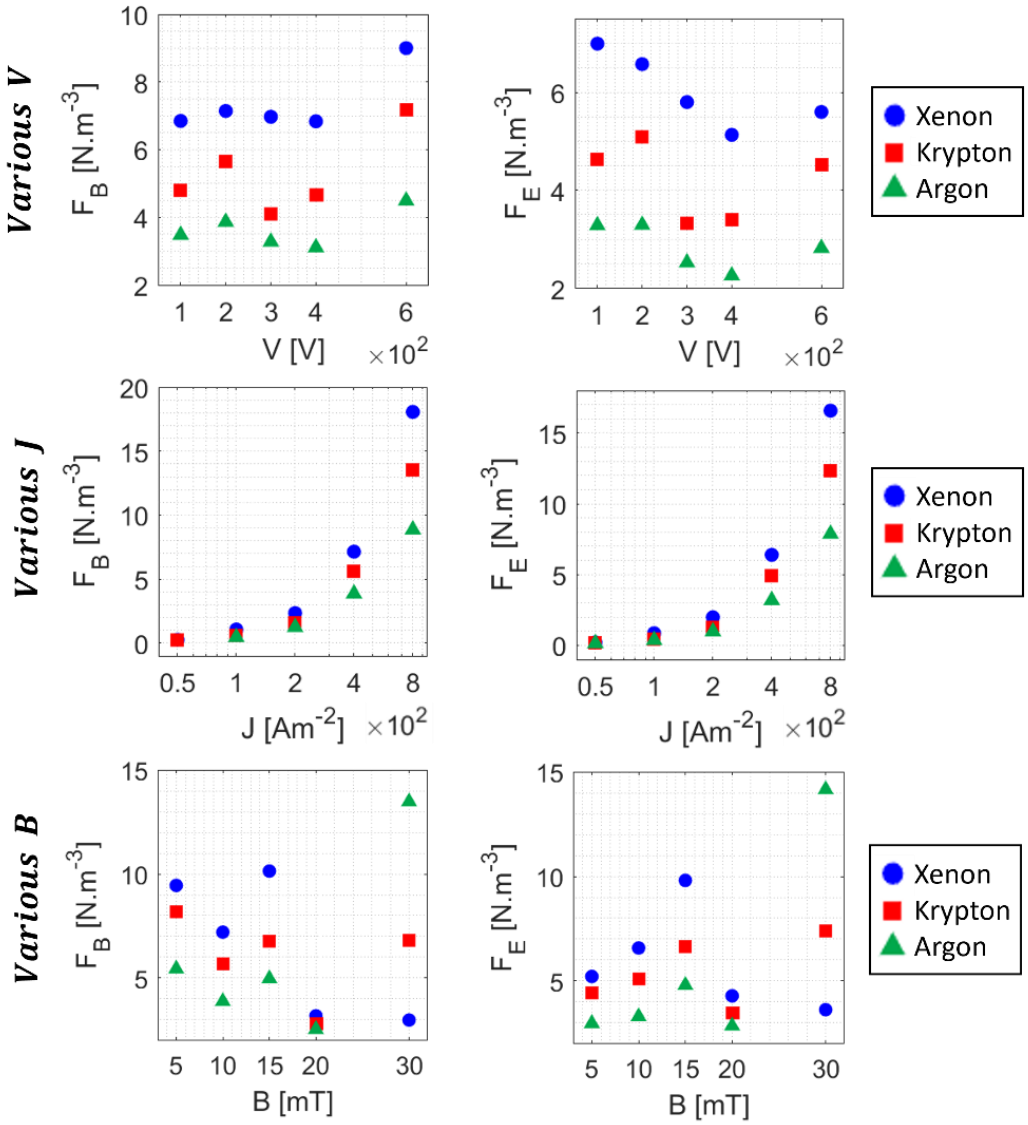


Fig. 5.14: Variation of spatiotemporally averaged (across entire domain and over $4\ \mu s$) magnetic force term F_B (left column) and electric force term F_E (right column) in Eq. 1.20 vs V (top row), vs J (middle row), and vs B (bottom row) for the three propellants.

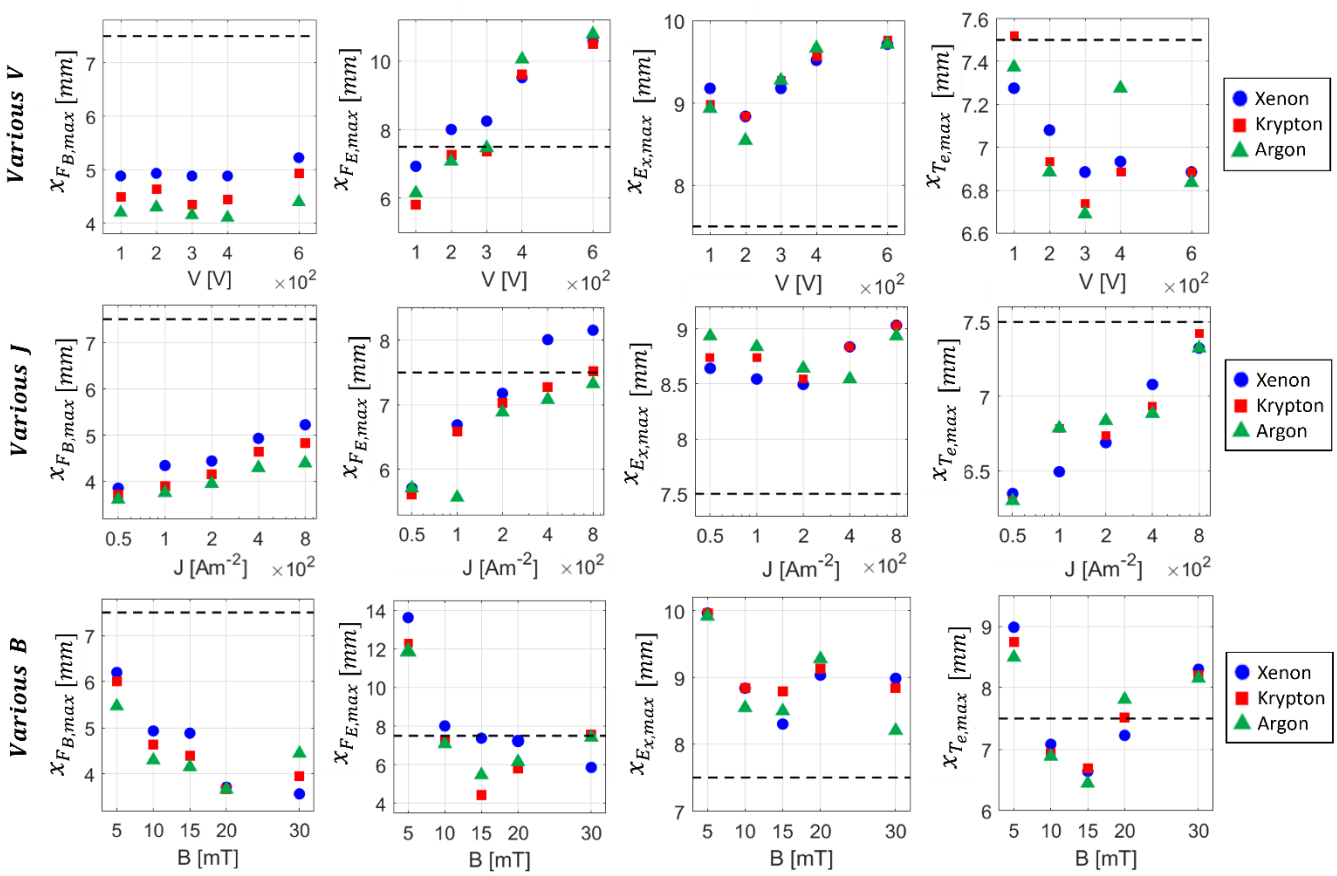


Fig. 5.15: Variation in the axial location of the peak values of different quantities vs V (top row), vs J (middle row), and vs B (bottom row) for the three propellants. From left to right, the axial location are associated with the peaks of the magnetic force term ($x_{F_{B,max}}$), electric force term ($x_{F_{E,max}}$), axial electric field ($x_{E_{x,max}}$), and electron temperature ($x_{T_{e,max}}$). Dashed black lines represent the location of the channel exit plane.

5.2.4. Variations in the ion distribution function

Fig. 5.16 presents the velocity distribution functions (IVDF) for various operating conditions, integrated over the plume region ($1.5\,cm < x < 2.5\,cm$), downstream of the acceleration zone. Additionally, the 1D1V ion distribution functions along the axial direction and the axial velocity component, under different J and B conditions are illustrated in **Fig. 5.17**. In these plots, we have also shown the ions' ideal exhaust velocity given by Eq. 5.1 for reference.

The broadening of IVDFs toward lower energies in **Fig. 5.16** is, in general, attributed to the overlap of the ionization and acceleration regions, and the degree of the broadening is corelated with the extent of this overlap. The spread of velocities is also evident in the plume region in the plots of **Fig. 5.17**. In particular, we notice that with increasing J, the spread of the velocities decreases and the ion population in the plume become increasingly closer to a beam-like distribution. At low J values ($J = 50 - 100 Am^{-2}$), the IVDFs show a notable spread over an extended range of energies and feature an oscillatory distribution as well. These oscillations are visible in the ion population in the plume (**Fig. 5.17**) and can also be seen (though not as evidently) in **Fig. 5.16** for $J = 50 - 100 Am^{-2}$. These observations are signature evidence of the presence of the ITTI instability, consistent with what is inferred from the DMD

mode plots in Ref. [138] for the low J values. Indeed, these perturbations root in the so-called "wave-riding" of the ions [18][159] as they interact with the ITTI waves. In this regard, the electric field oscillations associated with the ITTI create a back-and-forth movement of the acceleration region. When the acceleration region moves upstream, the ions already generated further downstream of the channel experience a reduced portion of the potential drop. Contrarily, when the acceleration zone moves downstream, these ions encounter a larger portion of the potential drop along their path. Accordingly, these oscillations result in ions being accelerated to velocities below and above the nominal speed, causing the oscillations in the ions' VDF in the plume and a larger velocity dispersion of the ion beam.

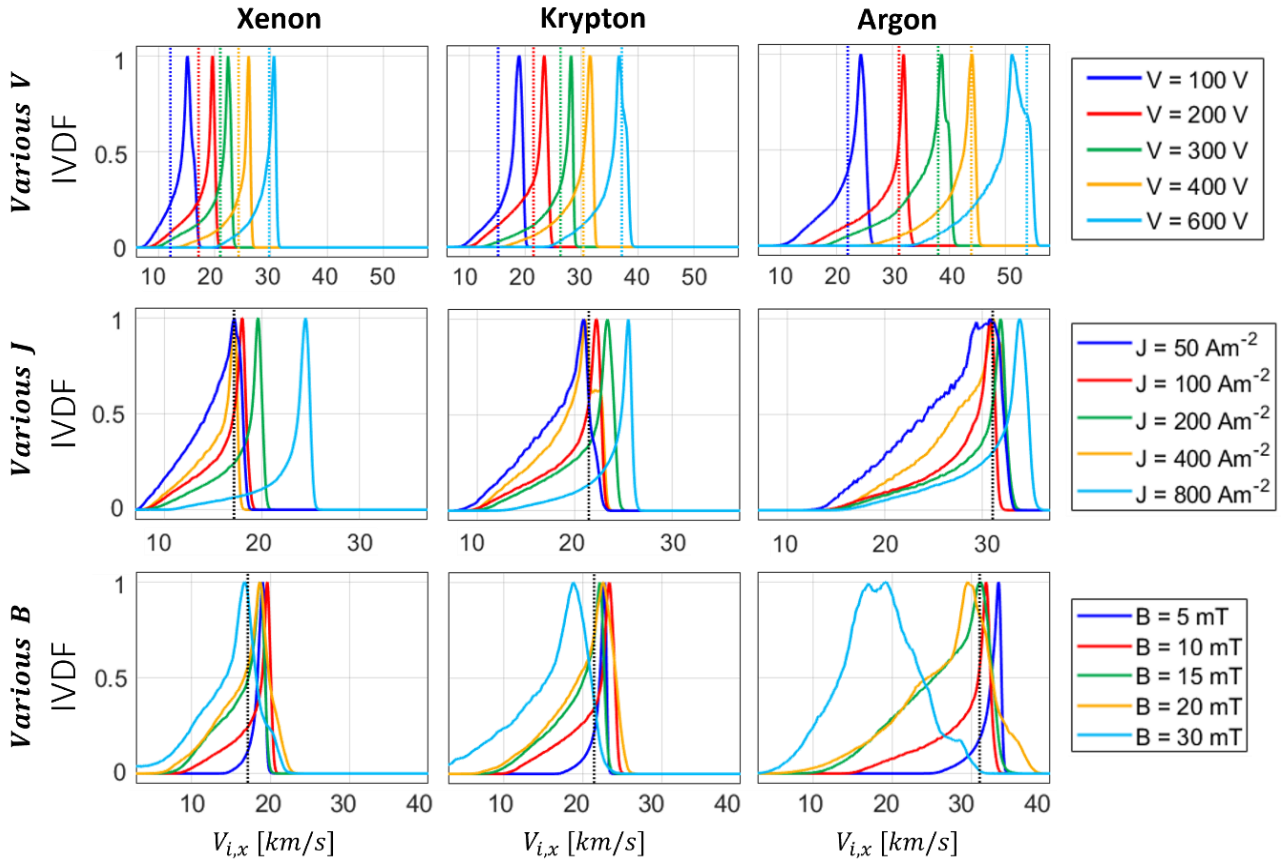


Fig. 5.16: Normalized ion axial velocity distribution function (IVDF) in the plume (over $1.5\ cm < x < 2.5\ cm$) at $t = 30\ \mu s$ for the three propellants with various V (top row), various J (middle row), and various B (bottom row). Dotted lines show the ions' ideal exhaust velocity given by Eq. 5.1.

At very low B-field intensity ($B = 5mT$), the IVDFs are highly beam-like. This is due to significant downstream shift of the acceleration region which has reduced its overlap with the ionization zone. Hence, most of the ions have experienced the full potential drop and accelerated to the same velocities. The velocity spread increases towards higher B inetnsities.

As was anticipated from the analyses of the waves' characteristics in Section 5.2.2, the rather turbulent state of plasma at the $B = 30\,mT$, in particular, have majorly affected the IVDFs of all propellants, especially those of the lighter mass gases, krypton and argon. Indeed, the peaks of IVDFs at $30\,mT$ have shifted toward lower velocities and the distributions feature strong broadening. Additionally, in this case, the ion beam is significantly perturbed (visible in **Fig. 5.17**). The notable spread in the ions' axial velocities as well as strongly perturbed ion beam can be associated with the

presence of strong axial instability such as ITTI waves [36][115][159] and the "wave-riding" mechanism in this case. The substantial scattering of the ions at $30\,mT$ leads to a strong heating of the ion population, which is evident from the time-averaged axial distributions of the ion temperature (T_i) at this B intensity (**Fig. 5.18**). These effects become more pronounced from xenon to argon.

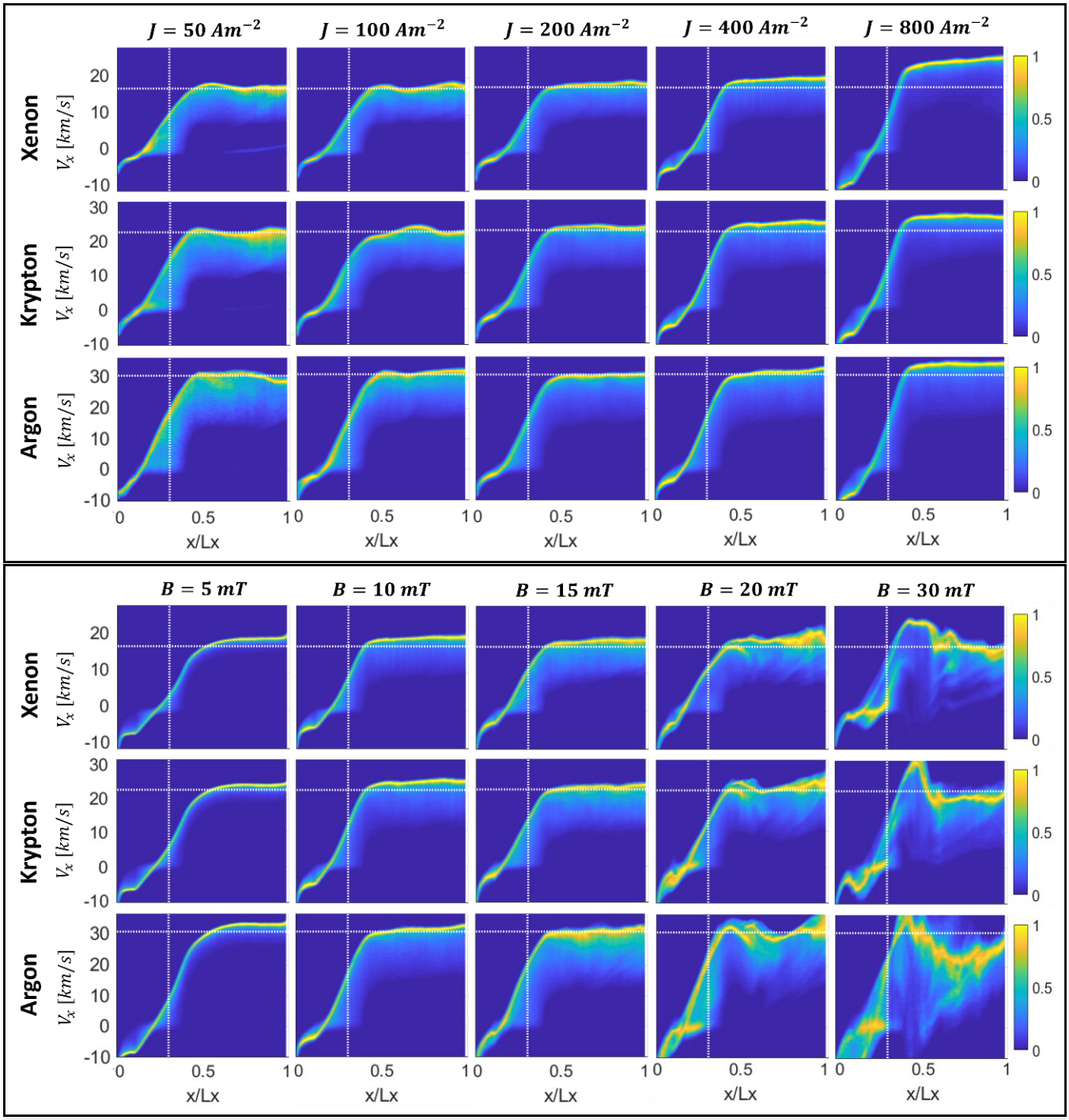


Fig. 5.17: Normalized 1D1V ions' distribution functions (at $t = 30\ \mu s$) along axial direction and axial velocity component for the three propellants with various J (top panel) and various B (bottom panel). Vertical dotted lines represent the location of the channel exit plane, and horizontal dotted lines show the ions' ideal exhaust velocity given by Eq. 5.1.

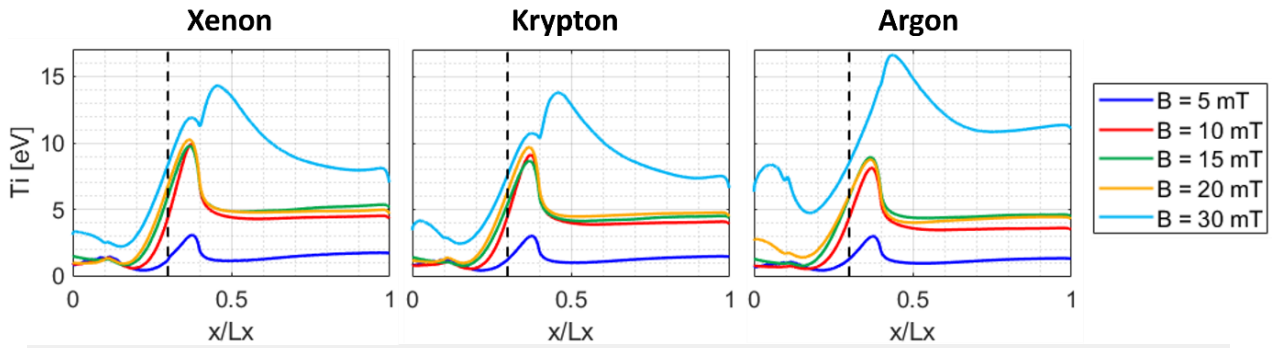


Fig. 5.18: Time-averaged (over $20 - 30\ \mu s$) axial profiles of ion temperature (T_i) for the three propellants with various B. Dashed black lines represent the location of the channel exit plane.

5.3. Influence of the axial profile of the applied magnetic field

To investigate the influence of the axial distribution of the applied radial magnetic field, we have systematically changed the B-field's profile using two parameters: 1) standard deviations (σ) in the B-field's Gaussian profile (Eq. 3.1) which alters the width of high magnetic field region, 2) location of the field's peak (x_p) which affects the overlap between the ionization and the acceleration regions. Note that changing either of the parameters alters the axial gradients of the B-field profile throughout the domain.

Fig. 5.19 (a) and (b) depict the axial distributions of the considered B-field profiles, respectively, with different standard deviations (σ) and the location of the field's peak (x_p). In these profiles $B(x = 0)$, $B(x = L_x)$ and $B(x = x_p)$ are kept the same as in baseline condition (refer to Section 3.1.1). The axial profile of the imposed ionization source in the simulations is shown on the plots to highlight the relative position of the ionization source with respect to the region of highest magnetic field intensities across various simulation cases. Referring to **Fig. 5.19** (a), by increasing the value of σ, the B-field profiles gradually approach the shape given by the case with $\sigma = inf$, which is associated with an arbitrarily large standard deviation value (set here to 100). The baseline value of σ (σ_0) is $0.625\ cm$.

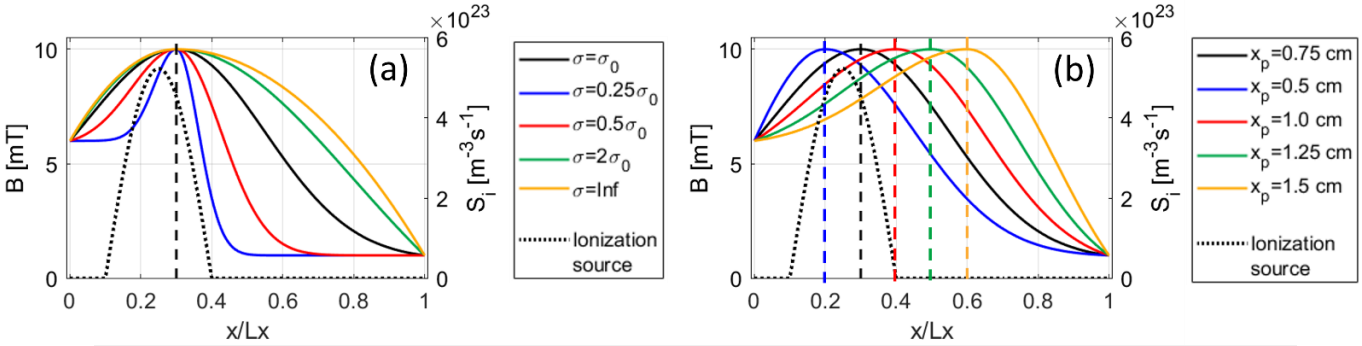


Fig. 5.19: Axial profiles of the applied radial magnetic field for simulations with different B-field distribution; (a) various values of standard deviations (σ), and (b) various axial locations of the magnetic field peak (x_p). The profile of the imposed ionization source is shown in both plots for reference. Dashed lines represent the location of the magnetic field peak in each case.

Note that A_k and C_k coefficients in Eq. 3.1 are determined in such a way as to constrain the values of the $B(x)$ profile at two boundaries of the domain which are different from $B(x_p)$. As a result, even at

very large values of σ (resembling σ approaching to infinity), the $B(x)$ profile is not flattened. Also, while we refer to σ in this case as approaching to infinity, in practice, its value is not infinite but rather set to a relatively large value, such as 100. In fact, the shape of the profile does not change appreciably for values of σ beyond a sufficiently large value, e.g. 10.

5.3.1. Variations in plasma profiles and currents

Fig. 5.20 shows the changes in the time-averaged axial plasma profiles for different axial distributions of the radial magnetic field.

Referring to these plots, a couple of interesting observations can be made. First, changing the standard deviation of the B-field's profile over a rather large range is seen to minimally affect the axial profiles of the plasma properties. The case with $\sigma = 0.25\sigma_0$ presents the most difference among all the cases, particularly in terms of the ion number density and the axial electric field. The plasma profiles are almost invariant with σ from $0.5\sigma_0$ to inf. These observations are significant because they highlight that, when the ionization process is modelled through a temporally invariant source, the variations in the width of the region of the high magnetic field intensities, does not majorly affect the distributions of the plasma properties. This contradicts the explanation provided in Ref. [156] to justify the experimental observation that the acceleration zone expands with the increasing B-field intensity.

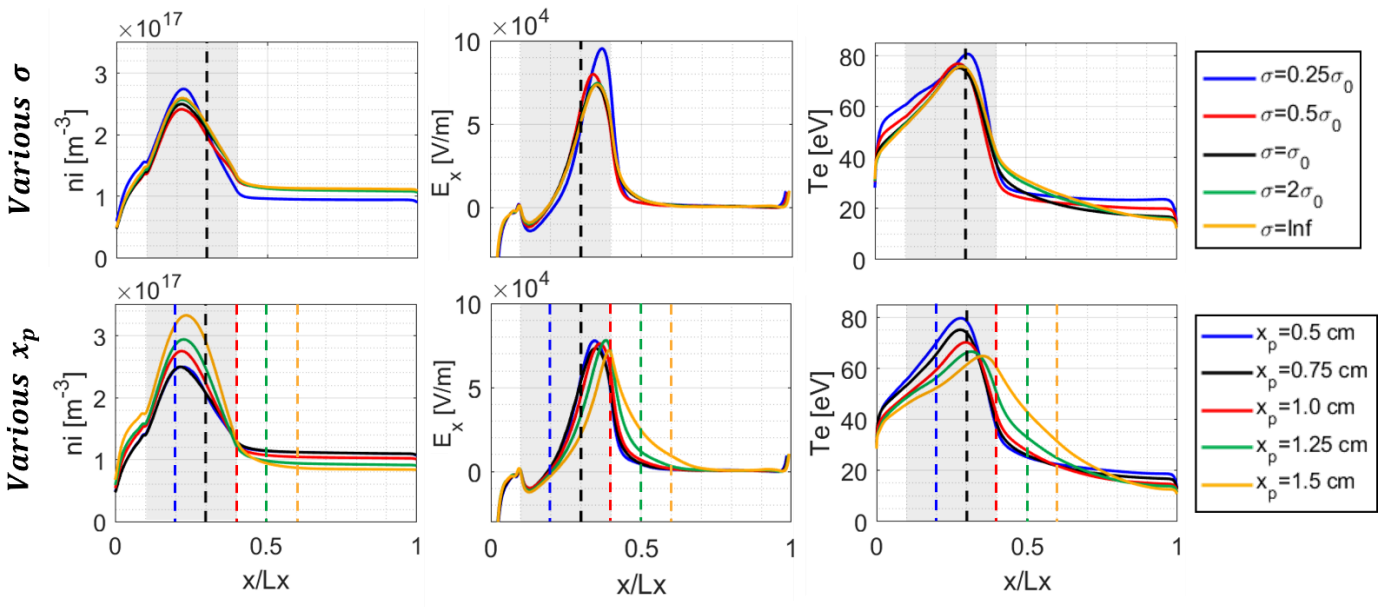


Fig. 5.20: Time-averaged (over $20 - 30\ \mu s$) axial profiles of ion number density (n_i), axial electric field (E_x), electron temperature (T_e) for xenon with various values of standard deviation of the magnetic field profile σ (top row), and various magnetic field's peak locations x_p (bottom row). Dashed lines represent the location of the channel exit plane in each case and grey boxes delimit the position of the ionization source.

This implies that significant alteration in the plasma profiles and performance of a Hall thruster when varying the width of B-field's profile in a real thruster setting [160]-[162] should primarily be attributed to the variations in the ionization process, including the efficiency of the ionization and the relative location of the ionization zone with respect to the acceleration region. Alternatively, variations in the axial gradient of the magnetic field can alter the curvature and radial gradient of the field topology. As

demonstrated in Section 4.3, the magnetic field's curvature can significantly influence plasma processes and conditions. Hence, alteration of the curvature of the magnetic field could also be another contributing factor in the experimentally observed changes in the performance when varying the width of the high magnetic field region.

Second, changes in the axial location of the peak B-field intensity are evident to have a more notable impact on the profiles of the plasma properties. In this respect, we see that, when x_p is varied from $0.5\ cm$ to $1.5\ cm$, the extent of overlap between the ionization zone and the acceleration zone is continuously reduced as the acceleration zone shifts progressively downstream toward the plume (as inferred from the E_x plot in **Fig. 5.20**). This downstream movement of acceleration zone leads to consistently larger ion velocities in the plume (**Fig. 5.21**), as well as increase in the peak n_i, a gradual reduction in the peak T_e values together with a downstream shift in the axial location of the peak T_e. Nevertheless, the extent of the downstream movement of the acceleration region does not match the extent of the shift in the location of the magnetic field peak. This is in part because the B-field value is fixed on the left boundary, thereby the B-field intensities are maintained at relatively high values upstream of the acceleration region (toward the anode side of the domain). As a result, the region of high B-field intensity, thus the acceleration zone does not move significantly with the change in x_p.

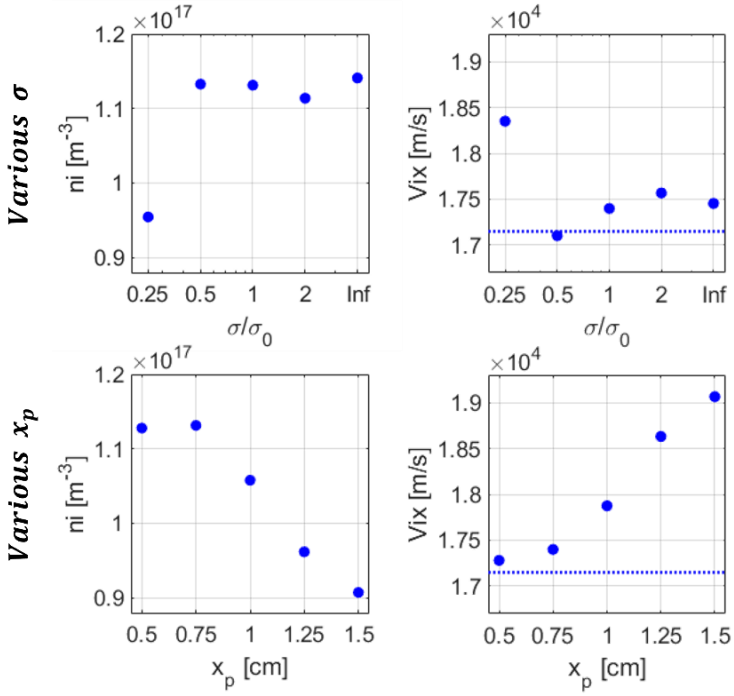


Fig. 5.21: Variation of spatiotemporally averaged (across axial extent of $1.5\ cm < x < 2.5\ cm$ and over $20 - 30\ \mu s$) ion number density (n_i) and ions' axial drift velocity in the plume vs σ (top row) and vs x_p (bottom row) for xenon. The dashed lines in the right-hand side plots represent the theoretical ideal exhaust velocity for ions from Eq. 5.1.

Despite the minor changes observed in the plasma profiles, the electron current (I_e) and thus, the discharge current (I_d) vary substantially with changes in the B-field's profile, as shown in **Fig. 5.22**. While the ion current (I_i) remains almost invariant with σ and x_p, the electron current decreases significantly as either σ or x_p increases. Indeed, as will also be seen in Section 5.3.2, the consistent

increase in the width of the relatively high magnetic field region with increasing σ or x_p leads to a continuous reduction in the overall electron transport.

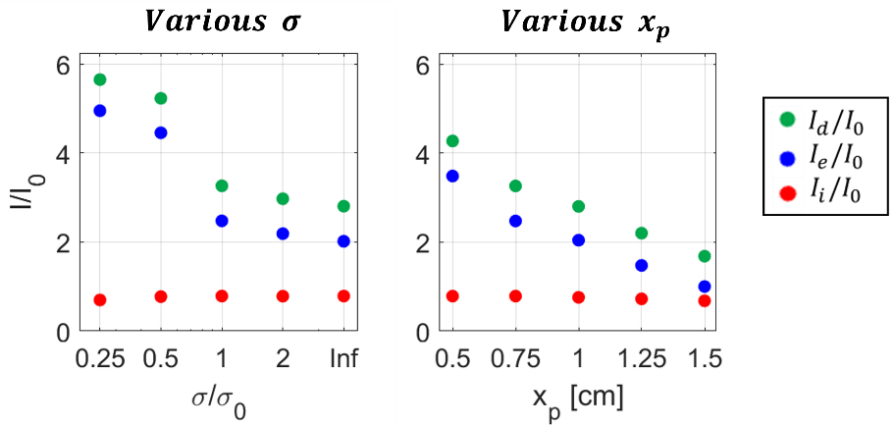


Fig. 5.22: Variation of the temporally averaged (over $20 - 30\ \mu s$) current terms vs σ (left), and vs x_p (right) for xenon propellant; I_0 is the nominal total ion current imposed by the ionization source. Note that the x-axis in the left hand-side plot is in logarithmic scale, and $\sigma_0 = 0.625\ cm$ is the standard deviation of the baseline B-field profile.

5.3.2. Variation in the electrons' cross-field transport

The time-averaged axial profiles of the of the force terms in Eq. 1.20 contributing to the electrons' axial transport in the presence of the studied magnetic field profiles are presented in **Fig. 5.23**.

Looking at the left column plots, it is noticed that as the parameter σ is increased, the axial distribution of the F_B (or equivalently the RHS term which is the sum of F_E, F_Π and F_I terms) tends to become more uniform. This behavior is related to the consistent reduction in the axial gradient of the B-field's profile. Additionally, the peak magnitude of F_B, along with the peak of the individual contributions (F_E, F_Π and F_I), consistently decreases with increasing σ.

Referring to the plots in the right column, when the axial location of the peak magnetic field intensity moves from $0.5\ cm$ to $1.5\ cm$, the profile of F_B is seen to become increasingly more flattened, with its upstream values dropping notably. At $x_p \geq 1\ cm$, the F_B profile begins to develop a peak at the x_p position, nearly as prominent as the upstream peak. For the large x_p values ($x_p \geq 1.25\ \ cm$), F_E and F_I terms demonstrate symmetrical oscillatory axial distributions across the domain.

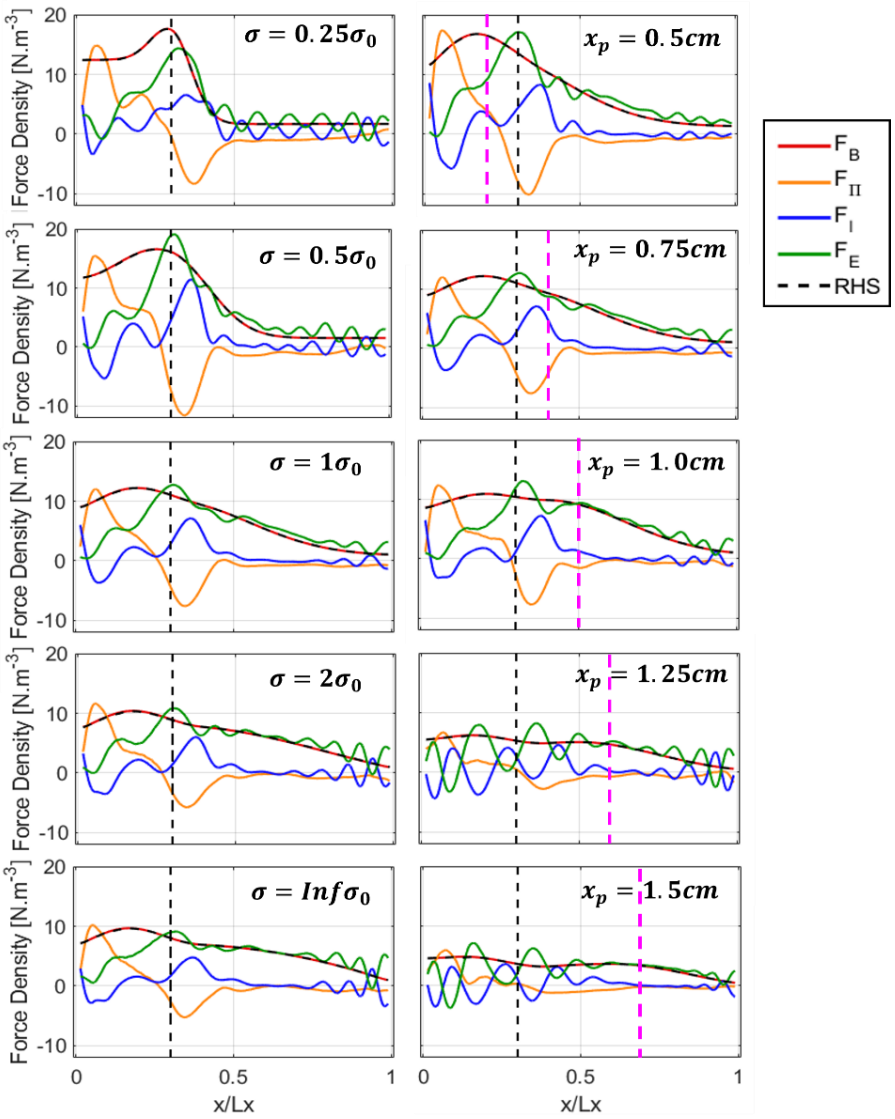


Fig. 5.23: Axial profiles of the transport terms in Eq. 1.20 for xenon propellant with various σ (left column), and various x_p (right column). The force terms are averaged over $4\ \mu s$. F_B is the magnetic force, F_Π is the viscous effects, F_I is the convective inertia force, F_E is the electric force term, and RHS represents the sum of F_Π, F_I and F_E . F_t (temporal inertia) contribution was almost zero, and it is thus not displayed. Dashed black lines represent the location of the peak B-field in the baseline case ($x_p = 0.75\ cm$), while dashed magenta lines in right column plots indicate the location of the peak B-field in the respective cases (x_p).

5.4. Conclusion

The complex and highly coupled nature of the plasma processes in a Hall thruster poses a great challenge on isolating and distinguishing how the variations in different parameters may alter the underlying phenomena and the global behavior of the discharge. In this regard, high-fidelity parametric sweeps in reasonably simplified controlled simulation environments are necessary to set the foundational understanding on the parametric variability of the system. Building upon the insights derived from the simplified parametric simulations, we can then methodically progress toward setups

that are increasingly more representative of the real world, and ultimately discover the parametric dependency of the plasma processes in realistic settings.

To this end, leveraging the substantial computational cost reduction achieved with RO-PIC, and following the parametric investigation in the radial-azimuthal configuration conducted in the previous chapter, we proceeded with performing a parametric study in the axial-azimuthal configuration with a simplified representative setup in this chapter. The parameters investigated include discharge voltage, ion current density (or, equivalently, mass flow rate which is controlled by the intensity of the ionization source), magnetic field intensity and its profile's shape. The most salient general findings in common among all operating conditions are:

- The numerical dispersion of the instabilities inside the channel and in the plume, overall, matches the nonlinear and linear IAI's theoretical dispersion relation, respectively across various operating conditions except for the very low current density ($J = 50$ and $100\ Am^{-2}$) and high magnetic field intensities ($N = 20$ and $30\ mT$), where indications of the presence of ITTI were noted. The development of strong ITTI modes at these conditions can be correlated with the insufficient levels of electrons' transport, which, according to Ref. [159], can trigger this instability mode.
- Evidence of the presence of ITTI in these conditions includes detection of the modes with non-zero axial wavenumber components from the DMD analysis in Refs. [138][139] and observation of the "wave-riding" ions in the IVDFs as well as notable broadening of the axial IVDFs. The frequency of the ITTI in these cases varies between $0.6 - 1.5\ MHz$.
- Ion-wave trapping which acts as the saturation mechanism for the instabilities was evidently observed across all operating conditions except for very low current density ($J = 50\ Am^{-2}$) and very high magnetic field intensity ($30\ mT$), where the instabilities were found to be weak.
- Theoretical predictions of the azimuthal wavenumber and the frequency of the dominant IAI's mode showed, respectively, up to 200% and up to $150\ \%$ error, in the respective simulated values across various operating conditions and propellants.
- Theoretical prediction for the saturated amplitude of IAI-induced plasma density fluctuations in the plume, based on ion-wave trapping saturation, is about 12% of the steady state plume density, while the simulated values vary between 8 to 15% across operating conditions.
- Regarding the distribution of individual contributions to the electrons' axial transport, in most conditions, viscous effects (F_Π) are the dominant term near the anode. However, in the rest of the domain, F_Π's contribution is nearly offset by convective inertia (F_I) term, leaving the instabilities' contribution (F_E) as the primary contributor to the transport.

Furthermore, the specific trends of variations with each operating condition are summarized below:

Effects of discharge voltage (V):

- The width of the acceleration zone progressively expands with increasing V and the location of the peak of the E_x profile shifts downstream.

- The deviation of the ion velocities in the plume (V_{ix}) from the ideal values ($v_{exhaust}$) is consistently increased at higher discharge voltages, with the deviation of the V_{ix} from $v_{exhaust}$ becomes more substantial from xenon to argon.
- The electron current (I_e) exhibits small variability across the voltages of 200 to $400\,V$ and jumps by a factor of about 1.5 from 400 to $600\,V$, which is due to increased role of viscous effects. Ion current density ratio (I_i/I_0) appears to reach a plateau beyond $V = 300\,V$ indicating the maximum ion beam current fraction that can be extracted with the imposed injection source intensity.
- The instabilities' characteristics show minor variability across the simulated voltage range.
- The F_Π term became increasingly more significant within a larger segment of the channel region as V increases, overtaking the instabilities' contribution to transport particularly at $600\,V$.

Effects of current density (J):

- The overlap between the acceleration and the ionization zones increases for small values of the current density (J) which reduces the ions' axial drift velocity in the plume.
- The fraction of the ion current collected at the cathode (I_i/I_0) became increasingly smaller than 1 as the J increased.
- The azimuthal wavenumber, frequency and amplitude of the instabilities increase with J and so does their induced electron transport.
- The ions' velocity distribution functions (IVDF) at low J values of 50 and $100\,Am^{-2}$ show the distinct features of the ions' interactions with the ITTI including oscillatory behavior and enhanced dispersion.

Effect of B-field intensity:

- Increasing B results in a continuous decrease in I_e until it reaches an asymptotic value between 20 and $30\,mT$. I_i, however, increases with B until it nearly plateaus around $15\,mT$.
- At the low B-field extreme ($B = 5\,mT$), the acceleration region is widened and shifts further downstream, reducing its overlap with the ionization region. Furthermore, at this field intensity, the electrons' transport within the channel is primarily driven by the F_Π term. Whereas, in the plume, the F_Π, F_I and F_E terms are of comparable magnitudes. However, the balance between of F_Π and F_I in the plume leaves F_E as the dominant transport mechanism in this region.
- At the high B-field extreme ($B = 30\,mT$, and to a lower extent $B = 20\,mT$), the discharge becomes turbulent, leading to ions' axial drift velocities much lower than the ideal $v_{exhaust}$. The non-idealities in acceleration substantially increase from xenon to argon. The turbulent fluctuations cause significant heating of the electron and ion populations and remarkably high electrons' transport in case of argon. The $30\,mT$ case indicates the most disparity in plasma behaviors among propellants.
- Inside the channel, the instabilities' wavenumber and frequency decrease with B, while they show no distinct trend in the plume. The most notable change in the wavenumber and amplitude of oscillations between the channel and the plume regions occurs at $B = 5\,mT$.

- At low B-fields ($B = 5\ mT$), the ions have a highly beam-like velocity distribution, whereas, at high B-fields ($B = 30\ mT$) the IVDFs exhibit “swirling” features as a result of their interactions with the turbulent fluctuations.

Effects of B-field profile:

- The axial profiles of plasma properties are minimally affected by varying the standard deviation (σ) of the B-field’s Gaussian profile. This limited sensitivity of plasma behavior to σ is, in part, attributed to the prescription of a fixed ionization source. This observation suggests that the significant changes in the plasma profiles and performance of a Hall thruster with variation in the width of B-field’s profile [160]-[162] is primarily due to the variations in the ionization process, and/ or the curvature of the magnetic field.
- Shifting the axial location (x_p) of the peak B-field intensity towards the downstream reduces the overlap between the ionization and acceleration zones, albeit to a lesser extent than downstream shift in x_p. The impact of shifting x_p is less than expected, partly due to the fixed and relatively high intensity of the B-field in the near-anode region and the invariant imposed ionization source.
- Despite minor changes in the plasma profiles and an almost invariant ion current (I_i) with σ and x_p, the electron current (I_e) and thus, the discharge current (I_d) decreases substantially with increasing σ and x_p. This is due to the consistent increase in the axial extent over which magnetic field is relatively high.
- In addition to the reduction in the overall electrons’ transport (F_B term), the profile of F_B tends to become more uniform as either σ or x_p increases.

As a final point, it is recognized that the imposed ionization source in the simulations may have to some extent affected the results. It is thus important to verify the outcomes from this work in an experimental setting or/and using 3D PIC simulations that self-consistently resolve the collisional processes (including the ionization) as well as the interactions with the radial walls.

Chapter 6 RO-PIC modelling of a high-power 20 kW-class industrial Hall thruster

High-power magnetically shielded Hall thrusters have emerged in recent years to meet the needs of the next-generation on-orbit servicing and exploration missions. Predictive models can significantly contribute to the design and development of these thrusters by reducing development costs and time to market, while enhancing their reliability for in-space operation. However, modeling such thrusters involves two main challenges.

First, due to their large size, self-consistent simulations of these thrusters using conventional multi-dimensional PICs without any physics-altering speed-up factors is unfeasible. In this regard, within this chapter, we demonstrate the applicability of the RO-PIC as a cost-efficient, self-consistent tool for prediction of the behavior of an industrial 20 kW-class magnetically shielded Hall thruster. To this end, the axial-azimuthal Q2D simulations are performed for three operating conditions. We have resolved self-consistently an unprecedented 650 μs of the discharge evolution without any ad-hoc electron mobility model, capturing several breathing cycles and approximating the experimental performance parameters with an accuracy of 70 to 80 % across the operating conditions. This has been made possible using single-region approximation of the RO-PIC which has provided a 400-fold speedup compared to a full-2D PIC, in these simulation cases.

Second, magnetically shielded thrusters feature highly curved magnetic field topology with large radial and axial gradients. This implies that the plasma configuration in these thrusters exhibits a more pronounced 3D nature than the Hall thrusters with conventional magnetic topologies. Accordingly, a 2D axial-azimuthal simulation resembles a rather simplified representation of the thruster's geometry. In any case, by performing the Q2D axial-azimuthal simulations using the single-region approximation, we intend to primarily investigate the level of accuracy at which such a self-consistent, low-computational-cost kinetic simulation can predict the experimental performance parameters and the global discharge dynamics.

In addition, radial-azimuthal simulations (at high-order approximation limit of RO-PIC) are carried out to complement the axial-azimuthal simulation by underlining the significance of the radial physics, including the radial gradients in the magnetic field, in the radial distribution

of the plasma properties and the involved plasma processes, in general. These simulations are performed for three radial-azimuthal cross-sections of the channel, at three different axial positions including near-anode, ionization and acceleration regions. The results of these studies are provided in Appendix A.7. However, the main insights gathered from the radial-azimuthal simulations and their relationship with the axial-azimuthal simulations are summarized at the end of the chapter.

6.1. RO-PIC as a tool to aid industrial development of plasma technologies

So far, we have showcased the efficacy of the RO-PIC in faithfully modeling plasma behavior in various plasma configurations within extensively large parameter spaces. In this chapter, we demonstrate the utility of RO-PIC as a tool to simulate full-size $\mathrm{E} \times \mathrm{B}$ devices, modeling which is currently unfeasible with the existing state-of-the-art numerical techniques in a self-consistent manner and within practical timeframes. To this end, we take a high-power magnetically shielded Hall thruster as an example of an industrially relevant device.

Today, innovative near-Earth and interplanetary space missions are being planned with the aim of enabling sustainable and responsible utilization of space and to expand humanity's exploration capabilities, from the Moon to Mars and beyond. High-power magnetically shielded Hall thrusters [52]-[55] are currently viewed as one of the leading candidates among the electric propulsion concepts to realize these novel missions due to their high-throughput, long-lifetime capabilities, and operational versatility.

Nevertheless, over the past decade, developing and testing this class of Hall thrusters has revealed the enormous cost and time required to mature this new technology to the qualified and flight-ready status. Simultaneously, extensive research into the Hall thrusters in the past years has highlighted the impact of the on-ground vacuum testing facilities on the performance and stability of Hall devices [163]-[168], which notably affects the reliability of the characterization/qualification test results with respect to the on-orbit operation. Finally, it is becoming globally acknowledged that the current qualification strategies, centered around pre-determined operating scenario(s), lack sufficient statistical data for reliable quantification of the risks and devising proper safety margins from a statistical perspective [169].

The above realizations have once again underscored the necessity of predictive models that can aid the design, development, and testing of Hall thrusters, thus, mitigating the required cost and time from one side and augmenting the reliability of this technology from the other side.

In this regard, although traditional PIC codes provide a high level of fidelity in predicting the behavior of thrusters, their computational cost (without any physics-altering speed-up scaling factors) are prohibitively high for real-size high-power Hall thrusters, rendering them impractical as a design and test-aiding tool. RO-PIC, however, can serve as a remarkably cost-efficient tool enabling self-consistent kinetic simulation of full-size $\mathrm{E} \times \mathrm{B}$ plasma devices, including high-power Hal thrusters. It can thus

enable the design of more efficient plasma technologies and facilitate their development by reducing the reliance on empirical, test-dependent practices.

Recalling that the Q2D simulations based upon the RO-PIC scheme enable a wide spectrum of resolution choices between full-1D and full-2D, thereby providing the flexibility to choose the optimal trade-off between the predictions' accuracy and the required computational resources. We have particularly demonstrated in Chapter 4 that, in the axial-azimuthal coordinates, the single-region Q2D simulation, which provides more than two orders of magnitude reduction in the computational cost, captures an average effect of the azimuthal instabilities on electrons' cross-field transport, that results in a reasonably accurate self-consistent prediction of the dynamics of the discharge. Accordingly, the maximum computational advantage (400 times in this case) provided by the single-region approximation limit of RO-PIC has been the main enabler of the present effort of simulating the extended domain of a 20kW-class Hall thruster over a $650\ \mu s$ duration.

We highlight that the single-region, as the lowest approximation limit of RO-PIC, is chosen to quantify the upper limit of the error in the prediction. Any approximation order above this limit is expected to improve the accuracy of the model. Moreover, due to the maximum computational gain, the single-region approximation limit can be the most practical choice for industrial applications to provide estimates of thruster behavior across the operational envelope.

6.2. Simulations' setup and conditions

The simulations are performed in the axial-azimuthal coordinate using the single-region Q2D approximation for a development model of a 20 kW-class magnetically shielded Hall thruster, SITAEL's HT20k, which is described in Refs. [168][170]. The computational domain is a Cartesian $x-z$ plane, with the x-coordinate along the axial direction and the z-coordinate along the azimuth. The anode is located at the left-hand side of the domain whereas the cathode boundary is at the right-hand end. Along the axial direction, the channel exit plane is located at the middle of the domain, i.e., $x/L_x = 1.0$. Accordingly, a plume length equal to the channel's axial extent is modelled. In the azimuthal direction, the computation domain is 2-cm-long.

At the beginning of the simulation, the electrons and ions are sampled from a Maxwellian distribution at $10\ eV$ for the electrons and $0.5\ eV$ for the ions and injected uniformly throughout the domain. At the cathode boundary, electrons are sampled from a half-Maxwellian at $5\ eV$ and are injected into the domain at each timestep according to the quasi-neutrality approach (see Section 1.4.2.2).

Dirichlet potential boundary conditions are applied at both axial ends of the domain, with the cathode side at $0\ V$ and the anode side at $300\ V$. In the azimuthal direction, a periodic boundary condition has been applied to either end. The axial and azimuthal potential boundary conditions are implemented in the RDPS as was described in Section 2.2.2.1.

Concerning the boundary conditions for the plasma particles, the azimuthal direction is assumed as periodic. Therefore, the particles leaving the domain at one end are injected back from the other end. Along the axial direction, both ions and electrons reaching either the anode or the cathode side of the

domain are removed from the simulation. However, ion recombination on the anode and the consequent injection of the neutrals are considered in the simulations.

The neutrals' dynamics is resolved in terms of their density and velocity evolution by solving a 1D axial Euler system of fluid equations (refer to Section 1.4.2.4). The adoption of a fluid description for neutrals is in line with the current practices being pursued by the community for axial-azimuthal simulations [115][171]. The benchmark results of our 1D Euler neutrals solver are provided in Appendix A.1.5. Furthermore, the application of this neutral's fluid solver (and its comparison with other neutral models) in 1D axial and quasi-2D axial-azimuthal simulations of a SPT100-type Hall thruster domain can be found in Ref. [106].

The flow of the neutrals is assumed to be isothermal at the temperature of $650\ K$. As the neutrals are treated as a fluid, to account for the neutrals created due to the ion recombination on the anode, the corresponding mass flow rate is calculated and added to the mass flow rate injected from the gas distributor [106]. The effects of the background pressure due to the residual neutrals in the vacuum chamber and the neutrals population in the cathode plume are not accounted for. Hence, no neutral injection is considered from the cathode boundary.

The simulations' physical and numerical parameters are summarized in **Table 6.1**.

Parameter	Value [unit]
Physical Parameters	
Initial plasma density (n_0)	1×10^{17} [m^{-3}]
Electron temperature, initial load ($T_{e,0}$)	10 [eV]
Electron temperature, cathode injection ($T_{e,c}$)	5 [eV]
Ion injection temperature ($T_{i,0}$)	0.5 [eV]
Neutral temperature ($T_{n,0}$)	650 [K]
Computational Parameters	
Time step (Δt)	2×10^{-12} [s]
Total simulation time (t_{sim})	650 [μs]
Cell size ($\Delta x = \Delta z$)	20 [μm]
Initial number of macroparticles per cells along axial direction ($N_{ppc,x}$)	50
Initial number of macroparticles per cells along axial direction ($N_{ppc,z}$)	600
Number of regions in Q2D simulations, NumR ($M = N$)	1 (single-region approximation)

Table 6.1: Summary of the main physical and numerical and parameters used for the Q2D axial-azimuthal simulations of HT20k.

The simulations are performed for three operating conditions of the HT20k where the thruster was operated on xenon as the propellant. An overview of the operating parameters is provided in **Table 6.2**. The values of the peak magnetic field intensity for the different operating conditions are normalized with respect to the peak field intensity of Case II, which is denoted as B_0. The axial profiles of the normalized radial magnetic field intensity for the three simulated operating conditions are shown in **Fig. 6.1** (a).

	Simulation case		
Operating condition	**Case I**	**Case II**	**Case III**
Discharge Voltage [V]	300	300	300
Anode Mass Flow Rate (AMFR) [mg/s]	25	30	35
Magnetic field peak intensity [mT]	$0.8B_0$	B_0	$1.5B_0$

Table 6.2: HT20k operating conditions used for the simulations.

The initial profiles of the neutrals' densities and axial velocities for the three cases are shown in **Fig. 6.1** (b). It is noted that the specific choice of the initial neutral density and velocity profile mostly affects the initial discharge transient, and simulations with different choices of these initial profiles shall eventually converge to a similar quasi-steady state. Accordingly, the initial profiles of **Fig. 6.1** (b) are not expected to notably influence the plasma behavior beyond the initial transient phase of the discharge evolution.

The electron-neutral collisions are resolved using the Monte Carlo Collisions (MCC) scheme (see Section 1.4.2.3). The collision events included in the MCC model include single ionization, four excitations and the elastic momentum-transfer collision. The cross-sections for these collisions are presented in **Fig. 1.12**.

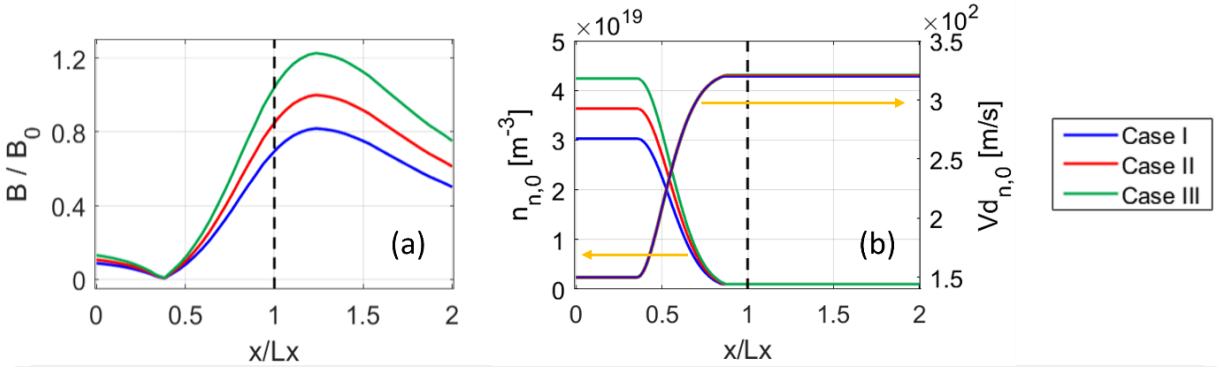


Fig. 6.1: Axial profiles of (a) the normalized radial magnetic field intensity (b) initial neutral density (left axis) and neutrals' axial velocity (right axis) used for the three operating conditions; Case I, Case II and Case III.

6.3. Results and discussions

In this section, we present the outcomes of the simulations in terms of global performance parameters, distribution of plasma properties and the azimuthal waves' characteristics. The predicted performance parameters are compared against the experimental data for HT20k thruster. We emphasize that intensive measurements of the plasma properties are not available for the HT20k to be used for validation of the simulation results. Nonetheless, since the simulations are fully self-consistent and do not include any tunning coefficient to be matched against the test data, comparing the performance parameters could serve as a suitable measure to quantify the accuracy of the predictions.

6.3.1. Global performance parameters and discharge current oscillations

We start discussing the results by comparing the predicted performance parameters from the Q2D axial-azimuthal simulations against the experimental data. **Table 6.3** shows the simulated performance parameters for each operating condition. In addition, **Fig. 6.2** compares the variation vs the anode mass flow rate (AMFR) of the simulated and measured performance parameters as was reported in Ref. [168]. The data are shown in a non-dimensional format in the figure at the request of SITAEL. In this regard, each simulated/measured performance parameter is normalized with respect to the corresponding measured value of that parameter for Case II.

As mentioned in Section 6.2, the neutrals' background pressure effects are not considered in the simulations and, as a result, our setup amounts to a thruster operating in space where the background pressure is indeed negligible. Accordingly, to gain insight into the extent of variation in performance parameters with background pressure, for the three simulated operating conditions, we have provided in **Fig. 6.2** the experimental performance at two background pressure levels, differing by a factor of 2.

The calculated performance values shown in **Table 6.3** are averaged over several breathing cycles. In this respect, the instantaneous value of the discharge current (I_d) is calculated in our simulations as the difference between the electron and ion flux reaching the anode at each time step. Furthermore, we have estimated the instantaneous values of thrust (T) and specific impulse (I_{sp}) during the simulation using the following relations:

$$T = \frac{A_{real}}{A_{sim}} \frac{1}{\Delta t} \sum_n \mathcal{W}_n M_i v_{ix,n}, \qquad \text{Eq. 6.1}$$

$$I_{sp} = \frac{\sum_n \mathcal{W}_n v_{ix,n}}{g_0 \sum_n \mathcal{W}_n}. \qquad \text{Eq. 6.2}$$

In the above relations, the summation is taken over ion particles crossing the cathode boundary at each timestep. Also, A_{real} and A_{sim} are the real and simulated thruster's cross-sectional area, respectively, $\mathcal{W}_n$ is the ion's macroparticle weight, $v_{ix,n}$ is the axial velocity of each exiting ion, M_i is the xenon ion mass, and g_0 is the gravitational acceleration at the sea level. The thrust efficiency is calculated using the time-averaged values of thrust and discharge current as

$$\eta_T = \frac{T^2}{2\dot{m}_n I_d V_a}, \qquad \text{Eq. 6.3}$$

in which, $\dot{m}_n$ is the injected xenon mass flow rate from the anode.

	Simulation case		
Performance Parameter	**Case I**	**Case II**	**Case III**
Discharge Current, I_d $[A]$	22.8	27.5	29.8
Thrust, T $[mN]$	350	456	510
Specific Impulse Isp $[s]$	1906	1834	1773
Thrust Efficiency η_T [%]	35.8	42	41.6

Table 6.3: Performance parameters from the Q2D simulations of the HT20k in the three operating conditions.

From **Fig. 6.2**, we observe that, as the mass flow rate increases from Case I to Case III, the simulated time-averaged thrust and discharge current show an increasing trend that is consistent with the

experimental trend. However, thrust efficiency and specific impulse show relatively minor variations with the mass flow rate, similar to the experimental observations.

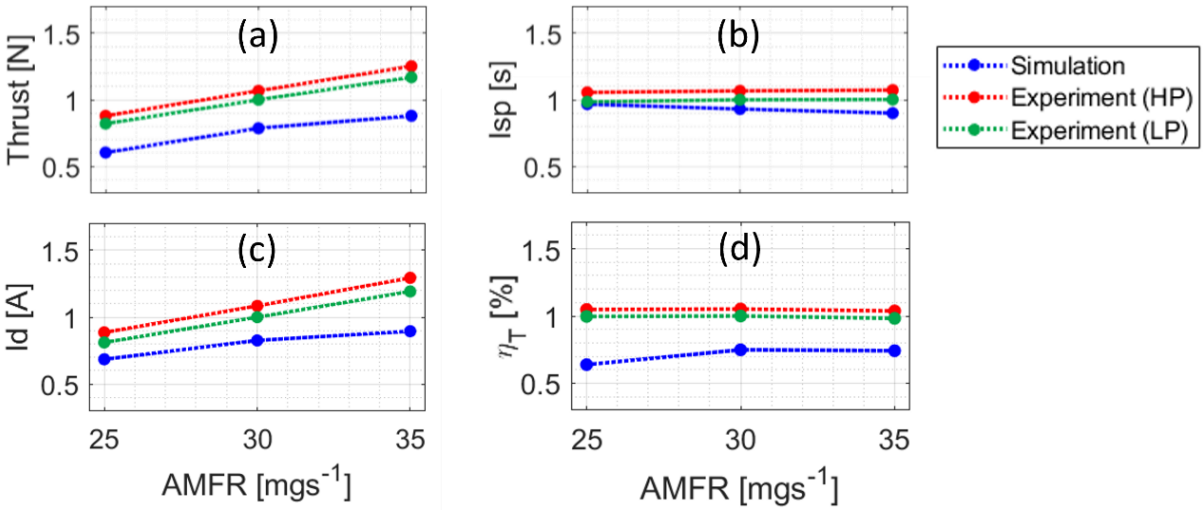


Fig. 6.2: Comparison of the normalized global performance parameters from the simulations against experimental values for the three operating conditions [168]; (a) thrust, (b) specific impulse, (c), discharge current, (d) thrust efficiency. The lower-pressure (LP) data corresponds to the performance measurements at a background pressure lowered by a factor of 2 compared to the higher-pressure (HP) points.

Referring to **Fig. 6.2**, the Q2D simulations across the simulated operating conditions, yield performance estimations that deviate from the experimental values at the reduced backpressure by the error ranges of $15-25\ \%$ in the discharge current, $20-25\ \%$ in the thrust, and $2-10\ \%$ in the specific impulse. The error in the thrust efficiency is also between $25-30\ \%$ for all cases compared to the experimental η_T.

With regard to the above errors in the performance parameters, we identified below, in the order of significance, the main factors that we consider as the root causes of the discrepancies observed between the experimental and simulated performance. Subject to further verification and detailed experimental validation of the simulated results, it is hypothesized that incorporating some of the factors outlined below in the simulation will yield calculated performance parameters that compare more closely with the experimental ones.

A) **Lack of resolving radial physics:** The inherently 3D nature of magnetically shielded Hall thrusters entails that radial processes and gradients play a crucial role in shaping plasma behavior and, consequently, device performance. In this regard, as demonstrated in Section 4.3, the curvature and the radial gradient of the magnetic field affects the plasma processes, regulating the electrons' energy as well as concentrating the plasma density toward the center. Furthermore, the results of the simulations along the radial-azimuthal cross section of the HT20k thruster presented in Appendix A.7 further underscore the impacts of the radial dynamics unresolved in the present axial-azimuthal simulations. According to these results, the absence of the radial coordinate in the axial-azimuthal simulations seems to be among the most influential factors behind the lower predicted thrust and discharge current relative to the experimental values. Indeed, as will be shown in section 0 (**Fig. 6.8**), a notable population of slow ions exists in the plume, which has been most

likely absent in the plume of the real thruster. This is believed to be due to the absence of the confining effect of the radial magnetic field curvature inherent to the magnetic shielding topology. The slow ion population, which does not significantly contribute to the ion current and thrust, become more significant as mass flow rates increases (**Fig. 6.8**), leading to a greater deviation in thrust and discharge current at higher mass flow rates.

As a result, in case the radial coordinate had been resolved, an enhancement of the ionization inside the channel could be expected which would have resulted in most of the ions to be created ahead of the region of maximum electric field intensity (the acceleration zone), thus, reducing notably the slow ion population. In this regard, it is highlighted that such a significant slow ion population has not been observed in the single region Q2D axial-azimuthal simulation of conventional SPT100-type thruster [106].

B) **Single-region approximation of the 2D problem**: Although the single-region approximation of an axial-azimuthal simulation domain has been demonstrated in Section 3.1.2 to self-consistently capture an average effect of the azimuthal instabilities on the electrons' transport, it is the simplest approximation that can be established for a 2D problem with the RO-PIC scheme. This implies that, because of the applied degree of order reduction, there can be an inherent error associated with the results of the single-region simulations.

C) **Absence of the background pressure and the additional neutrals' flow from the cathode**: The background neutrals in the testing facility and the cathode mass flow fraction, that determines the significance of the neutrals' population in the cathode plume, are well known to affect the performance of Hall thrusters [168][172]. These two factors, which are shown to have a similar effect on the discharge dynamics [172], increase the number density of the neutrals in the near-plume of Hall thrusters. The elevated neutral number density is, in part, ingested into the thruster's discharge channel, artificially increasing the effective thruster's mass flow rate [168]. The background and cathode neutrals also modify the global behavior of the thrusters by affecting the underlying processes such as the electrons' cross-field mobility [164][166][168]. Accordingly, we observe from **Fig. 6.2** that all measured performance parameters are lower at a reduced vacuum chamber pressure, and that the difference between the performance at higher and lower backpressures slightly increases with increasing mass flow rate.

D) **Neglecting the multiply charged ions**: The simulated cases correspond to the operating conditions at a relatively low discharge voltage of $300\,V$, which justifies the assumption of neglecting multiply charged ions in the simulations. However, in the real-world setting, a population of multiply charged ions, particularly doubly charged, is typically present and contributes to the discharge current, thrust, and specific impulse.

E) **Absence of ion-neutral charge-exchange (CEX) collisions**: The CEX collisions are known to be significant in the near-plume of Hall thrusters. It is additionally noted that CEX collisions can be important upstream of the acceleration zone as well due to a relatively high neutral density in that region. Accounting for CEX upstream of the acceleration zone can lead to lower ion velocities in the channel, thus, larger plasma densities. In any case, in Ref. [106], it was demonstrated that including CEX collisions in the axial and axial-azimuthal simulations, which do not capture plume

expansion can lead to the underpredicted ions' velocity and unrealistically high neutrals' temperature and velocity in the plume. As a result, the CEX collisions are not accounted for in the simulations here since an accurate capturing of the CEX collisions and their effects in the absence of resolving the radial coordinate is not believed to be practical.

Following the above remarks, we proceed with the presentation of the simulations' results by referring to **Fig. 6.3**, which shows the time evolution of the discharge current signal for the three simulation cases. In addition, we have plotted in **Fig. 6.4** the averaged temporal FFT of the respective ion number density signals to assess the frequency content of the axial discharge oscillations.

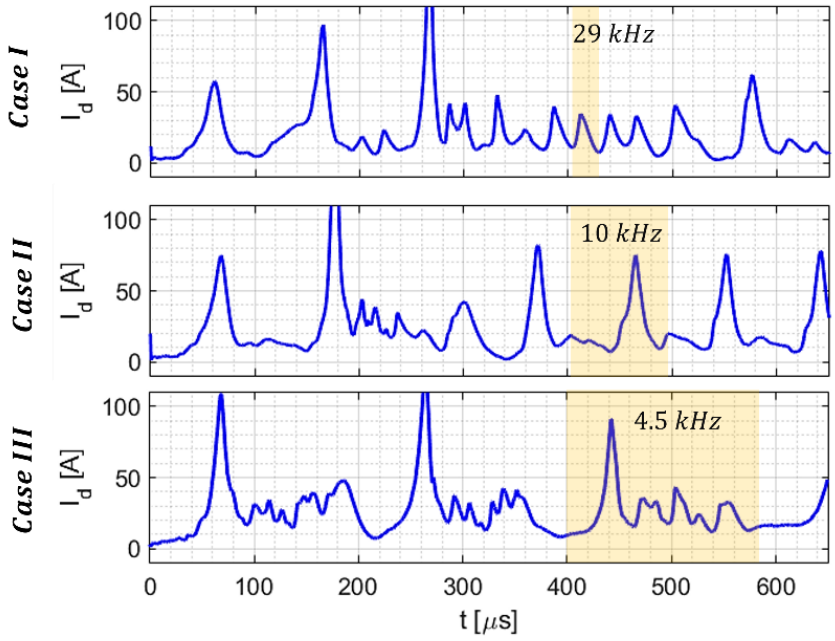


Fig. 6.3: Time evolution of the discharge current for the three simulated operating conditions. The highlighted areas isolate one cycle of the periodic behavior in the discharge after reaching the quasi-steady state.

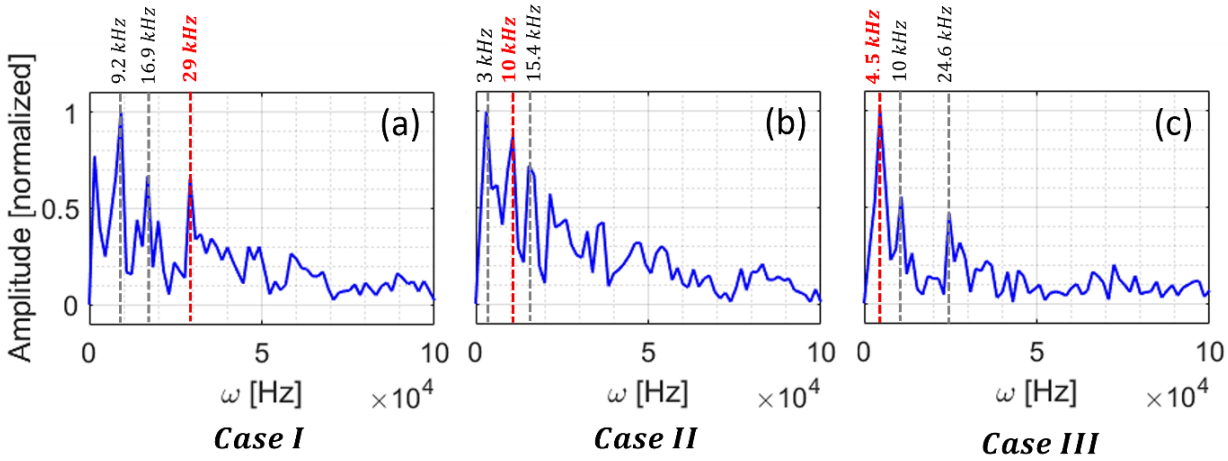


Fig. 6.4: Average (over all axial positions) temporal FFT plots of the ion number density signal, for the three simulated conditions. The two most dominant frequencies in the FFT plots are specified. The frequency highlighted in red corresponds to the frequency of the periodic pattern observable in the respective discharge current evolution plot in **Fig. 6.3**.

It is noted from **Fig. 6.3**, that all simulations have reached a quasi-steady state and exhibit periodic oscillations reminiscent of the breathing mode. This underlines that the average instability-induced electrons' axial transport is resolved adequately with the single-region Q2D simulations, enabling sustainment of the discharge and the development of the breathing mode oscillations.

Across various operating conditions, it is seen in **Fig. 6.3** that the amplitude and frequency of the discharge oscillations are different. However, all three cases exhibit both "low" and "high"-frequency global discharge oscillations, which are also distinctly evident from the corresponding FFT plots in **Fig. 6.4**. Looking at **Table 6.4**, the peak frequencies from the simulations are rather consistent with those observed in the experimental discharge current of the HT20k thruster. Even though we cannot entirely eliminate the possibility that the high frequency peaks in the experiments are associated with the cathode operation, they are most likely related to the thruster itself since they were not visible at higher magnetic field intensities.

	Current signal peak frequencies [kHz]		
	Case I	**Case II**	**Case III**
Simulation	$9.2, 16.9, 29$	$3, 10, 15.4$	$4.5, 10, 24.6$
Experiment	$\sim 9, 25$	$\sim 5, 20$	$\sim 5, 20$

Table 6.4: Comparison of the peak frequencies of the discharge current signal from the Q2D simulations of the HT20k in the three operating conditions with the corresponding experimental values.

Regarding the trend of variation of the frequency of breathing oscillations, the experimental results of Ref. [173] had also interestingly showed a decrease in the main frequency of the global discharge oscillations with increasing magnetic field intensity at discharge voltages around $300\,V$.

6.3.2. Distribution of plasma properties

Fig. 6.5 show the obtained spatiotemporal evolution of several macroscopic discharge properties for the three simulated operating conditions. It is noted that the point of ions' zero velocity, whose location is traced by the white curves on plots (b) and (c), indicates the axial location from where the ions start to backflow toward the anode.

It is seen in **Fig. 6.5** (a) that the evolution of the ion number density (n_i) is expectedly correlated with the discharge current. In fact, the peaks of the discharge current correspond to the maximum ion (plasma) number density near the anode. In addition, the acceleration and downstream propagation of the ions are observed from the ion axial velocity (Vd_i) plots in **Fig. 6.5** (b). In this regard, the ions created upstream the channel exit are accelerated to velocities of around $20\,km/s$ and propagate toward the plume. Accordingly, the location of the points of ions' zero velocity and sonic speed oscillates in time. The axial distance between these two characteristic ion velocity points is also noticed to vary in time such that it becomes maximum when the ions propagate toward the plume and is minimized when the ion front is upstream.

Looking at the evolution plots of n_i and Vd_i for each simulated case, the presence of a low-velocity ion population in the plume can be observed. It is evident from **Fig. 6.5** (a), that the significance of this slow ion population increases with the increase in anode mass flow rate from Case I to Case III. The

slow ion population is believed to be created due to occurrence of ionization over a relatively extended length of the domain (as will be shown in **Fig. 6.6** (c)), resulting in a large overlap between the ionization and acceleration regions. The ions born further downstream do not experience the entire plasma potential drop within the acceleration zone, hence they maintain relatively slow velocities in the plume.

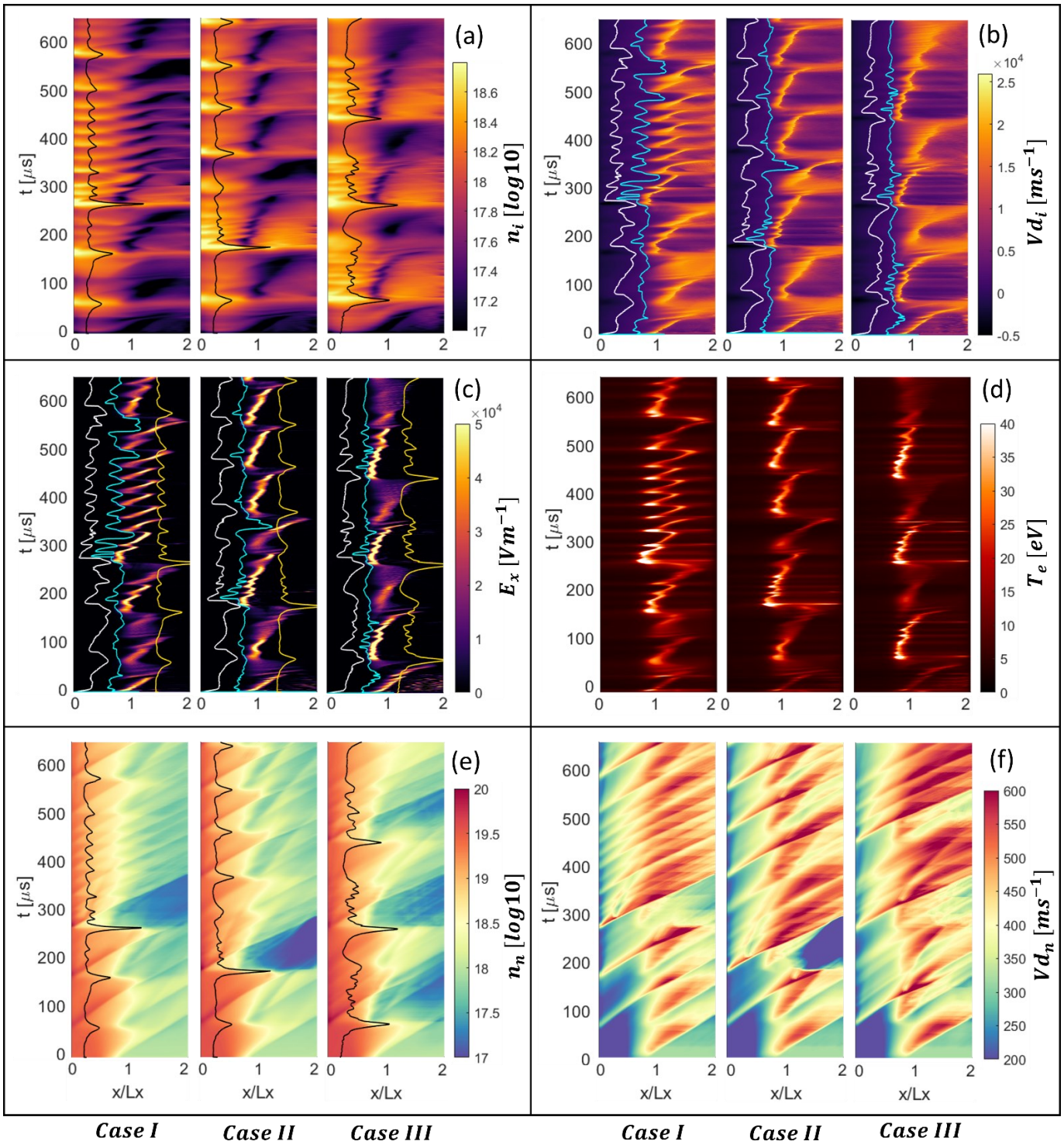


Fig. 6.5: Spatiotemporal maps of (a) ion number density (n_i), (b) ions' axial drift velocity (Vd_i), (c) axial electric field (E_x), (d) electron temperature (T_e), (e) neutral number density (n_n) and (f) neutrals' axial drift velocity (Vd_n) for the three simulated conditions. Black/yellow curves superimposed on (a), (c) and (e) plots are the normalized discharge current (I_d) signals. The white and cyan curves in (b) and (c) plots trace the axial positions of ions' zero velocity and ions' sonic speed, respectively.

Concerning the evolution of the axial electric field (**Fig. 6.5** (c)), we see that the typical back-and-forth movement of the acceleration zone, represented by the region of maximum electric field intensity, is captured in all cases. In this respect, as is reported in literature [115], the axial electric field peak shifts toward downstream of the exit plane ($x/L_x = 1$) during the current increase and retreats inside the channel when the current decreases. It is interesting to note that the extent of the acceleration zone is seen to change in time as well, which is reflected in the electric field plots as a broadening and narrowing of the region of maximum electric field with an associated variation in the peak field's intensity. In line with the movement of the acceleration zone, the axial distance between the points of ions' zero velocity and sonic speed shrinks when the acceleration zone moves upstream and expands when it shifts toward the plume.

The evolution of the electron temperature shown in **Fig. 6.5** (d) is noticed to be completely correlated with that of the electric field. This implies that, as could have been expected, the region of maximum electron temperature corresponds to the region of maximum electric field, i.e., the acceleration zone. Moreover, the electron temperature is seen to reach peak values of over $40\ eV$ in all Cases when the region of maximum electric field intensity is at its narrowest width.

Referring to **Fig. 6.5** (e), the neutral density profile is seen to be correlated with the discharge current evolution. Moreover, the neutral density at the anode location ($x = 0$) peaks for all cases almost immediately following the end of the discharge current drop. This can be due to an increase in the ion recombination on the anode when the discharge current decreases and the discharge moves toward the anode. Looking at the neutrals' axial velocity plots in **Fig. 6.5** (f), we observe that the axial velocity of the neutral flow varies from about $200\ m/s$ near the anode to about $600\ m/s$ in the plume. This observed variation in the axial velocity is in line with the experimental observations reported in the literature, that suggest a factor of 2 to 3 increase in the axial velocity of the neutrals in Hall thrusters as they propagate downstream [174].

The predicted axial distributions of the discharge properties averaged over entire simulation duration, are presented in **Fig. 6.6** for the three simulated cases. From these plots, it is first observed that, as the magnetic field peak intensity increases from Case I to Case III, so does the gradient of the plasma potential (plot (d)). However, the difference in the peak values of the electric field between Cases II and III is quite minimal (plot (b)). Second, it is noteworthy from the profiles in plots (b) and (h) that, in all cases, the ions are seen to reach the sound speed, i.e., Mach number of 1, slightly upstream of the electric field peak.

Third, the increase in the anode mass flow rate from Case I to Case III yields an increase in the ion number density (plot (a)). Consistent with the rise in the neutral number density (plot (e)) near the anode from Case I to III, the ionization rate (plot (c)) also increases. Nevertheless, the difference between the profiles of Cases II and III is again interestingly quite small. However, it is emphasized that the small difference between the results of Cases II and III are only in terms of the time-averaged plasma profiles. Indeed, the time evolution of the discharge is distinctly different across all simulated Cases. In addition, we observe in plot (c) that the ionization rate profiles are rather extended. As a result, significant ion particles are created beyond the electric field's peak. These ions, constituting the slow ion population

in the plume, contribute to increased plasma density within the plume, as is evident in plot (a). The density of the slow ion population in the plume increases from Case I to Case III.

Finally, concerning the axial profiles of the electron temperature (plot (g)), the time-averaged peaks are consistent with the results reported in Refs. [175][176].

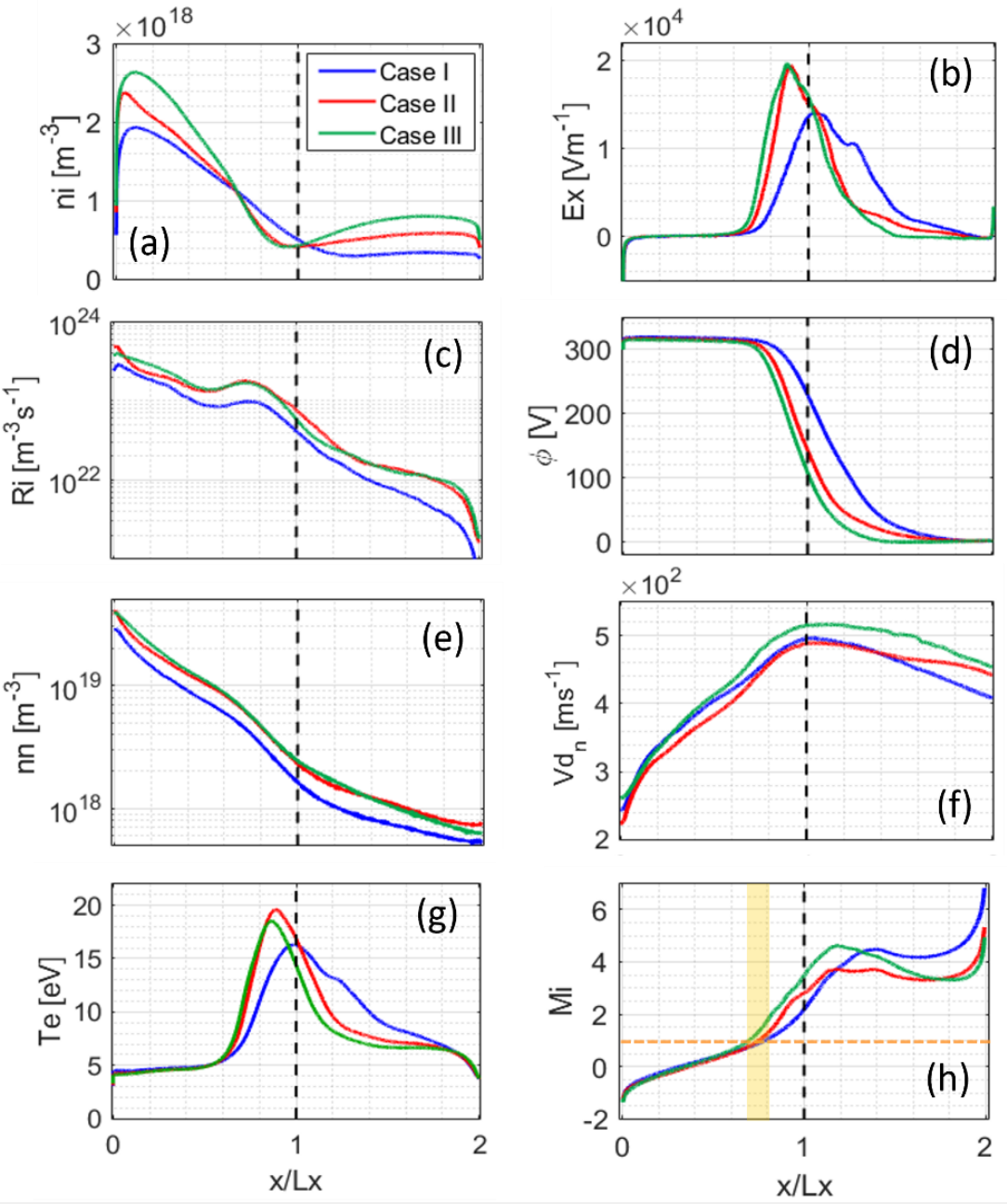


Fig. 6.6: Time-averaged axial profiles of plasma properties for the three simulated operating condition; (a) ion number density (n_i), (b) axial electric field (E_x), (c) ionization rate (R_i), (d) plasma potential (ϕ), (e) neutral number density (n_n), (f) neutrals' axial velocity (Vd_n), (g) electron temperature (T_e), and (h) ion Mach number (M_i). In the ion Mach number plot, the shaded area indicates the positions of the ion sonic point.

Fig. 6.7 compares the predicted profile of ions' axial velocity with LIF measurements at various axial locations for operating condition II. The plot indicates that the predicted ion velocity aligns well with experimental data.

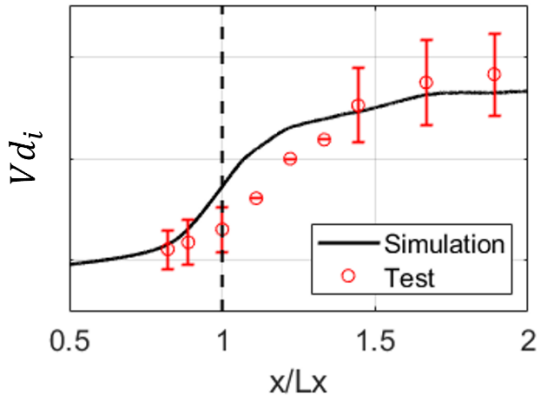


Fig. 6.7: Comparison of the predicted axial distribution of the ions' axial drift velocity (Vd_i) with the LIF measurements for operating condition II. The error bars on the test data represent one standard deviation of the measured distribution.

6.3.3. Ion velocity distribution function

Fig. 6.8 presents the 1D1V ion distribution functions (IVDFs) along the axial direction and axial velocity component at four time instances of the discharge evolution for the three operating conditions. The existence and evolution of the slow ion population in the plume can be more closely examined in these plots. Furthermore, the back-and-forth movement of the high E_x region (observed in **Fig. 6.5** (c)) during the discharge cycle, changes the overlap between ionization and acceleration regions. This will then manifest as the variation in the ions' velocity dispersion.

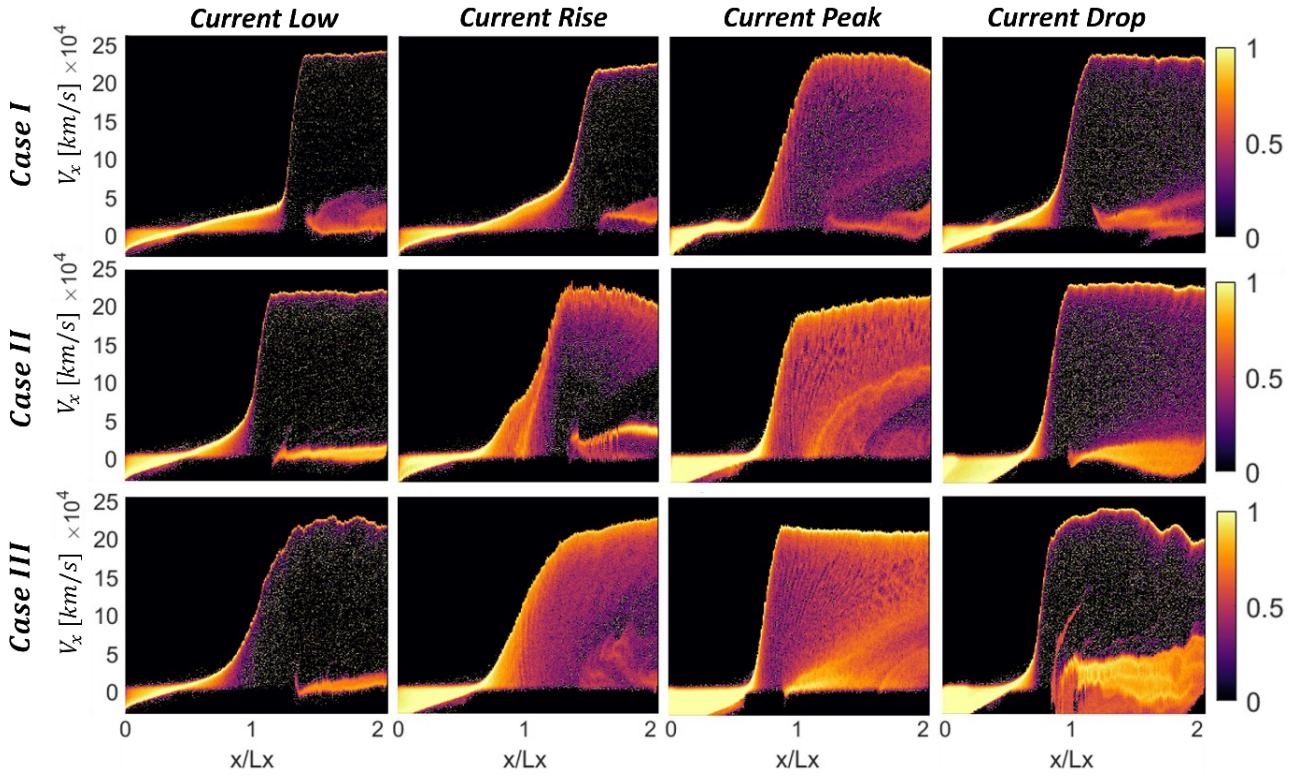


Fig. 6.8: 1D1V velocity distribution functions of the ions along the axial direction and axial velocity component for the three simulated operating conditions during different moments of the discharge evolution cycle.

It is noticed that, at the "current low" phase corresponding to minimum discharge current, two distinct nearly beam-like ion populations, one fast and one slow, exist in the plume (beyond $x/L_x = 1$). As the discharge current rises ("current rise" phase), the velocity dispersion of the two ion populations increases. The velocity dispersion is more pronounced for simulation Cases II and III. Ultimately, at the time of "current peak", the IVDFs exhibit maximum dispersion in the ion axial velocity such that the ions occupy the entire velocity range delimited by the slow and fast ion populations' velocities. During the "current drop", the dispersion of the ions' velocity in the plume reduces and the cycle repeats.

6.3.4. Characteristics of the azimuthal instabilities

The numerical dispersion maps of the azimuthal instabilities, obtained from the 2D FFT of the spatiotemporal azimuthal electric field signal over the time interval of $400 - 600\ \mu s$, are provided in **Fig. 6.9**. Note that, in the single-region approximation, there is only a single 1D azimuthal grid which captures average characteristics of the waves across the entire axial extent of the domain (see **Fig. 2.4**). Given the significant temporal and axial variation in plasma properties, the dispersion of the instabilities vary as the instabilities are convected downstream and throughout the discharge. Therefore, we superimposed the theoretical IAI's dispersion relation (given by Eq. 1.4), using a range of n_e and T_e encountered in each simulation case during the time interval of $400 - 600\ \mu s$ across entire domain. In particular, the cyan, yellow and white curves in **Fig. 6.9** indicate the theoretical IAI's dispersion relation evaluated using, respectively, average, highest and lowest n_e and T_e, over the time duration of $400 - 600\ \mu s$ across the domain for each simulated case.

We noticed that the numerical dispersion of the waves for the three cases features a rather continuous spectrum over a range of azimuthal wavenumbers (k_z) and a certain frequency (ω) bandwidth. This behavior is in part due to the average representation of the wave characteristics in the single-region approximation. In this regard, we see that the k_z spans and the ω bandwidths are bounded by the yellow and white curves.

In addition, as the discharge properties evolve in time, the numerical dispersion characteristics of the ion acoustic waves change between two rather distinct states, as evident from the bifurcated spectrum of the waves in the 2D FFT plots. The cyan lines delineate this bifurcation in the numerical dispersion plots, especially visible for $k_z\lambda_D$ values larger than 1. The two branches of the waves' numerical dispersions are speculated to represent the downstream convection of the waves, hence the change in their dispersion relation as the plasma properties vary along the axial direction.

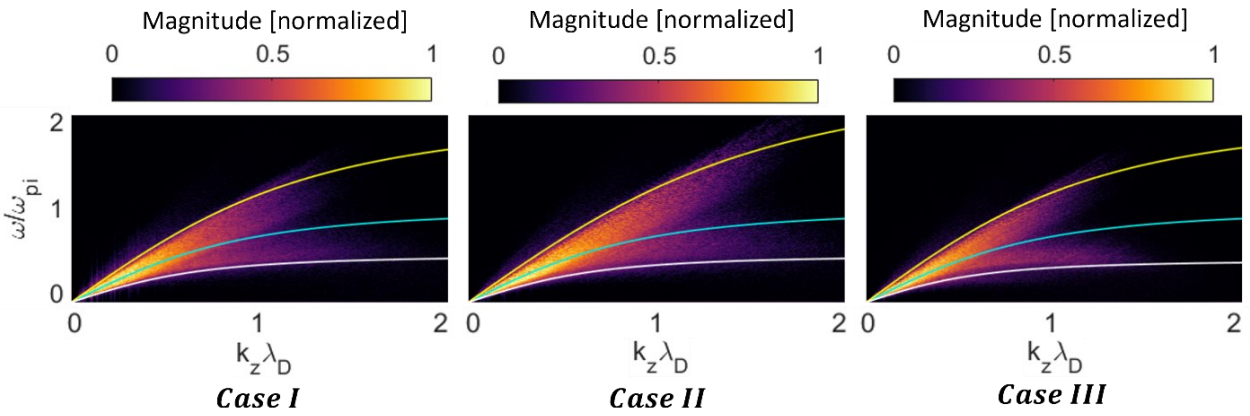


Fig. 6.9: Numerical dispersion plots of azimuthal instabilities for the three simulated conditions, obtained from 2D FFT of the spatiotemporal signal of azimuthal electric field fluctuations over the time window of $400 - 600\ \mu s$. Cyan, yellow and white curves represent the theoretical IAI's dispersion relation obtained from Eq. 1.4 using, respectively, the average, the maximum and the minimum values of the plasma density and the electron temperature across the domain during $400 - 600\ \mu s$. k_z and ω are normalized by the average λ_D and ω_{pi} across entire domain and over the considered time interval.

To characterize the dominant mode, we look at the azimuthal wavenumber and the frequency spectra of the azimuthal instabilities in **Fig. 6.10**.

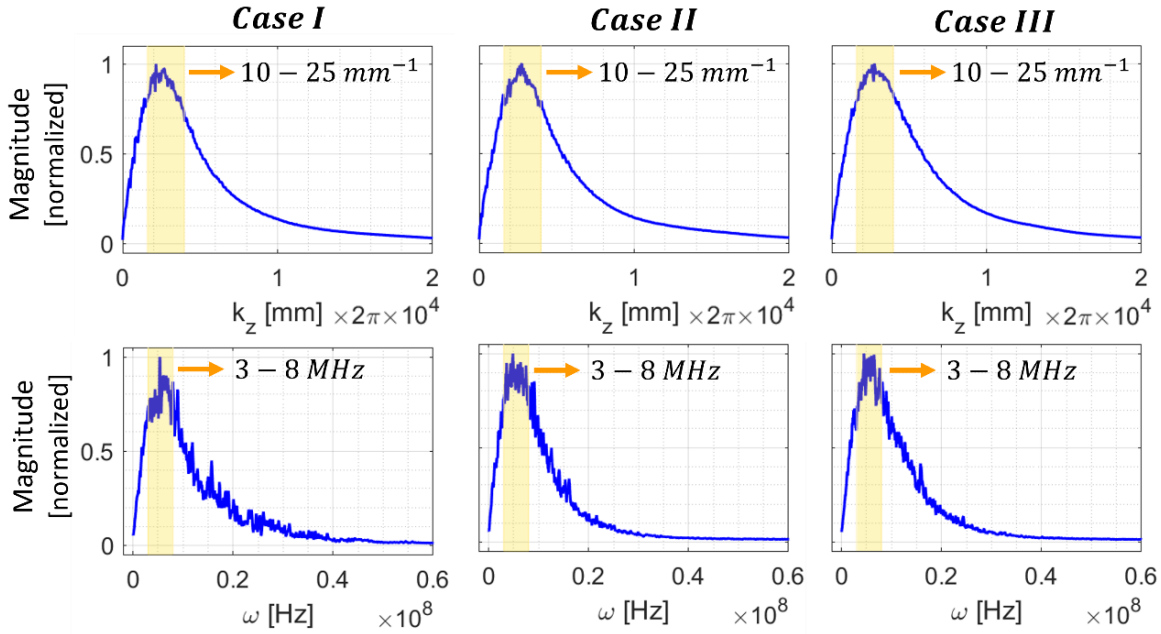


Fig. 6.10: Azimuthal wavenumber spectra (top row) and frequency spectra (bottom row) of instabilities obtained, respectively, from average spatial and temporal FFT of the azimuthal electric field signal from three simulations cases.

Assuming the axially averaged values of n_e and T_e to be about $1 \times 10^{18}\ m^{-3}$ and $10\ eV$ (from **Fig. 6.6**), the azimuthal wavenumber and the frequency of the IAI's fastest growing mode calculated from Eq. 1.7 are, respectively, $k_{z,max} \approx 30\ mm^{-1}$ and $\omega_{max} \approx 10\ MHz$. These theoretical values are quite consistent with the peak contents of the k_z and ω spectra of the instabilities in the simulations.

Furthermore, given the average values above, the estimated theoretical phase velocity of the IAI's fastest growing mode from Eq. 1.7 is $v_{ph,max} \approx 2\ km/s$. Referring to the time-averaged azimuthal

velocity distribution function (VDF) of the ions for the three simulated cases shown in **Fig. 6.11**, we observe a secondary peak in the VDF around the velocities of 2.5 to $4.5\ km/s$, which is rather close to the theoretical $v_{ph,max}$. The appearance of this secondary peak is due to the interactions with the azimuthal waves of the ions whose velocities are near the phase velocity of the wave.

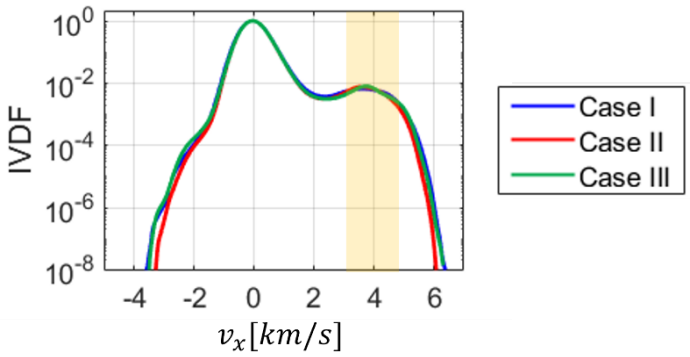


Fig. 6.11: Azimuthal VDF of the ions residing over the entire axial extent of the domain, averaged over $400 - 600\ \mu s$, for the three simulated cases. The shaded area indicates the secondary peak in the VDF associated with the ions interacting with the azimuthal waves.

6.4. Effects of radial dimension

To assess the unresolved effects of the radial direction in the axial-azimuthal simulations, we simulated the channel cross-section of the HT20k thruster at three axial positions including $x/L_x = 0.36, 0.68,$ and 0.88, which are representative of the radial-azimuthal dynamics at the near-anode (Section 3), ionization (Section 2), and acceleration (Section 1) regions, respectively. The radial-azimuthal cross-sections are simulated using high-order multi-region Q2D approximation with the initial plasma conditions corresponding to those at the respective axial locations obtained from the axial-azimuthal simulations of Case II. To distinguish the impact of magnetic shielding topology which involves substantial field's curvature and in turn radial gradients, we performed the simulations with both uniform purely radial and non-uniform curved magnetic fields. The detailed description of the simulation setups and the results are presented in Appendix A.7. A summary of the important average plasma parameters from these radial-azimuthal simulations is provided in **Table 6.5**, along with the corresponding values from the axial-azimuthal simulation (Case II) at the respective axial locations.

In the presence of the non-uniform curved magnetic field, particularly at Sections 1 and 2, the plasma becomes significantly concentrated near the center away from the radial walls. In particular, the plasma density at the centerline is larger than the average density in the domain by a factor of $1.5 - 1.8$. Furthermore, the electron temperature (T_e) at all sections is significantly higher in the radial-azimuthal simulations, whether with uniform or non-uniform B-field, compared to the T_e established in the axial-azimuthal simulations. This is an interesting point, because despite inclusion of the wall energy losses in radial-azimuthal simulations, the interaction of particles with the instabilities along the azimuthal and radial directions caused significant heating, which has led to larger T_e values. However, it is noted that the finite axial length considered in the radial-azimuthal simulations, as the typical measure to artificially introduce downstream convention of the waves and limit their growth, may have affected the energy

distribution of the particles to some extent. In any case, relying on the results we have so far, the elevated T_e along with the increased density concentration in the central region observed in the radial-azimuthal simulations (particularly in Section 2, which correspond to ionization region) can explain the less efficient ionization upstream of the acceleration region predicted by the axial-azimuthal simulations compared to reality. This has led to a more extended ionization region with a large overlap with the acceleration region, thus, existence of the low energy population in the near-plume region of the axial-azimuthal simulations.

Furthermore, when resolving the radial dimension, the instabilities whose wavevector includes a radial component such as the MTSI can be excited in the simulation. As a result, the energy cascade and thereby the instabilities' spectrum will be different from the instabilities developed in axial-azimuthal simulations. The instabilities developed in the radial-azimuthal simulation appear to induce a significant electrons' axial mobility in addition to a notable heating of electron population. As seen from **Table 6.5**, the mean electrons' axial current density and mobility in the radial-azimuthal configurations are about two orders of magnitude higher than the corresponding values in the axial-azimuthal simulations. The significant electrons' axial transport observed in the radial-azimuthal simulations could, in part, be attributed to the lack of self-consistent resolution in the axial direction in these simulations.

Finally, we observed that, in the radial-azimuthal simulations with non-uniform curved B-field associated with the shielded topology, the power deposition from the plasma species on the channel walls is reduced by several factors (see Appendix A.7) compared to that in the presence of a uniform B-field. This indicates that the magnetic shielding topology is effective in protecting the channel walls from erosion, especially at Sections 1 and 2.

					Radial-Azimuthal					
		Axial-Azimuthal			Uniform B-field			Non-uniform B-field		
Parameter	**Unit**	**Section 1**	**Section 2**	**Section 3**	**Section 1**	**Section 2**	**Section 3**	**Section 1**	**Section 2**	**Section 3**
Mean ion number density	$\times 10^{17} m^{-3}$	4.85	10.5	17.9	4.16	8.95	13.8	5.64	11.1	16.6
Peak ion number density	$\times 10^{17} m^{-3}$	–	–	–	5.27	11.7	17.8	8.56	19.8	18.6
Mean electron temperature	eV	19.5	7.70	4.64	64.9	18.3	29.8	53.5	12.2	17.9
Mean electrons' axial current density	kAm^{-2}	0.79	0.48	0.21	18.7	27.6	37.2	67.6	36.9	25.6
Mean electrons' axial mobility	$m^2V^{-1}s^{-1}$	0.14	2.4	24.3	16	190	1690	40	270	830

Table 6.5: Comparison of several plasma parameters in in axial-azimuthal and radial azimuthal configurations. The mean values correspond to spatiotemporal averages across the azimuthal extent of the domain for axial-azimuthal simulation, and across the radial and azimuthal extents of the domain for radial-azimuthal simulations and over entire simulation duration ($0 - 650\ \mu s$ in axial-azimuthal and $0 - 7\ \mu s$ in radial-azimuthal simulations). Sections 1, 2 and 3, correspond to axial locations of $x/L_x = 0.88, 0.68$, and 0.36, respectively, for operating condition of Case II.

These findings highlight that the axial-azimuthal and radial-azimuthal simulations, each capture different plasma processes and interactions, which once again underline the 3D nature of plasma configurations in Hall thrusters, especially with magnetically shielded configuration. We emphasize that in the absence of computationally affordable 3D models, our best attempt to characterize such 3D plasmas is to simulate 2D sections of the system in different 2D coordinates. However, the resulting picture from these studies is incomplete as they still do not capture the interdependency and coupling

among all three dimensions. This underscores the necessity of extending the RO-PIC to 3D in order to develop a computationally efficient Q3D PIC model as the next step.

6.5. Conclusion

We presented the results of the axial-azimuthal single-region Q2D PIC simulations of the HT20k Hall thruster in three operating conditions. These simulations are made possible by the cost-efficiency of the RO-PIC that enabled performing self-consistent and kinetic studies in an extended computational domain of HT20k thruster for an unprecedented duration of $650\ \mu s$, over a range of operating conditions.

The axial-azimuthal simulations amount to a rather simplified representation of the real-world thruster. Not resolving radial direction, the axial-azimuthal simulations do not account for the radial gradients in the magnetic field and the plasma properties that are inherent to the magnetic shielding topology. Additionally, the single-region approximation represents the lowest order of approximation of the 2D problem, offering the maximum computational gain. The main purpose of these simulations was, hence, to evaluate the utility of the single-region Q2D simulation for estimation of the plasma dynamics and global performance parameters in Hall thrusters. In this respect, we observed that the average instability-induced electron mobility resolved by the single-region simulations enabled resolving the plasma discharge behavior, without the need to use any ad-hoc electron transport model.

Moreover, keeping in mind the simplified problem description adopted and the approximation order used for the axial-azimuthal simulations, the calculated performance parameters were found to have a maximum error of $20 - 30\ \%$ across the three simulated operating conditions. It was highlighted that the main source of discrepancy between the simulated and the measured performance is the lack of resolving the important effects of the radial magnetic field gradient in the axial-azimuthal simulations. This justification was confirmed by the results of the HT20k radial-azimuthal simulations which showed that the radial gradients have a notable influence on the underlying plasma phenomena and regulating the macroscopic properties in magnetically shielded Hall thrusters.

The presented results in this chapter underline the efficacy and the promise of the RO-PIC scheme to serve as a robust numerical tool for prediction of the thruster behavior. Furthermore, when extended to 3D and properly validated, the RO-PIC model can effectively and reliably support the design and development of Hall thrusters and other plasma devices.

Chapter 7 Conclusions and future work

7.1. Summary and conclusions

The quest to unlock the mysteries of plasma and harness its potential in various technological applications demands computational tools capable of balancing accuracy with computational cost. However, on the one hand, the available conventional high-fidelity kinetic plasma models, such as PIC simulations, are prohibitively costly to simulate the multiscale, multi-dimensional plasma processes and interactions in real-size plasma devices such as Hall thrusters over realistic simulated timeframes. This enormous computational cost has rendered full-3D PIC simulations impractical if not unfeasible. On the other hand, less computationally demanding plasma codes, i.e., the fluid/hybrid models, inherently lack the ability to capture some important effects of the instabilities on plasma dynamics, such as wave-particle interactions and their induced electrons transport. Moreover, these models are not predictive since in the absence of rigorous and generalizable closure models they mostly rely on empirical relations and experimentally-tunned ad-hoc coefficients to close the involved system of equations.

In this work we introduced a novel reduced-order (RO) PIC scheme as a promising solution to this challenge. Based upon the invention of a reduced-dimension computational grid, the RO-PIC drastically reduces the computational complexity (by up to 1-2 orders of magnitude in 2D and 3-4 orders of magnitude in 3D) while preserving essential physics, serving as an alternative to the conventional PIC methods to simulate plasma dynamics with greater efficiency. The results from testing RO-PIC in diverse set of plasma configurations verifies the capability of RO-PIC in faithfully reproducing the behavior observed in full 2D simulations, thereby affirming its suitability for physics studies and engineering applications. The rigorous verification studies and detailed characterization of the convergence behavior of the RO-PIC scheme in various controlled benchmark cases lays a solid foundation for further exploration and application of RO-PIC in more complex plasma configurations.

The order (dimensionality) reduction technique underlying the RO-PIC features a unique flexibility, offering a continuous spectrum of resolution and accuracy choices (the order of approximation) and, in turn, the required computational resources. This allows for choosing an optimum trade-off between fidelity and computational gain of the simulation, enables “fit-for-purpose” kinetic simulations – simulations that tailor to various modelling purposes and needs.

RO-PIC has the potential to create a paradigm shift in computational plasma physics, offering a transformative tool to deepen our understanding of plasma phenomena and accelerate the development of plasma-based technologies. In this regard, the cost-efficiency, flexibility, and accuracy features of the RO-PIC have enabled conducting studies with both scientific and applied significance that were previously impractical with conventional PIC codes. These comprise (1) extensive high-fidelity parametric exploration of variations in the plasma phenomena and behaviors across vast parameter

spaces including plasma parameters and thrusters' operating conditions, and (2) self-consistent kinetic simulation of a full-size high-power (20kW-class) Hall thruster over time durations of real-world relevance.

The extensive parametric investigations performed in radial-azimuthal and axial-azimuthal $\mathrm{E} \times \mathrm{B}$ configurations unveiled intricate dependencies of plasma behavior on various operating parameters. These studies helped isolate the effects of various physical factors and mechanisms on the underlying microscopic processes as well as on the global macroscopic behavior of plasma. In particular, RO-PIC provided unprecedented aggregate insights into the impacts of the intensity of the applied electromagnetic field intensity and magnetic field curvature on plasma instabilities, electrons' cross-field transport, and ion beam divergence.

The presented parametric studies serve as demonstrative examples of the extent of insights that can be driven from such wide parametric assessment. Studies of this type can guide future research and/or development efforts by painting a comprehensive picture of the parametric variability of an $\mathrm{E} \times \mathrm{B}$ discharge configuration and identifying the critical conditions which require special attention.

In addition, the self-consistent simulations of a high-power Hall thruster over several breathing cycles without scaling physical parameters (for simulation speed-up) and with no ad-hoc parameter marks a pioneering endeavor toward the achievement of predictive capability enabled by RO-PIC. Such predictive models can be used to assess the influence of the design choices on the behavior of plasma and, in turn, on the global performance of the plasma thrusters within the practical timeframes. Integration of RO-PIC within the development cycle of plasma technologies enables methodical and cost-effective design, optimization, and testing of the devices by reducing the reliance on empirical, test-dependent practices. Additionally, it opens the door to the design of more efficient plasma technologies and can unlock new technological solutions.

Finally, the importance of experimental validation of the models and the numerical observations should not be overlooked. Experimental activities exclusively designed for model validations are necessary to confirm the applicability of simulation results in real-world scenarios and to gain further confidence in the reliability and robustness of the computational models for scientific discoveries and practical purposes.

7.2. Future works and research directions

This section outlines future avenues for further advancement of the RO-PIC scheme in order to expand its utility to broader scientific and engineering applications. In this regard, the proposed efforts include the extension of RO-PIC from 2D to 3D for achieving comprehensive kinetic modeling of real-size plasma devices, with the emphasis on code optimization and scalability enhancement for large-scale simulations. Potential pathways to utilize Machine Learning (ML) algorithms to enhance cost-efficiency and accuracy are identified which involve integration of Deep-Learning (DL) architectures into RO-PIC main loop and development of DL-augmented RO-PIC. Another proposed research direction involves making necessary modifications to the approach to ensure its compatibility with different

numerical discretization techniques, such as unstructured grids and the Finite Element Method (FEM), and/or to accommodate curvilinear coordinate systems.

Additionally, the chapter discusses extending the established reduced-order modelling framework to other PDEs systems and development of reduced-order Direct Numerical Simulation (RO-DNS) fluid solvers for fluid dynamics simulations and reduced-order Vlasov solvers. Lastly, we emphasize the importance of verifying the insights from 2D simulations in 3D configuration and experimental validation to gain a comprehensive understanding of plasma behavior and advance the computational tools.

7.2.1. 3D extension of the RO-PIC scheme

Following the successful verifications of the RO-PIC and demonstration of its capabilities in 2D, the next step is its extension to 3D to realize Q3D PIC simulations and enable the so far unachievable goal of 3D kinetic modeling of real-size plasm devices, e.g., the full-size 3D thruster plus its plasma plume over statistically representative number of breathing cycles. Additionally, this extension accounts for additional physics and effects (as enumerated in Chapter 6) that cannot be adequately captured in 2D settings.

We highlight that the RO-PIC's formulation is readily extensible to 3D. The extension of the RO-PIC formulation to 3D and derivation of the Q3D Poisson's equation is provided in Appendix A.2. However, most of the effort when developing Q3D PIC goes to code optimization and further improving the cost-efficiency of the approach so that it can provide highly accurate results with maximum computational gains (up to 3-4 orders of magnitudes) compared to a conventional 3D PIC simulation. If sufficiently optimized the Q2D/ Q3D PIC code can even be used to model entire vacuum test facility chamber within which thruster operates to account for the plume-facility interactions and the background pressures.

Achieving maximum cost-efficiency of the RO-PIC for large-scale 3D simulations involves two aspects. The first aspect is related to the code optimization and maximizing its scalability. The code is currently parallelized on CPUs (Central Processing Units), employing domain decomposition technique through Message Passing Interface (MPI). However, for a 3D simulation, the parallelization scheme needs to be adapted and optimized so as to ensure its scalability and its efficient deployment on large computer clusters. Additionally, deployment of the code on GPUs (Graphics Processing Units) and leveraging their massive parallelization capabilities could be an interesting option to explore.

The other aspect involves utilizing Machine-Learning (ML) algorithms to simultaneously achieve the maximum cost-efficiency and maximum accuracy characteristics of RO-PIC. One potential approach of integration of ML and PIC algorithms is briefly described in the following.

7.2.2. Integration of "super-resolution" deep-learning (DL) techniques to develop DL-PIC

As was demonstrated in Chapter 2 and Chapter 3, the accuracy and the computational cost of a RO-PIC simulation depends on the fineness of the coarse grid (**Fig. 2.1**), i.e., the number of regions to be used, which is problem-dependent. The RO-PIC approximations involving high number-of-regions are sufficiently accurate to provide speedup factors of about $5-10$ in 2D and $25-100$ in 3D.

Conversely, employing low number-of-regions sacrifices some accuracy but offers remarkable computational gains beyond 2 orders of magnitude in 2D and more than 4 orders of magnitude in 3D, compared to conventional PIC methods.

To minimize the computational cost while maximizing the fidelity and resolution of the Q3D simulation, one potential way is to incorporate the "super-resolution" deep-learning (DL) architectures within the RO-PIC scheme and development of a DL-enhanced RO-PIC code (or DL-PIC in short).

The super-resolution/sub-grid methods [177]-[182] have received substantial attention in recent years in computational fluid dynamics, particularly in turbulence modelling [177]. These multi-fidelity methods rely on a statistically representative high-resolution dataset to learn and infer the involved interactions in a flow [183]. These techniques can enhance the flow field obtained from a coarse-grid simulation, thus, enabling filling in the missing sub-grid scale details to account for the smaller-scale processes that are below the simulation's resolution [183]. Introducing a customized DL super-resolution architecture into the main loop of the RO-PIC enables using as few number-of-regions as possible while keeping the simulation resolution on a par with a full-2D/3D PIC simulation.

The DL network will act as a separate module of the simulation, interacting with other functions of the PIC code within the main loop. The focus of the DL architecture will be, in the first instance, on the electric potential, or equivalently the electric field, which is the main temporally evolving driving force in many "electrostatic" EP technologies. By enhancing the resolution of the electric field, the particles under the influence of the enhanced field can essentially experience the full-2D/3D effects in the simulation. A provisional schematic of the main loop of the DL-PIC is illustrated in **Fig. 7.1**.

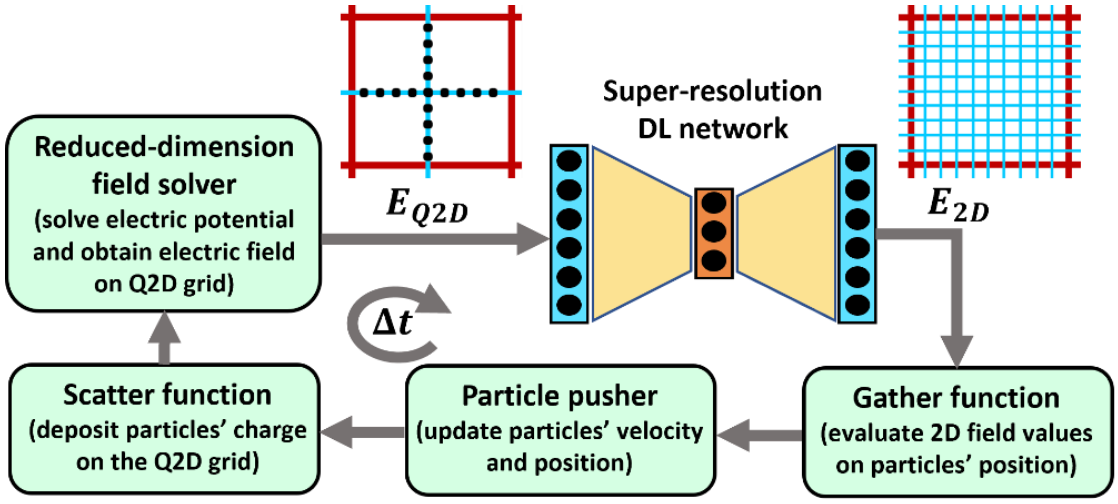


Fig. 7.1: Schematic of the main loop of the Q2D DL-PIC code. The same is valid for a Q3D case. Figure adopted from Ref. [183].

The integration of DL into RO-PIC establishes a framework for systematically coupling physics and data to develop a simulation tool for plasmas, which is both generalizable and computationally affordable. The physics part is covered through the solution of the RO-PIC simulation at each time step, and the data consists of a library of high-fidelity PIC simulation results based on which the DL network is trained to develop the data-driven sub-grid model. In contrast to pure DL-based models, the iteration

of the PIC and the DL model at each time step throughout the simulation can keep the error bounded since the field solver ensures strict satisfaction of Gauss's law at every time step.

The DL-enhanced RO-PIC, by virtue of cost-efficiency and accuracy, could potentially enable physics studies unattainable with the existing plasma simulation approaches and provide access to sufficiently large high-fidelity datasets that realistically resemble the real world, which are currently lacking. These datasets are essential for training Machine-learning (ML) and Data-Driven (DD) architectures to develop very fast predictive models. A thorough discussion of the most promising ML/DD architectures for plasma modeling can be found in Ref. [180].

7.2.3. Extension of the RO-PIC's dimensionality-reduction formulation to a magnetic-field-aligned mesh (MFAM)

Another approach to reducing the number of regions used in the RO-PIC simulation while maintaining a desired level of accuracy and resolution in the simulation is by adjusting the reduced-dimension grid according to the most suitable coordinate system for describing the dynamic in a plasma system. In general, we can adapt the definition of the course grid and the regions as well as the fine grids to be aligned with an arbitrary curvilinear coordinate system defined by natural features, geometrical/physical characteristics or dominant flow directions in the system. Since the gradients tend to occur mostly along these natural directions, adopting these coordinates can lead to a more natural representation of the physical phenomena, thereby minimizing the required number of regions without sacrificing accuracy.

Indeed, in Appendix A.4.4 we demonstrated how the adoption of non-uniform coarse grid, where the spacing between regions varies according to the steepness of gradients within the system, can reduce the required number of regions for accurate predictions. While this study involves a Cartesian grid system, the key takeaway remains valid: when the definition of the course grid (regions boundaries) is informed by the gradients in the system, a certain level of accuracy can be achieved with fewer number of regions, thereby at lower computational cost.

In partially magnetized plasmas, there exists a significant disparity in electrons' mobility along and across the magnetic field direction, indicating the substantial influence of the magnetic field topology in shaping the gradients in the plasma properties. Recalling the concept of the thermalized potential and the equipotentiality of the magnetic field lines introduced in Section 1.2.1.1, the electric potential tends to vary mostly in perpendicular direction to the magnetic field lines. As a result, the topology of the magnetic field can serve as a physical curvilinear coordinate system with the local direction of the magnetic field defining the bases of the coordinate system called magnetic field-aligned-mesh (MFAM).

In the presence of a stationary magnetic field ($\boldsymbol{B}$), which is irrotational ($\boldsymbol{\nabla} \times \boldsymbol{B} = 0$) in addition to being solenoidal ($\boldsymbol{\nabla}.\boldsymbol{B} = 0$), we can define magnetic potential function μ whose gradient is along $\boldsymbol{B}$ everywhere, and a magnetic stream function λ whose gradient is orthogonal to $\boldsymbol{B}$ such that

$$\boldsymbol{B} = \boldsymbol{\nabla}\mu\,, \qquad \text{Eq. 7.1}$$

$$\boldsymbol{B} = \boldsymbol{\nabla}\zeta \times \boldsymbol{\nabla}\lambda\,, \qquad \text{Eq. 7.2}$$

where ζ represent the third dimension. Note that both μ and λ functions satisfy the Laplace equation ($\nabla^2\mu = \nabla^2\lambda = 0$). In case of cylindrical geometries such as in Hall thrusters, the cylindrical coordinate is the natural choice for the third direction (ζ). Considering the cylindrical system represented by z as the axial direction, r as the radial direction and θ as the azimuthal direction, Eq. 7.1 and Eq. 7.2 can be rewritten as

$$B_r = \frac{\partial\mu}{\partial r}, \qquad B_z = \frac{\partial\mu}{\partial z}, \qquad \text{Eq. 7.3}$$

$$B_r = \frac{1}{r}\frac{\partial\lambda}{\partial z}, \qquad B_z = -\frac{1}{r}\frac{\partial\lambda}{\partial r}, \qquad \text{Eq. 7.4}$$

where, B_r and B_z are, respectively, the radial and azimuthal components of the magnetic field.

The local bases vectors ($\hat{e}_\mu$ and $\hat{e}_\lambda$) of the magnetic field-aligned coordinate system are obtained as

$$\hat{e}_\mu = \frac{B_z\hat{e}_z + B_r\hat{e}_r}{B}\,, \qquad \hat{e}_\lambda = \frac{B_r\hat{e}_z - B_z\hat{e}_r}{B}, \qquad \text{Eq. 7.5}$$

where B is the local intensity of the magnetic field. The magnetic-field-aligned reduced-dimension grid is schematically illustrated in **Fig. 7.2** for conventional and magnetically-shielded topologies in Hall thrusters. The boundaries of the regions and the computational grids in each region follow the μ and λ directions. The reduced-dimension Poisson's equation must be adapted in line with the definition of the coordinate system.

Considering the partial alignment of the electric potential and magnetic field, it is anticipated that solving the Q2D/Q3D Poisson's equation in magnetic-field-aligned reduced-dimension grid converges to the full-2D/full-3D solution with significantly fewer number-of-regions. However, this must be verified by a detailed comparison of the convergence characteristics of the magnetic-field-aligned RO-PIC against that of the Cartesian RO-PIC counterpart.

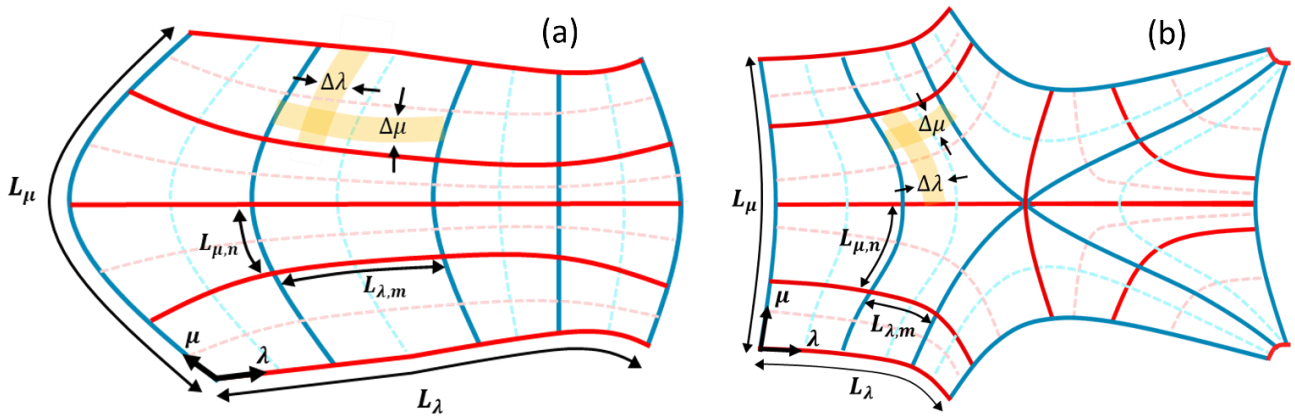


Fig. 7.2: Schematic of the magnetic-field-aligned coarse grid underlying the reduced-order scheme for two different magnetic field topologies corresponding to (a) conventional (unshielded) Hall thrusters and (b) magnetically-shielded Hall thrusters (refer to **Fig. 1.7**). Solid dark blue and red curves represent the regions' boundaries parallel (μ-direction) and perpendicular (λ-direction) to the magnetic field lines, respectively. Dashed light blue and pink curves represent the computational grids in each region along and across magnetic field, respectively.

7.2.4. Refinement of the RO-PIC's underlying formulation

An additional promising advancement path involves revisiting the underlying formulation by improving the core RO-PIC ansatz. The original formulation of RO-PIC represents a "zeroth-order" approximation across regions' extent. This approach can be extended by introducing, instead, a "first-order" approximation within each region.

The key distinction between the zeroth-order and the first-order formulations lies in how each approach treats the variation of grid-based data, within each region, perpendicular to the respective x-grid and the y-grid directions. In the zeroth-order formulation, the data within each cell is assumed to remain constant across the entire elongated extent of the cell, i.e., over l_y on the x-grid and over l_x on the y-grid. In contrast, the first-order formulation assumes that the grid-based data vary linearly across the elongated extent of the cells. This means that, instead of being constant, the data changes smoothly from one side of the cells to the other, providing a higher level of accuracy compared to the zeroth-order method. For the zeroth-order RO-PIC, these fine computational cells are placed in the middle of regions (see **Fig. 2.1**). Whereas, in the first-order version, the fine 1D computational cells are modified to coincide with the boundaries of the regions, as illustrated in **Fig. 7.3**.

In particular, with regards to the modified reduced-dimension Poisson's equation, the two-dimensional distribution of the electric potential (ϕ) is approximated as the linear superposition of potential functions ϕ^x and ϕ^y

$$\phi(x,y) \approx (1-\tilde{y})\phi_n^x(x) + \tilde{y}\phi_{n+1}^x(x) + (1-\tilde{x})\phi_m^y(y) + \tilde{x}\phi_{m+1}^y(y), \quad \forall \tilde{x},\tilde{y} \in \Omega_{n,m}\,, \qquad \text{Eq. 7.6}$$

where, $\tilde{x} = \frac{x-x_m}{l_x}$ and $\tilde{y} = \frac{y-y_n}{l_y}$ are linear interpolation weights, which are normalized relative coordinates within the region.

Following the procedure outlined in Section 2.2.2.2, substituting Eq. 7.6 into the 2D Poisson's equation and performing integration along the x-axis and then along the y-axis, over the respective extents of the region, we derive the new quasi-2D Poisson system of equations

$$\frac{l_y}{8}\left(\frac{d^2\phi_{n-1}^x}{dx^2} + 6\frac{d^2\phi_n^x}{dx^2} + \frac{d^2\phi_{n+1}^x}{dx^2}\right) + (1-\tilde{x})\left(\frac{\partial\phi_m^y}{\partial y}|_{y_N} - \frac{\partial\phi_m^y}{\partial y}|_{y_S}\right) + \tilde{x}\left(\frac{\partial\phi_{m+1}^y}{\partial y}|_{y_N} - \frac{\partial\phi_{m+1}^y}{\partial y}\right.$$
$$\left. + \frac{1}{l_y}(\phi_{n-1}^x - 2\phi_n^x + \phi_{n+1}^x) + \frac{1}{l_x}\int_{y_S}^{y_N}(\phi_{m+2}^y - 2\phi_{m+1}^y + \phi_m^y)dy = -\frac{1}{\epsilon_0}\int_{y_S}^{y_I}\right. \qquad \text{Eq. 7.7}$$

$$\frac{l_x}{8}\left(\frac{d^2\phi_{m-1}^y}{dy^2} + 6\frac{d^2\phi_m^y}{dy^2} + \frac{d^2\phi_{m+1}^y}{dy^2}\right) + (1-\tilde{y})\left(\frac{\partial\phi_n^x}{\partial x}|_{x_E} - \frac{\partial\phi_n^x}{\partial x}|_{x_W}\right)$$
$$+ \tilde{y}\left(\frac{\partial\phi_{n+1}^x}{\partial x}|_{x_E} - \frac{\partial\phi_{n+1}^x}{\partial x}|_{x_W}\right) + \frac{1}{l_x}(\phi_{m-1}^y - 2\phi_m^y + \phi_{m+1}^y) \qquad \text{Eq. 7.8}$$
$$+ \frac{1}{l_y}\int_{x_W}^{x_E}(\phi_{n+2}^x - 2\phi_{n+1}^x + \phi_n^x)dx = -\frac{1}{\epsilon_0}\int_{x_W}^{x_E}\rho dx.$$

In the above equations, x_W and x_E are the x-coordinates of the left and right boundaries of the region $\Omega_{n,m}$, while y_S and y_N represent the y-coordinates of the bottom and top boundaries of the region $\Omega_{n,m}$.

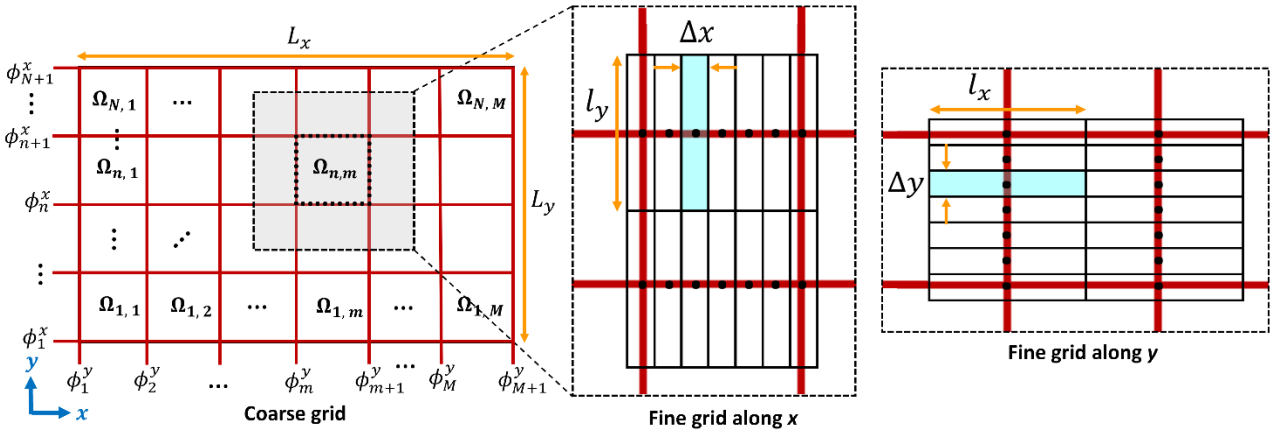


Fig. 7.3: Schematic of the domain decomposition corresponding to the reduced-dimension grid system for first-order RO-PIC; (**left**) decomposition into multiple "regions" using a coarse grid, (**right**) the 1D computational cells (fine grids) for the discretization of each region along the x and y directions. The red lines represent the boundaries between the regions which coincide with the computational grids.

The revised formulation is expected to lead to substantial improvements in both computational cost-efficiency and the overall accuracy characteristics of RO-PIC. As a result, the revisited RO-PIC can either achieve significantly greater computational speedups (beyond what was already offered by the original method) for the same accuracy level or deliver a significantly higher level of accuracy with the same computational resources.

7.2.5. Application of the RO-PIC's dimensionality-reduction formulation to other PDE systems

As mentioned in Chapter 2, the reduced-dimension grid underlying the RO-PIC provides a general framework for reduced-order modeling. In this regard, we demonstrated in Section 3.4, the applicability of the reduced-order scheme to DSMC simulations to provide a Q2D representation of the neutrals' flow in the thruster's plume. As a result, this framework can extend its utility beyond electrostatic PIC simulations to tackle other systems of partial differential equations such as Maxwell's equations for electromagnetic PIC, Vlasov equation for direct kinetic simulation of plasmas and even Navier-Stokes equations for fluid dynamics simulations. The extension of the reduced-order scheme to an arbitrary system of PDEs involves adopting the reduced-dimension grid and adjusting the system of equations of interest accordingly. This adjustment includes performing integrations over the extents of regions along the involved directions of the simulation separately, similar to the approach taken in for Poisson's equation in RO-PIC describe in Section 2.2.2. This will then lead to the development of quasi-multi-dimensional simulations which provide significant reduction of the number of computational cells in the same manner as in RO-PIC. However, the convergence characteristics of the reduced-order solution with the number-or-regions, used in the coarse grid, must be carefully examined for each of the system of equations. This can demonstrate the efficacy and versatility of the proposed reduced-order modeling framework across various simulation methods, verifying its applicability beyond PIC simulations and highlights its capacity to address computational challenges in various areas of scientific computation.

Exploring potential adjustments of the reduced-order scheme to accommodate different numerical discretization techniques, such as unstructured grids and the implementation of various computational methods like the Finite Element Method (FEM), can significantly expands the flexibility of the method in discretizing complex geometries and irregular domains. This makes the scheme well-suited for a wide range of engineering and scientific applications.

In the case of Navier-Stokes equations, the adoption of the reduced-order scheme yields reduced-order Direct Numerical Simulation (RO-DNS) fluid solver. It would be interesting to compare the performance of the RO-DNS, in terms of accuracy, resolution and cost-efficiency, with that of conventional computational schemes such as standard DNS, LES (Large Eddy Simulation) and RANS (Reynolds-Averaged Navier-Stokes). Such a comparison can establish the RO-DNS fluid solver as a potential alternative for these approaches.

We highlight that for the application of the reduced-order scheme to Vlasov equation, the reduced-dimension grid can be implemented along the configuration space or/ and the velocity space. For example, in a 2D2V setting, the distribution function, $f(x, y, v_x, v_y, t)$ in each 4-deimsional regions of the coarse grid can be approximated as

$$f(x, y, v_x, v_y, t) \approx f^x(x, t) + f^y(y, t) + f^{v_x}(v_x, t) + f^{v_y}(v_y, t), \quad \text{Eq. 7.9}$$

where f^x, f^y, f^{v_x} and f^{v_y} are the Q2DQ2V distribution components which are unique for each 4-dimensional region, thus, are valid within the bounds of that region. Substituting Eq. 7.9 into the Vlasov equation (Eq. 1.26) and integrating over each group of three dimensions across the regions' extents, separately, (along $x - v_x - v_y$, $y - v_x - v_y$, $x - y - v_x$ and $x - y - v_y$ subspaces) leads to Q2DQ2V description of the 2D2V Vlasov equation.

7.2.6. Verification of the 2D observations in 3D and validation with experiment

It is important to compare the insights and observed trends from parametric investigations conducted in 2D radial-azimuthal and axial-azimuthal Hall-thruster-representative cross-field discharge configurations in Chapter 4 and Chapter 5, with their 3D counterpart studies. This comparison allows us to infer how accounting for the third dimension self-consistently may influence the underlying phenomena and their parametric variations.

The 2D studies pointed to the variation in the dominant instability modes, and consequent behavior of plasma and performance of the device with the plasma/setup conditions (electric and magnetic field intensity, magnetic field curvature, ion mass, plasma density, etc.). Specifically, in 2D radial-azimuthal settings we observed distinct plasma regimes characterized by the dominance of different instabilities – ECDI, MTSI, longer-wavelength coherent structures – and consequently different plasma behaviors, including the nature of the anisotropy in and the spatial distributions of plasma properties. These insights need to be re-evaluated in a 3D setup and be validated experimentally. In particular, it is interesting to validate the nature of these regimes in reality and the ways by which they may possibly differ from the numerical observations. A worthwhile effort following a validation activity would be to explain the mechanisms that render this transition between the dominant instabilities with the plasma

conditions. In particular, it is essential to study more closely the energy transfer between various instability modes and the energy cascade in general, to explain the establishment of one or a set of dominant instabilities in the system under different plasma conditions.

Bibliography

[1] Kaganovich ID, Smolyakov A, Raitses Y, Ahedo E, Mikellides IG, Jorns B, Taccogna F, et al., "Physics of E × B discharges relevant to plasma propulsion and similar technologies," *Phys. Plasmas* **27**, 120601 (2020)

[2] Boeuf JP, Smolyakov A, "Physics and instabilities of low-temperature E × B plasmas for spacecraft propulsion and other applications," *Physics of Plasmas* **30**, 050901 (2023)

[3] Piragino A, Ferrato F, Faraji F, Reza M et al., "SITAEL's Magnetically Shielded 20 kW Hall Thruster Tests," IEPC-2019-879, *36th International Electric Propulsion Conference*, Vienna (2019)

[4] Chen FF, "Plasma Physics and Controlled Fusion", 2nd ed., Springer, New York, NY (2006)

[5] Gibbon P, "Introduction to Plasma Physics," Published by CERN in the Proceedings of the CAS-CERN Accelerator School: Plasma Wake Acceleration, Geneva, Switzerland, 23–29 November 2014, edited by B. Holzer, CERN-2016-001 (CERN, Geneva, 2016)

[6] Bittencourt JA, "Fundamentals of Plasma Physics," 3rd ed., Springer New York, NY (2004)

[7] Heron A, Adam JC, "Anomalous conductivity in Hall thrusters: Effects of the non-linear coupling of the electron-cyclotron drift instability with secondary electron emission of the walls," *Phys. of Plasmas* **20**, 082313 (2013)

[8] Hasegawa A, "Plasma Instabilities and Nonlinear Effects," *Physics and chemistry in space, Vol. 8, Springer-Verlag*, (1975)

[9] Landau L, "On the vibration of the electronic plasma," *JETP* 16 (1946), 574. English translation in *J. Phys. (USSR)* 10 (1946)

[10] Boeuf JP, "Tutorial: Physics and modeling of Hall thrusters", *Journal of Applied Physics* **121** 011101 (2017)

[11] Gary SP, Sanderson JJ, "Longitudinal waves in a perpendicular collisionless plasma shock: I. Cold ions," *Journal of Plasma Physics* **4**(4):739-751 (1970)

[12] Janhunen S, Smolyakov A, Sydorenko D, Jimenez M, Kaganovich I, Raitses Y, "Evolution of the electron cyclotron drift instability in two dimensions," *Phys. Plasmas* **25**, 082308 (2018)

[13] Tsikata S, Honore C, Gresillon DM, "Collective Thomson scattering for studying plasma instabilities in electric thrusters," *J. Instrum.* **8**, C10012 (2013)

[14] A. Ducrocq, J. C. Adam, A. Héron, and G. Laval, "High-frequency electron drift instability in the cross-field configuration of Hall thrusters," *Phys. Plasmas*, **13** 102111 (2006)

[15] Lazurenko A, Vial V, Bouchoule A, Prioul M, Adam JC, Heron A, Laval G, "Characterization of microinstabilities in Hall thruster plasma: experimental and PIC code simulation results," IEPC-2003-0218, *In Proceedings of International Electric Propulsion Conference*, Toulouse, France (2003)

[16] Cavalier J, Lemoine N, Bonhomme G, Tsikata S, Honore C, Gresillon D, "Hall thruster plasma fluctuations identified as the E×B electron drift instability: Modeling and fitting on experimental data," *Phys. Plasmas* **20**, 082107 (2013)

[17] Lafleur T, Baalrud SD, Chabert P, "Theory for the anomalous electron transport in Hall effect thrusters. I. Insights from particle-in-cell simulations," *Phys. Plasmas* **23**, 053502 (2016)

[18] Boeuf JP, Garrigues L, "E × B electron drift instability in Hall thrusters: Particle-in-cell simulations vs. theory," *Phys. Plasmas* **25**, 061204 (2018)

[19] Faraji F, Reza M, Knoll A, "Enhancing one-dimensional particle-in-cell simulations to self-consistently resolve instability-induced electron transport in Hall thrusters," *J. Appl. Phys.* **131**, 193302 (2022)

[20] Lampe M, Manheimer WM, McBride JB, Orens JH, Shanny R, and Sudan RN, "Nonlinear development of the beam-cyclotron instability," *Phys. Rev. Lett.* **26**, 1221 (1971)

[21] Lampe M, Manheimer WM, McBride JB, Orens JH, Papadopoulos K, Shanny R, and Sudan RN, "Theory and simulation of the beam cyclotron instability," *Phys. Fluids* **15**, 662 (1972)

[22] Smolyakov A, Zintel T, Couedel L *et al.,* "Anomalous Electron Transport in One-Dimensional Electron Cyclotron Drift Turbulence," *Plasma Phys. Rep.* **46**, 496–505 (2020)

[23] Katz I, Lopez Ortega A, Jorns BA, Mikellides IG, "Growth and Saturation of Ion Acoustic Waves in Hall Thrusters", AIAA 2016-4534, *In Proceedings of 52nd AIAA/SAE/ASEE Joint Propulsion Conference*, Propulsion and Energy Forum, Salt Lake City, UT (2016)

[24] Adam JC, Héron A, Laval G, "Study of stationary plasma thrusters using two-dimensional fully kinetic simulations", *Phys. of Plasmas* **11**, 295 (2004)

[25] Reza M, Faraji F, Andreussi T, Andrenucci M, "A Model for Turbulence-Induced Electron Transport in Hall Thrusters," IEPC-2017-367, *35th International Electric Propulsion Conference*, Atlanta, Georgia (2017)

[26] Janhunen S, Smolyakov A, Chapurin O, Sydorenko D, Kaganovich I, Raitses Y, "Nonlinear structures and anomalous transport in partially magnetized E×B plasmas," *Phys. Plasmas* **25**, 011608 (2018)

[27] Charoy T, Lafleur T, Tavant A, Chabert P, Bourdon A, "A comparison between kinetic theory and particle-in-cell simulations of anomalous electron transport in plasma discharges," *Phys. Plasmas* **27**, 063510 (2020)

[28] Taccogna F, Minelli P, Asadi Z, Bogopolsky G, "Numerical studies of the ExB electron drift instability in Hall thrusters," *Plasma Sources Sci. Technol.*, **28**(6):064002 (2019)

[29] Dewar R, "Saturation of kinetic instabilities by particle trapping," *Phys. Fluids* **16**, 431–435 (1973)

[30] Lafleur T, Chabert P, "The role of instability-enhanced friction on 'anomalous' electron and ion transport in hall-effect thrusters," *Plasma Sources Sci. Technol.*, **27**:015003 (2018)

[31] Degeling AW and Boswell RW, "Modeling ionization by helicon waves," *Phys. Plasmas* **4**, 2748 (1997)

[32] McBride JB, "Theory and Simulation of Turbulent Heating by the Modified Two-Stream Instability," *Physics of Fluids* 15.12 (1972)

[33] Petronio F, Tavant A, Charoy T, Alvarez-Laguna A, Bourdon A, Chabert P, "Conditions of appearance and dynamics of the Modified Two-Stream Instability in E×B discharges," *Phys. Plasmas* **28**, 043504 (2021)

[34] Petronio F, "Plasma instabilities in Hall Thrusters: a theoretical and numerical study," PhD dissertation, Paris Polytechnic Institute, NNT: 2023IPPAX030 (2023)

[35] Villafana W, Petronio F, Denig AC, Jimenez MJ, Eremin D et al., "2D radial-azimuthal particle-in-cell benchmark for E×B discharges," *Plasma Sources Sci. Technol.* **30** 075002 (2021)

[36] Barral S, Makowski K, Peradzyński Z, Dudeck M, "Transit-time instability in Hall thrusters," *Phys. Plasmas* **12**, 073504 (2005).

[37] Hagelaar GJM, Bareilles J, Garrigues L, Boeuf JP, "Role of anomalous electron transport in a stationary plasma thruster simulation," *J. Appl. Phys.* **93**, 67–75 (2003)

[38] Fernandez E, Scharfe MK, Thomas CA, Gascon N, Cappelli MA, "Growth of resistive instabilities in E×B plasma discharge simulations," *Phys. Plasmas* **15**, 012102 (2008)

[39] Choueiri EY, "Plasma oscillations in Hall thrusters," *Phys. Plasmas* **8**, 1411–1426 (2001)

[40] McDonald, M. S., and Gallimore, A. D., "Comparison of Breathing and Spoke Mode Strength in the H6 Hall Thruster Using High Speed Imaging," IEPC-2013-353, *33rd International Electric Propulsion Conference* (2013)

[41] Sekerak MJ, Gallimore AD, Brown DL, Hofer RR, Polk JE, "Mode Transitions in Hall-Effect Thrusters Induced by Variable Magnetic Field Strength," *Journal of Propulsion and Power* 32:4, 903-917 (2016)

[42] Boeuf JP, Garrigues L, "Low frequency oscillations in a stationary plasma thruster," *J. Appl. Phys.* **84**, 3541–3554 (1998)

[43] Fife J, Martinez-Sanchez M, Szabo J, "A numerical study of low-frequency discharge oscillations in Hall thrusters," AIAA 1997-3052, *33rd Joint Propulsion Conference and Exhibit* (1997)

[44] Barral S, Ahedo E, "Low-frequency model of breathing oscillations in Hall discharges," *Phys. Rev. E* **79**, 046401 (2009)

[45] Chapurin O, Smolyakov AI, Hagelaar G, Raitses Y, "On the mechanism of ionization oscillations in Hall thrusters," *J. Appl. Phys.* **129** (23): 233307 (2021)

[46] Hara K, Mikellides IG, "Characterization of low frequency ionization oscillations in Hall thrusters using a one-dimensional fluid model," AIAA 2018-4904, *2018 Joint Propulsion Conference* (2018)

[47] Lafleur T, Chabert P, Bourdon A, "The origin of the breathing mode in Hall thrusters and its stabilization," *J. Appl. Phys.* **130** (5): 053305 (2021)

[48] Dale ET, Jorn BA, "Two-zone Hall thruster breathing mode mechanism, Part I: Theory," IEPC-2019-354, *In Proceedings of 36th International Electric Propulsion Conference*, Vienna, Austria (2019)

[49] Goebel DM, Katz I, "Fundamentals of Electric Propulsion: Ion and Hall Thrusters," Wiley, 2008. DOI: 10.1002/9780470436448.

[50] Reza M, Ferrato E, Faraji F, Andreussi T, Andrenucci M, "Magnetic Circuit Optimization for Hall Thrusters Design," IEPC-2019-459, *In Proceedings of 36th International Electric Propulsion Conference*, Vienna, Austria (2019)

[51] Liang R, "The Combination of Two Concentric Discharge Channels into a Nested Hall Effect Thruster," PhD dissertation, University of Michigan (2013). Available on public domain.

[52] Mikellides IG, Katz I, Hofer RR, Goebel DM, "Magnetic shielding of a laboratory Hall thruster. I. Theory and validation," *Journal of Applied Physics* **115**, 043303 (2014)

[53] Hofer RR, Goebel DM, Mikellides IG, Katz I, "Magnetic shielding of a laboratory Hall thruster. II. Experiments," *Journal of Applied Physics* **115**, 043304 (2014)

[54] Giannetti V, Piragino A, Faraji F, Reza M, Leporini A et al., "Development of a 5kW Low-erosion Hall Effect Thruster," IEPC-2017-379, *In proceedings of 35th International Electric Propulsion Conference*, Atlanta, Georgia (2017)

[55] Piragino A, Ferrato E, Faraji F, Reza M, Giannetti V, et al., "SITAEL's magnetically shielded 20 kW Hall thruster tests," IEPC-2019-879, *In proceedings of 36th International Electric Propulsion Conference*, Vienna, Austria (2019)

[56] Morozov AI, Esipchuk YV, Tilinin GN, Trofimov AV, Sharov YA, Shchepkin GY, *Sov. Phys. Tech. Phys.* **17**, 38 (1972)

[57] Tsikata S, Honore C, Lemoine N, Gresillon DM, "Three-dimensional structure of electron density fluctuations in the Hall thruster plasma: E x B mode," *Phys. Plasmas* **17**, 112110 (2010)

[58] Charoy T, Boeuf JP, Bourdon A, Carlsson JA, Chabert P, Cuenot B, Eremin D et al., "2D axial-azimuthal particle-in-cell benchmark for low-temperature partially magnetized plasmas," *Plasma Sources Sci. Technol.* **28**, 105010 (2019)

[59] Barral S, Makowski K, Peradzyński Z, Gascon N, Dudeck M, "Wall material effects in stationary plasma thrusters. II. Near-wall and in-wall conductivity," *Phys. Plasmas* **10**, 4137–4152 (2003)

[60] Hara K, "An overview of discharge plasma modeling for Hall effect thrusters," *Plasma Sources Sci. Technol.* **28** 044001 (2019)

[61] Taccogna F, Garrigues L, "Latest progress in Hall thrusters plasma modelling," *Reviews of Modern Plasma Physics*, Springer Singapore, **3** (1) (2019)

[62] Hara K, Hanquist K, "Test cases for grid-based direct kinetic modeling of plasma flows," *Plasma Sources Sci. Technol.* **27**, 065004 (2018)

[63] Birdsall CK, Langdon AB, "Plasma Physics via Computer Simulation," CRC Press (1991)

[64] Taccogna F, Cichocki F, Eremin D, Fubiani G, Garrigues L, "Plasma propulsion modeling with particle-based algorithms," *J. Appl. Phys.* **134**, 150901 (2023)

[65] Vahedi V, Surendra M, "A Monte Carlo collision model for the particle-in-cell method: applications to argon and oxygen discharges," *Computer Physics Communications* **87** 179-198 (1995)

[66] Jorns B, "Predictive, data-driven model for the anomalous electron collision frequency in a Hall effect thruster," *Plasma Sources Sci. Technol.* **27** 104007 (2018)

[67] Marks TA, Jorns BA, "Challenges with the self-consistent implementation of closure models for anomalous electron transport in fluid simulations of Hall thrusters," *Plasma Sources Sci. Technol.* **32** 045016 (2023)

[68] Tavant A, "Study of the plasma-wall interaction and erosion on a plasma thruster of low power", Modeling and Simulation. Université Paris Saclay (COmUE), English (2019)

[69] Charoy T, "Numerical study of electron transport in Hall thrusters", Plasma Physics [physics.plasm-ph], Institut Polytechnique de Paris. English. ⟨NNT: 2020IPPAX046⟩ ⟨tel-02982367⟩ (2020)

[70] Villafana W, Cuenot B, Vermorel O, "3D particle-in-cell study of the electron drift instability in a Hall Thruster using unstructured grids," *Phys. Plasmas* **30**, 033503 (2023)

[71] Meyers MD, Huang CK, Zeng Y, Yi SA, Albright BJ, "On the Numerical Dispersion of Electromagnetic Particle-In-Cell Code: Finite Grid Instability," *Journal of Computational Physics* **297** (2014)

[72] Turner MM, "Numerical effects on energy distribution functions in particle-in-cell simulations with Monte Carlo collisions: choosing numerical parameters," *Plasma Sources Sci. Technol.* **22** 055001 (2013)

[73] Szabo JJ, "Fully Kinetic Numerical Modeling of a Plasma Thruster", PhD dissertation (2001)

[74] Werner GR, Jenkins TG, Chap AM, Cary JR, "Speeding up simulations by slowing down particles: Speed-limited particle-in-cell simulation," *Phys. Plasmas* **25** (12): 123512 (2018)

[75] Taccogna F, Minelli P, "Three-dimensional particle-in-cell model of Hall thruster: The discharge channel," *Phys. Plasmas* **25**, 061208 (2018)

[76] Brieda L, "Plasma Simulations by Example", CRC Press (2019)

[77] Lewis HR, "Energy-conserving numerical approximations for Vlasov plasmas," *Journal of Computational Physics*, Vol. **6**, Issue 1, pg. 136-141 (1970)

[78] Cohen BI, Langdon AB, Friedman A, "Implicit time integration for plasma simulation," *Journal of Computational Physics*, Vol. **46**, Issue 1, pg. 15-38 (1982)

[79] Sun H, Banerjee S, Sharma S, Powis AT, Khrabrov AV, Sydorenko D, Chen J, Kaganovich I, "Direct implicit and explicit energy-conserving particle-in-cell methods for modeling of capacitively coupled plasma devices," *Phys. Plasmas* **30** (10): 103509 (2023)

[80] Barnes DC, Chacón L, "Finite spatial-grid effects in energy-conserving particle-in-cell algorithms," *Journal of Computational Physics*, Vol. **258**, 107560 (2021)

[81] Cohen BI, Langdon AB, Hewett DW, Procassini RJ, "Performance and optimization of direct implicit particle simulation," *Journal of Computational Physics*, Vol. **81**, Issue 1, pg. 151-168 (1989)

[82] Eremin D, "An energy- and charge-conserving electrostatic implicit particle-in-cell algorithm for simulations of collisional bounded plasmas," *Journal of Computational Physics*, Vol. **452**, 110934 (2022)

[83] Zenger C, "Sparse Grids," In: W. Hackbusch, Ed., Notes on Numerical Fluid Mechanics, Vol. **31**, Vieweg, Braunschweig, pp. 241-251 (1991)

[84] Griebel M, Schneider M, Zenger C, "A combination technique for the solution of sparse grid problems," Technische Universität (1990)

[85] Griebel M, "Adaptive sparse grid multilevel methods for elliptic PDEs based on finite differences," *Computing*, **61**(2):151–179 (1998)

[86] Garcke J, Griebel M, Thess M, "Data mining with sparse grids," *Computing*, **67**(3):225–253 (2001)

[87] Bungartz HJ, Griebel M, "Sparse grids," *Acta numerical*, **13**(1):147–269 (2004)

[88] Ricketson LF, Cerfon AJ, "Sparse grid techniques for particle-in-cell schemes," *Plasma Phys. Control. Fusion* **59**, 024002 (2016)

[89] Garrigues L, Tezenas du Montcel B, Fubiani G, Bertomeu F, Deluzet F, Narski J, "Application of sparse grid combination techniques to low temperature plasmas particle-in-cell simulations. I. Capacitively coupled radio frequency discharges," *J. Appl. Phys.* **129**, 153303 (2021)

[90] Garrigues L, Tezenas du Montcel B, Fubiani G, Reman BCG, "Application of sparse grid combination techniques to low temperature plasmas particle-in-cell simulations. II. Electron drift instability in a Hall thruster," *J. Appl. Phys.* **129**, 153304 (2021)

[91] Deluzet F, Fubiani G, Garrigues L, Guillet C, Narski J, "Sparse grid reconstructions for particle-in-cell methods," *ESAIM: M2AN* **56**, 1809–1841(2022)

[92] Lapenta G, "Kinetic Plasma Simulation: Particle In Cell Method," available at URL, last accessed May 6, 2024

[93] Bezanson J, Edelman A, Karpinski S, Shah VB, "Julia: A Fresh Approach to Numerical Computing", *SIAM Review*, **59**: 65–98 (2017)

[94] Boris JP, "The acceleration calculation from a scalar potential", Plasma Physics Laboratory, Princeton University, MATT-152 (1970)

[95] Croes V, "Modélisation bidimensionnelle de la décharge plasma dans un propulseur de Hall," PhD thesis, Université Paris-Saclay, France (2018)

[96] Vaughan J, "A New Formula for Secondary Emission Yield," IEEE Trans. on Electron Devices 36, 9 (1989)

[97] Furman MA, Pivi MTF, "Probabilistic model for the simulation of secondary electron emission," *Phys. Rev. ST Accel. Beams* **5**, 124404 (2002)

[98] Sydorenko D, "Particle-in-Cell Simulations of Electron Dynamics in Low Pressure Discharges with Magnetic Fields," PhD Dissertation (2006)

[99] Box GEP, Muller ME, "A Note on the Generation of Random Normal Deviates," *The Annals of Mathematical Statistics*. **29** (2) (1958)

[100] Blackman D, Vigna S, "Scrambled linear pseudorandom number generators," *ACM Trans. Math. Softw.*, **47**:1–32 (2021)

[101] Alexander FJ, Garcia AL, "The Direct Simulation Monte Carlo method," *Computers in Physics* **11**, 588 (1997)

[102] Collision cross-sections data, URL: www.lxcat.net, accessed in May 2021

[103] Toro EF, Spruce M, Speares W, "Restoration of the contact surface in the HLL-Riemann solver," *Shock Waves* **4** (1994)

[104] Pawar S, San O, "CFD Julia: A Learning Module Structuring an Introductory Course on Computational Fluid Dynamics," *Fluids* **4** 159 (2019)

[105] Sod GA, "A Survey of Several Finite Difference Methods for Systems of Nonlinear Hyperbolic Conservation Laws," *J. Comput. Phys.* **27** (1978)

[106] Faraji F, Reza M, Knoll A, "Effects of the neutral dynamics model on the particle-in-cell simulations of a Hall thruster plasma discharge," *J. Appl. Phys.* **133**, 213301 (2023)

[107] Bird GA, "Molecular Gas Dynamics," Clarendon Press, London (1976)

[108] Boeuf JP, Smolyakov A, "Preface to Special Topic: Modern issues and applications of E × B plasmas," *Physics of Plasmas* **25**, 061001 (2018)

[109] Smolyakov A, "Towards predictive modeling of ExB plasma discharges," Report (2020). Accessed at URL: https://apps.dtic.mil/sti/pdfs/AD1105890.pdf on 30/08/2023.

[110] Croes V, Lafleur T, Bonaventura Z, Bourdon A, Chabert P, "2D particle-in-cell simulations of the electron drift instability and associated anomalous electron transport in Hall-effect thrusters," *Plasma Sources Sci. Technol.* **26**, 034001 (2017)

[111] Powis AT, Carlsson JA, Kaganovich ID, Raitses Y, Smolyakov A, "Scaling of spoke rotation frequency within a Penning discharge", *Physics of Plasmas*, **25**(7), 072110 (2018)

[112] Janes GS, Lowder RS, "Anomalous Electron Diffusion and Ion Acceleration in a Low-Density Plasma," *Phys. Fluids* **9**, 1115 (1966)

[113] Janes G, Dotson J, Wilson T, "Electrostatic acceleration of neutral plasmas - momentum transfer through magnetic fields," Technical Report No. NP-12154, Avco Corp. Avco-Everett Research Lab., Everett, MA (1962)

[114] See "https://jpb911.wixsite.com/landmark/copie-de-test-case-3-fluid-hybrid" for details of the Penning Discharge Benchmark activity (webpage last accessed on 25 May 2023)

[115] Charoy T, Lafleur T, Laguna Alvarez A, Bourdon A, Chabert P, "The interaction between ion transit-time and electron drift instabilities and their effect on anomalous electron transport in Hall thrusters," *Plasma Sources Sci. Technol.* **30** 065017 (2021)

[116] Reza M, Faraji F, Knoll A, Piragino A, Andreussi T, Misuri T, "Reduced-order particle-in-cell simulations of a high-power magnetically shielded Hall thruster," *Plasma Sources Sci. Technol.* **32**, 065016 (2023)

[117] Faraji F, Reza M, Knoll A, Kutz JN, "Dynamic Mode Decomposition for data-driven analysis and reduced-order modelling of E×B plasmas: I. Extraction of spatiotemporally coherent patterns," *J. Phys. D: Appl. Phys*. **57** 065201 (2024)

[118] Faraji F, Reza M, Knoll A, Kutz JN, "Dynamic Mode Decomposition for data-driven analysis and reduced-order modelling of E×B plasmas: II. Dynamics forecasting," *J. Phys. D: Appl. Phys.* **57** 065202 (2024)

[119] Croes V, Tavant A, Lucken R, Martorelli R, Lafleur T, Bourdon A, Chabert P, "The effect of alternative propellants on the electron drift instability in Hall-effect thrusters: Insight from 2D particle-in-cell simulations", *Physics of Plasmas* **25**, 063522 (2018)

[120] Lafleur T, Baalrud SD, Chabert P, "Theory for the anomalous electron transport in Hall effect thrusters. II. Kinetic model," *Physics of Plasmas* **23**(5), 053503 (2016)

[121] Marusov NA, Sorokina EA, Lakhin VP, Ilgisonis VI, Smolyakov AI, "Gradient-drift instability applied to Hall thrusters," *Plasma Sources Sci. Technol.* **28** 015002 (2019)

[122] Wang L, Yishen X, Ding Y, Xu F, Bao L, et. al., "Effects of the peak magnetic field location on discharge performance of a 100-W Hall thruster with large gradient magnetic field," *Vacuum* **199**, 110965 (2022)

[123] Ding Y, Li P, Zhang X, Wei L, Sun H, et. al. "Effects of the magnetic field gradient on the wall power deposition of Hall thrusters," *Journal of Plasma Physics*, **83**(2), 905830205 (2017)

[124] Hofer RR, "Development and Characterization of High-Efficiency, High-Specific Impulse Xenon Hall Thrusters," Ph.D. Dissertation, Aerospace Engineering, University of Michigan, Ann Arbor, Michigan (2004)

[125] Morozov AI, Esipchuk YV, Kapulkin AM, Nevrovskii VA, Smirnov VA, "Effect of the Magnetic Field on a Closed-Electron-Drift Accelerator," *Soviet Physics Technical Physics*, vol. 17, no. 3, (1972)

[126] Lopez Ortega A, Mikellides IG, Chaplin VH, "Numerical simulations for the assessment of erosion in the 12.5-kW Hall effect rocket with magnetic shielding (HERMeS)," IEPC-2017-154, in *35th International Electric Propulsion Conference*, (2017)

[127] Lopez Ortega A, Mikellides IG, Sekerak MJ, Jorns BA, "Plasma simulations in 2-D (r-z) geometry for the assessment of pole erosion in a magnetically shielded Hall thruster," *Journal of Applied Physics* **125**, 033302 (2019)

[128] Perales-Díaz J, Domínguez-Vázquez A, Fajardo P, Ahedo E, Faraji F, Reza M, Andreussi T, "Hybrid plasma simulations of a magnetically shielded Hall thruster," *Journal of Applied Physics* **131**, 103302 (2022)

[129] Perales-Díaz J, Domínguez-Vázquez A, Fajardo P, Ahedo E, Andreussi T, Piragino A, "Hybrid 2D plasma simulations of a 20kW-class magnetically shielded Hall effect thruster," IEPC-2022-322, *In proceedings of 37th International Electric Propulsion Conference*, Massachusetts Institute of Technology, Cambridge, MA (2022)

[130] Liu J, Li H, Hu Y, Liu X, Ding Y, et. al., "Particle-in-cell simulation of the effect of curved magnetic field on wall bombardment and erosion in a hall thruster," *Contributions to Plasma Physics* **59**: e201800001 (2019)

[131] Quan L, Cao Y, Tian B, Gong K, "The Influence of the Magnetic Field Line Curvature on Wall Erosion near the Hall Thruster Exit Plane," *Appl. Sci.*, **13**(6), 3547 (2023)

[132] Marin-Cebrián A, Domínguez-Vázquez A, Fajardo P, Ahedo E, "Kinetic plasma dynamics in a radial model of a Hall thruster with a curved magnetic field," *Plasma Sources Sci. Technol.* **31** 115003 (2022)

[133] Taccogna F, Longo S, Capitelli M, "Plasma Sheaths in Hall Discharges," *Phys. Plasmas* **12**, 093506 (2005)

[134] Kutz JN, Brunton SL, Brunton BW, Proctor JL, "Dynamic Mode Decomposition: Data-Driven Modeling of Complex Systems," *Society for Industrial and Applied Mathematics* (2016)

[135] Reza M, Faraji F, Knoll A, "Effects of the applied fields' strength on the plasma behavior and processes in E×B plasma discharges of various propellants: I. Electric field", *Phys. Plasmas.* **31**, 032120 (2024)

[136] Reza M, Faraji F, Knoll A, "Effects of the applied fields' strength on the plasma behavior and processes in E×B plasma discharges of various propellants: II. Magnetic field", *Phys. Plasmas.* **31**, 032121 (2024)

[137] Reza M, Faraji F, Knoll A, "Influence of the magnetic field curvature on the radial-azimuthal dynamics of a Hall thruster plasma discharge with different propellants," *J. Appl. Phys.* **134**, 233303 (2023)

[138] Reza M, Faraji F, Knoll A, "Plasma dynamics and electron transport in a Hall-thruster-representative configuration with various propellants: I. Variations with discharge voltage and current density," *Plasma* **7**(3), 651-679.

[139] Reza M, Faraji F, Knoll A, "Plasma dynamics and electron transport in a Hall-thruster-representative configuration with various propellants: II. Effects of the magnetic field topology," *Plasma* **7**(3), 680-704.

[140] Tsikata S, Lemoine N, Pisarev V, Grésillon DM, "Dispersion relations of electron density fluctuations in a Hall thruster plasma, observed by collective light scattering," *Phys. Plasmas* **16**, 033506 (2009)

[141] Lopez Ortega A, Katz I, Chaplin VH, "A First-Principles Model Based on Saturation of the Electron Cyclotron Drift Instability for Electron Transport in Hydrodynamics Simulations of Hall Thruster Plasmas," IEPC-2017-178, *In Proceedings of the 35th International Electric Propulsion Conference*, Atlanta, Georgia (2017)

[142] Conversano RW, Goebel DM, Mikellides IG, Hofer RR, Wirz RE, "Performance analysis of a low-power magnetically shielded hall thruster: computational modeling," *J Propuls Power* **33**:992–1001 (2017)

[143] Su LL, Vazsonyi AR, Jorns BA, "Performance of a 9-kW Magnetically-Shielded Hall Thruster with Krypton," AIAA-2020-3617, *In Proceedings of the AIAA Propulsion and Energy Forum* (2020)

[144] Tavant A, Croes V, Lucken R, Lafleur T, Bourdon A, Chabert P, "The effects of secondary electron emission on plasma sheath characteristics and electron transport in an E×B discharge via kinetic simulations," *Plasma Sources Sci. Technol.* **27** 124001 (2018)

[145] Taccogna F, Longo S, Capitelli M, "Plasma-surface interaction model with secondary electron emission effects," *Physics of Plasmas* **11** (3), 1220-1228 (2004)

[146] Sydorenko D, Smolyakov A, Kaganovich I, Raitses Y, "Modification of Electron Velocity Distribution in Bounded Plasmas by Secondary Electron Emission," *IEEE Trans. Plasma Sci* **34** (3), 815-824 (2006)

[147] Sydorenko D, Smolyakov A, Kaganovich I, Raitses Y, "Kinetic simulation of secondary electron emission effects in Hall thrusters," *Phys. Plasmas* **13**, 014501 (2006)

[148] Raitses Y, Kaganovich I, Khrabrov A, Sydorenko D, Fisch N, Smolyakov A, "Effect of Secondary Electron Emission on Electron Cross-Field Current in E × B Discharges," *IEEE Trans. Plasma Sci* **39**, 995 (2011)

[149] Taccogna F, Longo S, Capitelli M, Schneider R, "Anomalous transport induced by sheath instability in Hall effect thrusters," Appl. Phys. Lett. 94, 251502 (2009)

[150] Katz I, Chaplin VH, Ortega AL, "Particle-in-cell simulations of Hall thruster acceleration and near plume regions," *Phys. Plasmas* **25**, 123504 (2018)

[151] Lafleur T, Martorelli R, Chabert P, and Bourdon A, "Anomalous electron transport in hall-effect thrusters: Comparison between quasi-linear kinetic theory and particle-in-cell simulations," *Phys. Plasmas*, **25**(6):061202 (2018)

[152] Chernyshev T, Son E, Gorshkov O, "2d3v kinetic simulation of hall effect thruster, including azimuthal waves and diamagnetic effect," *J. Phys. D: Appl. Phys.*, **52**(44):444002 (2019)

[153] Chaplin VH, Jorns BA, Lopez Ortega A, Mikellides IG, Conversano RW, Lobbia RB, Hofer RR, "Laser-induced fluorescence measurements of acceleration zone scaling in the 12.5 kW HERMeS Hall thruster," *J. Appl. Phys.* **124** (18): 183302 (2018)

[154] Hargus WA, Nakles MR, "Ion Velocity Measurements Within the Acceleration Channel of a Low-Power Hall Thruster," in *IEEE Transactions on Plasma Science*, vol. **36**, no. 5, pp. 1989-1997 (2008)

[155] Mazouffre S, Gawron D, Kulaev V, Sadeghi N, "Xe+ Ion Transport in the Crossed-Field Discharge of a 5-kW-Class Hall Effect Thruster", in *IEEE Transactions on Plasma Science*, vol. **36**, no. 5, pp. 1967-1976 (2008)

[156] Gawron D, Mazouffre S, Sadeghi N, Héron A, "Influence of magnetic field and discharge voltage on the acceleration layer features in a Hall effect thruster," *Plasma Sources Sci. Technol.* **17** 025001 (2008)

[157] Mazouffre S, Kulaev V, Pérez Luna J, "Ion diagnostics of a discharge in crossed electric and magnetic fields for electric propulsion," *Plasma Sources Sci. Technol.* **18** 034022 (2009)

[158] Reza M, Faraji F, Knoll A, "Resolving multi-dimensional plasma phenomena in Hall thrusters using the reduced-order particle-in-cell scheme," *J Electr Propuls* **1**, 19 (2022)

[159] Coche P, Garrigues L, "A two-dimensional (azimuthal-axial) particle-in-cell model of a Hall thruster," *Phys. Plasmas* **21**, 023503 (2014)

[160] Zhurin VV, Kaufman H, Robinson R, "Physics of closed drift thrusters", *Plasma Sources Sci. Technol.* **8**, R1 (1999).

[161] Kaufman, HR, "Technology of closed-drift thrusters", *AIAA journal* **23**, no. 1 (1985): 78-87.

[162] Ahedo E, Escobar D, "Influence of design and operation parameters on Hall thruster performances", *J. Appl. Phys.* **96**, 983–992 (2004)

[163] Diamant KD, "The Effect of Background Pressure on SPT-100 Hall Thruster Performance," *In Proceedings of the 50th AIAA/ASME/SAE/ASEE Joint Propulsion Conference*, Cleveland, OH (2014)

[164] Huang W, Kamhawi H, Lobbia RB, Brown DL, "Effect of Background Pressure on the Plasma Oscillation Characteristics of the HiVHAc Hall Thruster," AIAA 2014-3708, *In Proceedings of 50th AIAA/ASME/SAE/ASEE Joint Propulsion Conference* (2014)

[165] Snyder JS, Lenguito G, Frieman JD, Haag TW, Mackey JA, "Effects of Background Pressure on SPT-140 Hall Thruster Performance," *Journal of Propulsion and Power* **36**:5, 668-676 (2020)

[166] Kamhawi H, Huang W, Haag TW, Yim J, Herman D et al., "Performance, Facility Pressure Effects, and Stability Characterization Tests of NASA's Hall Effect Rocket with Magnetic Shielding Thruster," *AIAA/SAE/ASEE Joint Propulsion Conference* (2016)

[167] Hofer RR, Anderson JR, "Finite Pressure Effects in Magnetically Shielded Hall Thrusters," *In Proceedings of the 50th AIAA/ASME/SAE/ASEE Joint Propulsion Conference*, Cleveland, OH, (2014)

[168] Piragino A, Faraji F, Reza M, Ferrato F et al., "Background Pressure Effects on the Performance of a 20 kW Magnetically Shielded Hall Thruster Operating in Various Configurations," *Aerospace* **8**(3), 69 (2021)

[169] Polk JE, Brophy JR, "Life Qualification of Hall Thrusters by Analysis and Test," SP00547, *In Proceedings of the Space Propulsion Conference*, Seville, Spain, (2018)

[170] Piragino A, Giannetti V, Reza M, Faraji F, Ferrato E, et al., "Development Status of SITAEL's 20 kW Class Hall Thruster", AIAA 2019-3812, *In Proceedings of AIAA Propulsion and Energy Forum*, Indianapolis, Indiana (2019)

[171] Petronio F, Charoy T, Alvarez Laguna A, Bourdon A, Chabert P, "Two-dimensional effects on electrostatic instabilities in Hall thrusters. I. Insights from particle-in-cell simulations and two-point power spectral density reconstruction techniques," *Physics of Plasmas* 30, 012103 (2023)

[172] Cusson SE, Dale ET, Jorns BA, Gallimore AD, "Acceleration region dynamics in a magnetically shielded Hall thruster," *Physics of Plasmas* **26**, 023506 (2019)

[173] Huang W, Kamhawi H, Haag TW, "Plasma Oscillation Characterization of NASA's HERMeS Hall Thruster via High Speed Imaging," AIAA-2016-4829, *In Proceedings of 52nd AIAA/SAE/ASEE Joint Propulsion Conference* (2016)

[174] Mazouffre S, Bourgeois G, Garrigues L, Pawelec E, "A comprehensive study on the atom flow in the cross-field discharge of a hall thruster," *J. Phys. D: Appl. Phys.* ***44*** *105203* (2011)

[175] Saravia MM, Giacobbe A, Andreussi T, "Bayesian analysis of triple Langmuir probe measurements for the characterization of Hall thruster plasmas," *Review of Scientific Instruments* **90**, 023502 (2019)

[176] Andreussi T, Saravia MM, Andrenucci M, "Plasma characterization in Hall thrusters by Langmuir probes", *JINST* **14** C05011 (2019)

[177] Kochkov D, Smith JA, Alieva A, Hoyer S, "Machine learning–accelerated computational fluid dynamics," *PNAS*, **118** (21) e2101784118 (2021)

[178] Fukami K, Fukagata K, Taira K, "Super-resolution reconstruction of turbulent flows with machine learning," *Journal of Fluid Mechanics*, **870**, 106-120 (2019)

[179] Maulik R, San O, Rasheed A, Vedula P, "Subgrid modelling for two-dimensional turbulence using neural networks," *J. Fluid Mech.* **858** 122-144 (2019)

[180] Faraji F, "Data-driven reduced-order modelling of the plasma systems dynamics", PhD thesis, Imperial College London (2024)

[181] Li Z, Kovachki N, Azizzadenesheli K, Liu B, Bhattacharya K, Stuart A, Anandkumar A, "Fourier Neural Operator for Parametric Partial Differential Equations," arXiv:2010.08895 (2021)

[182] Williams JP, Zahn O, Kutz JN, "Sensing with Shallow Recurrent Decoder Networks", arXiv:2301.12011v1 (2023)

[183] Faraji F, Reza M, Knoll A, "Machine-learning-enabled plasma modelling and prediction," AIAA-2024-2708, *In Proceedings of 2024 SciTech Forum conference*, Orlando, Florida (2024)

[184] Asadi Z, Taccogna M, Sharifian M, "Numerical Study of Electron Cyclotron Drift Instability: Application to Hall Thruster," *Front. Phys.* **7**:140 (2019)

[185] Turner MM, Derzsi A, Donkó Z, Eremin D, Kelly SJ, Lafleur T, Mussenbrock T, "Simulation benchmarks for low-pressure plasmas: Capacitive discharges," *Physics of Plasmas* **20** 013507 (2013)

[186] See https://jpb911.wixsite.com/landmark/test-case-3 for details of the benchmark case 3, webpage last accessed on May 10, 2024

[187] Hagelaar GJM, Bareilles J, Garrigues L, Boeuf JP, "Two-dimensional model of a stationary plasma thruster," *J. Appl. Phys.* **91** 5592 (2002)

[188] Panelli M, Morfei D, Milo B, D'Aniello FA, Battista F, "Axisymmetric Hybrid Plasma Model for Hall Effect Thrusters," *Particles*, **4** (2021)

Appendix

A.1 Results of the tests and benchmarking of the conventional branch of IPPL PIC code, IPPL-1D and IPPL-2D

A.1.1. Case 1: 1D simulation of two stream instability

According to the linear analysis, the dispersion relation of the instability resulting from N independent cold streams of species s is [63]

$$1 - \sum_{s=1}^{N} \frac{\omega_{ps}^2}{(\omega - \boldsymbol{k}.\boldsymbol{v}_{bs})^2} = 0\,, \qquad \text{Eq. A.1}$$

where, ω and $\boldsymbol{k}$ are the frequency and the wave vector of the waves, and ω_{ps} and $\boldsymbol{v}_{bs}$ are the plasma frequency and the beam velocity of species s. For two opposing cold streams of the same density and speed passing through an immobile ion background, Eq. A.1 after solving for ω is reduced to

$$\omega = \pm\sqrt{k^2 v_b^2 + \omega_p^2 \pm \sqrt{\omega_p(4k^2 v_b^2 + \omega_p^2)}}\,. \qquad \text{Eq. A.2}$$

The criterion for instability of perturbations is

$$\frac{k v_b}{\omega_p} < \sqrt{2}\,. \qquad \text{Eq. A.3}$$

Under this condition, the frequency has two imaginary (unstable) and two real (stable) solutions. Otherwise, all solutions are real and, therefore, perturbations remain stable. The results of 1D simulations for both unstable and stable conditions are provided below.

a) **Unstable Case:** The streams' properties were chosen such that $(k v_b)/\omega_p = 1 < \sqrt{2}$. The evolution of particles in 1D1V phase-space in **Fig. A.1.1** shows the diffusion of the beams' electrons in the velocity space and the non-linear growth of the instability. The particles are then trapped in the potential troughs of the waves, resulting in the saturation of the instability. **Fig. A.1.2** presents the evolution of particles' different energies. In these plots, DE, TE and PE denote drift, thermal and potential energies, respectively. Moreover, KE represents the total kinetic energy of the particles which is the sum of drift and thermal energy. E_tot represents the sum of the kinetic and potential energies. The particles drift energy turns quickly into thermal energy, indicating the thermalization of the beams which were initially cold. After this phase, the fluctuations saturate and remain at a constant amplitude. Additionally, the total energy plot confirms that the total energy of the system remains conserved.

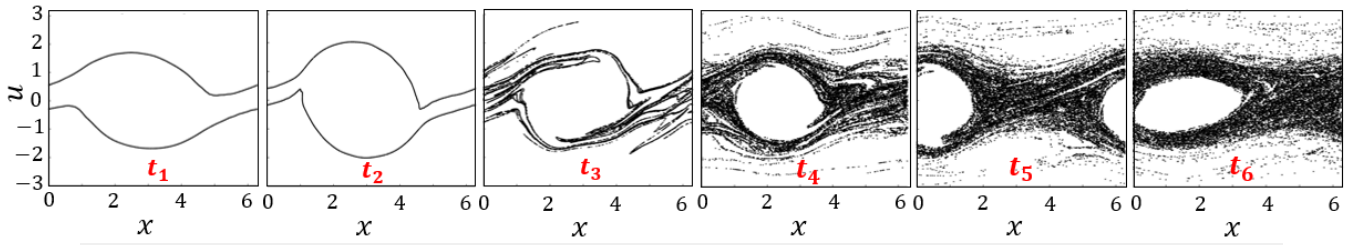


Fig. A.1.1 Particles phase-space plot at different times.

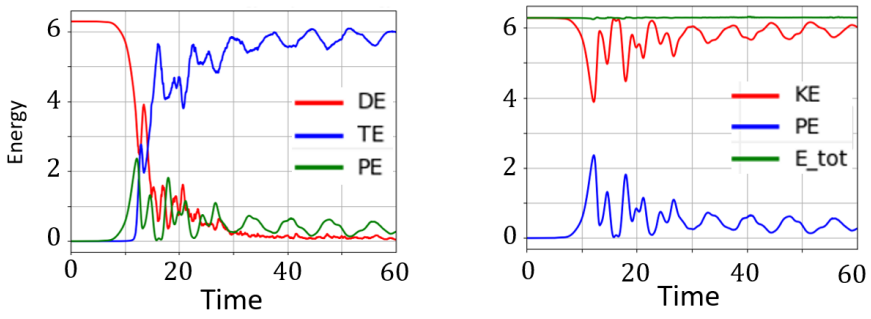


Fig. A.1.2: Time evolution of (a) total particles' drift (DE), thermal (TE) and potential (PE) energies, and (b) total particles' kinetic (KE), potential (PE) and total (E_tot) energies for unstable case.

b) Stable Case: The streams properties were chosen such that $(kv_b)/\omega_p > \sqrt{2}$. The stability of the oscillations is visible in particles phase-space plots in **Fig. A.1.3** (a) as well as in the energy plots in **Fig. A.1.3** (b). Furthermore, the frequency of oscillations (**Fig. A.3** (c)), predicted by the simulation, for various beam velocities perfectly agree with those obtained from the dispersion relation given by Eq. A.2.

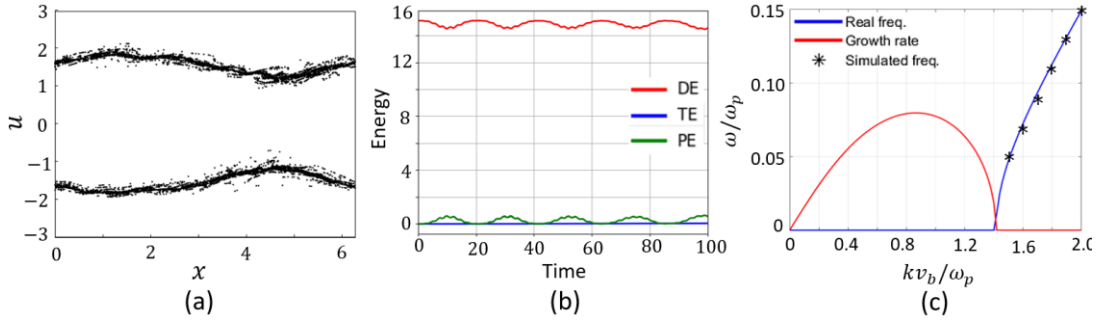


Fig. A.1.3: Plots for stable case of two stream instability; (a) particles phase-space plot, (b) time evolution of total particles' energies, (c) comparison of instability's frequency obtained from simulation with those from the dispersion relation given by Eq. A.2.

A.1.2. Case 2: Instabilities and electrons' axial transport in 1D azimuthal simulation

This 1D simulation case represents the azimuthal ($\mathrm{E} \times \mathrm{B}$) direction of Hall thrusters. Two distinct setups available in literature are used to test IPPL code's prediction of the instabilities along this direction.

a) Setup 1: The setup and conditions of this case are identical to those reported for the work in Ref. [17]. A uniform radial magnetic field with the intensity of $B_y = 20\,mT$ is applied. A

constant axial electric field of magnitude $E_x = 20\ kV/m$ is imposed. Initialization is performed by sampling electrons and ions from Maxwellian distributions at temperatures of $2\ eV$ and $0.1\ eV$, respectively, and loading them in the domain with a uniform density of $1 \times 10^{17} m^{-3}$. Neutrals are considered as a fixed background with a constant and uniform density of $3.2 \times 10^{22} m^{-3}$ and the temperature of $300\ K$. Electron-neutral collisions are included only to model the electrons energy loss and scattering. Thus, the plasma generation and neutral consumption in an ionization event are neglected to keep the density almost constant. A finite axial domain size (L_x) of $1\ cm$ is assumed. A periodic boundary condition is applied on particles and on the Poisson's equation along the azimuthal direction. Along the axial direction, electrons that leave the left boundary are resampled from their initial distribution and reloaded at the other end of the domain with a random azimuthal position. The same condition is applied to ions that leave the right boundary of the domain. The number of macroparticles per cell is 100. The domain azimuthal length (L_z) is $0.5\ cm$ with 100 number of grid nodes. The simulation is repeated with the same conditions but with h $L_z = 1\ cm$ and 200 grid nodes. The results are presented in **Fig. A.1.4**, which are in perfect agreement with the corresponding findings reported in Ref. [17], in particular in terms of the characteristics of the azimuthal instabilities established within the simulations.

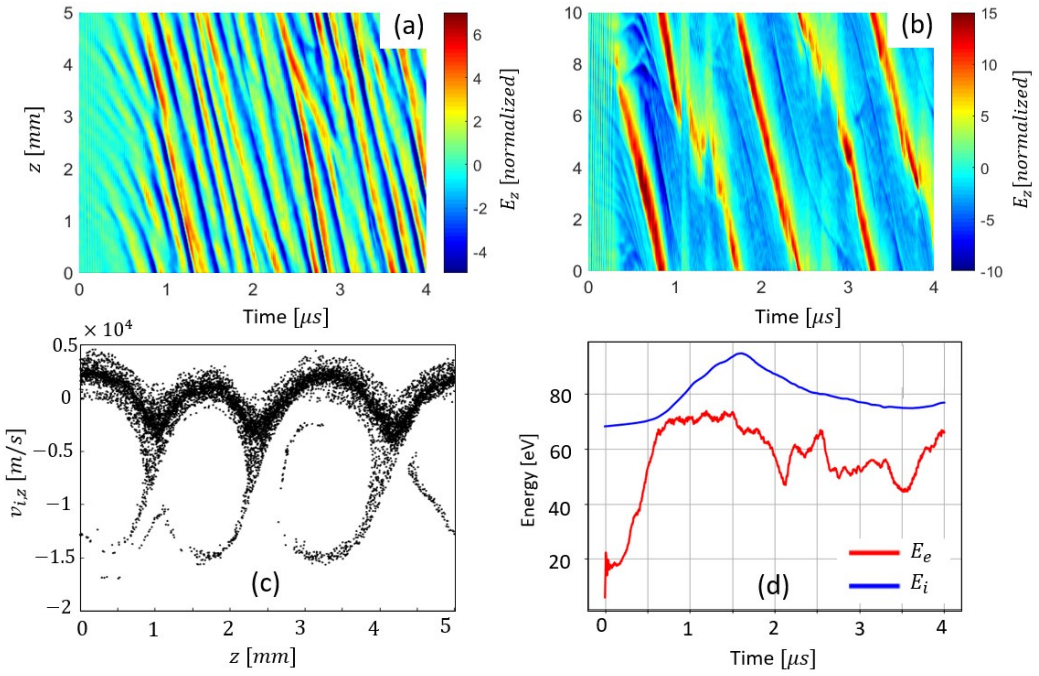


Fig. A.1.4: Spatiotemporal maps of normalized azimuthal electric fields in simulation with (a) $L_z = 0.5\ cm$ and (b) $L_z = 1cm$. (c) ion particles phase-space distribution and (d) electrons and ions total kinetic energies in simulation with $L_z = 0.5\ cm$.

Moreover, the ion-wave trapping, which is known as a saturation mechanism of azimuthal instabilities, is visible in the ions phase-space distribution in **Fig. A.1.4** (c). The total electron kinetic energy after nonlinear saturation of the instability, which takes about $0.5\ \mu s$, is $70\ eV$ and is consistent with what was presented in Ref. [17].

The instabilities developed in the simulation with an extended domain length ($L_z = 1\ cm$) exhibit higher amplitude, larger wavelength, and lower frequency – observations that are consistent with the results reported in Ref. [17]. Such a significant variation of waves characteristics with the domain azimuthal length is believed to be an artifact of the 1D simulation and its inability to adequately account for axial convection of the waves.

Additionally, the impact of instabilities on the electrons' axial transport is seen from **Fig. A.1.5** by comparing the electron mobilities in the absence and in the presence of the azimuthal fluctuations for a range of neutral number densities between 3×10^{18} and $3 \times 10^{23}\ m^{-3}$.

As suggested in Ref. [30], to obtain the electron mobility in the absence of instabilities, the waves are suppressed by setting the macroparticle weights to a very small amount. This leads to a very small charge density scattered on the grid and, thus, the azimuthal electric field will be almost zero ($E_z \approx 0$). In this case, at higher neutral densities, the classical mobility due to collisions of electrons with neutrals is the major transport mechanism. The relation for classical collisional mobility is derived from electrons' azimuthal momentum equation. Accordingly, neglecting the inertia and pressure terms leads to

$$\mu_{classical} = \frac{v_x}{E_x} = \frac{\frac{q}{m_e \nu_c}}{1 + \left(\frac{\omega_{ce}}{\nu_c}\right)^2}, \qquad \text{Eq. A.4}$$

where, ν_c is the electron-neutral momentum transfer collision frequency. In the case where we allow for the excitation of the instabilities, the enhanced mobility is obtained from the following equation [30]

$$\mu_{enhanced} = \frac{\frac{q}{m_e \nu_c}}{1 + \left(\frac{\omega_{ce}}{\nu_c}\right)^2}\left(1 - \frac{\omega_{ce}}{\nu_c}\frac{\langle n_e E_z \rangle}{n_e E_x}\right). \qquad \text{Eq. A.5}$$

In the above equation, $\langle\ \rangle$ represents the average over the entire azimuthal domain and over a time interval ($t_2 - t_1$) that is large compared to characteristic time of the instabilities

$$\langle n_e E_z \rangle = \frac{1}{(t_2 - t_1)}\frac{1}{L_z}\int_{t_1}^{t_2}\int_0^{L_z} n_e(z,t)\, E_z(z,t)\ dzdt. \qquad \text{Eq. A.6}$$

To calculate the mobility from simulation, we use

$$\mu_{sim} = \frac{1}{N}\frac{\sum_{i=1}^{N} v_{x,i}}{E_x}, \qquad \text{Eq. A.7}$$

where, N is the total number of macroparticles and $v_{x,i}$ is the electron particles' axial velocity.

Fig. A.1.5 (a) shows the electron mobility obtained from the simulation with the instabilities being suppressed (Eq. A.7) which, at higher neutral densities, aligns with the classical mobility calculated from Eq. A.4. The deviation at low neutral densities is due to the inertia and pressure effects which are neglected in the derivation of classical mobility. On the contrary, allowing for the instability to excite causes an enhanced transport across a wide range of neutral densities as displayed in **Fig. A.1.5** (b). In this figure, the theoretical mobility is calculated from Eqs. A.5 and A.6, which agree very well with the simulation's predictions.

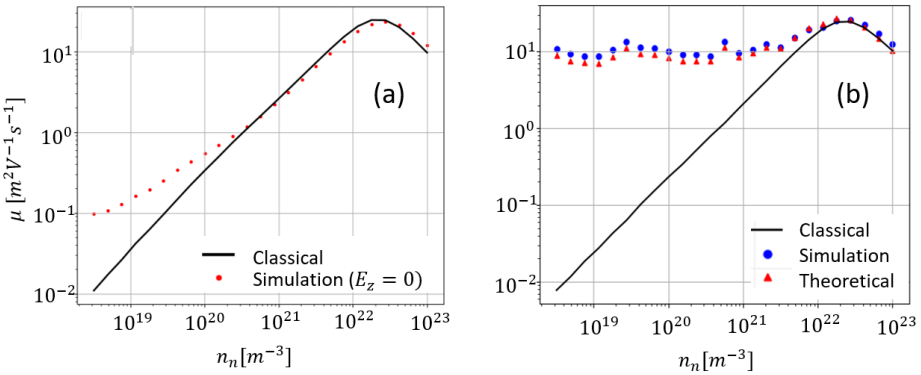


Fig. A.1.5: Electrons' axial mobility (a) in the absence of instabilities, (b) in the presence of instabilities.

b) Setup 2: In order to be able to observe more clearly the transition of the ECDI to the ion acoustic instability, we performed simulations with conditions similar to those in Ref. [184]. The main differences of this setup with respect to the setup 1 are the extended domain's azimuthal length ($L_z = 5.3\ cm$) and more rigorous requirements on the numerical parameters. Regarding the axial boundary condition, in this case, the particles which are reloaded at the axial boundaries maintain the azimuthal position at which they had left the domain from the opposing axial boundary of the domain (instead of being loaded at a random azimuthal position in setup 1). As demonstrated in Fig. A.1.6, the spatiotemporal maps of the azimuthal instabilities underline the existence of short-wavelength instabilities during the initial $1\ \mu s$ of the simulation and their transition to longer-wavelength structures after the saturation of the instability.

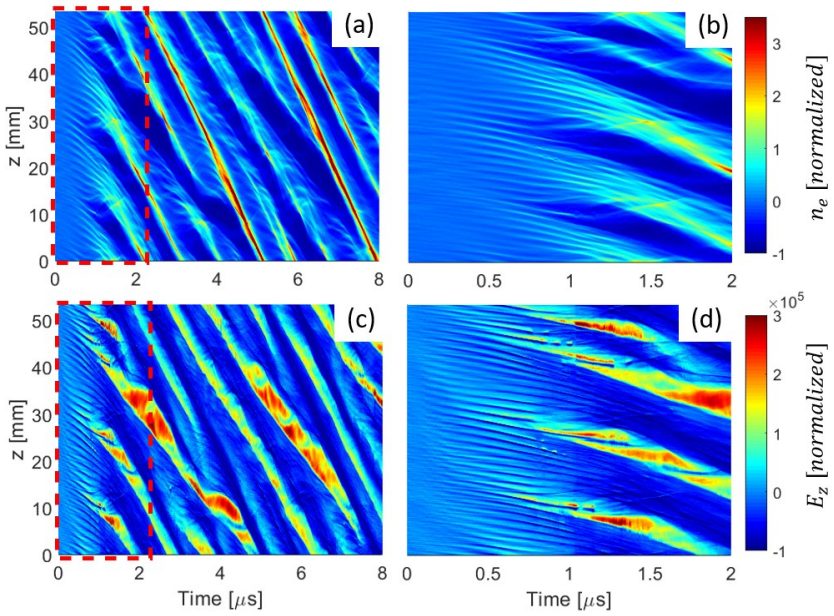


Fig. A.1.6: Spatiotemporal maps of (a) normalized azimuthal electric field and (c) normalized electron umber density. (b) and (d) are zoom-ins of (a) and (c), respectively over the initial $2\mu s$.

A.1.3. Case 3: Standalone test for the MCC collision rates

This case serves to verify the implementation of the standalone MCC module (described in Section 1.4.2.3) in being able to sample different collision events in accordance with their expected rates [95].

The collision rate is defined as

$$K(T) = \frac{1}{n}\int_0^\infty \sigma(v)\, vf(v)\ = \frac{\nu_c}{n_t}, \qquad \text{Eq. A.8}$$

in which σ is the collision cross section, ν_c is collision frequency, and n and n_t are the densities of colliding and target species, respectively. For a Maxwellian distribution function we have

$$K(T) = \left(\frac{m}{2\pi K_B T}\right)\int_0^\infty \sigma(v)\, v \exp\left(-\frac{mv^2}{2K_B T}\right) 4\pi v^2\, dv\,. \qquad \text{Eq. A.9}$$

The collision rates predicted by the MCC function are compared with their corresponding theoretical values. To obtain the theoretical collision rates, the integral in Eq. A.9 is numerically evaluated for a Maxwellian electron distribution with various temperatures across the range of $5 - 300\ eV$. The collision cross sections for electrons and xenon neutrals collisions (**Fig. 1.12**(a)) are used.

To calculate the collision rates from the simulation, a Maxwellian distribution of 10^6 immobile electrons at the corresponding temperature is loaded. The frequency of each collision is obtained by counting the number of each collision event and dividing it by the simulated time. The rate constants are then calculated per the right-hand side of Eq. A.8. As seen in **Fig. A.1.7**, the agreement of the simulated and analytical rates, across the entire range of electron energies, confirms that the simulated collision events happen at the correct rates.

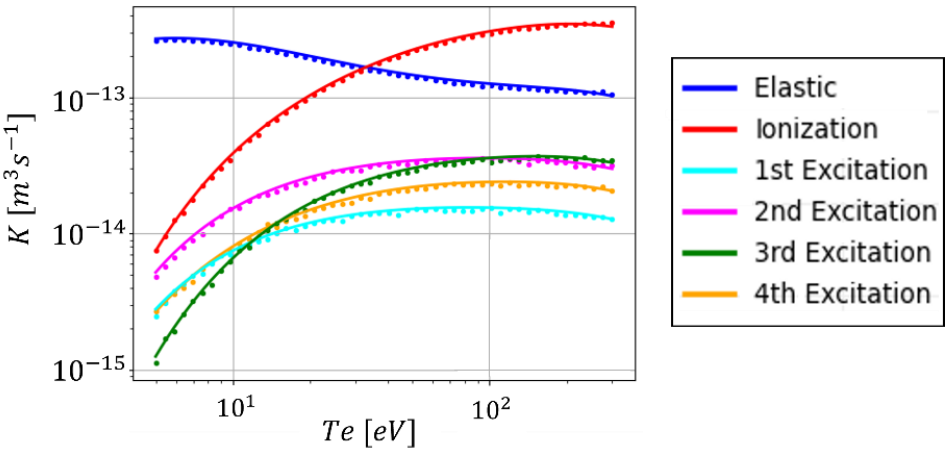


Fig. A.1.7: Comparison between collision rates from MCC function (dots) and their corresponding analytical rates (solid line) for various electron-neutral (xenon) collision types.

A.1.4. Case 4: 1D Capacitively Coupled Discharge (CCP) Benchmark

The CCP benchmark [185] is one of the most rigorous in the low-temperature plasma community. It consists of a one-dimensional Cartesian domain enclosed between two planar, parallel electrodes driven by a sinusoidal AC voltage source, fluctuating at 13.56 MHz. The domain is filled with Helium gas at a given temperature and pressure (number density) that remains unvarying throughout the simulation. the same collision cross-section data as in Ref. [185] were used. All physical and numerical parameters of the simulation have been set exactly as described in Table I of Ref. [185]. The ion number density has been suggested as the main parameter to use for comparison against benchmark results.

As such, in **Fig. A.1.8**, we have compared the ion number density profiles with respect to the published results in two cases, corresponding to Case I and Case II of Ref. [185]. It is observed that IPPL code's predictions are very closely aligned with the benchmark profiles in both cases.

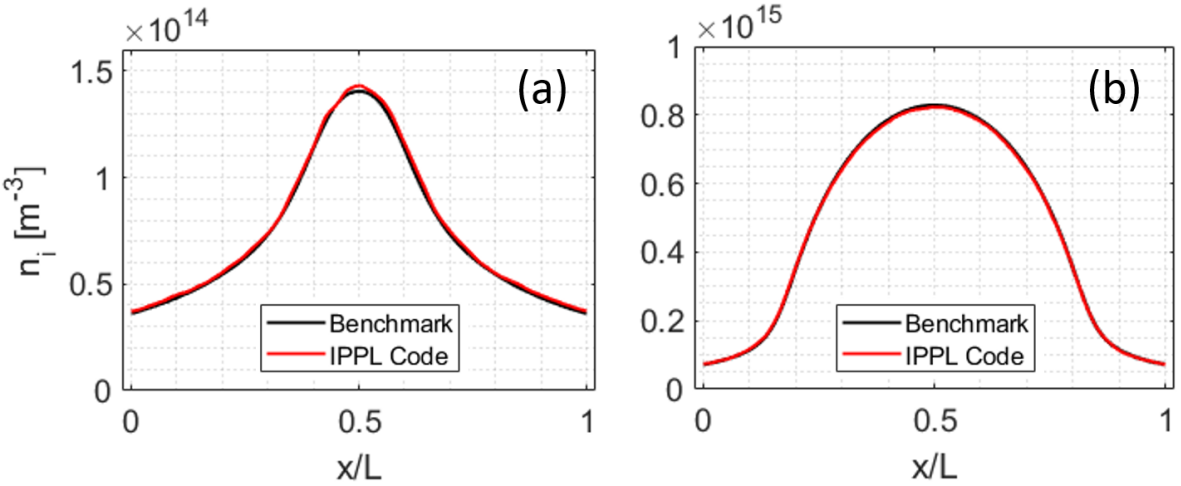


Fig. A.1.8: Comparison of ion number density distributions obtained from the IPPL code against those of the benchmark [185]: (a) Case I, (b) Case II.

A.1.5. Case 5: 1D Sod shock tube problem as standalone test for neutrals' fluid model

A simulation of the famous Sod shock tube problem [105] was carried out to verify the basic implementation of the neutrals' fluid model (Refer to Section 1.4.2.4). The problem is described by a source-free 1D Euler system of equations comprising the continuity, momentum, and energy conservation equations.

The simulation domain, shown in **Fig. A.1.9**, consists of a tube with high- and low-pressure regions separated by a diaphragm in the middle. The properties of the gas are uniform in each region and are given as initial conditions. At t_0, the diaphragm is removed and the gas from the high-pressure region quickly expands into the low-pressure region. This is accompanied by the occurrence of an expansion fan and a shock wave. In between, a contact discontinuity exists that separates the regions of different entropies (or total energy). Noting the presence of the discontinuities in the problem, the use of the HLLC Reimann solver for the inter-cell fluxes is warranted due to its ability to properly resolve the discontinuities in the solution.

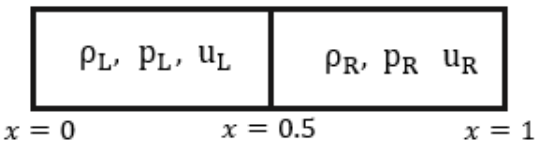


Fig. A.1.9: Simulation domain for the Sod shock tube benchmark.

In order to perform the simulation, a domain length of $1\ m$, a total simulation time of $0.2\ s$, and two different values of cell size were chosen. A simulation with 200 number of cells (N_{cell}) is performed to verify the accuracy of the results against an excessively high-resolution solution given by a simulation with $N_{cell} = 8000$, which effectively amounts to the analytical solution. Dirichlet boundary conditions are

applied to both ends of the domain. The CFL criterion of 0.5 is considered, and the following initial conditions is used:

$$\begin{pmatrix}\rho_L\\ p_L\\ u_L\end{pmatrix}=\begin{pmatrix}1.0\\ 1.0\\ 0.0\end{pmatrix} \text{ for } x<0.5, \quad \text{and} \quad \begin{pmatrix}\rho_R\\ p_R\\ u_R\end{pmatrix}=\begin{pmatrix}0.125\\ 0.1\\ 0.0\end{pmatrix} \text{ for } x>0.5. \qquad \text{Eq. A.10}$$

Fig. A.1.10 presents the results of the simulations with the two values of computational cells. It is observed that the approximate solution with 200 cells is in great agreement with the high-resolution solution with 8000 cells which is coincident with the exact steady-state solution of the problem. Only minor numerical oscillations can be noticed around the location of the discontinuities for the 200-cell simulation case. In addition, the variations in the gas properties due to the expansion fan and due to the contact and shock discontinuities are correctly captured.

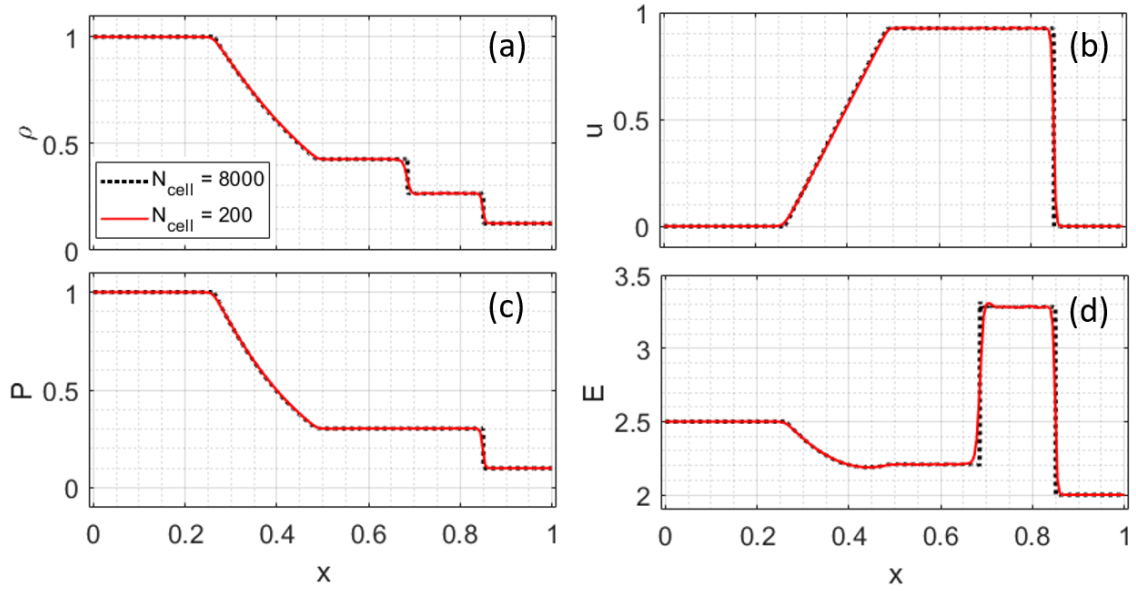


Fig. A.1.10: Profiles of the neutrals' properties from the neutrals' fluid model (1E Euler system of equations) at the end of the Sod test problem simulation; (a) density (ρ), (b) velocity (u), (c) pressure (p), and (d) total energy (E).

A.1.6. Case 6: 1D axial Hall thruster benchmark problem (LANDMARK project)

The setup of the simulation is, overall, based on a test case defined within the LANDMARK benchmarking project [186] for the verification of the 1D axial fluid and hybrid fluid/PIC codes. As a result, the simulations presented here extend the LANDMARK's 1D benchmark case to comprise the kinetic 1D axial simulation.

The domain is 5 cm-long in the x-direction which is discretized using $N_i = 2500$ nodes. The cross-sectional area of the channel $A = 40.035\ [cm^2]$. The adopted time step is $2.5 \times 10^{-12} s$ and the total simulated time is $400\ \mu s$. A Bohm-type transport model of the form $\nu_{Bohm} = \alpha\omega_{ce}$ is considered with $\alpha = 0.1$ and 1.0 for inside the discharge channel and for the near-plume as suggested in the LANDMARK case (**Fig. A.1.11** (a)). A radial magnetic field with a Gaussian distribution and peak value of $15\ mT$, as presented in **Fig. A.1.11** (a), is applied.

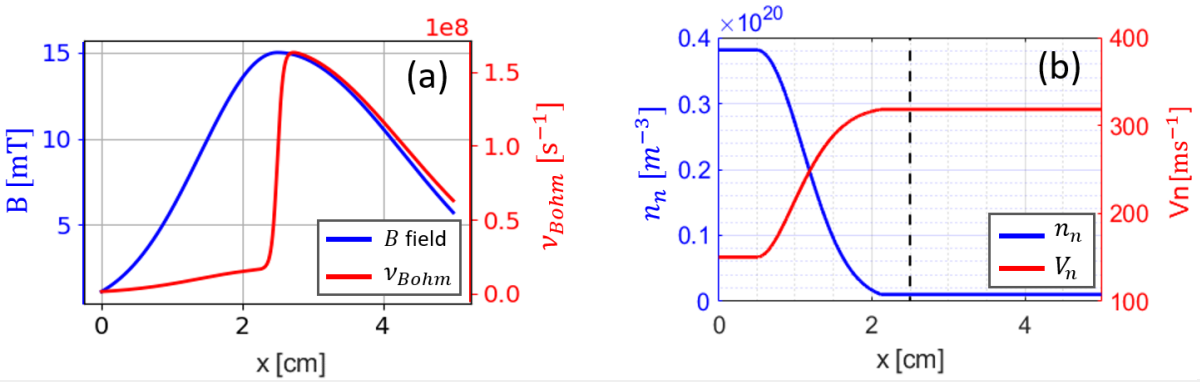


Fig. A.1.11: Axial profiles of (a) magnetic field intensity (B) and the Bohm collision frequency (ν_{Bohm}) and (b) initial number density and velocity of the neutrals.

Initially, the ions and electrons are loaded uniformly throughout the domain at a density of $5 \times 10^{17}\ m^{-3}$. The particles are sampled from a Maxwellian at a temperature of $0.5\ eV$ for the ions and $10\ eV$ for the electrons. To remain consistent with the benchmark results in which the neutrals are resolved using continuity equation alone, we used a fluid model for the neutrals. The results from the simulations are provided for two different models of the neutrals, one based on "continuity only" model (model 1) and the other "1D Euler" model (model 2) (See Section 1.4.2.4 for descriptions). The initial profile of the neutrals' number density and axial drift velocity are depicted in **Fig. A.1.11** (b).

Regarding the axial boundary conditions for the plasma potential, a Dirichlet boundary condition of $V_d = 300\ V$ is applied at the anode side of the domain ($x = 0$), whereas at the cathode side ($x = 5\ cm$), the potential is set at $0\ V$.

The particles' boundary conditions are implemented as follows: along the axial direction, electrons leaving the domain at the anode are removed from the simulation. The ion recombination on the anode surface is considered, by adding the flux of recombined neutrals to the anode particle flow rate ($\dot{m}_a = 5\ mg/s$). The ions leaving the domain from the cathode side are removed from the simulation. On the cathode boundary, electrons are injected into the domain according to the quasi-neutrality condition at the cathode plane (see Section 1.4.2.2). The injected electrons are sampled from a half-Maxwellian at the initial electrons' load temperature, i.e., $10\ eV$.

The collisions between the electrons and neutrals are resolved following the Monte Carlo Collisions (MCC) algorithm (See Section 1.4.2.3). In this regard, to be consistent with the reference LANDMARK case, only the ionization and the elastic momentum exchange collision are considered with the corresponding cross-sections shown in **Fig. 1.12** (a).

Finally, the electron-wall collisions and the associated energy losses are represented in an empirical manner, following the approach explained in Ref. [187] and also adopted in the LANDMARK simulation case. The electron-wall collisions are implemented as a fictitious collision event in the MCC module with the ad-hoc frequency of $\nu_{wall} = 1 \times 10^7\ s^{-1}$. In case of electron-wall collision event, the electron particle is isotopically reflected and loses a part of of its energy, which is calculated from the relation

$$\mathcal{W} = \epsilon \exp\left(-\frac{\mathcal{U}}{\epsilon}\right), \qquad \text{Eq. A.11}$$

in which ϵ is the electron's kinetic energy in eV, and $\mathcal{U}$ is a threshold electron energy that is set at $20\ eV$ according to the LANDMARK case description [186].

The results of these simulations, along with their comparison to the LANDMRK data (where available), are presented below. From the time-averaged axial profiles of plasma properties in **Fig.1. A.12**, it is observed that the PIC simulations with neutral model 1 (continuity only) are in great agreement with the LANDMARK profiles. This is because, in the LANDMARK simulation, only the evolution of the neutrals' density was resolved using continuity equation. The only major difference is noticed to be in the axial electric field profile (**Fig. A.1.12** (e)) where the discontinuity in the LANDAMRK's profile is absent in our result. This is associated with the kinetic treatment of the electrons in our simulations compared to the fluid description of the electron species in the LANDMARK.

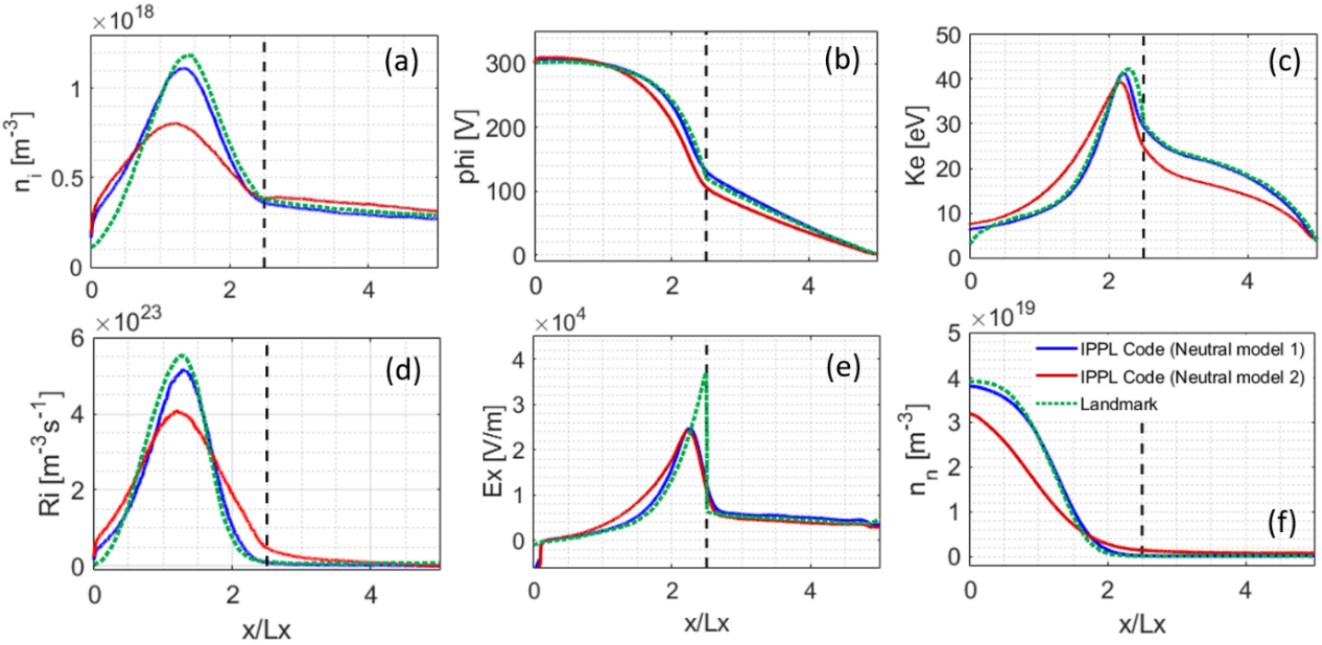


Fig. A.1.12: Time-averaged (over 400 μs) axial profiles of the plasma properties from 1D axial PIC simulations with different neutrals' fluid models together with the LANDMARK results from Ref. [186]. (a) ion number density (n_i), (b) electric potential (phi), (c) electron kinetic energy (Ke), (d) ionization rate (R_i), (e) axial electric field (E_x), and (f) neutral number density (n_n). Dashed black lines show the location of channel exit plane.

Furthermore, from the time evolution plots in **Fig. A.1.13**, it is noticed that, in case of the "Continuity Only" model, the breathing oscillations are rather weak and are damped early in the simulation. The discharge in this case becomes almost steady after approximately $150\ \mu s$. However, resolving the variations in the neutrals' velocity in the neutral model 2 (1D Euler equations) results in stronger breathing oscillations.

The performance parameters, namely, thrust (T), specific impulse (I_{sp}), and thrust efficiency (η_T) are calculated using the Eqs. A.12 to A.14 and provided in **Table A.1.1**.

$$T = \frac{Am_i}{kN_i} \sum_{ts=1}^{k} \sum_{j=1}^{N_i} n_i(j,t)\ V_{i,x}^2(j,t)\,, \qquad \text{Eq. A.12}$$

$$I_{sp} = \frac{1}{gkN_i} \sum_{ts=1}^{k} \sum_{j=1}^{N_i} V_{i,x}(j,t) \qquad \text{Eq. A.13}$$

$$\eta_T = \frac{T^2}{2\,\dot{m}_a\, I_d V_a}. \qquad \text{Eq. A.14}$$

In the above equations, the summation $\Sigma_{ts=1}^{k}$ denotes the temporal average, which is taken over $400\ \mu s$ of the simulation time. In addition, the summation $\Sigma_{j=1}^{k}$ denotes the spatial average, which is taken over the last 100 cells of the domain (near cathode boundary). The thrust and the specific impulse due to the neutrals were found to be negligible and are, thus, neglected.

The values of the current components predicted by the IPPL code with neutral are in line with the corresponding values reported for the LANDMARK.

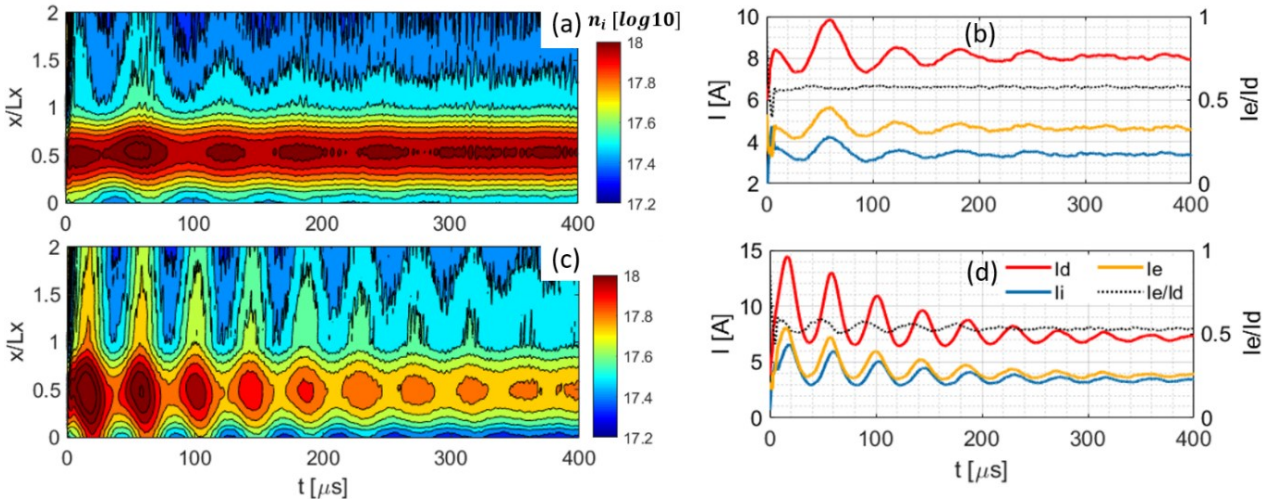


Fig. A.1.13: Spatiotemporal evolutions of ion number density (a and c) and time evolutions of total discharge current (I_d), and the electron (I_e) and ion (I_i) current components (b and d). Top row is for simulation with neutral model 1 and bottom row is for simulation with neutral model 2.

	I_d [A]	I_i [A]	I_e [A]	T [mN]	Isp [s]	η_T [%]
IPPL Code (Neutral model 1)	8.11	3.44	4.67	94	2052	36.3
IPPL Code (Neutral model 2)	7.99	3.70	4.29	93	1897	36
Landmark	8.15 – 8.36	3.67 – 3.68	4.48 – 4.67	---	---	---

Table A.1.1: Comparison of the predicted performance parameters from IPPL-1D axial PIC simulations using two different neutral models and the LANDMARK results [186].

A.1.7. Case 7: 2D radial-azimuthal E × B discharge benchmark problem

The setup and conditions of this test case follow exactly those of the benchmarking activity in Ref. [35] and described in Section 3.2.1. This problem was used in Section 3.2.2 to verify the IPPL-Q2D simulations in the radial-azimuthal configuration. Here we focus on benchmarking the IPPL-2D code.

Fig. A.1.14 shows the comparison between the radial distributions of the time-averaged ion number density and electron temperature from IPPL-2D and from the benchmark's 2D code, CERFACS [35]. Referring to Ref. [35], the participating codes in the radial-azimuthal benchmarking activity had a prediction error withing a band of $\pm$ 2.5 % in their predictions with respect to the CERFACS code.

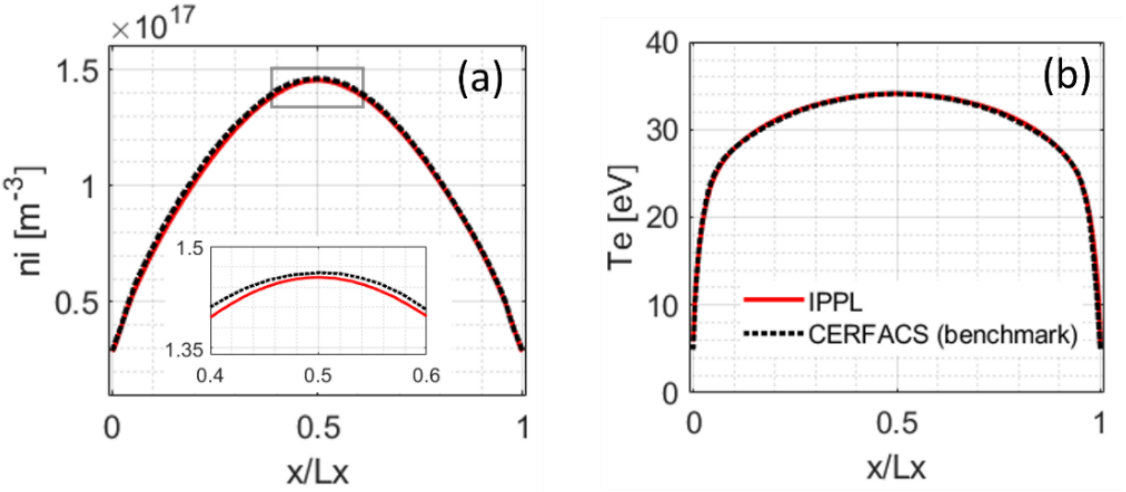


Fig. A.1.14: Comparison between the time-averaged (over $25 - 30\ \mu s$) radial profiles of (a) ion number density (n_i) and (b) electron temperature (T_e), obtained from the IPPL-2D and the CERFACS code [35].

It is seen in **Fig. A.1.14** that the time-averaged radial distributions from IPPL-2D are almost identical to those from CERFACS, with only a negligible difference of about $0.5\ \%$ visible in the zoomed-in view of the ion number density profile.

Moreover, the time evolution of the spatially averaged ion number density and the radial component of the electron temperature (T_{ex}) from IPPL-2D are shown in **Fig. A.1.15**. Comparing these evolution plots with those published in Fig. 7 of the benchmarking article [35], we found that the resolved trends from IPPL-2D are very similar to those from the 2D codes that involved in the benchmark, both over the initial $3\ \mu s$ transient state (**Fig. A.1.15** (a)) and as well as the quasi-steady state throughout the rest of simulation duration (**Fig. A.1.15** (b)).

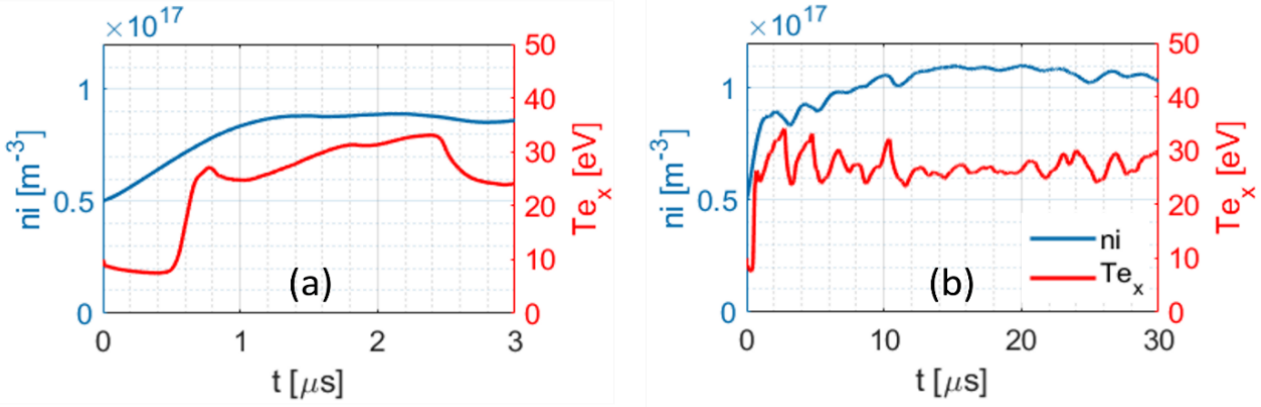


Fig. A.1.15: Time evolution of the ion number density (n_i) and the radial component of the electron temperature (T_{ex}) over (a) the initial $3\ \mu s$ of the simulation time and, (b) over the entire simulation duration. The left y-axis in both plots corresponds to the ion number density, whereas the right y-axis represents the radial electron temperature.

A.2 Extension of the underlying formulation of RO-PIC to 3D

The underlying formulation of RO-PIC is readily extensible to 3D. In the following we derive the Q3D Poisson's equation underpinning the electrostatic Q3D RO-PIC simulation. In 3D, the coarse grid comprises $M \times N \times P$ regions. The Q3D Poisson's solution within each region $\Omega_{n,m,p}$, where $m \in [1, M]$, $n \in [1, N]$ and $p \in [1, P]$ is approximated as the sum of three potential functions $\phi^x_{n,p}$, $\phi^y_{m,p}$ and $\phi^z_{n.m}$

$$\phi(x,y,z) \approx \phi^x_{n,p}(x) + \phi^y_{m,p}(y) + \phi^z_{n.m}(z)\,, \qquad \forall x,y,z \in \Omega_{n,m,p}, \qquad \text{Eq. A.15}$$

where,

$$\phi^x_{n,p} = \phi^x_{n,p}(x); \quad \forall x \in [0, L_x]\,, \quad y \in \left[y_{g,n} - \frac{L_{y,n}}{2}, y_{g,n} + \frac{L_{y,n}}{2}\right], \qquad z \in \left[z_{g,p} - \frac{L_{z,p}}{2}, z_{g,p} + \frac{L_{z,p}}{2}\right], \qquad \text{Eq. A.16}$$

$$\phi^y_{m,p} = \phi^y_{m,p}(y); \quad \forall x \in \left[x_{g,m} - \frac{L_{x,m}}{2}, x_{g,m} + \frac{L_{x,m}}{2}\right], \quad y \in [0, L_y], \qquad z \in \left[z_{g,p} - \frac{L_{z,p}}{2}, z_{g,p} + \frac{L_{z,p}}{2}\right], \qquad \text{Eq. A.17}$$

$$\phi^z_{n.m} = \phi^z_{n.m}(z); \quad \forall x \in \left[x_{g,m} - \frac{L_{x,m}}{2}, x_{g,m} + \frac{L_{x,m}}{2}\right], \quad y \in \left[y_{g,n} - \frac{L_{y,n}}{2}, y_{g,n} + \frac{L_{y,n}}{2}\right], \qquad z \in [0, L_z]. \qquad \text{Eq. A.18}$$

In the above equations, $L_{x,m}, L_{y,n}$ and $L_{z,p}$ represent the regions' extents along x, y and z directions, respectively, while L_x, L_y and L_z are the domain's lengths along the respective directions. Also, $x_{g,m}, y_{g,n}$ and $z_{g,p}$ denote, respectively, the x, y and z coordinated of the center of region $\Omega_{n,m,p}$.The domain decomposition in 3D and the reduced-dimension computational grid are illustrated in **Fig. A.2.1.**

For simplicity let us assume $x_W = x_{g,m} - \frac{L_{x,m}}{2}$, $x_E = x_{g,m} + \frac{L_{x,m}}{2}$, $y_S = y_{g,n} - \frac{L_{y,n}}{2}$, $y_N = y_{g,n} + \frac{L_{y,n}}{2}$, $z_B = z_{g,p} - \frac{L_{z,p}}{2}$ and $z_F = z_{g,p} + \frac{L_{z,p}}{2}$. Similar to the procedure followed in 2D, we substitute Eq. A.15 in the 3D Poisson's equation and integrate separately over $x-y$, $x-z$ and $y-z$ planes within each region. **Fig. A.2.2** illustrates the computational elements associated with the Q3D scheme along with the electric field components which are integrated over. The resulting coupled system of equations is given by Eqs. A.19 – A.21, which can be solved in the same manner as described in Chapter 2.

$$\left(\frac{d^2\phi^x_{n,p}}{dx^2}\right)L_{y,n}L_{z,p}+\frac{L_{z,p}}{\Delta x}\int_{y_S}^{y_N}\left(\frac{\partial\phi^y_{m,p}}{\partial x}|_E-\frac{\partial\phi^y_{m,p}}{\partial x}|_W\right)dy+\frac{L_{y,n}}{\Delta x}\int_{z_B}^{z_F}\left(\frac{\partial\phi^z_{n,m}}{\partial x}|_E-\frac{\partial\phi^z_{n,m}}{\partial x}|_W\right)dz$$

$$+L_{z,p}\left[\left(\frac{\partial\phi^x_{n,p}}{\partial y}+\frac{\partial\phi^y_{m,p}}{\partial y}+\frac{\partial\phi^z_{n,m}}{\partial y}\right)_N-\left(\frac{\partial\phi^x_{n,p}}{\partial y}+\frac{\partial\phi^y_{m,p}}{\partial y}+\frac{\partial\phi^z_{n,m}}{\partial y}\right)_S\right]$$

$$+L_{y,n}\left[\left(\frac{\partial\phi^x_{n,p}}{\partial z}+\frac{\partial\phi^y_{m,p}}{\partial z}+\frac{\partial\phi^z_{n,m}}{\partial z}\right)_F-\left(\frac{\partial\phi^x_{n,p}}{\partial z}+\frac{\partial\phi^y_{m,p}}{\partial z}+\frac{\partial\phi^z_{n,m}}{\partial z}\right)_B\right] \qquad \text{Eq. A.19}$$

$$=-\frac{1}{\epsilon_0}\int_{z_B}^{z_F}\int_{y_S}^{y_N}\rho(x,y,z)dydz\,,$$

$$\left(\frac{d^2\phi^y_{m,p}}{dy^2}\right)L_{x,m}L_{z,p}+\frac{L_{z,p}}{\Delta y}\int_{x_W}^{x_E}\left(\frac{\partial\phi^x_{n,p}}{\partial y}|_N-\frac{\partial\phi^x_{n,p}}{\partial y}|_S\right)dx+\frac{L_{x,n}}{\Delta y}\int_{z_B}^{z_F}\left(\frac{\partial\phi^z_{n,m}}{\partial y}|_N-\frac{\partial\phi^z_{n,m}}{\partial y}|_S\right)dz$$

$$+L_{z,p}\left[\left(\frac{\partial\phi^x_{n,p}}{\partial x}+\frac{\partial\phi^y_{m,p}}{\partial x}+\frac{\partial\phi^z_{n,m}}{\partial x}\right)_E-\left(\frac{\partial\phi^x_{n,p}}{\partial x}+\frac{\partial\phi^y_{m,p}}{\partial x}+\frac{\partial\phi^z_{n,m}}{\partial x}\right)_W\right]$$

$$+L_{x,m}\left[\left(\frac{\partial\phi^x_{n,p}}{\partial z}+\frac{\partial\phi^y_{m,p}}{\partial z}+\frac{\partial\phi^z_{n,m}}{\partial z}\right)_F-\left(\frac{\partial\phi^x_{n,p}}{\partial z}+\frac{\partial\phi^y_{m,p}}{\partial z}+\frac{\partial\phi^z_{n,m}}{\partial z}\right)_B\right] \qquad \text{Eq. A.20}$$

$$=-\frac{1}{\epsilon_0}\int_{z_B}^{z_F}\int_{x_W}^{y_E}\rho(x,y,z)dxdz\,,$$

$$\left(\frac{d^2\phi^z_{n,m}}{dz^2}\right)L_{x,m}L_{y,n}+\frac{L_{x,m}}{\Delta z}\int_{y_S}^{y_N}\left(\frac{\partial\phi^y_{m,p}}{\partial z}|_F-\frac{\partial\phi^y_{m,p}}{\partial z}|_B\right)dy+\frac{L_{y,n}}{\Delta z}\int_{x_W}^{x_E}\left(\frac{\partial\phi^x_{n,p}}{\partial z}|_F-\frac{\partial\phi^x_{n,p}}{\partial z}|_B\right)dx$$

$$+L_{y,n}\left[\left(\frac{\partial\phi^x_{n,p}}{\partial x}+\frac{\partial\phi^y_{m,p}}{\partial x}+\frac{\partial\phi^z_{n,m}}{\partial x}\right)_E-\left(\frac{\partial\phi^x_{n,p}}{\partial x}+\frac{\partial\phi^y_{m,p}}{\partial x}+\frac{\partial\phi^z_{n,m}}{\partial x}\right)_W\right]$$

$$+L_{x,m}\left[\left(\frac{\partial\phi^x_{n,p}}{\partial y}+\frac{\partial\phi^y_{m,p}}{\partial y}+\frac{\partial\phi^z_{n,m}}{\partial y}\right)_N-\left(\frac{\partial\phi^x_{n,p}}{\partial y}+\frac{\partial\phi^y_{m,p}}{\partial y}+\frac{\partial\phi^z_{n,m}}{\partial y}\right)_S\right] \qquad \text{Eq. A.21}$$

$$=-\frac{1}{\epsilon_0}\int_{y_S}^{y_N}\int_{x_W}^{x_E}\rho(x,y,z)dxdy\,.$$

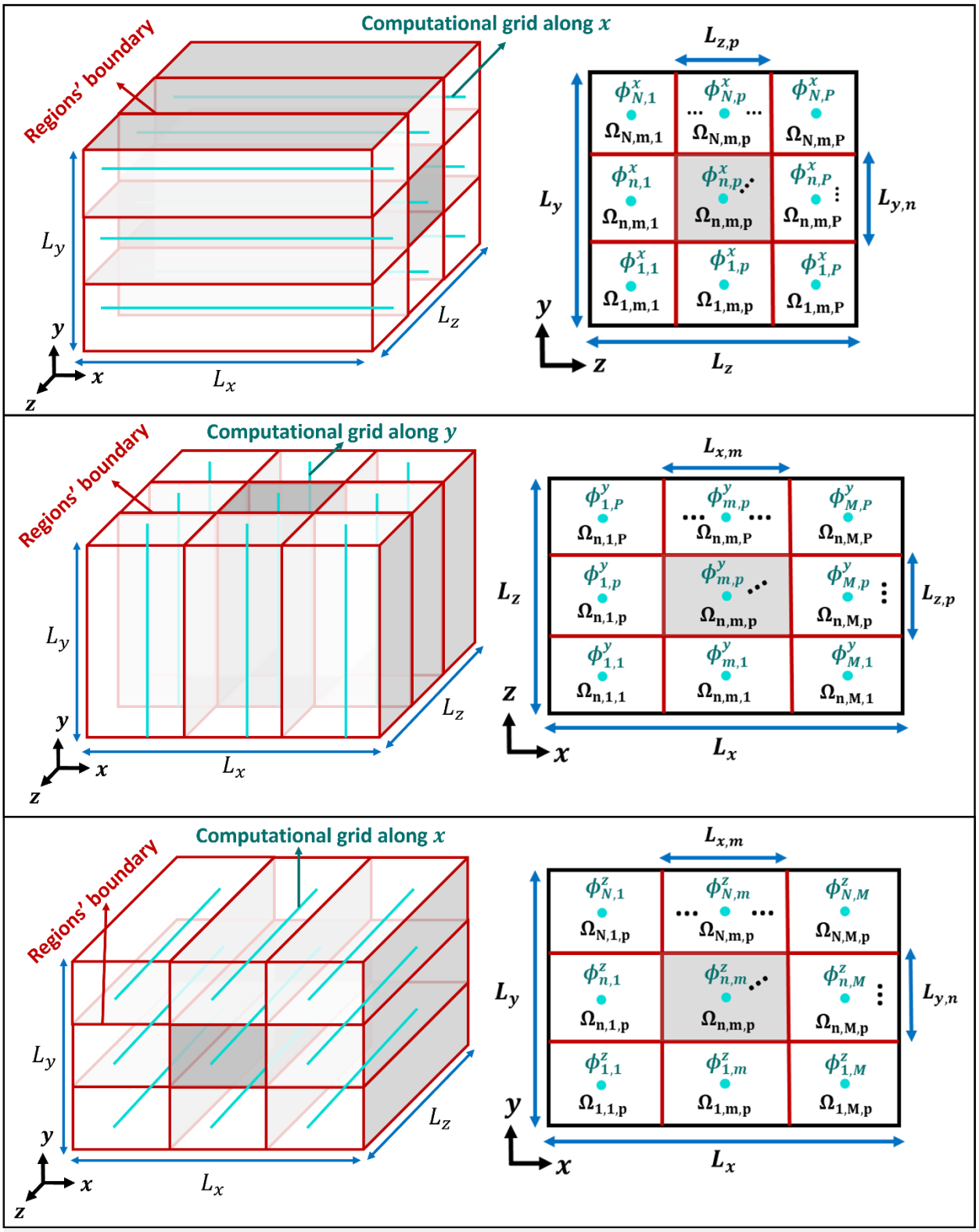


Fig. A.2.1: Schematic of Q3D grid and the multi-region domain decomposition for the reduced-dimension Q3D Poisson's equation. The illustrations on the left demonstrate the 3D view of domain decomposition (including the regions' boundaries and computational grid) along x-axis (top panel), along y-axis (middle panel) and along z-axis (bottom panel). The illustrations on the right show the cross-sections of the domain along $y-z$ plane (top panel), $x-z$ plane (middle panel), and $x-y$ plane (bottom panel).

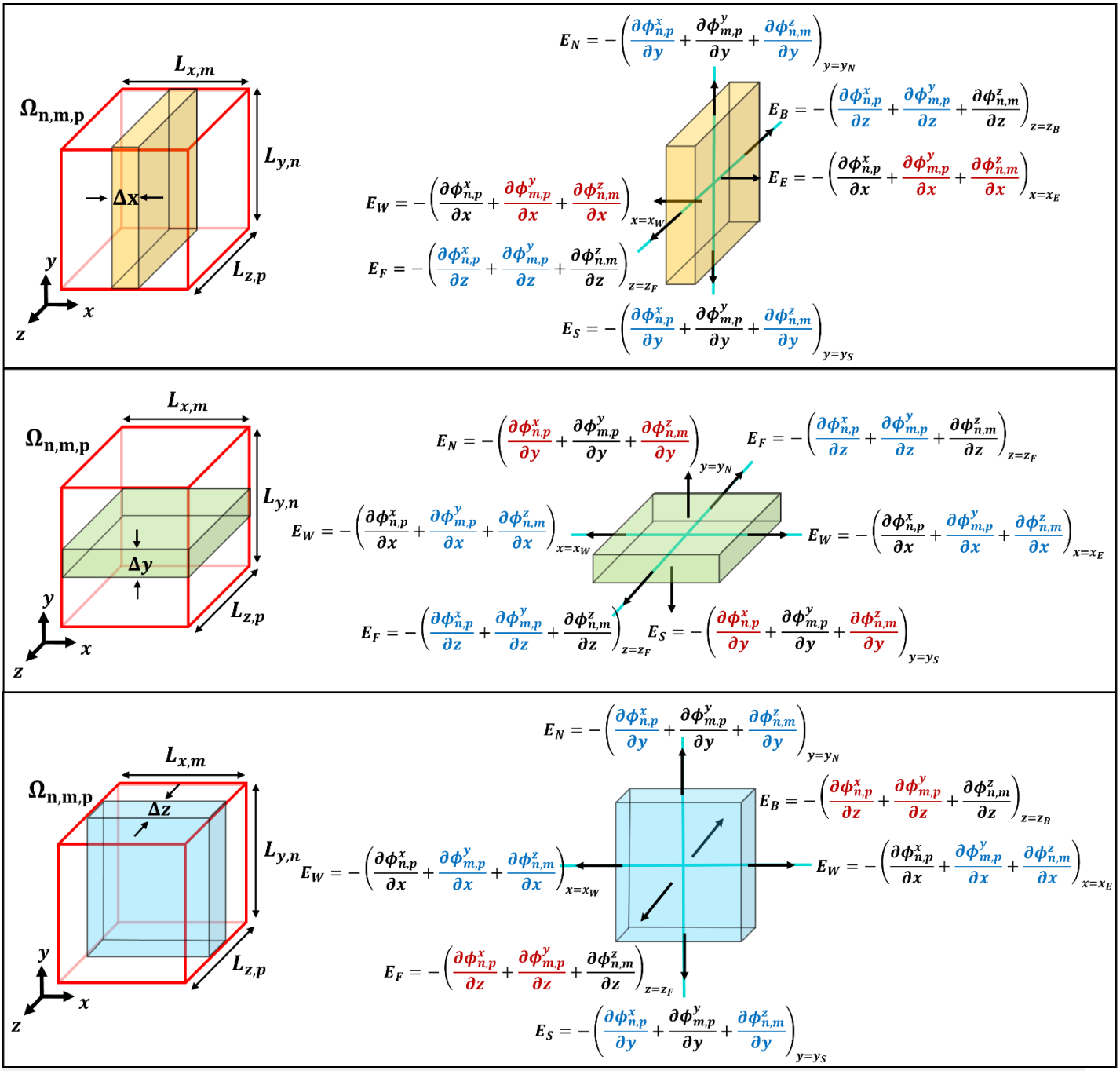


Fig. A.2.2: Schematic of the computational elements associated with the dimensionality-reduction approach in region $\Omega_{m,n,p}$ (left) and electric field components across sides of the element (right); (top panel) computational element along x-axis for solving potential function $\phi^x_{n,p}$ from Eq. A.19, (middle panel) computational element along y-axis for solving potential function $\phi^y_{m,p}$ from Eq. A.20, (bottom panel) computational element along z-axis for solving potential function $\phi^z_{n,m}$ from Eq. A.21.

A.3 Additional standalone test cases for reduced-dimension Poisson solver (RDPS)

In addition to the test cases presented in Section 2.4 for standalone verification of the RDPS, we provide two sets of additional cases here. The first set represents a problem with an oscillatory source term distribution (ρ) across the domain with different wavenumbers and zero-value Dirichlet boundary condition along the four boundaries (Case No 1 to 4 in **Table A.3.1**). This is a common situation occurring in an $\mathrm{E}\times\mathrm{B}$ plasma discharge, especially along the azimuthal coordinate where small-wavelength fluctuations in charge density develop. This test case verifies the ability of the approach to accurately resolve the potential distribution in the presence of small-scale density gradients. The second set involves oscillatory Dirichlet boundary conditions with various wavenumbers along the boundaries and no source term (Case No 5 to 8 in **Table A.3.1**). The number of computational cells along either x or y direction is 100.

Case No.	Source terms ($S(x,y)$)	Boundary Conditions
1, 2, 3, 4	$S = sin(n\pi y)\, sin(n\pi x);\ \ n = 1, 3, 5, 10$	$\phi(0,y) = \phi(L_x,y) = 0$ $\phi(x,0) = \phi(x,L_y) = 0$
5, 6, 7, 8	$S = 0$	$\phi(0,y) = \phi(L_x,y) = sin(n\pi y)\, sin(n\pi x);\ \ n = 1, 3, 5, 10$ $\phi(x,0) = \phi(x,L_y) = sin(n\pi x)\, sin(n\pi x);\ \ n = 1, 3, 5, 10$

Table A.3.1: Definition of the 2D Poisson problems for additional standalone verification of RDPS.

The error convergence plots of the reduced-order solution for the defined problems using RDPS with various number of regions are provided in **Fig. A.3.1**. The error is computed according to Eq. 2.40 and with respect to the corresponding full-2D solution. Furthermore, the contour maps of the solutions with various number of regions are presented in **Fig. A.3.2** and **Fig. A.3.3**, for cases 1-4 and 5-8, respectively. These figures clearly illustrate the convergence of solution accuracy and the enhancement of the smoothness of the Q2D potential profile as the number of regions increases.

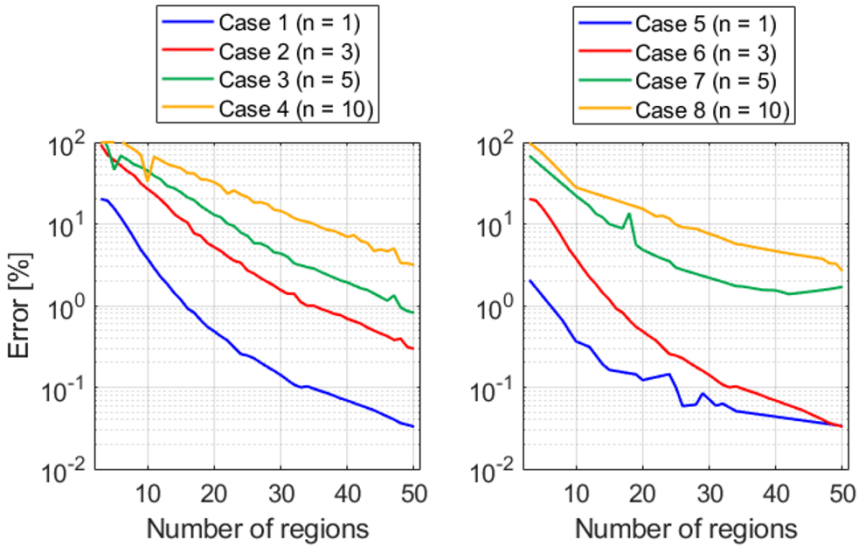


Fig. A.3.1: Error convergence of the RDPS's solution; variation of the normalized L2 error (Eq. 2.40) between the full-2D solution and the approximate Q2D solution from the RDPS when increasing number of regions for (left) cases 1-4 defined, and (right) cases 5-8 defined in **Table A.3.1.** The y-axis in both plots is in logarithmic scale.

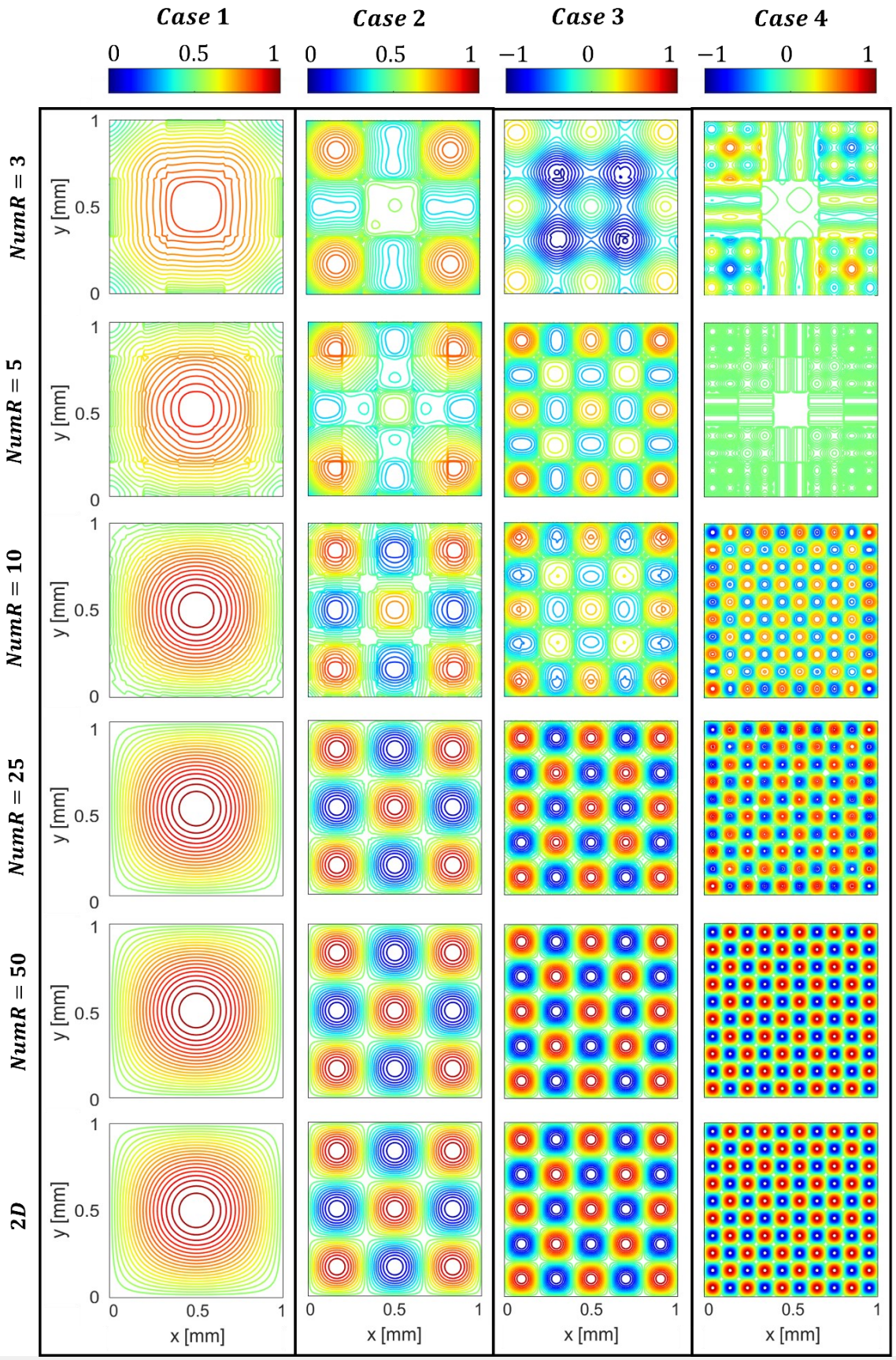


Fig. A.3.2: Contour map representation of the RDPS's solutions with various number of regions against the corresponding full-2D solution (bottom row) for cases 1-4 defined by **Table A.2.1**. The numbers of regions are equal along both dimensions ($M = N$) which are denoted by *NumR*.

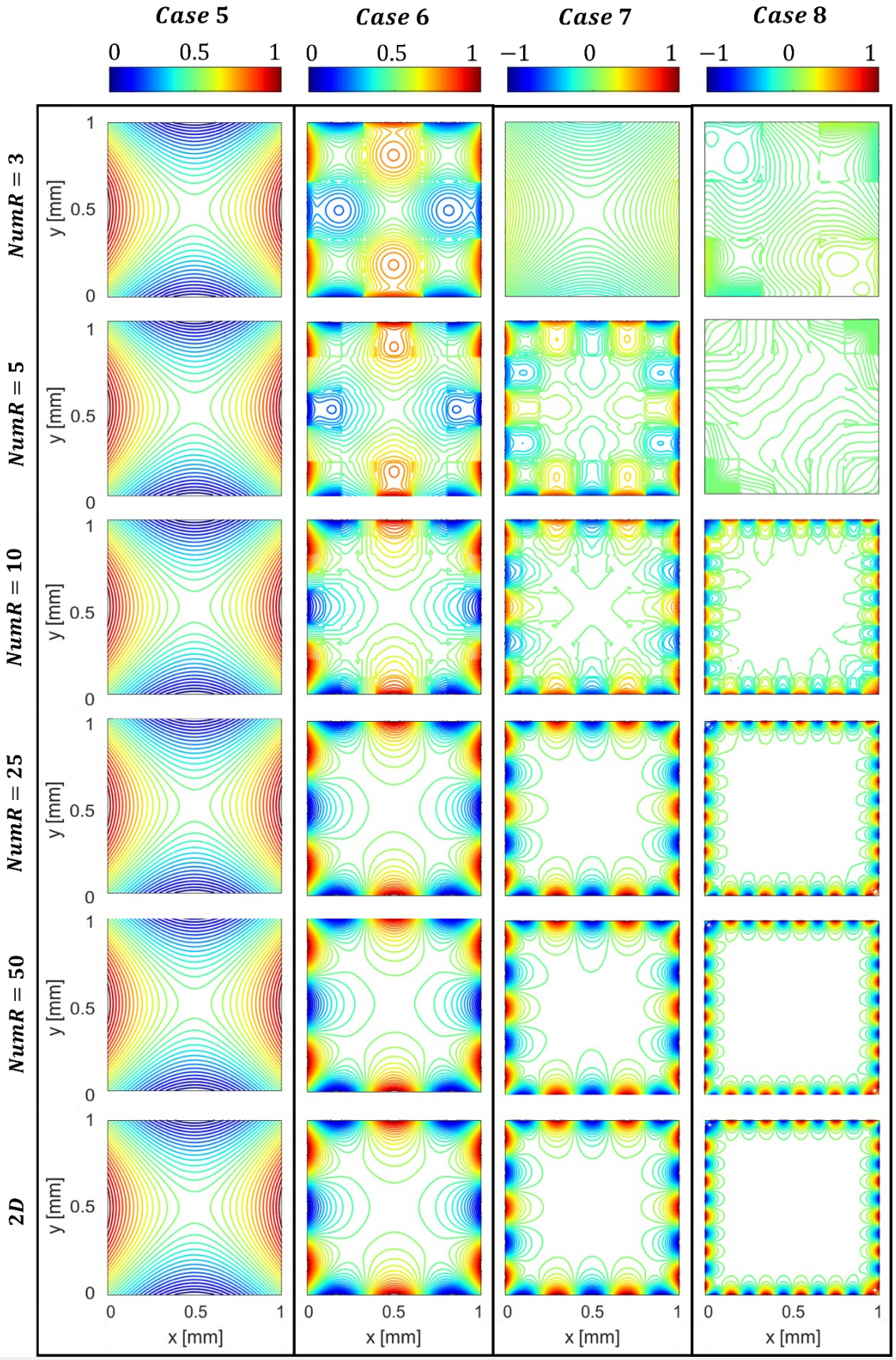


Fig. A.3.3: Contour map representation of the RDPS's solutions with various number of regions against the corresponding full-2D solution (bottom row) for cases 5-8 defined by **Table A.3.1**. The numbers of regions are equal along both dimensions ($M = N$) which are denoted by *NumR*.

A.4 Additional tests on the reduced-order PIC code (IPPL-Q2D)

A.4.1. Axial-azimuthal Hall thruster configuration

A) Various operating conditions: The low-number-of-region Q2D simulations, which were verified for the nominal condition ($J = 400\ Am^{-2},\ B = 10\ mT$) of the axial-azimuthal benchmark problem in Section 3.1.2, namely, single-region ($N = 1,\ M = 1$), double-region ($N = 1,\ M = 2$) and triple-region ($N = 1,\ M = 3$). These simulations are now tested across various operating conditions. The simulations' setup and conditions follow those outlined in Section 3.1.2 except for the operating ion current density (J) and the applied magnetic field peak (B).

The simulation conditions correspond to two sets of cases: the first set includes different current densities (i.e., $J = 50,\ 100,\ 200$ and $400\ A/m^2$) with the magnetic field peak intensity being fixed at $10\ mT$. The second set is related to various magnetic field peak intensities (i.e., $B = 5,\ 10,\ 15$ and $20\ mT$), with the maximum current density maintained at $400\ A/m^2$. These correspond to a subset of conditions for which the results of high-number-of-region simulations are discussed in Chapter 5. The profiles of the ionization source and the applied magnetic field are according to **Fig. 5.1**.

The comparison of the outcomes of the Q2D simulations in terms of the time-averaged axial profiles of ion number density (n_i) and axial electric field (E_x) against the corresponding full-2D results reported in Ref. [69] are presented in **Fig. A.4.1** and **Fig. A.4.2**, respectively.

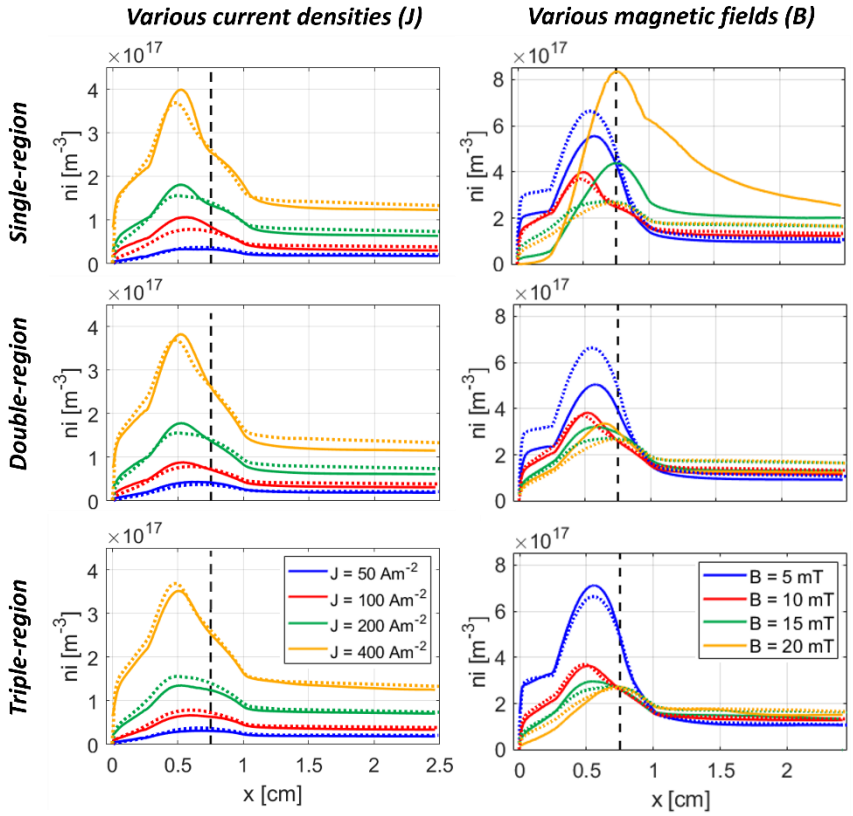


Fig. A.4.1: Time-averaged (over $16 - 20\ \mu s$) axial profiles of ion number density (n_i) from low-number-of-region Q2D simulations for various operating conditions. The dashed lines show the corresponding full-2D results from Ref. [69]. Dashed black lines show the location of magnetic field's peak.

Referring to left column (various J) in **Fig. A.4.1** and **Fig. A.4.2**, it is observed that the single-region quasi-2D simulations provide a very consistent approximation of the results from the full-2D simulations. Nevertheless, the double-region and triple-region simulations demonstrate an improvement in the prediction of the axial distribution of plasma properties. In this respect, the trend of n_i and E_x predicted by the triple-region simulations resemble very closely the reference profiles from the 2D simulations, with only a slight difference observed near the peak of the respective profiles.

Looking at the right column (various B) in **Fig. A.4.1** and **Fig. A.4.2,** it is seen that the single-region simulations are unable to properly approximate the plasma properties in the $15\ mT$ and $20\ mT$ cases. In fact, in these two cases, the resolved average instability-induced electron cross-field transport is not enough to allow for a sufficient electron current toward the anode. As a result, the electrons and, hence, the plasma generated in the ionization zone (defined by the extent over which the ionization source is imposed) do not fill the near-anode region. This is evident in n_i plot which shows very low densities near the anode in the cases with high magnetic field peaks. Therefore, the high magnetic-field-peak simulation conditions represent the limiting cases for the single-region Q2D simulations. In any case, it is important to note that this limitation of the single-region approximation might be specific to the adopted simulation case and due to the disparity between the strength of the imposed ionization source ($400\ A/m^2$) and the magnetic field intensity, not reflecting realistic operating conditions of Hall thruster.

The double-region and triple-region simulations are, nonetheless, able to properly predict the plasma profiles across the considered range of magnetic field intensities. In this regard, the plots show a reasonable consistency between the Q2D and full-2D simulation results. Furthermore, as it was the case for the simulations with various current densities, the triple-region simulations for different magnetic field peaks provide results that are in closest agreement with the 2D profiles, especially in terms of the ion number density.

However, concerning the case with the lowest magnetic field intensity ($B = 5\ mT$), although all Q2D simulations provide an acceptable approximation of the plasma profiles, in none of the simulations, a perfect agreement with the reference 2D results is achieved. This is again conjectured to be as a consequence of the extreme condition in this case.

We highlight that these predictions accuracies across the wide range of operating conditions are achieved with the computational costs equivalent to those of a 1D PIC simulation, i.e. only $0.4\ \%$ of the computational cost of a full-2D simulation.

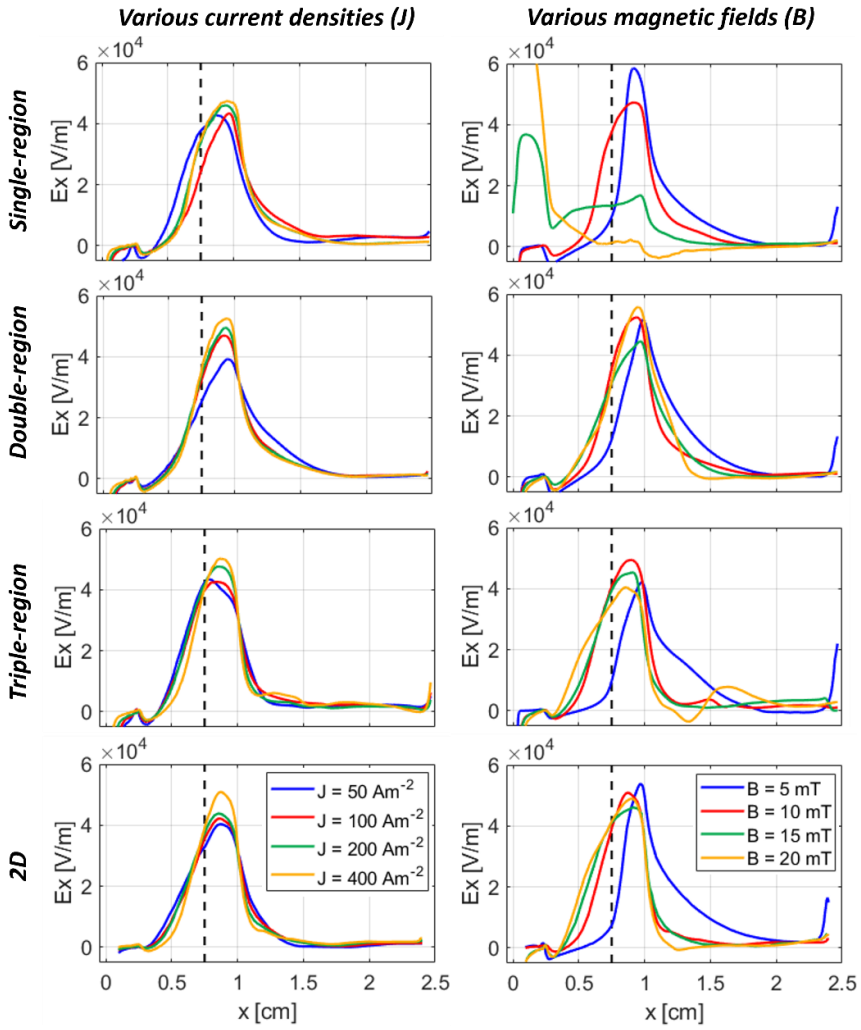


Fig. A.4.2: Time-averaged (over $16 - 20\ \mu s$) axial profiles of axial electric field (E_x) from low-number-of-region Q2D simulations for various operating conditions. The bottom row plots show the corresponding full-2D results from Ref. [69]. Dashed black lines show the location of magnetic field's peak.

B) Sensitivity to the azimuthal extent of the domain: Due to computational impracticality of simulating the entire circumference of a Hall thruster has with conventional full-2D simulations, it is customary to instead simulate a limited portion of the circumferential extent and apply a periodic boundary condition on both ends of the domain along the azimuthal direction. Hence, it is necessary to analyze the sensitivity of the results to the simulated azimuthal length. In this regard, we present a comparison between the results from the triple-region simulations for azimuthal lengths of $L_z = 0.64,\ 1.28$ and $2.56\ cm$.

Concerning the axial distribution of the time-averaged plasma parameters, **Fig. A.4.3** illustrates a very minor sensitivity of the predicted profiles to the azimuthal length of the domain. The observed sensitivity of the Q2D simulation is found to be very similar to the sensitivity to the azimuthal length reported for the full-2D simulations [69].

Furthermore, from the spatiotemporal maps of the azimuthal electric field fluctuations shown in **Fig. A.4.4** in each region, we notice that the waves' azimuthal wavenumber, frequency and amplitude in each region are almost identical for all simulated azimuthal domain lengths.

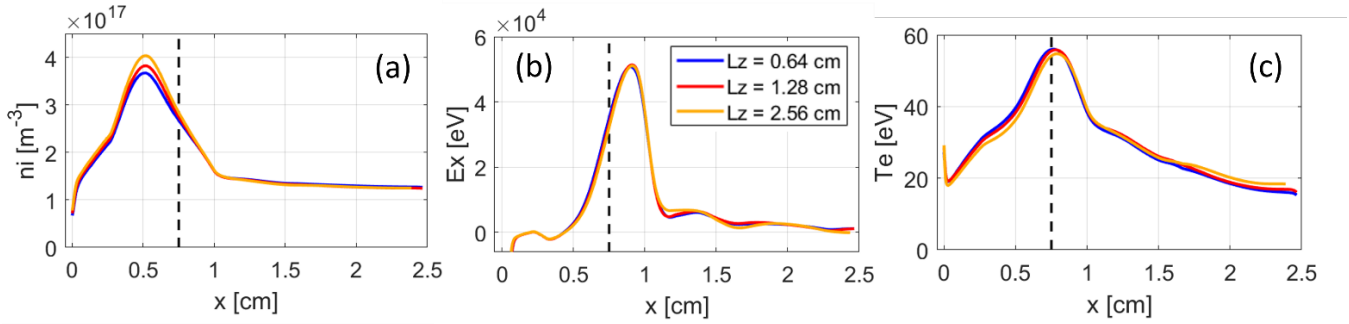


Fig. A.4.3: Comparison between the axial profiles of the time-averaged (over $16 - 20\ \mu s$) plasma properties from the triple-region simulations with various azimuthal extents; (a) ion number density (n_i), (b) axial electric field (E_x), and (c) electron temperature (T_e). Dashed black lines show the location of magnetic field's peak.

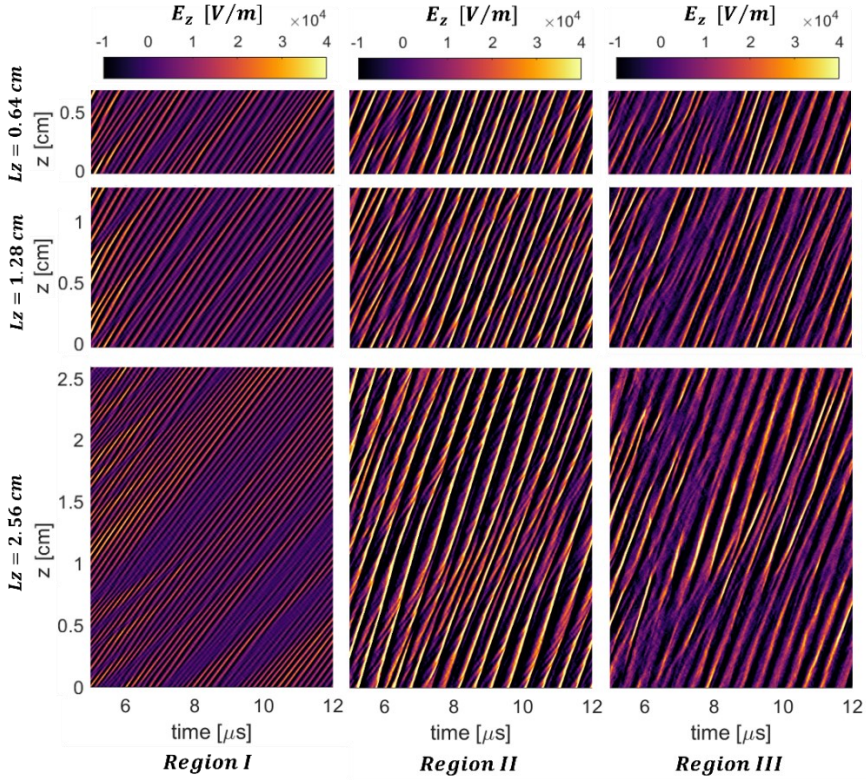


Fig. A.4.4: Spatiotemporal maps of the azimuthal electric field fluctuations in different regions of the triple-region simulations with various azimuthal lengths.

A.4.2. Axial-radial Hall thruster configuration

The setup of the axial-radial simulations is inspired from the one reported in Ref. [188]. The computation domain is a rectangular Cartesian $x - y$ plane, resembling the channel and the near-plume a SPT100-type Hall thruster. The x-axis is parallel to the thruster's channel axial centerline, and the y-axis is directed along the radial direction. The axial extent of the domain is $4\ cm$, covering the $2.5\ cm$-long channel of the thruster and $1.5\ cm$ of the near plume. The radial length of the domain is $1.5\ cm$. The number of cells along the axial and the radial direction is 2000 and 750, respectively.

The simulated operating condition corresponds to a discharge voltage of $300\ V$, an anode mass flow rate of $5\ mg/s$, and a peak magnetic field intensity of $16\ mT$. The imposed magnetic field is purely radial with an axial profile being the same as that shown in Fig. 9 of Ref. [188].

At the beginning of the simulation, the electrons and ions are sampled from a Maxwellian distribution at $10\ eV$ and $0.5\ eV$, respectively and loaded uniformly throughout the domain. Electrons are sampled from a half-Maxwellian at $4\ eV$ and are injected into the domain from the cathode boundary at each timestep according to the quasi-neutrality approach (refer to Section 1.4.2.2).

An anode temperature of $750\ K$ and a wall temperature of $850\ K$ are assumed. The neutral particles are sampled from a Maxwellian at the anode temperature and are loaded into the domain according to an initial profile given in Ref. [106]. The neutral density at the anode in the beginning of the simulation is $1 \times 10^{19}\ m^{-3}$. The evolution of the neutrals is resolved kinetically using the Q2D DSMC module, which was verified in Section 3.4.

The neutrals that are injected at the constant operating mass flow rate as well as those created due to ion recombination on the anode surface are sampled from a half-Maxwellian at the anode temperature. Ion recombination on the channel walls is also considered and the corresponding neutrals are sampled from a half-Maxwellian at the wall temperature. The secondary electron emission (SEE) from the channel walls is accounted for following the linear SEE model, described in Section 1.4.2.2.

The electrons' collisions with the neutrals are resolved through the Monte Carlo Collisions (MCC) scheme (See Section 1.4.2.3). The collision events that are considered include single ionization, four excitations, and elastic momentum-transfer collision.

Finally, concerning the "anomalous" electrons' axial mobility, noting that the axial-radial simulations do not resolve the effects of azimuthal instabilities on cross-field transport, an ad-hoc electron mobility model based on the Bohm collision frequency is implemented in the simulations. In this regard, following the approach pursued in Ref. [188], a "two-zone" mobility model of the general form $\nu_{Bohm} = \left(\frac{\alpha}{16}\right)\omega_{ce}$ is used, with the tuning coefficient $\alpha = 0.035$ inside the channel and $\alpha = 5$ in the near-plume.

The axial-radial Q2D simulations are conducted using various numbers of regions along the axial and the radial directions denoted by M and N, respectively. These configurations include case $\boldsymbol{i}$: $N = 4$, $M = 8$, case $\boldsymbol{ii}$: $N = 8$, $M = 16$, case $\boldsymbol{iii}$: $N = 12$, $M = 24$. The Q2D implementation of the DSMC algorithm (Q2D DSMC) is integrated within the Q2D PIC resulting in a RO-PIC-DSMC scheme. The time step is $2 \times 10 - 12\ s$ and the total simulation duration is $20\ \mu s$.

The comparison of the 2D distribution of various plasma properties predicted from Q2D PIC-DSMC simulations at $t = 20\ \mu$s is presented in **Fig. A.4.5**. The plasma distributions demonstrate significant similarities across different numbers of regions. However, with an increase in the number of regions, the 2D profiles become smoother. The results presented in this figure are sufficient for the purposes of the testing of the IPPL-Q2D in the axial-radial coordinates, as they clearly demonstrate that the main expected axial-radial behaviors are indeed represented across the different approximation orders.

Cases $\boldsymbol{i}$, $\boldsymbol{ii}$ and $\boldsymbol{iii}$ result in 250-, 125- and 83-times speedup, respectively, compared to a full-2D simulation. The main observed behaviors from **Fig. A.4.5** are the concentration of the plasma number density (n_e) in the domain's center, as well as the influence of the sheath's potential drop near the radial walls of the discharge channel on the overall distribution of plasma potential (ϕ) within the domain.

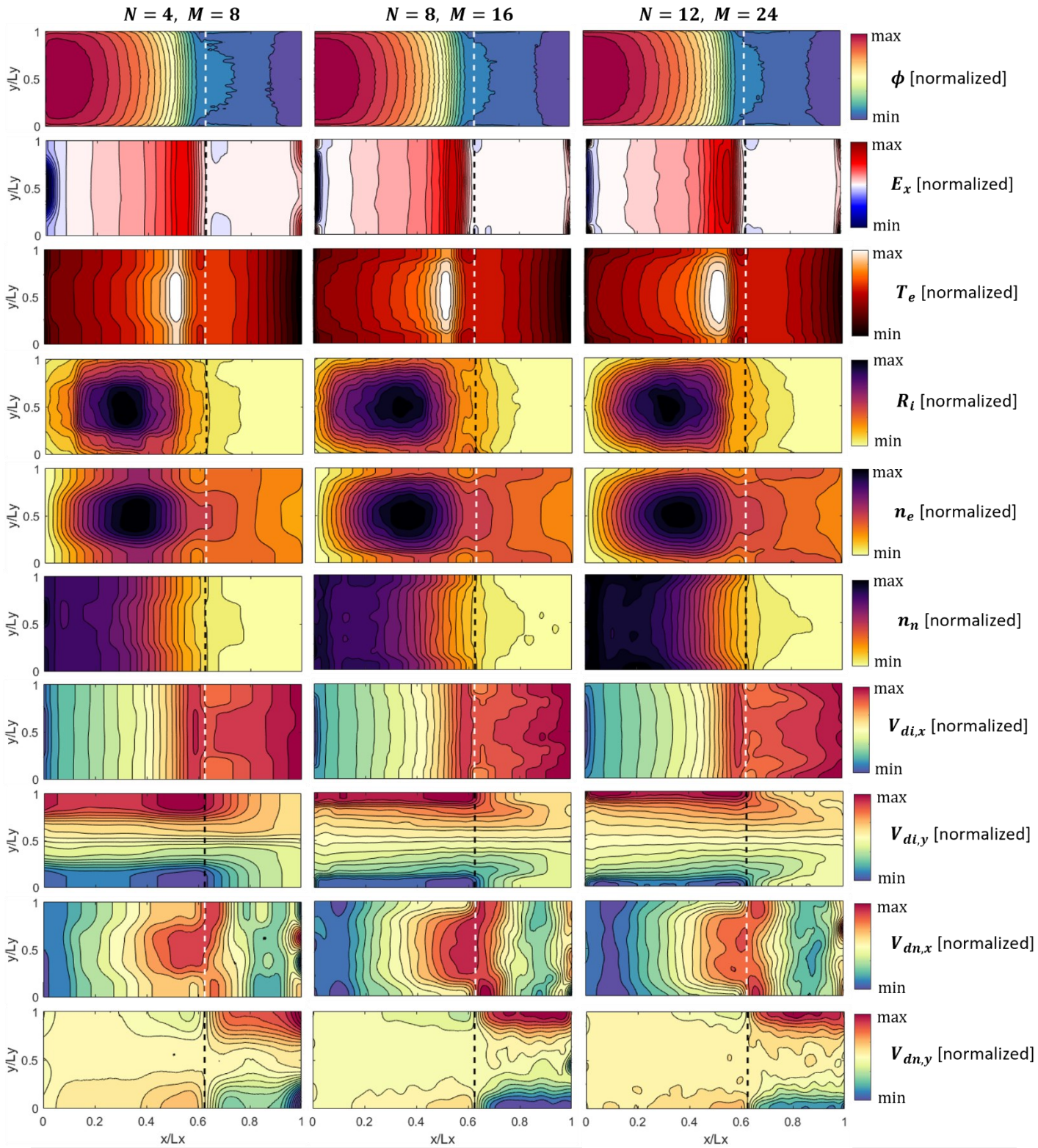


Fig. A.4.5: Normalized 2D snapshots of plasma properties at $t = 20\ \mu$s from the Q2D PIC-DSMC simulations of the axial-radial Hall thruster test case with various numbers of regions along the axial (M) and the radial (N) directions; The rows from top to bottom represent the electric potential (ϕ), the axial electric field (E_x), the electron temperature (T_e), the ionization rate (R_i), the electron number density (n_e), the neutral number density (n_n), the ions' axial and radial drift velocities ($V_{di,x}$ & $V_{di,y}$), and the neutrals' axial and radial drift velocities ($V_{dn,x}$ & $V_{dn,y}$). Dashed black /white lines show the location of the exit plane of the channel.

We also notice the consistency between the location of the maximum axial electric field intensity (E_x) upstream of the channel exit plane, representing the so-called "acceleration zone", with the region of the peak electron temperature (T_e). The radial flow of the neutrals after the exit plane of the channel is evident from their radial velocity ($V_{dn,y}$) plots. The ions have larger radial velocity components ($V_{di,y}$) inside the channel due to their fall through the radial plasma sheaths.

A.4.3. Penning discharge benchmark problem: variability of the results over an extended run

The 100-region Q2D simulation of the Penning discharge benchmark problem [114], whose results for $t = 0 - 500\ \mu s$ duration of the discharge evolution was verified in Section 3.3, is extended here to simulate a longer duration (up to $t = 1100\ \mu s$) of the discharge, and to investigate the variability of the results over various time spans.

Fig. A.4.6 shows the comparison of the time-averaged plasma profiles over three consecutive $300\ \mu s$-long time windows alongside a "long average" over the cumulative span of the three time windows ($200 - 1100\ \mu s$). The maximum variability of the results relative to the "long average" profiles are as follows: ± 1.7 % for the ion number density, ± 1.5 % for the electron temperature and ± 1 % for the electric potential profiles.

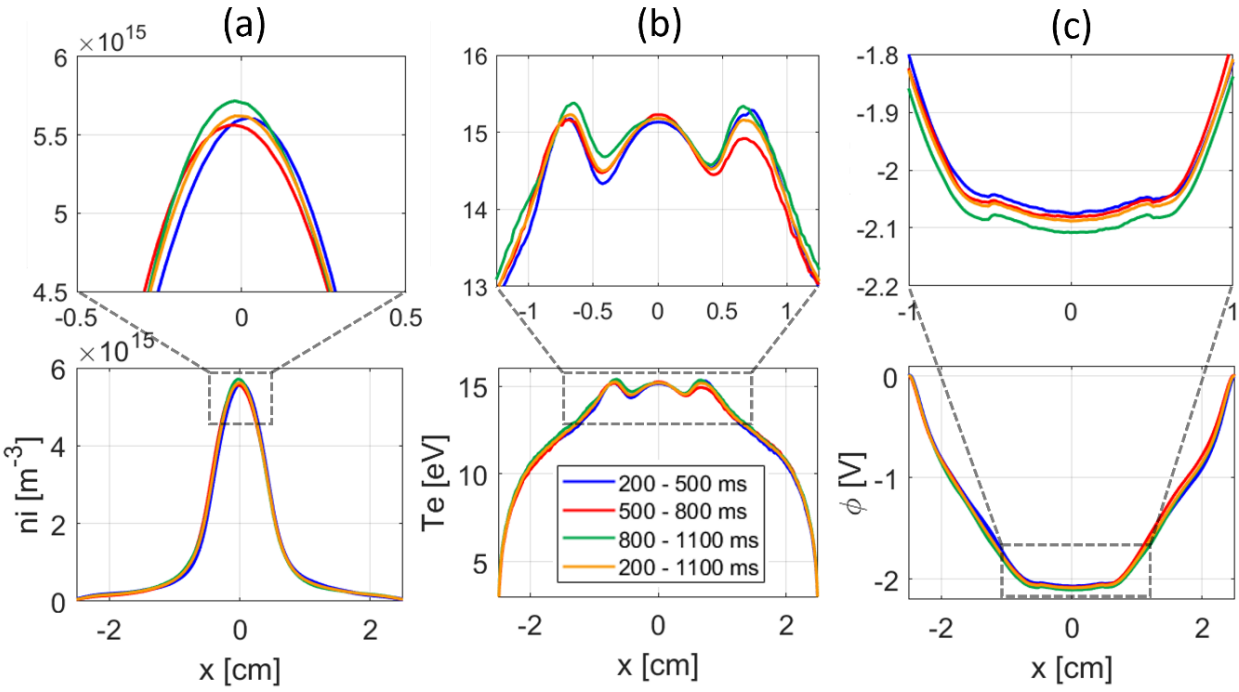


Fig. A.4.6: Comparison of the profiles of plasma properties at the mid-plane of the domain along the y-direction from the 100-region Q2D simulation, averaged over different timeframes, f; (a) ion number density (n_i), (b) electron temperature (T_e), and (c) plasma potential (ϕ). Top row shows the zoom-ins of the respective profiles within the grey box.

The density probe's signal which shows the time evolution of the local ion number density at the midpoint between the domain's center and the wall along the x-axis is presented in **Fig. A.4.7.** The signal exhibits a regular quasi-periodic behavior throughout the entire shown time interval.

Furthermore, **Fig. A.4.8** provides the comparison between the frequency spectra obtained from the temporal FFT of the signal taken separately over the three time windows and over the entire duration of the signal shown in **Fig. A.4.7**. The spoke's frequency, indicated by the highest peak in the FFT spectra, exhibits a minor variation across different time windows, ranging from 41 to $42\ kHz$.

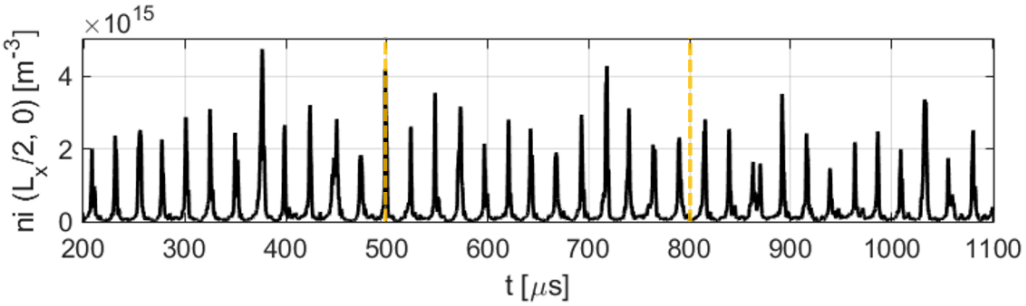


Fig. A.4.7: Time evolution of the local ion number density at the location of the virtual density probe from 100-region Q2D simulation over long simulated time. The dashed yellow lines divide the signal into the three equal time windows.

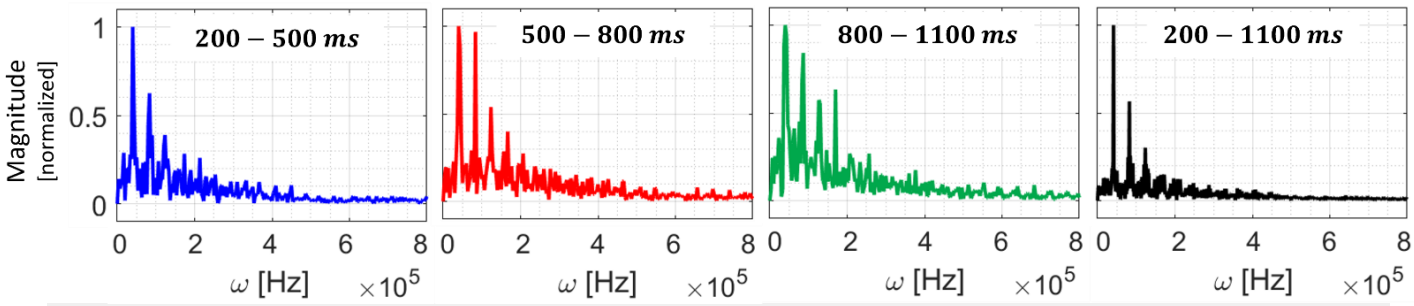


Fig. A.4.8: Temporal FFT spectra of different time periods of the density probe's signal from 100-region Q2D simulation. The highest peak corresponds to the spoke's frequency.

A.4.4. Q2D simulation with non-uniform regions' extent

The Q2D simulations results presented and discussed in Chapter 3, all featured uniform region extents along both directions of the simulation. Here, we verify the functionality of RO-PIC with non-uniform region extent(s) along either one or two dimensions. We then compare the Q2D predictions with non-uniform vs uniform region extents.

We will test the Q2D simulations with non-uniform region extents in the radial-azimuthal $\mathrm{E} \times \mathrm{B}$ discharge and the Penning discharge benchmark problems for which the Q2D simulations using uniform regions had been verified in Sections 3.2 and 3.3, respectively.

A non-uniform distribution of region extents could be useful for the scenarios where the scale macroscopic gradients vary significantly across the domain. In such cases, instead of choosing a fixed length for all regions based on the smallest gradient scale throughout the domain, we can refine the distribution of the regions according to the local gradients. This would avoid unnecessarily large number of regions, thereby further optimizing computations. However, with the variable area of the computational cells, we must ensure that the initial number of macroparticles per cell (N_{ppc}) remains consistent with the minimum necessary in the smallest cell. Note that, here by the cell size, we are referring to the length along the long side, which is equal to the regions' extent along the coarse grid

(refer to **Fig. 2.1**). Along the fine x and y grids, the cell sizes are uniform and compatible with the "smaller than Debye length" criterion.

A) Radial-azimuthal $\mathbf{E} \times \mathbf{B}$ discharge benchmark problem: In this problem, we aim to assess that, by using more refined regions near the walls, where the potential gradient is steep due to the plasma sheath, whether a Q2D simulation with an overall number of regions significantly lower than 100 can provide results close to those from the 100-region Q2D simulation. In this study, the regions along the azimuthal direction are spaced uniformly. Furthermore, it is emphasized that the extent of the regions and the cells' size remain constant in time throughout the simulation duration. **Fig. A.4.9** (a) illustrates the schematic of a 2D domain with a non-uniform domain decomposition along the x-direction and uniform decomposition along y-direction. **Fig. A.4.9** (b) compares the normalized radial extent of the regions ($\frac{L_{x,m}}{L_x}$) in the three cases investigated here against the three reference Q2D simulations with uniform region definition, namely, the 10-, 25-, and 100-region simulation.

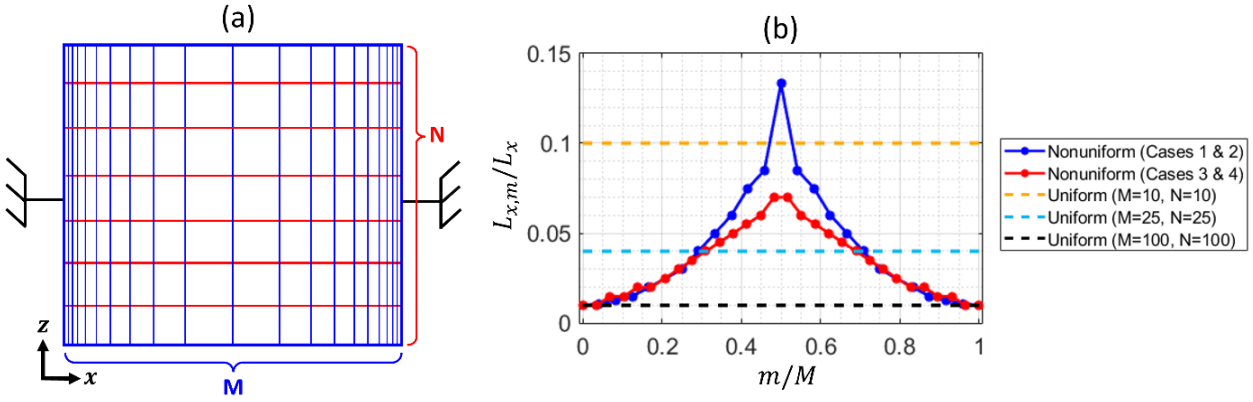


Fig. A.4.9: (a) Illustration of non-uniform regions' extent along the radial direction for radial-azimuthal $\mathrm{E} \times \mathrm{B}$ discharge benchmark problem, (b) comparison of the variation in regions' extent along the radial direction in the different cases investigated. Note that plot (a) shows the coarse grid, and the lines indicate the regions' boundaries. The values on the x-axis of the plot (b) represent regions' number (m) normalized by total number of regions along x-direction (M).

Cases 1 and 2 have a total number-of-region count along the radial direction (M) of 25, whereas, in cases 3 and 4, M is equal to 30. Cases 1 and 2 differ only in terms of the number of initial numbers of macroparticles per cell. The difference in cases 3 and 4 is in their number of regions along the azimuthal direction (N) which is 10 for case 3 and 100 for case 4. It is observed from **Fig. A.4.9** (b) that, in all cases, the extent of the smallest radial region near the walls is equivalent to that of the 100-region simulation. Moving toward the center of the domain along the radial direction, cases 1 and 2 have a region in the middle of the domain whose radial length is larger than that in the 10-region simulation. In cases 3 and 4, several regions in the middle have radial lengths larger than that in the 25-region simulation but smaller than the 10-region. This information is summarized in **Table A.4.1.**

The simulation setup and conditions are exactly the same as those described in Section 3.2.

	M (nonuniform)	N (uniform)	N_{PPC} (In smallest cell)	N_{PPC} (In largest cell)
Case 1	25	10	100	1330
Case 2	25	10	25	332
Case 3	30	10	33	231
Case 4	30	100	100	700

Table A.4.1: Summary of the numerical parameters used for the Q2D simulations with non-uniform radial region extents.

The results from the non-uniform Q2D simulations in terms of the time-averaged plasma profiles are compared in **Fig. A.4.10** against the 10-region, 25-region, and 100-region Q2D simulations with uniform radial domain decomposition. It is observed that, overall, by refining the regions' extent near the walls, the ion number density (n_i) and the radial electron temperature (T_{ex}) distributions closely follow the 100-region profiles. In particular, case 3 with only 30 radial regions can almost exactly reproduce the 100-region results in terms of n_i and T_{ex} profiles.

Nevertheless, the T_e and T_{ez} profiles are seen to only approach the 100-region results in case 4 where the number of azimuthal regions is increased to 100. Also, the T_e and T_{ez} profiles for cases 1 to 3 (with 10 azimuthal regions) are similar to the T_{ez} profile from the 10-region Q2D simulation. Thus, it seems that the accuracy in the prediction of the T_{ez} profile is controlled through the regions' resolution along the azimuthal direction.

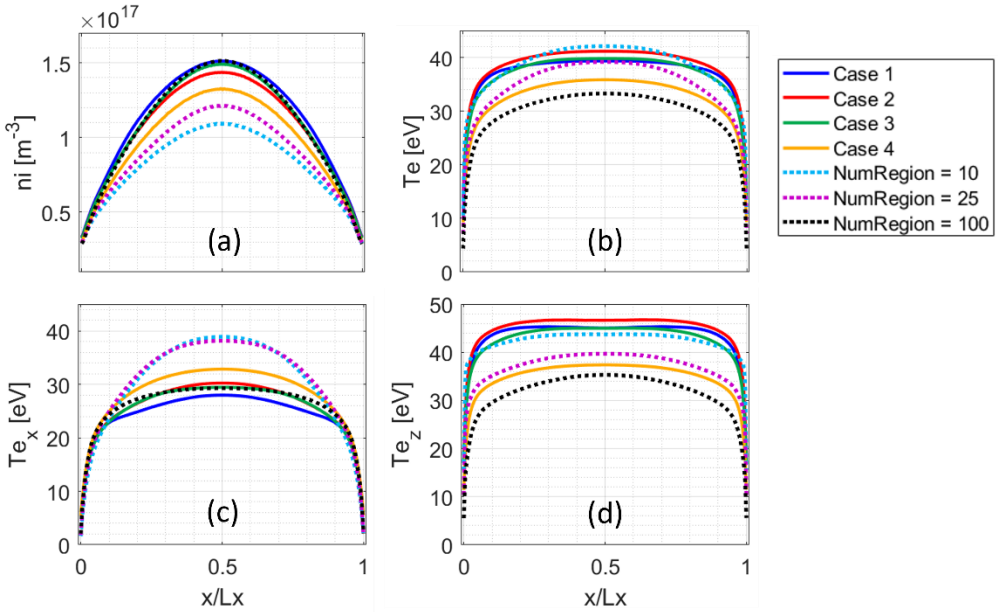


Fig. A.4.10: Comparison of time-averaged (over 25-30 μs) radial profiles of (a) ion number density (n_i), (b) electron temperature (T_e), and (c) & (d) radial and azimuthal electron temperatures (Te_x & Te_z) from Q2D simulations with the non-uniform and uniform regions' extents.

Having a fine regions' resolution along the azimuth in case 4 yields improved predictions of T_e and T_{ez}, whereas the n_i and T_{ex} profiles are noticed to deviate to some extent from the 100-region profiles. A plausible reason for this observation for such behavior is the disparate resolution of the plasma potential gradient along the radial and the azimuthal coordinates.

Moreover, comparing the profiles of the plasma properties from cases 1 and 2 in **Fig. A.4.10**, it is noticed that the distributions are almost similar. Noting that the difference between these two cases is only their initial number of macroparticles, we conclude that a lower N_{ppc} in the smallest regions near the walls does not have a noticeable influence on the results.

Finally, **Fig. A.4.11** shows the 2D snapshots of the plasma properties for cases 2 to 4 as well as the uniform 25-region simulation and the full-2D (as reference) at a time instance corresponding to the local maximum of the spatially averaged T_{ex}. Refinement of the regions near the walls is seen to have, overall, a minor effect on the 2D snapshots of plasma properties and waves' characteristics. Nevertheless, it is interesting to note that, in case 4, the small-scale features and patterns visible in the snapshots of the full-2D simulation are more closely captured.

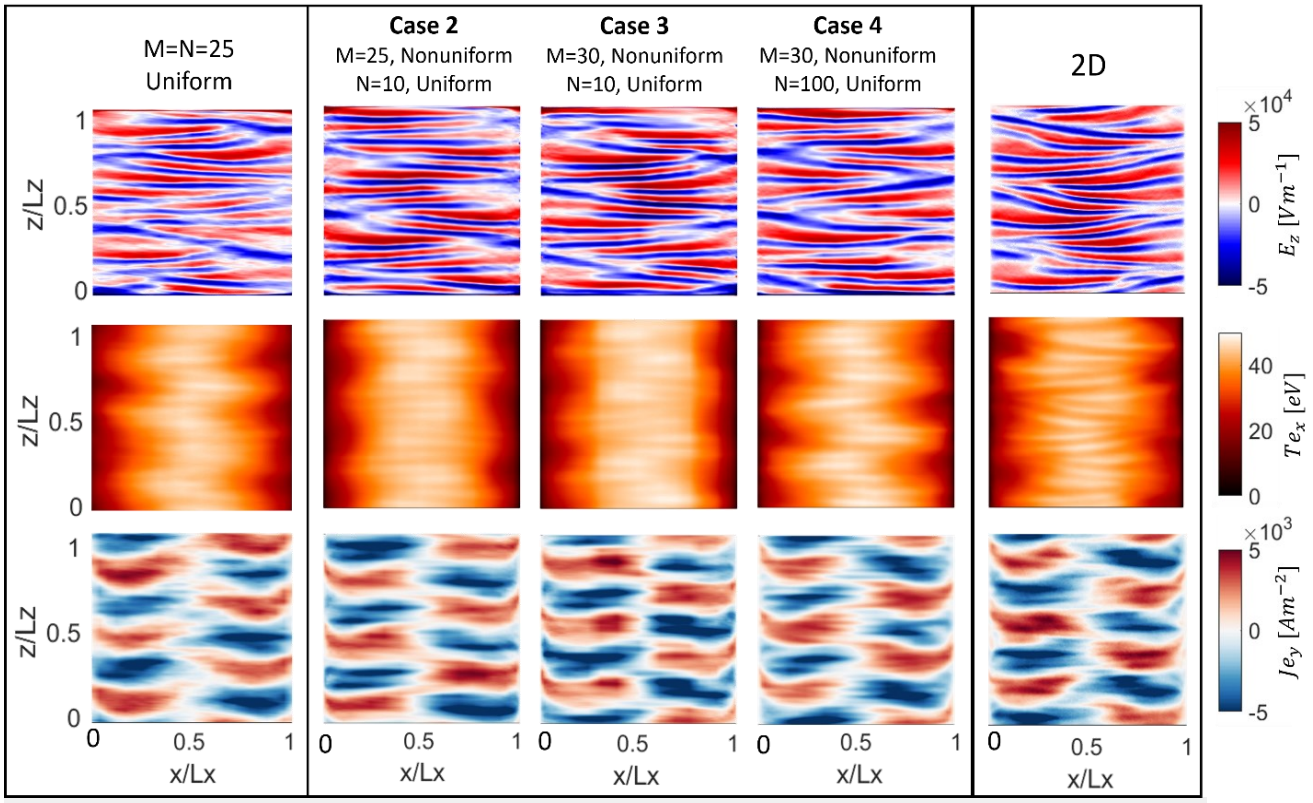


Fig. A.4.11: 2D snapshots of the plasma properties at the time of local maximum of the radial electron temperature from the non-uniform Q2D simulations (cases 1 to 3) in comparison with those from the uniform 25-region Q2D simulation and the full-2D simulations. The rows, from top to bottom, represent the azimuthal electric field (E_z), the radial electron temperature (T_{ex}), and the axial electron current density (J_{ey}).

B) **Penning discharge benchmark problem:** In this case, the regions' extents are nonuniform along both simulation directions. We use 31 regions along each direction. As seen in **Fig. 3.24**, the scale of the processes becomes smaller towards the center of the domain. Accordingly, we chose the regions such that their lengths along both directions are coarser near the boundaries of the domain and become increasingly refined towards the domain's center. The distribution of the regions' extents across the domain is illustrated in **Fig. A.4.12** (a) with their quantitative values being shown in **Fig. A.4.12** (b). The two largest regions near domain's boundaries have extents larger than the regions in the15-region Q2D simulation, while the smallest region in the middle is as small as the regions in 100-region Q2D with uniform regions.

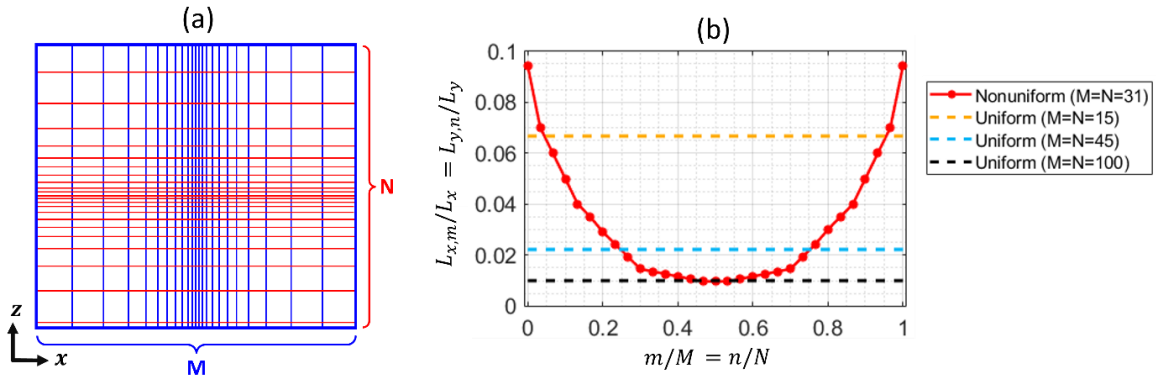


Fig. A.4.12: (a) Illustration of non-uniform region extents along the x and y directions for Penning discharge benchmark problem, (b) the variation in region extents along both simulation directions. Note that plot (a) shows the coarse grid, and the lines indicate the regions' boundaries. The values on the x-axis of the plot (b) represent regions' number (m & n) normalized by total number of regions along respective direction (M & N).

The simulation setup and conditions are kept the same as those introduced in Section 3.3.

The resulting time-averaged profiles from the Q2D simulation with 31 non-uniformly distributed regions are compared against the Q2D simulations with uniforms regions in **Fig. A.4.13**.

It is noticed that the ion number density and the electric potential profiles in the central area of the domain almost match the respective profiles from 100-region Q2D and the full-2D simulations. The electric potential profile exhibits slight deviations from the 2D simulation's predictions, moving from the center towards the walls due to the progressively coarser regions. The accuracy of the predicted electron temperature also diminishes away from the center. However, in the central regions, the electron temperature closely aligns with the predictions of the 45-region simulation, while the deviation from the 2D values becomes more pronounced farther away from the center. Note that, besides the improvement of the plasma properties in the central regions, the plasma profiles near the walls show significant improvement over the results from the 15-regions simulation too, despite the larger size of regions near the walls compared to those in the 15-region simulation.

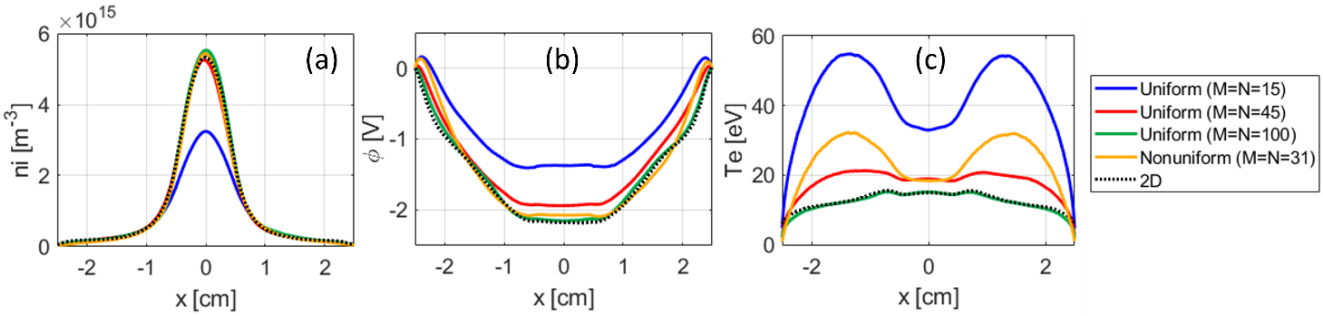


Fig. A.4.13: Comparison of time-averaged (over $200 - 500\ \mu s$) profiles of (a) ion number density (n_i), (b) electron temperature (T_e), and (c) plasma potential (ϕ) from Q2D simulations with non-uniform and uniform region extents.

These results are interesting as they demonstrate that by adjusting the sizes of the regions according to the physics of the problem, we can attain maximum speed up and accuracy beyond what is achieved with the uniformly distributed regions. Indeed, local refinement of the regions can improve the prediction of the properties not only in those localities but also in the whole simulation domain.

A.5 Supplementary analyses for parametric variability studies along the radial-azimuthal coordinate

A.5.1. Comparison of the instabilities' spectra obtained from Q2D and 2D simulations for $E = 5E_0$ and $B = 1.5B_0$ cases

Fig. A.5.1 provides a comparison between the frequency and the azimuthal wavelength spectra of the instabilities as obtained from the Q2D and full-2D simulations of the cases with extreme electric and magnetic field intensities, namely, $E = 5E_0$ and $B = 1.5B_0$. The spectra are obtained from average spatial and temporal FFTs of the azimuthal electric field fluctuations. The results show that the Q2D predictions are in great agreement with the 2D results, providing further confidence in the reliability of the Q2D simulations and the insights derived from the simulations presented in Section 4.2.

Moreover, for the $1.5B_0$ case, the results additionally serve to verify the prediction of the Q2D concerning the azimuthal wavenumber of the MTSI in this case. It is recalled that, from **Fig. 4.9** (bottom panel), there was some discrepancy between the simulated MTSI's azimuthal wavenumber and its theoretical value from Eq. 1.11. In this regard, **Fig. A.5.1** (bottom row), shows that the peaks associated with the MTSI mode in the spatial FFT spectra of the Q2D and the 2D simulations are coincident (at $\frac{k_z}{k_0} = 0.188$). However, in both simulations, the FFT spectrum around this peak is broadened over a finite wavenumber interval of $\frac{k_z}{k_0} = 0.125 - 0.188$. As a result, we can expect the MTSI's azimuthal wavenumber to be somewhere within this interval.

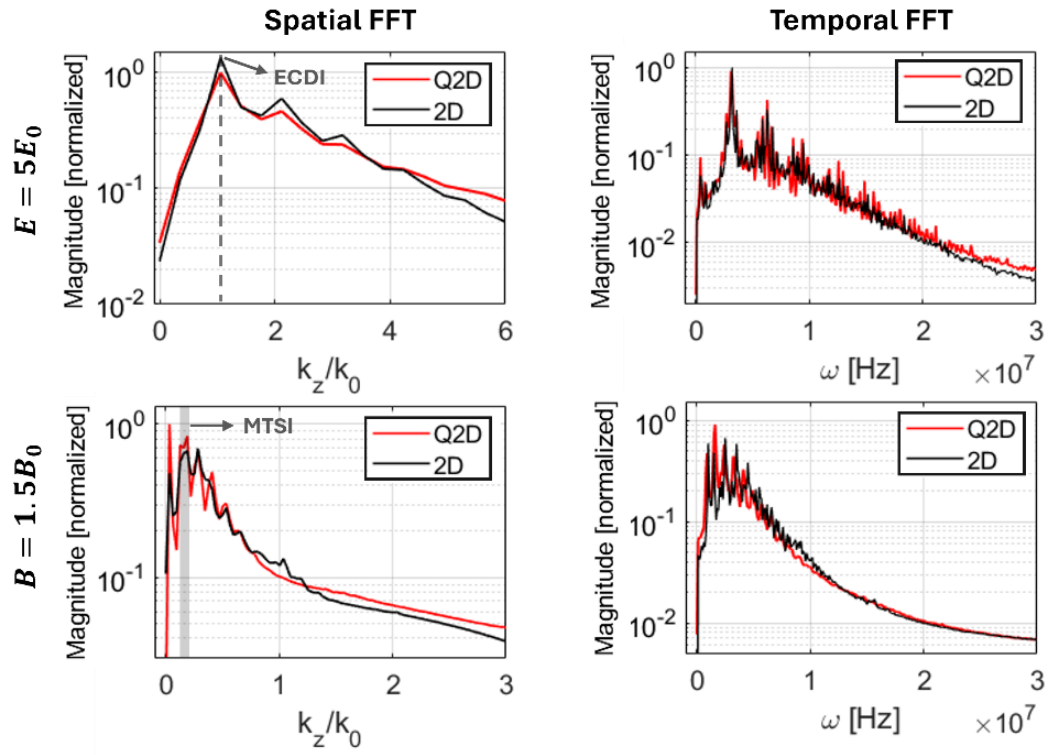


Fig. A.5.1: Comparison of the averaged spatial and temporal FFT spectra of the azimuthal electric field fluctuations for the $E_y = 5E_0$ and $B_x = 1.5B_0$ cases with xenon propellant as obtained from the Q2D and full-2D simulations. The averaging is consistent with the averaging performed for the FFT analyses in Section 4.2.2.

A.5.2. Impact of the domain's extent on the instabilities' spectra for the $E = 5E_0$ case

To evaluate the impact(s) of the domain's size on the instabilities established in the simulations, we carried Q2D simulations of the case with the extreme electric field of $E_y = 5E_0$ with various lengths of the domain. In this regard, the size of the domain was once doubled along the radial direction, once along the azimuth, and once along both directions. The resulting azimuthal wavenumber (k_z) and the frequency (ω) spectra of the azimuthal fluctuations are compared in **Fig. A.5.2**.

From the k_z plot, it is evident that increasing the domain's length along the azimuthal direction does not remarkably change the relative spectral amplitudes of the instabilities, and the ECDI remains the dominant mode. However, doubling the radial length of the domain (or both the radial and azimuthal lengths) leads to the formation of the long-λ mode (with $\frac{k_z}{k_0} \approx 0.35$) with a larger amplitude compared to the ECDI. In these cases, an inverse energy cascade seems to have transferred energy toward larger structures and, hence, resulted in the growth of the long-λ mode. The azimuthal wavelength of this mode is $1.28\ cm$, and it is the same mode that was observed to be dominant in the case of $E = 0.5E_0$. The long-λ mode has been also observed from the spatial FFT spectra in Section 4.2.2 to be present in the baseline condition as well ($E = 1E_0$), though with a small amplitude.

The fact that the MTSI is not observed from the present simulations with various domain's lengths ensures that the mitigation of this mode for the $5E_0$ case (as an extreme studied value of the E-field) is not an artifact of the limited domain's size. Rather, the MTSI's mitigation is the aggregate consequence of the conditions of the plasma when subject to large axial electric fields.

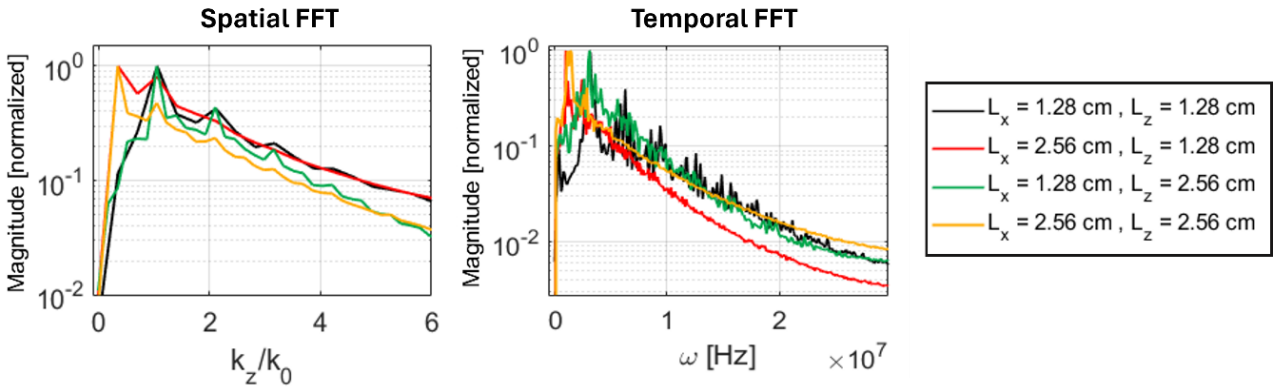


Fig. A.5.2: Comparison of the averaged spatial and temporal FFT spectra of the azimuthal electric field fluctuations for the $E = 5E_0$ case with the xenon propellant as obtained from the Q2D simulations with different lengths of the domain along the radial and azimuthal directions.

This analysis further evidences the validity of the arguments made in Section 4.2 regarding the relative dominance of the instabilities under different E-field conditions. In this regard, we underline that, whereas a low sensitivity of the results to the adopted azimuthal extent of the simulations is a crucial point to demonstrate, a larger dependence of the instabilities' spectra to the simulations' radial extent does not constitute a point of concern. This is because it is along the azimuthal direction that only a limited portion of the plasma discharge is simulated, and periodic behavior is assumed. However, the radial dimension of a simulation represents an actual (physical) characteristic length of the plasma

system under study. In this sense, altering the radial length of the simulation amounts to changing the plasma geometry, in which case some degree of change in the underlying plasma phenomena could be consequently expected.

A.5.3. Comparison of instabilities' numerical dispersion map with the IAI's dispersion relation

Comparing the dispersion maps of the azimuthal instabilities predicted by the simulations with the theoretical dispersion relation of the Ion Acoustic Instability (IAI), can provide insights into whether the ECDI in the simulations has transitioned to the IAI waves. These comparisons are provided in **Fig. A.5.3** and **Fig. A.5.4** for various simulation cases discussed in Chapter 4. The numerical dispersion plots are obtained from the 2D spatiotemporal FFT of the azimuthal electric field signal at the mid-radial location of the domain over the duration of $t = 20 - 30\ \mu s$. The superimposed yellow curves are the IAI's theoretical dispersion relation given by Eq. 1.4, calculated using the time-averaged (within $20 - 30\ \mu s$ window) plasma properties at the mid-radial location.

From these plots we observe that in some cases such as the baseline configuration ($E = E_0,\ B = B_0,\ S = S_0$), the projection of the linear part of the IAI's dispersion relation is fitted well on the dispersion plot of the wave modes. Whereas, in other cases, clear deviation from the linear and nonlinear IAI's dispersion relation is apparent. Additionally, most cases exhibit some extent of resonance broadening around the mode(s) with the largest magnitude, which is a characteristic feature of the transition of the ECDI modes to the IAI.

Besides, in some cases, particularly, $B = 0.5B_0$ in **Fig. A.5.3** and, $S = 3S_0$ and $S = 6S_0$ in **Fig. A.5.4** significantly turbulent nature of the fluctuations is evident from their dispersed 2D dispersion plots. Moreover, the concentration of the dispersion of the waves near the origin in cases of $B = 0.25B_0$ in **Fig. A.5.3** and $config\ 2$ in **Fig. A.5.4** represent the formation of the larger structures corresponding to the long-λ mode with low frequency.

For the case of $E = 0.5E_0,\ B = 1.25B_0$ in **Fig. A.5.3** and $\epsilon^* = 5$ and $15\ eV$ in **Fig. A.5.4**, the dispersion plots are characterized by a broadband spectrum around the frequency and wavenumber of the ECDI with a few distinct modes aligned at an angle with respect to the linear IAI's dispersion. We can also notice the presence of numerous harmonic modes in the case of $E = 5E_0$.

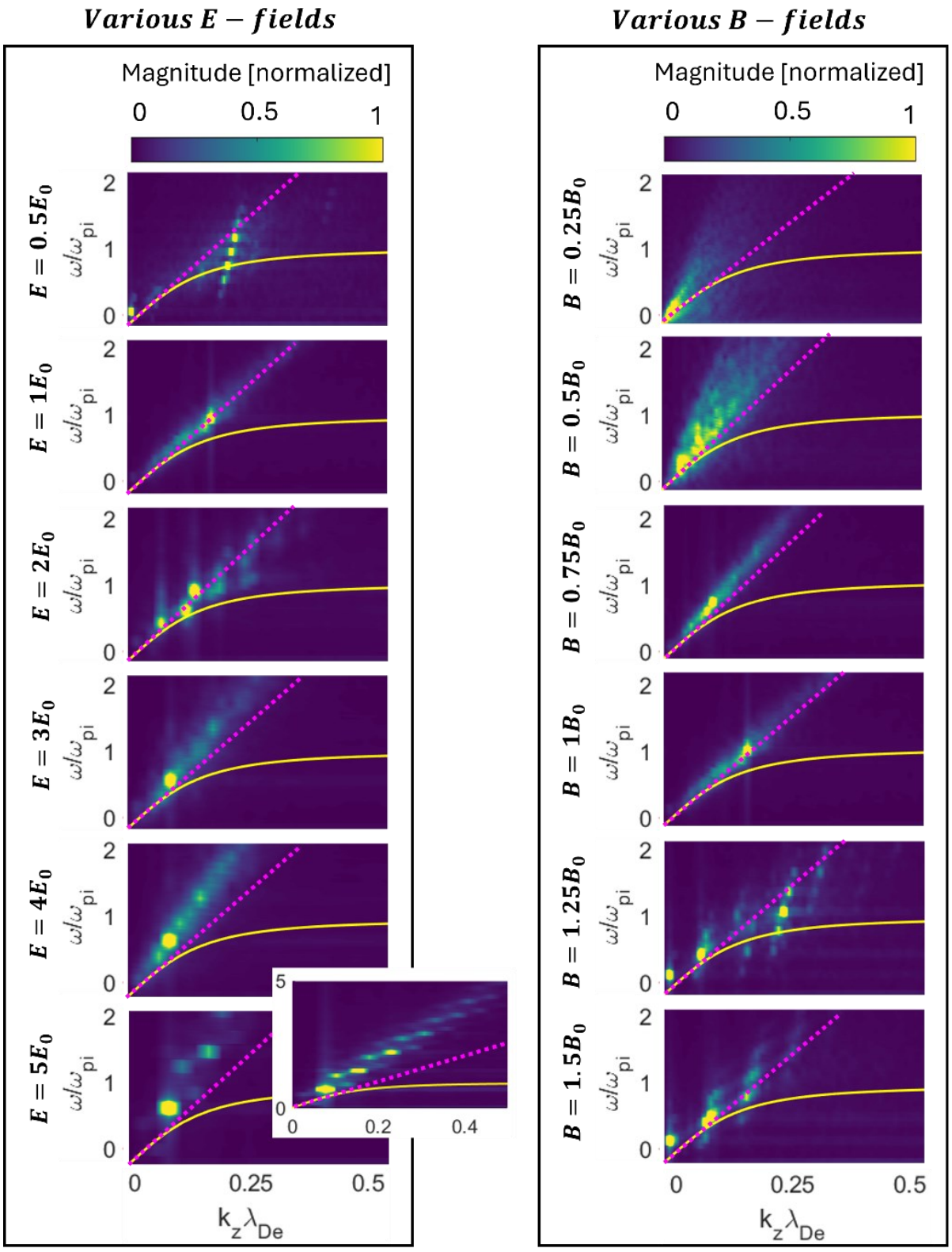


Fig. A.5.3: Comparisons of the numerical dispersion maps of the azimuthal electric field fluctuations and theoretical dispersion relation of IAI given by Eq. 1.4 (yellow curves), for xenon propellant with various E_y (left column) and various B_x (right column). The magenta lines represent the linear dispersion relation of the ion sound waves (Eq. 1.6).

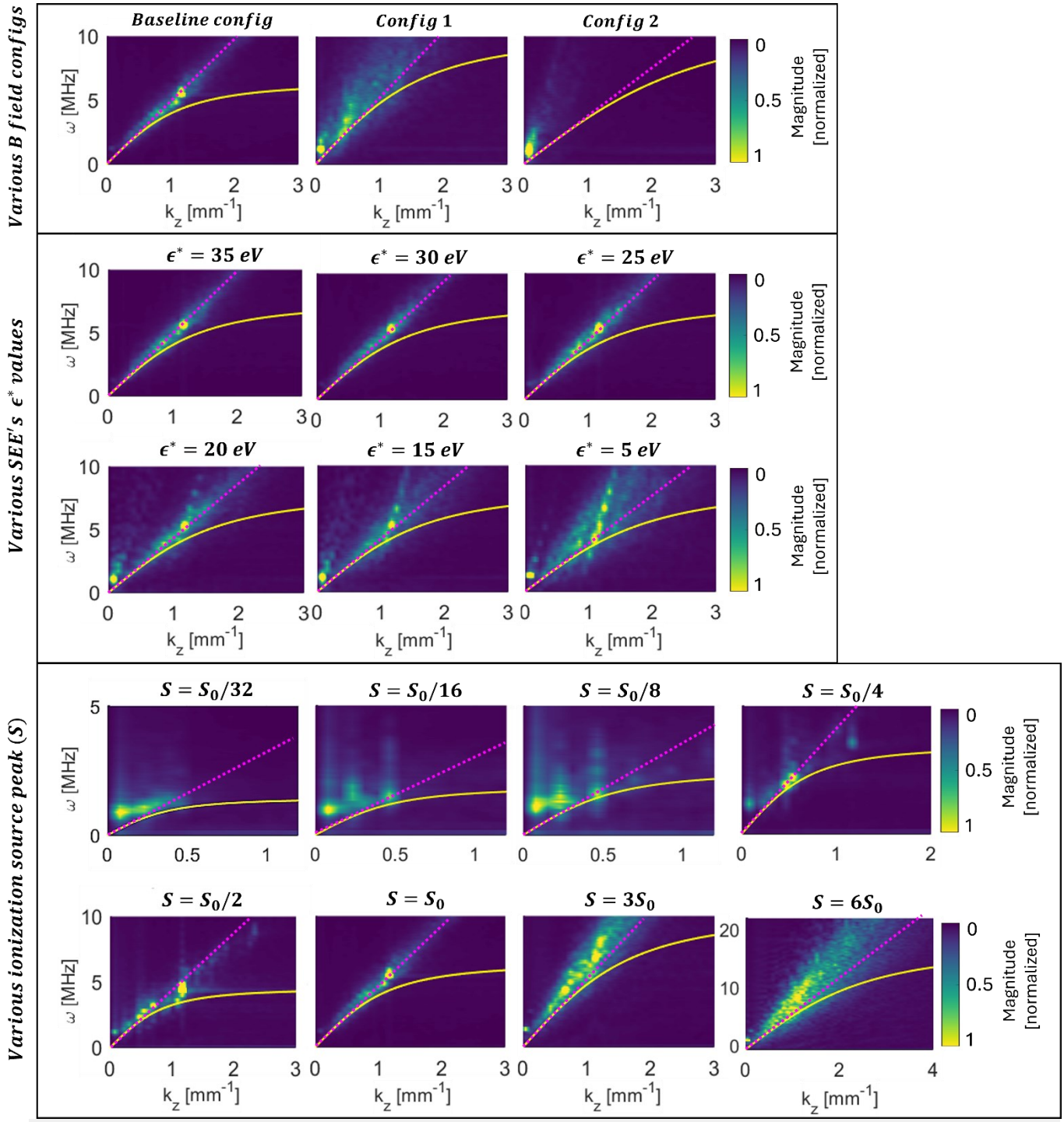


Fig. A.5.4: Comparisons of the numerical dispersion maps of the azimuthal electric field fluctuations and theoretical dispersion relation of IAI given by Eq. 1.4 (yellow curves), for xenon propellant with various magnetic field configurations (top panel), various SEE's ϵ^* values (middle panel), and various ionization source peak intensities (S). The magenta lines represent the linear dispersion relation of the ion sound waves (Eq. 1.6).

A.5.4. Spectral cascade of the azimuthal instabilities

Fig. A.5.5 and **Fig. A.5.6** illustrate the temporal evolution of the azimuthal wavenumber (k_z) spectrum of the instabilities across various simulation cases discussed in Chapter 4. The k_z spectra are obtained from averaged (over all radial locations) spatial FFT of the azimuthal electric field signal at each time. These plots demonstrate the energy transfer between various instability modes due to their

nonlinear interaction. These interactions lead to the cyclic behavior of the discharge characterized by growth and damping of the main instability modes within the system.

Most notably, the growth and damping of the MTSI is seen in the presence of large negative magnetic curvatures ($\theta = -60$ and -45 degrees in **Fig. A.5.5** and config.2 in **Fig. A.5.6**). In these cases, the damping of the MTSI modes is noticed to be associated with an inverse energy cascade toward longer wavelengths that leads to the formation of a long-λ mode. Furthermore, in cases such as $E = 0.5E_0$, $B = 1.25B_0$ and $1.5B_0$, $\theta = -30$ and -15 degrees, $\epsilon^* = 5$ and $15\ eV$, and $S = 3S_0$ and $6S_0$, the long-λ instability establishes in the first few microseconds of the simulation and persists throughout the discharge with relatively constant amplitudes. In particular, the energy cascade from the MTSI harmonics towards the long-λ mode is clearly visible in cases of $\theta = -30$ degrees and $E = 0.5E_0$.

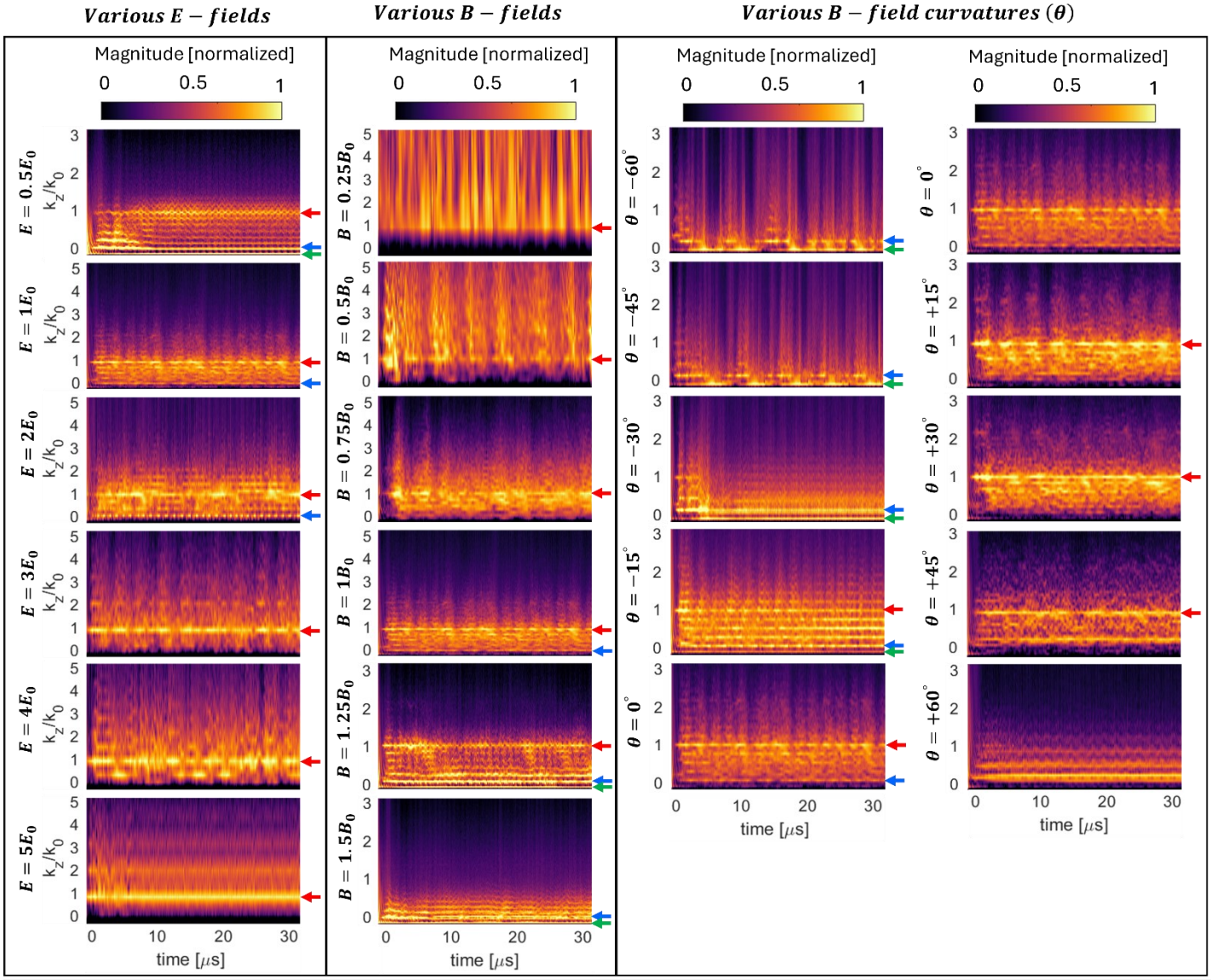


Fig. A.5.5: Time evolution of the k_z spectrum of the azimuthal fluctuation for xenon propellant with various E_y (first column), various B_x (second column), and various θ (third and fourth columns). k_z spectra are normalized by k_0 which is the ECDI's fundamental wavenumber ($k_0 = \frac{\omega_{ce}}{V_{de}}$). The red, blue and greens arrows indicate the wavenumbers associated with the ECDI, the MTSI and the long-λ mode, repectively. Note the y-axis in some plots has different scales.

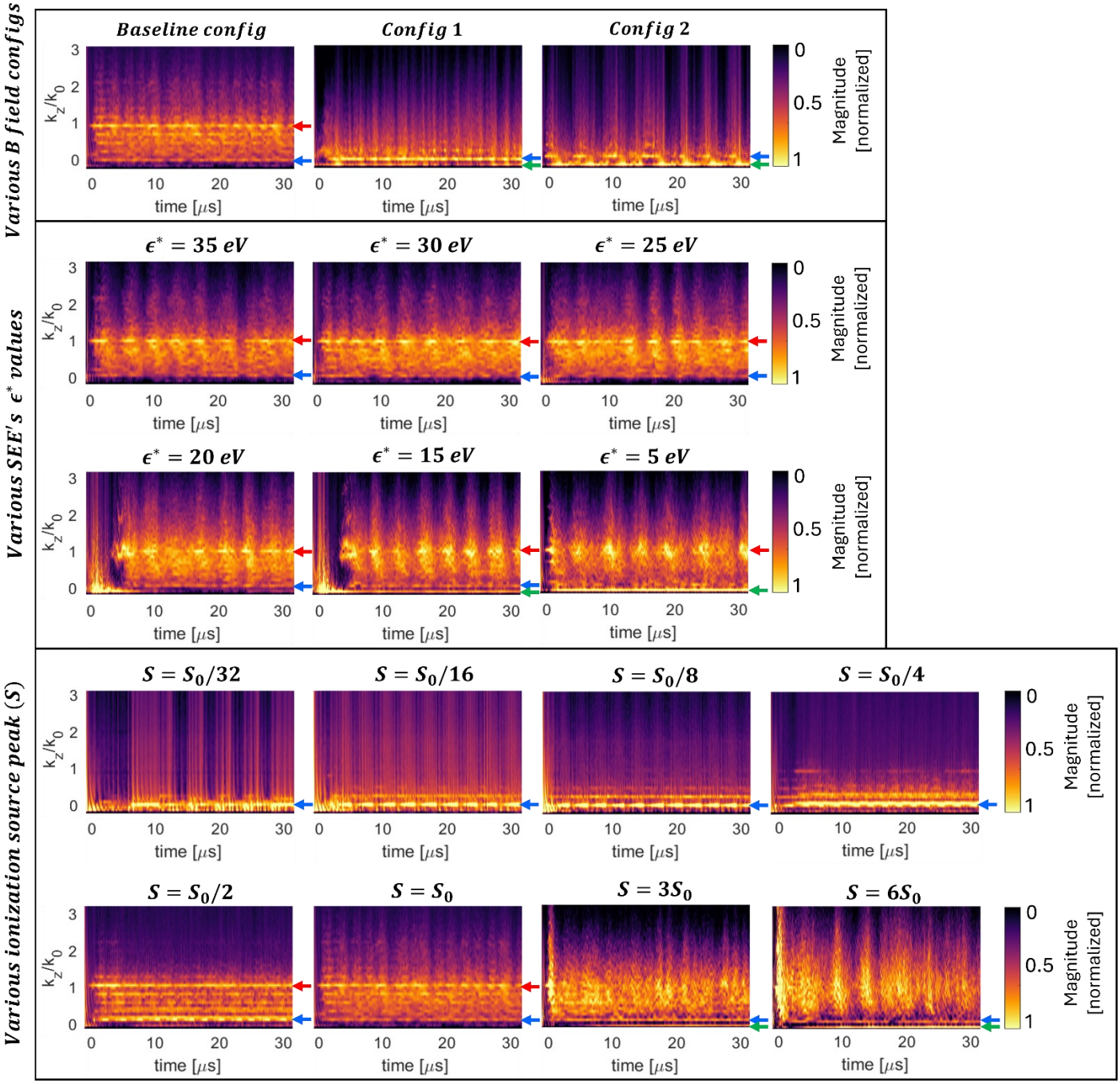


Fig. A.5.6: Time evolution of the k_z spectrum of the azimuthal fluctuation for xenon propellant with various magnetic field configurations (top panel), various SEE's ϵ^* values (middle panel), and various ionization source peak intensities (S). k_z spectra are normalized by k_0 which is the ECDI's fundamental wavenumber ($k_0 = \frac{\omega_{ce}}{V_{d_e}}$). The red, blue and greens arrows indicate the wavenumbers associated with the ECDI, the MTSI and the long-λ mode, repectively.

A.5.5. Correlation between instabilities and electrons' cross-field mobility

Fig. A.5.7 presents the temporal evolution of the amplitude of the dominant azimuthal instability modes (discussed in Section 4.2.2) in the simulations with various E_y and B_x. The instability's amplitude at each time instant is determined by averaging the spatial FFT spectra of the azimuthal electric field fluctuations across all radial positions at each time instant. The resulting instantaneous amplitude

corresponding to the wavenumber of each specific instability is then plotted over time. The plots also include the time evolution of electrons' cross-field (axial) mobility.

It is underlined that, from **Fig. A.5.7**, we can infer the instability that has the dominant contribution to the electrons' mobility. This can be done by observing the correlation between the electrons' mobility oscillations and the oscillations in the instabilities' amplitude.

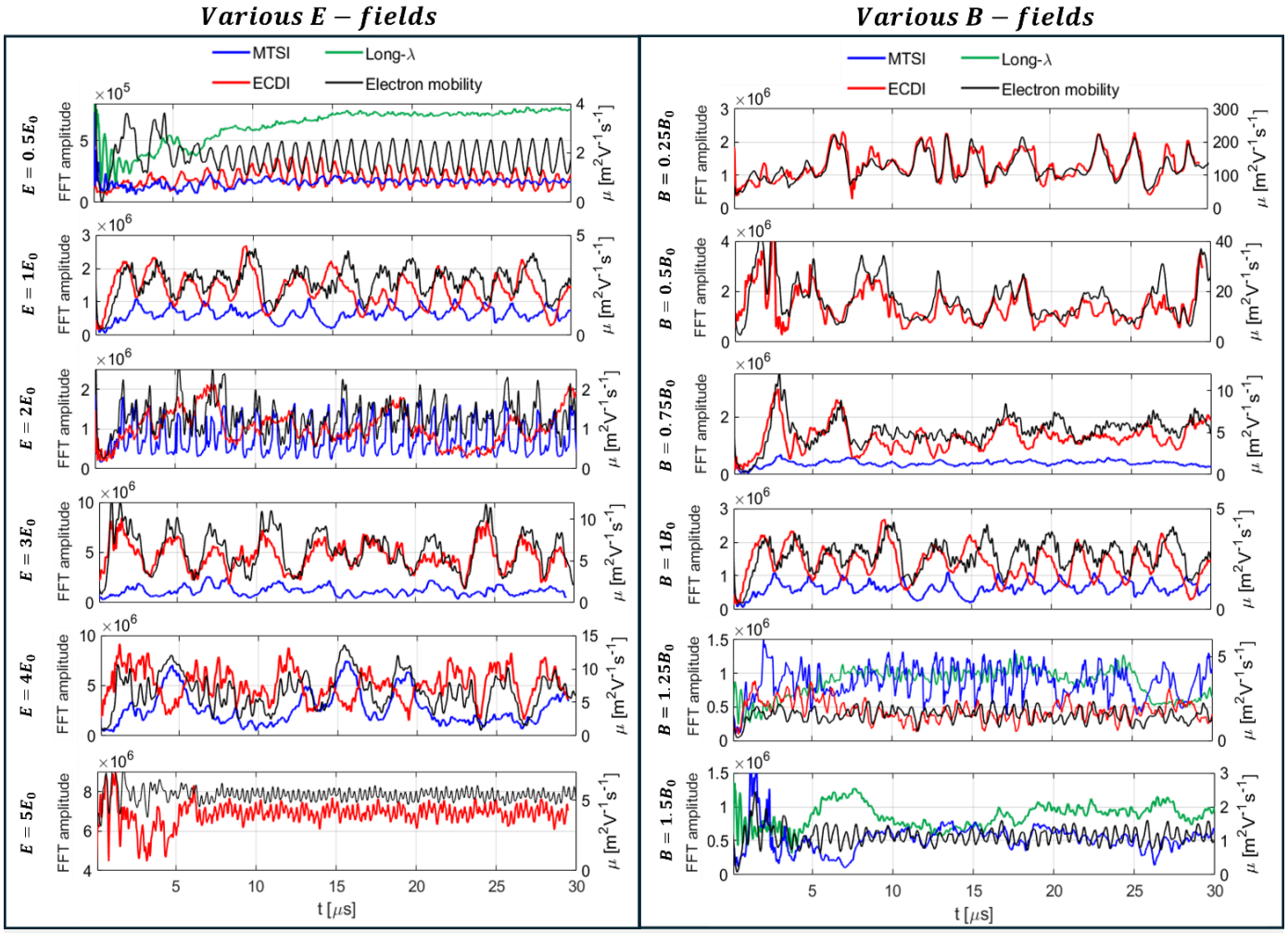


Fig. A.5.7: Time evolution of the amplitude of the dominant azimuthal modes (left axes) and the spatially averaged electrons' mobility (right axes) from the simulations with various E_y (left column) and various B_x (right column) for xenon propellant.

A.5.6. Comparison between the results from the 1D and the Q2D simulations in the presence of magnetic field's curvature

In this section we aim to assess the differences between a 1D radial and a Q2D radial-azimuthal study in terms of the observed effects of the magnetic field curvature. The B-field curvature effects on plasma dynamics have been studied in the literature in a 1D radial Hall thruster case [132]. It is, therefore, highly important to investigate the significance of the roles likely to be played by the *azimuthal* physics and the changes that resolving azimuthal processes can induce in the reported insights from 1D studies.

The 1D simulations are carried out in the radial direction of the thruster's domain using IPPL-1D code for xenon propellant with various curvature levels of the magnetic field lines. The same setup and conditions as those of Q2D simulations described in Section 4.3, are adopted for the 1D simulations except for the exclusion of the azimuthal direction and all the associated conditions. Maintaining similarity between the 1D and the 2D setups is necessary to enable a direct comparison between the results from the Q2D and the 1D simulations. In addition, such comparison allows distinguishing the processes driven primarily by the azimuthal dynamics from the processes along the radial direction associated with the plasma-wall interactions and magnetic field curvature.

The comparison of the 1D and Q2D simulation results are presented in **Fig. A.5.8** and **Fig. A.5.9** in terms of spatiotemporal average of the plasma parameters and the radial profiles of plasma properties, respectively.

In particular, in the plots of the normalized ion density ($n_i/n_{i,mean}$) in **Fig. A.5.8** (a) and **Fig. A.5.9** (a), it is observed that the impact of the negative curvature of the B-field is more pronounced in the 1D simulations compared to the Q2D simulations. In the 1D simulations, the density becomes progressively more confined toward the center as the angle θ changes from 0 to -60 degrees. However, the concentration effect of the negative curvature of the B-field is mitigated in Q2D simulations due to presence of the azimuthal instabilities and their consequences on plasma properties, which will be discussed shortly. Contrarily, for the positive curvature values, the $n_i/n_{i,mean}$ values are in good agreement with the Q2D simulations.

Referring to the radial electron temperature (T_{ex}) in **Fig. A.5.8** (c) and **Fig. A.5.9** (c), it is noticed that T_{ex} is much higher in the Q2D simulations compared to the 1D simulations. This is due to the electrons' heating effect of the instabilities captured in the Q2D simulations. In contrast to the Q2D simulations, in the 1D simulations, T_{ex} exhibits a monotonic increase as the θ varies from zero toward more negative values. The positive curvatures of the B-field leads to more uniform profiles across the radial extent both in the 1D and the Q2D simulations. The dependency of T_{ex} on the field's curvature is also minor across the positive values of θ.

Comparing the magnitudes of the electrons' mobility from the Q2D and the 1D simulations **Fig. A.5.8** (d) and **Fig. A.5.9** (d), it is evident that, across all curvature cases, the μ is consistently higher in the 1D simulations. The disparity in the values of μ is particularly significant in the cases of positive curvature. This is a noteworthy observation considering that the 1D simulations do not resolve the azimuthal instabilities and their induced electrons' transport. Even though the Q2D simulations capture the additional contribution of the instabilities, the resulting electrons' mobility in the Q2D simulations is lower compared to that observed from the 1D simulations. Moreover, in the 1D simulations, the electrons' mobility shows a very small variation along the radial extent of the domain and across various curvature levels. In the negative-curvature cases, the mobility exhibits a slight increase near the walls, whereas, in the positive-curvature cases, it becomes slightly more pronounced toward the center.

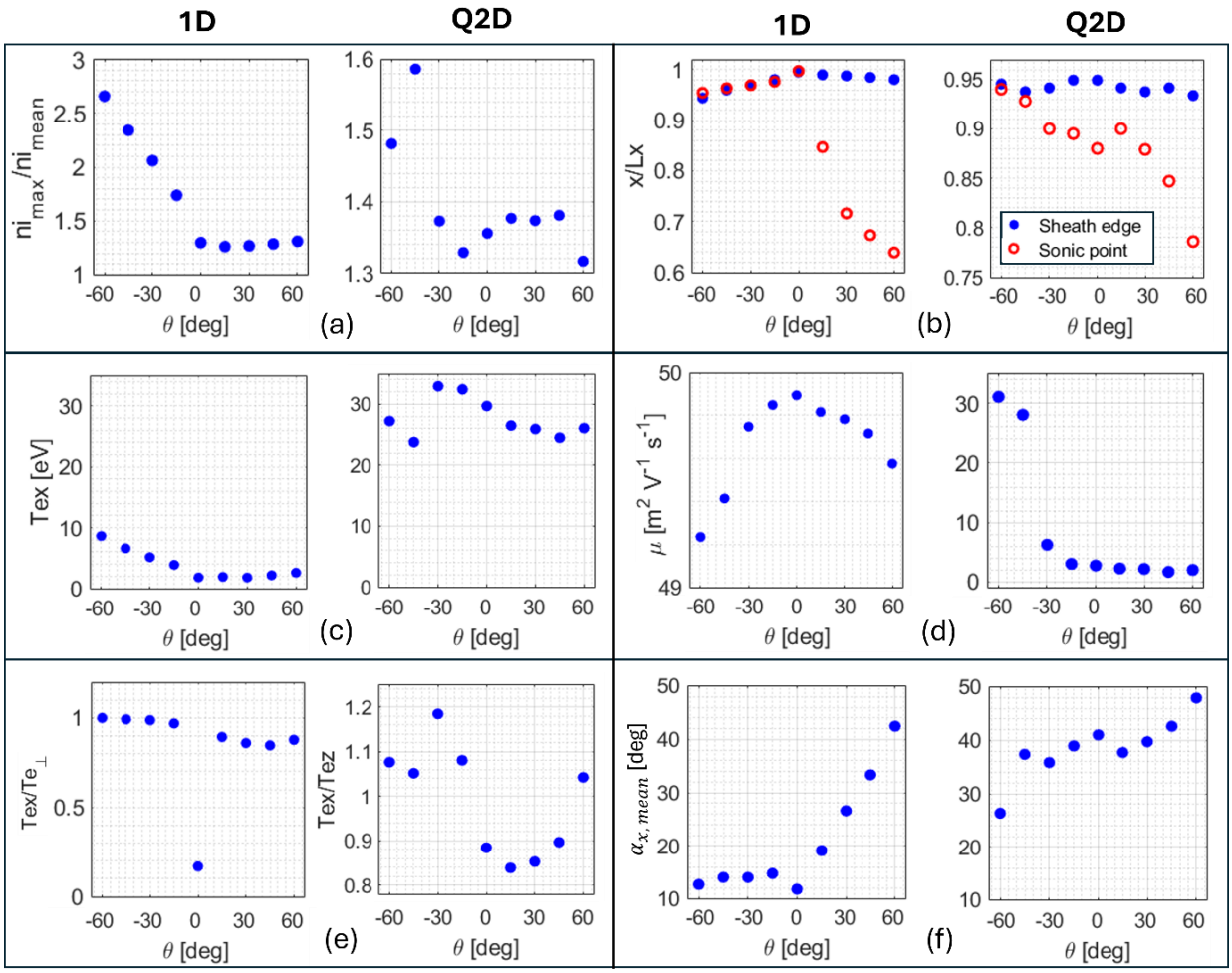


Fig. A.5.8: Comparison of spatiotemporally averaged (across entire domain and over $20-30\ \mu s$) plasma properties vs θ for xenon propellants from 1D radial and Q2D radial-azimuthal simulations; (a) normalized ion number density ($n_i/n_{i,mean}$), (b) normalized radial location (x/L_x) of the sheath edge and ion sonic point, (c) radial electron temperature (T_{ex}), (d) electrons' axial mobility (μ), (e) electron temperature anisotropy (parallel-to-perpendicular electron temperature ratio in 1D ($T_{ex}/T_{e\perp}$) and radial-to-azimuthal electron temperature ratio in Q2D (T_{ex}/T_{ez})), and (f) ion beam divergence angle ($\alpha_{x,mean}$) due to the radial velocity component calculated per Eq. 4.2.

Now, focusing on the electron temperature anisotropy from the 1D simulations in **Fig. A.5.8** (e), we notice that, introducing any level of B-field curvature significantly enhances the temperature isotropy in the system, which is in line with the observed behavior in Ref. [132]. In fact, for a purely radial B-field ($\theta = 0$), $T_{ex}/Te_{\perp} \approx 0.2$. However, this ratio shifts to around 1 in the presence of the negative field curvature and stays almost constant across $\theta = -60$ to -15 degrees. For the positive curvatures, the $T_{ex}/Te_{\perp}$ ratio is slightly lower but still significantly higher compared to the scenario of purely radial B-field. These trends are different from the temperature anisotropy behavior observed in the Q2D simulations, where even in the absence of field curvature the anisotropy level is not that high.

Another interesting discrepancy between the 1D and the Q2D simulations relates to the radial location of the ion sonic point which is presented in **Fig. A.5.8** (b). The time-averaged radial distribution of the ion Mach number (M_i) from the Q2D and the 1D simulations are also provided in **Fig. A.5.9** (b).

Interestingly, in the Q2D simulations, as θ increases from -60 to 60 degrees, the ion sonic point continuously progresses toward the bulk plasma away from the walls. Contrary to the Q2D results, in the 1D setting, the location of the sonic point slowly gets closer to the walls when θ varies from -60 degrees to 0, whereas it moves rapidly away from the walls as θ increases for the positive curvatures. Note that the y-axis scales in **Fig. A.5.8** (b) are different between the 1D and the Q2D plots.

Our observation from the 1D simulations is consistent with the variation of the location of the ion sonic point with the field's curvature, reported in Ref. [132]. The general behavior of the sonic point is, however, only in line with the Q2D simulations' results for the positive B-field curvatures. Even in this case, though, the sensitivity of the position of the ion sonic point to the curvature of the magnetic field is more significant in a 1D setting.

The occurrence of the sonic condition for ions within the plasma bulk, where the quasi-neutrality holds, renders the Bohm's criterion inadequate in establishing the boundary (edge) of the sheath. Thus, as also suggested in Ref. [132], in these situations, the non-quasineutrality serves instead as the appropriate criterion to determine the sheath's edge. According to this criterion [132], the sheath's boundary is defined to coincide with the location where the non-quasineutrality exceeds a certain threshold, typically beyond 5% of the bulk ion density, i.e.,

$$\frac{|n_i - n_e|}{n_i} \approx 0.05\,. \qquad \text{Eq. A.22}$$

Fig. A.5.8 (b) additionally compares the location of the sheath' edge as described by the non-quasineutrality condition (Eq.A.23) in the vicinity of the right-hand side wall of the domain in comparison to the position of the ion sonic point in the 1D and Q2D simulations. According to these plots, in the 1D simulations and across the negative curvatures, the Bohm's criterion agrees with the non-quasineutrality condition in determining the location of the sheath's edge. However, in the cases of positive curvature, there is a notable disparity between the two criteria in the 1D cases. In the Q2D setting, apart from the positive-curvature cases, the disagreement of the two criteria extends to the negative curvatures as well including the cases with $\theta = -15$ and -30 degrees.

The discrepancy between the criteria for the sheath's edge from the Q2D simulations indeed bears a more significant implication for the negative curvatures. This is because, in a typical Hall thruster design, the magnetic field features negative curvatures within the discharge channel where the formation of a plasma sheath near the walls actually becomes relevant. Hence, the observation that the 1D simulations falsely show a consistency between the sheath's edge criteria for the negative field curvatures points to an important shortcoming of the 1D simulations.

Finally, the divergence of the ion beam due to the radial component of the ions' velocities are represented in **Fig. A.5.8** (f), **Fig. A.5.9** (e) and **Fig. A.5.9** (f). From **Fig. A.5.9** (e), it is observed that in the Q2D simulations across all curvature cases, the Γ_x demonstrates a spread over a broader range of angles compared to the 1D simulations. Moreover, in the 1D simulations, the ion beam's radial divergence angle ($\alpha_{x,avg}$) does not exhibit significant sensitivity to the degree of negative B-field curvature. On the contrary, the variation of the $\alpha_{x,avg}$ with positive curvature is exaggerated in the 1D

setting relative to the smaller degrees of change observed in in the Q2D simulations. Also, in the 1D setting, in general, the divergence angle remains low over a larger extent of the plasma bulk, contrary to the Q2D simulations. Thus, a 1D radial analysis can misleadingly point to a low divergence-angle ion beam or, equivalently, an artificially elevated beam divergence efficiency.

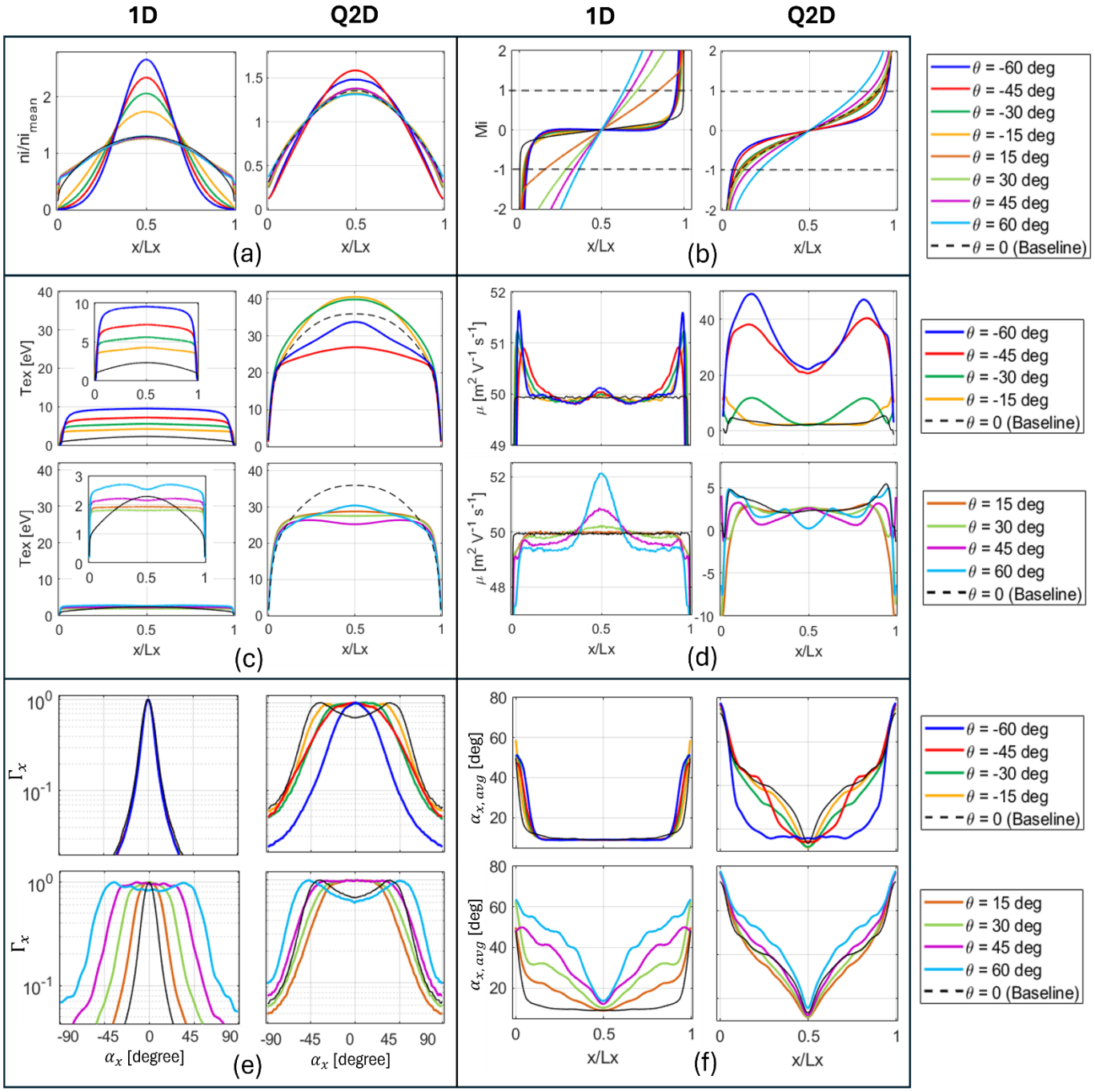


Fig. A.5.9: Comparison of radial profiles of plasma properties averaged over $20 - 30\ \mu s$ (and over all azimuthal locations for Q2D results) for xenon propellant with various θ from 1D radial and Q2D radial-azimuthal simulations; (a) normalized ion number density ($n_i/n_{i,mean}$), (b) ion Mach number (M_i), (c) radial electron temperature (T_{ex}), (d) electrons' axial mobility (μ), (e) ion divergence-angle distribution function due to the ions' radial velocity component (Γ_x), and (f) ion beam divergence angle ($\alpha_{x,avg}$) due to the ions' radial velocity component calculated per Eq. 4.2.

A.6 Supplementary analyses for parametric variability studies in axial-azimuthal coordinates

Fig. A.6.1 presents the numerical dispersion maps of the azimuthal instabilities in various operating conditions, at two axial positions, corresponding to the mid-location in the channel ($x = 0.375\ cm$) and midway in the near-plume ($x\ 0.625\ cm$). The theoretical nonlinear and linear dispersion relation of IAI (given by Eq. 1.4 and Eq. 1.6) are superimposed on these plots. These comparisons are provided for xenon propellant. It is seen that, overall, within the channel, the numerical dispersion of the instabilities is consistent with the IAI's *nonlinear* dispersion at this location, while in the plume, the instabilities align with the local *linear* dispersion relation of ion sound waves.

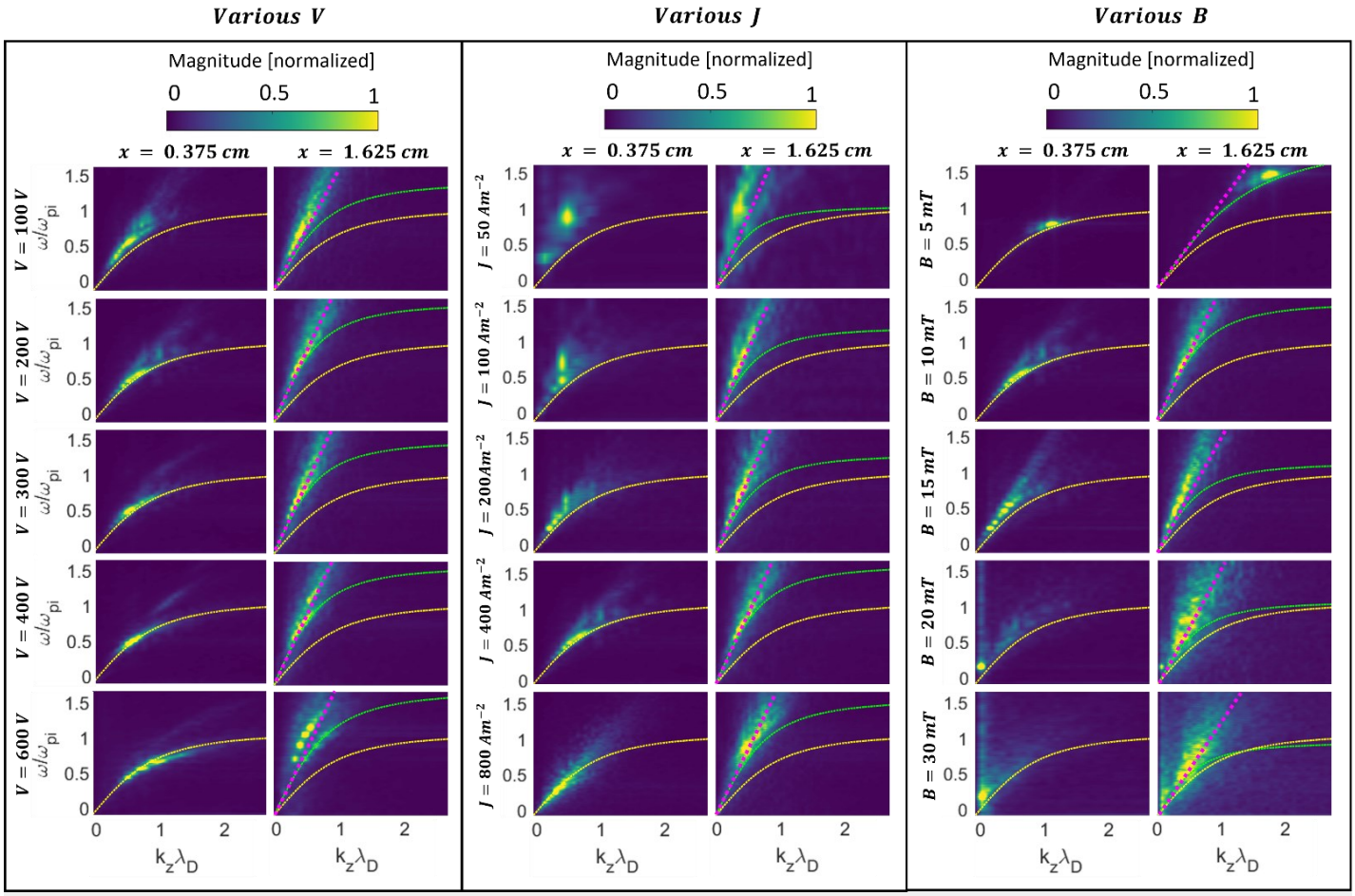


Fig. A.6.1: Numerical dispersion plots of azimuthal instabilities obtained from 2D FFT of the spatiotemporal signal of azimuthal electric field fluctuations at two axial locations (inside the channel at $x = 0.375$ and in the plume at $1.625\ cm$) for xenon with various V (left panel), various J (middle panel), and various B (right panel). Yellow curves are the local IAI's dispersion, and the green curves are the dispersion relation of the IAI at $x = 0.365\ cm$ obtained from Eq. 1.4, using the average local plasma properties at respective axial positions. The magenta lines represent the linear dispersion relation of the ion sound waves (Eq. 1.6).

Fig. A.6.2 and **Fig. A.6.3** show, respectively, the azimuthal wavenumber (k_z) and frequency (ω) spectra of the azimuthal instabilities at $x = 0.375\ cm$ and $x = 1.625\ cm$. The instabilities' k_z and ω spectra are derived from 1D spatial and the 1D temporal FFT of the azimuthal electric field fluctuation from the simulations with various propellants under various operating conditions. From these figures, we most notably observe that the case with the B intensity of $5\ mT$ exhibits a distinctly different spatial

and temporal FFT spectrum compared to the other cases. The k_z spectrum within the channel is dominated by two clear peaks across all the three propellants. These peaks have been smeared out in the k_z spectrum within the plume. The corresponding frequency spectra inside the channel also show three distinct peaks, with the peaks at the higher frequencies being the harmonics of the mode at the frequency of about $7.5\ MHz$.

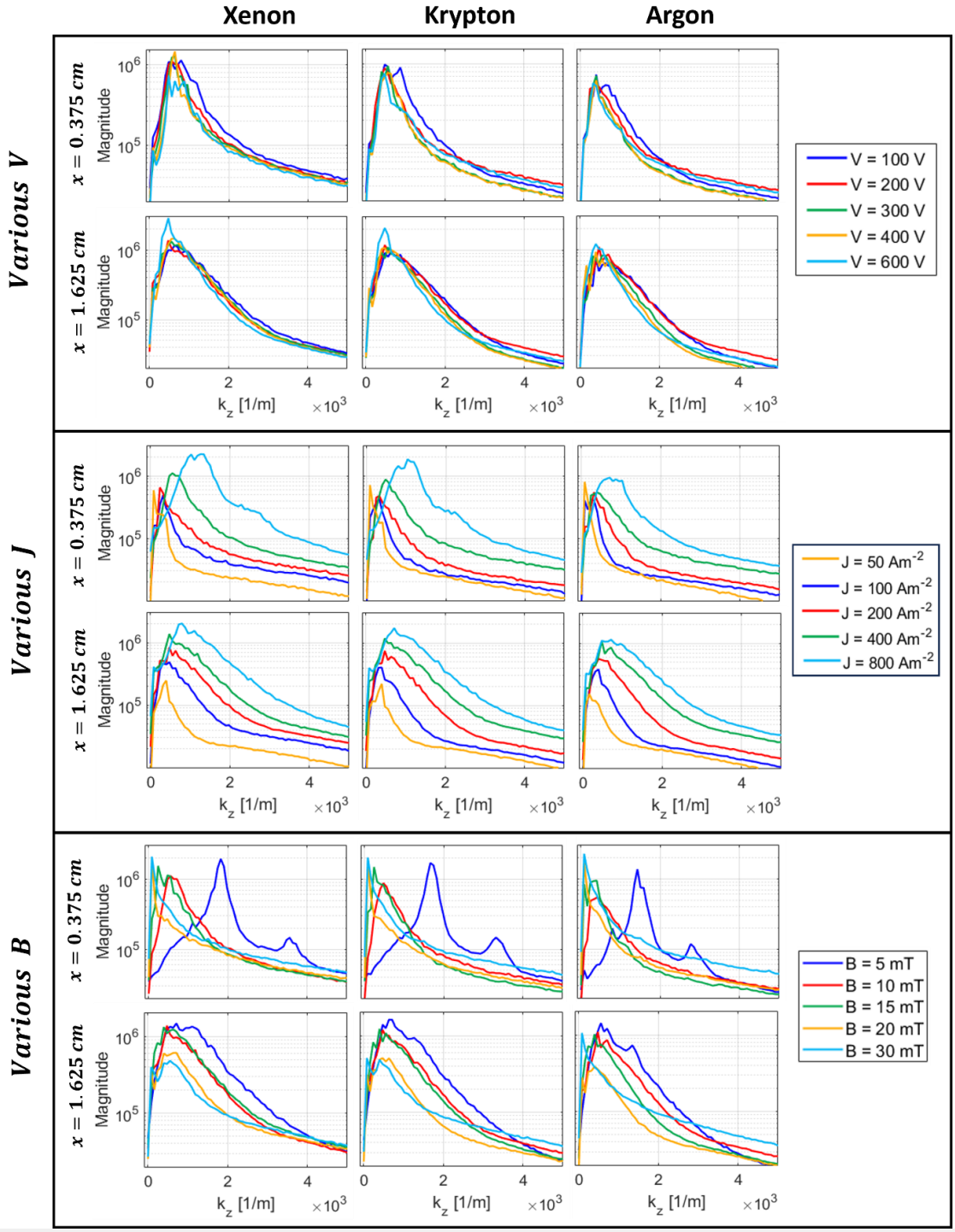


Fig. A.6.2: Azimuthal wavenumber spectra (k_z) of instabilities obtained from average (over $20 - 30\ \mu s$) spatial FFTs of the azimuthal electric field signal at two axial locations (inside the channel at $x = 0.375$ and in the plume at $1.625\ cm$) in simulations with various V (top panel), various J (middle panel), and various B (bottom panel) for the three propellants.

Furthermore, we notice that at 20 and $30\ mT$, inside the channel, the amplitude floors of the k_z and ω spectra are much higher compared to the lower B intensity cases, for which the spectra are seen to rapidly fall off in magnitude toward high frequencies and wavenumbers. The elevated magnitudes of the tail of the spectra for the $20\ mT$ and the $30\ mT$ cases point to a turbulent state of the plasma.

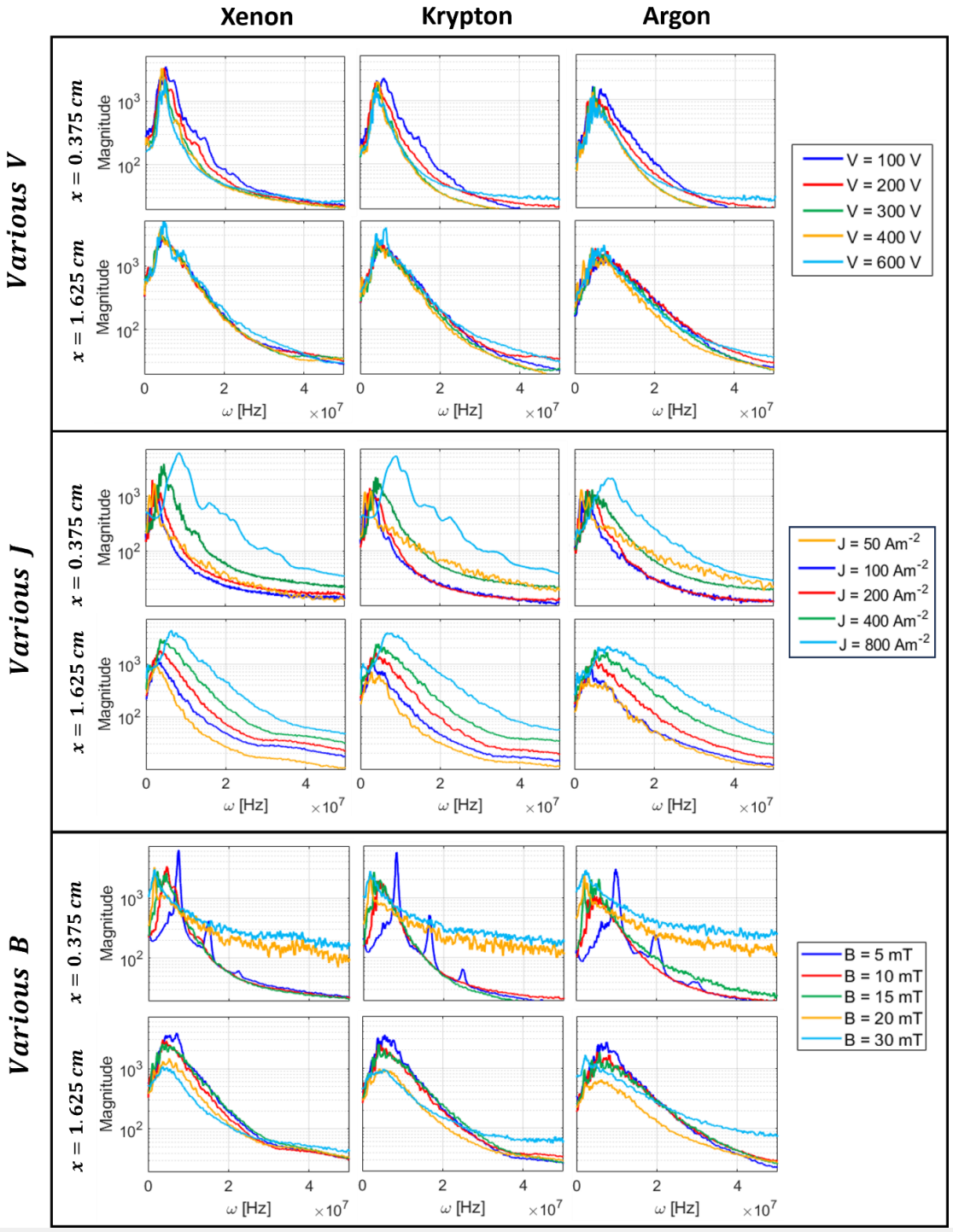


Fig. A.6.3: Frequency spectra of instabilities obtained from average (over all azimuthal locations) temporal FFTs of the azimuthal electric field signal at two axial locations (inside the channel at $x = 0.375$ and in the plume at $1.625\ cm$) in simulations with various V (top panel), various J (middle panel), and various B (bottom panel) for the three propellants.

A.7 Simulation of radial-azimuthal channel cross-sections of high-power 20 kW-class industrial Hall thruster

Here we present the Q2D simulation results of the radial-azimuthal cross sections at three different axial locations of the HT20k's thruster domain. The purpose of these simulations is to evaluate the effects that were not accounted for in the axial-azimuthal simulations discussed in Chapter 6 due to not resolving the radial direction. These include the impact that the radial magnetic field gradient and curvature in a magnetically shielded Hall thruster has on the radial distribution of the plasma properties and the underlying processes such as instabilities and the electrons' transport.

A.7.1. Simulations' setup and conditions

The Q2D radial-azimuthal simulations are carried out using a multi-region decomposition of the simulation domain, which is represented by a Cartesian $y-z$ plane. The y-axis is along the radial coordinate and the z-axis is along the azimuth. We have simulated radial-azimuthal cross-sections of the HT20k at three different axial (x) locations. These three sections and the distribution of the magnetic field along the radius in each section are illustrated in **Fig. A.7.1**. From the field topology plot shown in **Fig. A.7.1** (a), it is seen that Section 1 corresponds to the beginning of the chamfered region of the discharge channel upstream the exit plane, Section 2 is inside the channel at a location where the magnetic field lines are almost axial adjacent to the walls, and Section 3 is located at a position within the channel where the magnetic flux is nearly zero in the center of the domain.

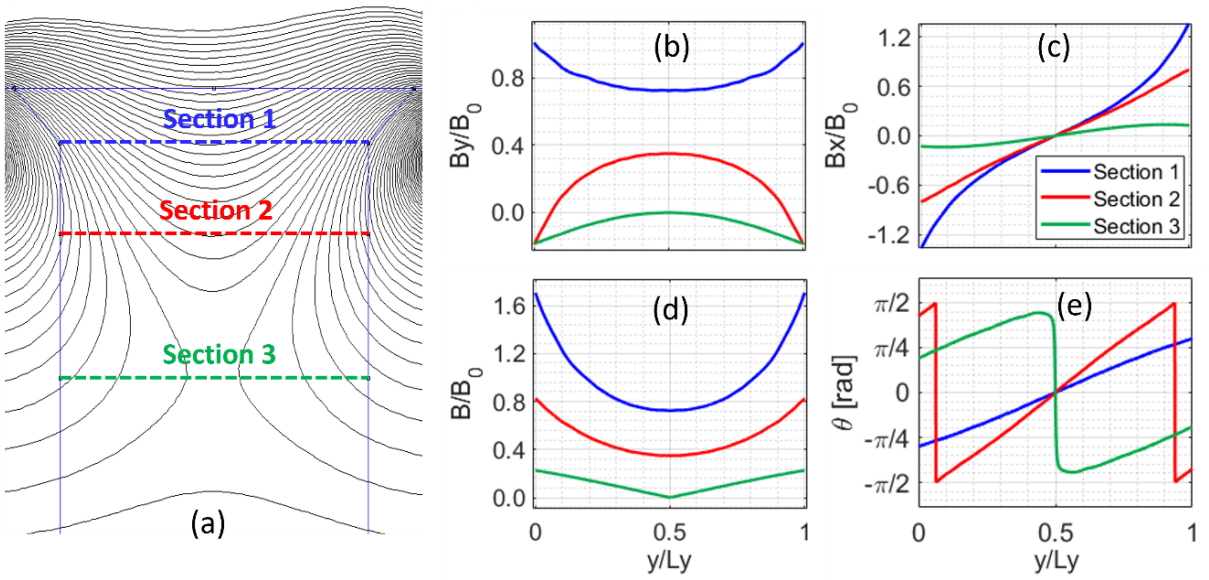


Fig. A.7.1: (a) A schematic of the adopted field topology and the three simulated cross-sections. (b) to (e) Radial profiles of the magnetic field properties at the three studied Sections; (b) normalized radial component (B_y), (c) normalized axial component (B_x), (d) normalized field intensity (B), and (e) angle between the tangent to the magnetic field lines and the x-axis. The normalization factor, B_0, is the peak magnetic field intensity for Case II of the axial-azimuthal simulations.

The operating condition of the HT20k, for which the radial-azimuthal simulations are performed, corresponds to that of Case II of the axial-azimuthal simulations in Chapter 6. Accordingly, the initial bulk plasma properties at each simulated cross-section are taken from the time-averaged axial distribution of the properties obtained from the axial-azimuthal simulation of Case II (**Fig. 6.6**) at the respective axial location. These values (physical parameters) along with the numerical parameters used in the simulations are provided in **Table A.7.1.**

Note that, referring to the **Fig. 6.5** and **Fig. 6.6**, Section 1 falls within the acceleration zone, Section 2 is inside the ionization zone, and Section 3 corresponds to the near-anode zone.

As a reference, we have additionally performed, for each cross-section, a Q2D simulation with a purely radial and uniform magnetic field distribution whose intensity is equal to the value of the field at the centerline of the channel (given in **Table A.7.1**) at the respective cross-section. This set of simulations with uniform radial B-field profile also enables us to distinguish the influence of the near-wall plasma sheath and its interactions with the bulk plasma processes.

The axial electric field in all simulations is assumed to be radially constant.

The neutrals are present in the radial-azimuthal simulations as a uniform background with the constant density values provided in **Table A.7.1** for each simulated Section. The MCC model is used to resolve the collisions between the electrons and the xenon atoms. The types of collision events considered, and the collision cross-sections used are the same as those mentioned in Section 6.2 in order to remain consistent with the setup of the axial-azimuthal simulations. An electron undergoing any collision event is isotopically scattered. In the event of an inelastic collision, the particle will experience an energy loss. In the event of ionization collision, only the associated energy loss and scattering are considered for the incident electron and no new plasma particles are created.

The Secondary Electron Emission from the channel walls is neglected so as to isolate the effect of the radial magnetic field gradient. We have followed the approach suggested in Ref. [95] to partially compensate for the radial flux of particles lost to the walls. Accordingly, we inject electron-ion pairs randomly in the domain at each timestep. The number of pairs to inject is estimated as the minimum between the number of electrons and the number of ions reaching the wall at every timestep [95]. This is necessary because the simulations do not self-consistently resolve the axial inflows and outflows of the particles. It is noteworthy that the adopted approach only partially compensates for the particle wall loses, which implies that the plasma density gradually decreases over time. Accordingly, we limited the duration of the radial-azimuthal simulations to $7\ \mu s$ to maintain the radially averaged plasma densities, on average (over time), close to those at the axial-azimuthal simulations at each cross-section.

The simulation domain features a virtual axial length of $1\ cm$ in line with the common practices in the 1D and 2D PIC simulations that do not resolve the axial flux of the particles self-consistently [17][35]. Particles crossing the boundary along the x-direction (at $L_x = \pm 1\ cm$) from the simulation plane are resampled from their initial Maxwellian distribution and are re-introduced onto the simulation plane, maintaining their azimuthal and radial positions.

The simulations are initialized by loading the electrons and ions uniformly throughout the simulation domain at an initial number density of 5×10^{17} m^{-3} for Section 1, 1.3×10^{18} m^{-3} for Section 2, and 2.35×10^{18} m^{-3} for Section 3. These initial plasma densities are a factor of 1.2 higher than the plasma density obtained from the axial-azimuthal simulation of Case II at the location of each simulated Section, so that the average density of the plasma over the duration of the simulation for each cross-section remains close to the corresponding value from the axial-azimuthal simulation. The plasma species are sampled from a Maxwellian at the initial load temperatures reported in **Table A.7.1** for each Section.

The radial extent of the domain is twice its azimuthal length. The Q2D simulations are conducted using 50 regions along radial and 25 regions along the azimuthal direction, resulting in a 30-fold computational gain relative to a corresponding conventional full-2D PIC simulation.

	Value [unit]		
Parameter	**Section 1**	**Section 2**	**Section 3**
Physical Parameters			
Axial position of the simulated Section (x/L_x)	0.88	0.68	0.36
Initial plasma density (n_0)	6.5×10^{17} [m^{-3}]	1.3×10^{18} [m^{-3}]	2.35×10^{18} [m^{-3}]
Background neutral density ($n_{n,0}$)	3.5×10^{17} [m^{-3}]	7×10^{18} [m^{-3}]	1.3×10^{19} [m^{-3}]
Axial electric field (E_x)	1.8×10^{4} [Vm^{-1}]	1×10^{3} [Vm^{-1}]	1×10^{2} [Vm^{-1}]
Normalized magnetic field at the channel centerline (B/B_0)	0.73	0.34	≈ 0
Initial electron temperature ($T_{e,0}$)	20 [eV]	8 [eV]	5 [eV]
Initial ion temperature ($T_{i,0}$)	0.5 [eV]		
Neutral temperature (T_n)	650 [K]		
Computational Parameters			
Time step (Δt)	2×10^{-12} [s]		
Total simulation time (t_{sim})	7 [μs]		
Cell size ($\Delta x = \Delta z$)	20 [μm]		
Initial number of macroparticles per cell	100		
Number of regions along radial direction (M)	50		
Number of regions along azimuthal direction (N)	25		

Table A.7.1: Summary of physical and numerical parameters used in the Q2D radial-azimuthal simulations of HT20k.

A.7.2. Results and discussion

Fig. A.7.2 shows the time evolution of the spatially averaged ion number density (n_i) from simulations. Overall, the n_i decreases over time across all simulated Sections, albeit at varying rates influenced by the distribution and the intensity of the B-field. Section 3 resembles an electrostatic problem due to very low magnetic field intensities, where n_i decreases quite rapidly. In simulations with non-uniform B-field distribution show, the rate of decrease in n_i is reduced compared to the simulations with uniform purely radial B-fields. Indeed, the negative curvature of the B-field has a confining effect which lowers the flux of plasma particles toward the walls.

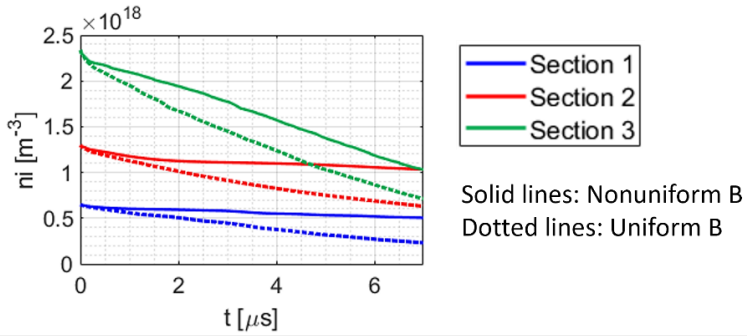


Fig. A.7.2: Time evolution of the ion number density (n_i) for the three studied Sections with non-uniform (solid curves) and uniform (dotted curves) B-field profiles.

The confinement of the plasma in the presence of non-uniform B-field can also be noticed from time-averaged ion density (n_i) profiles in **Fig. A.7.3** (a). We observe that at Sections 1 and 2 with non-uniform B-field profiles, the density is concentrated toward the center of the domain compared to their counterpart simulations with uniform B-fields. In particular, at Section 2, situated within the ionization region, the peak of the n_i profile is almost twice the average density ($\sim 10^{18} m^{-3}$) established within the axial-azimuthal simulation at the corresponding axial location in Case II (refer to **Fig. 6.6**). Furthermore, **Fig. A.7.3** (b) shows that the electron temperatures (T_e) in the radial-azimuthal simulations in all sections either with uniform or non-uniform B-field are higher compared to the average T_e in the axial-azimuthal simulations at the respective axial locations. The elevated temperature is mainly due to interaction with the spectrum of instabilities captured in radial-azimuthal simulation, which are not accounted for in axial-azimuthal simulations, particularly those involving radial wavenumber component.

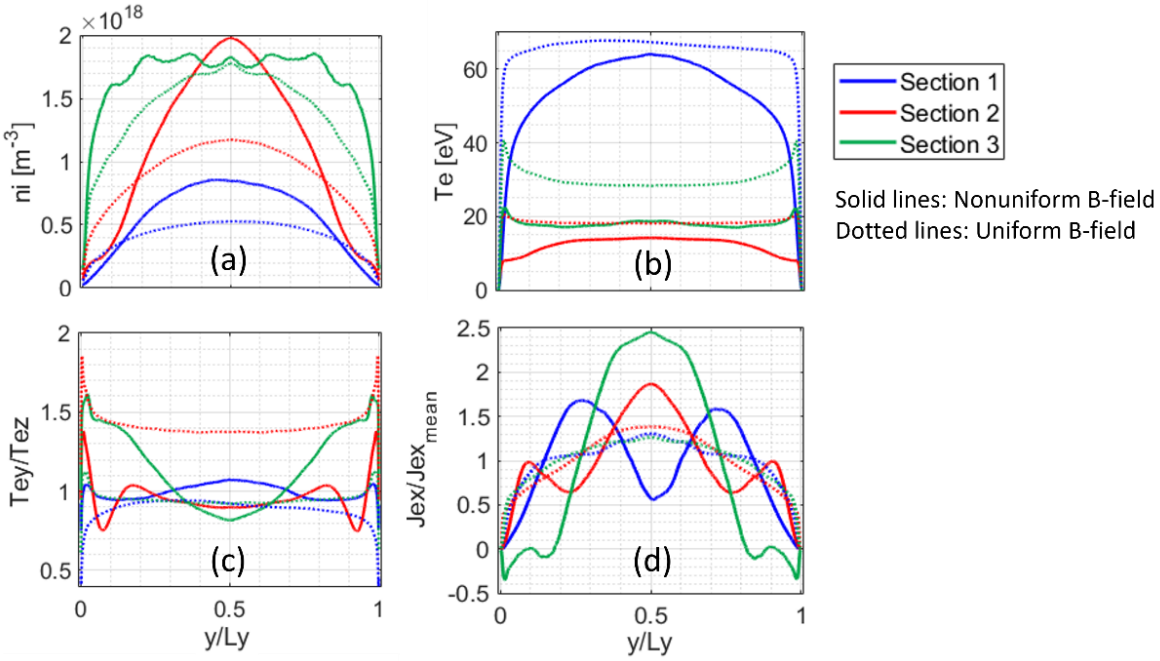


Fig. A.7.3: Time-averaged (over $0 - 7\ \mu s$) radial profiles of the plasma properties for the three simulated Sections; (a) ion number density (n_i), (b) electron temperature (T_e), (c) radial-to-azimuthal electron temperature ratio (T_{ey}/T_{ez}), and (d) normalized axial electron current density ($J_{ex}/J_{ex,mean}$). The solid curves correspond to the simulations with non-uniform B-field distribution and the dotted curves are from the simulations with uniform B-field profile.

In **Fig. A.7.3** (c), it is observed that the nonuniform distribution of the magnetic field has significantly decreased the temperature anisotropy (represented by T_{ey}/T_{ez} ratio) for Section 2.

The normalized electrons' axial current density ($J_{ex}/J_{ex,mean}$) in **Fig. A.7.3** (d) indicates different distribution among the simulated Sections in the presence of non-uniform B-field.

The time-averaged radial profiles of the electrons' axial (μ_x) and cross-field ($\mu_\perp$) mobilities are shown in **Fig. A.7.4**. μ_x and $\mu_\perp$ are obtained according to Eq. 4.6 – Eq. 4.9. Note that in cases with uniform B-field, the axial and cross-field electrons' mobility are equivalent, due to the purely radial B-field.

At Section 3 with non-uniform B-field, it is observed that the electrons funnel out of the simulation plane from the central part of the domain where the magnetic flux is almost zero. In the case of uniform radial B-field, the electrons move along the axial electric field almost freely throughout the domain, resulting in a high and nearly uniform axial electrons' mobility.

The radially-averaged values of electrons' axial mobilities in Section 2 and 3 increase, respectively, from 16 and $190\ m^2V^{-1}s^{-1}$ in case of uniform B-fields to 40 and $270\ m^2V^{-1}s^{-1}$ in the presence of non-uniform B-fields.

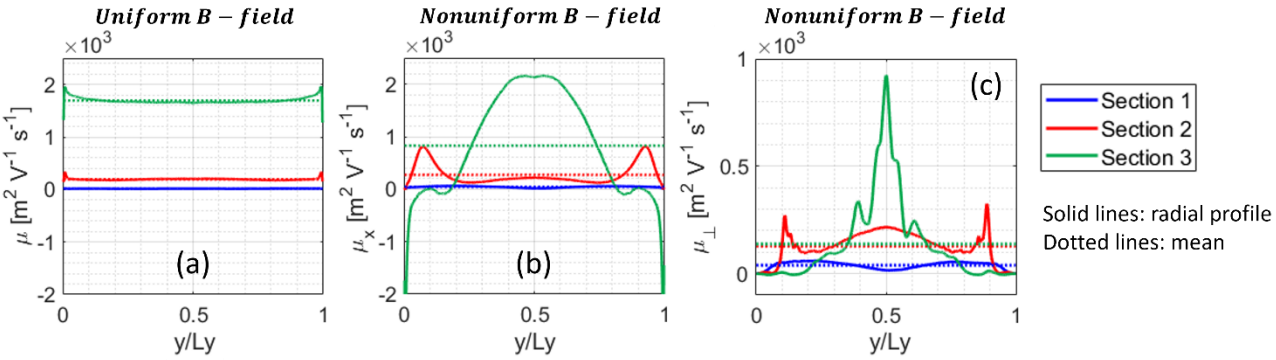


Fig. A.7.4: Time-averaged (over $0 - 7\ \mu s$) radial profiles of (a), (b) electrons' axial mobility with uniform and nonuniform B-field profiles, respectively, and (c) cross-field electrons' mobility for the three simulated Sections with nonuniform B-field distribution for the three simulated Sections. The dotted curves represent the radially-averaged (mean) value of the respective profiles.

The main purpose of the magnetic shielding topology is to mitigate the power deposition mainly from the ions on the channel walls, particularly around the exit plane, so as to lower the erosion rate of the ceramic channel and, hence, to extend the thruster's lifetime [52]. Accordingly, we present, in **Table A.7.2**, the spatiotemporally averaged electron (P_e) and ion (P_i) power deposition on the channel walls for various simulated Sections. Comparing the values from the simulations with non-uniform and uniform radial B profiles, we notice that the radial gradient of the magnetic field associated with the shielding topology has indeed reduced the ion power deposition at Sections 1 and 2 by a factor of about 4 and 8, respectively. Moreover, P_i at Section 3 is lowered by a factor of 1.5. Similarly, referring to **Table A.7.2**, the P_e values are also lowered as a result of the magnetic shielding topology (by a factor of 2 and 8 at Sections 1 and 2, respectively).

	Uniform B-field		Non-uniform B-field	
Section	$P_i\ [W]$	$P_e\ [W]$	$P_i\ [W]$	$P_e\ [W]$
Section 1	67	7	16	3
Section 2	62	12	7.5	1.5
Section 3	455	117	302	101

Table A.7.2: Average (across internal and external wall's extents and over time of $0-7\ \mu s$) ion (P_i) and electron (P_e) power deposition on the walls for the three simulated Sections with non-uniform and uniform B-field distributions.

To assess the characteristics of the azimuthal instabilities we look at the azimuthal wavenumber (k_z) and frequency (ω) spectra of the instabilities shown in **Fig. A.7.5**. We observe that, at Section 1, the dominant frequency and wavenumber content of the azimuthal electric field fluctuations changes in the presence of the radial magnetic field gradient. Indeed, in the case of uniform B-field profile the dominant frequency content includes a distinct mode with $1.2\ MHz$ and wavelength of about $18\ mm$ corresponding to MTSI, in addition to a broad spectrum of ECDI-like modes with frequency range of $4-10\ MHz$ and wavelength of $1-2\ mm$. Whereas in the case of non-uniform radial B profile, the dominant waves are concentrated around the frequencies of $1-1.5\ MHz$ and wavelength of $9\ mm$ representing the MTSI's waves. However, for Sections 2 and 3, it is seen that the radial magnetic field gradient does not significantly change the frequency and azimuthal wavenumber contents of instabilities.

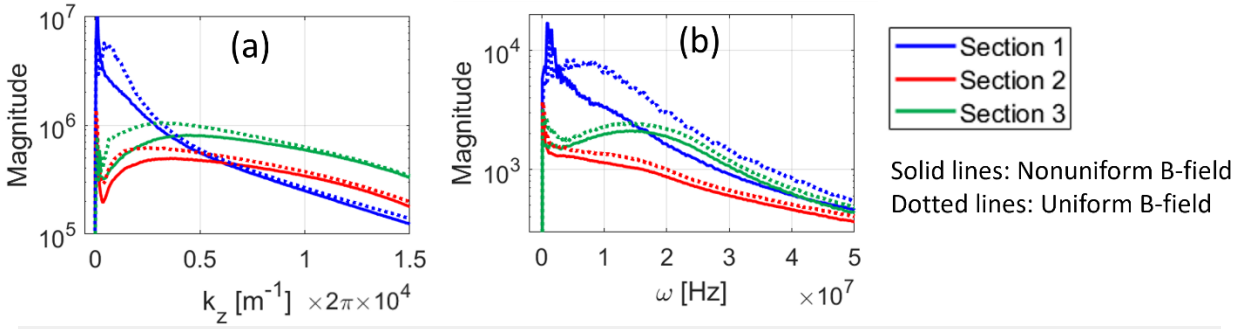


Fig. A.7.5: (a) temporal, and (b) spatial FFT plots of the azimuthal electric field signal, averaged over all radial positions, for the three simulated Sections. The spatial FFTs are also averaged over $7\ \mu s$ of the simulations' time. The solid curves correspond to the simulations with non-uniform B-field distribution and the dotted curves are from the simulations with uniform B-field profile.

The dynamics of the azimuthal waves at Section 1 in the presence and absence of the radial B-field gradient is shown in **Fig. A.7.6** in terms of 2D snapshots of the electrons' axial current density (J_{ex}) at six different time instances through the one cycle of the discharge evolution. Also, **Fig. A.7.7** compares the 2D snapshots of various plasma properties from the simulations with non-uniform and uniform radial B-fields at a time corresponding to the beginning of the evolution cycles in **Fig. A.7.6**, i.e., the upper left-most subplots in each panel.

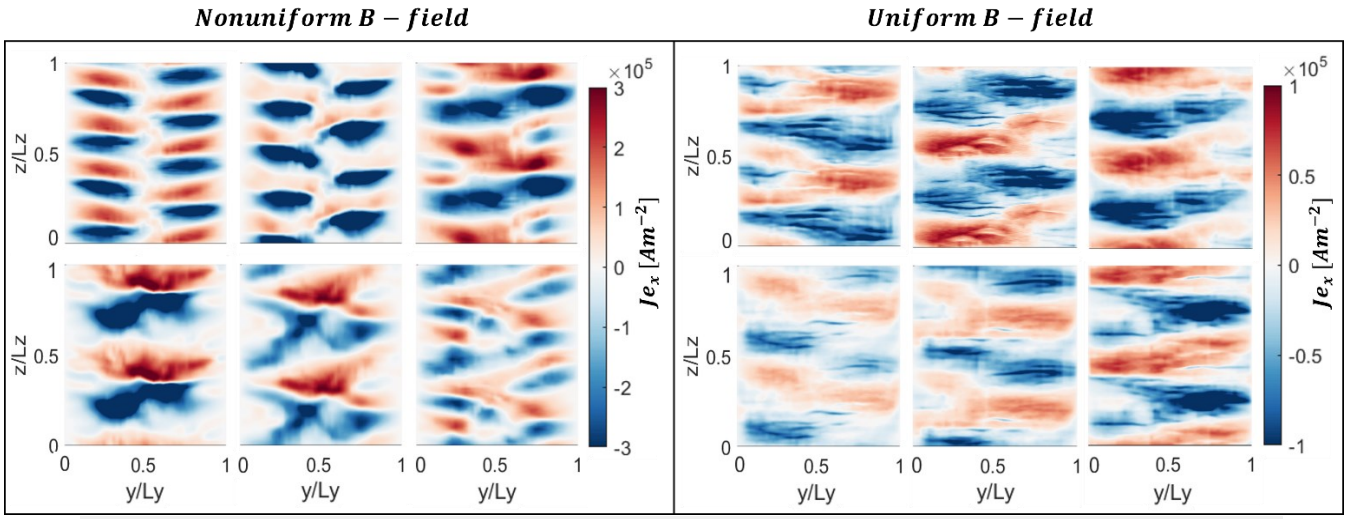


Fig. A.7.6: 2D snapshots of the axial electron current density (J_{ey}) at six different moments through the discharge evolution at Section 1 with non-uniform (left panel), and uniform (right panel) B-field. The time advances from left to right at each row.

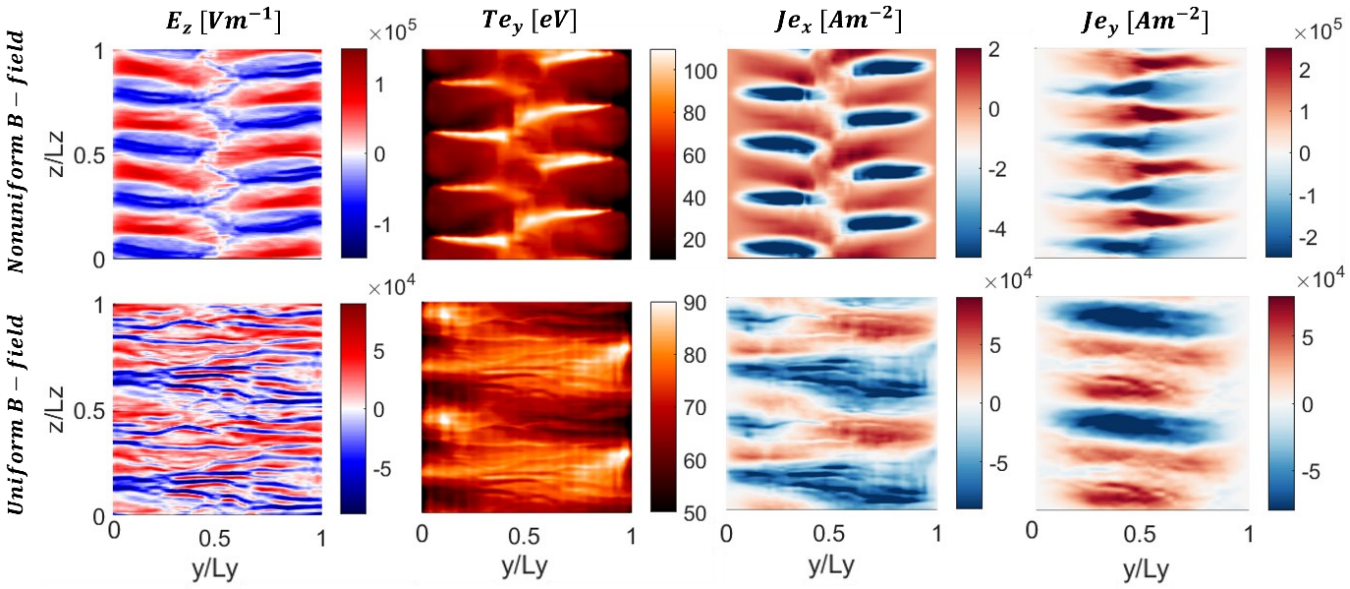


Fig. A.7.7: 2D snapshots of the plasma properties at Section 1 with non-uniform (top row), and uniform (bottom row) B-field profile. The columns, from left to right, represent the azimuthal electric field (E_z), radial electron temperature (T_{ey}), and the axial and radial electron current densities (J_{ex} and J_{ey}).